

Physicochemical Problems of Mineral Processing

Index No. 32213X



ISSN 1643-1049

Volume 50, Issue 1

January 1, 2014

Physicochemical Problems of Mineral Processing

Volume 50, Issue 1, January 1, 2014

www.minproc.pwr.wroc.pl/journal
www.dbc.wroc.pl/dlibra/publication/11251

Faculty of Geoengineering, Mining and Geology
Wroclaw University of Technology

Wydział Geoinżynierii, Górnictwa i Geologii
Politechniki Wrocławskiej
Wrocław 2014

Editor-in-Chief
Jan Drzymala

Editors
Christian Jungnickel, Przemyslaw B. Kowalczyk,
Pawel Nowak, Orhan Ozdemir

Editorial advisory board
Ashraf Amer, Alicja Bakalarz, Marian Brozek, Stanisław Chibowski, Tomasz Chmielewski,
Andrzej Heim, Jan Hupka, Teofil Jesionowski, Janusz Laskowski, Andrzej Luszczykiewicz,
Kazimierz Malysa, Andrzej Pomianowski, Pradip, Fereshteh Rashchi, Zygmunt Sadowski,
Oktay Sahbaz, Stanisława Sanak-Rydlewska, Barbara Tora, Adriana Zaleska

Production Editor
Marek J. Battek

The papers published in the Physicochemical Problems of Mineral Processing journal are abstracted in BazTech, Chemical Abstracts, Coal Abstracts, EBSCO, Google Scholar, Scopus, Thomson Reuters (Science Citation Index Expanded, Materials Science Citation Index, Journal Citation Reports) and other sources

This publication was supported in different forms by
Komitet Górnictwa PAN (Sekcja Wykorzystania Surowców Mineralnych)
Akademia Górniczo-Hutnicza w Krakowie
Politechnika Śląska w Gliwicach
Politechnika Wroclawska

© Copyright by Faculty of Geoengineering, Mining and Geology Wrocław University of Technology

ISSN 1643-1049 (print)
previously 0137-1282
ISSN 2084-4735 (online)

Faculty of Geoengineering, Mining and Geology Wrocław University of Technology
Wybrzeze Wyspianskiego 27, 50-370 Wrocław, Poland

CONTENTS

N. J. Coleman, Q. Li, A. Raza, <i>Synthesis, structure and performance of calcium silicate ion exchangers from recycled container glass</i>	5
J.S. Laskowski, S. Castro, O. Ramos, <i>Effect of seawater main components on frothability in the flotation of Cu-Mo sulfide ore</i>	17
T. Guler, K. Sahbudak, U. Akdemir, S. Cetinkaya, <i>Impact of ovalbumin on pyrite flotation in the absence and presence of metal ions</i>	31
S. Kursunoglu, M. Kaya, <i>Dissolution and precipitation of zinc and manganese obtained from battery powder</i>	41
D. Kondej, T.R. Sosnowski, <i>Physicochemical mechanisms of mineral nanoparticles effects on pulmonary gas/liquid interface studied in model systems</i>	57
B. Rewerski, D. Ruskowski, E. Chajduk, A. Sklodowska, <i>Environmental aspects of post mining uranium wastes deposited in Radoniow, Poland</i>	71
H. Wang, S. Lu, <i>Modifying effect of electron beam irradiation on magnetic property of iron-bearing minerals</i>	79
R. Matlakowska, A. Wlodarczyk, B. Slominska, A. Sklodowska, <i>Extracellular elements-mobilizing compounds produced by consortium of indigenous bacteria isolated from Kupferschiefer black shale – implication for metals biorecovery from neutral and alkaline polymetallic ores</i>	87
W. Pocwiardowski, P. Wodzinski, J. Kaniewska, <i>The concept of the scientific standpoint of the rolling-screw screen. Partial automation of the screening process</i>	97
A. Muszer, <i>Silicide spherules from Permian sediments of the Fore-sudetic monocline (SW Poland)</i>	107
F. Ciesielczyk, P. Bartczak, L. Klapiszewski, D. Pauksza, A. Piasecki, T. Jesionowski, <i>Influence of calcination parameters on properties of co-precipitated magnesium silicate</i>	119
E. Radzimska-Lenarcik, M. Ulewicz, <i>The use of 1-alkylimidazoles for selective separation of zinc ions in the transport process across a polymeric inclusion membrane</i>	131
J. Zawala, E. Malysa, M. Krzan, K. Malysa, <i>Monitoring of contamination of coal processing plants and environmental waters using bubble velocity measurements – advantages and limitations</i>	143
A. Lutynski, M. Lutynski, <i>Assessment of coal slurry deposits energetic potential and possible utilization paths</i>	159
H. K. Basaran, T. Tasmemir, <i>Determination of flocculation characteristics of natural stone powder suspensions in the presence of different polymers</i>	169
D. Jamroz, T. Niedoba, <i>Application of the Observational Tunnels Method to select a set of features sufficient to identify a type of coal</i>	185
N.E. Altun, T. Weatherwax, B. Klein, <i>Upgrading valuable mineralization and rejecting magnesium silicates by pre-concentration of mafic ores</i>	203
M. Kotyczka-Morańska, G. Tomaszewicz, <i>Application of modified calcium sorbents in carbonate looping</i>	217
A. Kolodziejczak-Radzimska, M. Samuel, D. Pauksza, A. Piasecki, T. Jesionowski, <i>Synthesis of hydroxyapatite in the presence of anionic surfactant</i>	225

M. Kolodziejaska, C. Kozlowski, J. Kozlowska, M. Ulewicz, <i>Selective removal of Ag(I) and Cu(II) by plasticizer membranes with N-(diethylthiophosphoryl)-aza[18]crown-6 as a carrier</i>	237
A. Tasdemir, P.B. Kowalczyk, <i>Application of statistical process control for proper processing of the Fore-Sudetic Monocline copper ore</i>	249
K. Siwinska-Stefanska, D. Paukszta, A. Piasecki, T. Jesionowski, <i>Synthesis and physicochemical characteristics of titanium dioxide doped with selected metals</i>	265
B. Sayiner, N. Acarkan, <i>Effect of silver, nickel and copper cyanides on gold adsorption on activated carbon in cyanide leach solutions</i>	277
M. Lutynski, T. Suponik, <i>Hydrocarbons removal from underground coal gasification water by organic adsorbents</i>	289
X. Gui, Y. Wang, H. Zhang, S. Li, <i>Effect of two-stage stirred pulp-mixing on coal flotation</i>	299
L. Gofryd, G. Pietek, Z. Szolomicki, K. Becker, <i>Recovery of major components of spent zinc electrolyte with di(2-ethylhexyl)phosphoric acid (DEHPA) used as a zinc(II) extractant</i>	311
K. Ochromowicz, M. Jeziorek, K. Wejman, <i>Copper(II) extraction from ammonia leach solution</i> ..	327
T. Gawenda, D. Saramak, <i>Influence of selected work parameters of the rolling screen operation on screening effects</i>	337
R.O. Ajemba, O.D. Onukwuli, <i>Assessing influence of hydrochloric acid leaching on structural changes and bleaching performance of Nigerian clay from Udi</i>	349
T. Suponik, M. Blanco, <i>Removal of heavy metals from groundwater affected by acid mine drainage</i>	359
I. Cichowska-Kopczynska, M. Joskowska, R. Aranowski, <i>Wetting processes in supported ionic liquid membranes technology</i>	373
D.W. Pawlak, J.L. Parus, E. Skwarek, W. Janusz, <i>A study of selected properties of rhenium sulphide dispersion</i>	387
O. Gok, C.G. Anderson, G. Cicekli, E.I. Cocen, <i>Leaching kinetics of copper from chalcopyrite concentrate in nitrous-sulfuric acid</i>	399

Received March 16, 2013; reviewed; accepted May 8, 2013

SYNTHESIS, STRUCTURE AND PERFORMANCE OF CALCIUM SILICATE ION EXCHANGERS FROM RECYCLED CONTAINER GLASS

Nichola J. COLEMAN*, **Qiu LI****, **Atiya RAZA***

* School of Science, University of Greenwich, Chatham Maritime, Kent, ME4 4TB, UK;
nj_coleman@yahoo.co.uk

** School of Civil Engineering, University of Leeds, Leeds, LS2 9JT, UK.

Abstract: Numerous technical, economic and societal factors limit the recycling of waste soda-lime-silica glass back into the primary production process and accordingly alternative applications for this material are sought. This study demonstrates that waste soda-lime-silica container glass is a suitable feedstock material for the production of tobermorite, a calcium silicate cation exchanger. Tobermorites were synthesised at 100 °C from stoichiometric mixtures of container glass and lime under alkaline hydrothermal conditions. Increasing concentrations of sodium hydroxide (between 1.0 M and 4.0 M) in the reaction mixture promoted the formation and crystallisation of tobermorite, and also resulted in greater fragmentation of the silicate chains along the b-axis direction. The maximum removal capacities of these tobermorite specimens for Cd²⁺ (441 mg g⁻¹) and Zn²⁺ (122 mg g⁻¹) compared well with those of other waste-derived sorbents. Superior Cd²⁺- and Zn²⁺-uptake capacities and kinetics were observed for the least crystalline tobermorite specimen, indicating that stacking defects facilitate the transport and exchange of cations within the lattice.

Keywords: tobermorite, sorbent, hydrothermal synthesis, cullet, recycling, ion-exchange

Introduction

Discarded soda-lime-silica glass containers constitute a significant and increasing proportion of the urban waste stream in every developed nation (Pontikes et al., 2007). The reuse and recycling potential of waste container glass (cullet) back into the primary production process is limited by a range of political, societal and technical obstacles (Coleman, 2011). In response to this problem, a variety of research projects has been carried out to identify alternative applications for waste cullet as a secondary feedstock in the production of aggregates, concretes, ceramics, abrasives and water filtration media (Ayadi et al., 2011; Coleman, 2011; Korkosz et al., 2012; Matteucci et al., 2002; Park et al., 2002).

Tobermorites are a family of naturally occurring calcium silicate hydrate minerals which are also readily synthesised under hydrothermal conditions between 80 and 225 °C (Coleman, 2005; El-Hemaly et al., 1977; Nelson and Kalousek, 1977). Their structure comprises a double Ca-O sheet bound on both sides by anionic wollastonite-like silicate chains running along the *b*-axis, as indicated in Fig. 1. The interlayer region houses labile charge-balancing cations and water molecules. Members of this family are characterised in terms of the length of their *c*-axis, which is dependent on the number of water molecules *per* unit formula. There are three principal polytypes of this mineral, *viz.* 14, 11 and 9 Å tobermorite, whose names relate to the approximate *d*-spacings of their (0 0 2) Bragg reflections.

11 Å tobermorite ($\text{Ca}_2\text{Si}_6\text{O}_{16}(\text{OH})_2 \cdot 4\text{H}_2\text{O}$) is of particular interest as it is the primary binder in autoclaved cements and also functions as a basic catalyst for organic synthesis and as an adsorbent for carbon dioxide and aqueous heavy metal contaminants (Al-Wakeel et al., 2001; El-Hemaly et al., 1977; Komarneni et al., 1986; Lima et al., 2008; Reinik et al., 2011). 11 Å tobermorite specimens exhibit a range of thermal behaviour: those which convert to 9 Å tobermorite at ~ 300 °C by the loss of molecular water are referred to as ‘normal’ tobermorites; whereas those which do not are described as ‘anomalous’ (El-Hemaly et al., 1977).

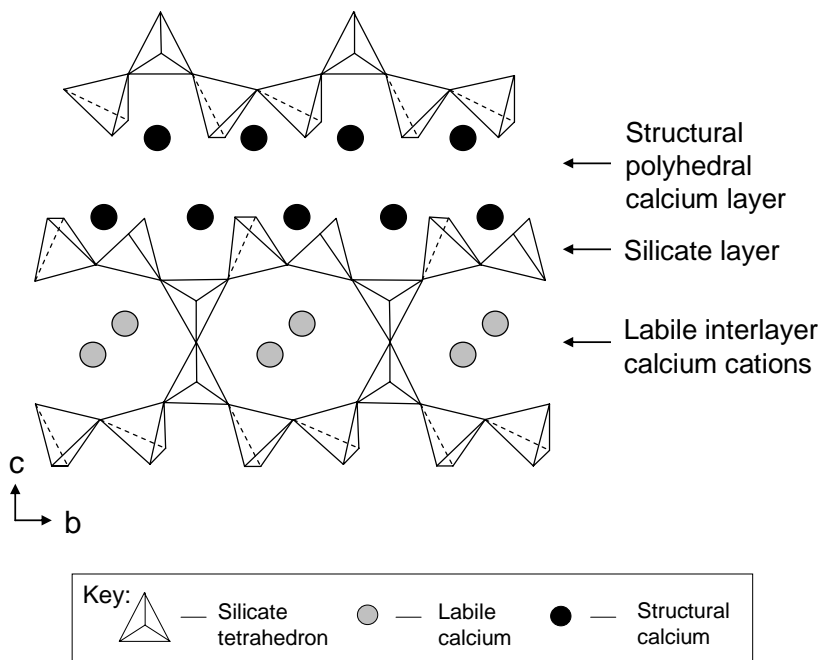


Fig. 1. Projection of 11 Å tobermorite in the *bc*-plane

The synthesis of 11 Å tobermorites reported in the literature has generally been carried out using analytical grade reagents such as sodium silicate and fumed silica; however, more recently, tobermorites have been prepared from industrial waste materials such as oil shale ash, cement kiln dust and paper recycling residue (Coleman, 2005; Coleman et al., 2009; Reinik et al. 2011). Recent research has also demonstrated that it is possible to prepare 11 Å tobermorite from waste container glass and that this material is an effective sorbent for divalent lead and cadmium ions (Coleman, 2011).

In the present study, waste soda-lime-silica container glass was used as the silicate feedstock for the hydrothermal synthesis of 11 Å tobermorites at 100 °C under conditions of varying alkalinity. The structures of the tobermorite products were analysed by powder X-ray diffraction (XRD) and solid-state ^{29}Si nuclear magnetic resonance spectroscopy (NMR). The relationship between structure and ion-exchange behaviour was explored *via* batch sorption of divalent cadmium and zinc ions.

Materials and methods

Materials, synthesis and characterisation

Flint soda-lime-silica glass (SLSG) containers were collected from the urban waste stream in Rochester, Kent, UK, and milled to pass 125 μm . An oxide analysis of the SLSG, obtained by X-ray fluorescence spectroscopy (XRF) at the Materials Research Institute, Sheffield Hallam University, Sheffield, UK, is given in Table 1.

Reaction mixture compositions and synthesis regimes are summarised in Table 2. All syntheses were carried out in triplicate by heating at 100 °C in hermetically sealed PTFE reaction vessels under autogenous pressure for 7 days. Samples Tob-1, Tob-2 and Tob-4 were prepared from mixtures of 3.5 g of SLSG and 1.5 g of CaO in 60 cm^3 of 1.0 M, 2.0 M and 4.0 M sodium hydroxide solution, respectively. The products of each synthesis were washed with deionised water to pH \sim 7 and dried to constant mass in air at 40 °C. Oxide analyses for each of the SLSG-derived tobermorite products are given in Table 1.

The reaction products were analysed by powder XRD using a Siemens Kristalloflex 810 X-ray diffractometer. To determine whether the tobermorite products exhibited normal or anomalous thermal behaviour, the samples were heated to 300 °C for 10 hours in air and re-analysed by powder XRD.

The silicate structures of the tobermorite products were analysed by solid state ^{29}Si NMR, as described elsewhere (Coleman and Brassington, 2003). The free induction decay profiles were processed by Delta software (provided by JEOL) to obtain spectra which were then analysed and deconvoluted using Igor Pro software.

Table 1. Composition of SLSG and tobermorite products

Oxide Component	SLSG (mass %)	Tob-1 (mass %)	Tob-2 (mass %)	Tob-4 (mass %)
SiO ₂	72.1	40.12	43.15	41.76
Na ₂ O	13.4	5.44	3.44	3.16
CaO	11.3	28.76	31.42	32.52
MgO	1.30	0.56	0.91	0.64
Al ₂ O ₃	1.14	0.68	0.91	0.76
K ₂ O	0.39	0.10	0.04	0.04
SO ₃	0.21	0.28	0.13	0.13
Fe ₂ O ₃	0.08	0.04	0.04	0.04
TiO ₂	0.05	Nil	Nil	Nil
Mn ₃ O ₄	0.03	Nil	Nil	Nil
Loss on ignition	Nil	23.76	19.84	20.72

Table 2. Reaction conditions and mixture compositions

Sample	Reaction conditions	Si : Ca : Al : Na molar ratios
Tob-1	100 °C, 168 h, 1.0 M NaOH _(aq)	1.00 : 0.80 : 0.02 : 1.79
Tob-2	100 °C, 168 h, 2.0 M NaOH _(aq)	1.00 : 0.80 : 0.02 : 3.21
Tob-4	100 °C, 168 h, 4.0 M NaOH _(aq)	1.00 : 0.80 : 0.02 : 6.07

Notation used to describe the silicate structure of the tobermorites is such that the symbol Q represents one SiO₄⁴⁻ tetrahedron and a superscript denotes the number of other Q units to which it is bonded. Substitution of Q units by tetrahedra other than SiO₄⁴⁻ is indicated in parentheses, for example, a mid-chain SiO₄⁴⁻ unit linked to one other SiO₄⁴⁻ unit and one AlO₄⁵⁻ unit would be represented as Q²(1Al).

The silicate chain configurations of the SLSG-derived tobermorite products were evaluated in terms of their ‘mean chain length’ (MCL). MCL is a measure of the average number of tetrahedra linked along the *b*-axis direction between breaks in the chain, and is given by (Richardson and Groves, 1997):

$$MCL = \frac{2 \left(Q^1 + Q^2 + Q^3 + \frac{3}{2} [Q^2(1Al) + Q^3(1Al)] \right)}{Q^1} \quad (1)$$

where, in this instance, Qⁿ symbols represent the relative intensities of the deconvoluted ²⁹Si resonances arising from the associated silicate tetrahedra.

The specific surface areas of the tobermorite products were determined according to ISO 9277:1995(E) by nitrogen gas sorption at 77.4 K using a Micromeritics Gemini VI analyser.

Batch sorption of Cd²⁺ and Zn²⁺

The uptake of Cd²⁺_(aq) and Zn²⁺_(aq) by Tob-1, Tob-2 and Tob-4 was determined by single metal batch sorption at 25 °C. In each case, 50 mg of tobermorite product were contacted with 200 cm³ of metal nitrate solution at an approximate metal concentration of 0.5 mM in screw-capped polypropylene bottles. Contact times for specimens were between 1 and 168 hours, after which, the supernatant liquors were recovered by centrifugation at 3000 rpm and analysed by atomic absorption spectrophotometry using a Pye Unicam SP 9 spectrophotometer. Each experiment was carried out in triplicate and the relative standard deviations of the mean metal-uptake data were lower than 5% in all cases.

Results and discussion

Characterisation of SLSG

The major oxide components of SLSG used in this study (listed in Table 1) are in the system SiO₂-Na₂O-CaO-MgO-Al₂O₃ in proportions which are typical of container cullet (Park et al., 2002). K₂O, SO₃, Fe₂O₃, TiO₂ and Mn₃O₄ are also present at concentrations below 0.5% by mass. The ²⁹Si NMR spectrum of SLSG (Fig. 2(a)) shows a broad asymmetric signal of maximum intensity at ~-95 ppm with a shoulder to high field which is consistent with a range of amorphous Q¹ to Q⁴ silicate units comprising a predominance of Q³ species. Powder X-ray diffraction analysis (not shown) also confirmed that SLSG is amorphous.\

Preparation and characterisation of SLSG-derived tobermorites

Powder XRD diffraction patterns of the SLSG-derived tobermorite products are shown in Fig. 3(a-c) and closely resemble those of phase-pure 11 Å tobermorites reported in the literature which have been prepared from reagent grade materials (Al-Wakeel et al., 2001; Mitsuda and Taylor, 1975). The comparatively broad and weak (0 0 2) basal reflection and poor resolution of the (2 2 0) and (2 2 2) reflections (at 2θ = 28.9° and 29.9°, respectively) in the XRD pattern of Tob-1 indicate that this specimen is less crystalline than its counterparts, Tob-2 and Tob-4, which were produced under conditions of increasing alkalinity (Fig. 3(a-c)). All SLSG-derived tobermorite products exhibited 'normal' thermal behaviour in that they dehydrated to form 9 Å tobermorite when heated to 300 °C (Fig. 3(d-f)). This finding is in agreement with those of other researchers who report that relatively low reaction temperatures (< 140 °C) and short processing times (< 14 days) generally give rise to normal tobermorite (El-Hemaly et al., 1977).

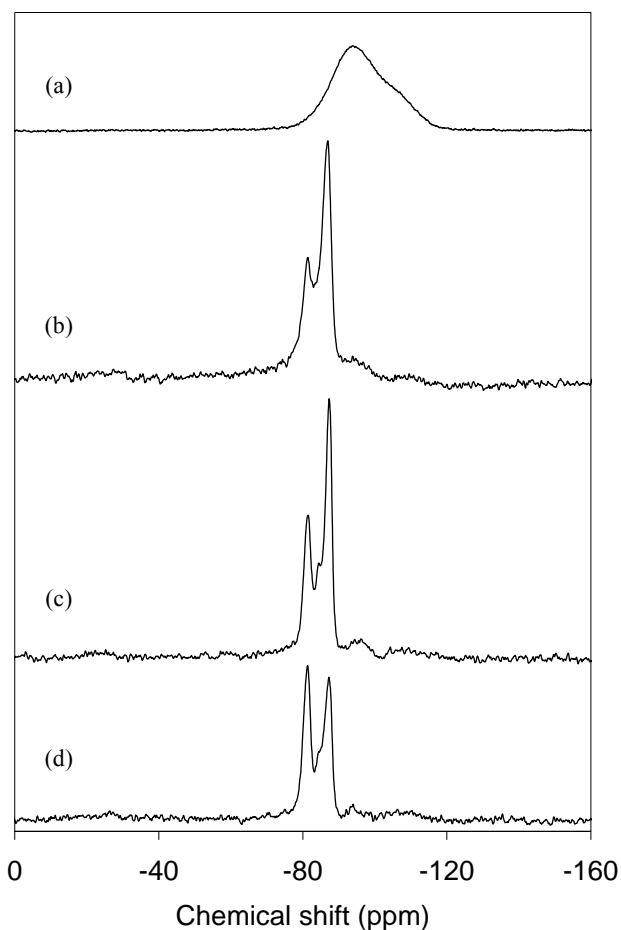


Fig. 2. ^{29}Si NMR spectra of (a) SLSG, (b) Tob-1, (c) Tob-2 and (d) Tob-4

The ^{29}Si NMR spectra of samples Tob-1, Tob-2 and Tob-4 (Fig. 2(b-d)) are consistent with the presence of crystalline phase-pure 11 Å tobermorites (Komarneni et al., 1985; Wieker et al., 1982). Terminal Q^1 silicate tetrahedra of the wollastonite-like chains and isolated silicate dimers are denoted by resonances at -81.6 ppm. Mid-chain Q^2 tetrahedra give rise to the resonances at -87.4 ppm and the low field shoulder at -85.2 ppm is assigned to $\text{Q}^2(1\text{Al})$ species. The low intensity signals at ~ 95 ppm arise from bridging Q^3 species and minor proportions of residual SLSG may also contribute to the signals in this region of the spectrum. The mean silicate chain lengths (MCL) of the SLSG-derived tobermorite products are listed in Table 3 and indicate that MCL decreases from 18.5 to 4.1 units as the sodium hydroxide concentration of the hydrothermal system is increased from 1.0 M to 4.0 M. Nitrogen gas sorption analysis demonstrated that the BET specific surface areas of the tobermorite products were also

influenced by the alkalinity of the reaction mixture (Table 3). These data, and those obtained by other researchers (Reinik et al., 2011), indicate that specific surface area tends to decrease as a function of increasing pH of the reaction mixture.

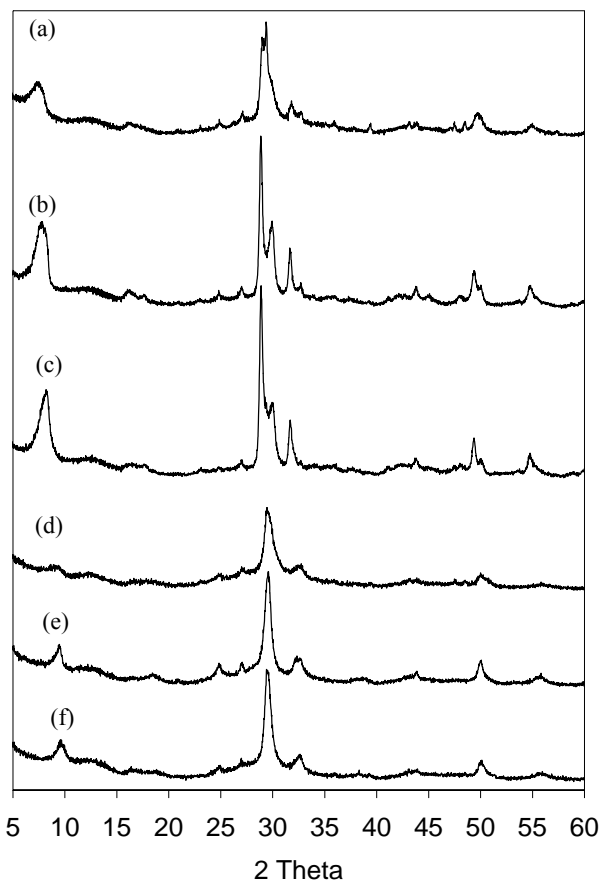


Fig. 3. Powder XRD patterns of SLSG-derived tobermorites (a) Tob-1, (b) Tob-2, (c) Tob-4; and tobermorite after heating at 300 °C (d) Tob-1, (e) Tob-2, (f) Tob-4

Table 3. Mean silicate chain length (MCL), BET specific surface area and metal ion uptake data for tobermorite products

Sample	MCL	Surface area (m^2g^{-1})	Cd^{2+} -uptake at 168 h		Zn^{2+} -uptake at 168 h	
			(mg g^{-1})	(mg m^{-2})	(mg g^{-1})	(mg m^{-2})
Tob-1	18.5	16.1 ± 0.2	441	27.4	122	7.58
Tob-2	5.7	27.1 ± 0.3	374	13.8	96	3.54
Tob-4	4.1	26.0 ± 0.4	325	12.5	78	3.00

This study has demonstrated that phase-pure 11 Å tobermorites can be synthesised from a stoichiometrically appropriate mixture of SLSG and calcium oxide *via* one-step hydrothermal processing at 100 °C under alkaline conditions. Unlike many industrial and municipal waste materials, SLSG does not require pre-treatment such as leaching or chemical conditioning prior to use. This research has also revealed that increasing concentrations of sodium hydroxide in this hydrothermal system increase the degree of crystallinity and surface area, yet reduce the average silicate chain length of the resulting product.

Mitsuda and Taylor observed that the development of tobermorite proceeds *via* the formation of a poorly structured calcium silicate hydrate gel phase (C-S-H) similar to that found in hydrating cement (Mitsuda and Taylor, 1975). This observation was subsequently confirmed in a real-time synchrotron study, which revealed that the first hydrothermal reaction product formed during tobermorite synthesis is a C-S-H gel with good periodicity in the *ab*-plane and poor organisation parallel to the *c*-axis (Shaw et al., 2000). Other studies have indicated that increasing alkalinity generally enhances the rate of tobermorite formation; whereas, increasing concentrations of Na⁺ ions are reported to stabilise the intermediate C-S-H gel phase and impede the development of the tobermorite product (Nocun-Wczelik, 1999; Shaw et al., 2000). SLSG-derived tobermorites confirm these observations, as increasing sodium hydroxide concentrations resulted in an enhanced reaction rate (i.e. superior crystallinity) at the expense of mean silicate chain length.

Batch sorption of Cd²⁺ and Zn²⁺ ions

The sorption profiles for the removal of Cd²⁺ and Zn²⁺ ions from single metal nitrate solutions by Tob-1, Tob-2 and Tob-4 under batch conditions are shown in Fig. 4. The uptakes of Cd²⁺ and Zn²⁺ after 168 hours as functions of mass and of BET surface area are also listed in Table 3. These data demonstrate that the rates and extents of sorption of both Cd²⁺ and Zn²⁺ ions by the SLSG-derived tobermorites are of the following order: Tob-1 > Tob-2 > Tob-4.

Despite a steadily increasing body of data, the mechanisms and extents of ion exchange reactions between heavy metal cations and 11 Å tobermorites remain disputed. For example, Komarneni et al. (1986 and 1988) report that essentially all of the Ca²⁺ ions within the tobermorite structure can be exchanged for Co²⁺ or Ni²⁺ ions; whereas, in a similar investigation, Shrivastava and Glasser (Shrivastava and Glasser, 1986) found that fewer than 20% of the total Ca²⁺ ion content was available for exchange by these heavy metal cations. It is clear that these and other such discrepancies arise from differences in structural features which have not been identified to date. Indeed, very little is presently known of the relationship between tobermorite structure and ion exchange behaviour.

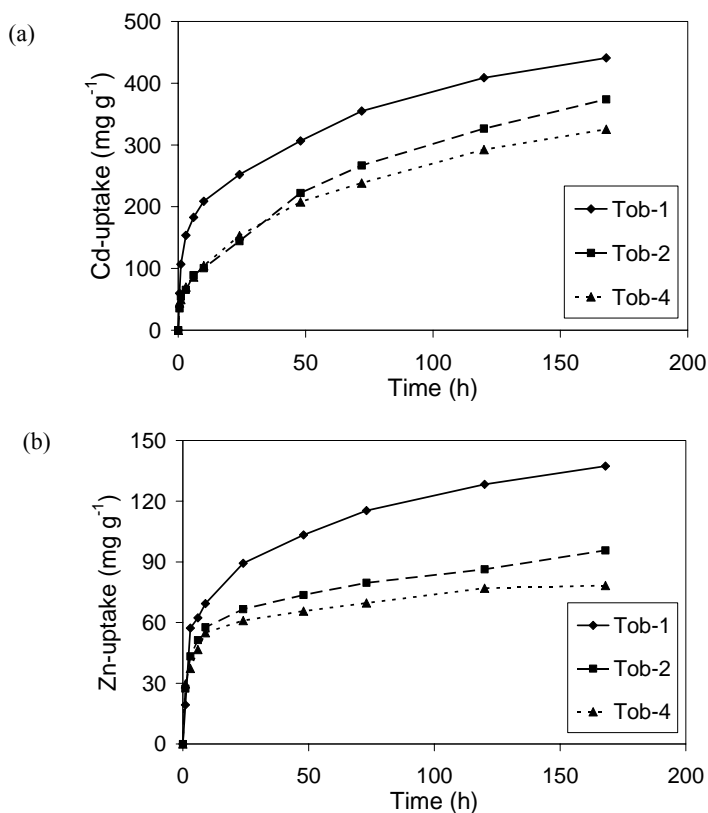


Fig. 4. The uptake of (a) Cd²⁺ ions and (b) Zn²⁺ ions by SLSG-derived tobermorites

The results obtained in this investigation indicate that low crystallinity, specifically arising from stacking disorders, assists the transport and ion-exchange of Cd²⁺ and Zn²⁺ ions within the tobermorite lattice. Conversely, these findings have also demonstrated that structural defects arising from breaks along the silicate chains do not facilitate these transport and ion-exchange processes.

Table 4. Cd²⁺ and Zn²⁺ sorption capacities for a range of waste-derived sorbents

Sorbent	Cd ²⁺ -uptake (mg g ⁻¹)	Zn ²⁺ -uptake (mg g ⁻¹)	Reference
Red mud	68	133	Vaclavikova et al. (2005)
Modified chestnut shell	10.14	9.26	Vázquez et al. (2012)
Bone char	53.6	33.0	Choy and McKay (2005)
Papaya wood	19.99	14.44	Saeed et al. (2005)
Rice husk	16.7	8.14	Krishnani et al. (2008)

For comparison, the maximum Cd^{2+} and Zn^{2+} sorption capacities for a range of waste-derived sorbents are listed in Table 4 (Choy and McKay, 2005; Krishnani et al., 2008; Saeed et al., 2005; Vaclavikova et al., 2005; Vazquez et al., 2012). It should be noted that the original data were reported in a variety of units which have been converted to mg g^{-1} for convenience. In general, the sorption capacity of SLSG-derived tobermorites for both metal cations compares favourably with those of other waste materials such as bone char, papaya wood, rice husk and modified chestnut shells; however, their performance was inferior to that of red mud with respect to the removal of Zn^{2+} ions. Further work is now in progress to more fully characterise the ion-exchange properties and potential for post-use regeneration of SLSG-derived tobermorite sorbents.

Conclusions

The findings of this study have demonstrated that waste soda-lime-silica container glass is a suitable feedstock material for the one-step hydrothermal synthesis of ion-exchangeable tobermorites. Unlike many industrial wastes, discarded container glass does not require leaching or chemical pre-treatment prior to use in this application.

All tobermorites synthesised at 100 °C from stoichiometric mixtures of waste glass, lime and sodium hydroxide solution were structurally similar to those prepared from analytical grade reagents and exhibited normal thermal behaviour. Increasing concentrations of sodium hydroxide (between 1.0 M and 4.0 M) in the reaction mixture promoted the formation and crystallisation of tobermorite, although also resulted in greater fragmentation of the silicate chains along the b-axis direction. Superior Cd^{2+} and Zn^{2+} ion-exchange capacities and kinetics were observed for the least crystalline tobermorite specimen, indicating that stacking defects in the c-axis direction facilitate the transport and exchange of cations within the lattice.

References

- AL-WAKEEL E.I., EL-KORASHY S.A., EL-HEMALY S.A.S., RIZK M.A., 2001, *Divalent Ion Uptake of Heavy Metal Cations by (Aluminum plus Alkali Metals)-Substituted Synthetic 1.1 nm-Tobermorites*, J. Mater. Sci. 36, 2405-2415.
- AYADI A., STITI N., BOUMCHEDDA K., RENNAI H., LERARI Y., 2011, *Elaboration and Characterization of Porous Granules Based on Waste Glass*, Powder Technol. 208, 423-426.
- CHOY K.K.H., MCKAY G., 2005, *Sorption of Cadmium, Copper and Zinc Ions onto Bone Char using Crank Diffusion Model*, Chemosphere 60, 1141-1150.
- COLEMAN N.J., BRASSINGTON D.S., 2003, *Synthesis of Al-substituted 11 Å Tobermorite from Newsprint Recycling Residue: a Feasibility Study*, Mater. Res. Bull. 38, 485-497.
- COLEMAN N.J., 2005, *Synthesis, Structure and Ion Exchange Properties of 11 Å Tobermorites from Newsprint Recycling Residue*, Mater. Res. Bull., 40, 2000-2013.
- COLEMAN N.J., TRICE C.J., NICHOLSON J.W., 2009, *11 Å Tobermorite from Cement Bypass Dust and Waste Container Glass: a Feasibility Study*, Int. J. Miner. Process. 93, 73-78.

- COLEMAN N.J., 2011, *11 Å Tobermorite Ion Exchanger from Recycled Container Glass*, Int. J. Environ. Waste Manage. 8, 366–382.
- EL-HEMALY S.A.S., MITSUDA T., TAYLOR H.F.W., 1977, *Synthesis of Normal and Anomalous Tobermorites*, Cem. Concr. Res., 7, 429–438.
- KOMARNENI S., ROY R., ROY D.M., FYFE C.A., KENNEDY G.J., BOTHNER-BY A.A., DADOK J., CHESNICK A.S., 1985, *^{27}Al and ^{29}Si Magic Angle Spinning Nuclear Magnetic Resonance Spectroscopy of Al-substituted Tobermorites*, J. Mater. Sci. 20, 4209–4214.
- KOMARNENI S., ROY R., ROY D.M., 1986, *Pseudomorphism in Xonotlite and Tobermorite with Co^{2+} and Ni^{2+} Exchange for Ca^{2+} at 25 °C*, Cem. Concr. Res. 16, 47–58.
- KOMARNENI S., BREVAL E., ROY R., ROY D.M., 1988, *Reactions of Some Calcium Silicates with Metal Cations*, Cem. Concr. Res. 18, 204–220.
- KORKOSZ A., PTASZYNSKA A., HANEL A., NIEWIADOMSKI M., 2012, *Cullet as a Filter Medium for Swimming Pool Water Treatment*, Physicochem. Probl. Miner. Process. 48, 295–301.
- KRISHNANI K.K., MENG X., CHRISTODOULATOS C., BODDU V.M., 2008, *Biosorption Mechanism of Nine Different Heavy Metals onto Biomatrix from Rice Husk*, J. Hazard. Mater. 153, 1222–1234.
- LIMA S., DIAS A.S., LIN Z., BRANDÃO P., FERREIRA P., PILLINGER M., ROCHA J., CALVINO-CASILDA V., VALENTE A.A., 2008, *Isomerization of D-Glucose to D-Fructose over Metallosilicate Solid Bases*, Appl. Catal. A: General. 339, 21–27.
- MATTEUCCI F., DONDI M., GUARINI G., 2002, *Effect of Soda-Lime Glass on Sintering and Technological Properties of Porcelain Stoneware Tiles*, Ceram. Int. 28, 873–880.
- MITSUDA T., TAYLOR H.F.W., 1975, *Influence of Aluminium on the Conversion of Calcium Silicate Hydrate Gels into 11 Å Tobermorite at 90 °C and 120 °C*, Cem. Concr. Res. 5, 203–210.
- NELSON E.B., KALOUSEK G.L., 1977, *Effects of Na_2O on Calcium Silicate Hydrates at Elevated Temperatures*, Cem. Concr. Res. 7, 687–694.
- NOCUÑ-WCZELIK W., 1999, *Effect of Na and Al on the Phase Composition and Morphology of Autoclaved Calcium Silicate Hydrates*, Cem. Concr. Res. 29, 1759–1767.
- PARK S.B., LEE B.C., KIM K.H., 2002, *Studies on Mechanical Properties of Concrete Containing Waste Glass Aggregate*, Cem. Concr. Res. 34, 2181–2189.
- PONTIKES Y., ESPOSITO L., TUCCI A., ANGELOPOULOS G.N., 2007, *Thermal Behaviour of Clays for Traditional Ceramics with Soda-Lime-Silica Waste Glass Admixture*, J. Eur. Ceram. Soc. 27, 1657–1663.
- REINIK J., HEINMAA I., KIRSO U., KALLASTE T., RITAMÄKI J., BOSTRÖM D., PONGRÁCZ E., HUUTANEN M., LARSSON W., KEISKI R., KORDÁS K., MIKKOLA J-P., 2011, *Alkaline Modified Oil Shale Fly Ash: Optimal Synthesis Conditions and Preliminary Tests on CO_2* , J. Hazard. Mater. 196, 180–186.
- RICHARDSON I.G., GROVES G.W., 1997, *The Structure of the Calcium Silicate Hydrate Phases Present in Hardened Pastes of White Portland Cement/Blast Furnace Slag Blends*, J. Mater. Sci. 32, 4793–4802.
- SAEED A., AKHTER M.W., IQBAL M., 2005, *Removal and Recovery of Heavy Metals from Aqueous Solution Using Papaya Wood as a New Biosorbent*, Sep. Purif. Technol. 45, 25–31.
- SHAW S., CLARK S.M., HENDERSON C.M.B., 2000, *Hydrothermal Formation of the Calcium Silicate Hydrates, Tobermorite ($\text{Ca}_5\text{Si}_6\text{O}_{16}(\text{OH})_2 \cdot 4\text{H}_2\text{O}$) and Xonotlite ($\text{Ca}_6\text{Si}_6\text{O}_{17}(\text{OH})_2$): an In Situ Synchrotron Study*, Chem. Geol. 167, 129–140.
- SHRIVASTAVA O.P., GLASSER F.P., 1986, *Ion-Exchange Properties of 11-Å Tobermorite*, React. Solids 2, 261–268.

- VACLAVIKOVA M., MISAEELIDES P., GALLIOS G., JAKABSKY S., HREDZAK S., 2005, *Removal of Cadmium, Zinc, Copper and Lead by Red Mud, an Iron Oxides Containing Hydrometallurgical Waste*, *Studies in Surface Science and Catalysis* 155, 517–525.
- VAZQUEZ G., MOSQUERA O., FREIRE M.S., ANTORRENA G., GONZALEZ-ALVAREZ J., 2012, *Alkaline Pre-Treatment of Waste Chestnut Shell from a Food Industry to Enhance Cadmium, Copper, Lead and Zinc Ions Removal*, *Chem. Eng. J.* 184, 147–155.
- WIEKER W., GRIMMER A-R., WINKLER A., MÄGI M., TARMAK M., LIPPMA E., 1982, *Solid-State High-Resolution ^{29}Si NMR Spectroscopy of Synthetic 14 Å, 11 Å and 9 Å Tobermorites*, *Cem. Concr. Res.* 12, 333–339.

Received May 8, 2013; reviewed; accepted May 30, 2013

EFFECT OF SEAWATER MAIN COMPONENTS ON FROTHABILITY IN THE FLOTATION OF Cu-Mo SULFIDE ORE

J.S. LASKOWSKI*, **S. CASTRO****, **O. RAMOS****

* NB Keevil Institute of Mining Engineering, University of British Columbia, Vancouver, Canada,
jsl@mining.ubc.ca

** Department of Metallurgical Engineering, University of Concepcion, Chile

Abstract: The main problem in the flotation of Cu-Mo sulfide ores in seawater is poor floatability of molybdenite at pH>9.5. Froth stability plays a very important role in determining concentrate grade and recovery in flotation operations and in this paper both floatability and frothability have been tested. The frothability have been studied by measuring froth equilibrium layer thickness in a modified laboratory flotation cell. Two chemical aspects of seawater need to be considered: the content of NaCl (around 87% of salinity), and the concentration of secondary ions (around 13%) (sulfate, magnesium, calcium, bicarbonate ions, etc.). Seawater, NaCl solutions, and seawater's ions were found to depress frothability. The effect of pH on frothability over the pH range from 9.5 to 11, which is very strong in freshwater, becomes negligible in seawater and the tested electrolyte solutions. The analysis of the relationship between the mechanisms of molybdenite depression and the loss of frothability in seawater implies that the effects of the studied ions on molybdenite floatability and on pulp frothability are different. While depression of molybdenite floatability could be tracked down to magnesium hydroxide precipitation as a main culprit, the depression of frothability is a much more complicated issue.

Keywords: *seawater, froth stability, Cu-Mo flotation, magnesium ions, molybdenite flotation*

Introduction

Many large mineral deposits are located in the areas with limited resources of fresh water. The Atacama Desert, with a major portion of Chilean Copper Industry situated in this area, exemplifies such problems very well. In such cases flotation in seawater becomes an increasingly important issue. However, the use of seawater could become a sustainable solution only if it could deliver the metal recoveries and concentrate grades comparable to those that can be obtained when using freshwater.

Molybdenum recovery plays a very important role in making Cu-Mo processing plants economically viable, and the major problem in the use of seawater in flotation of Cu-Mo sulfide ores results from a poor flotation of molybdenite at $\text{pH} > 10$ (Castro et al., 2012c; Castro, 2012; Laskowski and Castro, 2012). This loss of Mo is particularly obvious when the ore also contains pyrite/pyrrhotite, the minerals which are conventionally depressed with lime at a high pH.

Molybdenite is a mineral with natural hydrophobicity and its anisotropic laminar crystal structure (non-polar faces and polar edges) is similar to that of talc and graphite. Along with graphite, talc, sulfur, and also coal, it belongs to a group of inherently hydrophobic solids. These minerals were shown to float very well in concentrated electrolyte solutions (e.g. 0.5 M NaCl) without any organic flotation agents in the process referred to as salt flotation (Klassen and Mokrousov, 1963; Castro and Laskowski, 2011; Castro and Laskowski, 2012). It is therefore surprising that in the flotation of Cu-Mo sulfide ores in seawater molybdenite is depressed. However, while seawater is a concentrated solution of NaCl (about 0.6 mol/dm^3), it also contains some secondary ions (such as, magnesium, calcium, sulfate, bicarbonate, etc.), and precipitating magnesium hydroxide was found to be the major culprit responsible for depressing molybdenite when flotation is carried out in seawater over alkaline pH range (when pH exceeds $\text{pH } 9.5\text{--}10.0$) (Castro et al., 2012c; Castro, 2012; Laskowski and Castro, 2012).

Flotation process requires formation of a froth layer that is to some extent stable. Frothing agents prevent bubble coalescence and reduce bubble size (Cho and Laskowski, 2002a; 2002b). It is known that foams are stabilized not only by surface-active compounds (frothers) but also by surface-inactive compounds (inorganic ions) (Quinn et al., 2007; Castro et al., 2010). Foamability of frothing agents in distilled water does not necessarily predict frothability under flotation conditions. Lekki and Laskowski (1975) showed that frothers do not have to be strongly surface active agents. For example, di-acetone alcohol, a commercial flotation frother which was used by the copper industry in Poland, is not a surface active agent but it was performing very well as a frothing agent. While there was no foam when foamability tests were carried out in the presence of this agent in distilled water, the three-phase froth was sufficiently stable. The same phenomenon has been reported for pine oil. While there was no foam when the foamability was tested with pine oil, both in fresh water and in seawater, the presence of hydrophobic particles was found to strongly stabilize the pine oil froth (Castro et al., 2012b). A strong foaming agent does not necessarily produce the most stable froths. Melo and Laskowski (2007) found that DF-1012 frother ($\text{CH}_3(\text{PO})_{6,3}\text{OH}$ where PO stands for propylene oxide group) generated the most stable foams and carried most water, but in the presence of hydrophobic bituminous coal particles produced remarkably less voluminous froth when this frother was utilized. The same phenomenon was observed by Kuan and Finch (2010) who studied the effect of hydrophobic talc particles on the properties of foams in the presence of a polyglycol frother.

Frothing agents are employed in flotation to facilitate air dispersion into fine bubbles and to stabilize the froth. Froth stability depends on the frother type and concentration, but also is a function of other variables, such as particle size, hydrophobicity, solids content, pH, airflow rate, etc. For example, as reported by Tao et al. (2000), coal particles can stabilize or destabilize the froth. This depends both on the size of these particles as well as on their concentration. The -150 μm size fraction destabilized froth at lower concentrations but stabilized it at higher concentrations, while micronized coal particles showed froth-breaking power. Kurniawan et al. (2011) found a correlation between coal recovery and bubble size and claimed that fine coal floats better in electrolyte solutions because finer bubbles are produced in such systems. Zanin et al. (2009) derived models relating the froth stability and bubble size on top of the froth to the amount of hydrophobic material present in the froth. In this work the variables affecting froth stability are extended to electrolyte concentration and ionic composition, particularly to seawater.

Replacement of fresh water with seawater in flotation pulps brings about other factors. Foaming characteristics of MIBC (methyl isobutyl carbinol) and DF-250 ($\text{CH}_3(\text{PO})_4\text{OH}$) frothers in NaCl solutions and in seawater have been studied by Castro et al. (2010; 2012a). The two-phase foaming was characterized through measurements of the dynamic foamability index (DFI) for both frothers at various NaCl concentrations, and in seawater. Foamability of both, MIBC and DF-250 frothers, were much stronger in seawater than in distilled water. However, the frothability tests carried out during rougher flotation of Cu-Mo sulfide ores (Castro et al., 2012b) revealed that in the presence of polyglycol frothers (DF-250 and DF-1012) the frothability was much lower when measured in seawater as compared with that in fresh water.

To sum it up, the available evidence indicates that while depression of molybdenite in the flotation of Cu-Mo sulfide ores containing pyrite can be related to the precipitation of magnesium hydroxide, an explanation of the phenomena associated with frothing in the flotation of Cu-Mo ores is still missing.

Experimental

Material and methods

In our previous tests the samples of Cu-Mo sulfide ores from three different plants in Chile were used (Castro et al., 2012b). The experimental work described in this paper has been carried out with the use of Sample No. 3 (from the previous tests). The sample contained 0.43% Cu, 6.26% Fe and 0.008% Mo.

The laboratory flotation tests have been carried out with the use of the same reagents which are employed at the plant from which the sample was obtained and under the same conditions. The ore sample weight per one test was 1,161 g; impeller speed rate, 900 rpm; 34% solids; and air flow rate, 10 dm^3/min . MX-7017 thionocarbamate (26 g/Mg); MX-945 (21 g/Mg); MIBC, methyl isobutyl carbinol (21

g/Mg) were used as reagents. Grinding test: $P_{80} = 150 \mu\text{m}$ (20% +150 μm and 60.3% – 75 μm). The conditioning time was 5 min and flotation time 10 min.

The froth phase was studied by measuring the maximum froth layer thickness in a laboratory flotation cell so modified that it operates without discharge of concentrate. The LA-500 Agitair flotation cell with a volume of 2.7 dm³ was adapted for the frothability tests, as was described elsewhere (Castro et al., 2012b). In these tests air flow rate was 10 dm³/min at 900 rpm (other conditions similar to the flotation tests). The froth thickness was measured during 60 s by using a digital photographical method coupled to image analysis with the ImageJ software. The system was continuously

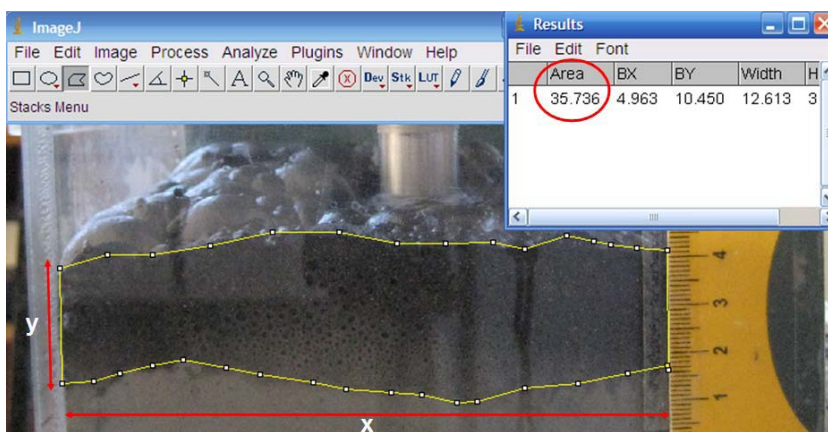


Fig. 1. Measurement of the area occupied by froth with the use of the ImageJ program

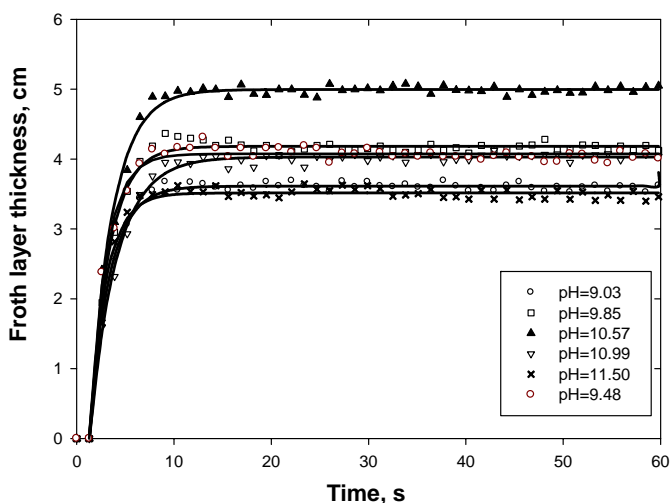


Fig. 2. Kinetics of rougher froth layer thickness growth in fresh water as a function of pH

determining the area occupied by the froth and was converting it to a rectangle; its height was taken as a mean froth layer thickness. The height of the froth in the cell was measured versus time (growth kinetic), and the maximum froth layer thickness was determined at the equilibrium time (t_e) (Figs. 1 and 2).

Examples of the results that can be generated using this technique are shown in Fig. 2.

Results

The flotation results in seawater given in Figs. 3 and 4 indicate that molybdenite recovery is sensitive to pH. A strong depression of molybdenite takes place at a pH higher than pH 9.5-10.0, and it was demonstrated that molybdenite is depressed by precipitating colloidal magnesium hydroxide (Castro et al., 2012c).

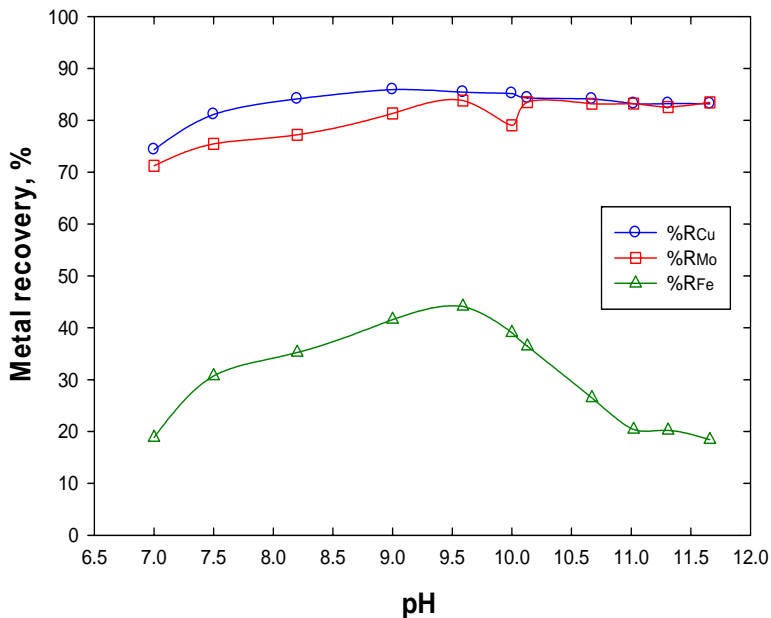


Fig. 3. Rougher recovery (Cu, Mo and Fe) as a function of pH in fresh water

Figure 5 shows that the frothability of the flotation pulp in the tests carried out in fresh water is very different from all other tests in other solutions (0.6 M NaCl, 0.6 M NaCl with 1,350 mg/dm³ of Mg²⁺ ions, fresh water with 1,350 mg/dm³ of Mg²⁺ ions, and seawater). All these cases, different from fresh water, are either concentrated NaCl solutions or contain a divalent cation (Mg²⁺ ions).

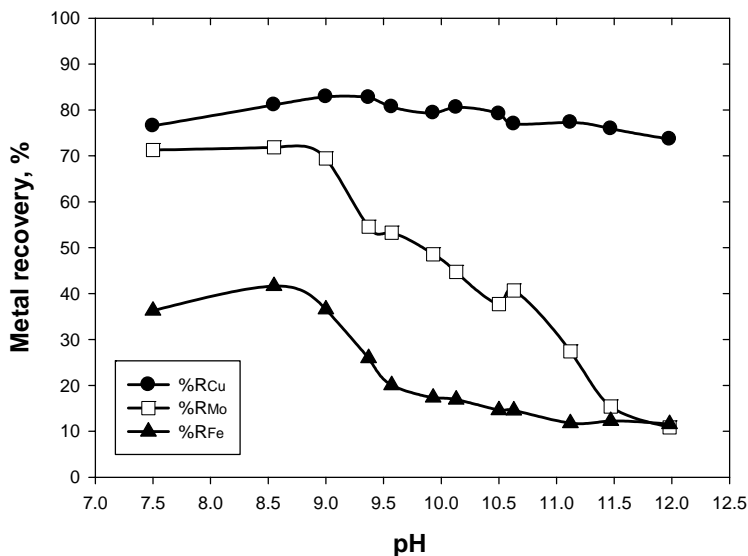


Fig. 4. Rougher recovery (Cu, Mo and Fe) as a function of pH in seawater

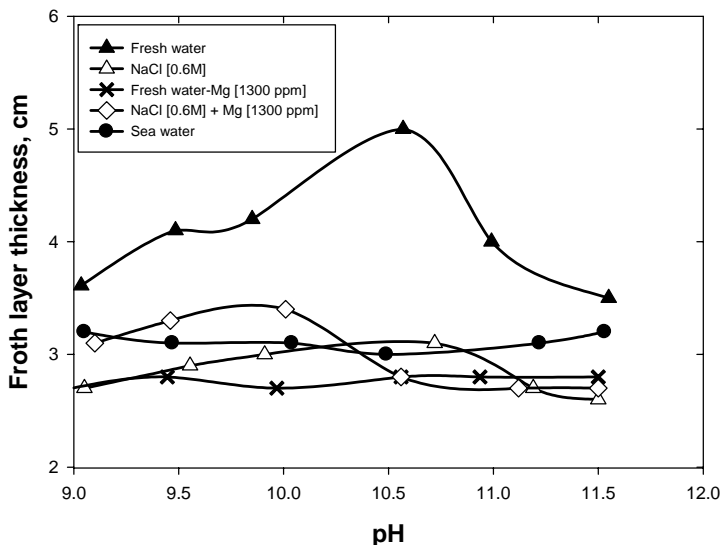


Fig. 5. Profile of equilibrium froth layer thickness as a function of pH in fresh water, NaCl 0.6M; fresh water-Mg²⁺ 1300 ppm, 0.6M NaCl-Mg²⁺ 1300 ppm, and seawater

As Figure 6 demonstrates, the ionic strength has a strong effect on frothing of the pulp under flotation conditions. Figure 7 shows that the concentration of Mg²⁺ ions in fresh water also strongly affects pulp frothability.

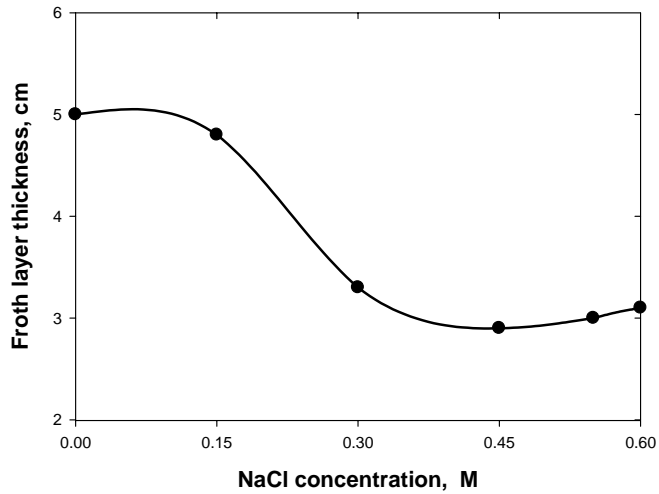


Fig. 6. Profile of equilibrium froth layer thickness as a function of sodium chloride concentration at pH 10.5

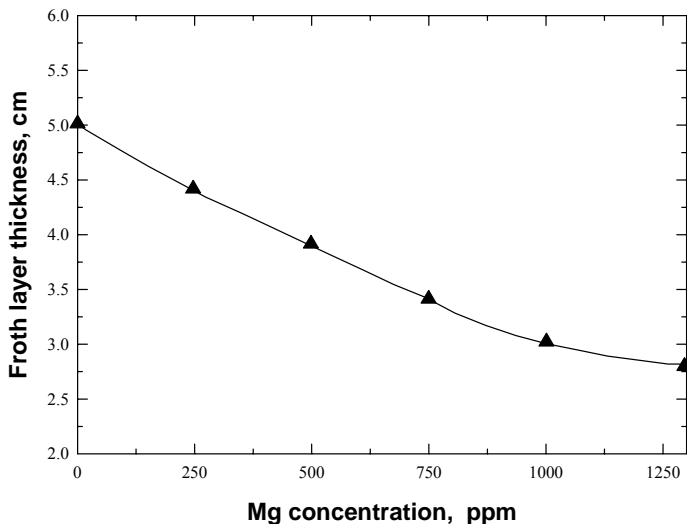


Fig. 7. Froth layer thickness as a function of Mg^{2+} ions concentration in fresh water at pH 10.5

Seawater contains various ions and their effect on frothability is compared in Fig. 8. These tests were carried out in fresh water with addition of some ions that appear in sea water (e.g. SO_4^{2-} , Mg^{2+} , Ca^{2+}) at pH of 10.5.

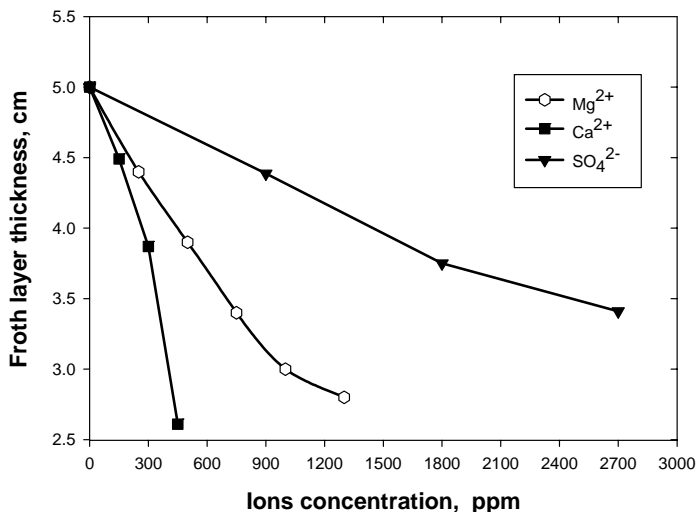


Fig. 8. Froth layer thickness as a function of Ca^{2+} , Mg^{2+} and SO_4^{2-} ions concentration in fresh water at pH 10.5

Discussion

Frothability in seawater

Inorganic electrolytes and seawater prevent bubble coalescence and decrease bubble size. Figure 9 confirms that without frother (in our tests MIBC) fine bubbles cannot be produced in fresh water. It is totally different in seawater where fine bubbles can be obtained even without the frother (Castro et al., 2010).

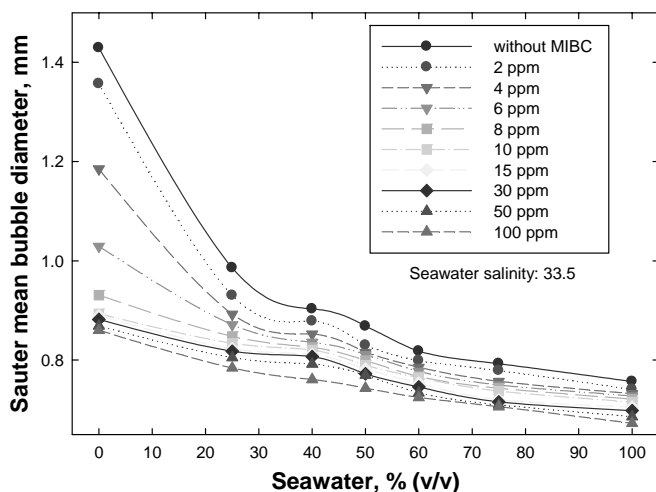


Fig. 9. Effect of seawater and MIBC frother on bubble size (Castro et al., 2010)

While critical coalescence concentration CCC values reported for MIBC frother are in the range of a few ppm (about 11 ppm that is 0.1 mmole/dm^3) (Laskowski et al., 2003), for NaCl solutions CCC was measured at 0.78 mole/dm^3 (Castro et al., 2012a). That means that when frother concentration is greater than CCC both in frother solutions and in electrolyte solutions bubbles do not coalesce. In seawater, bubbles are quite stable and frother is not needed to stabilize them further. In both cases what is stabilizing bubbles are water molecules bound to the bubbles. In the case of frothers, which molecules adsorb at the gas/liquid interface, some amount of water is bound to the bubbles by hydrogen bonding to the adsorbed frother molecules. In the case of electrolytes, the water layer is formed around bubbles since inorganic ions are surface-inactive, they increase water surface tension because they are expelled from the surface layer. Thus, in both cases different is only the mechanism by which water molecules accumulate around the bubbles.

The effect of magnesium ions on air bubbles

The results reported in this paper also indicate that frothability in fresh water is highly influenced by pH and shows a peak around pH 10.5. However this strong effect of pH is not observed in the frothability tests in seawater (or in general, in electrolyte solutions).

In flotation of Cu-Mo sulfide ores, lime is commonly applied to depress pyrite/pyrrhotite. The best pH range for pyrite depression is between 10 and 12, and over this pH range, when the flotation process is carried out in seawater, magnesium hydroxide precipitates. As Figure 10 shows, magnesium hydroxide may start precipitating around pH 9.5 as the process depends not only on pH but also on initial Mg^{2+} concentration (Li and Somasundaran, 1991). It is not yet possible to clarify whether molybdenite depression is just caused by a precipitating hydroxide (which happened to be magnesium hydroxide), or whether this phenomenon results from the ability of Mg(OH)^+ ions and/or colloidal $\text{Mg(OH)}_{2(s)}$ to accumulate on the surface of bubbles.

Eigeles and his co-workers (Eigeles and Volvenkova, 1963; Eigeles and Volova, 1964; 1968) studied in the 60's the effect of colloidal species accumulated on the surface of bubbles on flotation. They pointed out that adsorption on solid particles, which are in general heterogeneous, does not lead to an even distribution of the adsorbed surfactant on the solid surface but creates islands, and this does not necessarily affect flotation. On the other hand, accumulation of such species on the surface of bubbles always affects flotation, and translates into a strong depression when these species are hydrophilic.

The zeta potential measurements on air bubbles indicate that the iso-electric point of bubbles is around pH 2–4 (Li and Somasundaran, 1992; Yang et al., 2001; Oliveira and Rubio, 2011), and, practically, is not affected by the adsorption of flotation frothers (Elmahdy et al., 2008). Bubbles in alkaline pH are negatively charged in

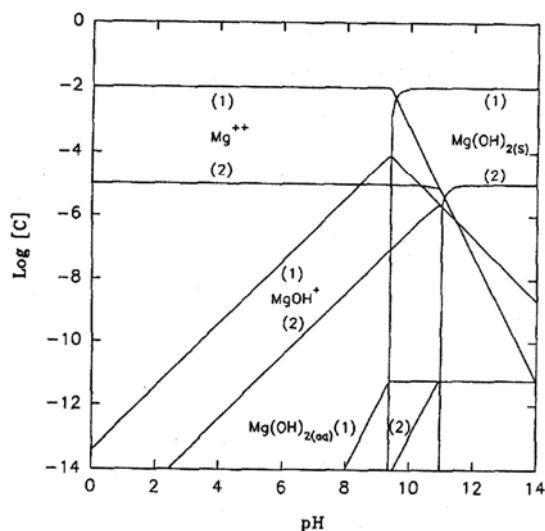


Figure 10. Magnesium species distribution as a function of pH at $1 \cdot 10^{-2}$ mol/dm³ (1) and $1 \cdot 10^{-5}$ mol/dm³ (2) MgCl₂ solutions (Li and Somasundaran, 1991, with the permission of Elsevier)

water and in NaCl solutions. However, in the presence of hydrolysable divalent cations the zeta-potential may, depending on pH, reverse its sign. Li and Somasundaran (1992) showed that the electrical charge change from negative to positive takes place when Mg²⁺ ions are present in the system in the pH range from 9 to 11. This was explained by coating of the bubbles by precipitating Mg(OH)_{2(s)}. Han et al (2004) confirmed a very high affinity of Mg(OH)⁺ and Mg(OH)_{2(s)} to bubble surface. It is therefore quite likely that the highly depressing effect of precipitating Mg(OH)₂ on molybdenite flotation results from the fact that these species tend to accumulate on air bubbles and the fact that such bubbles are positively charged may also play an important role.

The effect of ions present in the pulp

Inorganic electrolytes inhibit bubble coalescence and increase foamability (Castro et al., 2010). However, frothability, that is the stability of a three-phase froth, the system which may contain quite different solid particles, may behave differently. As Figure 8 shows, at pH of 10.5, the froth height decreases in 0.6 M NaCl solutions, and in fresh water containing SO₄²⁻, Mg²⁺ and Ca²⁺ ions up to the concentration similar to those in seawater (400 ppm in the case of Ca²⁺ ions, 1300 ppm for Mg²⁺ ions, and 2700 ppm for SO₄²⁻ ions).

In our study the depressing effect of Ca²⁺ ions in fresh water on frothability was higher than the effect of Mg²⁺ ions. This is completely different to what takes place in molybdenite depression by the same ions, where the effect of Mg²⁺ ions is stronger than

that of Ca^{2+} ions (Castro et al., 2012c; Laskowski and Castro, 2012). The surface precipitation and/or hetero-coagulation of colloidal $\text{Mg}(\text{OH})_{2(s)}$ has been suggested as the main depression mechanism. Because magnesium hydroxide is much less soluble than calcium hydroxide, whenever lime is added to seawater (to depress pyrite) and pH exceeds 9.5–10.0 magnesium hydroxide starts precipitating (Castro et al., 2012c).

On the other hand, the depressing effect of Ca^{2+} ions on frothability produced in fresh water at pH 10.5 takes place before the precipitation of $\text{Ca}(\text{OH})_{2(s)}$, and when zeta potential of bubbles is negative (Yang et al., 2001; Han et al., 2004). Mg^{2+} ions are able to reduce frothability at pH 9 (Fig. 5), i.e., below the critical pH of precipitation of colloidal $\text{Mg}(\text{OH})_{2(s)}$ (around pH 10). Apparently, the adsorption of the hydroxylated species, $\text{Ca}(\text{OH})^+$ and $\text{Mg}(\text{OH})^+$, on air bubbles, which concentration is predominant before the hydroxide precipitation, may be involved in the loss of frothability.

Of particular note, not only hydrolysing divalent cations showed a deleterious effect on frothability. Electrolytes, such as NaCl also reduce frothability (Figs. 6 and 8). It must be noted that, with the exception of fresh water, in all other cases the frothability was practically independent on pH, contrarily to molybdenite depression which takes place at the critical pH of magnesium hydroxide precipitation. Therefore, the inhibition of frothability (by secondary seawater's ions and NaCl solution), and molybdenite depression, seem to be quite independent phenomena. Depression of the frothability in NaCl solutions takes place at NaCl concentration of about 0.3 M NaCl (Fig. 6), in the solutions containing Mg^{2+} ions similar effect is observed at a concentration of about 0.05 M, while for Ca^{2+} this was observed at around 0.01 M. The fact that much higher concentrations were needed in case of NaCl than in the case of divalent cations of Mg^{2+} and Ca^{2+} may as well indicate that the phenomena discussed here result from coagulation of solid particles.

In general, it can be concluded that while we were able to demonstrate that poor floatability of molybdenite in seawater can be tracked down to the precipitation of magnesium hydroxide when pH is raised above 10 (to depress pyrite), the situation with frothability in such systems is a much more complicated issue.

Conclusions

In the lab flotation tests with Cu-Mo sulfide ore the froth layer thickness (frothability) was measured and compared with Cu and Mo recoveries. The tested parameters included pH, fresh and seawater, and 0.6 M NaCl solutions with addition of various ions that appear in seawater. Several conclusions are evident from the data:

- Frothability in fresh water was higher than in seawater, and it shows a maximum froth layer thickness around pH 10.5.
- In all cases in which either ionic strength of the pulp was high (0.6 M NaCl solution, sea water) or divalent cations (e.g. Mg^{2+}) were present in fresh water, the

frothability was depressed over the 9 to 11.5 pH range, that is over the range over which the frothability in fresh water was very high.

- The loss of frothability was observed whenever the prepared aqueous solutions contained the main components of seawater: NaCl or ions such as Mg^{2+} , Ca^{2+} and SO_4^{2-} at concentrations similar to those in seawater.
- The obtained results imply that while the effects detected when studying
- frothability result from the phenomena driven by coagulation, the molybdenite depression by Mg^{2+} ions takes place only above the critical pH of $Mg(OH)_{2(s)}$ precipitation.
- The results suggest that in flotation of Cu-Mo sulfide ores, the effect of seawater's ions on molybdenite depression is very different from the role these ions play in stabilizing the froth.

References

- BICAK, O, EKMEKCI, Z., CAN, M., OZTURK, Y., 2012. *The effect of water chemistry on froth stability and surface chemistry of the flotation of a Cu-Zn sulfide ore*, Int. J. Miner. Process., 102–103, 32–37.
- CASTRO S., VENEGAS I, LANDERO A., LASKOWSKI J.S., 2010. *Frothing in seawater flotation systems*, Proc. 25th International Mineral Processing Congress. Brisbane, 4039–4047.
- CASTRO S., LASKOWSKI J.S., 2011. Froth flotation in saline water. KONA, No 29, 4–15.
- CASTRO S., TOLEDO P., LASKOWSKI J.S., 2012a. *Foaming properties of flotation frothers at high electrolyte concentrations*. Water in Mineral Processing – Proc. of the First International Symposium (J. Drelich, ed.), SME, 51–60.
- CASTRO S., RAMOS O., CANCINO J.P., LASKOWSKI J.S., 2012b. *Frothing in the flotation of copper sulfide ores in sea water*. Water in Mineral Processing – Proc. of the First International Symposium (J. Drelich, Ed.), SME, 211–223.
- CASTRO S., RIOSECO P., LASKOWSKI J.S., 2012c. *Depression of molybdenite in seawater*. Proc. 26th Int. Mineral Processing Congress, New Delhi, 739–752.
- CASTRO S., 2012. *Challenges in flotation of Cu-Mo sulfide ores in sea water*, Water in Mineral Processing – Proc. of the First International Symposium (J. Drelich, Ed.), SME, 29–40.
- CHO Y.S., LASKOWSKI J.S., 2002a. *Effect of flotation frothers on bubble size and foam stability*, Int. J. Miner. Process., 64, 69–80.
- CHO Y.S., LASKOWSKI J.S., 2002b. *Bubble coalescence and its effect on dynamic foam stability*. Can. J. Chem. Eng., 80, 299–305.
- EIGELES M.A., VOLVENKOVA V.S., 1963. *Inorganic Electrolytes and Colloids in Elementary Flotation*, Proc. 6th Int. Mineral Processing Congress (A. Roberts, ed.), Peramon Press, 513–525.
- EIGELES M.A., VOLOVA M.L., 1964. *On the Mechanism of Activating and Depressant Action in Soap Flotation*, Proc. 7th Int. Mineral Processing Congress (N. Arbitter, ed.), Gordon and Breach, Vol. 1, 269–277.
- EIGELES M.A., VOLOVA M.L., 1968. *Activating of air bubbles by the insoluble products of reactions in flotation*, Proc. 8th Int. Mineral Processing Congress, Leningrad, Vol. 2, 353–364 (in Russian).
- ELMAHDY A.M., MIRNEZAMI M., FINCH J.A., 2008. *Zeta potential of air bubbles in presence of frothers*. Int. J. Miner. Process., 89, 40–43.
- HAN M.Y., AHN H.J., SHIN M.S., KIM S.R., 2004. *The effect of divalent metal ions on the zeta potential of bubbles*, Water Sci. and Technology, 50, 49–56.

- KLASSEN V.I., MOKROUSOV V.A., 1963. *An Introduction to the theory of flotation*, Butterworths, London.
- KUAN S.H., FINCH J.A., 2010. *Impact of talc on pulp and froth properties in F150 and 1-pentanol frother systems*, Miner. Eng., 23, 1003–1009.
- KURNIAWAN A.U., OZDEMIR O., NGUYEN A.V., OFORI P., FIRTH B., 2011. *Flotation of coal particles in $MgCl_2$, $NaCl$, and $NaClO_3$ solutions in the absence and presence of Dowfroth 250*. Int. J. Miner. Process., 98, 137-144.
- LASKOWSKI J.S., CASTRO S., 2012. *Hydrolyzing ions in flotation circuits: seawater flotation*, Proc. 13th Int. Mineral Processing Symp., Bodrum (Turkey), 219–228.
- LASKOWSKI J.S., TLHONE J., WILLIAMS P., DING K., 2003. *Fundamental properties of the polyoxypropylene alkyl ether flotation frothers*, Int. J. Miner. Process., 72, 289–300.
- LEKKI J., LASKOWSKI J.S., 1975. *A new concept of frothing in flotation systems and general classification of flotation frothers*, 11th Int. Mineral Processing Congress, Cagliari, 427–448.
- LI C., SOMASUNDARAN P., 1991. *Reversal of bubble charge in multivalent inorganic salt solutions – effect of magnesium*. J. Colloid Interface. Sci., 146, 215–218.
- LI C., SOMASUNDARAN P., 1992. *Reversal of bubble charge in multivalent inorganic salt solutions – effect of aluminium*. J. Colloid Interface Sci., 148(2), 587–591.
- MELO F., LASKOWSKI J.S., 2007. *Effect of frothers and solid particles on the rate of water transfer to froth*, Int. J. Miner. Process., 84, 33–40.
- OLIIVEIRA C., RUBIO J., 2011. *Zeta potential of single and polymer-coated microbubbles using an adapted microelectrophoresis technique*. Int. J. Miner. Process., 98, 118–123.
- QUINN J.J., KRACHT W., GOMEZ C.O., GAGNON C., FINCH J.A., 2007. *Comparing the effect of salts and frother (MIBC) on gas dispersion and froth properties*, Miner. Eng., 20, 1296–1302.
- TAO D., LUTTRELL G.H., YOON R-H., 2000. *A parametric study of froth stability and its effect on column flotation of fine particles*, Int. J. Miner. Process., 59, 25–43.
- YANG C., DABROS T., LI D., CZARNECKI, MASLIYAH J. H., 2001. *Measurements of the zeta potential of gas bubbles in aqueous solutions by microelectrophoresis method*. J. Colloid Interface Sci., 243, 128–135.
- ZANIN M., WIGHTMAN E., GRANO S.R., FRANZIDIS J.P., 2009. *Quantifying contributions to froth stability in porphyry copper plants*, Int. J. Miner. Process., 91, 19–27.

Received April 8, 2013; reviewed; accepted July 1, 2013

IMPACT OF OVALBUMIN ON PYRITE FLOTATION IN THE ABSENCE AND PRESENCE OF METAL IONS

Taki GULER^{*}, Kemal SAHBUDAK^{**}, Unal AKDEMIR^{***},
Sevil CETINKAYA^{****}

^{*} Mugla Sitki Kocman University, Mining Eng. Dept., Mugla, Turkey, takiguler@mu.edu.tr

^{**} Cumhuriyet University, Metallurgical and Materials Eng. Dept., Sivas, Turkey

^{***} Cumhuriyet University, Mining Eng. Dept., Sivas, Turkey

^{****} Cumhuriyet University, Chemical Eng. Dept., Sivas, Turkey

Abstract: Recovery of gangue pyrite and its accidental activation are vital issues in flotation of complex sulfide ores. This work was performed by cyclic voltammetry (CV) and flotation tests to elucidate applicability of ovalbumin (OVA) as depressant for pyrite. The synergetic effect of metal ions in addition to its possible use in case of accidental activation by metal ions. CV tests stated that OVA adsorbed irreversibly on pyrite, and restricted electron transfer up to moderately oxidizing potentials due to electrostatic interaction together with weak hydrophobic interactions. At highly oxidizing potentials, adsorption occurred through electrochemical mechanisms through formation of metal-OVA chelates. Rate of pyrite depression with OVA was found to be potential dependent reaching its peak point around moderately oxidizing potentials both in absence and presence of metal ions. Electrochemically active metals display synergetic effect with OVA on pyrite depression, whereas noble metals activate pyrite and reduced depressing potency of OVA.

Keywords: *pyrite, ovalbumin, metal ion, flotation, redox potential*

Introduction

Pyrite (FeS₂) is the most widespread sulfide mineral in earth crust. It is the major gangue of most sulfide ores and is rejected in flotation processes. Flotation practices revealed that there is a potential problem arising from concentrate dilution with recovery of gangue-pyrite in froth even in alkaline pulp due primarily to accidental activation. Its hydrophobization may result from dissolved metal ions from constituent of ore, and/or intentionally used ions as modifying agent to satisfy selectivity (Chandra and Gerson, 2009). Commonly encountered metal ions in flotation pulps are Cu⁺², Pb⁺² and Fe⁺². First two of them may come from constituent of ore in addition to

intentionally added ones to improve selectivity, while a comminution circuit is major source of Fe^{+2} . Iron ions significantly depress ore-pyrite from neutral to mildly-alkaline pHs (Jiang et al., 1998). Activation by Cu-ions occurs through direct adsorption instead of one-to-one exchange with lattice. Cu^{+2} ions reduce into Cu^{+} on pyrite by reducing components chiefly coming from grinding circuit and new Cu^{+} -sulfide phase forms (Weisener and Gerson, 2000; Chandra and Gerson, 2009). Similarly, activation by Pb^{+2} ions does not obey exchange with lattice cation. Lead activation occurs by deposition of dissolved or precipitated lead oxidation species on pyrite. In contrast to Cu^{+2} -activation, electrochemical potential was found to have no effect on pyrite activation by Pb^{+2} ions (Peng et al., 2012).

Various inorganic agents were used as pyrite depressant despite environmental concerns. Their consumptions have increased day by day due to need to process more complex and lower grade ores. However, selectivity has still remained as significant problem. By the time, researchers engaged more on the use of environmentally-friendly organic depressants as a result of strict environmental regulations and necessity to process low grade complex ores at low cost. However, ovalbumin (OVA) has not taken enough interest as a modifying agent in spite of being a good candidate as an adsorbent of metal ions (Maruyama et al., 2007).

OVA is a chicken egg protein having a molecular weight of 45000 g/mol. It is composed of amino acid subunits forming backbone structure and sidechains. The backbone structure contains 385 amino acids having carboxyl ($-\text{COOH}$) and amine ($-\text{NH}_2$) groups. The chemical structure and elemental constituent of sidechains of amino acids determine protein type. OVA exhibits electrochemically active behavior in aqueous environment due to presence of one disulfide (S-S) in cystine and four sulfhydryl ($-\text{SH}$) bonds in cysteine groups in sidechains (Fothergill and Fothergill, 1970).

Investigations on the use of OVA in mineral processing are limited. Bastrzyk et al. (2008) separated magnesite from quartz with anionic collector by using OVA as modifier. Guler et al (2013) emphasized importance of redox potential on OVA-pyrite interaction based on FTIR spectroscopy and cyclic voltammetry (CV). Ying et al (2004) stated that adsorbed albumin was stable on Au at potential range $-200+600$ mV, and could partly block redox reactions. Liu et al. (2006) attributed cysteine adsorption on pyrite to chemical interaction. Rojas-Chapana and Tributsch (2001) explained cysteine-pyrite interaction with disulfide formation between sulfhydryl groups of cysteine and free-SH groups from pyrite.

Since OVA is easily suppliable, abundant and cheap in addition to its affinity to interact with heavy metals depending on redox condition, its use as an environmentally friendly depressant with metal ions has rather not been considered yet. This work was made to elucidate impact of electrochemical condition on pyrite depression with OVA in absence and presence of metal ions by CV and flotation tests.

Experimental

Pyrite sample was supplied from Artvin-Murgul deposits in Turkey. Chemical and mineralogical analysis showed that pyrite was highly pure (>98% FeS₂) and major impurity was quartz. Mineralogical analysis was made by Bruker D8 Advance X-ray diffractometer. Pyrite was ground in a ceramic mill for flotation tests, sized (-212+75 μm) and stored in glass tubes under nitrogen atmosphere to eliminate surface oxidation.

Tetraborate (0.05 M Na₂B₄O₇·10H₂O) buffer solution (pH 9.2) was used in experimental works. O₂ content of buffer was reduced down to 1 ppm by intensive bubbling of nitrogen (>99.998% N₂) for at least 15 minutes. It was controlled by a YSI-5100 oxymeter. CuSO₄·5H₂O, Pb(NO₃)₂ and FeCl₂·7H₂O were used as sources of Cu⁺², Pb⁺², Fe⁺² ions. Highly pure OVA (98%) supplied by Merck was tested as the environmentally-friendly organic modifier. Metal ion concentration was applied as 10⁻⁴ M and 250 g/Mg in CV and flotation tests, respectively. A 500 ppm of OVA in CV tests and 50 g/Mg in flotation study was used.

Three-electrode system cells were used in polarization works. Calomel electrode and Pt-foil were used as reference and counter electrodes, respectively. The working electrode was Pt-wire (150 cm) for flotation tests mounted to inner side of cell, while it was a shaped pyrite crystal in CV setup. Electrochemical works were performed using Gamry PCI-750 potentiostat and PHE-200 Physical Electrochemistry software of Gamry Co. Flotation tests were carried out in a specially designed closed cell system (Güler et al., 2013). Polarization was applied potentiostatically for 10 minutes, and then, froth was collected for 5 minutes.

Results and discussions

Pyrite reacts with surroundings in aqueous medium due to its semiconducting property, and surface state is established through electrochemical mechanisms in addition to possible chemical reactions. Electrochemistry of pyrite is a well-documented issue. Pyrite oxidizes first to release Fe⁺² and S⁰ (Ekmekci and Demirel, 1997). Fe⁺² ion is not stable, and oxidizes to form ferric oxy-species at higher potentials, which reduces to ferrous hydroxides at lower potentials during cathodic scan. Fe⁺²/Fe⁺³ redox of iron hydroxides drew distinctive oxidation (A1) and reduction (C1) peaks on pyrite voltammogram (Fig. 1a). Peak A2 arose chiefly from oxidation of S⁰ to sulfate. Further oxidation of pyrite surface to Fe⁺³-oxyhydroxides, and decomposition of H₂O to release O₂ did also contribute to charge transfer, which shaped peak A2. Oxidation products were reduced in cathodic scan, and increased current flow at lower potentials. Therefore, size of C1 ($Q_{C1} = 821 \mu\text{C}$) was greater than that of A1 ($Q_{A1} = 615 \mu\text{C}$) (Güler et al., 2013).

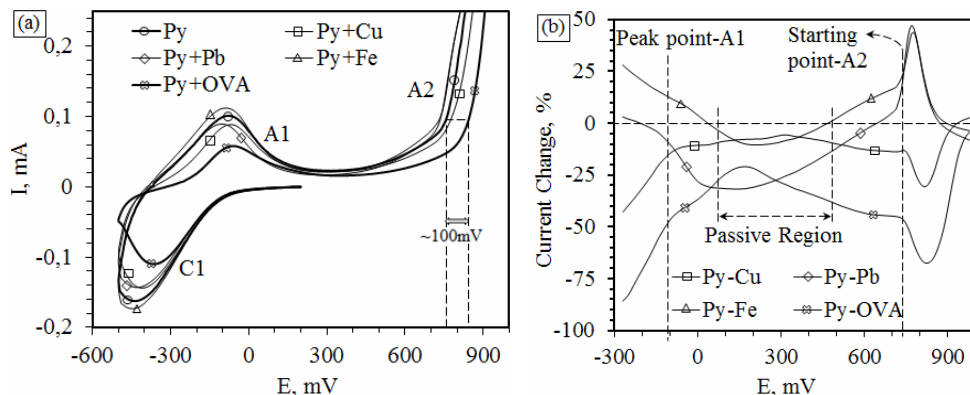


Fig. 1. Effect of metal ions and OVA on (a) electrochemical behavior of pyrite, and (b) percentage change in anodic current respons of pyrite electrode

Pyrite floatability curves were thought to be shaped by dominating surface hydroxy species in the examined range (Fig. 2). The recovery curve drew an arch-shape. It reached a plateau around 200 mV owing to formation of hydrophobic elemental sulfur S^0 , together with possible hydrophobic polysulfides. Self-induced floatability left at lower rates in moderate to highly oxidizing potentials due to presence of ferric-hydroxides and hydrophilic sulfoxy species while ferrous species and HS^- inhibited pyrite flotation at reducing potentials (Ekmekci and Demirel, 1997).

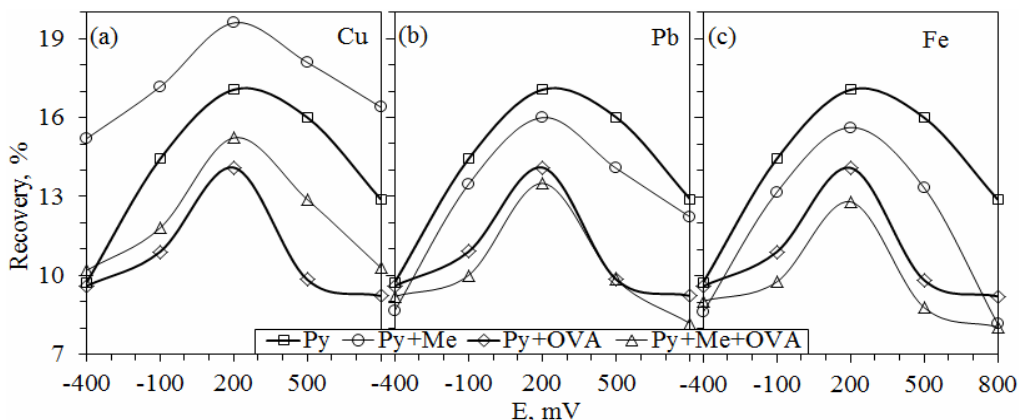


Fig. 2. Pyrite flotation in the absence and presence of metal ions (Me) and OVA

Electrochemistry of pyrite-metal ion interaction was investigated both in absence and presence of OVA. Examined metal ions were opted depending on abundance in sulfide ores, and their standard formation potentials E° . From the selected ions Fe (E° for Fe^{+2}/Fe is -440 mV) is the most active one, while Pb (E° for Pb^{+2}/Pb is -126 mV) is ready to oxidize around open circuit potential (OCP) of pyrite, and Cu (E° for Cu^{+2}/Cu is 337 mV) is the most noble one.

Metal ions did not significantly alter pyrite voltammograms (Fig. 1a) except slight changes in current flow rate. Then, percentage variation in anodic current by metal ions with respect to reference value of bare pyrite was also considered (Fig. 1b). Positive values mean that modifying agents increase electron transfer rate, while negative ones show inhibition of charge transfer and passive layer formation. Electrochemical activity of pyrite was at minimal level in slight to moderately oxidizing potentials, in which region, amount of charge transferred was out of significance regardless of percentage magnitude of calculated value. Beyond this range, all the constituents affected current flow. Fe-ions displayed added-effect on the activity of $\text{Fe}^{+2}/\text{Fe}^{+3}$ redox couple, and enhanced anodic current flow (Fig. 1). Depressing effect of Fe^{+2} ions became more predominant at oxidizing potentials. Since, number of surface sites covered by hydrophilic ferric species increased at higher potentials. Pb^{+2} ions adsorbed onto pyrite as Pb-complexes independent of applied potential. Adsorbed layer has porous structure (Nava et al., 2002; Güler, 2012), and does not inhibit anodic processes occurring on pyrite at moderate to highly oxidizing potentials. Therefore, Pb^{+2} ion also increased anodic current flow at moderate to highly oxidizing potentials. On the other hand, Cu-ions confined electron flow at changing rate among potential range. Potential increased from reducing to slightly oxidizing values. Electrochemical activity increased on the surface. Redox processes completed at certain rate releasing ferric hydroxide and S° , at which point passivation by Cu^{+2} was significantly overcome (Fig. 1). Simultaneously, Cu-ions adsorbed on pyrite as hydrophobic CuS-like species and upgraded recovery. They are not stable at moderate to highly oxidizing potentials, and then Cu-hydroxides form on mineral surface. Hence, recovery started to decrease again at higher potentials with combined effect of ferric species and Cu-oxyhydroxides (Peng et al., 2012; Weisener and Gerson, 2000).

Isoelectric point of OVA is at pH 4.6 (Bastrzyk et al., 2008) and it has net negative charge at pH 9.2. Pyrite is also negatively charged in alkaline condition at OCP, which is around 200 mV at pH 9.2 (Kocabağ and Güler, 2008). Therefore, amount of adsorbed OVA on pyrite is expected to increase at positive potentials above OCP due to supply of more binding sites (Ying et al., 2004). OVA adsorption under reducing to slightly oxidizing conditions is also possible due to conformational changes in protein structure, which occurs at lower rates since OVA is hard protein (Nakanishi et al., 2001). OVA has electrochemically active sulfhydryl groups in addition to amine and carboxyl functional groups (Fothergill and Fothergill, 1970). These groups are anticipated to influence OVA-pyrite interaction related to potential.

Role of sulfhydryl residues on OVA-pyrite interaction did not appear on E-I spectrum up to about 750 mV besides passivation (Fig. 1). Since both OVA and pyrite have the same sign at lower potentials and around OCP, the passivation was not expected due to electrostatic repulsion. Therefore, the passivation would mainly be referred to irreversible adsorption of OVA during repeated cycling. The flotation results clarified role of OVA and passive layer formation (Fig. 2). Although weak

conformational changes in OVA molecule verified protein-pyrite interaction under OCP, electrostatic repulsion restricted the adsorbed amount (Ying et al., 2004). The monolayer coverage was thought to be satisfied at low OVA concentrations in slightly reducing condition due to large molecular size and side-on-type configuration (Liu et al., 2006). OVA loses only a small fraction of its secondary structure (α -helix) during adsorption on hydrophilic surface, which takes long time to reach equilibrium when conformational change or rearrangement of molecular structure occurs (Nakanishi et al., 2001). Moreover, collectorless flotation of pyrite was already achieved at its minimum value under reducing condition, and then electron blocking and depressing effect by electrostatic interaction could be only partially reflected on self induced floatability.

Figure 3 shows depression rate of pyrite with respect to applied potential drawn using experimental data:

$$\text{Depression rate} = (R_{M+Py} - R_{PY})/R_{PY},$$

where $R_{M+Pyrite}$ and R_{PY} are pyrite recovery with and without modifying agent(s), respectively. Hydrophobic redox products made pyrite more floatable around OCP, and reduced depressing effect of OVA (Figs. 2 and 3). Conversely, hydrophobic redox products may behave as tools for OVA adsorption through hydrophobic interaction in addition to weak conformational changes (Nakanishi et al., 2001; Bastrzyk et al., 2008; Güler et al., 2013). At moderately oxidizing potentials, OVA accumulation took place through ionic interaction between OVA and OH^- group of oxidized surface (Parida et al., 2006) and recovery drop reached peak point (Fig. 3). Effect of sulfhydryl groups became apparent at highly oxidizing potentials (Fig. 1). OVA shifted peak A2 to higher potentials, which was attributed to formation of metal-OVA chelate (Maruyama et al., 2007). OVA adsorption might also proceed through disulfide bond formation between sulfhydryl groups of OVA and $-\text{SH}$, oxidation product of pyrite (Rojas-Chapana and Tributsch, 2001). Although rate of recovery drop with OVA was significantly high at cited potentials, role of electrochemical interaction could not be clarified due to lower recovery values in collectorless condition both in absence and presence of OVA.

A combined effect of OVA+metal ions on electrochemical behavior of pyrite was given in Fig. 4. No peculiar peak did appear besides present ones. Instead, metal ions enhanced passivizing effect of OVA. The maximum passivation was observed with $\text{OVA}+\text{Fe}^{+2}$. The polarization potential vs. rate of pyrite depression curve for $\text{OVA}+\text{Fe}^{+2}$ did also exhibit similar results (Fig. 3). In general, curves in Fig. 3 assumed an “M-shape” and two maxima appeared at -100 mV and 500 mV. Recovery drop decreased down to minimum point at about 200 mV between two maxima due to hydrophobization of pyrite surface. Since hydrophilic surfaces bound significantly more protein than hydrophobic ones due to less charged property of hydrophobic surfaces, and binding of protein to hydrophobic surfaces by unspecific hydrophobic and van der Waals interactions. Under OCP, where first peak appeared, both OVA and

pyrite were negatively charged. Metal ions served as bridging medium between OVA and pyrite through ion attachment to peptide chain leading to unfolding (Nakanishi et al., 2001; Jansson and Tengvall, 2004; Ying et al., 2004). Conversely, OVA is known to have high internal stability, and there would be significant electrostatic repulsion between OVA and pyrite in alkaline condition. So, OVA adsorption by bridging action of metal ions occurred in limited rate, which referred to limited pyrite depression with OVA+metal ion as seen in Figs. 2 and 3. Positive applied potential satisfied significant electrostatic interaction of OVA with metal-oxyhydroxides (Parida et al., 2006). Rate of pyrite depression reached its maxima, and almost kept on at higher potentials with negligible decrease.

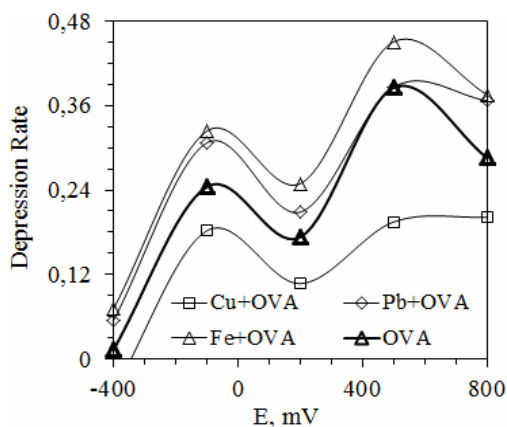


Fig. 3. Relationship between applied potential and depression rate

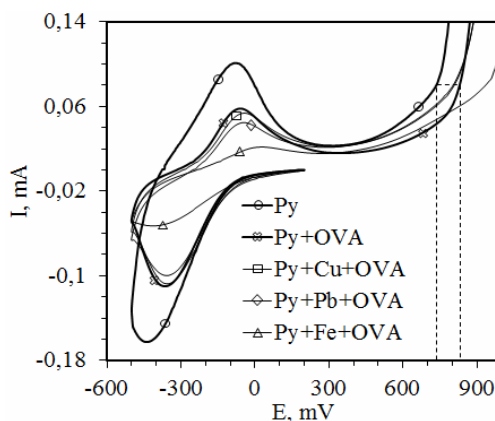


Fig. 4. Effect of modifying agents on voltammetric behavior of pyrite

Cu^{+2} ion activated pyrite (Fig. 2a) and reduced depressing potency of OVA from about 40% down to 20% at moderate to highly oxidizing potentials (Fig. 3). On the other hand, Pb^{+2} and Fe^{+2} exhibited synergetic effect with OVA except that depression effect of Pb^{+2} left at negligible rate in slight to moderately oxidizing potential range. Effect of metal ions on OVA-pyrite interaction was thought to depend mainly on their formation potentials. Then, impact of OVA on pyrite flotation was also depicted on contour maps concerning rate of pyrite depression with OVA+metal ion (Fig. 5a) and depression rate of metal-interacted pyrite with OVA (Fig. 5.b). In general, depressing effect of OVA+metal ion was in increasing order by applied potential, and a formed M-shape curve with peaks at slightly reducing and moderately oxidizing potentials almost for all E° values. The curve for OVA from Fig. 3 was overlapped in Fig. 5a. This curve intersected E° value of about 0 mV indicating that metal ion with positive E° could not be applicable as depressant with OVA in pyrite flotation. Metal ions should have negative E° to enhance depressing potency of OVA on pyrite, and flotation should be performed at moderately oxidizing potentials. The overlapped OVA curve did almost draw frontier line. More noble metals having positive E°

behave as activator, whereas more active metals with lower E° depress pyrite. On the other hand, OVA was found to be effective in depressing activated pyrite with more noble metals almost only at highly oxidizing potentials (Fig. 5b). Depression rate of activated pyrite with OVA did also form a peak around slightly reducing potentials for noble metals. In case of flotation application at slightly reducing potentials, OVA might then be preferred as pyrite depressant.

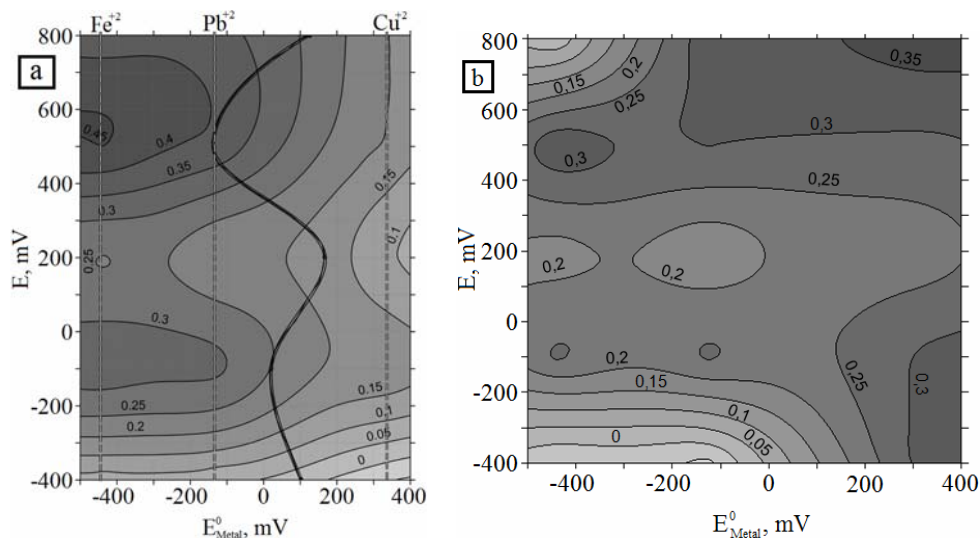


Fig. 5. Rate of recovery drop of (a) bare pyrite with the synergetic effect of metal ions and OVA, and (b) metal-interacted pyrite with OVA depending on standard formation potential of metal ion (E_{Metal}^0) and applied potential (E)

Conclusions

Adsorption and depressing effects of OVA on pyrite in absence and presence of metal ions were investigated by CV and flotation tests. The following conclusions can be drawn.

1) Flotation reached peak point around OCP of pyrite due to hydrophobization. Beyond this range, the hydrophilic redox products decreased pyrite recovery. Cu^{+2} activated pyrite, whereas Fe^{+2} exhibited depressing effect. Pb^{+2} did also depressed but at negligible rate.

2) OVA reduced flotation both in absence and presence of metal ions.

3) Pyrite depression with OVA can be controlled by applied potential. Electrostatic interaction as a result of conformational changes in OVA molecule, together with hydrophobic interaction, caused nearly insignificant depression in reducing to slightly oxidizing potentials. OVA adsorption through ionic interaction induced the maximum depression at moderately oxidizing potentials, which level was almost kept at highly oxidizing potentials due to formation of metal-OVA chelates.

4) Metal ions with more negative E° enhanced depressing potency of OVA, whereas those with positive E° could not be used as alternative depressant with OVA.

5) Activated pyrite with metal ions having positive E° can be depressed with OVA at moderate to highly oxidizing potentials. Reasonable depression might also be possible at slightly reducing condition.

ACKNOWLEDGEMENTS: The financial support of Cumhuriyet University Scientific Research Project Unit (Project No: M-279) is gratefully acknowledged.

References

- BASTRZYK A., POLOWCZYK I., SZELAG E., SADOWSKI Z., 2008, *The Effect of Protein-Surfactant Interaction on Magnesite Rock Flotation*, Physicochem. Probl. Miner. Process. 42, 261–269.
- CHANDRA A.P., GERSON A.R., 2009, *A Review of the Fundamental Studies of the Copper Activation Mechanisms for Selective Flotation of the Sulfide Minerals, Sphalerite and Pyrite*, Adv. Colloid Interf. Sci. 145, 97–110.
- EKMEKCI Z., DEMIREL H., 1997, *Effect of Galvanic Interaction on Collectorless Flotation Behaviour of Chalcopyrite and Pyrite*, Int. J. Miner. Process., 52, 31–48.
- FOTHERGILL L.A., FOTHERGILL J.E., 1970, *Thiol and Disulphide Contents of Hen Ovalbumin C - Terminal Sequence and Location of Disulphide Bond*, Biochem. J. 116, 555–561.
- GULER T., 2012, *Galena oxidation in alkaline condition*, 13th International Mineral Processing Symposium, Bodrum, Turkey, 239–246.
- GULER T., ŞAHBUDAK K., ÇETINKAYA S., AKDEMİR U., 2013, *An Electrochemical Study on Pyrite-Ovalbumin Interaction in Relation to Flotation*, Trans. Nonferrous Met. Soc. China, accepted for publication.
- JANSSON E., TENGVALL P., 2004, *Adsorption of Albumin and IgG to Porous and Smooth Titanium*, Colloids Surf. B, 35, 45–51.
- JIANG C.L., WANG X.H., PAREKH B.K., LEONARD J.W., 1998, *The Surface and Solution Chemistry of Pyrite Flotation with Xanthate in the Presence of Iron Ions*, Coll. Surf. A: Physicochem. Eng. Aspects, 136, 51–62.
- KOCABAG D., GULER T., 2008, *A Comparative Evaluation of the Response of Platinum and Mineral Electrodes in Sulfide Mineral Pulps*, Int. J. Miner. Process. 87, 51–59.
- LIU J.S., WANG Z.H., LI B.M., ZHANG Y.H., 2006, *Interaction between Pyrite and Cysteine*, Trans. Nonferrous Met. Soc. China, 16, 943–946.
- MARUYAMA T., MATSUSHITA H., SHIMADA Y., KAMATA I., HANAKI M., SONOKAWA S., KAMIYA N., GOTO M., 2007, *Proteins and Protein-Rich Biomass as Environmentally Friendly Adsorbents Selected for Precious Metal Ions*, Envir. Sci. Technol., 41, 1359–1364.
- NAKANISHI K., SAKIYAMA T., IMAMURA K., 2001, *On the Adsorption of Proteins on Solid Surfaces, a Common but very Complicated Phenomenon*, J. Biosci. Bioeng. 91, 233–244.
- NAVA J.L., OROPEZA M.T., GONZÁLEZ I., 2002, *Electrochemical Characterisation of Sulfur Species Formed During Anodic Dissolution of Galena Concentrate in Perchlorate Medium at pH 0*, Electrochim. Acta, 47, 1513–1525.
- PARIDA S.K., DASH S., PATEL S., MISHRA B.K., 2006, *Adsorption of Organic Molecules on Silica Surface*, Adv. Colloid Interf. Sci. 121, 77–110.
- PENG Y., WANG B., GERSON A., 2012, *The Effect of Electrochemical Potential on the Activation of Pyrite by Copper and Lead Ions during Grinding*, Int. J. Miner. Process. 102–103, 141–149.

- ROJAS-CHAPANA J.A., TRIBUTSCH H., 2001, *Biochemistry of Sulfur Extraction in Bio-Corrosion of Pyrite by Thiobacillus Ferrooxidans*, *Hydrometallurgy*, 59, 291–300.
- WEISENER C., GERSON A., 2000, *Cu(II) Adsorption Mechanism on Pyrite: An XAFS and XPS Study*, *Surface Interf. Analysis*, 30, 454–458.
- YING P., VIANA A.S., ABRANTES L.M., JIN G., 2004, *Adsorption of Human Serum Albumin onto Gold: A Combined Electrochemical and Ellipsometric Study*, *J. Colloid Interf. Sci.* 279, 95–99.

Received February 21, 2012; reviewed, accepted July 3, 2013

DISSOLUTION AND PRECIPITATION OF ZINC AND MANGANESE OBTAINED FROM SPENT ZINC-CARBON AND ALKALINE BATTERY POWDER

Sait KURSUNOGLU, Muammer KAYA

Eskisehir Osmangazi University, Department of Mining Engineering, Division of Mineral Processing, 26480 Eskisehir, Turkey, Tel.: +90 222 239 37 50 – Ext.: 3147, skursunoglu@ogu.edu.tr (S. Kursunoglu)

Abstract: The aim of this study was to investigate manganese and zinc recoveries from spent zinc-carbon and alkaline battery powder. The effect of sulfuric acid concentration, ascorbic acid dosage, reaction temperature and leaching time on zinc and manganese dissolutions was investigated. The optimum reductive acid leaching conditions were determined as: 3 hours, 70 °C, 0.5 M of sulfuric acid concentration, 13 g/dm³ of ascorbic acid dosage, 1/20 g/cm³ of solid/liquid ratio and 200 rpm of stirring speed. Under these conditions, dissolution efficiencies were 99.99% for Zn and 99.25% for Mn. In addition, dissolution kinetics of manganese was undertaken, and the activation energy was found to be 7.04 kJ/mol. Using 3 M NaOH as precipitating agent at room temperature, 95.35% of Zn (at pH 8) and 93.66% of Mn (at pH 10) were precipitated from the leaching solution. Under the same conditions, using 3 M KOH, precipitations of Zn and Mn were 91.63% and 96.39%, respectively. Based on the experimental results, a flowsheet of zinc and manganese recovery was proposed.

Keywords: *leaching, ascorbic acid, manganese, zinc, precipitation*

Introduction

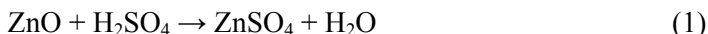
Manganese is a key element in the development of different industrial fields such as zinc-carbon and alkaline batteries, steel production, preparation of dietary additives, fertilizers, fine chemicals, non-ferro alloys as well as some medicines (Sahoo et al., 2001; Ghafarizadeh et al., 2011). The world annual production of the total manganese alloys passed 10 Tg and it will increase (Lasheen et al., 2009).

A consumption of relatively rich manganese ores has focused attention on the possible exploitation of its low grade ores and wastes. Besides, the low grade manganese ores and wastes have also generated a lot of interest as a potential source of associated metal value such as zinc, nickel, copper, vanadium, chromium and molybdenum (Ghafarizadeh et al., 2011). Therefore, several hydrometallurgical

processes have been developed for these ores and wastes such as, dissolving manganese as a soluble sulphite or nitrate, purifying a obtained liquor each by different techniques such as precipitation (as sodium or potassium hydroxide), solvent extraction and electro-winning (Salgado et al., 2003; Mantuano et al., 2004; De Souza and Tenorio, 2004; Veleso et al., 2005; De Michelis et al., 2007; Sayilgan et al., 2010).

Recently, numerous reduction methods in acid media has been investigated such as lactose reduction leaching (Veglio et al., 2000), sucrose reduction leaching (Veglio et al., 1994), corncob reduction leaching (Tian et al., 2010), oxalic acid reduction leaching (Sahoo et al., 2001; Sayilgan et al., 2009), waste newspaper reduction leaching (Biswal et al., 2011), hydrogen peroxide reduction leaching (El Hazek et al., 2006; Zhang and Cheng, 2007), ascorbic/oxalic acid reduction leaching (Sayilgan et al., 2010; Kaya and Kursunoglu, 2012) and activated carbon powder reduction leaching (Kursunoglu and Kaya, 2013).

In the present work, the zinc-carbon and alkaline battery powder is reduced to zinc sulfate and manganese sulfate by employing ascorbic acid in sulfuric acid solution. The following reactions can be considered for the dissolution of zinc oxide and manganese dioxide from zinc-carbon and alkaline battery powder. According to Eq. (1), zinc oxide fully dissolves in sulfuric acid solution. On the other hand, Eq. (2) indicates that ascorbic acid can be used to dissolve manganese dioxide in sulfuric acid solution:



The aim of this study is to investigate manganese and zinc recovery from spent battery powder by sulfuric acid leaching in the presence of ascorbic acid as a reducing agent. The effects of dissolution time, sulfuric acid concentration, ascorbic acid dosage and temperature were investigated to determine dissolution kinetics of manganese in this system. In addition, precipitation studies were conducted to reveal structure of manganese hydroxide.

Experimental

Spent AA and AAA sized zinc-carbon and alkaline batteries were collected from Eskisehir Osmangazi University battery collection bins in Turkey. The batteries were first dismantled by a laboratory hammer crusher and then dry screened by a 2 mm sieve to remove manually steel cases, plastics and papers. Spent battery cells contain 55.3% battery powder, 28.94% steel cases, 6.12% papers and 2.25% plastics. The obtained black battery powder was put into oven at $105 \pm 5^\circ\text{C}$ for 24 h. The moisture content of the battery powder was found to be 7.4%. The dried battery powder was mixed carefully to ensure the homogeneity and then ground to the required particle

size of $-88 \mu\text{m}$ for 30 min in a laboratory Bond ball mill. All leaching tests were performed with the battery powder.

A semi-quantitative analysis of the battery powder was carried out using a Philips PW-2404 X-Ray Fluorescence spectrometer (XRF) for Mn, Zn, Cl, Fe, Si, Ni, Al, S, Mg and K after neutral leaching. The mineralogical composition of the washed battery powder was determined by a Bruker AXS-D8 Advance X-Ray Diffractometer (XRD), using Cu $K\alpha$ radiation generated at 30 mA and 40 kV.

The chemical composition of the washed battery powder was 32.80% Mn, 32.92% Zn, 1.29% Cl, 0.84% Fe, 0.62% Si, 0.54% Ni, 0.30% Al, 0.28% S, 0.27% Mg, and 0.24% K. The presence of Cl is due to ammonium chloride that is the electrolytes of zinc-carbon batteries (De Souza et al., 2001; Ferella et al., 2008). Based on the XRD analysis (Fig. 1) the major phases in the washed battery powder were manganese oxides (MnO_2 and Mn_3O_4), simonkolleite ($\text{Zn}_5(\text{OH})_8\text{Cl}_2 \cdot \text{H}_2\text{O}$), graphite (C) and zinc oxide (ZnO).

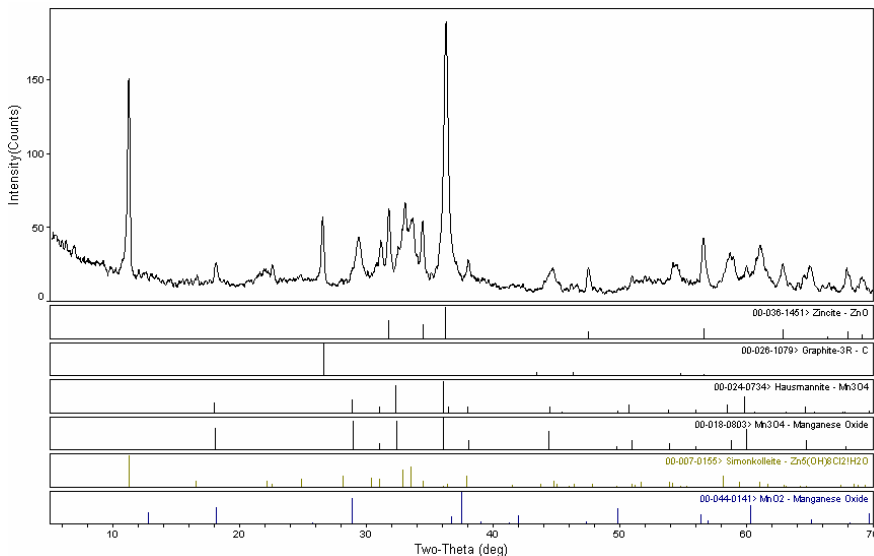


Fig. 1. XRD pattern of washed battery powder

Before reductive acid leaching tests, neutral leaching tests were performed in a 250 cm^3 Erlenmeyer flasks at a constant stirring speed of 200 rpm. The temperature was maintained at $60 \text{ }^\circ\text{C}$. The neutral leaching was carried out at solid/liquid ratio of $1/20 \text{ g/cm}^3$ and leaching time was 3 hours. After neutral leaching, the final solution pH was measured between 8.7 and 9.0 using a digital pH-meter (Hach, 40d).

In reductive acid leaching tests the battery powder was leached using ascorbic acid as a reducing agent in sulfuric acid solution. The 250 cm^3 Erlenmeyer flasks were dipped in a temperature-controlled water-bath. The slurry was agitated using a magnetic stirrer (Advantec, TBS 541 PA) at 200 rpm. Glass condensers were fitted

on the Erlenmeyer flasks in order to prevent liquid evaporation. The experimental set up used in experiments is shown in Fig. 2.

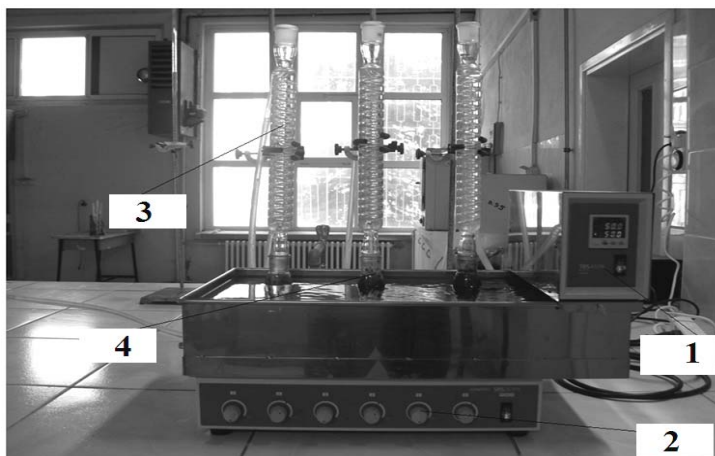


Fig. 2. Experimental set-up. 1 – temperature controlled water bath, 2 – stirring speed controller, 3 – glass condenser, 4 – 250 cm³ Erlenmeyer flask

After the reductive acid leaching step, selective precipitation tests were carried out at room temperature in a 1 dm³ beaker under constant stirring by a magnetic stirrer. A solution of 3 M NaOH or KOH was added slowly to the leach solution to increase the pH up to 11. The pH of the solution was controlled during precipitation test. A 5 cm³ sample was withdrawn at determined pH values, and then the samples were diluted with distilled water by 1:100. Zinc and manganese concentrations in the diluted solutions were determined by an Atomic Absorption Spectrometer (AAS). At the end of the precipitation, the solution in the beaker was filtered and the solid residue remained in the filter paper was dried in an oven at 105 °C for 24 hours. The dried solid residue was analyzed by the SEM-EDX to display its structure.

Results and discussion

Preliminary leaching tests

In order to determine the effect of sulfuric acid concentration on the zinc and manganese dissolution, the preliminary leaching tests were carried out at different sulfuric acid concentrations (0.05-3 M), a solid/liquid ratio of 1/20 g/cm³, stirring speed of 200 rpm and leaching temperature of 70°C for 3 hours leaching time in the absence of a reducer. The results obtained are given in Fig. 3. It shows that zinc dissolution increased significantly with increasing sulfuric acid concentration up to 0.15 M, and then gradually increased after that point. It can be seen that 98.25% of

zinc was dissolved in 0.5 M sulfuric acid concentration and thereafter remained constant.

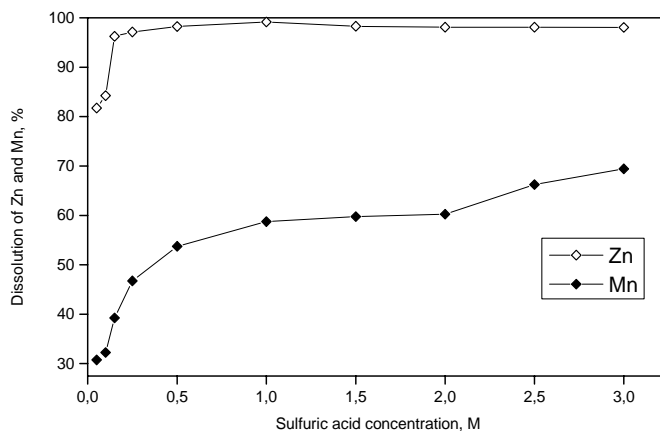


Fig. 3. Effect of acid concentration on dissolution of zinc and manganese (70 °C, 1/20 g/cm³, 200 rpm and 3 hours)

Manganese dissolution gradually increased with increasing sulfuric acid concentration. The maximum manganese dissolution at 3 M sulfuric acid concentration was found to be 69.42%. These results showed that sulfuric acid concentration was very effective on dissolution of zinc and manganese from zinc-carbon and alkaline battery powder, which is consistent with the results of previous studies (El-Nadi et al., 2007; Sayilgan et al., 2009; Gega et al., 2011). In order to dissolve zinc and manganese, ascorbic acid was used as a reducing agent to improve manganese dissolution. For this reason and environmental considerations, low sulfuric acid concentrations were chosen for the subsequent reductive acid leaching tests.

Reductive acid leaching tests

The effect of ascorbic acid dosage on the dissolution of manganese from zinc-carbon and alkaline battery powder was carried out at different ascorbic acid dosages (10-15 g/dm³) using 0.5M sulfuric acid concentration, at 70 °C, stirring speed of 200 rpm, solid/liquid ratio of 1/20 g/cm³ for 3 hours of leaching time. Figure 4 shows that the manganese dissolution increased with increasing ascorbic acid dosage. A 13 g/dm³ of ascorbic acid dosage was sufficient to leach almost all manganese from zinc-carbon and alkaline battery powder. After 13 g/dm³ of ascorbic acid dosage, manganese dissolution increased slightly remaining almost constant. There were small increases in the manganese dissolution values when the leaching tests were performed up to 15 g/dm³ ascorbic acid dosage.

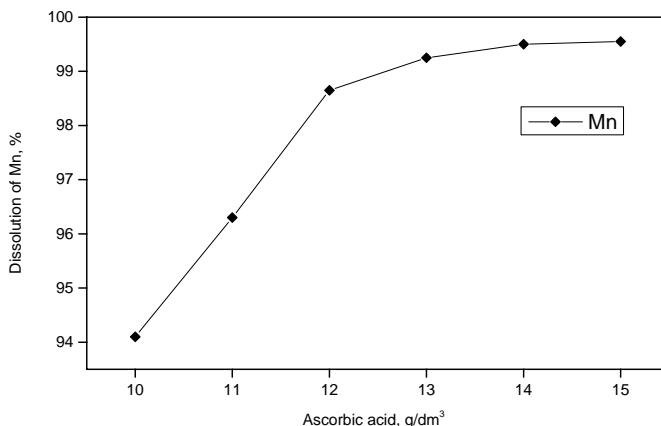


Fig. 4. Effect of ascorbic acid on dissolution of manganese (0.5 M sulfuric acid concentration, 70 °C, 200 rpm, 1/20 g/cm³ and 3 hours)

The effect of sulfuric acid on dissolution of zinc from zinc-carbon and alkaline battery powder was studied using 13 g/dm³ of ascorbic acid dosage, at 70 °C, stirring speed of 200 rpm, solid/liquid ratio of 1/20 g/cm³ for 3 hours of leaching time. Figure 5 shows that zinc dissolution increased with an increased sulfuric acid concentration up to 0.5 M and then remained constant. The maximum reached value of Zn dissolution was 99.99%.

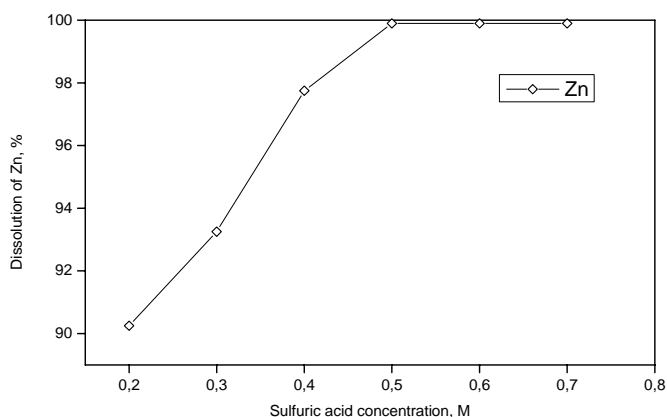


Fig. 5. Effect of sulfuric acid concentration on dissolution of zinc (13 g/dm³ of ascorbic acid dosage, 70 °C, 200 rpm, 1/20 g/cm³ and 3 hours)

Effect of solid/liquid ratio

Dissolution of zinc and manganese from zinc-carbon and alkaline battery powder by 0.5 M sulfuric acid concentration, 13 g/dm³ of ascorbic acid dosage, at 70 °C, stirring

speed of 200 rpm for 3 hours leaching time was tested by varying the solid/liquid ratios (1/20, 1/16, 1/10 and 1/5), as given in Fig. 6. Zinc and manganese dissolution significantly decreased with increasing solid/liquid ratio. When the solid/liquid ratio was lower than 0.10, leaching of zinc and manganese significantly increased, since most of zinc and manganese were leached into the solution to form ZnSO_4 and MnSO_4 . The highest dissolutions were found at solid/liquid ratio of 0.05 ($1/20 \text{ g/cm}^3$).

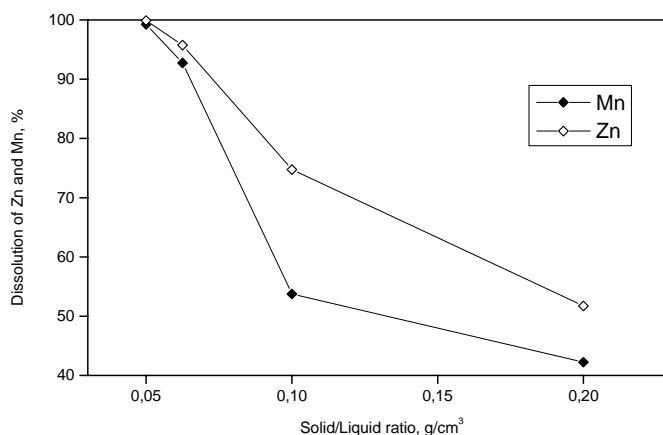


Fig. 6. Effect of solid/liquid ratio on dissolution of zinc and manganese (0.5 M sulfuric acid concentration, 13 g/dm^3 of ascorbic acid dosage, $70 \text{ }^\circ\text{C}$, 200 rpm and 3 hours)

Effects of leaching time and temperature

To determine the effects of time and temperature on dissolution of zinc and manganese from zinc-carbon and alkaline battery powder more accurately, leaching experiments were performed under constant conditions of 0.5 M sulfuric acid concentration, 13 g/dm^3 of ascorbic acid dosage, $1/20 \text{ g/cm}^3$ of solid/liquid ratio, 200 rpm stirring speed and $20\text{-}70 \text{ }^\circ\text{C}$ temperature range. The results obtained are shown in Fig. 7. Dissolution of manganese increased with increasing temperature. The maximum manganese dissolution values were 92.06% at $20 \text{ }^\circ\text{C}$, 98% at $50 \text{ }^\circ\text{C}$ and 99.75% at $70 \text{ }^\circ\text{C}$.

Zinc dissolution slightly increased with increasing leaching time. Zinc was almost fully dissolved at $70 \text{ }^\circ\text{C}$ for 3 hours leaching time. Dissolution behavior of zinc and manganese showed a similar trend for all temperatures and leaching times. Figure 7 shows that temperature and leaching time are important factors that affect the leaching process. After one hour of leaching at $20 \text{ }^\circ\text{C}$ in 0.5 M sulfuric acid solution using 13 g/dm^3 of ascorbic acid, dissolutions of manganese and zinc were 91.2% and 90.76%, respectively. However, when leaching temperature and time were $70 \text{ }^\circ\text{C}$ and 3 hours, dissolution of zinc and manganese increased to 99.99% and 99.25%, respectively.

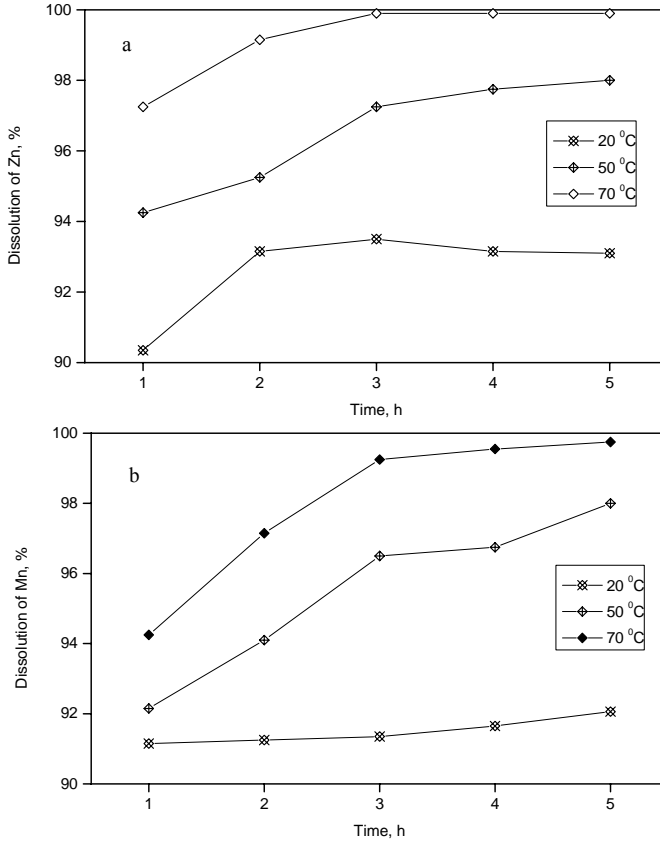


Fig. 7. Effect of leaching time on Zn and Mn dissolution at different leaching temperature (0.5 M sulfuric acid concentration, 13 g/dm³ of ascorbic acid dosage, 200 rpm, 1/20 g/cm³)

Kinetics of manganese from zinc-carbon and alkaline battery powder

Kinetics data collected at different temperatures for 0.5 M sulfuric acid, 13 g/dm³ of ascorbic acid dosage, 200 rpm of stirring speed, 1/20 of solid/liquid ratio for 3 hours leaching time were evaluated according to shrinking core model (Sohn and Wadsworth, 1979; Levenspiel, 1999). To determine chemical rate constant (k_p) of manganese dissolution in the temperature range of 20–70 °C (Fig. 8), the best linear relationship for manganese was obtained from equation:

$$1 - \frac{2}{3}x - (1-x)^{\frac{2}{3}} = k_p t, \quad (3)$$

where k_p is chemical rate constant (cm·min⁻¹), t time (min), x fraction reacted of manganese.

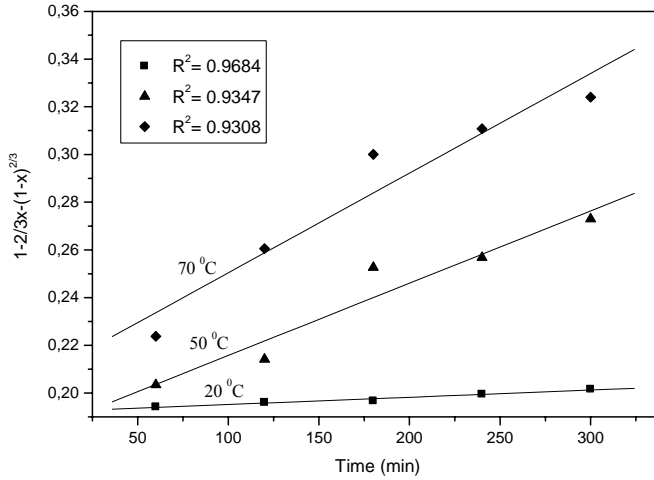


Fig. 8. Plot of $1 - \frac{2}{3}x - (1-x)^{\frac{2}{3}}$ versus time. R^2 is determination coefficient

The Arrhenius plot (Fig. 9) was constructed using the experimentally determined $\ln k_p$ values as a function of the reciprocal of leaching temperature ($1000/T$) as shown in Fig. 9. The activation energy for manganese dissolution was calculated to be 7.04 kJ/mol, which is consistent with the values of activation energy reported for diffusion-controlled leaching process (Habashi, 1969).

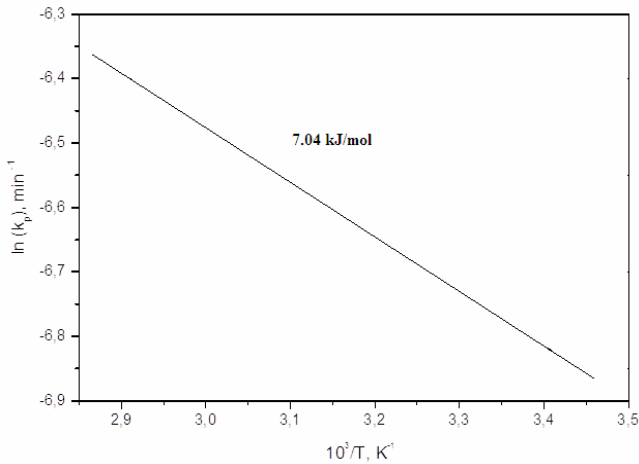


Fig. 9. The Arrhenius plot for manganese dissolution

Comparison of previous studies with present study

Table 1 compares the data between this paper and previous studies reported on the reductive acid leaching of zinc and manganese from zinc-carbon and alkaline battery powders or manganese dioxide ores. It is clear that present work has some advantages over other studies. For instance, the sulfuric acid and reductants concentrations and leaching temperature are lower and manganese dissolution is relatively higher than in previous studies.

Table 1. Comparison of the conditions and dissolutions of recent and present studies

	Battery/Ore Type	Leaching agents	Temperature (°C)	Leaching time (min)	S/L ratio	Dissolution of Zn (%)	Dissolution of Mn (%)
Sahoo et al. (2001)	Manganese dioxide ore	0.543 M H ₂ SO ₄ + 30.6 g/dm ³ oxalic acid	85	105	1/20	-	98.4%
Ferella et al. (2006)	Zn-C and Alkaline	1.8 M H ₂ SO ₄ + 59.4 g/dm ³ oxalic acid	80	300	1/20	100%	70%
Sayilgan et al. (2009)	Zn-C and Alkaline	+30 stoichiometric ratio H ₂ SO ₄ + -30 stoichiometric ratio oxalic acid	45	180	1/10	Full	91.2%
Sayilgan et al. (2010)	Zn-C and Alkaline	stoichiometric ratio H ₂ SO ₄ + (1.7 M) stoichiometric ratio ascorbic acid	45	180	1/15	Full	97%
Tian et al. (2010)	Manganese dioxide ore	1.9 M H ₂ SO ₄ + 3 g corncob	85	60	1/10	-	92.8%
Present Study	Mixed AA-AAA sized	0.5 M H ₂ SO ₄ + 13g/dm ³ ascorbic acid	70	180	1/20	99.99%	99.25%

Precipitation tests

Selective precipitation was previously reported by Veleso et al. (2005), De Michelis et al. (2007) and Poravazi et al. (2011) to separate metals present in spent batteries. In the current study, the precipitation tests were conducted using aqueous liquor obtained under the optimum test conditions found in the study of the reductive acid leaching tests (Table 2).

Table 2. Optimum reductive acid leaching test conditions

Sulfuric acid concentration (M)	Ascorbic acid dosage (g/dm ³)	Temperature (°C)	Time (hour)
0.5	13	70	3

Precipitations of zinc and manganese at different pH values adjusted with NaOH or KOH are given in Fig. 10. It shows that precipitation ratio of zinc and manganese increased with increasing pH value. The zinc precipitation increased from about 20-30% to near-complete precipitation with increasing solution pH from 6 to 8. The manganese precipitation gradually increased with increasing pH value up to pH 8. Nearly all manganese precipitation was achieved around pH 10 for both NaOH and KOH, which is consistent with previous study (Veleso et al., 2005). These results indicate that zinc and manganese can be selectively separated by adjusting solution of pH using NaOH or KOH (Zhang and Cheng, 2007).

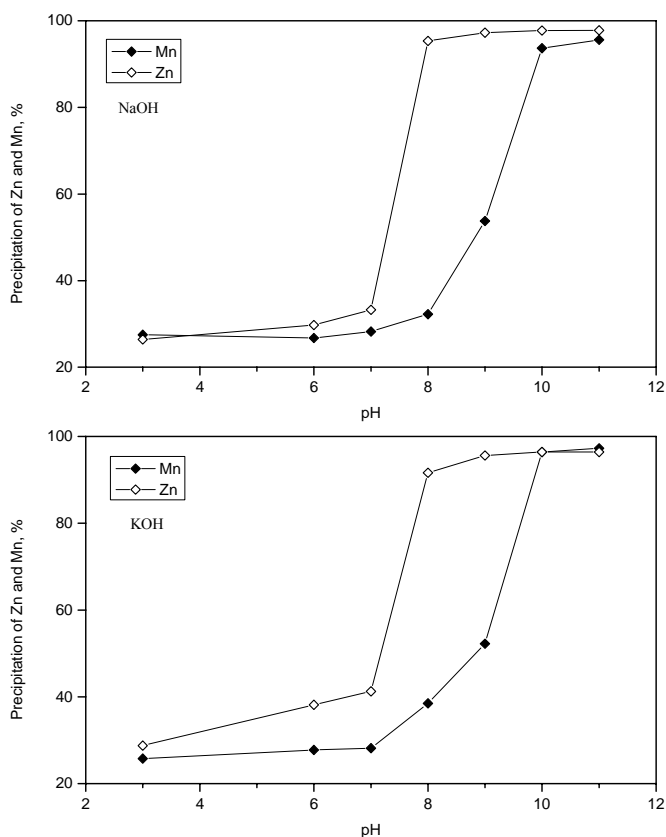


Fig. 10. Precipitation of Mn and Zn in the presence of NaOH and KOH at different pH's

The SEM-EDX images of the precipitated manganese hydroxide are given in Fig. 11. The manganese hydroxide particles precipitated by NaOH were heterogeneous in size and had a fractured structure. This may be resulted from hydrogen embrittlement.

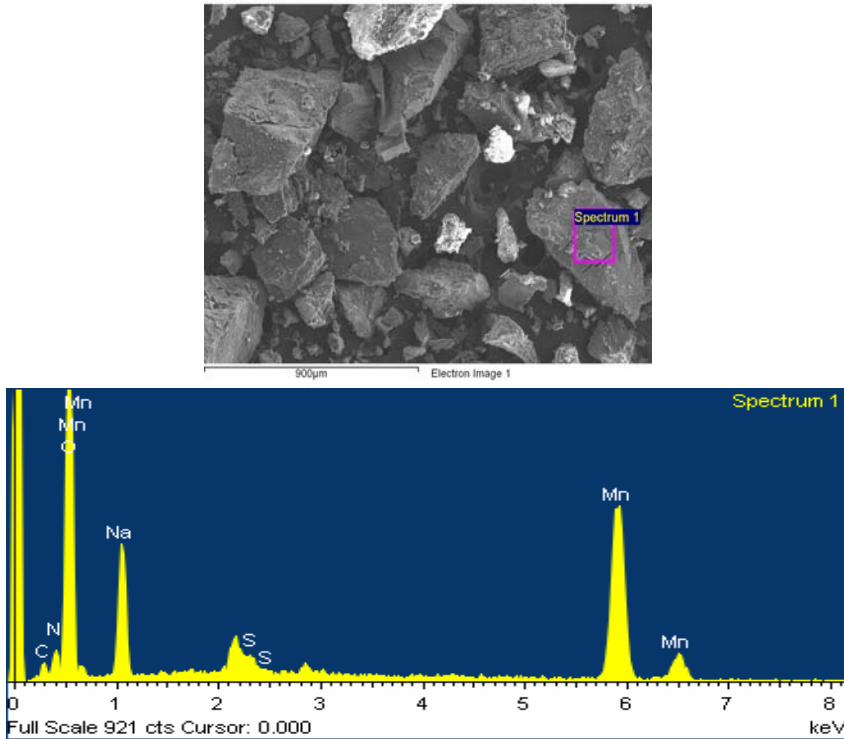


Fig. 11. SEM-EDX images of precipitated manganese hydroxide

Table 3. EDX analysis

Element	Weight (%)	Atomic (%)
C	4.57	8.13
N	7.53	11.49
O	40.45	54.09
Na	14.23	13.24
S	0.40	0.27
Mn	32.83	12.78
Totals	100	

For the spot indicated as spectrum 1, EDX analysis was performed and the results are given in Table 3. It shows that manganese and oxygen contents were detected in that point, indicating the presence of large amount of manganese hydroxide. The EDX

analysis also indicated a small amount of sulfur in the sample. This may originate from the elemental sulfur, which starts to form and produce a layer around particles during the reductive acid leaching process.

Leaching and precipitation conditions and proposed process flowsheet

The optimum leaching and precipitation variables are given in Table 4. Figure 12 shows the proposed flowsheet by referring our laboratory experimental tests. The results show that it was possible to dissolve 99.99% of zinc and 99.25% of manganese from the battery powder. In the precipitation stage, zinc and manganese sulfates were precipitated in as zinc and manganese hydroxides. It was possible to precipitate more than 95% of zinc at pH value of 8 and 96% of manganese at pH value of 10.

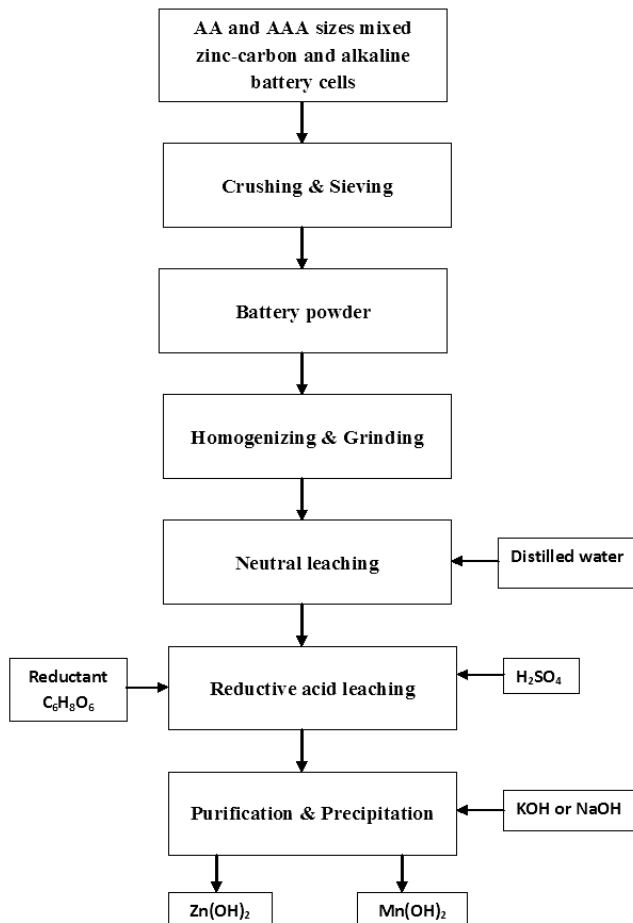


Fig. 12. Hydrometallurgical flowsheet proposed for zinc and manganese recovery zinc-carbon and alkaline battery cells

Table 4. The optimum leaching and precipitation experimental laboratory conditions

Sulfuric acid concentration (M)	Ascorbic acid dosage (g/dm ³)	Temperature (°C)	Time (hour)	Precipitation stage	pH	pH
				NaOH or KOH concentration (M)	Zn	Mn
0.5	13	70	3	3	8	10

Conclusions

In this study, simultaneous zinc and manganese recoveries from zinc-carbon and alkaline battery powder were studied. A hydrometallurgical flowsheet was developed for recovery of zinc and manganese from spent AA and AAA sized zinc-carbon and alkaline battery cells. The optimum reductive acid leaching conditions were determined as 3 hours of leaching time, 70 °C of leaching temperature, 0.5 M of sulfuric acid concentration, 13 g/dm³ of ascorbic acid dosage, 1/20 g/cm³ of solid/liquid ratio and 200 rpm of stirring speed. Under these conditions, the dissolution efficiencies were 99.99% for Zn and 99.25% for Mn. An activation energy of 7.04 kJ/mol was determined for manganese dissolution, which indicates that this is a diffusion-controlled leaching process. Using 3 M NaOH as precipitating agent at room temperature, a 95.35% of Zn (pH 8) and 93.66% of Mn (pH 10) were precipitated from the leaching solution. Under the same conditions, using 3 M KOH, precipitations of Zn and Mn were 91.63% and 96.39%, respectively.

Acknowledgements

This work was supported by Research Projects Funding Unit of Eskisehir Osmangazi University (Project no: ESOGU BAP 2009/15018) in Eskisehir, Turkey.

References

- BISWAL A., SANJAY K., GHOSH M.K., SUBBAIAH T., MISHRA B.K., 2011. *Preparation and characterization of electrolytic manganese dioxide (EMD) was prepared from manganese cake-A by product of manganese nodule processing*. Hydrometallurgy, Hydrom-03419.
- DE MICHELIS I., FERELLA F., KARAKAYA E., BEOLCHINI F., VEGLIO F., 2007. *Recovery of zinc and manganese from alkaline and zinc-carbon spent batteries*. J. Power Sources 172, 975–983.
- DE SOUZA C.C.B.M., TENORIO J.A.S., 2004. *Simultaneous recovery of zinc and manganese dioxide from household alkaline batteries through hydrometallurgical processing*. J. Power Sources 136, 191–196.
- EL-NADI Y.A., DAOUD J.A., ALY H.F., 2007. *Leaching and separation of zinc from the black paste of spent MnO₂-Zn dry cell batteries*. J. Hazard. 143, 328–334.
- EL HAZEK M.N., LASHEEN T.A., HELAL A.S., 2006. *Reductive leaching of manganese from low grade Sinai ore in HCl using H₂O₂ as reductant*. Hydrometallurgy 84, 187–191.
- FERELLA F., DE MICHELIS I., PAGNANELLI F., BEOLCHINI F., FURLANI G., NAVARRA M., VEGLIO F., TORO L., 2006. *Recovery of zinc and manganese from spent batteries by different leaching systems*. Acta Metallurgica Slovaca 12, 95–104.
- GEGA J., WALKOWIAK W., 2011. *Leaching of zinc and manganese from used up zinc-carbon batteries using aqueous sulfuric acid solutions*. Physicochem. Probl. Miner. Process. 46, 155–162.

- GHAJARIZADEH B., RASHCHI F., VAHIDI E., 2011. *Recovery of manganese from electric arc furnace dust of ferromanganese production units by reductive leaching*. Minerals Engineering, 24, 174-176.
- HABASHI F., 1969. *Principles of Extractive Metallurgy*, Vol. 1. Gordon & Breach, New York.
- KAYA M., KURSUNOGLU S., 2012. *Dissolution of Mixed Zinc-Carbon and Alkaline Battery Powders in Sulphuric Acid Using Ascorbic/Oxalic Acid as a Reductant*, [in:] EPD Congress 2012 (eds. L. Zhang, J. A. Pomykala and A. Ciftja), John Wiley & Sons, Inc., Hoboken, NJ, USA. doi 10.1002/9781118359341.ch32.
- KURSUNOGLU S., KAYA M., 2013. *Recovery of Manganese from Spent Batteries Using Activated Carbon Powder as Reductant in Sulfuric Acid Solution*. Asian Journal of Chemistry, 25, 1975-1980.
- LASHEEN T. A., EL-HAZEK M. N., HELAL A. S., EL-NAGAR W., 2009. *Recovery of manganese using molasses as reductant in nitric acid solution*. Int. J. Miner. Process. 92, 109-114.
- LEVENSPIEL O., 1972. *Chemical Reaction Engineering*, 3rd ed., Wiley, New York, NY.
- MANTUANO D.P., DORELLA G., ELIAS R.C.A., MANSUR M.B., 2006. *Analysis of a hydrometallurgical route to recover base metals from spent rechargeable batteries by liquid-liquid extraction with Cyanex 272*, J. Power Sources 159, 1510-1518.
- PROVAZI K., CAMPOS B.A., ESPINOSA D.C.R., TENORIO J.A.S., 2011. *Metal separation from mixed types of batteries using selective precipitation and liquid-liquid extraction techniques*. Waste Management 31, 59-64.
- SALGADO A.L., VELOSO A.M.O., PEREIRA D.D., GONTIJO G.S., SALUM A., MANSUR M.B., 2003. *Recovery of zinc and manganese from spent alkaline batteries by liquid-liquid extraction with Cyanex 272*. J. Power Sources 115, 367-373.
- SAYILGAN E., KUKRER T., FERELLA F., AKCIL A., VEGLIO F., KITAS M., 2009. *Reductive leaching of manganese and zinc from spent alkaline zinc-carbon batteries in acid media*. Hydrometallurgy 97, 73-79.
- SAYILGAN E., KUKRER T., YIGIT N.O., CIVELEKOGLU G., KITAS M., 2010. *Acid leaching and precipitation of zinc and manganese from spent battery powders using various reductants*. J. Hazard. 173, 137-143.
- SAHOO R.N., NAIK P.K., DAS S.C., 2001. *Leaching of manganese from low-grade manganese ore using oxalic acid as reductant in sulfuric acid solution*. Hydrometallurgy 62, 157-163.
- SOHN H. Y., WADSWORTH M. E., *Rate processes of extractive metallurgy*, Plenum, New York and London, 1979, 136-151.
- TIAN X., WEN X., YANG C., LIANG Y., PI Z., WANG Y., 2010. *Reductive leaching of manganese from low-grade manganese dioxide ores using corncob as reductant in sulfuric acid solution*. Hydrometallurgy 100, 157-160.
- VEGLIO F., TORO L., 1994. *Fractional factorial experiments in the development of manganese dioxide leaching by sucrose in sulfuric acid solutions*. Hydrometallurgy, 36, 215.
- VEGLIO F., VOLPE I., TRIFONI M., TORO L., 2000. *Surface response methodology and preliminary process analysis in the study of manganese ore leaching by using whey or lactose in sulfuric acid solutions*. Ind. Eng. Chem. Res., 39, 2947.
- VELOSO L.R.S., RODRIGUES L.E.O.C., FERREIRA D.A., MAGALHAES F.S., MANSUR M.B., 2005. *Development of a hydrometallurgical route for the recovery of zinc and manganese from spent alkaline batteries*. J. Power Sources 152, 295-302.
- ZHANG, W., CHENG C.Y., 2007. *Manganese metallurgy review. Part II: Manganese separation and recovery from solution*. Hydrometallurgy 89, 160-177.

Received May 5; reviewed; accepted July 4, 2013

PHYSICOCHEMICAL MECHANISMS OF MINERAL NANOPARTICLES EFFECTS ON PULMONARY GAS/LIQUID INTERFACE STUDIED IN MODEL SYSTEMS

Dorota KONDEJ*, Tomasz R. SOSNOWSKI**

* Central Institute for Labour Protection – National Research Institute, Czerniakowska 16, 00-701 Warsaw, Poland, dokon@ciop.pl

** Warsaw University of Technology, Faculty of Chemical and Process Engineering, Warynskiego 1, 00-645 Warsaw, Poland, T.Sosnowski@ichip.pw.edu.pl

Abstract: Inhaled mineral nanoparticles which are deposited on the lung surface may influence the gas/liquid barrier and the pulmonary surfactant (PS) which constitutes the vital element of the respiratory system. This research is focused on the physicochemical effects caused by selected clay nanoparticles (bentonite, halloysite, montmorillonites) interacting with PS and changing its original surface activity. Using three measuring methods (pulsating bubble technique, Langmuir balance and drop shape analysis), we demonstrated the influence of different mineral nanoparticles on the dynamic surface tension of animal-derived PS material (Survanta[®]) and main surfactant phospholipid (DPPC). The results which are dependent on material properties and concentration allow to hypothesize possible pathways of health effects from inhalation of mineral nanoparticles. This may help to set the guidelines in defining occupational safety standards and methods of protection of the respiratory system against inhaled mineral dusts.

Keywords: *inhalation, nanoparticles, gas/liquid interface, dynamic surface tension*

Introduction

Inhalation of dusts formed of mineral materials may contribute to respiratory symptoms and undesired health effects. Aerosol deposition in the respiratory system is a complex problem governed by airflow pattern and particle dynamics in a complicated geometrical structure of the upper airways and bronchial tree (Zhang et al., 2003; Rostami, 2009; Sosnowski, 2011; Longest and Holbrook, 2012). Depending on size and shape, inhaled particles can penetrate to deep lungs with different efficiency. It is recognized that compact (spherical-like) particles larger than 10 μm have a low chance to get to the bronchial tree as they are primarily deposited in the

mouth and throat (e.g. Sosnowski et al., 2006). On the other hand, elongated (needle-like) particles, such as of asbestos, easily penetrate deeply into lungs even if their length exceeds 20 μm . It is due to reorientation of needles during flow via curved airways and narrowings, which allows to avoid the deposition in upper airways and bronchi (Zhang et al., 1996). Health effects from inhaled nano-sized or nano-structured particles attract much attention nowadays (Oberdorster, 2001; Maynard and Kuempel, 2005; Marijnissen and Gradon, 2010; Bakand et al., 2012). Due to small size and low inertia nanoparticles can be effectively transported to the pulmonary (alveolar) region with inhaled air.

Particles which are deposited in deep lungs come into contact with the pulmonary surfactant (PS) which constitutes an important component of the respiratory system (Zuo et al., 2008; Rugonyi et al, 2008). PS has the extraordinary dynamic surface activity which is expressed during variations of pulmonary gas-liquid surface area caused by breathing. PS is responsible for a significant reduction of the surface tension during surface contraction (related to air exhalation from the lungs), what reduces the effort of lung inflation. Surface tension hysteresis observed during periodic interfacial area variations is important for the stability of the alveolar network of the lungs. In addition, the local variations of the surface tension result in Marangoni effects and superficial flows - these phenomena are important for the mass transfer in the respiratory system (Gradoń and Podgorski, 1989; Sosnowski et al., 1998). All the mentioned facts indicate the necessity of maintaining the specific composition and surface activity of the pulmonary surfactant, and, accordingly, any notable disturbances of surfactant quality should be expected as harmful to the lungs (Sosnowski et al, 2000).

Within this work we focus on mechanisms of direct physicochemical interactions between selected inhalable mineral nanoparticles and the pulmonary surfactant, which can be studied using selected *in vitro* experimental systems.

Materials and Methods

Nanoparticles

Five types of mineral nanoparticles have been tested in this study. All selected nanopowders are commercially available aluminosilicates (Sigma Aldrich) being used as mineral nanofillers in polymer industry. They are of natural origin, however they are standardized regarding the purity, and some of them are chemically modified to produce surface hydrophobicity required in technological applications. The list of used nanomaterials is given in Table 1, together with the indications of nanoparticle morphology, characteristic size and the specific surface area, which were determined in the separate study (Kondej and Sosnowski, 2013).

Table 1. Mineral nanoparticles used in the study

Particle designation	Material name, morphology and characteristic particle size	Specific surface area [m^2/g]
HN	HALLOYSITE Morphology: needles (nanotubes), diameter <100 nm, length - up to a few μm	25.5
PGV	BENTONITE Morphology: nanoplates, thickness < 200 nm	67.3
I.28.E	MONTMORILLONITE modified by trimethyl stearyl ammonium: Morphology: flakes, thickness < 200 nm	9.6
I.30.E	MONTMORILLONITE modified by octadecylamine Morphology: flakes, thickness < 200 nm	14.0
I.31.PS	MONTMORILLONITE modified by octadecylamine and aminopropyltriethoxysilane Morphology: flakes, thickness < 200 nm	13.5

Pulmonary surfactants

Two types of pulmonary surfactant models have been used:

a) pure 1,2-dipalmitoyl-sn-glycero-3-phosphocholine (DPPC – Sigma Aldrich) – the predominant natural phospholipid found in the natural PS. It is recognized as a key surface-active component of the pulmonary fluid.

b) Survanta[®] (Abbott Laboratories, France) – an animal-derived standardized whole PS which is used to treat surfactant deficiencies in humans (surfactant replacement therapy – e.g. Lam et al., 2005; Engle et al., 2008).

Measuring methods and procedures

Experiments have been done using three independent techniques allowing to study different aspects of the influence of mineral nanoparticles on the interfacial activity of model pulmonary surfactants. A Langmuir-Wilhelmy film balance (model Mini – KSV, Finland) was used to study surface-tension effects induced by nanoparticles interacting with PS phospholipid at air-liquid interface. The measurements were done for gradually decreased interfacial area mimicking the behavior of the lung surface during air exhalation. The gas-liquid area was compressed by two barriers sliding in the predefined manner on the top of the saline (0.9%) covered by DPPC monolayer – a model of physiological lung fluid, Figure 1.

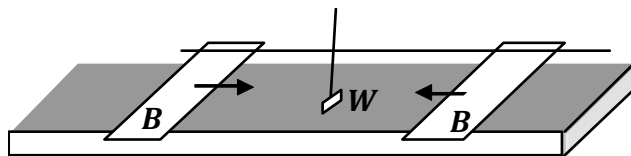


Fig. 1. The schematic of the Langmuir-Wilhelmy film balance. Two movable barriers (*B*) compress the interface while the surface pressure (eq. 2) is measured by Wilhelmy plate (*W*) connected to an electronic sensor

To study the effects of nanoparticles on the surfactant phospholipid, the liquid phase was prepared as a suspension of the known amounts of particles determined by calculations of lung deposition of dusts inhaled at occupational environments (Kondej and Sosnowski, 2013). Several nanoparticles concentrations ($0.1\text{--}1\text{ mg/cm}^3$) in the saline were used in measurements conducted at physiological temperature ($37 \pm 0.5\text{ }^\circ\text{C}$).

A more realistic representation of the pulmonary surfactant system is available in the oscillating bubble tensiometry (PBS device - Electronics Corp., USA). These experiments rely on measuring a pressure difference Δp during continuous pulsations of an air bubble (diameter $0.8\text{--}1.1\text{ mm}$) submerged in Survanta[®] (concentration: 1.25 mg/cm^3 ; volume: 30 mm^3). The pulsation were done at the frequency corresponding to the breathing rate (15 min^{-1}). The instantaneous, dynamic surface tension at the interface of a bubble with radius r , is found from the Young-Laplace equation:

$$\sigma = \frac{r\Delta p}{2} \quad (1)$$

The experimental system and measuring procedure have been described in details recently (Kondej and Sosnowski, 2013). Nanoparticles concentrations used in this study were similar to the ones tested in the Langmuir-Wilhelmy balance experiments. The temperature of measurements was set to $37 \pm 0.5\text{ }^\circ\text{C}$.

The third method used in this study to characterize the physicochemical interactions between nanoparticles and the pulmonary surfactant was the drop shape analysis (DSA – using the equipment made at the Faculty of Chemistry, Warsaw University of Technology). The dynamic surface tension of tested suspensions was determined in this case from the pending drop profile (Figure 2).

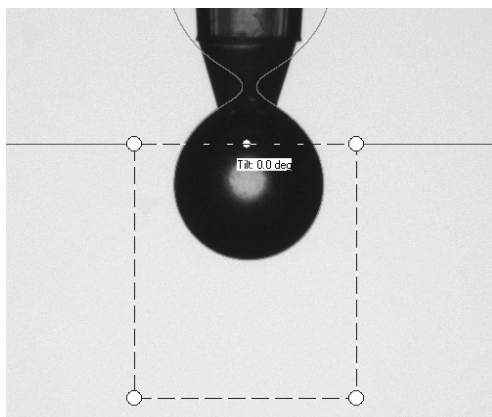


Fig. 2. An example of a picture of pending drop (volume of approximately 3 mm^3) in DSA method

This type of measurements allows to monitor the long-time evolution (up to several hours) of the dynamic surface tension, so it helps to study slow adsorption of surface-active material on a gas-liquid interface. It should be noted, however, that the system offers an incomplete analogy to the physiological system. Firstly, the experimental interface is stationary, secondly – the ratio of liquid volume to the interfacial area is much higher in the measuring system than in the real pulmonary fluid, and finally, the available observation times are much longer than a duration of a single breathing cycle. Therefore, these data can be used only as a supportive information during recognition of mechanisms by which nanoparticles interact with PS in the dynamic system. In DSA experiments we used the same concentrations of mineral nanomaterials as in the two other studies. However, due to technical limitations, the measurements were done only at room temperature (23 ± 0.5 °C) although the samples were pre-thermostated at 37 °C.

Results and data analysis

The methods of reduction of raw experimental data obtained with different techniques need additional explanation before results are presented and discussed. In all experimental systems the dynamic surface tension, σ (or surface pressure, π), is found as a function of either time, τ , or the time-dependent interfacial area, $A(\tau)$. Let us note that the surface pressure is defined as:

$$\pi = \sigma_w - \sigma \quad (2)$$

where σ_w denotes the surface tension of water (70 mN/m at 37 °C).

Univocal comparison of the dynamic surface tension evolution requires data reduction and defining some numerical indicators. For data obtained with the oscillating bubble method (an outline of a typical result is shown in Figure 3) it will be informative to find the minimum surface tension, σ_{min} , during pulsations as a measure of the highest surface activity at the tested surface oscillations. It is obvious that σ_{min} depends on the total surfactant concentration but also on its composition which governs the surface activity. For comparative purposes done in this study, when it is essential to assess the σ_{min} deviation after surfactant contact with nanomaterials, it is convenient to indicate the percent change of σ_{min} , defined as:

$$\Delta\sigma_{min\%} = \left(\frac{\sigma_{min}}{\sigma_{min}^*} - 1 \right) 100\% \quad (3)$$

where σ_{min}^* denotes the minimum surface tension of the control surfactant sample (no particles). Positive values of $\Delta\sigma_{min\%}$ indicate the increased minimum surface tension when compared to the control case, i.e. a loss of surface activity, while negative values suggest a stronger lowering of the surface tension (increased interfacial activity).

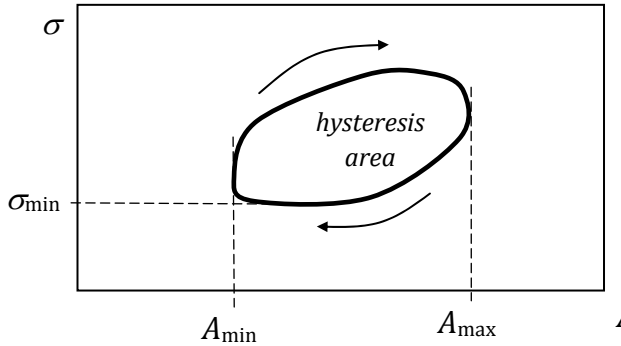


Fig. 3. A sketch of a characteristic result from oscillating bubble experiments

Another indicator of dynamic surface activity in this measurement is the size (area) of surface tension hysteresis, schematically drawn in Fig. 3. The hysteresis reflects dissipative processes during surface area cycling. It is recognized that the hysteresis for physiologically active pulmonary surfactant remains higher than in case of surfactant inactivation caused by lung diseases (Clements et al., 1961; Notter et al., 1982). The mathematical formula to find the area confined size by the σ -hysteresis loop is given by:

$$HA = \left[\int_{A_{\min}}^{A_{\max}} \sigma dA \right]_{\text{expansion}} - \left[\int_{A_{\min}}^{A_{\max}} \sigma dA \right]_{\text{contraction}} \quad (4)$$

HA should be normalized against the applied surface compression (e.g. Notter et al., 1982), however for all oscillating bubble measurements in this study, the compression was always the same ($A_{\min}/A_{\max} = 0.53$), so the additional calculation is not needed.

By analogy to eq. (3), the relative percent change of HA induced by nanoparticles added to PS can be expressed as:

$$\Delta HA_{\%} = \left(\frac{HA}{HA^*} - 1 \right) 100\% \quad (5)$$

where HA^* denotes the hysteresis area in the control surfactant sample (no particles). Here, the decrease of dynamic surface activity will be indicated by negative values of $\Delta HA_{\%}$.

Experimental results from the oscillating bubble studies were obtained for the complete pulmonary surfactant under physiological conditions (dynamic breathing-like surface pulsations). These results are the most informative, but simultaneously the most difficult to interpret on the physicochemical basis. The values of two parameters defined by eqs. (3) and (5) at nanoparticles concentration of 0.5 mg/ml is presented in Fig. 4.

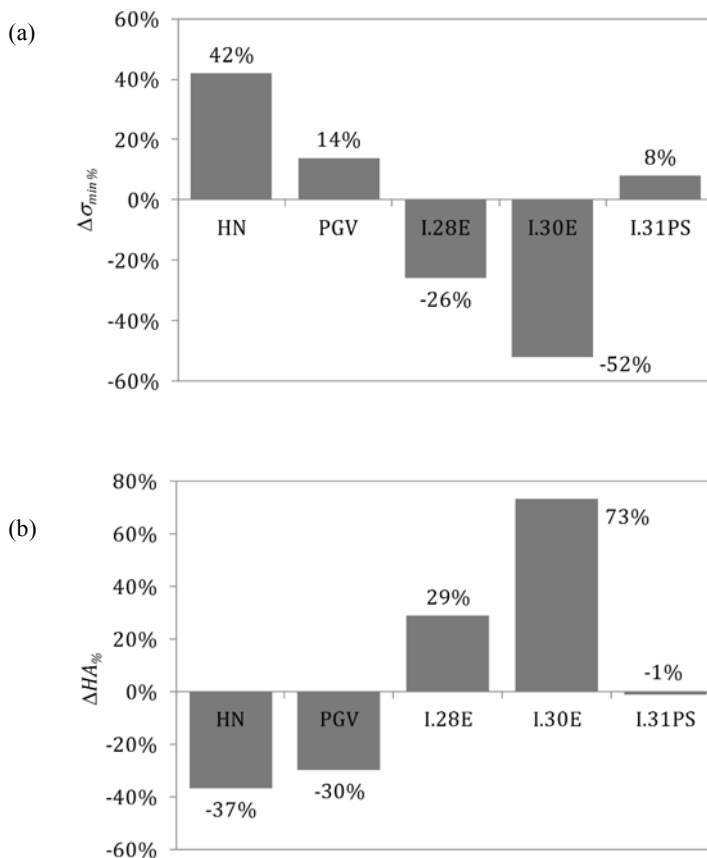


Fig. 4. Relative change of (a) – the minimum surface tension ($\Delta\sigma_{min}\%$) and (b) – the hysteresis area ($\Delta HA\%$) for different mineral nanoparticles at concentration of 0.5 mg/cm^3

It is visible that the response of the system depends on type of nanoparticles. For three kinds of minerals (HN, PGV and 1.31 PS) there is an increase of the minimum surface tension and a decrease of the surface tension hysteresis, suggesting an evident decline of the original PS surface activity. For montmorillonites 1.28E and 1.30E there is a reduction of the minimum surface tension and a simultaneous increase of the hysteresis. In this case the surface activity of the PS is changed in the opposite way than for the other mineral particles. Similar responses of model PS system can be observed for lower (down to 0.1 mg/cm^3) and higher (up to 1 mg/cm^3) dust contents, and the extent of change of discussed parameters is well correlated with nanoparticles concentration.

Studies done with the Langmuir–Wilhelmy balance support the results obtained with the oscillating bubble method. In these experiments, the compression isotherms for DPPC at 37°C were obtained - an example in the presence of bentonite

nanoparticles (PGV) is presented in Figure 5. To facilitate the comparison of all data obtained for different mineral nanoparticles at variable concentrations, we propose to derive a single parameter as an indicator of the surface tension reduction effectiveness in each tested system. Here we define MA_{30} to denote the molecular surface area at which the initial surface tension in the system is reduced by 30 mN/m (i.e. the surface pressure is increased by the same value – Figure 5). Higher values of MA_{30} indicate that smaller surface compressions are required to obtain low surface tensions, that is the interface contains a more active surfactant.

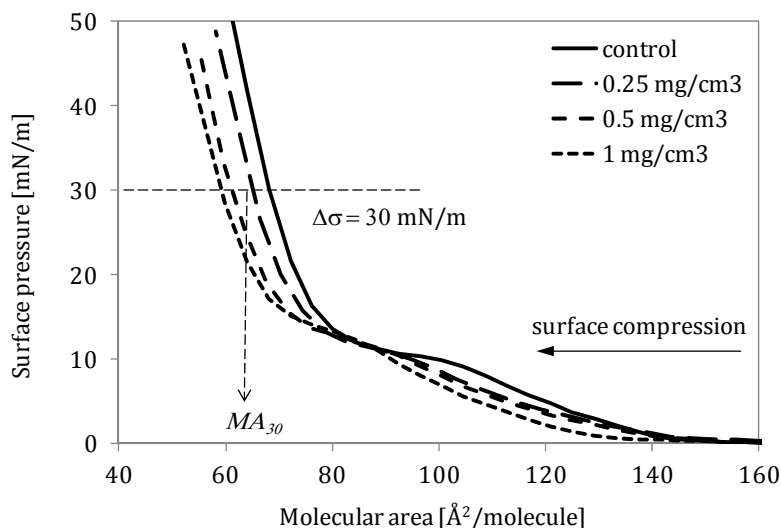


Fig. 5. Compression isotherms (37°C) for DPPC in the presence of bentonite (PGV) nanoparticles. Dashed line illustrates the meaning of MA_{30} parameter

From Fig. 5 it is visible that the compression isotherms are deformed due to surfactant interactions with the particles. It can be also seen that the phospholipid without particles exhibits the highest value of MA_{30} what means that low surface tension is attained already at a low degree of surface compression. The surface needs to be more compressed when PGV nanoparticles are added to the system.

The comparative results of MA_{30} for all tested nanoparticles at different concentrations are shown in Fig. 6.

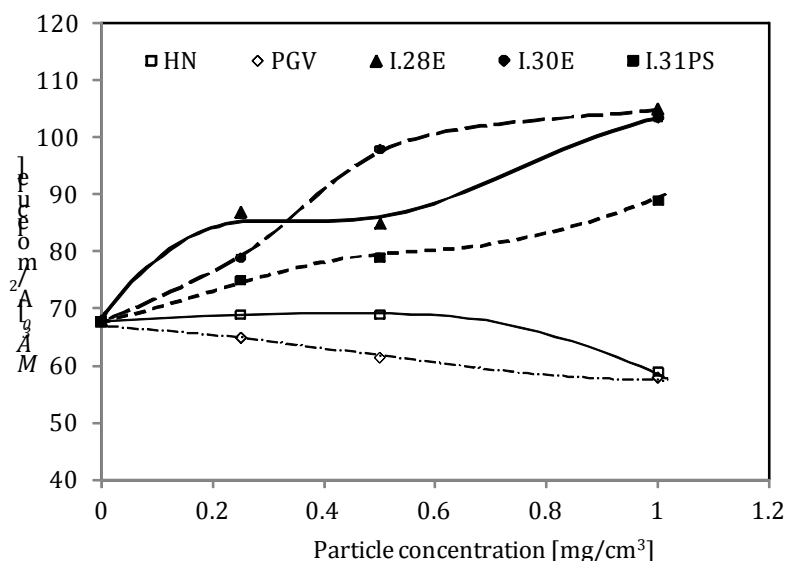


Fig. 6. The dependence of MA_{30} on particle type and concentration

In case of HN or PGV particles added to the system, the molecular area parameter is equal or smaller than for the pure phospholipid monolayer, and it implies that a higher compression of the interfacial area is required to obtain the expected low surface tension value. This reveals an impairment of DPPC surface activity by these two types of nanoparticles. On the contrary, if I.28E, I.30E and I.31PS particles are present in the system, they promote an increase of MA_{30} , suggesting an additional surface-active effect allowing to reduce surface tension at a lower interfacial compression. The mechanism of the observed effect remains unclear unless additional surface-visualization studies are done (e.g. Guzman et al. 2011). However, one can postulate that an improved surface activity observed for surface-modified montmorillonites results from an extra surface tension lowering properties of either these nanoparticles themselves or the compounds that are released (washed out) from the nanomaterials. Such conclusions correspond to the data from the oscillating bubble experiments, where also two different types of system response was found – a decrease of the surface activity by HN or PGV nanoparticles, and its moderate increment by modified montmorillonites: I.28E or I.30E. Moreover, such a correlation suggests that DPPC is indeed the most important compound in the regulating the dynamic surface tension of the whole PS.

In the DSA method of testing PS surface activity in the presence of mineral nanoparticles, the parameter $\Delta\sigma_{\%}$ is used by analogy to the parameter defined by eq. (3). It represents the temporary change of the dynamic surface tension in the given system, $\sigma(\tau)$, in respect to the temporary surface tension of the pure surfactant, $\sigma^*(\tau)$:

$$\Delta\sigma_{\tau\%} = \left(\frac{\sigma(\tau)}{\sigma^*(\tau)} - 1 \right) 100\% \quad (6)$$

The interpretation of $\Delta\sigma_{\tau\%}$ values is similar to that of $\Delta\sigma_{\min\%}$ in the discussion presented earlier. Figure 7 shows the comparison of $\Delta\sigma_{\tau\%}$ averaged in the first 10 minutes of monitoring the dynamic surface tension of Survanta[®] containing different mineral nanoparticles (concentration 0.5 mg/cm³).

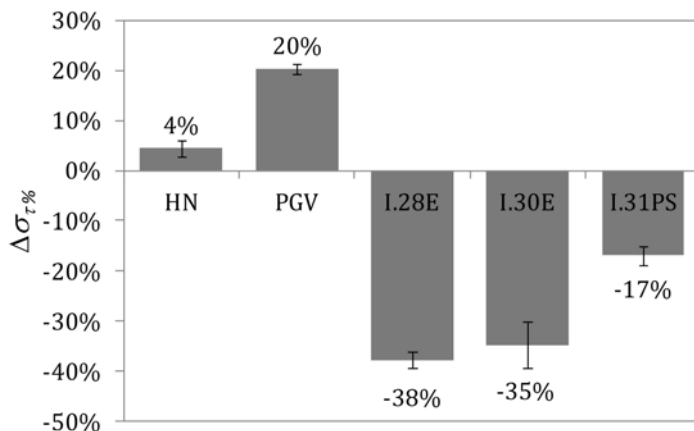


Fig. 7. Comparison of $\Delta\sigma_{\tau\%}$ value for PS with different mineral nanoparticles (0.5 mg/cm³).

Interestingly, data obtained with DSA studies are also supportive for the findings from two other experimental approaches. Both HN and PGV nanoparticles decrease the activity of the surfactant while each of three modified montmorillonites (I.28E, I.30E and I.31.PS) acts in synergy with the surfactant in lowering the surface tension. The changes are different numerically than the ones found in the oscillating bubble studies, however it should be reminded that these two experimental systems differ in a few essential aspects, as discussed earlier. It is striking however, that the overall trend of changes of the surface activity in the PS-nanoparticles system remains similar to the obtained in two other sets of experimental data.

Discussion

Our results provide an apparent support that mineral nanoparticles influence the properties of the pulmonary surfactant due to physicochemical interactions related either to changes in adsorption dynamics at a gas-liquid interface or altering the surface tension lowering capabilities of the adsorbed compounds. However, at dynamic conditions which are indispensable associated with the breathing cycle, the mechanisms interfacial phenomena become more difficult to trace and identify. There is a vast number of published data recognizing that different micro- and nanoparticles,

as well as gaseous contaminants, influence surface processes in the model PS systems (e.g., Sosnowski et al., 2000; Podgórski et al., 2001; Wallace et al., 2007; Bakshi et al., 2009; Kondej and Sosnowski, 2010; Harishchandra et al. 2010; Fan et al. 2011; Guzman et al. 2011). Some theoretical interpretations employ also mathematical modeling of mass transfer phenomena (e.g. Sosnowski, 2001) or molecular dynamics analysis (Choe et al., 2008; Sosnowski et al., 2012), still giving only partial explanation of the observed effects. Several studies confirm that ultrafine particles present in the PS system provide an additional interface for adsorption, so PS components can be collected on solids. In this way the concentration, and – consequently – the surface activity of PS at gas-liquid interface may be reduced. In our studies this mechanism can feasibly elucidate the influence of HN and PGV particles on the surfactant. Other types of particles produce the opposite effects and this may be explained rather by a synergy in dynamic surface activity between the PS and the particles or the compounds they transport into the system.

The fundamental question which needs to be answered during discussion of the results is if the effects revealed in the specialized *in vitro* experimental systems are indeed taking place in the real physiological system. It is known that homeostatic biological environment of the lungs is equipped with specialized mechanisms which protect against the elevation of the concentration of deposited inhaled nanomaterials in the pulmonary fluids (e.g. mucociliary clearance, chemotactic activity of alveolar macrophages). This environment is also effectively buffered and continuously refreshed by surfactant production and turnover – such processes are absent in all laboratory settings. So, keeping in mind that tensiometric approaches tested within this work should be considered only as simplistic models of physiologically-related systems, they allow to speculate that accidental or repetitive overdosing of inhaled mineral nanoparticles (e.g. at the workplace) may cause a runaway of the physiological system from a natural dynamic equilibrium. In such a situation, the initiated biological response can lead to a pulmonary dysfunction or disease.

Conclusions

It was demonstrated that the evaluation of dynamic surface activity of a model pulmonary surfactant (PS) or its main phospholipid constituent (DPPC), obtained from three different tensiometric techniques, allow to investigate the plausible interactions of inhaled mineral nanoparticles in the liquids covering lung surface. It was shown that the response of the model system depends on particle type and concentration, and that different nanoparticles may decrease or increase the surface tension of the PS. The exact physiological implication of these findings cannot be straightforwardly interpreted, however it may be expected that alteration of the original surface activity of the surfactant in the lungs can initiate a biological response which will lead to undesired health effects. As the surfactant also regulates pulmonary defense mechanisms against inhaled aerosol deposits, the induced changes of PS properties

may result in an increased susceptibility to lung infections or allergies. This conclusion confirms that it is essential to minimize the breathing with air contaminated with mineral dusts. It can be achieved by using personal protection equipment (filtering facial masks or respirators) which must be properly designed to collect airborne nanoparticles.

Acknowledgments

This paper has been prepared on the basis of the results of research project No. I.B.10 carried out within the National Program "Improvement of safety and working conditions" partly supported in 2011-2013 within the scope of research and development by the Ministry of Science and Higher Education. CIOP-PIB has been the Program main coordinator.

The activity of one co-author (T.R.S.) is related to his activity in COST Action MP1106 "Smart and green interfaces – from single bubbles and drops to industrial, environmental and biomedical applications"

The author also wish to thank prof. Kamil Wojciechowski from Department of Microbioanalytics, Faculty of Chemistry WUT, for providing the access to DSA equipment.

References

- BAKAND S., HAHES A., DECHSAKULTHORN F., 2012. *Nanoparticles: a review of particle toxicology following inhalation exposure*. *Inhal. Toxicol.* 24, 125–135.
- BAKSHI M.S., ZHAO L., SMITH R. et al., 2008. *Metal nanoparticle pollutants interfere with pulmonary surfactant function in vitro*. *Biophys. J.* 94, 855–868.
- CHOE S., CHANG R., JEON J., VIOLI A., 2008. *Molecular Dynamics simulation study of a pulmonary surfactant film interacting with a carbonaceous nanoparticle*. *Biophys. J.* 95, 4102–4114.
- CLEMENTS J.A., HUSTEAD R.F., JOHNSON R.P., 1961. *Pulmonary surface tension and alveolar stability*. *J. Appl. Physiol.* 16, 444–450.
- ENGLE W.A. AND THE COMMITTEE ON FETUS AND NEWBORN, 2008. *Surfactant-replacement therapy for respiratory distress in the preterm and term neonate*. *Pediatrics* 121, 419–432.
- FAN Q., WANG Y.E., ZHAO X. et al., 2011. *Adverse biophysical effects of hydroxyapatite nanoparticles on natural pulmonary surfactant*. *ACS Nano* 5, 6410–6416.
- GRADOŃ L., PODGÓRSKI A., 1989. *Hydrodynamical model of pulmonary clearance*. *Chem. Eng. Sci.* 44, 741–749.
- GUZMAN E., LIGGIERI L., SANTINI E., FERRARI M., RAVERA F., 2011. *Effect of hydrophilic and hydrophobic nanoparticles on the surface pressure response of DPPC monolayers*. *J. Phys. Chem. C*, 115, 21715–21722.
- HARISHCHANDRA R.K., SALEEM M, GALLA H.-J., 2010. *Nanoparticle interaction with model lung surfactant monolayers*. *J. R. Soc. Interface* 7, S15–S26.
- LAM B.C., NG Y.K., WONG K.Y., 2005. *Randomized trial comparing two natural surfactants (Survanta vs. bLES) for treatment of neonatal respiratory distress syndrome*. *Pediatr. Pulmonol.* 39, 64–69.
- LONGEST P.W., HOLBROOK L.T., 2012. *In silico models of aerosol delivery to the respiratory tract – development and applications*. *Adv. Drug Del. Rev.* 64, 296–311.
- KONDEJ D., SOSNOWSKI T.R., 2010. *The influence of metal-containing occupational dust on pulmonary surfactant activity*. *Chem. Eng. Trans.* 19, 315–320.
- KONDEJ D., SOSNOWSKI T.R., 2013. *Alteration of biophysical activity of pulmonary surfactant by aluminosilicate nanoparticles*. *Inhal. Toxicol.* 25, 77–83.

- MARIJNISSEN J.C.M., GRADOŃ L., 2010. *Nanoparticles in medicine and environment: inhalation and health effects*. Springer, Berlin.
- MAYNARD A.D., KUEMPEL E.D., 2005. *Airborne nanostructured particles and occupational health*. J. Nanoparticle Res. 7, 587–614.
- NOTTER R.H., TAUBOLD R., MAVIS R.D., 1982. *Hysteresis in saturated phospholipid and its potential relevance in vivo*. Exp. Lung. Res. 3, 109–127.
- OBERDÖRSTER G., 2001. *Pulmonary effects of inhaled ultrafine particles*. Int. Arch. Occup. Environ. Health 74, 1–8.
- ROSTAMI A.A., 2009. *Computational modeling of aerosol deposition in respiratory tract: a review*. Inhal. Toxicol. 21, 262–290.
- RUGONYI S., BISWAS S.C., HALL S.B., 2008. *The biophysical function of pulmonary surfactant*. Resp. Physiol. Neurobiol. 163, 244–255.
- SOSNOWSKI T.R., 2001. *Sorption-induced Marangoni microflows in the pulmonary surfactant system*. Inż. Chem. Proces. 22, 251–267.
- SOSNOWSKI T.R., 2011. *Importance of airway geometry and respiratory parameters variability for particle deposition in the human respiratory tract*. J. Thorac. Dis. 3, 153–155.
- SOSNOWSKI T.R., GRADOŃ L., PODGÓRSKI A., 2000. *Influence of insoluble aerosol deposits on the surface activity of the pulmonary surfactant: a possible mechanism of alveolar clearance retardation?* Aerosol Sci. Techn. 32, 52–60.
- SOSNOWSKI T.R., GRADOŃ L., SKOCZEK M., DROŹDZIEL H., 1998. *Experimental evaluation of importance of the pulmonary surfactant for oxygen transfer rate in human lungs*. Int. J. Occup. Safety Ergon. 4, 391–409.
- SOSNOWSKI T.R., KOLIŃSKI M., GRADOŃ L., 2012. *Alteration of surface properties of dipalmitoyl phosphatidylcholine by benzo[a]pyrene: a model of pulmonary effects of diesel exhaust inhalation*. J. Biomed. Nanotechnol. 8, 818–825.
- SOSNOWSKI T.R., MOSKAL A., GRADOŃ L., 2006. *Dynamics of oro-pharyngeal aerosol transport and deposition with the realistic flow pattern*. Inhal. Toxicol. 18, 773–780.
- WALLACE W.E., KEANE M.J., MURRAY D.K. et al., 2007. *Phospholipid lung surfactant and nanoparticle surface toxicity: lessons from diesel soots and silicate dusts*. J. Nanopart. Res. 9, 23–38.
- ZHANG Z., KLEINSTREUER C., KIM C.S., 2002. *Cyclic micron-size particle inhalation and deposition in a triple bifurcation lung airway model*. J. Aerosol Sci. 33, 257–281.
- ZHANG, L., ASGHARIAN, B., ANJILVEL, S., 1996. *Inertial and interceptional deposition of fibers in a bifurcating airway*. J. Aerosol Med. 9, 419–430.
- ZUO Y.Y., VELDHUIZEN R.A.W., NEUMANN A.W., PETERSEN N.O., POSSMAYER F., 2008. *Current perspectives in pulmonary surfactant – Inhibition, enhancement and evaluation*. Biochim. Biophys. Acta 1778, 1947–1977.

Received June 2, 2013, reviewed, accepted July 8, 2013

ENVIRONMENTAL ASPECTS OF POST MINING URANIUM WASTES DEPOSITED IN RADONIOW, POLAND

Bartosz REWERSKI*, **Dariusz RUSZKOWSKI***, **Ewelina CHAJDUK****,
Aleksandra SKLODOWSKA*

* Laboratory of Environmental Pollution Analysis, Faculty of Biology, University of Warsaw, Miecznikowa 1, 02-096 Warsaw, Poland; corresponding author: asklodowska@biol.uw.edu.pl

** Laboratory of Nuclear Analytical Methods, Institute of Nuclear Chemistry and Technology, Dorodna 16, 03-195 Warsaw, Poland

Abstract: Post mining uranium wastes from Radoniów were analysed and chemical, mineralogical and petrographic characteristics were performed. Additionally, the size parameters of dumps and direction of water runoff were estimated using LIDAR data. Bioaccumulation of uranium in different plants covering dump's surface was shown.

Keywords: *uranium, post mining wastes, bioaccumulation, LIDAR*

Introduction

The Radoniów deposit is located in the northern part of the Izera Metamorphic Complex (Poland). This unit is composed of granitic gneisses, quartz-biotiteschists, mylonites and breccias with trace amounts of sulphides. Primary and secondary uranium minerals have been found. The primary minerals are pitchblende, uraninite with blue fluorite, and hematite. Between secondary minerals, metatorbernite, metauranocircite, metaautunite and uranophane were recognized (Piestrzynski et al., 2006). Uranium mining has started in 1954 and was continued until 1960.

Post-mining wastes were deposited in the dump located near the mine. Originally the dump covered an area of about 25 000 m² and γ -measurements made in 1971 showed elevated radiation (about 500 μ R/h (~5 μ Sv/h)), reaching a maximum dose rate of 2000 μ R/h (about 20 μ Sv/h) (Piestrzynski et al., 1996). During the next twenty years the dump was reexploited for local purposes (mainly for construction of local

roads and sometimes for buildings). In 1994 the average noted dose rate was about $80\mu\text{R/h}$ with maximum $105\mu\text{R/h}$ (about $0.8\text{--}1.05\mu\text{Sv/h}$).

All data collected by Piestrzynski et al. (1996) show that the rocks deposited on the dump reveal a significant amount of uranium. The available data are not sufficient to present quantitative figures of uranium content in the dump and its dispersion around the dump.

In presented research we try to quantify material collected in two dumps (actually, after reexploitation two dumps exist – one small and the second much larger) and describe mineral and chemical character of the deposited wastes.

Materials and methods

Sampling

Wastes were collected from two dumps located in Radoniow (Large Dump –N $51^{\circ}00'13.39$;E $15^{\circ}29'00.16$, Small Dump - N $51^{\circ}00'15.55$; E $15^{\circ}28'53.68$). Plants were collected from the surface of dumps.

XRD Analyses

A Philips X'Pert PW 3020 X-ray diffraction analyzer was utilized to characterize the mineral composition of wastes. Co radiation (K-Alpha1 [\AA]- 1.78901 K-Alpha2 [\AA]- 1.79290 K-Beta [\AA]- 1.62083 ;K-A2 / K-A1 Ratio- 0.50000) was used at 30 mA , and 40 kV .

Petrography

Light petrographic microscopy of thin section of polished waste sample was used for petrographic characteristic.

Chemical analysis

Uranium in wastes was analyzed using the ICP-MS technique according to the procedure described by Chajduk et al. (2013). Extraction analysis with EDTA, phosphate buffer and 0.11 M acetic acid ($\text{pH } 3.0$) was done for determination of uranium bioavailability. Uranium and other metals in plants were analyzed in Polish Geological Institute-National Research Institute using the ICP-MS technique according to the certified procedure used in Central Chemical Laboratory (Polish Centre of Accreditation certificate No. AB 283).

Electron Microscopy

Scanning Electron Microscopy analysis was done in the Paleozoology Department of Museum and Institute of Zoology, Polish Academy of Sciences. HITACHI S-3400N Scanning Electron Microscope equipped with an EDS X-ray microanalyser, (Superdry II detector) was used for examination of polished section of wastes and crushed wastes

(fraction 250–500 μm). Acceleration voltage was 20.0 kV. Thin sections of polished waste sample were examined.

Analysis of the dump size and direction of water runoff

The pictures taken in 2011 in the LAS format and containing data from laser scanning ground – LIDAR with spatial resolution of 12 points per square meter were used for analysis. Basing on the point of altitude (altitude above sea level), triangulation model TIN (Triangulated Irregular Network) was created. It was then converted into a GRID model based on a grid. Resolution of this model was 0.5 m. Analysis was carried out in the Space Research Centre of Polish Academy of Sciences.

Results and discussion

Waste dumps in Radoniow are localized in the vicinity of Radoniow village and they are surrounded by agricultural lands (Fig. 1). The surface of dumps is is tightly folded (especially the surface of the large dump) and clear signs of erosion are visible (Fig. 2).



Fig. 1. Post mining waste in the dumps in Radoniow (www.geoportal.gov.pl)

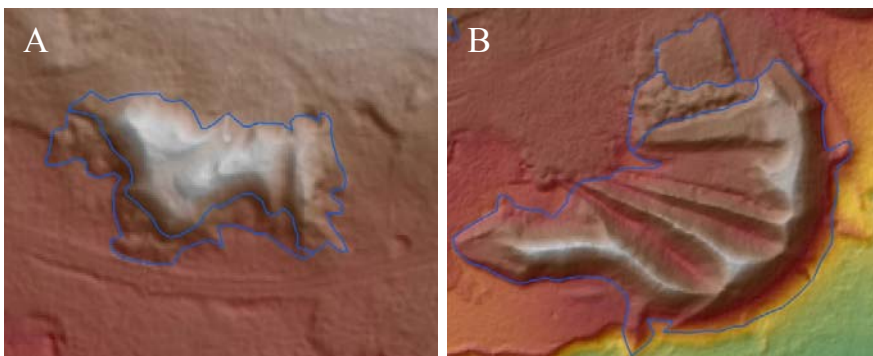


Fig. 2. Shape of small dump (A) and large dump (B)

Geometrical parameters of dumps are presented in Table 1. Total surface occupied by dumps in 2011 (7368 m²) decreased significantly in comparison to 1971 when it was about 25 000 m². The total volume of dumps in 1971 is unknown and now is 44 803 m³. Uranium concentration in waste is still high. An average uranium concentration is about 153 mg/kg with minimum about 60 mg/kg and maximum 806 mg/kg. The richer uranium wastes were found in the small dump. Total amount of uranium deposited in the dumps basing on our studies is about 17,97 Mg (volume × density (~2.65 kg/m³)). A large amount of aggregate showing uranium concentration between 358 mg/kg and about 2000 mg/kg (single stones) was observed around the dumps in 2012. The dose rate noted on the surface of the dump in 2012 was 0.86 – 4.4 μSv/h. The minimum was similar to the radiation level noted by Piestrzynski et al. (1996) in 1994 but the maximum dose rate is only slightly lower than this one noted in 1971. Single stones around the dumps show very high radiation with the dose rate reaching 20 μSv/h.

Table 1. Dumps size parameter calculated using LIDAR data

Model LAS 0.5 m	Total	Small dump	Large dump
surface projection [m ²]	7368	1176	6192
body surface [m ²]	8621	1350	7271
altitude minimum [m]	402.3	407.1	402.3
altitude maximum [m]	414.6	414.6	414.1
height difference [m]	12.3	7.5	11.8
volume [m ³]	44803	4573	40230

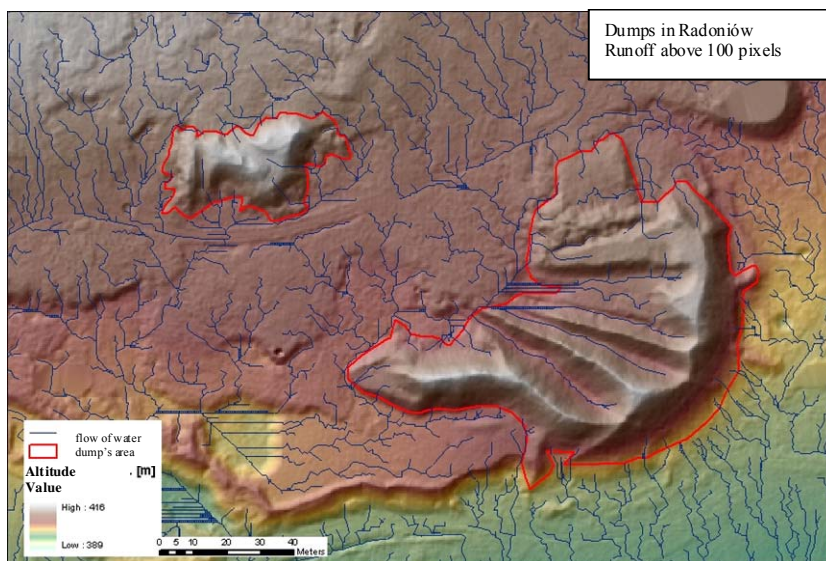


Fig. 3. The intensity of surface water runoff calculated basing on LIDAR data

The main direction of water runoff in the large dump is West, except northern part of dump where outflow to the East and North is observed. In the small dump water runoff to the South prevails. Petrographic studies of the waste materials revealed gneiss with laminar and eye texture as the main building material. Gneiss contains following minerals: quartz, K-feldspar, plagioclase and mica (mainly muscovite). In some parts of material gneiss is transformed to mylonite with thin slots filled by fluorite and iron oxyhydroxides. Ore minerals are also present between which pyrite is most abundant (Fig. 3). Pyrite occurs in gneiss and in mylonite. Uranium mineral were not found in petrographic studies.



Fig. 4. Pyrite occurrence: single crystals and pyrite aggregates (A); in gneiss (B) and mylonite(C).

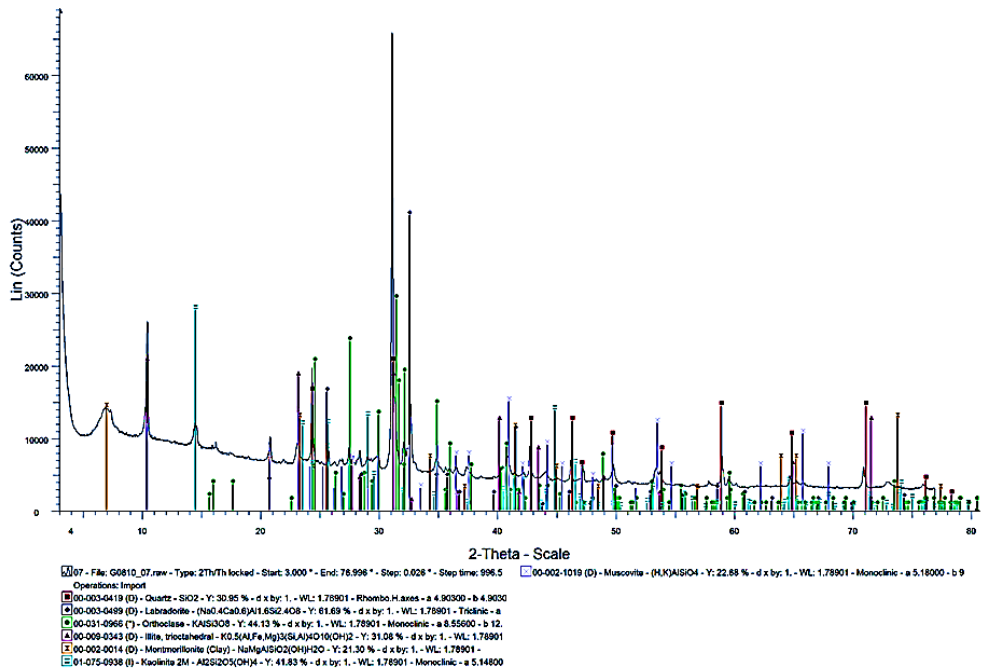


Fig. 5.XRD analysis of waste material taken from the small dump

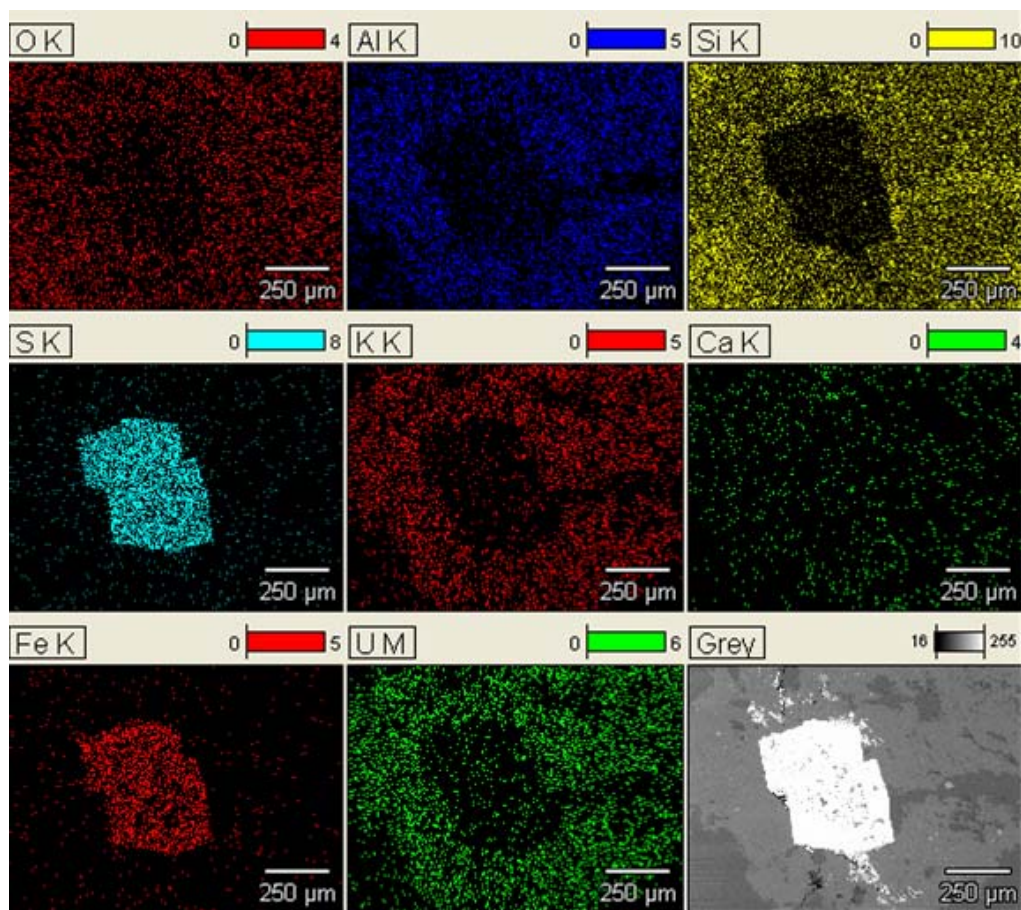


Fig. 6. Results of EDS-X ray analysis made in SEM

In XRD analysis (Fig. 5) quartz, orthoclase, montmorillonite, kaolinite, illite and labradorite were found. XRD profiles of samples from the dumps were very similar and uranium minerals were not found. Uranium presence in material from the dumps has been only shown in scanning electron microscope with the use of EDS-X ray microanalyzer. Its occurrence is strongly correlated with potassium and aluminum and uranium minerals often surrounding pyrite aggregates (Fig. 6).

Lack of detection of uranium in the XRD and petrographic analysis is a proof of its wide dispersion in waste material deposited in the Radoniow dumps. However, uranium concentration as well the level of radiation is relatively high, which brings serious environmental issues. The presence of pyrite and relatively low pH (below 6.0) facilitates leaching and bioleaching processes. We described earlier (Rewerski et al., 2013) that indigenous microorganisms living in wastes are able to oxidize iron what can cause uranium leach up to 30% of its total content in nearly neutral pH and 90%

under acidic conditions. The extraction analysis shows that 21–25% of uranium is associated with the carbonate fraction, 5.8–10.6% occurs in soluble fraction (respectively in the large and small dump) and 0.1–2.7% is bioavailable (respectively in the small and large dump).

Table 2. Uranium concentration found in plants covering the surface of dumps.

Dump	Plant	mg U/kg dry weight (ppm)	
Radoniow	berd vetch (<i>Vicia cracca</i>)	stalk	0.57
		leaves	0.73
		root	9.96
	ribwort (<i>Plantago lanceolata</i>)	flower	2.69
		stalk	2.76
		leaves	14.64
	clover (<i>Trifolium hybridum</i>)	root	56.40
		flower	0.80
		stalk	2.24
	alfalfa (<i>Medicago lupulina</i>)	leaves	2.83
		root	71.54
		flower	4.10
	white sweet clover (<i>Melilotus albus</i>)	stalk	2.25
		leaves	5.37
		root	0.55
	orchard grass (<i>Dactylis glomerata</i>)	stalk	2.02
		leaves	3.76
		root	10.24
	flower	3.65	
	stalk	0.25	
	leaves	3.22	
	root	77.54	

Therefore we decided to check accumulation of uranium in plant tissue. Plant's samples were collected in the runoff because only there was enough vegetation developed. Uranium is accumulated mainly in the roots reaching the maximum concentration at 77.54 mg/kg (dry weight) in the roots of orchard grass. Leaves accumulate much lower uranium amount and maximum of bioaccumulation was noted in ribwort's leaves (14.6 mg/kg). Surprisingly a relatively high uranium level was noted in flowers of alfalfa and orchard grass.

Distribution of uranium in the individual extraction fractions, its accumulation in plants and earlier information concerning its bioleaching by indigenous microorganisms (Rewerski et al. 2013) clearly show that uranium deposited in dumps may be disseminated in the environment causing contamination of soil, surface water and groundwater.

Conclusions

Post mining wastes deposited in Radoniow contain a significant amount of uranium. The concentration of uranium and level of radiation in some parts of dumps is still hazardous for the environment and availability of dumps should be limited. The indigenous plants accumulating uranium in leaves, e.g. ribwort, may be useful for bioremediation.

Acknowledgement

This work was supported by strategic research project No. SP/J/3/143045/11 from The National Centre for Research and Development (NCBiR), Poland. We also wish to thank Dr. Edyta Wozniak from Space Research Centre of Polish Academy of Sciences for her contributions to the work in creation of spatial model of dumps.

References

- CHAJDUK E., BARTOSIEWICZ I., PYSZYNSKA M., CHWASTOWSKA J., POLKOWSKA-MOTRENKO H., 2013, *Determination of uranium and selected elements in Polish dictyonema shales and sandstones by ICP-MS*, Journal of Radioanalytical and Nuclear Chemistry, 295 (3), 1913–1919.
- PIESTRZYNSKI J., PIECZONKA W., MIELNICZUK E., CHRUSCIEL P., JODŁOWSKI P., 1996, *Effects of uranium mining on the contamination of some areas in Poland*, in: *Planning for environmental restoration of radioactively contaminated sites in central and eastern Europe*, Volume 1; Identification and characterization of contaminated sites, IAEA-Vienna 1996, TECDOC-865, 193–216.
- REWERSKI B., MIELNICKI S., BARTOSIEWICZ I., POLKOWSKA-MOTRENKO H., SKŁODOWSKA, A., 2013, *Uranium post-mining wastes as a potential reserve source of uranium for nuclear energy plants*, Physicochemical Problems of Mineral Processing, 49 (1), 5–11.

Received February 28, 2013; reviewed; accepted July 9, 2013

MODIFYING EFFECT OF ELECTRON BEAM IRRADIATION ON MAGNETIC PROPERTY OF IRON-BEARING MINERALS

Huaifa WANG*, **Shouci LU****

* College of Mining Engineering, Taiyuan University of Technology, Taiyuan 030024, China, tyut01@126.com

** School of Civil and Environmental Engineering, University of Science and Technology Beijing, Beijing 100083, China

Abstract: The effect of electron beam irradiation on magnetic property of iron bearing minerals was investigated by susceptibility measurements. The results show that the magnetic susceptibility of iron bearing sulfide minerals can be enhanced remarkably by strong beam current irradiation, while the magnetic susceptibility of oxidized iron minerals keeps unchanged and even is slightly reduced. The magnetic susceptibility of arsenopyrite can reach the ferromagnetic level. The particle size of irradiated minerals makes notable effects on magnetic susceptibility. The magnetic susceptibility of irradiated minerals is enhanced greatly with reduction of particle size, and the irradiation dose corresponding to the maximum magnetic susceptibility is decreased simultaneously. Exposure of pyrite to small beam current electron irradiation can only enhance its magnetic susceptibility from 4 to 5-fold. Enhancement of magnetic property by radiation induced defects and excitation in minerals is limited. Strong beam current electron irradiation provides a novel approach to enlarge the magnetic property differences between iron bearing minerals.

Keywords: *magnetic susceptibility, iron bearing mineral, sulfide, electron beam irradiation*

Introduction

Exposure of solids to high-energy radiation is known to result in radiation-induced defects and leads to related process acceleration, such as diffusion controlled reaction in solid and solid phase synthesis (Gribkov et al., 1995; Auslender et al., 1997, 1999). It also makes possible to create new conditions for changes in solid materials properties e.g. the mechanical strength, electric, magnetic and surface properties, floatability of minerals and others. The difference between minerals with close physical and physicochemical properties can be markedly enlarged (Florek, 1995; Bochkarev et al.,

1997; Milkhilov et al., 1998; Kovalyov et al., 1999; Chanturiya et al., 1999; Wang et al., 2002a; Wang et al., 2002b; Wang et al., 2002c). The study of the effect of accelerated electron energy on magnetic separation of iron bearing ores showed that the preliminary treatment of raw ores by electron beam irradiation enables to increase the concentrate grade and decrease the loss of valuable constituents in tailing. This promising technique was successfully used to treat in laboratory scale iron, iron containing tin and chalcopyrite and others ores (Bochkarev et al., 1992, 1997; Florek et al., 1992; Ostopenko et al., 1992).

The objective of this work is the study of the electron irradiation effect on magnetic property of iron bearing minerals such as pyrite, arsenopyrite, chalcopyrite, marmatite, hematite and siderite. The magnetic susceptibility change of weakly magnetic iron bearing minerals induced by electron beam irradiation is investigated and analyzed.

Experimental

Materials

The iron-bearing minerals such as pyrite, arsenopyrite, chalcopyrite, marmatite hematite and siderite were picked from real ores and purified using suitable mechanical measures. The pure mineral samples were first ground in mortar and then classified into several size fractions. The minerals samples with size range of -180+75, -75+53 and -53 μm were subjected to electron irradiation treatment.

Methods

The samples were irradiated with an electron accelerator at a steady-state regime. The low irradiation dose experiments were conducted on the type BF-5 experimental accelerator installed at Beijing Normal University. The electron beam parameters were as follows: the incident electron energy 1.5 MeV, irradiation dose rate 100 Gy/s (Gray, $\text{Gy} = \text{m}^2/\text{s}^2$), current intensity were altered from 90 to 150 μA . The high irradiation dose experiments were conducted on the type GJ-15 industrial accelerator installed at Tianjin Institute of Technical Physics. The fixed electron beam parameters were as follows: electron energy 1.5 MeV, current intensity 6 mA. The irradiation dose was varied in accordance with the problems stated. The magnetic susceptibility was measured on a multi-purposes magnetism analyzer model WCF2-65. The exciting current was set at 1.0 A for all tests.

Results and discussions

Small beam current irradiation

Arsenopyrite and two types of pyrite (sample A from Hunan Leiyang mine, sample B from Zhejiang Longyou mine) were exposed to electron beam irradiation under low dose and small beam current. Under such irradiation conditions the thermal effect on

irradiated minerals is negligible. As shown in Table 1, the magnetic susceptibility of arsenopyrite after irradiation increases. At beam current 115 μA and dose $23 \cdot 10^3 \text{ m}^2/\text{s}^2$, the magnetic susceptibility of arsenopyrite increases 5 times than that prior to irradiation. The beam current and irradiation dose are the major parameters for changes in magnetic properties.

Table 1. Effect of current density and irradiation dose on magnetic susceptibility of arsenopyrite. Magnetic susceptibility of arsenopyrite prior to irradiation is $5.39 \cdot 10^{-6} \text{ cm}^3/\text{g}$ and particle size $\sim 180 \mu\text{m}$

Current density (μA)		115				
Irradiation dose ($\text{kGy} = 10^3 \text{ m}^2/\text{s}^2$)	2.3	4.6	6.9	9.2	11.5	
Susceptibility $10^{-6} (\text{cm}^3/\text{g})$	12.72	15.52	18.83	14.28	9.38	
Current density (μA)		115				
Irradiation dose ($\text{kGy} = 10^3 \text{ m}^2/\text{s}^2$)	13.8	16.1	18.4	20.7	23.0	
Susceptibility $10^{-6} (\text{cm}^3/\text{g})$	11.16	13.14	26.77	28.35	30.72	
Current density (μA)		90				
Irradiation dose ($\text{kGy} = 10^3 \text{ m}^2/\text{s}^2$)	12	14	16	18	20	
Susceptibility $10^{-6} (\text{cm}^3/\text{g})$	7.35	19.68	9.28	20.17	22.94	

The magnetic properties of irradiated pyrite A and B are given in Tables 2 and 3, respectively. The results show that the changes in magnetic susceptibility fluctuate. At electron current density 150 and 115 μA , the magnetic susceptibility even decreases under low irradiation dose. Under high irradiation dose (above $10 \cdot 10^3 \text{ m}^2/\text{s}^2$ for 150 μA , and above $20.7 \cdot 10^3 \text{ m}^2/\text{s}^2$ for 115 μA) the magnetic susceptibility of pyrite A becomes higher than the initial value. Under current density 120 μA the result is

Table 2. Effect of current density and irradiation dose on magnetic susceptibility of pyrite A. Magnetic susceptibility of pyrite A prior to irradiation is $7.89 \cdot 10^{-6} \text{ cm}^3/\text{g}$ and particle size $\sim 180 \mu\text{m}$

Current density (μA)		150				
Irradiation dose ($\text{kGy} = 10^3 \text{ m}^2/\text{s}^2$)	2	4	6	8	10	
Susceptibility $10^{-6} (\text{cm}^3/\text{g})$	0.7	1.46	1.68	4.89	22.69	
Current density (μA)		120				
Irradiation dose ($\text{kGy} = 10^3 \text{ m}^2/\text{s}^2$)	2	4	6	8	10	
Susceptibility $10^{-6} (\text{cm}^3/\text{g})$	15.83	20.47	16.50	18.03	7.09	
Current density (μA)		115				
Irradiation dose ($\text{kGy} = 10^3 \text{ m}^2/\text{s}^2$)	13.8	16.1	18.4	20.7	23.0	
Susceptibility $10^{-6} (\text{cm}^3/\text{g})$	3.01	3.65	4.17	9.26	22.69	

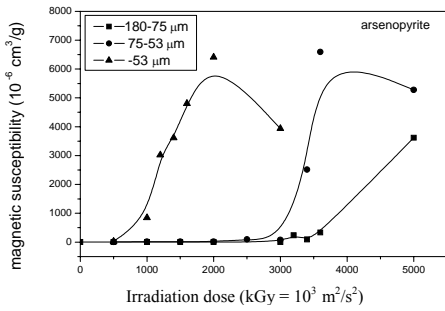
different as the magnetic susceptibility increases under the irradiation dose from $2 \cdot 10^3 \text{ m}^2/\text{s}^2$ to $8 \cdot 10^3 \text{ m}^2/\text{s}^2$, and then decreases at higher irradiation dose $10 \cdot 10^3 \text{ m}^2/\text{s}^2$. Generally, the magnetic susceptibility of irradiated pyrite B increases, however, a significant decrease can be observed for the current density $120 \mu\text{A}$ with irradiation dose $6 \cdot 10^3 \text{ m}^2/\text{s}^2$, $115 \mu\text{A}$ with $16.1 \cdot 10^3 \text{ m}^2/\text{s}^2$ and $90 \mu\text{A}$ with $14 \cdot 10^3 \text{ m}^2/\text{s}^2$. The reason of such fluctuating changes for mineral pyrite A and B is still unclear. It may be related to the extent of crystalline perfection, specific defects and geologic environment of mineralization of pyrite. Further study is needed.

Table 3. Effect of current density and irradiation dose on magnetic susceptibility of pyrite B. Magnetic susceptibility of pyrite B prior to irradiation is $7.89 \cdot 10^{-6} \text{ cm}^3/\text{g}$ and particle size $\sim 180 \mu\text{m}$

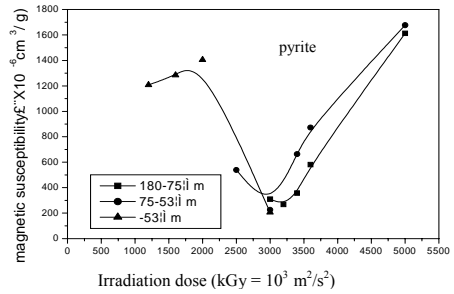
Current density (μA)		150				
Irradiation dose ($\text{kGy} = 10^3 \text{ m}^2/\text{s}^2$)	2	4	6	8	10	
Susceptibility $10^{-6} (\text{cm}^3/\text{g})$	12.17	15.14	16.26	20.17	16.05	
Current density (μA)		120				
Irradiation dose ($\text{kGy} = 10^3 \text{ m}^2/\text{s}^2$)	2	4	6	8	10	
Susceptibility $10^{-6} (\text{cm}^3/\text{g})$	29.58	22.04	4.51	13.5	22.77	
Current density (μA)		115				
Irradiation dose ($\text{kGy} = 10^3 \text{ m}^2/\text{s}^2$)	13.8	16.1	18.4	20.7	23.0	
Susceptibility $10^{-6} (\text{cm}^3/\text{g})$	12.59	6.4	11.85	19.95	12.37	
Current density (μA)		90				
Irradiation dose ($\text{kGy} = 10^3 \text{ m}^2/\text{s}^2$)	12	14	16	18	20	
Susceptibility $10^{-6} (\text{cm}^3/\text{g})$	10.91	4.68	38.43	15.57	15.03	

Strong beam current irradiation

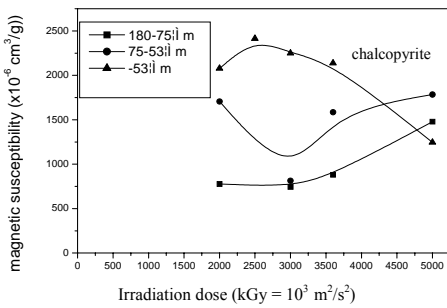
The effect of strong beam current irradiation on magnetic susceptibility of arsenopyrite, pyrite, chalcopyrite and marmatite is given in Figs. 1a–d. From Fig. 1 it can be seen that magnetic susceptibility of irradiated minerals under strong beam current irradiation changes remarkably. However, the response of minerals to irradiation is different. With increase in irradiation dose the magnetic susceptibility of minerals increases sharply reaching its maximal value and then decreases. Hence, there is a critical irradiation dose for each mineral. Furthermore, the critical irradiation dose is dependent upon the particle size. The coarser particle size, the higher value of the critical irradiation dose.



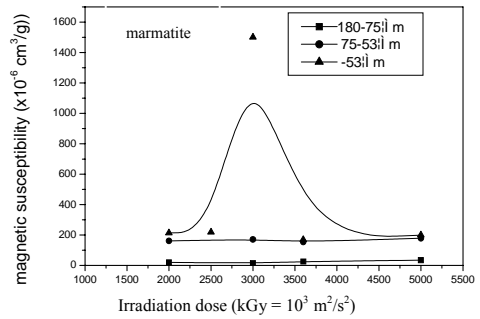
(a)



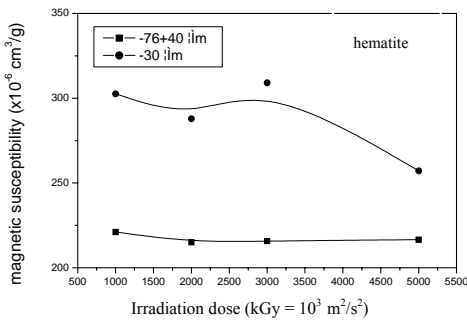
(b)



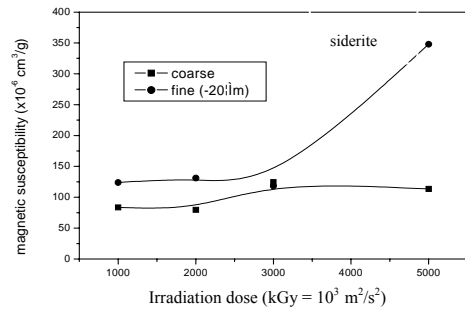
(c)



(d)



(e)



(f)

Fig. 1. Magnetic susceptibility of arsenopyrite (a), pyrite (b), chalcopyrite (c), marmatite (d), hematite (e) and siderite (f) as a function of irradiation dose

The magnetic susceptibility of arsenopyrite with size $-75+53 \mu\text{m}$ increases sharply with the irradiation dose, reaching the maximum value at $6.6 \cdot 10^{-3} \text{ cm}^3/\text{g}$, which is higher than the minimum level of ferromagnetic scope $3 \cdot 10^{-3} \text{ cm}^3/\text{g}$ (Liu, 1994). After irradiation the magnetic susceptibility of pyrite sized $75-53 \mu\text{m}$ reaches maximum at $1.7 \cdot 10^{-3} \text{ cm}^3/\text{g}$ (Fig. 1b). For chalcopyrite the maximum magnetic susceptibility is

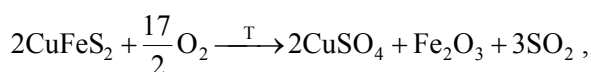
obtained for particle size $-53 \mu\text{m}$ and is equal to $2.4 \cdot 10^{-3} \text{ cm}^3/\text{g}$ (Fig. 1c). The magnetic susceptibility of marmatite remains almost unchanged, except for $-53 \mu\text{m}$ fraction (Fig. 1d).

The results show that the particle size has a notable effect on the magnetic susceptibility of the irradiated minerals. For arsenopyrite as an example, the corresponding irradiation dose is $2000 \cdot 10^3 \text{ m}^2/\text{s}^2$ for $-53 \mu\text{m}$, $3600 \cdot 10^3 \text{ m}^2/\text{s}^2$ for $-75+53 \mu\text{m}$ and $5000 \cdot 10^3 \text{ m}^2/\text{s}^2$ for $-180+75 \mu\text{m}$. Further increase in the irradiation dose causes sharply decreases in the magnetic susceptibility. It may be due to greater specific surface and reaction rate constant for finer particles. Exceeded irradiation may result in overoxidation of minerals and in decrease of magnetic susceptibility of irradiated minerals (Wang, 2002 d).

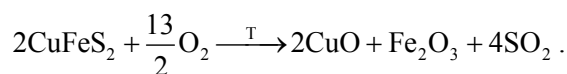
The irradiation effect of the magnetic susceptibility of hematite and siderite is given in Figs. 1e–f. It can be seen that the magnetic susceptibility of hematite after irradiation remains almost unchanged and even slightly reduced. The magnetic susceptibility of siderite fine particles increases to a great extent under irradiation dose of $5000 \cdot 10^3 \text{ m}^2/\text{s}^2$.

Collision of incident electron with mineral crystal lattice causes temperature rising and leads to the thermolysis of mineral (Bochkarev et al., 1997; Milkhilov et al., 1998; Wang, 2002 d; Wang et al., 2004). Under certain conditions, the ferromagnetic phases are formed that enhances magnetic property of minerals.

Decomposition of chalcopyrite in atmosphere occurs in the manner of oxidation and sulfation. The oxidation and sulfation processes may be markedly intensified at higher temperature. The partial and complete oxidations of chalcopyrite by conventional heating occur at temperature of $680 \text{ }^\circ\text{C}$ and $850 \text{ }^\circ\text{C}$, respectively. The sulfation process of chalcopyrite at $600 \text{ }^\circ\text{C}$ can be expressed as follows:

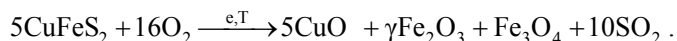


while complete oxidation occurs at temperature 850°C :



Ferric oxide (Fe_2O_3) produced in both reactions enhances the magnetic properties of chalcopyrite. Furthermore, Fe_3O_4 phase may also form as a product of chalcopyrite thermolysis when the temperature exceeds $500 \text{ }^\circ\text{C}$. The thermolysis products of chalcopyrite excited by radiation-thermal treatment using XRD spectrum were previously studied by Florek et al. (1992) and Wang et al. (2004). The results of XRD analysis (Fig. 2) indicate that other iron oxide phases such as $\gamma\text{Fe}_2\text{O}_3$ and Fe_3O_4 also appear. Therefore, the thermolysis process of chalcopyrite excited by radiation-

thermal treatment is distinct from conventional thermolysis and might be expressed by the following reaction:



In addition, the thermolysis process is largely excited by radiation-thermal treatment. The partial and complete thermolysis occurs at lower temperature at about 400 °C and 600 °C, respectively. Consequently, temperature of thermolysis can be reduced about 280 °C and 250 °C, respectively. Intensification of thermolysis is probably due to that the defects resulted by electron beam irradiation may accelerate the diffusion and reaction process inside the solid phase.

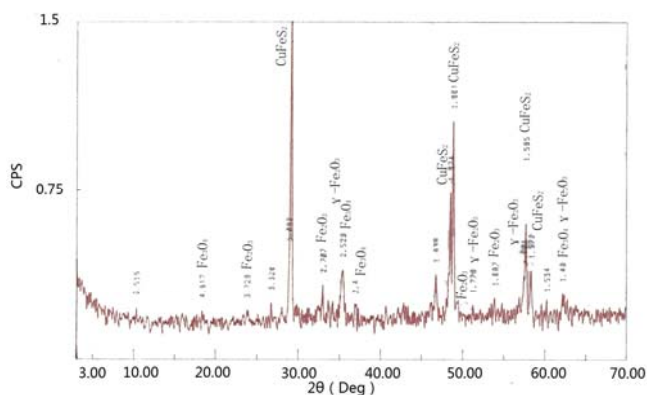


Fig. 2. XRD analysis of chalcopyrite after irradiation pretreatment at maximum temperature 600 °C

Conclusions

Changes of magnetic properties of pyrite by electron beam irradiation under small beam current and low irradiation dose resulted from radiation induced defects and excitation in minerals. As a result, the magnetic susceptibility enhancement is limited.

Strong beam current electron irradiation enhances the magnetic susceptibility remarkably. The magnetic susceptibility of iron bearing sulfide is easier to enhance by irradiation than that of oxidized iron minerals.

The particle size of minerals has notable effect on the magnetic susceptibility. The magnetic susceptibility of irradiated minerals is enhanced greatly with finer particle size, the irradiation dose corresponding to maximal magnetic susceptibility can be decreased.

Radiation defects diffusion and radiation enhanced diffusion process should be responsible for the difference between electron beam radiation induced phase conversion and conventional heat one.

Acknowledgments

This work was financially supported by the National Natural Science Foundation of China (59874002).

References

- AUSLENDER V.L., BOCHKAREV I.G., BOLDYREV V.V., 1997, *Electron Beam Induced Diffusion Controlled Reaction in Solids*. Solid State Ionic, 101–103.
- AUSLENDER V.L., BOCHKAREV I.G., VORONIN A.P., 1999, *Radiation-thermal Process in Solid Inorganic Systems*. Radtech-Euroasia, (2).
- GRIBKOV O.S., VORONIN, A.P. AND AUSLENDER, V. L., 1995, *The use of electron accelerators in the processes of high temperature solid phase synthesis*, Radiation Physics and Chemistry, 46(4–6).
- BOCHKAREV G.R., CHANTURIYA V.A., VIGDERGAUS V.E. et al., 1997, *Prospects of Electron Accelerators Used for Realizing Effective Low-cost Technologies of Mineral Processing*, [in:] H. Hoberg and H.V. Blottnitz eds., Proceedings of the XX IMPC. Aachen, Germany.
- MILKHILOV A.M., ROSTOVTSEV V.I., 1998, *Mechanism of the weakening and fracture of mineral by an electron beam*, Journal of Mining Science, 34(2), 180–184.
- KOVALYOV A.T., 1999, *Possibility of Applying Radiative Electrization for Electrical Separation of Pulverized Mineral Mixture*, Journal of Mining Science, 35(2).
- CHANTURIYA V.I., IVNOVA T.I., LUNIN V.D., 1999, *Influence of Liquid Phase and Products of Its Radiolysis on Surface Properties of Pyrite and Arsenopyrite*, Journal of Mining Science, 35(1).
- FLOREK I., 1995, *The Effects of Radiation Pretreatment on the Flotability of Magnesite and Siderite*, Minerals Engineering, 8(3).
- WANG, H. F., LU, S. C., and XIE, L. Q., 2002a, Effect of radiation on wettability and floatability of sulfide minerals, Journal of University of Science and Technology Beijing, 9 (4).
- WANG H. F., LU S.C., CUI S.F. et al., 2002b, *Electrification of mineral particles by electron beam irradiation*, Journal of University of Science and Technology Beijing, 9(5).
- WANG H., BOCHKAREV G.R., ROSTOVTSEV V.I. et al., 2002c, *Intensification of polymetallic sulfide ore dressing by high-energy electrons*, Journal of Mining Science, 38(5).
- FLOREK I., CERNY V., 1992, *Intensification of the Magnetic Separation of Fine Chalcopyrite Ores by Means of Irradiation by Electrons*, [in:] Proceedings of the First International Conference on Modern Process Mineralogy and Mineral Processing, September 22–25, Beijing, China.
- BOCHKAREV G.R., ROSTOVTSEV V.I., VEIGEL'T, YU. P. et al, 1992, *Effects of Accelerated Electrons on Structural and Technological Properties of Ores and Minerals*, Journal of Mining Science, 28(6).
- OSTOPENKO P.E., SMOLYAKOV A.R., TRUFANOVA I.M. et al, 1993, *Directional Change of Technological Properties of Rare Metal Mineral By Means of the Radiation-Thermal action*, Journal of Mining Science, 29(1).
- LIU S.Y., 1994, *Principle of Magnetic and Electrical Beneficiation* (in Chinese) [M], Central South University of Technology Press, Changsha, China.
- WANG H.F., 2002d, *Study on Mechanism and Application Fundamental of Minerals Modification by Electron Beam Irradiation* (in Chinese), Doctoral Dissertation, Beijing, China.
- WANG H., BOCHKAREV G. R., ROSTOVTSEV V.I., VEIGEL'T Y.P., LU S., 2004, *Improvement of the magnetic properties of iron-bearing minerals during radiation-thermal treatment*, Journal of Mining Science, 40 (4), 399–408 .

Received June 1, 2013; reviewed; accepted July 3, 2013

EXTRACELLULAR ELEMENTS-MOBILIZING COMPOUNDS PRODUCED BY CONSORTIUM OF INDIGENOUS BACTERIA ISOLATED FROM KUPFERSCHIEFER BLACK SHALE – IMPLICATION FOR METALS BIORECOVERY FROM NEUTRAL AND ALKALINE POLYMETALLIC ORES

**Renata MATLAKOWSKA, Agnieszka WŁODARCZYK, Beata SŁOMINSKA,
Aleksandra SKŁODOWSKA**

Laboratory of Environmental Pollution Analysis, Faculty of Biology, University of Warsaw, Miecznikowa 1,
02-096 Warsaw, Poland, rmatlakowska@biol.uw.edu.pl

Abstract: Extracellular compounds produced by a consortium of indigenous bacteria interact with the polymetallic Kupferschiefer black shale and implicate for elements mobilization and/or complexation. The extracellular compounds were identified by GC-MS as carboxylic acids, but also aromatic acids and alcohols. Due to their action in batch experiment 16 elements were mobilized from black shale. Among mobilized elements precious metals (Cu, Ni, Co, V) as well as toxic heavy metals (As) were determined. Extracellular metabolites produced by studied consortium may be utilized in non-contact biorecovery of precious metals from neutral or slightly alkaline ores, and in the bioremediation of heavy metal-contaminated sites.

Keywords: *microbial consortium, extracellular compounds, black shale, metals mobilization*

Introduction

Mineralytic effect of microorganisms based on the acidolysis and/or complexolysis is an integral process of rock bioweathering. Solubilization of mineral elements and the breakdown of minerals can be caused by a wide range of microbial extracellular metabolites. One group of such compounds responsible for bioweathering are by-products of microbial metabolisms. During degradation of organic matter heterotrophic microorganisms produce variety of low molecular weight organic acids such as carbonic, aliphatic, phenolic and amino acids. Beside the dissolution of minerals and elements mobilization some of them have also ability to complex

elements. The chemistry and role of such compounds have been reviewed by Birch and Bachofen (1990).

Besides the role of such extracellular metabolites in geochemical cycling of elements in natural environment they are also of potential use in biotechnologies of the recovery of metals from deposits and wastes. This phenomenon is of great importance especially in the case of neutral or slightly alkaline ores where acidic leaching is not applicable. Copper bearing alkaline ultrabasic and carbonatite deposits made up 4% of worldwide copper mining activity. This type of ore is located among other in the middle of Europe in a great area from Middle Germany (the eastern edge of the Harz Mountains and the Saale river) to Fore-Sudetic Monocline and North Sudetic Trough (SW Poland). These copper deposits called Kupferschiefer are ranked as one of the largest and the richest of Cu and Ag deposits in the world (Oszczepalski, 1999). The concentrations of copper and silver in the black shale profile range from a few to up to 10 wt. % and up to 100 ppm, respectively. Beside these two main elements Kupferschiefer contains also considerable reserves of other basic and highly valuable and rare elements (cobalt, nickel, vanadium) as well as toxic elements (arsenic, lead). The major difficulties restricting the exploitation of such abundant resources is the low efficiency of the conventional technical methods for recovering valuable metals, from mining extraction to metallurgical processing. Metal bearing minerals are mostly merged with sandstone (24-85 %) and dolomite (11-62 %). In this situation all known methods of acid metals bioleaching widely used throughout the world are not useful.

Bioshale project was one of first projects dedicated to development of biotechnology for safe, clean and viable beneficiation of black shale ores in Europe and to propose an innovative, environmentally and socially favourable model of mining activities and metals recovery (d'Hugues et al., 2008). In frame of Bioshale project the consortium of indigenous microorganisms was isolated from Kupferschiefer black shale (Matlakowska and Skłodowska, 2009). During our last studies we demonstrated that indigenous bacteria play a prominent role in the weathering of black shale and in the biogeochemical cycles of elements occurring in this rock (Matlakowska et al., 2010; Matlakowska et al., 2012). It was shown that bacteria directly interact with black shale organic matter and indirectly influence on ore minerals. As a result of bacterial activity the redistribution of P, Al, Si, Ca, Mg, K, S, Cu and Pb was confirmed. Continuing these studies we focused on the analysis of non-contact action of microbial extracellular products on the rock components and potential implication of these processes. The analysis of such phenomenon is important not only to understand the role of microorganisms in ancient black shale transformations but also to find the methods of precious elements biomining from neutral or slightly alkaline ores. In presented study we describe the impact of extracellular metabolites produced under laboratory conditions by a consortium of bacteria isolated from Kupferschiefer black shale on the biotransformation of elements present in this rock and we discuss the potential role of these processes in biomining.

Materials and methods

Geological materials

Material for the study representing highly mineralized Kupferschiefer black shale was sampled at the underground Lubin mine below 600 m (Fore-Sudetic Monocline, SW, Poland). The crushed black shales with diameter fall in range: 0.25–0.5 mm; 1–2 mm and 3–4 mm were used. The whole rock analyses of the Kupferschiefer shale used in this study were performed by ACME Analytical Laboratories Ltd. Vancouver, Canada (<http://www.acmelab.com>) and its chemical composition is presented in Table 1.

Table 1. Chemical composition of Kupferschiefer black shale used in this study

Element (wt. %)		Element (mg kg ⁻¹)	
Na ₂ O	0.16	Cu	34958
K ₂ O	4.23	Co	1287
SiO ₂	34.50	Ni	336
Al ₂ O ₃	13.50	V	943
MgO	6.80	Mo	169
CaO	9.20	Mn	2224
Fe ₂ O ₃	3.50	Zn	26
S	1.89	As	1598
MnO	0.29	Fe	2450

Microorganisms

Bacterial strains were originally isolated from black shale (Lubin copper mine) and have been described previously (Matlakowska and Sklodowska, 2009). The mixed culture of microorganisms contained equal numbers of: *Microbacterium* sp. LM1 (EU821337), *Microbacterium* sp. LM2 (EU821338), *Acinetobacter* sp. LM3 (EU821339), *Bacillus* sp. LM4 (EU821340), *Pseudomonas* sp. LM5 (EU821341), *Pseudomonas* sp. LM6 (EU821342), *Pseudomonas* sp. LM7 (EU821343) and *Pseudomonas* sp. LM8 (EU821344).

Growth media

Luria-Bertani medium (LB) (Sambrook and Russell, 2001) was used for inoculum preparation. The mineral basal salts (MBS) medium containing glucose at concentration 20 mM (Hartmans et al., 1989) was used for production of extracellular metabolites.

Microorganisms cultivation

The mineral MBS medium was inoculated with an exponentially growing bacterial culture that had been cultivated in LB medium and then centrifuged (10 000 x g, at 4 °C, 10 min). Cultures were carried out in 500 millilitre flasks containing 250 ml of

mineral medium and were maintained in aerobic conditions, on a rotary shaker (150 rpm) at temperature 22 °C for 7 days. Sterile mineral medium with glucose was used as a control. Bacterial growth was monitored by plating diluted samples on solid LB medium to determine the number of CFU (colony forming units) and growth curves were plotted. The pH of bacterial culture and sterile control was measured at the end of experiment.

Dissolved organic carbon (DOC) analysis

The concentration of dissolved organic carbon (DOC) in the liquid phase of cultures was determined with Shimadzu TOC analyser TOC 5050A. A combustion/non-dispersive infrared gas analysis method was employed.

The analysis of extracellular compounds produces by bacterial consortium

Bacterial culture and sterile control were centrifuged (10 000 x g, at 4 °C, 10 min). 25 ml of samples of the cell-free supernatants was extracted with chloroform and then dried with anhydrous Na₂SO₄. Chloroform solutions were evaporated and then samples were prepared through the derivatization using BSFTA:TMCS 99:1 as silylating agent (Supelco, USA). GC-MS analyses were performed using an Agilent 7890A gas chromatograph associated to an electron impact ionization source 5975 series MSD (Agilent Technologies, USA). Identifications were carried out on a HP-5MS column (30 m long, 0.25 mm I.D., 0.25 µm film **thickness**, Agilent Technologies, USA) using He as carrier gas at 1 ml/min and an injection volume of 0.1 µl. The ion source was maintained at 230 °C; the GC oven was programmed with a temperature gradient starting at 100 °C for 3 min to 280 °C at 8 °C/min. MS analysis was carried out in the electron-impact mode at an ionizing potential of 70 eV. Compounds represented in the eluted peaks were identified by computer analysis using Wiley's mass spectra library (version 3.2, Copyright 1988–2000 by Palisade Corporation with The Wiley Registry of Mass Spectral Data, 8th Edition with Structures, Copyright 2000 by John Wiley and Sons, Inc.).

Elements mobilization from black shale by extracellular metabolites

10 g of crushed black shale was incubated with 100 ml of filter sterilized (pore size 0.22 µm) cell-free supernatant of bacterial culture in aerobic conditions on a rotary shaker (150 rpm) at temperature 22 °C for 24 hours. Sterile mineral medium supplemented with black shale were control for this experiment. All experiments were performed in triplicate. For chemical analysis the samples were centrifuged (10000 x g at 20 °C, 10 min), the supernatant was filtrated (pore size 0.22 µm) and mineralized with 65% nitric acid.

Elements concentration analysis

The chemical composition of cell-free supernatants of bacterial culture after incubation with crushed shale was determined by inductively coupled plasma emission

spectrometry (ICP-ES) using an Optima 5300 DV spectrometer (Perkin-Elmer, USA). All analyses were performed in triplicate.

Results and discussion

One of the processes responsible for elements redistribution in environment is their mobilization and/or complexation by a variety of extracellular organic substances produced by microorganisms. Low molecular organic acids and alcohols are released as a by-product of microbial metabolism due to incomplete metabolic pathways (Birch and Bachofen, 1990). A majority of organic acids are generated by microorganisms as a byproduct of fermentation or aerobic respiration of glucose.

In this study the growth of consortium of indigenous microorganisms on liquid mineral medium with glucose under aerobic condition and the concentration of total dissolved carbon was monitored for 7 days (Fig. 1). A typical growth curve was observed. During bacterial growth the carbon concentration decreased during first 4 days and then it started to increase up to the end of experiment (Fig. 1).

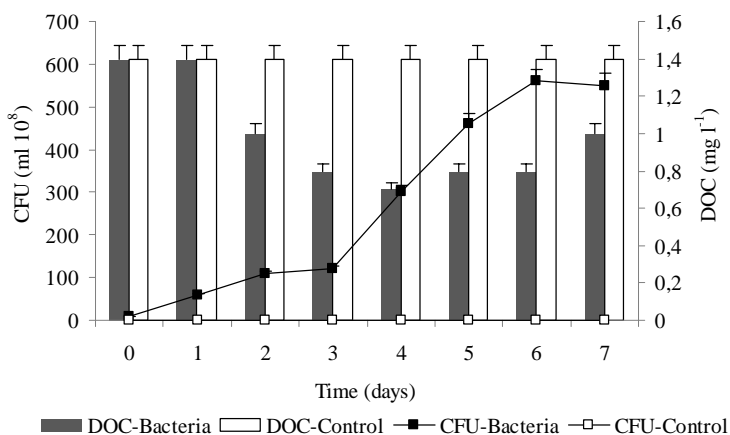


Fig. 1. The growth (CFU) of consortium of indigenous microorganisms on liquid mineral medium with glucose and the concentration of dissolved organic carbon (DOC)

The changes of the dissolved carbon concentration during bacterial growth suggest the utilization of glucose at the first days (decrease of the carbon concentration) and then the production of extracellular metabolites (increase of the carbon concentration). The pH of bacterial culture monitored during the bacterial growth decreased from 7.0 to 4.2 while the pH of sterile mineral medium (control) was stable (7.0).

The results of qualitative analysis of chemical compounds produced by consortium of indigenous microorganisms are presented in Table 2. Between compounds identified in culture sample 14 aliphatic (C7–C18) and 3 aromatic (C7–C8) carboxylic

acids were found (Table 2). In addition 5 alcohols were identified. All signals in the chromatogram of control sample (sterile mineral medium) originated from BSTFA:TMCS mixture.

The microbial extracellular metabolites such as organic acids increase mineral dissolution and mobilize elements by displacement of metal ions from the ore matrix by hydrogen ions or by the formation of metal complexes and chelates. The impact of organic acids and other metabolites on bioextraction of metal sulphide ore have been known for a long time. Parés (1964 a, b, c) described the solubilization of copper and other metals associated with laterite and clays using extracellular ligands formed by *Serratia marcescens*, *Bacillus subtilis*, *Bacillus sphaericus* and *Bacillus firmus*.

Table 2. The qualitative composition of extracellular compounds produced by mixture of microorganisms

Aliphatic carboxylic acids
heptanoic acid, octanoic acid, nonanoic acid, decanoic acid, undecanoic acid, 4-oxo-pentanoic acid, 5-dodecenoic acid, dodecanoic acid, 3-hydroxycapric acid, phenylpyruvic acid, 1,2-hydroxylauric acid, hexadecanoic acid, octadecanoic acid, 2,3-bishydroxypropyl laurate, 3-hydroxypalmitic acid
Aromatic carboxylic acids
benzoic acid, benzeneacetic acid, methyl benzoic acid
Alcohols
benzyl alcohol, glycerol, dodecanol, hexadecanol, octadecanol

Such species as *Bacillus circulans* and *Bacillus mucilaginosus* were described as able to leach manganese from ores using different organic compounds as reducing agents (Groudev, 1987). The most effective in metal solubilization are fungi: *Aspergillus* and *Penicillium* (Burgestaller and Schinner, 1993; Bosecker, 1997). Wenberg et al. (1971) reported the isolation of the fungus *Penicillium* sp. from a mine-tailing pond which produced unidentified metabolites that could mobilize copper from sedimentary ores of the White Pine deposit (Michigan, USA). Anjum et al. (2010, 2012) described the role of organic acids produced by *A. niger* in mobilization of copper, cobalt and zinc from black shale located in Pakistan. Also our studies of yeast *Rhodotorula mucilaginosa* sp. LM9 isolated from Kupferschiefer black shale showed that organic acids (malic and oxalic) produced by this strain can effectively mobilize copper from this sedimentary rock (Rajpert et al., 2013).

Despite extensive information on this topic in the literature, up to our knowledge this paper for the first time presents the simultaneous mobilization of dozen of elements from multielements sedimentary rock by the action of compounds of bacterial origin. Figure 2 shows the concentrations of nine elements after 24 hours of black shale incubation with cell-free supernatant containing bacterial metabolites and sterile mineral medium (control) and Table 3 presents the efficiency of mobilization of all studied elements.

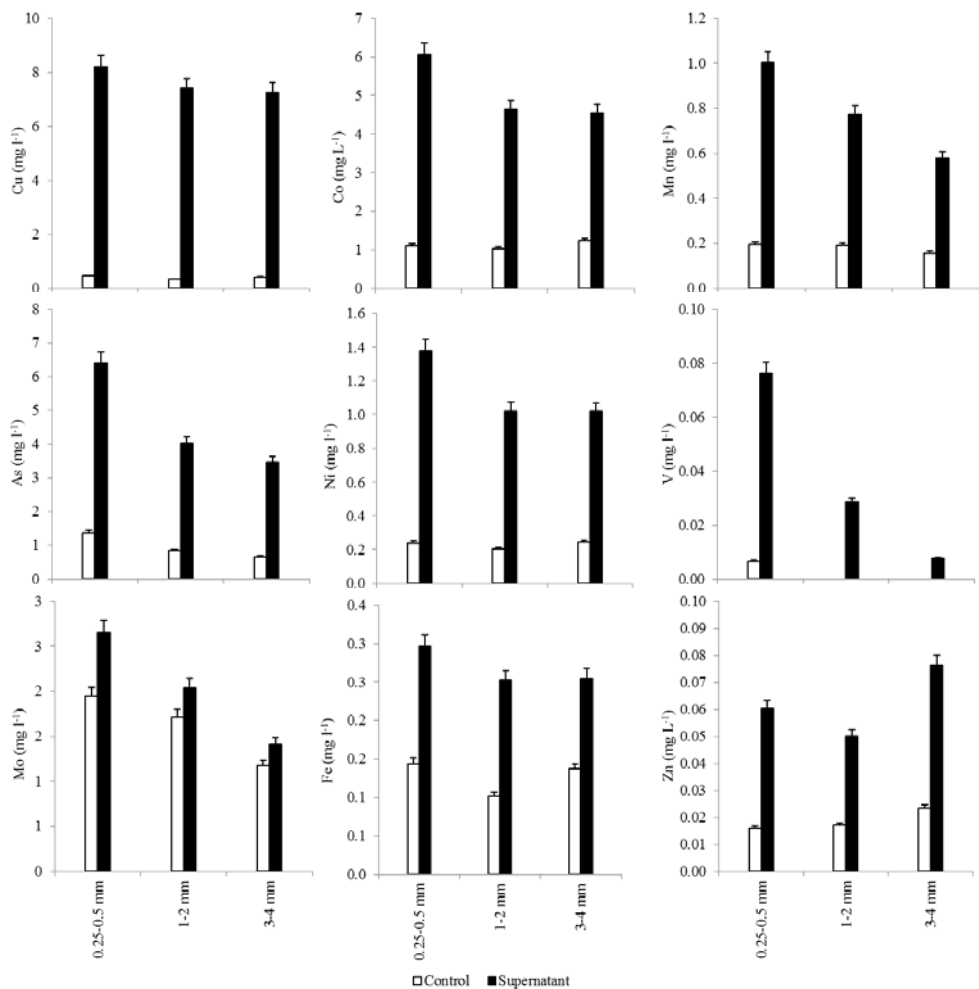


Fig. 2. Concentrations of elements mobilized from black shale by cell-free supernatant of bacterial cultures and sterile mineral medium (control) after 24 hours of incubation. Bars represent the standard deviation of measurements

The role of bacterial extracellular metabolites in mobilization of Ca, Na, Mg, Si, Al, Cu, Co, As, V, Zn, Ni, Mo, Fe, and Mn was clearly evident. The concentrations of K and S were lower in studied sample than in control where only chemical weathering was observed. The mobilization of elements was depended on the diameter of crushed shale and it was the highest in the case of fine crushed shale (0.25–0.5 mm) that could be simply explained by the differences in active surface area of different fractions used in this study.

The extracellular metabolites can be beneficial for microorganisms – they can be utilized as a means of sequestering of some metals from external environment to

supplement their nutritional needs. They can be also used as a way of detoxication against toxic elements. Black shale represents a type of extreme environment characterized by high concentrations of heavy metals and limited access to sources of carbon and energy. According to detailed petrographic and geochemical characterization of Kupferschiefer black shale performed by Speczik (1994) and Oszczepalski (1999) about 60 different major and trace elements in more than 100 different minerals occur in this ore. Rock-forming minerals such clay minerals, feldspars, dolomites and calcites are potential sources of Na, K, Al, Si, Ca and Mg. Such elements as Cu, Zn, Fe, Mo, S are mobilized from ore minerals - Cu-S, Cu-Fe-S, Cu-As-Sb-S, Pb-S and Zn-S Cu-Mo-S Mo-S. A part of mobilized elements can originated from metalloorganic compounds and geoporhyrins. Among them is first of all vanadium, but also it can be nickel, cobalt and molybdenum (Matlakowska et al., 2013).

Table 3. The efficiency (%) of elements mobilization from black shale by a microbial extracellular compounds

Element	Fraction size					
	0.25–0.5 mm		1–2 mm		3–4 mm	
	Supernatant	Control	Supernatant	Control	Supernatant	Control
Na	3.56	0	2.94	0	2.61	0
K	0.79	0.94	0.48	0.74	0.42	0.60
Al	0.011	0.0023	0.0098	0.00054	0.0069	0.00068
Si	0.035	0.025	0.025	0.022	0.023	0.021
Mg	0.31	0.31	0.29	0.24	0.27	0.19
Ca	1.3	0.76	0.83	0.52	0.73	0.38
Fe	0.012	0.0058	0.010	0.0042	0.010	0.0056
Mn	0.45	0.087	0.34	0.084	0.26	0.07
S	3.54	5.32	2.17	3.49	2.17	3.33
Cu	0.23	0.013	0.22	0.0092	0.21	0.012
Co	4.69	0.85	3.59	0.79	3.52	0.94
Ni	4.08	0.71	3.04	0.61	3.03	0.73
V	0.08	0.0074	0.03	0	0.0085	0
Mo	15.68	11.48	12.01	10.11	8.34	6.92
Zn	2.3	0.62	1.92	0.65	2.92	0.88
As	4.02	0.85	2.52	0.53	2.18	0.41

The efficiency of elements mobilization was the highest for cobalt (4.69%), nickel (4.08%) and arsenic (4.02%). The distribution of arsenic in black shale is very similar

to that of cobalt and nickel. Biorecovery of nickel and cobalt by mean of extracellular metabolites is very promising solution but also the mobilization of toxic arsenic is of great importance. Arsenic is an element that is very often associated in copper minerals. Contamination of copper ore with this metalloids is troublesome for hydrometallurgical processes. During smelting processes the volatile arsenic compounds are released into the atmosphere, which due to the toxicity of these compounds is a significant environmental hazard. Besides volatile arsenic compounds, high concentrations of arsenic are found also in the dust from tailings ponds. For this reason, very important, both from an economic and environmental point of view, is to develop effective methods for controlled removal of arsenic from copper deposits.

Conclusion

Taken together, the results of present study increase our knowledge about black shale bioweathering and confirm that bacteria may indirectly influence on the simultaneous mobilization of elements from sedimentary rock. This phenomenon has the potential application in biorecovery of metals from neutral or alkaline ores and wastes containing such ores and it could be used as the non-contact and environmentally friendly method of metal recovery.

The application of this biotechnology requires further research focused on finding a cheap source of extracellular compounds and process optimization. Another aspect requiring further analysis is the possibility of including these microbial metabolites into hydrometallurgical processes and recovering the mobilized metals as well as re-using the solutions.

References

- ANJUM F., SHAHID M., AKCIL A., 2012, *Biohydrometallurgy techniques of low grade ores: A review on black shale*. Hydrometallurgy 117–118, 1–12.
- ANJUM F., BHATII H.N., ASGHER M., SHAHID M., 2010, *Leaching of metal ions from black shale by organic acids produced by Aspergillus niger*. J. App. Clay Sci. 47, 356–361.
- BIRCH L., BACHOFEN R., 1990, *Complexing agents from microorganisms*. Experientia 46, 827–834.
- BOSECKER K., 1997, *Biorecovery: metal solubilization by microorganisms*. FEMS Microbiol. Rev. 20, 591–604.
- BURGSTALLER W., SSHINNER F., 1993, *Leaching of metals with fungi*. J Biotechnol. 27, 91–116.
- GROUDEV S.N., 1987, *Use of heterotrophic microorganisms in mineral biotechnology*. Acta Biotechnol. 7, 299–306.
- HARTMANS S., SMITS J.P., VAN DER WERF M.J., VOLKERING F., DE BONT J.A.M., 1989, *Metabolism of styrene oxide and 2-phenylethanol in the styrene-degrading Xanthobacter strain 124X*. Appl. Environ. Microbiol. 55, 2850–2855.
- d'HUGES P., NORRIS P.R., HALLBERG K.B., SANCHEZ F., LANGWALDT J., GROTOWSKI A., CHMIELEWSKI T., GROUDEV S., BIOSHALE CONSORTIUM, 2008, *Bioshale FP6 European project: exploiting black shale ores using biotechnologies?* Minerals Engineering 21, 111–120.

- MATLAKOWSKA R., SKIODOWSKA A., 2009, *The culturable bacteria isolated from organic-rich black shale potentially useful in biometallurgical procedures*. J. Appl. Microbiol. 107, 858–866.
- MATLAKOWSKA R., NARKIEWICZ W., SKIODOWSKA A., 2010, *Biotransformation of organic-rich copper bearing black shale ore by indigenous microorganisms isolated from Lubin copper mine (Poland)*. Environ. Sci. Technol. 44, 2433–2440.
- MATLAKOWSKA R., SKIODOWSKA A., NEJBERT K., 2012, *Bioweathering of Kupferschiefer black shale (Fore-Sudetic Monocline, SW Poland) by indigenous bacteria: implication for dissolution and precipitation of minerals in deep underground mine*. FEMS Microbiol. Ecol. 81, 99–110.
- MATLAKOWSKA R., RUSZKOWSKI D., SKIODOWSKA A., 2013, *Microbial transformations of fossil organic matter of Kupferschiefer black shale – elements mobilization from metalloorganic compounds and metalloporphyrins by a community of indigenous microorganisms*. Physicochem. Probl. Miner. Process. 49, 223–231.
- OSZCZEPALSKI S., 1999, *Origin of the Kupferschiefer polymetallic mineralization in Poland*. Mineral Deposita 34, 599–613.
- PARES Y., 1964a, *Intervention des bacteries dans la solubilisation du cuivre*. Ann. Inst. Pasteur (Paris) 107, 132–135.
- PARES Y., 1964b, *Action de Serratia marcescens dans le cycle biologique des metaux*. Ann. Inst. Pasteur (Paris) 107, 136–141.
- PARES Y. 1964c, *Action d'Agrobacterium tumefaciens dans la mise en solution de l'or*. Ann. Inst. Pasteur (Paris) 107, 141–143.
- RAJPERT L., SKŁODOWSKA A., MATLAKOWSKA R., 2013, *Biotransformation of copper from Kupferschiefer black shale (Fore-Sudetic Monocline, Poland) by yeast Rhodotorula mucilaginosa LM9*. Chemosphere 91, 1257–1265.
- SAMBROOK J., RUSSEL D.W., 2001, *Molecular cloning: A laboratory manual*. 3rd edn. New York USA: Cold Spring Harbor Laboratory Press.
- SPECZIK S., 1994, *Kupferschiefer mineralization in the light of organic geochemistry and coal petrology studies*. Geol. Quarterly 38, 639–650.
- WENBERR G.M., ERBISH F.H., VOLIN M., 1971, *Leaching of copper by fungi*. Trans. Soc. Min. Eng. AIME 250, 207–212.

Received May 7, 2013; reviewed; accepted July 9, 2013

THE CONCEPT OF THE SCIENTIFIC STANDPOINT OF THE ROLLING -SCREW SCREEN. PARTIAL AUTOMATION OF THE SCREENING PROCESS

Wojciech POCWIARDOWSKI*, **Piotr WODZINSKI****, **Joanna KANIEWSKA***

* University of Technology and Life Sciences, Faculty of Chemical Technology and Engineering
ul. Seminaryjna 3, 85-326 Bydgoszcz, e-mail: wojciech.pocwiardowski@utp.edu.pl

** Politechnika Lodzka, W 10, K 101, 175 Wolczańska Street, 90-924 Lodz, wodzinsk@wipos.p.lodz.pl

Abstract. The study presents suggestions of partial automation of the screening process with the use of the rolling-screw screen. The principles of screening using such a screen was also briefly described in the study.

Keywords: *screening, rolling-screw screens, automation*

Introduction

Rolling screens (rolling-screw screens) are machines designed for the realization of granular materials sieve classification processes. It refers, first of all, to fine and very fine-grained granular mixtures, which due to their particle size, cannot be screened using other known sieves. These machines perform a complex, spatial, rotational movement, being so-called “drunken barrel” movement. The screening process of these machines is performed through putting the feed centrally onto the highest located (within sieving layer sets) sieve (of the biggest holes). The above-sieved products X1, X2... are collected through side gutters whilst the below-sieved products Y1, Y2... form the feed for further, lower located sieves (Fig. 1) (Pocwiardowski and Wodzinski 2011a, Pocwiardowski and Korpala 2010, Pocwiardowski 2012, Wodzinski 1997).

During the screening process we deal with a number of parameters, which need both monitoring and controlling. To fulfill these needs the elements of mechatronics registering and supervising these parameters could be introduced.

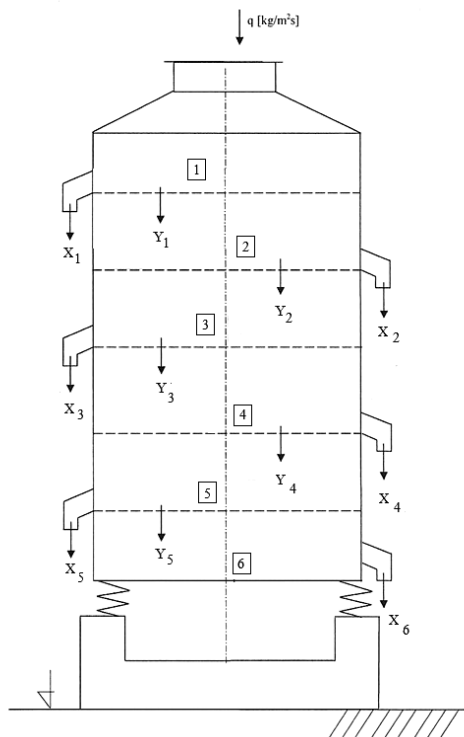


Fig. 1. The diagram of the screening process using a rolling-screw screen

The aim an the scope of the study

The aim of the study is to propose a solution to the screening of granular materials process automation using a rolling-screw screen.

The guidelines on the screening process automation

The project includes the place for screening granular materials of fine and very fine grain-size, which consists of the following:

- gutter feeder (website of VIBRO-EKO-TECH) operating within the influx intensity q within the range from 5 to 50 kg/h. The influx intensity is adjusted by feeding voltage of the electromagnetic vibrator with the use of the inverter. Additionally, the feeder is equipped with an electronic sliding bolt in a place where a charging hopper is,
- a rolling-screw screen consisting of seven sieving panels, which enables to achieve up to eight fractions within one passage (Fig. 2),



Fig. 2. A rolling-screw screen with a fraction receiver (Pocwiardowski and Wodzinski 2011b)

- a sieving fraction receiver (Fig. 2) located on electronic industrial scales (website of RADWAG) enabling monitoring of mass increment of collected fractions,
- an inverter, which is used for switching on and off the screen, as well as for changing the angular speed of motor-vibrators, and adjustment of granular materials influx (Catalog page of inverter MX2 OMRON),
- Bruel&Kjaer SYSTEM PULSE used for the measurement of oscillation amplitude of the screen within three axis plane x,y,z ,
- computer PC, which controls the entire process and is connected to the monitoring sensors of the scening process.

The mechatronics system guidelines

- the control of sieving fractions mass influx, which enables indirectly the monitoring whether the sieves have not been blocked by the materials being screened;
- the measurement of oscillation amplitude within three axis plane x, y, z ,
- change of the angular speed of motor-vibrators (the phenomenon of the sieve blockage by the sieving material),
- dosage of the granular materials.

The implementation of the mechatronics system

- mass influx is monitored with the use of an industrial scale of RADWAG WPW 60 H5/K with a maximum load 60kg and readout accuracy 20g, and output signal RS 232/RS 485,
- the oscillation amplitude within three axis plane x,y,z is measured with an Bruel&Kjaer Triaxial delta tron accelerometer type 4524-b-001. The signal from a sensor is converted in the Bruel&Kjaer SYSTEM PULSE measuring box connected to the PC via a cable,
- the change of the angular speed of motor-vibrators is done with the use of OMRON inverter OMRON mx2, class 400v, with signal output RS485 ModBus RTU,
- the dosage of the granular materials is done with the use of a gutter feeder connected to OMRON mx2 inverter and equipped with an electro -valve (numerically controlled (I/O)) placed in the charge basket opening,
- the connection to the computer via USB-COM-4S equipped with four ports RS 485, the computer equipped with an USB input and a card system.

Table 1. A sample solution to the implementation of the mechatronics system for a rolling-screw screen

No.	Given parameters	Solution	Apparatus
1	Receivers mass influx	An industrial scales of max. load 60kg with readout accuracy 20g, and output signal RS 232/RS 485.	e.g., RADWAG scales model WPW 60 H5/K
2	oscillation amplitude within three axis plane x,y,z	Accelerometer measuring oscillation amplitude within three axis plane x,y,z w within frequency 0.25–3000 Hz	e.g., Triaxial delta tron accelerometer model 4524-b-001 operated by Bruel&Kjaer SYSTEM PULSE
3	The adjustment of the angular speed of motor-vibrators	Inverter class 400v, with signal capacityRS485 ModBus RTU with a possibility of connecting to PC	e.g., Omron inverter mx2
4	dosage of the granular materials	Gutter feeder (dosing capacity up to 50 kg/h) connected to an inverter and equipped with an electro -valve (numerically controlled (I/O)) placed in the charge basket opening	e.g., Gutter feeder – vibratory Omron inverter mx2 an electro-valve (numerically controlled (I/O))

The description of the system operation – the stages of the process

Initial research

Before commencing the screening process with the use of a rolling-screw screen, the sieving analysis of the researched material should be performed (suggested shaker Fritsch) in order to determine the percentage composition of individual sieving fractions.

The dosage process

The feed is put centrally onto the highest located sieve of the screen pillar (of the biggest sieving holes) with the use of a gutter feeder driven electromagnetically. The change in current frequency causes the change of engine rotation frequency thus the material dosage amount adjustment onto the screen. The feeder gutter is placed on a springy suspension. The gutter is activated by the engine therefore it performs reciprocating motion. The motion makes the granular material shift onto the screen. The charging hopper opening of the feeder is equipped with an electronically controlled electro -valve, which adjusts the dosage with influx intensity q [kg/h]. In case there is a screen running stoppage (messages: SIEVES BLOCKAGE, RECEIVERS CHANGE, SCREENING FINISHED) the computer sends a signal to the electro -valve in order to cut out the granular material influx onto the screen.

The screening process

The granular material dosed onto the rolling-screw screen is directed from sieving panels via side gutters onto the receivers. The receivers are placed on the electronic industrial scales, enabling the monitoring of mass increment of the particular fraction. When the receivers are filled (the mass of the received fraction exceeded the maximum mass of the receiver) a message RECEIVERS CHANGE is displayed, the screen is stopped by the inverter and the electro-valve is closed. After the receivers change the screen turns on again via the inverter controlled by a computer PC. In case there is too large amount of one of the sieving fractions (the receiver mass is too large due to the percentage contents of particular sieving fractions of the researched material) a message SIEVES BLOCKAGE is displayed. The system sends signal to the inverter in order to increase the motor-vibrators rotational speed until the sieve is unblocked (the completion of the process is indirectly noticeable via the particular fractions mass)

The control of the SYSTEM PULSE

The Bruel&Kjaer SYSTEM PULSE analyzer operated by PULSE LabShop program reads the signal from the sensor: Triaxial delta tron accelerometer type 4524-b-001 (Bruel&Kjaer official website). With the use of this sensor the sieving oscillation amplitude within three axis plane x,y,z is recorded. In case of too low or too high amplitude value on particular axis, a message SERVICE is displayed. The deviating amplitude values on particular axis might mean:

- wrong set-up angle of the side motor-vibrators,
- wrongly screwed screen,
- screen resonance occurs.

In each of the above cases the system turns of the screen via the inverter and cuts out the influx of the granular material onto the screen.

The sensor mounting diagram (Fig. 3) on the rolling screen as well as actual measurement of the sieving oscillation amplitude within three axis plane x,y,z (Fig. 4–8) were presented below.

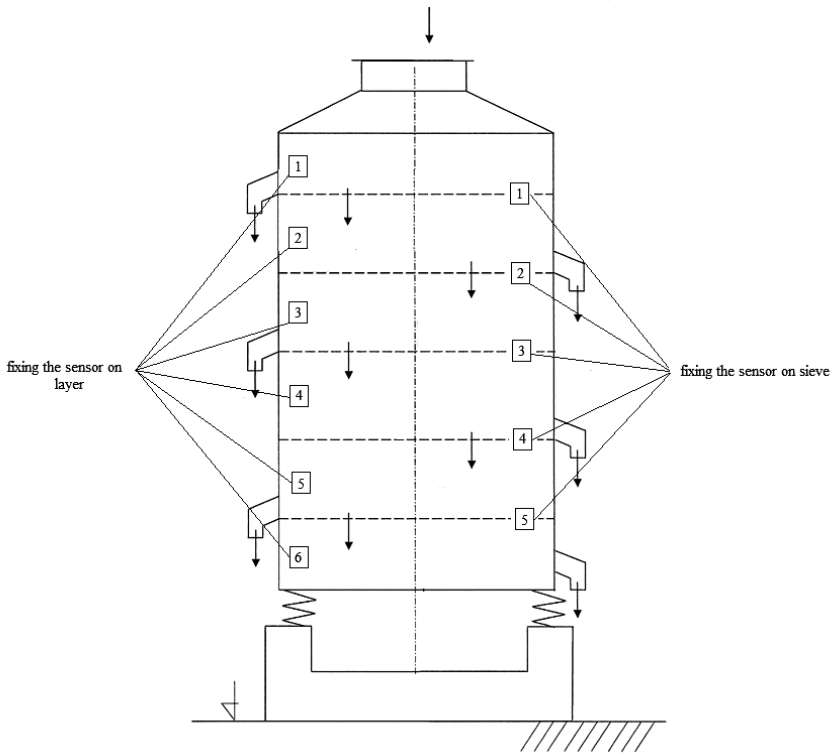


Fig. 3. The sensor (accelerometer) mounting diagram on a rolling scree

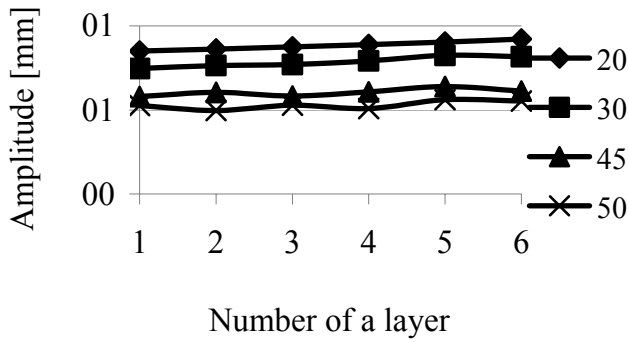


Fig. 4. Layer oscillation amplitude within X axis in the screen with various inclination angles of the motor-vibrators

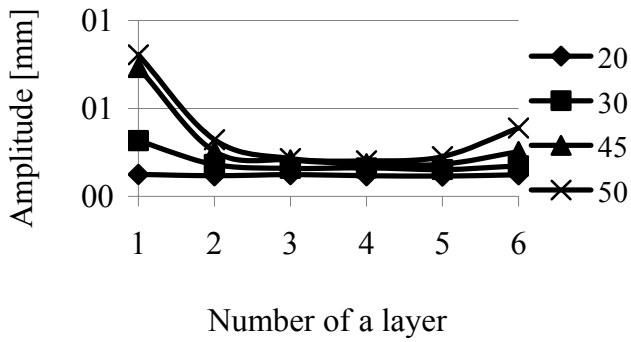


Fig. 5. Layer oscillation amplitude within Y axis in the screen with various inclination angles of the motor-vibrators

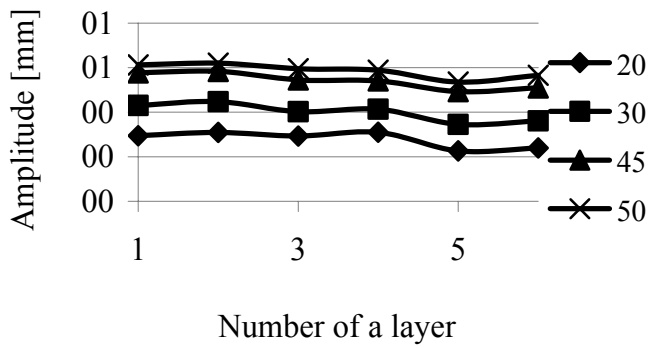


Fig. 6. Layer oscillation amplitude within X axis in the screen with various inclination angles of the motor-vibrators

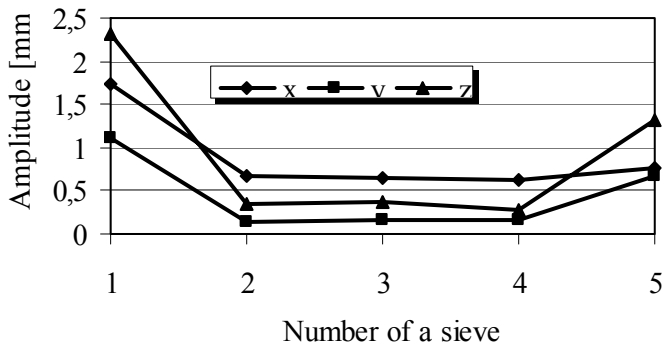


Fig. 7. Sieves oscillation amplitude within X, Y, Z axis with the motor-vibrators inclination angle of 20°

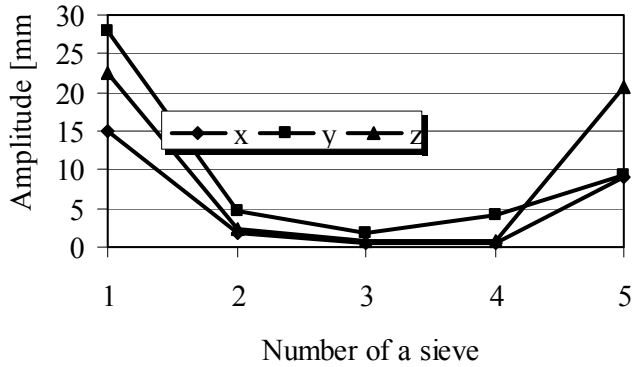


Fig. 8. Sieves oscillation amplitude within X, Y, Z axis with the motor-vibrators inclination angle of 45°

The mechatronics system diagram was presented below in Fig. 9.

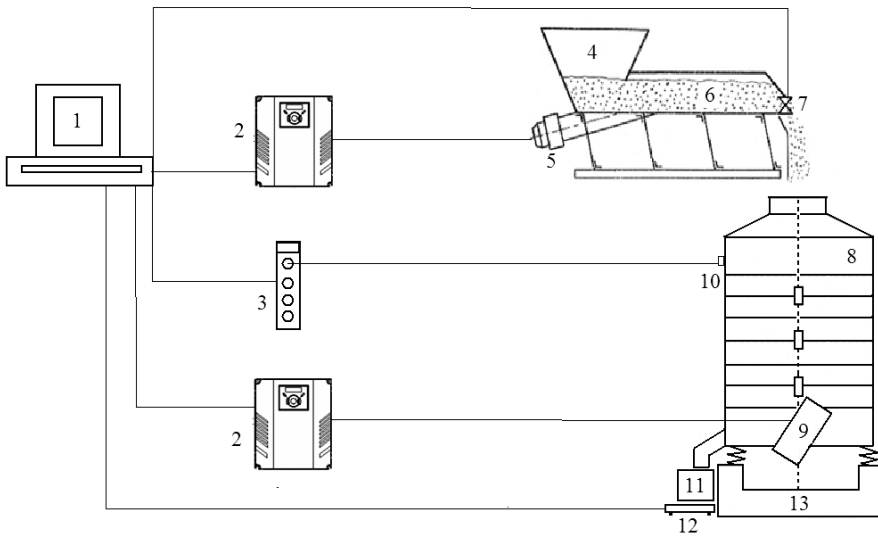


Fig. 9. The mechatronics system diagram

- 1 – computer, 2 – inverter, 3 – SYSTEM PULSE box, 4 – gutter feeder – vibratory,
 5 – feeder engine, 6 – gutter feeder on a springy suspension, 7 – feeder electro-valve,
 8 – rolling-screw screen, 9 – side motor-vibrators, 10 – accelerometer, 11 – receiver,
 12 – industrial scales, 13 – screen base.

Conclusions

1. The mechatronics system allows controlling most of the screening processes via the computer panel.

2. The application of this solution enables early reaction to the problems arising during the process.
3. The set of the sensors enables the visualization of particular parameters of the process.
4. The screening process automation enables process run reports making.
5. The above research standpoint is to be made in order to test its possibility.

Acknowledgement

This work was done within the framework of statutory activity of Procedural Apparatus Faculty of Lodz University of Science: W-10/16/2012/Dz.st.

References

Inverter catalog card MX2 OMRON.

POCWIARDOWSKI W., KORPAL W. (2010): *The analysis of sieving carrot seeds via the sieves of rolling screen*, Agricultural engineering, 4 (122), 179–187.

POCWIARDOWSKI W., WODZINSKI P. (2011a): *The sieving of mineral resources on the rolling screen*. The Research Studies of the Science Institute of Mining, Institute of Technology – Wrocław, 132, 225–236.

POCWIARDOWSKI W., WODZINSKI P. (2011b): *The sieving of biological material on the rolling screens*, Environment Protection Yearbook, 13, 1115–1131.

POCWIARDOWSKI W., WODZINSKI P., KANIEWSKA J. (2012): *The sieving of calcareous aggregate on the rolling-screw screen*, Mining and geology XVII – Agricultural engineering; 134.

WODZINSKI P. (1997): *Sieving and screens*. Institute of Technology, Lodz.

RADWAG official website – Electronic and Multifunction scales WPW, 2012, Online access: www.radwag.pl/e-sklep/2a_wpwc.htm, access 03-09-2012.

Bruel&Kjaer official website, Products, 2012, Online access: www.bksv.com/Products/Transducers/Conditioning/vibration-transducers/accelerometers/accelerometers/4524B001.aspx?tab=specifications, access 03-09-2012.

VIBRO-EKO-TECH official website, Vibration feeders and batcher, Online access: www.vet.com.pl/?a=document&documentId=868#, access 03-09-2012.

Received December 12, 2013; reviewed; accepted July 10, 2013

SILICIDE SPHERULES FROM PERMIAN SEDIMENTS OF THE FORE-SUDETIC MONOCLINE (SW POLAND)

Antoni MUSZER

Institute of Geological Sciences, University of Wrocław, Pl. Maksa Borna 9, 50-205 Wrocław, Poland

Abstract: The presence of Fe-silicides, extremely rare mineral phases were documented in the Permian Cu-bearing ore formation in the Fore-Sudetic Monocline (Polkowice-Sieroszowice and Rudna mines, SW Poland). It is a first report of their occurrence within rocks of Late Palaeozoic age. The Fe-Si alloys form spherules of various structure and chemical composition. The silicide spherules were found in the flotation concentrates prepared from the copper ore. Their composition varies from FeSi (fersilicite) to Fe₂Si₃ or Fe₄Si₉. A dominant constituent is Fe₅Si₃ (xifengite) with admixtures of P, Ti, Cr and Mn. Native Si and Ti were detected in the marginal part of spherules. The current knowledge do not permit to determine unequivocally whether the Fe-silicide spherules formed as a result of Permian cosmic dust or constitute terrestrial magmatic material of ultramafic character transported into a sedimentary basin from the adjacent terrain.

Keywords: Permian, Fe-silicide spherules, cosmic dust, ore minerals, Fe-Si alloy

Introduction

During routine research of copper flotation concentrates from the Polkowice-Sieroszowice Mine (SW-Poland, Fig. 1) the presence of very rare minerals, such as iron silicide was discovered (Muszer, 2007). On the basis of this analysis new research was designed to determine the location of their occurrence in the Permian rocks.

Silicides still remain relatively poorly investigated and exotic mineralogical compounds. First report about naturally occurring Fe-Si compounds was published by Gevorky'en (1969). Recently a newly discovered Fe-Si phase was described from the Tibetan mines (Bai et al., 2007). On the other hand, from the chemical point of view, silicides has been known for over 100 years. Alloys of Si with another metallic element, e.g. TiSi₂ and CoSi₂, found industrial use as joints of various metals in semiconductors. Natural Fe-silicides were found in meteorites (Mason, 1962; Judin and Kolomenskij, 1987), sedimentary (Gevork'yen et al., 1969; Novosielova, 1975), metamorphic (Xiongjian, 1991) as well as mafic (Bai et al., 2007) and felsic igneous

rocks (Jakabska and Rozložník, 1989). This mineral group comprise fersilicite FeSi , hapkeite Fe_2Si , gupeite Fe_3Si , suessite Fe_3Si , xifengite Fe_5Si_3 , luobusaite $\text{Fe}_{0.84}\text{Si}_2$ and ferdasilicite (leboite) FeSi_2 . Fersilicite was recorded from the Poltava sandstones of the Donyeck area in Ukraine (Gevork'yen, 1969; Gevork'yen et al., 1969). Suessite was discovered in the North Haig ureilite meteorite (achondrite) from South Australia in 1980 (Keil et al., 1982; Judin and Kolomenskij, 1987). According to Keil et al. (1982) it was formed during the fall as a result of silica reacting with carbonaceous matrix. Gupeite and xifengite were detected in cosmic dust from Yanshan province (China) in the paragenesis with kamacite, taenite, magnetite, wüstite and maghemite (Zuxiang, 1984). Similarly to fersilicite from Ukraine, they were found in heavy mineral concentrates obtained from alluvial deposits.



Fig. 1. Location of sampling points in SW Poland

Luobusaite $\text{Fe}_{0.84}\text{Si}_2$ was found at the Cr-Fe Luobusa mine in the Autonomic Xizang Region (Tibet) in 2007 (Bai et al., 2007). It occurs as irregular grains in Cretaceous ophiolitic rocks accompanied by numerous alloys of Fe-Si, Ni-Fe, Fe-Cr, Ir-Fe, W-Co, Cr-C, Ti-N, Si-Ca as well as abundant oxides, sulphides, arsenides and extremely rare Si spinels (Bai et al., 2007).

Another IMA-approved natural Fe-Si species are hapkeite and ferdasilicite. Hapkeite Fe_2Si was described from Lunar meteorite breccia Dh-280 found in the Dhofar Province, Oman (Anand et al., 2004). It occurs in weathered plagioclase together with fersilicite, Fe-Ni alloys and ferdasilicite FeSi_2 . According to Anand et al. (2004), hapkeite formed as a result of meteorite fall onto the Lunar regolith. Ferdasilicite (leboite) FeSi_2 is known from the sedimentary Poltava sequence in the Donyeck area (Ukraine) and the concentrates of metamorphic rocks from Longquan, Zhejiang Province, China (Xiongjian, 1991). In both occurrences it coexists with other Fe-Si compounds, i.e. Fe_5Si_2 , xifengite (Fe_5Si_3) and a mixture of phases with varying Fe-Si proportions. Ferdasilicite was also found in the kimberlites of Sytykanskaya (Russia) where it is accompanied by native Si and other Fe-silicides (Pankov and Spetsius, 1989). Unnamed are such phases as Fe_4Si_9 , Fe_5Si_3 and Fe_2Si_3 . They occur as

intergrowths with moissanite (SiC) found in Lower Cambrian carbonaceous rocks of the Sayan Mts, Russia (Novosielova, 1975). According to Novosielova and Bagdasarova (1979) they are of meteoritic origin.

Samples

Three samples, about 10 kg each, were chosen to investigate the presence of Fe-silicides in the Permian rocks of SW Poland (Fig. 1). The samples were: ore-bearing formation of the Polkowice-Sieroszowice copper mines (KGHM Polska Miedz S.A.), ore material processed in the Polkowice-Sieroszowice Ore Concentrator and a sample of tailing stored in the Zelazny Most tailings pond (Rudna Ore Concentrator). The first one consists of reddish-brown dolomitic shale and represents marine sediments of the Rotliegendes/Zechstein boundary (Werra cyclothem). It was obtained from the side-wall of the gallery in the G-31 mining section of the Polkowice-Sieroszowice mine (Fig. 2). The laminated aleurite-pelitic rock contains carbonates (calcite, dolomite), clay minerals and detritic quartz with minor anatase and titanite. Opaque phases constitute from 0.1 to 1% of its volume. Dominating chalcopyrite is dispersed in the rock, while subordinate chalcocite, covellite, digenite, pyrite together with uncommon bornite, native Au and electrum (up to 35.5% Ag) form laminae. Chalcopyrite aggregates reach 200 µm in diameter. Pyrite forms subhedral grains up to 50 µm across. Other sulphides rarely exceed 30 µm. Native gold and electrum form intergrowths and clusters with digenite. Au-bearing ore minerals, dominated by native Au with small admixture of Ag < 2.45 wt %, are of various size: from several to several dozens µm.

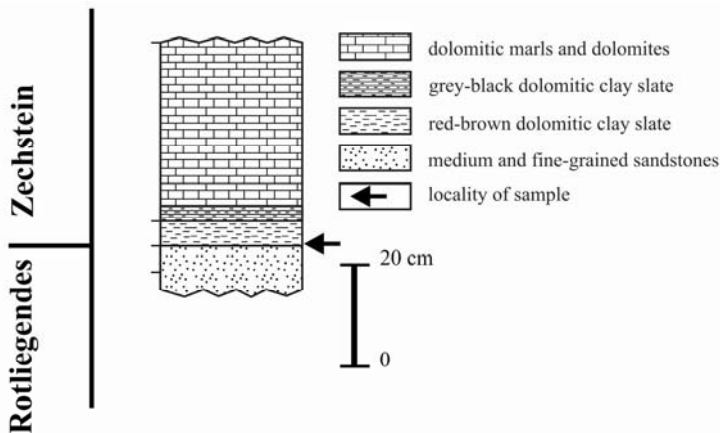


Fig. 2. Lithological profile of the side-wall of mine gallery in mining section G-31 (Polkowice-Sieroszowice mine)

The sample of material processed in the Polkowice-Sieroszowice Ore Concentrator consists of Cu-bearing, streaky dolomite and dolomite. The sample from the Rudna Ore Concentrator represents flotation tailings.

Methods

The Permian rocks were crushed in a Fritsch jaw crusher into <0.25 mm fraction and then enriched by flotation and magnetic separation (Nd-magnet, 6000 Gs and 9000 Gs). A Joy-Denver flotation cell was used to concentrate minerals and spherules. Cu- and Fe-bearing concentrates together with spherules built of various minerals constituted 0.01 and 0.02% of the initial weight of the first and second sample, respectively.

Magnetic and non-magnetic spherules were separated from other mineral phases present in the concentrates using an experimental ramp-like device developed by Muszer (2007). As a result, a satisfying number of objects was obtained to use statistical approach in describing structural and microtextural features of individual spherule types as well as to characterise their chemical composition.

Polished sections were prepared following the standard procedure used for ore minerals and metallographic material (Samuels, 1982; Muszer, 2000). DP-Mol, DP-Dur and DP-Nap Struers polishing cloths were used with precisely controlled granulation of diamond pastes.

An optiphot 2-Pol Nikon microscope was used for observations in reflected light. Ore minerals were distinguished basing on their optical and physical properties (Uytenbogaardt and Burke, 1971; Ramdohr, 1973, 1975; Criddle and Stanley, 1993; Muszer, 2000; Bernhard, 2008). Planimetric analysis, coupled with the Lucia M software, was employed to establish the proportions between minerals, spherules and microporosity in the studied samples. The spherules were subdivided into several types basing on the concentration of a dominant mineral or alloy (i.e. into aluminosilicate, silicate and silicide types).

Chemical point analyses of the spherules and accessory minerals were conveyed using SEM-515 (Philips) and JOEL JSM-55800LV electron microscopes. A MIKROSKAN MK-9 Cambridge electron microprobe was used in case of bigger mineral grains or homogeneous spherules. The analyses were carried out in the Institute of Low Temperature and Structure Research (Polish Academy of Sciences, Wroclaw), Institute of Materials Science and Applied Mechanics (Wroclaw University of Technology) and Department of Mineralogy and Petrology (Institute of Geological Sciences, University of Wroclaw). Pure (99.99%) metal of Fe, Ni, Co, Mn, Al, Cu and Zn as well as pure SiO₂ and Al₂O₃ were used as standards.

Results

In the analysed samples Fe-silicides occur within spherules, which are present in the red shale obtained at the Rotliegendes/Zechstein boundary in the Polkowice-Sierszowice mine as well as in the tailings from the Rudna Ore Concentrator. In the ore from the Polkowice-Sierszowice mine only metallic sulphides together with magnetite, magnetite-hematite and Fe-spherules were detected (Muszer, 2007).

The silicide spherules are present in parasteresis with Cu-, Zn- and Pb-sulphides as well as other minerals typical of the ore-bearing rock series of the Lubin-Glogow Mining Area: chalcocite, bornite, chalcopyrite, covellite and others. The chemical composition and microtexture of the Fe-spherules in both samples are alike. However they differ in the spherules size. In the red shale Fe-silicide spherules reach 50 μm and often exceed 150 μm in the tailings.

Spherules from red-brown shale (Polkowice-Sierszowice mine)

Magnetite, hematite, Fe-silicides, arsenopyrite, pyrrhotite, bornite, covellite, pyrite and goethite were detected in a magnetic concentrate prepared from the red shale (Polkowice-Sierszowice mine). Rock fragments incrustated by Fe-hydroxides, i.e. goethite and hydrogoethite constitute 60.45% of the sample volume. Only magnetite grains from several to 200 μm across were not intergrown with rock fragments and other minerals. Pyrrhotite spherical forms, with the diameter ranging from 2 to 25 μm , occur within rock fragments enriched in Fe-hydroxides. A 25 μm big pyrite framboids coexists with bornite. Covellite was also found in rock fragments (up to several dozens μm) impregnated with Fe-hydroxides (Fig. 3).

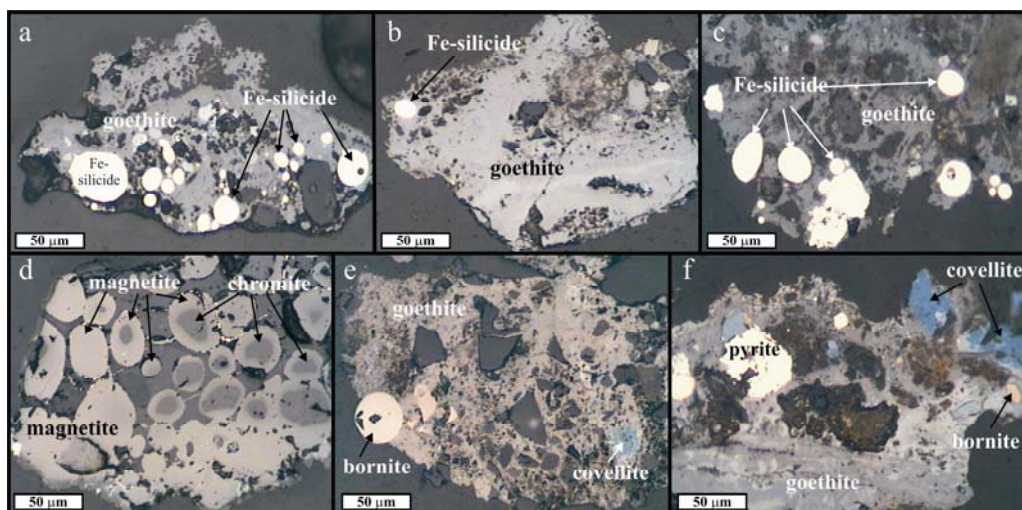


Fig. 3. Forms of spherules in a magnetic concentrate from the red shale (Polkowice-Sierszowice mine), reflected light, without analyser

The spherules from this concentrate are mainly built of Fe-silicides (Fe-spherules, Table 1, Fig. 3a–c), magnetite (Fig. 3d), silicates with goethite and recrystallized bornite framboids (Fig. 3e, Table 1). Most of the spherules (>95%) are massive (Table 2). Porous microtexture was observed only in the magnetite spherules. In this sample spherical forms are dominated by the Fe-spherules with the composition of Fe_5Si_3 with minor amounts of P, Ti, Cr and Mn (Table 3). They are small, between several and 50 μm , oval or slightly flattened, massive and relatively homogeneous as concerns their chemical composition (Table 3).

Table 1. Distribution of spherule types from the red shale (Polkowice-Sieroszowice mine)

Spherule		Spherule type	wt %	
Fe-oxide	Magnetite		5.41	13.52
	Silicate with goethite		8.11	
Iron	Iron (Fe-silicide)		86.36	83.36
Sulphide	Bornite		0.13	0.13
Total			100.00	100.00

Table 2. Distribution of microstructures in spherules from the red shale (Polkowice-Sieroszowice mine)

Spherule type	microtexture, %		Total
	porous	massive	
Magnetite	3.25	2.16	5.41
Silicate with goethite	–	8.11	8.11
Iron (Fe-silicide)	–	86.36	86.36
Bornite	–	0.13	0.13
Total	3.25	96.80	100.00

The silicide spherules are present in goethite aggregates or occur separately. Within the aggregates they occur together with magnetite, covellite and pyrite grains as well as silicate spherules (Fig. 4). The latter are very small and do not exceed 25 μm . The spherules built of bornite are of comparable size. Such forms are most probably an effect of recrystallization of framboids enclosed in the shale ore, which were originally composed of bornite.

The magnetite spherules present in the concentrate are usually porous (Table 2). The core of the porous magnetite spherules is granular, while the massive spherules contain chromite cores (Fig. 3).

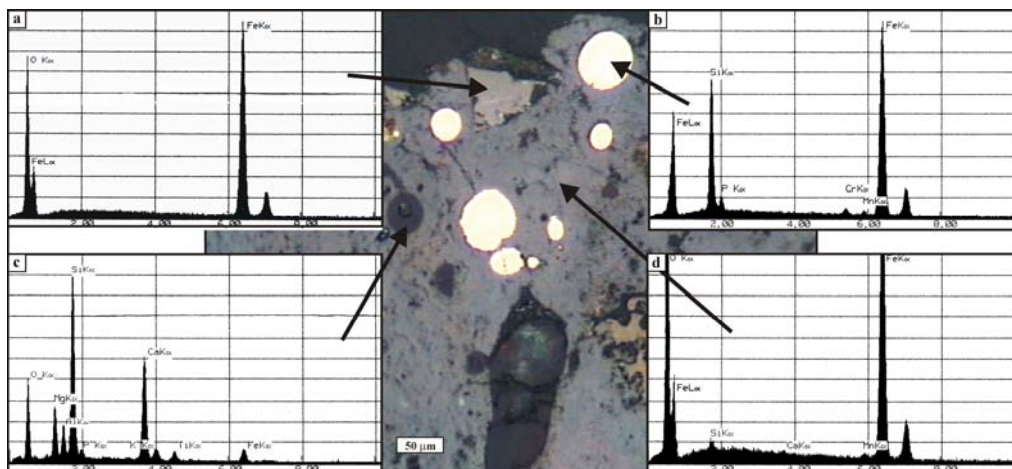


Fig. 4. Analyses of minerals in goethite aggregate from the red shale (Polkowice-Sierszowice mine). Reflected light, without analyser. Spectra of typical X-ray radiation of
 a – magnetite grain, b – Fe-Si-spherule, c – silicate spherule, d – goethite, excitation voltage 20 kV

Table 3. Contents of elements in Fe-silicide spherules from the red shale (Polkowice-Sierszowice mine)

Element	wt %									
	1	2	3	4	5	6	7	8	9	10
P	3.96	2.17	2.05	1.10	0.56	3.92	0.24	2.10	0.76	0.37
Ti	0.22	1.25	1.20	–	–	0.2	0.65	1.13	–	0.63
Cr	1.03	–	–	0.99	0.55	1.05	0.65	–	1.19	0.91
Mn	0.56	0.11	–	0.55	–	0.51	0.51	–	0.57	–
Fe	72.49	74.12	74.65	74.64	76.27	72.53	75.13	74.66	74.86	75.27
Si	21.74	22.35	22.10	22.72	22.62	21.79	22.82	22.11	22.62	22.82

Spherules from Rudna tailing

Mineralogical composition of the tailings sample from the Rudna Ore Concentrator differs significantly from those of the Polkowice-Sierszowice ore. The following phases were recognised: (with decreasing amount) bornite, pyrite (+marcasite), covellite, chalcocite (+digenite), sphalerite and galenite. Minor amounts of rammelsbergite-safflorite, zircon and various types of spherules also occur. Bornite, pyrite and covellite form over 70% of ore minerals in the sample. Magnetite, magnetite-hematite, Fe-silicides and Fe-silicates spherules predominate (Table 4). Massive microtexture is far more common than porous (Table 5).

Table 4. Distribution of spherules in a concentrate from tailings of Rudna Ore Concentrator

Spherule	Spherule type	wt %	
Fe-oxides	magnetite	81.81	90.91
	magnetite-hematite	9.09	
Fe	Fe-silicides	4.75	9.10
	Fe-silicates	4.35	
Total		100.00	100.00

The size of the spherical forms (50–250 μm) is comparable to those from the Polkowice-Sierszowice mine. Their surface is smooth with high metallic lustre. The magnetite spherules are granular and contain pores but lack discernible grain boundaries when their microtexture is massive (Fig. 5, Table 5).

The amount of magnetite spherules with skeletal magnetite crystals is low and does not exceed 15,5 % of the total spherule number. Magnetite is often replaced by hematite. Martitization develops outwards if the spherule core is empty, but in the opposite direction if the spherule do not possess granular structure. Magnetite crystals replace a minor admixture of Mn (<1.65 wt%).

Table 5. Distribution of microstructures in spherules from tailings of Rudna Ore Concentrator

Spherule type	Microstructure, %		Total
	porous	massive	
	40.91	59.09	
Magnetite	31.82	49.99	81.81
Magnetite-hematite	9.09	–	9.09
Fe-silicides	–	4.75	4.75
Fe-silicates	–	4.35	4.35

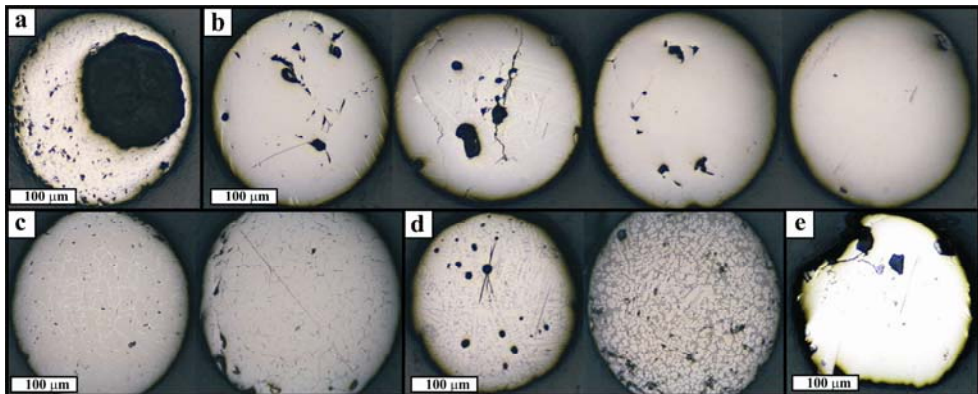


Fig. 5. Spherules in a concentrate from tailings of Rudna Ore Concentrator. Reflected light, without analyser: a – granular and porous magnetite spherule, b – magnetite spherules with invisible microtexture or of net-like texture, c – magnetite spherules with granular texture, martitization and silicates, d – magnetite spherules with skeletal texture, e – Fe-silicide spherule with inclusions of native silicon (grey)

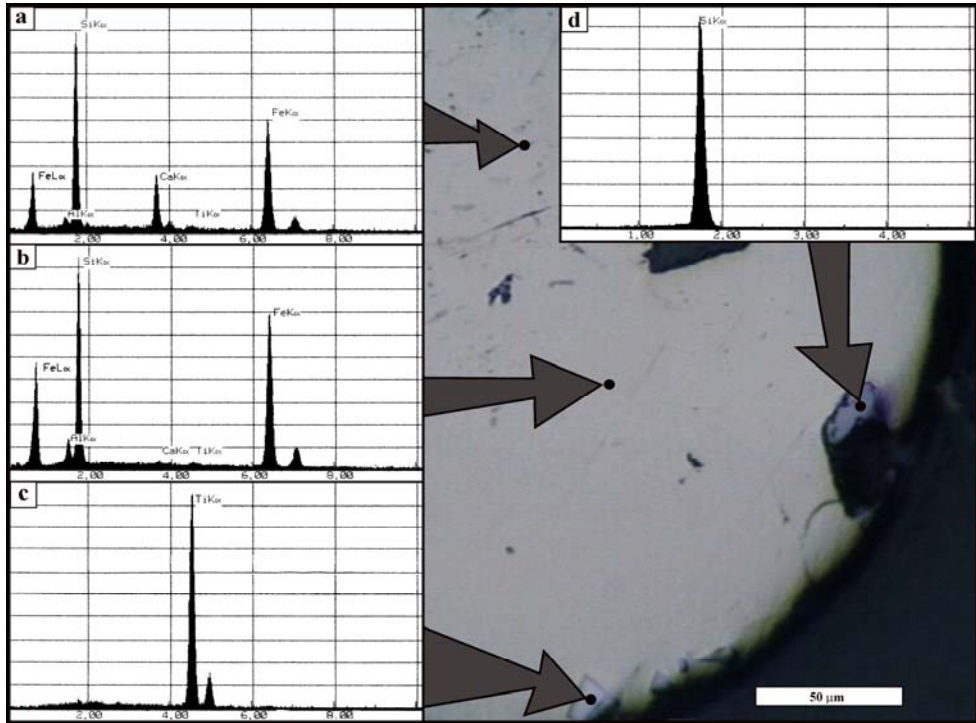


Fig. 6. Analyses of mineral phases in an Fe-silicide spherule from Rudna Ore Concentrator. Reflected light, without analyser. Spectra of typical X-ray radiation of: a – Fe_2Si_3 , b – FeSi , c – Ti crystal, d – Si crystal, excitation voltage 20 kV

Magnetite-hematite spherules are rare in this concentrate. All of them are porous with highly developed net-like structure that results from martitization of magnetite. The spherules built mainly of native Fe or Fe with admixtures of Si show a different structure that is reflected by Fe-Si compounds. Their size varies from 100 to 150 μm and the chemical composition changes over several μm . Although the differences are not readily discernible in BSE images, they become pronounced in reflected light. The composition varies from FeSi to Fe_2Si_3 or from FeSi to Fe_4Si_9 . The margins contain crystals of native Si or Ti (Fig. 6). Tabular-lenticular unmixing structures, present in central parts of the spherules, display an increase of Al and Ca (from 0 to 3.95 wt%). Ti concentration varies between 0 and 0.65 wt%. The spherules surface is rough comparing to the magnetite spherules. During polishing the silicide spherules crumble away along the margins.

Discussion and conclusion

A characteristic feature of Fe-silicides in described spherules is their occurrence in paragenesis with native Si. The latter is an extremely rare mineral, reported from the

Neogene volcanic rocks found on the Mediterranean beaches, 150 km NW of Izmir, Turkey. It forms intergrowths with moissanite (Di Pierro et al., 2003; Robinson et al., 2004). Native Si was also reported from volcanic rocks of Tolbachik in Kamchatka (Russia) and volcanic exhalations in the ophiolitic complex of Nuevo Potosí (Cuba). In the latter case it forms inclusions in native gold (Novgorodova et al., 1989). A 19-80 μm big regular octahedrons of native Si are known from the Kola Peninsula and from the Jakutia kimberlites near Sytykanskaya, Russia (Pankov and Spetsius, 1989). The crystals from the Kola Peninsula occur in paragenesis with graphite, moissanite as well as native Fe, Au and Cu-bearing Zn (Novgorodova et al., 1989). Native Si was also observed as inclusions in natural SiC and native Fe (Bauer et al., 1963) as well as in Fe-silicides, e.g. ferdasilicide Fe_3Si_7 (Marshintsev, 1990).

The samples of Permian rocks from Polkowice and Rudna belong to one ore-bearing formation on the Fore-Sudetic Monocline. Ore minerals, mainly chalcocite, bornite, chalcopyrite, covellite, galenite, sphalerite, pyrite and uncommon Ni-Co arsenides belong to medium- and low-temperature phases. The accompanying spherulitic forms are characteristic for very high crystallization temperatures (magnetite, silicide and silicate spherules). Their shape implies surface tension operating during their formation and indicates liquid or gaseous conditions (Muszer, 2007). The comparison of the textural and the elementary composition with other spherules described in the bibliography showed numerous analogies of the internal structure. Necessary high temperature may be achieved when meteoritic dust travels through upper parts of the troposphere. Alternatively, it may be related to magmatic (volcanic) terrestrial conditions. The described Fe-silicides and other magnetite and silicate spherules are exoclasts within the rocks sampled.

The current research do not permit to determine unequivocally whether the Fe-silicide spherules formed as a result of Permian cosmic dust or constitute terrestrial magmatic material of ultramafic provenance transported into a sedimentary basin from the adjacent terrain. Their co-occurrence with Fe-hydroxides resembles the position of suessite Fe_3Si from the North Haig achondrite from South Australia (Keil et al., 1982; Judin and Kolomenskij, 1987). In both cases silicides are surrounded by goethite (originally probably native Fe) but they do not yield to oxidation themselves. The spherules from the Permian rocks, composed of Fe-silicides did not oxidize either although the process transformed the primary Fe-bearing minerals into goethite. Besides, crystals of native Si and Ti were detected in the silicide spherules from the concentrate obtained from tailings of the Rudna Ore Concentrator (Fig. 5). Such paragenesis in the spherules is similar to the one described from the Luobusa Cr-Fe ore, Autonomic Xizang Region, Tibet (Bai et al., 2007).

The composition of silicide spherules varies from FeSi (fersilicite) to Fe_2Si_3 or from FeSi to Fe_4Si_9 . The spherules composed of Fe_5Si_3 (xifengite) with admixture of P, Ti, Cr and Mn dominate. This composition does not allow determining their origin. It corresponds however to silicides reported from meteorites (Judin and Kolomenskij, 1987; Novosielova and Bagdasarova, 1979) as well as the ones from sedimentary,

metamorphic and igneous rocks (Gevork'yen et al., 1969; Novosielova and Bagdasarova, 1979; Xiongjian, 1991; Bai et al., 2007).

References

- ANAND M., TAYLOR L.A., NAZAROV M.A., SHU J., MAO H.K., HEMLEY R.J., 2004. *Space weathering on airless planetary bodies: Clues from the lunar mineral hapkeite*. Proc. Nat. Acad. Sci., 101, 6847–6851.
- BAI W.J., SHI N., FANG Q., LI G., YANG J., XIONG M., RONG H., 2007. *Luobusaite – a new mineral*. Acta Geologica Sinica 80 (10), 1487–1490. (Chinese with English abstract).
- BAUER J., FIALA J., HRICHOVÁ R., 1963. *Natural α -silicon carbide*. American Mineralogist. 48. 620–634.
- BERNHARD P., 2008. *The Ore Minerals Under the Microscope*. Elsevier.
- CRIDDLE A.J., STANLEY C.J., 1993. *Quantitative data file for ore minerals*. 3rd edition, Chapman & Hall, London-New York-Madras.
- DI PIERRO S., GNOS E., GROBETY B.H., ARMBRUSTER T., BERNASCONI S.M., ULMER P., 2003. *Rock-forming moissanite (natural-silicon carbide)*. American Mineralogist. 2003. 88. 1817–1821.
- GEVORK'YEN V. Ku, 1969. *The occurrence of natural ferrosilicon in the northern Azov region*. Dokl. Akad. Nauk.S.S.S.R. 85. 416–418 (in Russian).
- GEVORK'YEN V. Ku., LITVIN A. L., POVARENENYKH A.S., 1969. *Occurrence of the new minerals fersilicite and ferdasilicate*. Geol. Zh. (Ukraine) 29, 2. 62–71 (in Russian).
- JAKABSKÁ K., ROZLOŽNÍK L., 1989. *Spherical accessories („spherules”) in gemeric granites (West Carpathians – Czechoslovakia)*. Geol. Zbor. 40. 3. 305–322.
- JUDIN I.A., KOLOMENSKIJ W.D., 1987. *Mineralogy of meteorites*. Svierdlovsk. A.N. Uralskij Naucznyj Centr (in Russian).
- KEIL K., BERKLEY J.L., FUCHS L.H., 1982. *Suessite, Fe_3Si : a new mineral in the North Haig ureilite*. American Mineralogist: 67. 126–131.
- MARSHINTSEV V.K., 1990. *Nature of silicon carbide in kimberlite rocks of Yakutia*. Mineralogicheskij Zhurnal. 12 (3). 17–26 (in Russian).
- MASON B., 1962. *Meteorites*. New York. Wiley. 305.
- MUSZER A., 2000. *Outline of ore microscopy*, University of Wrocław, Wrocław (in Polish).
- MUSZER A., 2007. *Characteristic of the spherules and accessory minerals from selected phanerozoic and anthropogenic sediments*, Wrocław, Fundacja Ostoja, (in Polish).
- NOVGORODOVA M.I., BORONIKHIN V.A., GENERALOV M.E., KRAMER H., 1989. *On native silicon in association with native gold and other metals*. Doklady Akad. Nauk SSSR., 309 (5), 1182–1185 (in Russian).
- NOVOSIELOVA L.H., 1975. *Fe-silicides in the Lower Cambrian limestone, Bazaiha (pritok Enisieja)*. Krasnojarskij kraj. Zap. Wsesojuz. Min., 104 (2), 228–234 (in Russian)
- NOVOSIELOVA L.H., BAGDASAROVA E.A., 1979. *New dates about Fe-silicides*. Zap. Wsesojuz. Min., 108 (3), 326–333 (in Russian)
- PANKOV V.YU., SPETSIVS Z.V., 1989. *Inclusions of iron silicides and native silicon in moissanite from the “Sytykanskaya” kimberlite pipe*. Doklady Akad. Nauk SSSR 305, 704–707 (in Russian).
- RAMDOHR P., 1973. *The opaque minerals in Stony Meteorites*. Berlin.
- RAMDOHR P., 1975. *Die Erzminerale und ihre Verwachsungen*. Berlin.

- ROBINSON P.T., BAI W.J., MALPAS J., YANG J.S., ZHOU M.F., FONG Q.S., HU X., CAMERON S., STAUDIGEL H., 2004. *Ultra-high pressure minerals in the Luobusa ophiolite, Tibet, and their tectonic implications*. In: Malpas J., Fletcher L.J.N., Ali J.R., Aitchison J.C. (eds.). *Aspects of the Tectonic Evolution of China*. Geological Society London Special Publications. 226 (1), 247–271.
- SAMUELS L.E., 1982. *Metallographic polishing by mechanical methods*. American Society for Metals. Metals Park, Ohio.
- UYTENBOGAARDT W., BURKE E.A.J., 1971. *Tables for Microscopic Identification of Ore Minerals*. Elsevier. Amsterdam–London–New York.
- XIONGJIAN Hu, 1991. *A preliminary study on ferrosilicium from the Proterozoic, southwestern Zhejiang Province*. Acta Mineral. Sinica, 11(3), 285–289 (in Chinese, English abs.).
- ZUXIANG Yu., 1984. *Two new minerals gupeiite and xifengite in cosmic dusts from Yanshan*. Acta Petrologica Mineralogica et Analytica. 3, 231–238.

Received May 17, 2013; reviewed; accepted July 15, 2013

INFLUENCE OF CALCINATION PARAMETERS ON PHYSICOCHEMICAL AND STRUCTURAL PROPERTIES OF CO-PRECIPIATED MAGNESIUM SILICATE

Filip CIESIELCZYK*, Przemysław BARTCZAK*, Lukasz KLAPISZEWSKI*,
Dominik PAUKSZTA*, Adam PIASECKI**, Teofil JESIONOWSKI*

* Poznan University of Technology, Faculty of Chemical Technology, Institute of Chemical Technology and Engineering, M. Skłodowskiej-Curie 2, PL-60-965, Poznan, Poland, Filip.Ciesielczyk@put.poznan.pl

** Poznan University of Technology, Faculty of Mechanical Engineering and Management, Institute of Materials Science and Engineering, Jana Pawła II 24, PL-60-965, Poznan, Poland

Abstract: Physicochemical properties of different oxide systems depend mostly on the method of their preparation and classification, so the main aim of the study was to obtain the MgO·SiO₂ hybrid in an aqueous solution and its calcination under assumed conditions. Research scope included evaluation of the effect of the basic parameters of the calcination process (time and temperature) on the structural properties of the final materials. Products obtained by the proposed method were thoroughly characterized. The chemical composition, crystalline structure, morphology and nature of the dispersion as well as parameters of the porous structure were established. The results of research in a decisive manner confirmed the possibility of designing the properties of inorganic oxide systems such as MgO·SiO₂, which will definitively be scheduled into potential directions for their use.

Keywords: *magnesium silicate, precipitation, calcination, WAXS, porous structure*

Introduction

Naturally occurring oxide materials are the largest group of minerals that create the Earth's crust. They are among the most important mineral resources, both in terms of quantity and availability of their deposits. Such systems are becoming increasingly applied in terms of technological and economic development. Thanks to its unique physicochemical properties they are used in many industries. They have become the basic raw material for ceramics, paints, lacquers, plastics and bioceramics (Qiu, 2013; Johnson, 2004; Lu, 2012).

Today's technology is gaining more and more interest in oxide materials obtained in the laboratory. Synthetic powders may have similar or quite different properties in

comparison to their natural substituents. The use of synthetic oxide materials is increasing and is a result of the ability to control and improvement of their physicochemical properties (Baldyga, 2012; Modrzejewska-Sikorska, 2012; Laurentowska, 2012; Yamagata, 2013). These properties depend mostly on the preparation process parameters, such as concentration of reagents, the direction and speed of dosing, temperature and pH. In addition, synthetic powders can be subjected to numerous chemical modifications, changing the spectrum of a wide range of application. The modification is carried out with the use of a large group of organic compounds which provide products with specific hydrophilic-hydrophobic properties and surface activity (Bhardwaj, 2012, Zhang, 2013). In addition to these processes, important is the final step of oxide materials classification, including thermal treatment (calcination). Selection of the calcination process parameters of these powders is important from the point of view of porous structure, hydrophilic-hydrophobic nature, crystalline structure and dispersion characteristics (Ibrahim, 2012; Ren, 2013; Saruchi, 2013).

The calcination process is generally carried out at a temperature lower than the melting point of the calcinated product. In various research papers the influence of calcination on the physicochemical properties of oxide materials was described so far. Choi et al. (2012) have shown that the structure of mesoporous (granular) systems of titanium dioxide and aluminum oxide ($\text{TiO}_2/\text{Al}_2\text{O}_3$) can be easily controlled by calcination temperature and the ratio of reagents. The calcination was carried out at three different temperatures: 450, 600 and 750 °C. It was found that the higher the calcination temperature the pore size increases and the volume as well as the bending strength slightly decrease, which directly translates to surface area development. Other researchers (Yu, 2006) have proved that the calcination process affects morphology, surface area, structure and photocatalytic properties of titanium nanotubes. Titanium nanotubes calcinated in the temperature range 400–600 °C had a larger surface area and greater pore volume than the starting material. A further increase in calcination temperature (700–900 °C) caused a decrease in photocatalytic properties and pore volume, reduction of the surface area, as a result of the formation of the rutile structure. Mohammadi et al. (2003) conducted a study on the effect of calcination of kaolin used for zeolite membranes. It was found that an increase in the calcination temperature improves the strength properties of kaolin, which is caused by the formation of the two forms of the compound above 1000 °C – mullite and spinel and the increase in pore diameter. In other work (Guo, 2010), calcination process at four different temperatures (200–500 °C) and five different times (1–5 h) was realized for sodium silicate, in order to obtain a product characterized with the best properties for biodiesel production (sodium silicate acted as the solid catalyst of the transesterification process). The optimum calcination condition of Na_2SiO_3 for biodiesel production from soybean oil was at temperature of 400 °C and calcination duration – 2 h. In subsequent scientific reports Yan et al. (2010) studied the effect of temperature of calcination process in the production of calcium sorbents. Best results were obtained at 503 °C to

607 °C as a process temperature. Tangchupong and co-authors (2010) studied the effect of calcination temperature on the properties of sulfated zirconia – commercial and synthetic obtained via precipitation method. It has been shown that change in the calcination temperature from 450 °C to 750 °C significantly influences surface properties, and also the acid-base character of the surface of such systems. Using a commercial product in the conversion of carbon monoxide, it was found that the reaction rate decreases with increasing calcination temperature. For the product precipitated and calcinated in the temperature range of 450–600 °C, the conversion of CO increased, and after calcination at 750 °C it decreased.

Calcination process is gaining importance in area of today's technology, giving the ability to control the physicochemical properties of calcinates (moisture content, sorption capacity, diameter and pore volume, surface activity, the hydrophilic-hydrophobic character), resulting in subsequent directions of their use, despite various costly modifications with other compounds.

Experimental

Synthesis of MgO·SiO₂ powder and its calcination

The magnesium silicate powder was obtained in a process of precipitation from aqueous solutions of sodium silicate and magnesium sulfate, as described earlier (Ciesielczyk, 2011). Precipitation of MgO·SiO₂ powder was realized in the QVF Mini Plant Pilot-Tec reactor having 10 dm³ capacity, equipped with a high speed stirrer (2000 rpm). Five dm³ of 5% magnesium sulfate solution was previously placed in the reactor. After that, the 5% solution of sodium silicate in appropriate amount was dosed to the reactor (1 dm³/h) using a peristaltic PP2B-15 pump. The product obtained – MgO·SiO₂ in a form of white powder – was washed and filtrated, and then dried at 105 °C for 24 h. The prepared powders were additionally calcinated, using a Controller P320 oven made by Nabertherm, at 300, 450, 600, 750, 900 and 1000 °C. For each of these temperatures of calcinations, the process lasted for 1 and 2 h, respectively.

Physicochemical properties evaluation

The dispersive characteristic of the MgO·SiO₂ oxide material and its calcinates was determined using a Mastersizer 2000 apparatus made by Malvern Instruments Ltd., by using the laser diffraction method and measuring particles of sizes from 0.2 to 2000 μm. The morphology and microstructure of the materials obtained were analyzed using a Zeiss EVO40 scanning electron microscope. The observations permitted evaluation of the dispersion degree, the structure of particles and their tendency towards aggregation or agglomeration. Moreover, the surface composition of calcinates (contents of Mg, Si and O) was analyzed by energy dispersive X-Ray spectroscopy (EDS) using a Princeton Gamma-Tech unit equipped with a prism digital

spectrometer. The calcinates of $\text{MgO}\cdot\text{SiO}_2$ were also subjected to crystalline structure determination using the WAXS method. The results were analyzed employing a XRAYAN software. The diffraction patterns were taken using a TUR-M62 horizontal diffractometer equipped with an HZG-3 type goniometer. The surface area A_{BET} (BET method) was calculated based on data measured by low-temperature adsorption of nitrogen. The isotherms of nitrogen adsorption/desorption were measured at $-196\text{ }^\circ\text{C}$ using an ASAP 2020 apparatus made by Micromeritics Instrument Co. With regard to the high accuracy of the instrument used ($\pm 0.0001\text{ m}^2/\text{g}$) the surface area values were rounded up to interger numbers, and the mean pore size (S_p) and total pore volume (V_p), calculated using the BJH algorithm, were rounded to one and two decimal places respectively.

Results and discussion

Dispersive and morphological characteristics of $\text{MgO}\cdot\text{SiO}_2$ calcinates

In the first stage of study, the dispersion characteristics and morphology of the obtained $\text{MgO}\cdot\text{SiO}_2$ calcinates were established. Table 1 shows the dispersive parameters, and Figure 1 shows SEM images of the precipitated powder, additionally calcinated at different temperatures. The data indicate that the largest average particle diameter ($25.9\text{ }\mu\text{m}$) was in sample PB 0, that was not calcinated $\text{MgO}\cdot\text{SiO}_2$. The largest volume contribution (4.9%) in this sample is represented by the particles of $39.8\text{ }\mu\text{m}$ in diameter. This sample contains 10% of the particles having a diameter less than $3.6\text{ }\mu\text{m}$, 50% of the particles having a diameter less than $18.0\text{ }\mu\text{m}$ and 90% of particles smaller than $60.7\text{ }\mu\text{m}$. The SEM image of this sample shows particles smaller than $10\text{ }\mu\text{m}$, as well as the bigger ones, which directly confirms the obtained particle sizes (see Fig. 1a). Sample PB 7 calcinated at $750\text{ }^\circ\text{C}$, PB 3 calcinated at $450\text{ }^\circ\text{C}$ and PB 1 calcinated at $300\text{ }^\circ\text{C}$ show the most similar nature of dispersion as compared to the not calcinated sample, which is evidenced by the values of $d(0.1)$ $d(0.5)$ $d(0.9)$ parameters, as well as by the average particle diameter in the range of $21.6\text{--}22.5\text{ }\mu\text{m}$. The smallest particle sizes were obtained in sample PB 11 calcinated at $1000\text{ }^\circ\text{C}$. Its average particle diameter in hole volume of the sample is $14.8\text{ }\mu\text{m}$. Other samples were characterized by similar values of individual parameters falling within the range of $d(0.1) = 18.1\text{--}18.7\text{ }\mu\text{m}$, $d(0.5) = 12.4\text{--}13.0\text{ }\mu\text{m}$ and $d(0.9) = 40.1\text{--}42.8\text{ }\mu\text{m}$.

Carrying out the process of calcination for 2 h, it was found that the largest average particle diameter in the entire volume of the sample has a powder calcinated at $1000\text{ }^\circ\text{C}$ (PB 12) – $24.6\text{ }\mu\text{m}$. Samples characterized with the smallest particle sizes were those calcinated at $750\text{ }^\circ\text{C}$ (PB 8) – $12.1\text{ }\mu\text{m}$ and at $300\text{ }^\circ\text{C}$ (PB 2) – $12.8\text{ }\mu\text{m}$. Other samples were characterized by similar dispersion parameters ($d(0.1) = 3.1\text{--}3.2\text{ }\mu\text{m}$, $d(0.5) = 11.3\text{--}13.7\text{ }\mu\text{m}$ and $d(0.9) = 36.7\text{--}45.8\text{ }\mu\text{m}$). The average particle diameter for samples PB 10, PB 6 and PB 4 are respectively 19.9 , 18.8 and $16.5\text{ }\mu\text{m}$.

Analyzing the results concerning the characteristics of the dispersion and morphology it was proved that calcination process contributes to significant changes

in these properties. Change in the size of the particles (the nature of the dispersion) is determined by the temperature and time of calcination. The most significant changes were observed when comparing the $\text{MgO}\cdot\text{SiO}_2$ powder calcinated at $750\text{ }^\circ\text{C}$ and $300\text{ }^\circ\text{C}$, however, definitely the best dispersive-morphological parameters have calcinates obtained in a 2-hours calcination process. Experimental data are confirmed by Fig. 1. The scanning electron microscopy images of selected calcinates are analogous to the data presented in the literature concerning the thermal treatment of other precipitated powders (Kim, 2002).

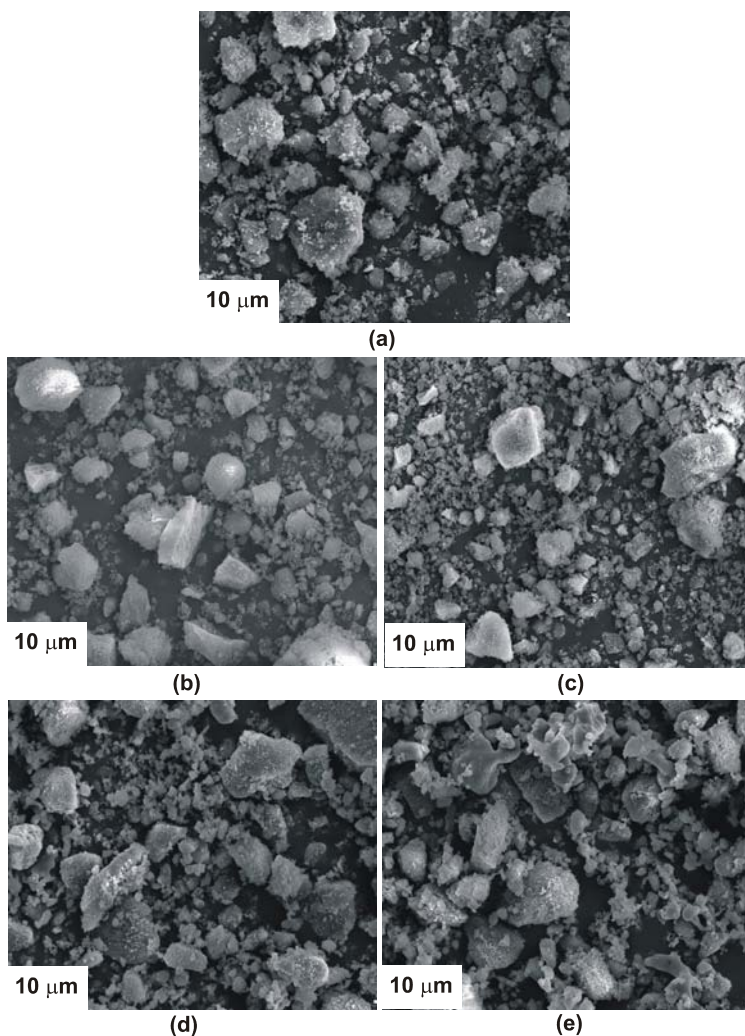


Fig. 1. SEM images of $\text{MgO}\cdot\text{SiO}_2$ powder (a) without calcination, (b) and (c) calcinated at $450\text{ }^\circ\text{C}$ and (d) and (e) calcinated at $1000\text{ }^\circ\text{C}$ for 1 or 2 h, respectively

Table 1. Dispersive parameters of MgO·SiO₂ powder calcinated at different temperatures

Sample symbol	Calcination temperature (°C)	Calcination time (h)	Diameter (μm)			
			<i>D</i> (4.3)	<i>d</i> (0.1)	<i>d</i> (0.5)	<i>d</i> (0.9)
PB 0	–	–	25.9	3.6	18.0	60.7
PB 1	300	1	22.2	3.4	14.8	51.8
PB 3	450		22.5	3.4	15.0	52.9
PB 5	600		18.7	3.1	12.4	42.8
PB 7	750		21.6	3.2	15.2	49.6
PB 9	900		18.1	3.1	13.0	40.1
PB 11	1000		14.8	3.6	12.4	29.2
PB 2	300	2	12.8	2.7	7.1	21.7
PB 4	450		16.5	3.1	11.3	36.7
PB 6	600		18.8	3.2	12.6	43.0
PB 8	750		12.1	2.7	8.1	23.1
PB 10	900		19.9	3.1	13.7	45.8
PB 12	1000		24.6	5.6	20.1	50.5

Chemical composition of calcinates

Table 2 shows the results of EDS analysis of the calcinates received after 1-hour calcination, which confirms the presence of characteristic elements present in the structure of MgO·SiO₂ powder. The presented experimental data proved that together with an increase in the calcination temperature the mass contribution of magnesium and silicon, which are part of material structure, slightly increases.

Table 2. Chemical composition of MgO·SiO₂ powder calcinated at different temperatures for 1 h

Element	Mass contribution (%)						
	PB 0	PB 1	PB 3	PB 5	PB 7	PB 9	PB 11
Mg	8.02	8.12	8.08	8.27	8.32	8.45	8.56
Si	35.59	34.55	34.72	36.88	36.87	36.99	37.99
Na	1.29	0.89	1.05	1.10	0.98	1.11	0.97
K	0.03	0.02	0.03	0.03	0.03	0.03	0.02
Ca	0.01	0.01	0.01	0.01	0.01	0.01	0.01
O	55.06	56.99	54.88	54.32	53.86	53.08	52.34

The presence in the structure of MgO·SiO₂ such elements as sodium, potassium or calcium is a result of composition of raw materials, especially of sodium silicate solution, used in the synthesis process. However, the oxygen content is slightly reduced, which is directly associated with the constitutional water loss, released during calcination, especially at higher temperatures. Calcination of the powder, performed for 2 h, gave analogous results.

WAXS analysis

In order to compare the crystalline structures of $\text{MgO}\cdot\text{SiO}_2$ powders calcinated at different temperatures for 1 and 2 h, Fig. 2 shows their XRD patterns. As a reference the sample of noncalcinated material was used. Analyzing collected data it was found that with increasing calcination temperature, regardless of time, the crystalline structure of the material is changing. The transition from amorphous to crystalline form occurs not earlier than at $750\text{ }^\circ\text{C}$. The well-defined crystalline structure was obtained in the case of the samples calcinated at high temperature – $1000\text{ }^\circ\text{C}$ (samples PB 11 and PB 12), both for 1 h and 2 h. However, samples calcinated at $900\text{ }^\circ\text{C}$ (samples PB 9 and PB 10) and $750\text{ }^\circ\text{C}$ (sample PB 7 and PB 8) have not fully formed crystalline structure. In the case of the other samples, there was no characteristic diffraction peaks, indicating an amorphous structure of the tested powders. Identification of the diffraction patterns obtained using X-RAYAN software, demonstrated that the diffraction peaks for selected calcinates appear at values of 2θ ranging sequentially 22.06, 28.45, 31.26, 36.05 and 57.09, which clearly indicate the appearance of the synthetic cristobalite (SiO_2) structure in obtained powders.

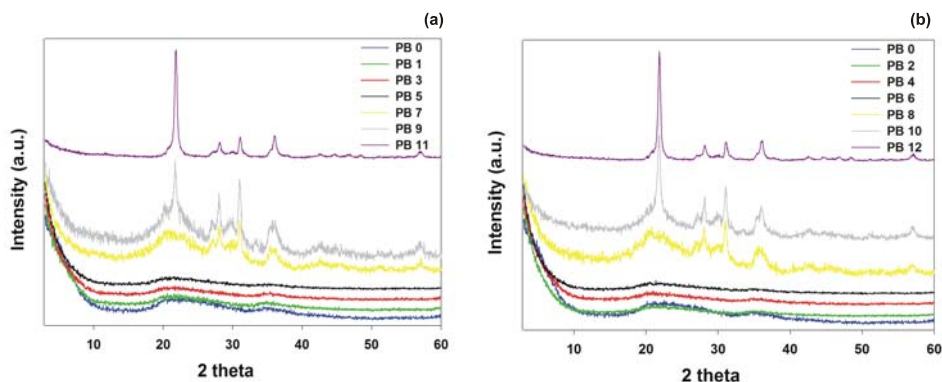


Fig. 2. WAXS patterns of $\text{MgO}\cdot\text{SiO}_2$ calcinates obtained for (a) 1 h and (b) 2 h calcination at different temperatures

Analyzing the obtained results it was found that the calcination process plays a crucial role in changing of the crystalline structure, which is better formed at higher temperatures of the process. This is analogous to the calcination process of selected powders such as TiO_2 . In the case of such monoxide or its mixture ($\text{TiO}_2\cdot\text{SiO}_2$), calcination temperature determines the variation of its crystalline structure. Calcination of these materials at temperature below $700\text{ }^\circ\text{C}$ leads to anatase and the thermal treatment above this temperature results in forming of rutile (Lee, 2007; Siwińska-Stefańska, 2011). These aspects are also correlated with the properties of the obtained materials based on TiO_2 , which determines their potential directions of use.

Porous structure properties

The next step was to determine the parameters of the porous structure of MgO·SiO₂ calcinates. Figure 3 shows the isotherms of nitrogen adsorption/desorption of the MgO·SiO₂ powder calcinated at different temperatures for 1 h and 2 h. The isotherms indicate that the calcination process conditions have an important impact on the parameters of the porous structure. Significant changes were observed in the case of calcinates received at different temperatures of calcination process. However, no significant changes were noted comparing the samples prepared at the same temperatures but at a different time of calcination. The nature of the isotherms obtained indicates the mesoporous character of obtained powders.

For not calcinated sample (PB 0) as well as for calcinates obtained at 300, 450 and 600 °C it was observed that the amount of nitrogen adsorbed slowly increases up to a value of relative pressure equals 0.8. After that the amount of nitrogen adsorbed increases rapidly. For sample not calcinated amount of nitrogen adsorbed at $p/p_0 = 1$ reaches a value of 345 cm³/g. For samples calcinated at temperatures of 300, 450 and 600 °C, this values does not differ in any significant way and are in the range of 305-335 cm³/g (at $p/p_0 = 1$). However, for the samples calcinated at higher temperatures, the difference in the amounts of adsorbed nitrogen is very large. The samples calcinated at 750 °C adsorbed almost half of the amount of nitrogen (210 cm³/g) than the not calcinated sample. The smallest amount of nitrogen adsorbed was observed in the case of the MgO·SiO₂ samples calcinated at 900 and 1000 °C. These values were 60, 40, 15 and 10 cm³/g, respectively.

As in the case of amount of nitrogen adsorbed, the calcination temperature significantly affected the changes in the basic parameters of the porous structure, such as surface area and pore volume and diameter. It was noted that the surface area of obtained powders decreases with increasing temperature of the calcinations process. The largest surface area of 427 m²/g was reached for not calcinated material. However, the largest surface area from all of the analyzed calcinates was obtained for sample PB 11 – 399 m²/g. As the calcination temperature increases the surface area gradually decreases up to the lowest value for powders obtained after calcination of MgO·SiO₂ at 1000 °C. The value of surface area (A_{BET}) is 6 m²/g for the sample calcinated at this temperature for 1 h and 4 m²/g - calcinated for 2 h. Extension of calcination time resulted in a further, slight decrease in the individual parameters of the porous structure. Noteworthy is also the fact that the calcination temperature increase resulted in a decrease of the pore volume from 0.49 and 0.51 cm³/g, respectively, for samples PB 1 and PB 2 (calcinated at 300°C) to a value of 0.02 and 0.01 cm³/g for samples PB 11 and PB 12 calcinated at 1000 °C respectively. Moreover, the pore diameter increases with increasing calcination temperature only up to 750 °C. Above this temperature the pore diameter changes are completely random.

Once again, it was confirmed that the implementation of the calcination of MgO·SiO₂ under certain conditions, led to significant changes in the physicochemical properties of obtained powders. As a confirmation, a number of scientific literature

reports can be used (Choi, 2012; Yu, 2006), which show that too high temperature of calcination reduces the activity of the prepared products and causes a significant reduction in the value of individual parameters of the porous structure.

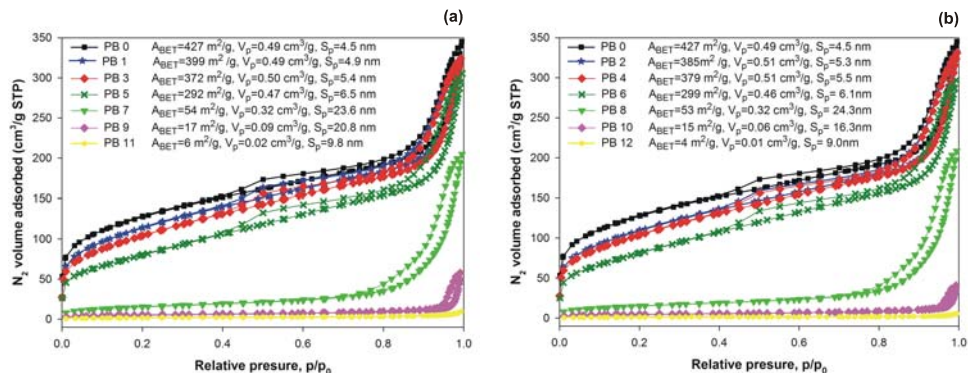


Fig. 3. Characteristics of the porous structure of MgO·SiO₂ powder calcinated for (a) 1 h and (b) 2 h at different temperatures

Conclusions

The study demonstrated that the process of heat treatment of the MgO·SiO₂ powder, implemented via calcination, is a very effective method to change their physicochemical and structural properties. The dispersive characteristics of obtained calcinates depend mainly on the temperature and time of calcination. All powders were characterized with a smaller particle size as compared to not calcinated sample. Insignificant changes were observed while analyzing the chemical composition of the prepared products. The only dependency that was observed was the increase in the percentage contribution of magnesium and silicon in relation to oxygen in the structure of calcinates obtained at higher temperatures.

Calcination of precipitated magnesium silicate at temperatures above 750 °C led to the formation of the crystalline structure corresponding to the structure of synthetic cristobalite. Formation of this structure was noted in the case of calcinates obtained during thermal treatment, implemented at 1000 °C, regardless of the time of calcination. Samples of MgO·SiO₂ calcinated at temperatures below 750 °C were of typical amorphous form.

A significant change in various parameters of the porous structure of obtained powders was also observed, depending on the calcination temperature. It was found that the surface area and pore volume decrease with increasing temperature of the process, while the pore diameter increased only for samples calcinated at temperatures up to 750 °C. Above this temperature changes of this parameter were completely random. The best parameters of the porous structure were exhibited by the system that

was not calcinated ($A_{\text{BET}} = 427 \text{ m}^2/\text{g}$, $V_p = 0.49 \text{ cm}^3/\text{g}$, $S_p = 4.5 \text{ nm}$), whereas the worst by $\text{MgO}\cdot\text{SiO}_2$ calcinated at $1000 \text{ }^\circ\text{C}$ ($A_{\text{BET}} = 4 \text{ m}^2/\text{g}$, $V_p = 0.01 \text{ cm}^3/\text{g}$, $S_p = 9.0 \text{ nm}$).

Acknowledgements

The study was financed within the Polish National Centre of Science funds according to decision no. DEC-2011/03/D/ST5/05802.

References

- BALDYGA J., JASINSKA M., JODKO K., PETELSKI P., 2012, *Precipitation of amorphous colloidal silica from aqueous solutions-aggregation problem*, Chem. Eng. Sci., 77, 207–216.
- BHARDWAJ D., SHARMA M., SHARMA P., TOMAR R., 2012, *Synthesis and surfactant modification of clinoptilolite and montmorillonite for the removal of nitrate and preparation of slow release nitrogen fertilizer*, J. Hazard. Mater., 227–228, 292–300.
- CHOI J., KIM J., YOO K.S., LEE T.G., 2008, *Synthesis of mesoporous $\text{TiO}_2/\gamma\text{-Al}_2\text{O}_3$ composite granules with different sol composition and calcinations temperature*, Powder Technol., 181, 83–88.
- CIESIELCZYK, F., NOWACKA, M., PRZYBYLSKA, A., JESIONOWSKI, T., 2011, *Dispersive and electrokinetic evaluations of alkoxy silane-modified $\text{MgO}\cdot\text{SiO}_2$ oxide composite and pigment hybrids supported on it*, Colloids Surf. A: Physicochem. Eng. Asp., 376, 21–30.
- GUO F., PENG Z.G., DAI J.Y., XIU Z.L., 2010, *Calcinated sodium silicate as soil base catalyst for biodiesel production*, Fuel Process. Technol., 91, 322–328.
- IBRAHIM S.S., SELIM A.Q., 2012, *Heat treatment of natural diatomite*, Physicochem. Probl. Miner. Process., 48, 413–424.
- JOHNSON J.H., MCFARLANE A.J., BORMANN T., MORAES J., 2004, *Nano-structured silica and silicates: new materials and their applications in paper*, Cur. Appl. Phys., 4, 411–414.
- KIM D.J., HAHN S.H., OH S.H., KIM E.J., 2002, *Influence of calcination temperature on structural and optical properties of TiO_2 thin films prepared by sol-gel dip coating*, Mat. Lett., 57, 355–360.
- LAURENTOWSKA A., JESIONOWSKI T., 2012, *$\text{ZnO}\cdot\text{SiO}_2$ oxide composites synthesis during precipitation from emulsion system*, Physicochem. Probl. Miner. Process., 48, 63–76.
- LEE C.-K., WANG C.-A., LYU M.-D., JUANG L.-C., LIU S.-S., HUNG S.-H., 2007, *Effects of sodium content and calcination temperature on the morphology, structure and photocatalytic activity of nanotubular titanates*, J. Colloid Interface Sci., 316, 562–569.
- LU B.-Q., ZHU Y.-J., AO H.-Y., QI C., CHEN F., 2012, *Synthesis and characterization of magnetic iron oxide/calcium silicate mesoporous nanocomposites as a promising vehicle for drug delivery*, Appl. Mater. Interfaces, 4, 6969–6974.
- MODRZEJEWSKA-SIKORSKA A., CIESIELCZYK F., JESIONOWSKI T., 2012, *Synthesis and characterisation of precipitated $\text{CuO}\cdot\text{SiO}_2$ oxide composites*, Pigm. Resin Technol., 41, 71–80.
- MOHAMMADI T., PAK A., 2003, *Effect of calcinations temperature of kaolin as a support for zeolite membranes*, Sep. Purif. Technol., 30, 241–249.
- QIU Z.-Y., NOH I.-S., ZHANG S.-M., 2013, *Silicate-doped hydroxyapatite and its promotive effect on bone mineralization (review)*, Front. Mater. Sci., 7, 40–50.
- REN C., QIU W., CHEN Y., 2013, *Physicochemical properties and photocatalytic activity of the $\text{TiO}_2/\text{SiO}_2$ prepared by precipitation method*, Sep. Purif. Technol., 107, 264–272.
- SARUCHI, SURBHI, AGHAMKAR, P., KUMAR S., 2013, *Neodymia-silica nanocomposites: synthesis and structural properties*, Adv. Mater. Lett., 4, 78–81

- SIWINSKA-STEFANSKA K., PAUKSZTA D., JESIONOWSKI T., 2011, *Physicochemical properties of TiO₂/SiO₂ oxide composites produced by nucleation of reaction system*, Przem. Chem. 90, 1009–1010.
- TANGCHUPONG N., KHAODEE W., JONGSOMJIT B., LAOSIRIPOJAN N., PRASERTHDAM P., ASSABUMRUNGRAT S., 2010, *Effect of calcination temperature on characteristic of sulfated zirconia and it's application as catalyst for isosynthesis*, Fuel Process. Technol., 91, 121–126.
- YAMAGATA C., ELIAS D.R., PAIVA M.R.S., MISSO A.M., CASTANHO S.R.H.M., 2013, *Facile preparation of apatite-type lanthanum silicate by a new water-based sol-gel process*, Mater. Res. Bull., 48, 2227–2231.
- YAN CH.F., GRACE J.R., LIM C.J., 2010, *Effects of rapid calcinations on properties of calcium based sorbents*, Fuel Process. Technol., 91, 1678–1686
- YU J., YU H., CHENG B., TRAPALIS C., 2006, *Effects of calcinations temperature on the microstructures and photocatalytic activity of titanate nanotubes*, J. Mol. Catal., 249, 135–142.
- ZHANG J., GUO Z., ZHI X., TANG H., 2013, *Surface modification of ultrafine precipitated silica with 3-methacryloxypropyltrimethoxysilane in carbonization process*, Colloids Surf. A: Physicochem. Eng. Asp., 418, 174–179.

Received June 20, 2013; reviewed, accepted July 26, 2013

THE USE OF 1-ALKYLIMIDZOLES FOR SELECTIVE SEPARATION OF ZINC IONS IN THE TRANSPORT PROCESS ACROSS A POLYMERIC INCLUSION MEMBRANE

Elzbieta RADZYMINSKA-LENARCIK*, Malgorzata ULEWICZ**

* Department of Inorganic Chemistry, University of Technology and Life Sciences, Seminaryjna 3, 85-326 Bydgoszcz, e-mail: elaradz@utp.edu.pl

** Czestochowa University of Technology, Dąbrowskiego 69, 42-201 Czestochowa, e-mail: ulewicz@onet.eu

Abstract: The transport of Zn(II) ions from different aqueous nitrate(V) source feeding phases ($c_{Me} = 0.001 \text{ mol/dm}^3$, pH 6.0) across polymer inclusion membranes (PIMs) doped with 1-alkylimidazole as an ion carrier was reported. Alkyl substituents in position 1 of imidazole ring have an effect on hydrophobic properties of the carriers and the initial flux of the transported metal ions. The membranes were characterized by an atomic force microscopy (AFM). The results show that the Zn(II) ions could effectively be separated from other transition metal cations such as Co(II) and Ni(II) from different equimolar ion mixtures. Also, the thermal stability of PIM doped with 1-decylimidazole was studied in replicate experiments. The highest separation coefficients for the Zn(II)/Co(II) and Zn(II)/Ni(II) systems, equal to 9.4 and 11.9 were recorded for the equimolar Zn(II)-Co(II)-Ni(II) mixture for 1-hexylimidazole as a carrier, while using 1-decylimidazole resulted in the highest values of initial flux of the Zn(II) ions transport across the polymeric membrane.

Keywords: *polymer inclusion membrane (PIM), separation ions, cobalt(II), nickel(II), zinc(II), alkylimidazole*

Introduction

Non-ferrous metals recovering from ores and metal-bearing wastes such as flue dusts, melting losses, slimes and spent technological liquors is based either on pyrogenic or hydrometallurgical (wet) technologies. Selection of an appropriate manufacturing process depends on a useful metal content. In a typical wet process, among the four basic technologies, i.e. leaching, phase separation, extraction of metal ions from aqueous solutions and deposition of the ions from the aqueous phase, of particular interest is separation of the ions in an aqueous solution, which has direct bearing on

the purity of a final product. In a modern wet process of non-ferrous metals recovery, separation of the ions is usually conducted by solvent extraction or ion-exchange (Habashi, 1999; Bartsch and Way, 1996). The separation of the non-ferrous metal ions in aqueous solutions or industrial waste waters in a laboratory scale is carried out using membrane-based techniques. A characteristic feature of liquid membranes is that both the extraction and re-extraction steps can be conducted simultaneously, which enabled the implementation of a continuous process eliminating the need of intermediate operations. The combined extraction-reextraction regime, also named a pertraction process, offers a considerable advantage, as compared to that of solvent extraction (Bond et al., 1999). The liquid membranes, as far as their constructional features are concerned, can be divided in four basic categories: thick-layer (BML), immobilised liquid (SCM), emulsion liquid (ELM) and polymeric inclusion (PIM) membranes.

The efficiency of separation of metal ions using liquid membranes depends mainly on the type and concentration of the ion carriers. Commercial carriers used in laboratory experiments ensure the effective separation of the ions but their selectivity is rather poor. Therefore, new complexing reagents are sought enabling the effective separation of the ions from aqueous solutions. During the past few years, macrocyclic compounds, such as laryate ethers, calixarenes, calixcrowns and cyclodextrins were successfully used as the ion carriers (Ulewicz, 2001, 2008; Walkowiak and Kozłowski, 2009; Nghiem et al., 2006). Moreover, other organic compounds, e.g., imidazole and its derivatives were also used for the purpose. Imidazole (1,3-diazole) belongs to a class of five-member heterocyclic bases known as azoles. According to the Pearson's classification, imidazole is a medium-class base with pK_a of 7.14 (Barszcz and Lenarcik, 1989). It forms stable complexes with soft Lewis acids (Schaekers and du Preez, 2004). The substitution of an alkyl to position 1 of the azole only slightly strengthens the basicity of the electron-donating nitrogen atom of 1-alkylimidazoles ($pK_a = 0.0222n + 7.165$, where n is the number of the carbon atoms in the alkyl substituent) (Lenarcik and Ojczenasz, 2002). At the same time, the stability of their metal complexes is slightly enhanced. Water-insoluble alkylimidazoles were used for the solvent extraction of a number of metal ions, e.g., Co^{2+} , Ni^{2+} , Cu^{2+} , Zn^{2+} and Cd^{2+} (Cuprey, 1974; Lenarcik and Barszcz, 1977, 1979; Lenarcik et al., 1977; Schaekers and du Preez, 2004; Lenarcik and Ojczenasz, 2004; Lenarcik and Kierzkowska, 2004; Lenarcik and Rauckyte, 2004; Radzaminska-Lenarcik, 2007, 2008). 1-Decylimidazole was used for extraction of Co^{2+} , Ni^{2+} and Cu^{2+} from their chlorate(VII), chloride and thiocyanate solutions (du Preez et al., 2001). Moreover, azocrown ethers and thiaazocrown ethers were also reported as the ion carriers of Pb^{2+} , Zn^{2+} , Cd^{2+} , Ni^{2+} and Co^{2+} in the transport processes across the polymeric inclusion membranes (Ulewicz et al., 2007a,b, 2009), and 1-vinylimidazole was used for separation of the Cu^{2+} and Fe^{3+} ions (Ajjji and Ali, 2010). Recently, the imidazole derivatives were used by Ulewicz and Radzaminska-Lenarcik (Ulewicz and Radzaminska-Lenarcik, 2011, 2012; Radzaminska-Lenarcik and Ulewicz, 2012a) for

separation of the Cu²⁺ ion from the equimolar mixtures in the Cu²⁺-Co²⁺-Zn²⁺-Ni²⁺ systems.

A metallurgical waste is subjected to recovery processes, as far as these are technologically feasible and cost-effective. By the end of 2007 year, about 8.9 Tg of waste came from the copper metallurgy processes. The post-neutralization deposits of a waste-water treatment plant (80 Mg/24 hours) were found to contain 11.5% of zinc. Hence, our interest is zinc recovery. In the literature, there are many reports on the processes of zinc and other metals recovery (Beniot et al., 1996; Cuprey, 1974; Schaekers and du Preez, 2004).

The present article deals with a competitive transport of the zinc(II) ions from the dilute aqueous solutions using PIM doped with 1-alkylimidazoles. The initial fluxes and selectivity coefficients of zinc(II), cobalt(II) and nickel(II) ions transport across PIM doped with 1-alkylimidazole from the aqueous source phase containing equimolar mixture of all metals are also investigated.

Experimental

Preparation of polymeric inclusion membranes

The polymeric inclusion membranes (PIM) were synthesized using the following solutions: 1.25 g of cellulose triacetate (CTA) in 100 cm³ of dichloromethane, 10% plasticizer solution (o-nitrophenyl pentyl ether, o-NPPE; FLUKA) in dichloromethane and 0.10 mol/dm³ 1-alkylimidazoles (ion carrier) (Fig.1) solution in dichloromethane. The carrier was synthesized using a literature procedure (Pernak et al. 1987).

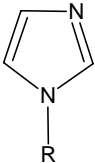
	No	R-:	pK _a
	<u>1</u>	-C ₆ H ₁₃	7.30
	<u>2</u>	-C ₇ H ₁₅	7.32
	<u>3</u>	-C ₈ H ₁₇	7.34
	<u>4</u>	-C ₉ H ₁₉	7.39
	<u>5</u>	-C ₁₀ H ₂₁	7.43

Fig. 1. Formulas of 1-alkylimidazoles

To prepare a membrane, the CTA solution was mixed with the plasticizer solution and that of the carrier and the mixture was poured into a mould consisting of a glass ring (6 cm in diameter). The membrane was formed after solvent evaporation during 12 hours at ambient temperature and subsequently it was conditioned in distilled water for further 12 hours. For preparation of the membrane, 2.67 cm³ of o-NPPE/1.0 g of CTA and 1.0 mole of 1-alkylimidazoles, based on the weight of the plasticizer, were used. A fresh membrane was prepared for each experiment. Highly magnified images of the polymeric membranes were recorded using an atomic force microscopy (AFM)

MultiMode instrument (Veeco) equipped with type E scanner with the maximum scanning area of $10 \times 10 \times 2.5 \mu\text{m}$. The NanoScope IIIa and Quadrex control systems were employed. The equipment was operated as the atomic force microscope in the Tapping Mode. The HA_NC Etalon probes manufactured by NT-MDT were used and a resonance frequency was set at 110 KHz. In the separation process, distilled water (conductance of $5 \mu\text{S/m}$) was the receiving phase. The thermal stability of the polymeric inclusion membranes was determined over the range of $20 - 700^\circ\text{C}$ under nitrogen, in ceramic crucibles. An empty crucible served as a reference. The apparatus used was a SDT 2960 simultaneous DSC-TGA-TA instrument operated at a heating rate of 10°C/min and a nitrogen flow rate of $100 \text{ cm}^3/\text{min}$. The sample weight was 10 mg throughout.

Investigation of transport across polymeric inclusion membranes

The following metal nitrate(V) solutions were used for preparation of the aqueous solutions: $\text{Zn}(\text{NO}_3)_2$, $\text{Co}(\text{NO}_3)_2$, $\text{Ni}(\text{NO}_3)_2$, and NaNO_3 (all of analytical reagent grade, purchased from POCh, Gliwice, Poland). The transport of the metal ions across PIM was determined in equimolar solutions (0.001 mol/dm^3 each), containing the following ion systems: Zn(II)–Ni(II), Zn(II)–Co(II), and Zn(II)–Co(II)–Ni(II) placed in a cell fitted with a membrane separating both aqueous phases (feeding and receiving), stirred at 600 rpm. The metal ion concentrations were determined by an atomic absorption spectrometry using a Solaar 939 (Unicam) spectrometer.

The efficiency of the ionic transport was estimated using the following quantities.

- Initial flux:

$$J_0 = -\frac{V}{A} k c_0 \quad (1)$$

where J_0 is the flux at $t = 0$ ($\text{mol/m}^2\text{s}$), A an effective surface area of the membrane (m^2), V volume of the feeding phase (m^3), and c_0 is the initial concentration of the metal ion (mol/dm^3). The rate constant, k (s^{-1}) for the first-order kinetics was defined as:

$$\ln \frac{c}{c_0} = -kt \quad (2)$$

High correlation coefficients R^2 falling in the range of 0.971–0.997 indicated a linear relationship of $\ln(c/c_1)$ against time t .

- The separation factor of ions was defined as:

$$S_{M1/M2} = \frac{J_{0,M1}}{J_{0,M2}} \quad (3)$$

where $J_{0, M1}$ and $J_{0, M2}$ are initial fluxes of metal ions M_1 and M_2 , respectively.

- The percentage of the metal ions transport from the feeding to receiving phase, RF, was defined as:

$$RF = \frac{c_i - c}{c_i} \cdot 100\% \tag{4}$$

where c_i is the initial concentration of metal ion in the receiving phase and c is the concentration in that phase after time t .

Results and discussion

The selectivity of transport of metal ions across the liquid membranes depends both on physicochemical characteristics of solutions, such as the metal ion concentration in the feeding phase, its pH and the presence of extraneous ions, the characteristics of membrane and plasticizer used and concentration of the carrier (Ulewicz et al., 2007a,b; 2009; Ajji and Ali, 2010; Ulewicz and Radzaminska-Lenarcik, 2011, 2012). One of the crucial factors affecting the selectivity of membrane is the ion carrier

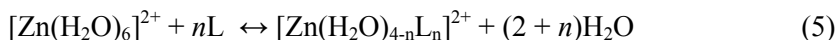
Table 1. Initial flux, selectivity order and selectivity coefficients for competitive transport of Zn(II), Co(II), and Ni(II) ions across PIM doped with 1-alkylimidazole; membrane: 2.6 cm³ *o*-NPPE /1g CTA and 1.0 M carriers calculated on plasticizer; source phase: [Me(II)] = 0.001M each, receiving phase: deionized water. * data from Radzaminska-Lenarcik and Ulewicz (2012b)

Carrier	Metal ions	J, μmol/m ² ·s	S _{Zn(II)/Me(II)}
1	Zn(II)	1.79	Zn(II) > Co(II) > Ni(II) 9.4 11.9
	Co(II)	0.19	
	Ni(II)	0.15	
2	Zn(II)	1.86	Zn(II) > Co(II) > Ni(II) 7.4 9.3
	Co(II)	0.25	
	Ni(II)	0.20	
3	Zn(II)	1.95	Zn(II) > Co(II) > Ni(II) 6.9 8.1
	Co(II)	0.28	
	Ni(II)	0.24	
4	Zn(II)	2.29	Zn(II) > Co(II) > Ni(II) 6.7 7.0
	Co(II)	0.34	
	Ni(II)	0.29	
5*	Zn(II)	2.50	Zn(II) > Co(II) > Ni(II) 6.4 7.8
	Co(II)	0.39	
	Ni(II)	0.32	

nature. Therefore, the kind of substituent at the imidazole molecule on the separation efficiency of the Zn(II), Co(II) and Ni(II) ions from their equimolar mixture was studied. The initial fluxes of ions J_o and their transportation selectivity rank orders depending on the carrier used are presented in Table 1. Table 1 shows that the Zn(II) ions are transported from the feeding to receiving phase faster than the Co(II) and Ni(II) ions. Irrespective of the substituent chain length, the selectivity of transport of the ions across polymeric membranes doped with 1-alkylimidazole declines in the order Zn(II) > Co(II) > Ni(II).

This finding can be interpreted in terms of the kinetic factors involved in a complex formation of metal ions at the membrane/feeding phase interface. The stability constants of the Zn(II) complexes are higher than those of the Co(II) and Ni(II) (Table 2). With increasing chain length from $-C_6H_{13}$ to $-C_{10}H_{21}$, associated with pK_a increase of the carrier, the initial fluxes of metal ions increase, while the selectivity coefficients of Zn(II) against those of the remaining metals decrease. This decrease is due to faster increase in the transportation fluxes of remaining metals as compared with the increasing transportation fluxes of the Zn(II) ions.

The differences in the transport efficiency of metal ions can be explained by structural features of their complexes with 1-decylimidazole. This compound forms Zn(II) complexes of distorted tetrahedral geometry just at the first complexation steps ($n = 1, 2..$) (Lenarcik and Kierzkowska, 2004) according to equation:



where L denotes the 1-decylimidazole molecule.

The tetrahedral Zn(II) complexes are more compact than the octahedral, thus there are more readily transported across the pores of membranes. The Co(II) ions form tetrahedral complexes in the 3rd and 4th complexation steps at high alkylimidazole concentrations (Lenarcik and Ojczenasz, 2004). Consequently, much more readily are formed more bulky complexes of those ions. Under these conditions, the Ni(II) ions form exclusively 6-coordinate species (Lenarcik and Rauckyte, 2004).

Table 2. Comparison of stability constants β_n of Co(II), Ni(II), and Zn(II) complexes with 1-alkylimidazoles. x denotes a number of carbon atoms in alkyl chain at position 1 in the 1-alkylimidazoles. Data from: * Lenarcik and Ojczenasz (2004), ** Lenarcik and Rauckyte (2004), *** Lenarcik and Kierzkowska (2004)

$\log \beta_n$	Co(II)*	Ni(II)**	Zn(II)***
$\log \beta_1$	$y = 0,302x + 1,653$	$y = 0,161x + 2,631$	$y = 0,229x + 1,986$
$\log \beta_2$	$y = 0,342x + 3,592$	$y = 0,164x + 5,290$	$y = 0,229x + 4,500$
$\log \beta_3$	$y = 0,377x + 4,881$	$y = 0,164x + 7,233$	$y = 0,229x + 6,700$
$\log \beta_4$	$y = 0,434x + 5,780$	$y = 0,166x + 8,653$	

Table 3. Kinetic parameters and selectivity factors for the transport of the metal ions across polymeric membranes doped with 1-hexylimidazole (**1**) and 1-decylimidazole (**5**).
* data from Radzimska-Lenarcik and Ulewicz (2012^b)

Carrier	Mixture	Ions	$J, \mu\text{mol}/\text{m}^2\cdot\text{s}$	$S_{\text{Zn(II)/Me(II)}}$
1	Zn(II)/Co(II)	Zn(II)	1.98	Zn(II) > Co(II)
		Co(II)	0.21	9.4
	Zn(II)/Ni(II)	Zn(II)	2.04	Zn(II) > Ni(II)
		Ni(II)	0.19	10.7
5*	Zn(II)/Co(II)	Zn(II)	2.65	Zn(II) > Co(II)
		Co(II)	0.30	8.8
	Zn(II)/Ni(II)	Zn(II)	2.67	Zn(II) > Ni(II)
		Ni(II)	0.28	9.5

The selectivity of separation of Zn(II) from binary solutions was studied during the transportation process across polymeric membranes doped with carriers **1** and **5**, i.e. those exhibiting respectively the highest and lowest selectivity of separation of the Zn(II) ions from the equimolar ternary mixture, Zn(II) – Co(II) – Ni(II). The results are given in Table 3. The highest separation factor among the Zn(II)/Me(II) systems was 10.7 for the Zn(II) – Ni(II) pair using carrier **1** and 9.5 for carrier **5**. From the Zn(II) – Co(II) – Ni(II) mixture, the separation efficiency for the Zn(II) ions was 89.3% and from the binary ion mixtures it exceeded 90% (Fig. 2). By comparing data from Tables 1 and 3, it can be seen that the Zn(II) ions were transported most effectively from all the investigated mixtures.

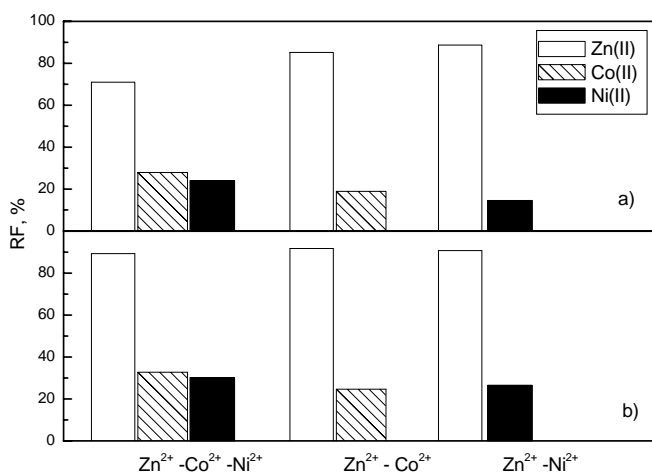


Fig. 2. Transport of metal ions from feeding phase after 24 hours, from different mixtures, during transport across the 1-hexylimidazole (a) and 1-decylimidazole (b) doped PIM

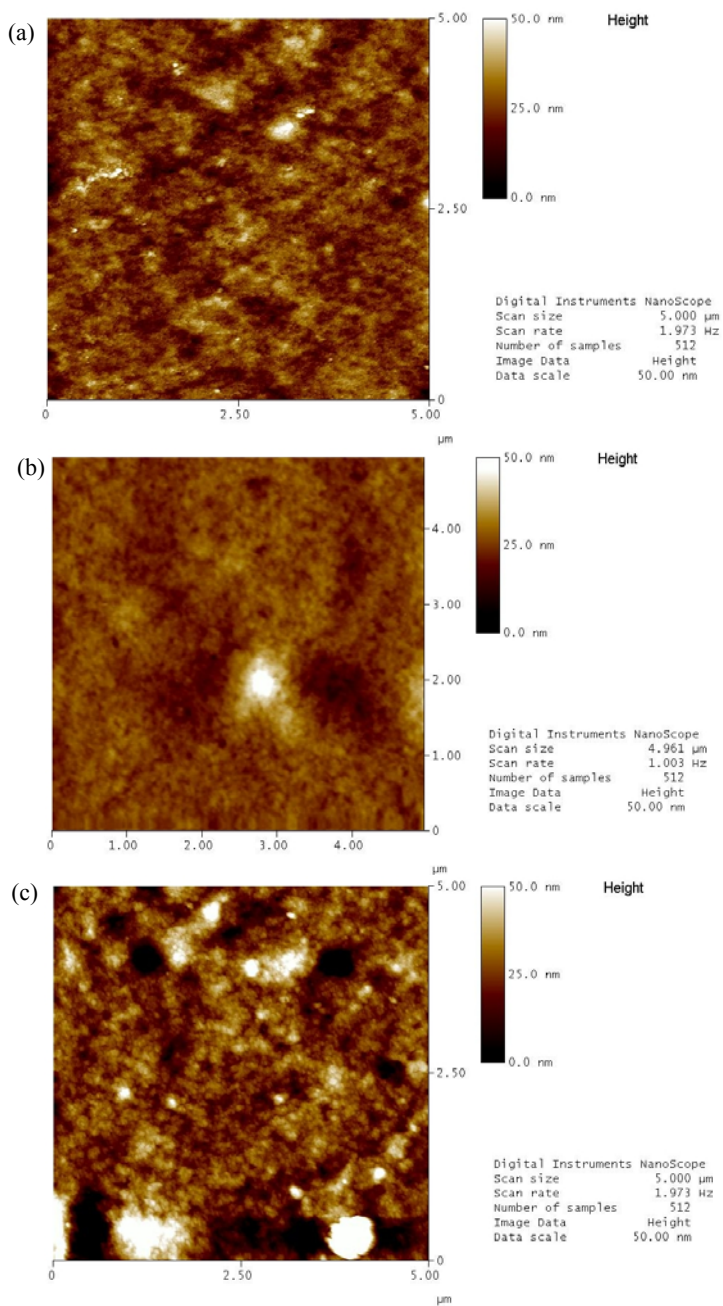


Fig. 3. 2D-view AFM images of the CTA - *o*-NPPE membrane (a), CTA - *o*-NPPE - carrier 1 (b), and CTA - *o*-NPPE - carrier 5 (c)

Since, as demonstrated in many papers (Ulewicz, 2001; Nghiem et al., 2006; Ulewicz et al., 2007a, Arous et al., 2004a), the selectivity of transportation of metal ions is affected by the physicochemical characteristics of the membrane, also the porosity and roughness of membranes were determined. Figure 3 shows the AFM image of the polymeric inclusion membranes doped with 1-hexylimidazole (membrane b) and 1-decylimidazole (membrane c) and, for the sake of comparison, that of a membrane consisting of support (CTA) and plasticizer (*o*-NPPE) only (membrane a).

The calculated mean roughness values, based on Ulewicz et al. (2009), for membranes 3a, 3b and 3c (surface area of 25 μm^2) are respectively 6.8, 8.1 and 3.9 nm. In Figures 3b and 3c the inclusions of organic phase are seen as large pores of 39.9 and 35.5 nm. The degree of porosity of *o*-NPPE-CTA membranes doped with carriers **1** and **5** was 21.1 and 18.7%, respectively.

Finally, thermal stability was examined for the membranes, which depends, among other things, on the polymer internal structure, its networking, presence of degradable aromatic and functional groups in the plasticizer and ion carrier. It was demonstrated (Gherrou et al. 2004, 2005; Arous et al., 2004b) that the degradation of CTA-made membrane occurs in two steps, the first over the range of 292–320 °C (main step) and the other over the range of 450–476 °C (charring of products). It was also shown that in thermal degradation of the CTA – *o*-NPOE – crown ether membranes, an additional

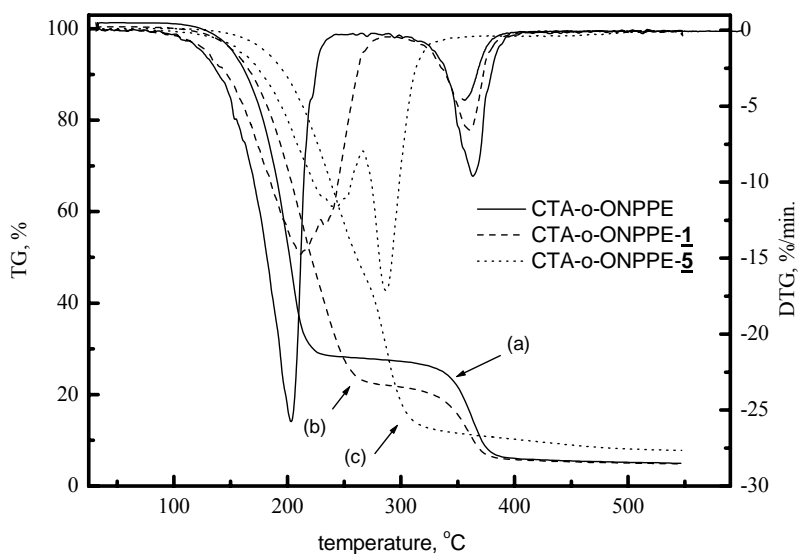


Fig. 4. TG-DTA curves for membranes: CTA-*o*-NPPE and CTA-*o*-NPPE + carrier **1**, and CTA-*o*-NPPE + carrier **5**

step emerges, which is assigned to degradation of the crown ether (ion carrier). For the series of crown ethers this step was recorded at 238.2 °C, 250.0 °C, 298.7 °C, and 273.4 °C for DB18C6, HT18C6, DA18C6, and HA18C6, respectively.

Figure 4 shows the thermograms of CTA-o-NPPE membranes with and without 1-hexylimidazole and 1-decylimidazole. Degradation of the membranes without the carrier occurs in two steps. In the first one, at 203.1 °C, 73.5% loss in mass was recorded, and in the second, at 363.3 °C, the loss was 19.9%. For the 1-hexylimidazole doped membrane corresponding losses of 74.63% and 13.9% occurred at 211.3 °C and 360.7 °C, respectively, while for the 1-decylimidazole doped membrane corresponding losses of 61.3% and 18.9% occurred at 227.7 °C and 358.6 °C, respectively.

Conclusion

The effective transport of the Zn(II) ions across 1-alkylimidazoles doped polymeric membranes was studied from both binary Zn(II) – Ni(II) and Zn(II) – Co(II) mixtures and ternary Zn(II) – Ni(II) – Co(II) mixture. The selectivity of separation declined in the series Zn(II) > Co(II) > Ni(II). The initial flux of the zinc(II) transport across PIM increases slightly with increasing alkyl chain length of the alkyl substituent in a molecule of the carrier in the order: **1** < **2** < **3** < **4** < **5**. The highest separation coefficient for the Zn(II)/Co(II) and Zn(II)/Ni(II) systems, equal 9.4 and 11.9, respectively, were determined for the equimolar Zn(II) – Co(II) – Ni(II) mixture using carrier **1**. Application of this carrier enables also to obtain higher selectivity factors for the Zn(II) ions from equimolar binary systems Zn(II) – Co(II) and Zn(II) – Ni(II). PIMs doped 1-hexyl- and 1-decylimidazole are thermally stable up to 210°C and they enable separation of Zn²⁺ with efficiencies better than 72% and 90% respectively within 24 hours.

References

- AJJI Z., ALI A. M. (2010). *Separation of copper ions from iron ions using PVA-g-(acrylic acid/N-vinyl imidazole) membranes prepared by radiation-induced grafting*. J. Hazardous Materials, 173, 71–74.
- AROUS O., KERDJOU DJ H., SETA P. (2004)a. *Comparison of carrier-facilitated silver(I) and copper(II) ions transport mechanism in a supported liquid membrane and in a plasticized cellulose triacetate membrane*. J. Membr. Sci., 241, 177–185.
- AROUS O., AMARA M., KERDJOU DJ, H. (2004)b. *Synthesis and characterization of cellulose triacetate and poly(ethylene imine) membranes containing a polyether macrobicyclic: Their application to the separation of copper(II) and silver(I) ion*. J. Applied Polymer Sci., 93, 1401–1410.
- BARSZCZ B., LENARCIK B. (1989). *Complexes of Mn(II) with azoles. Part II. Studies on the stability of Mn(II) complexes with diazoles and their methyl derivatives in aqueous solution*. Pol. J. Chem., 63, 371–380.
- BARTSCH R.A., WAY J.D. (1996). *Chemical separation with liquid membranes*, ACS Symp. Series Washington DC, Vol. 642

- BENIOT R., MENOYO B., ELIZALDE M.P. (1996). *Extraction equilibria of Zn(II) from chloride medium by Cyanex 302 in toluene*. Hydrometallurgy, 40, 51–63.
- BOND A.H., DIETZ M.L., ROGERS R.D. (1999). *Metal-ion separation and preconcentration. Progress and Opportunities*, ACS, Washington, DC.
- CUPREY M.E. (1974). *N-Imidazole compounds and their complex metal derivatives*. US Patent, 3,843,667, October 22.
- du PREEZ J.G.H., GERBER T.I.A., EGDE W., MTOTYWA V.L.V., van BRECHT J.A.M. (2001). *Nitrogen Reagents in Metal Ion Separation. XI. The Synthesis and Extraction Behavior of a New NS Imidazole Derivative*. Solvent Extr. Ion Exch. 19 (1), 143–154.
- GHERROU A., KERDJOUDJ H., MOLINARI R., SETA P., DRIOLI E. (2004). *Fixed sites plasticized cellulose triacetate membranes containing crown ethers for silver(I), copper(II) and gold(III) ions transport*. J. Membr. Sci., 228, 149–157.
- GHERROU A., KERDJOUDJ H., MOLINARI R., SETA P. (2005). *Preparation and characterization of polymeric plasticized membranes (PPM) embedding a crown ether carrier application to copper ions transport*. Mat. Sci. Eng. C, 25, 436–443.
- HABASHI R. (1999). *A textbook of hydrometallurgy*, 2nd ed. Metallurgy Extractive Quebec, Quebec City, Canada.
- LENARCIK B., BARSZCZ B. (1977). *Stability and structure of transition metal complexes with azoles in aqueous solutions. Part XIV. Complex formation between N-methylimidazole and Co(II), Ni(II), Cu(II) and Zn(II)*. Roczniki Chem., 51, 1849–1855.
- LENARCIK B., BARSZCZ B. (1979). *Stability and structure of transition metal complexes with azoles in aqueous solutions. Part XIX. Structural effects during complexation of Co(II), Ni(II), Cu(II) and Zn(II) with 1-ethyl- and 1-propylimidazoles*. Pol. J. Chem., 53, 963–971.
- LENARCIK B., BARSZCZ B., KULIG J. (1977). *Stability and structure of transition metal complexes with azoles in aqueous solutions. Part XI. A study on complex formation between n-butylimidazole and Co(II), Ni(II), Cu(II) and Zn(II)*. Roczniki Chem., 51, 1315–1323.
- LENARCIK B., OJCZENASZ P. (2002). *The influence of the size and position of the alkyl groups in alkylimidazole molecules on their acid – base properties*. J. Heterocyclic Chem. 39, 287–290.
- LENARCIK B.; OJCZENASZ P. (2004). *Investigation of the Stability Constants of Co(II) Complexes with a Homologous Series of 1-Alkylimidazoles in Aqueous Solution by Using a Partition Method with Several Solvents*, Sep. Sci. Technol., 39, 199–226.
- LENARCIK B.; KIERZKOWSKA A. (2004). *The Influence of Alkyl Length on Stability Constants of Zn(II) Complexes with 1-Alkylimidazoles in Aqueous Solutions and Their Partition Between Aqueous Phase and Organic Solvent*, Solv. Extr. Ion Exch., 22, 449–471.
- LENARCIK B., RAUCKYTE T. (2004). *The Influence of Alkyl Length on Extraction Equilibria of Ni(II) Complexes with 1-Alkylimidazoles in Aqueous Solution / Organic Solvent Systems*, Sep. Sci. Technol., 39, 3353–3372.
- NGHIEM L.D., MORNANE P., POTTER I.D., PERERA J.M., CATTRALL R.W., KOLEV S.D. (2006). *Extraction and transport of metal ions and small organic compounds using polymer inclusion membranes (PIMs)*, J. Membrane Sci., 281, 7–41.
- PERNAK J., KRYSINSKI J., SKRZYPCZAK A. (1987) *Bakterizide wirkung von iminiumverbindungen*, A. Tenside Surfact. Det., 24, 276–286.
- RADZYMINSKA-LENARCIK E. (2007). *The influence of the alkyl chain length on extraction equilibrium of Cu(II) complexes with 1-alkylimidazoles in aqueous solution/organic solvent systems*. Solvent Extr. Ion Exch. 25, 53–64.

- RADZYMINSKA-LENARCIK E. (2008). *Search for the possibility of utilizing the differences in complex-forming capacities of alkylimidazoles for selective extraction of some metal ions from aqueous solutions*. Pol. J. Chem. Technol., 10, 73–78.
- RADZYMINSKA-LENARCIK E., ULEWICZ M. (2012)a. *Selective transport of Cu(II) across polymer inclusion membranes with 1-alkylimidazole from nitrate solutions*. Sep. Sci. Technol., 47, 1113–1118.
- RADZYMINSKA-LENARCIK E., ULEWICZ, M. (2012)b. *Selective transport of Zn²⁺ ions across polymer inclusion membranes doped with 1-decylimidazole*. Proceedings., 47, 1 of the 39th International Conference of Slovak Society of Chemical Engineering, Tatranske-Matliare, Slovakia, 724–732.
- SCHAEKERS J.M., du PREEZ, J.G.H. (2004). *Solvent extraction mixture comprising substituted imidazole or benzimidazole for the purification of groups of base metals*. US Patent, US 2004/0208808 A1, October 21.
- ULEWICZ M. (2001). *Separacja jonów metali nieżelaznych w procesie transportu przez ciekłe membrany zawierające związki makrocycliczne*. Wydawnictwo WIPMiFS, Seria Monografie 20, Częstochowa.
- ULEWICZ M. (2008). *Application of macrocyclic compounds to the transport of Zn(II), Cd(II) and Pb(II) ions cross the polymer inclusion membrane (PIM)*, Polish J. Chem., 82, 1237–1244.
- ULEWICZ M., RADZYMINSKA-LENARCIK E. (2012). *Application of supported and polymer membrane with 1-decyl-2-methylimidazole for separation of transition metal ions*. Physicochemical Problems of Mineral Processing, 48, 91–102.
- ULEWICZ M., RADZYMINSKA-LENARCIK E. (2011). *Transport of metal ions across polymer inclusion membrane with 1-alkylimidazole*. Physicochemical Problems of Mineral Processing, 46, 119–130.
- ULEWICZ M., SADOWSKA K., BIERNAT J.F. (2007)a. *Facilitated transport of Zn(II), Cd(II) and Pb(II) across polymer inclusion membrane doped with imidazole azocrown ethers*. Desalination, 214, 352–364.
- ULEWICZ M., SADOWSKA K., BIERNAT J.F. (2007)b. *Selective transport of Pb(II) across polymer inclusion membrane using imidazole azocrown ethers as carriers*. Physicochemical Problems of Mineral Processing, 41, 133–143.
- ULEWICZ M., SZCZYGELSKA-TAO J., BIERNAT J.F. (2009). *Selectivity of Pb(II) transport across polymer inclusion membranes doped with imidazole azothiacrown ethers*, J. Membr. Sci., 344, 32–38.
- WALKOWIAK W., KOZŁOWSKI C. (2009). *Macrocyclic carriers for separation of metal ions in liquid membrane processes – a review*, Desalination, 240, 186–197.

Received May 31, 2013; reviewed; accepted July 16, 2013

MONITORING OF CONTAMINATION OF COAL PROCESSING PLANTS AND ENVIRONMENTAL WATERS USING BUBBLE VELOCITY MEASUREMENTS – ADVANTAGES AND LIMITATIONS

Jan ZAWALA^{*}, Ewa MALYSA^{}, Marcel KRZAN^{*}, Kazimierz MALYSA^{*}**

^{*} Jerzy Haber Institute of Catalysis and Surface Chemistry Polish Academy of Sciences, Krakow

^{**} AGH University of Science and Technology, Dept. Environmental Engineering & Mineral Processing, Krakow

Abstract: The paper presents fundamentals of a simple physicochemical method (SPMD) and analysis of results obtained when the method was applied for detection of organic contaminations (surface-active substances SAS) in samples of environmental and industrial waters. The method is based on measurements of variations of air bubble local velocities, which can be significantly changed in presence of surface-active contaminants. Lowering of the bubble velocity is a consequence of a motion induced dynamic adsorption layer (DAL) formed over surface of the rising bubble. The DAL formation retards the surface fluidity and the bubble rising velocity can be lowered by over 50% when the bubble surface is completely immobilized. We showed that the SPMD is a very sensitive tool (detection limit even below 1 ppm) for detection of various kinds of surface-active substances (ionic, non-ionic) in water samples. On the basis of results obtained using precise laboratory set-up, an accuracy of the SPMD is discussed. Moreover, effect of inert electrolyte addition on the bubble velocity lowering and value of detection limit of the SPMD is discussed. Simple approach, enabling quantitative analysis of the surface-active contaminants in samples collected, based on “equivalent concentrations” determination, is proposed. Results obtained for industrial (Jankowice and Knurow coal processing plants, Jaslo Refinery channel) and environmental waters (Wisloka and Ropa river) are used for detailed analysis and critical discussion of advantages and limitations of the SPMD.

Keywords: *bubble velocity, water purity, surface-active contaminants, method of detection, adsorption layer*

Introduction

Contaminations of environmental waters are caused by different areas of human activities, mainly industrial and domestic (households). Increasing applications of various detergents, washing/cleaning powders and liquids, cosmetics, pharmaceutical

products means also an increasing volume of municipal sewages containing various surface active substances. Agriculture with growing application of fertilizers, herbicides and pesticides, and various branches of industry, such as, for example petroleum, cosmetics, pulp and paper, pharmaceutical, mineral processing industries are also large sources of organic wastes contaminating environmental waters. Generally, organic substances (pollutants) show low affinity to the aqueous phase, and therefore adsorption at the liquid/gas interface formation of adsorption layer is a typical feature of all kind of surfactants and surface active substances. Certainly, the surface activity of various organic substances (pollutants) depends on their chemical structure and can differ by orders of magnitude. Nevertheless, their adsorption at the liquid/gas interface means that their presence in waters can be detected through measurements of velocity of the rising bubble, which is highly affected by formation of the adsorption layer over the bubble surface.

The bubble velocity is very sensitive to presence of surface active substances (SAS) in water since the adsorption layer formed over surface of the rising bubble retards fluidity of the bubble surface (Levich, 1962). In clean water, devoid of any SAS, the bubble surface is fully mobile, and therefore its velocity is higher than that of a solid sphere of identical density and diameter, which surface is immobile (no-slip conditions). This is clearly seen comparing the predictions of the Hadamard–Rybczynski theory (motion of bubbles and drops in pure liquids under creeping flow conditions) and Stokes law (motion of solid particles under creeping flow conditions). Under creeping flow conditions (Reynolds number, $Re < 1$) the bubble and drop velocity is 50% higher than velocity of a rigid sphere of the same diameter and density difference. At higher Reynolds number the bubble surface immobilization by the SAS adsorption caused similarly high lowering velocity of the rising bubble (Clift et al., 1978; Sam et al., 1996; Bel Fdhila and Duineveld, 1996; Zhang and Finch, 1996; Ybert and di Meglio, 1998; Ybert and di Meglio, 2000; Liao and McLaughlin, 2000; Zhang et al., 2001, Krzan and Malysa, 2002ab; 2009; 2012; Krzan et al., 2004; 2007; Malysa et al., 2005; 2011).

Degree of adsorption coverage of the bubble, formed in SAS solutions at a capillary orifice, is determined by the adsorption kinetics and velocity of the bubble surface growth. The equilibrium adsorption coverage over the bubble surface is attained only, when the adsorption kinetics is faster than the rate of bubble surface growth. Nevertheless, independently if there was or was not the attained equilibrium adsorption coverage, the adsorption coverage over surface of the detaching bubble is uniform. When the bubble starts to float then a non-uniform distribution of the adsorbed molecules, called dynamic adsorption layer (DAL), starts to be formed over surface of the rising bubble (Levich, 1996; Dukhin et al., 1995; Dukhin et al., 1998, Zholkovskij et al., 2000; Malysa et al., 2005 and 2011; Krzan et al., 2007) as a result of the viscous drag exerted by fluid on the moving bubble. Formation of this dynamic structure of the adsorption layer means that the adsorption coverage is much lower at the upstream pole of the moving bubble than at the rear pole. This difference in

adsorption coverage means induction of the surface tension gradients over the bubble surface, which - depending on degree of adsorption coverage (Dukhin et al. 1995; Levich, 1996; Dukhin et al., 1998; Zholkovskij et al., 2000; Krzan and Malysa, 2002ab) cause either partial or a complete immobilization of the bubble surface. As showed elsewhere (Krzan and Malysa, 2002ab; 2009; 2012; Krzan et al., 2004; 2007; Malysa et al., 2005; 2011) the degree of adsorption coverage needed for complete immobilization of the bubble surface varies for different surface active substances, but generally is rather low, a few percent in the case of non-ionic surfactants and up to ca. 30% for ionic SAS. On the other hand, the time of the DAL formation depends on concentration of SAS solutions. It needs to be underlined here that, as even traces of surfactant can lower the bubble velocity, monitoring the bubble motion in waters can be used as sensitive tool for detection of surface active contaminations. Loglio et al. (1989) were probably the first who applied measurements the time of bubbles rising at different heights of the column for detection surfactants presence in water. They pointed out that the velocity of the rising bubbles (2–3 mm diameter) decreased when an amount of surfactant increased. Recently, Zawala et al. (2007) carried out systematic studies on influence of various contaminants on the bubble rising velocity and proposed a simple physicochemical method (SPMD) for detection of organic contaminations in water. The details of the SPMD are described below.

The paper analyses possibilities, advantages and limitations of application of the bubble velocity measurements in monitoring presence and concentration of organic contaminants in environmental and industrial waters. Influence of ionic and nonionic surface active substances on motion of the rising bubble and the experimental data obtained for samples collected in two polish rivers (Zychowska, 2012) and in water circulating system of the coal processing plants (Malysa et al., 2009) are presented and discussed.

Experimental

The bubble velocity measurements were carried out using the precise laboratory set-up, called here Moticam-2000 and the SPMD set-up elaborated, described in details by Zawala et al. (2007). The Moticam 2000 set-up described in details by Krzan and Malysa (2002a) consists of the following main elements (Fig. 1, right): i) a square glass column of cross section 40x40 mm with the capillary of inner diameter 0.075 mm, ii) syringe pump for gas supply with high precision control of the flow rate, iii) stroboscopic illumination system, and Moticam-2000 CCD camera coupled with PC computer for the images recording, and iv) image analysis software. The bubble local velocity was determined as

$$U = \frac{\sqrt{(x_{i+2} - x_{i+1})^2 + (y_{i+2} - y_{i+1})^2}}{\Delta t}, \quad (1)$$

where (x_{i+2}, y_{i+2}) and (x_{i+1}, y_{i+1}) are the coordinates of the subsequent positions of the bubble bottom pole and Δt is the time interval between stroboscopic lamp flashes. In majority of the experiments Δt is equal to 0.01 s. The bubble terminal velocity was calculated as an average for distances, where values of the bubble local velocity started to be constant. In distilled water, the bubble formed at the capillary used in the experiments had the radius of 0.74 mm.

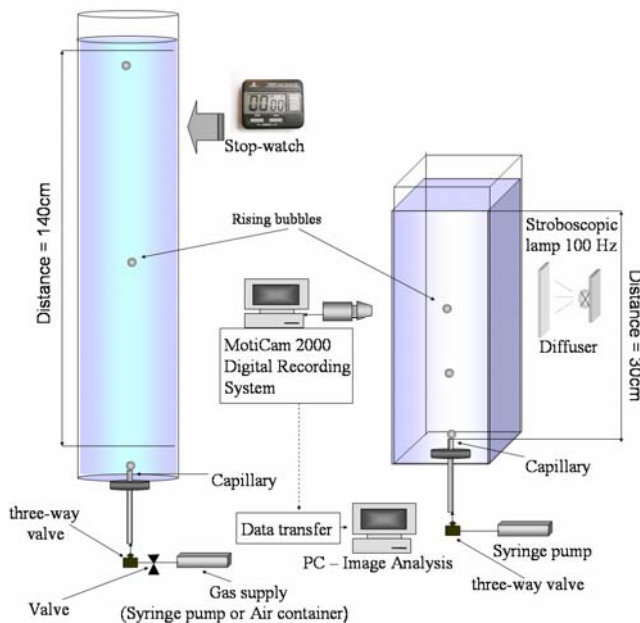


Fig. 1. Sketch of the MotiCam 2000 and SPMD set-ups

Simplicity of measurements and low cost of the experimental set-up were the main aims of elaboration of the simple physicochemical method for detection (SPMD) of organic contaminants in water (Zawala et al., 2007). The SPMD set-up (Fig. 1, left) consists of: i) a long (ca. 1600 mm) glass tube with the glass capillary sealed at the bottom, ii) a stop-watch, and iii) air supply system with a controlled flow rate. We used either a compressed air container with a precise valve or the syringe pump. Single bubbles were formed at the capillary orifice with time interval above 10 s between each subsequent bubble. The time of bubble passage of the distance 140 mm (t_i) was measured manually using stop-watch. The choice of this measurement distance is a compromise between a convenience of the bubble observation and compactness of the set-up. When the time intervals are determined manually using the stop-watch, then we should have long distance of the bubble passage to measure the time values with a satisfactory accuracy and precision. To increase the precision of determination, the measurements were repeated at least 20 times (the passage time of

20 bubbles was measured and the average value was calculated for every sample). The time interval (t_i) was started to be measured when the bubble was passing the point marked 60 mm above the capillary orifice, i.e. after acceleration period of the bubble motion (Krzan et al., 2007; Zawala et al., 2007) and the bubble velocity (U_i) was determined as:

$$U_i = \frac{140}{t_i}. \quad (2)$$

Results and discussion

Sequences of images of the bubbles rising in $3 \cdot 10^{-5}$, $1 \cdot 10^{-4}$ and $3 \cdot 10^{-3}$ M sodium n-dodecyl sulfate (SDDS) solutions are presented in Fig. 2. Figure 2 shows the bubbles motion immediately after detachment (acceleration stage of the rising bubble motion) and at the distance $L=30$ cm from the capillary. The experiments were carried out under identical frequency of stroboscopic illumination (100 Hz), therefore the photos clearly illustrate the following features of the bubble motion: i) the detached bubble increases rapidly its rising velocity, ii) at distance $L = 30$ cm the bubble velocity seems to be constant (does not change with distance), iii) with increasing the SDDS concentrations the bubble velocity decreases, iv) spherical bubbles formed at the capillary orifice started to be deformed immediately after their detachment, and v) degree of the bubble shape deformation was decreasing with the SDDS concentration.

Figure 3 (left) presents quantitative data on influence of the SDDS concentration on the bubble local velocities. A similar data for Persil (a popular washing powder used in Polish households) as an comparison are given in Fig. 3 (right). It needs to be underlined, that the washing powder Persil is a commercial product and similarly as all commercial detergents it is not a well-defined surfactant but a “formulation”, that is a mixture of ionic and non-ionic surfactants containing many different additives. We carried out measurements to check if the bubble velocity is changing in similar way in Persil solutions as in solutions of well-defined ionic and non-ionic surfactants. The general features of the bubble local velocity profiles (Fig. 3) show that variations of the bubble local velocities with distance are similar for the SDDS and Persil solutions. Immediately after detachment, the bubbles velocity monotonically increases and far away from the capillary, a tendency to attain a constant value (terminal bubble velocity) can be noted for all concentrations of SDDS and Persil solutions. Moreover, at low concentrations of SDDS and Persil there are maxima on local velocity profiles. As it was already showed before (Krzan et al., 2004; Malysa et al., 2005 and 2011; Krzan et al., 2007), the occurrence of the maximum on the local velocity profile indicates that dynamic architecture of the adsorption layer (DAL), causing immobilization of the bubble interface as a result of the surface tension gradients inducement, was not established during the acceleration stage of the bubble motion.

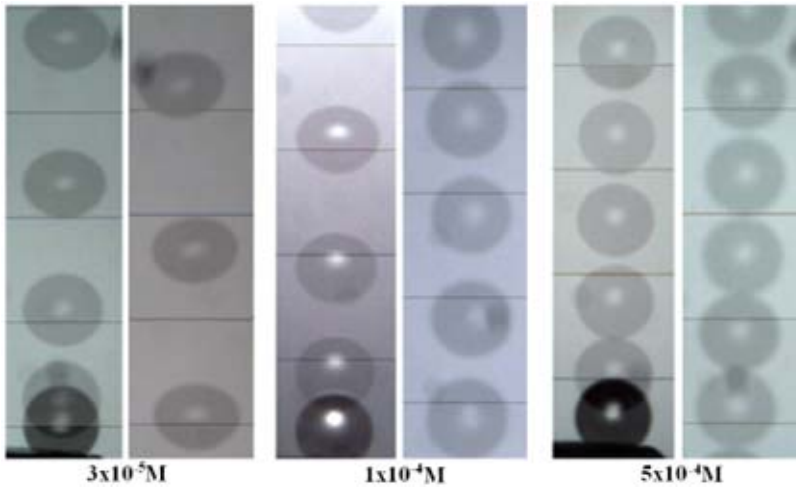


Fig. 2. Sequences of photos (3 pairs) showing rising bubbles in SDDS solutions, immediately after detachment (left side sequences) and far away (30 cm) from the capillary. Time interval between the stroboscopic lamp flashes $\Delta t = 0.01$ s

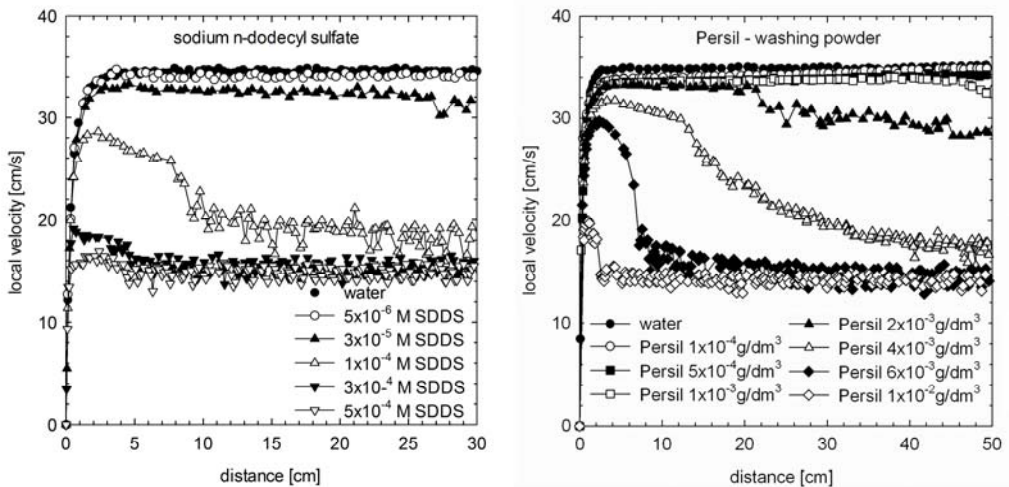


Fig. 3. Bubble local velocities as a function of distance in SDDS (left) and Persil washing powder (right) solutions of different concentrations

The influence of electrolyte concentration on the bubble velocity in solutions of ionic and nonionic surface active substances is compared in Figs. 4 and 5. Sequences of photos presented in Fig. 4 illustrate that addition of inert electrolyte (NaCl) had practically no influence on the bubble velocity ($L = 30$ cm) in $2 \cdot 10^{-4}$ M n-hexanol solution (non-ionic surface active substance) and caused a significant lowering the bubble velocity in $3 \cdot 10^{-5}$ M SDDS solution (anionic surfactant). It needs to be underlined that without ionic surfactant presence, the bubble velocity in 0.05 M NaCl

solution is identical as in distilled water (Krzan and Malysa, 2012). Thus, the electrolytes affect the bubble velocity in solutions of ionic surfactants through variation of their adsorption at the bubble surface and /or their surface activity and dissociation degree.

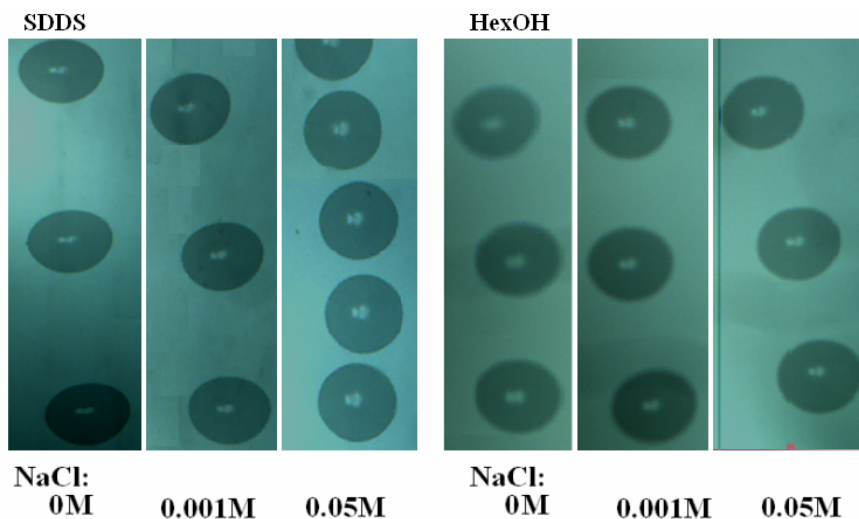


Fig. 4. Sequences of photos (2 sets) showing the influence of electrolyte on bubble motion in $3 \cdot 10^{-5}$ M SDDS and $2 \cdot 10^{-4}$ M n-hexanol solutions far away (30 cm) from the capillary. Time interval between the stroboscopic lamp flashes $\Delta t = 0.01$ s

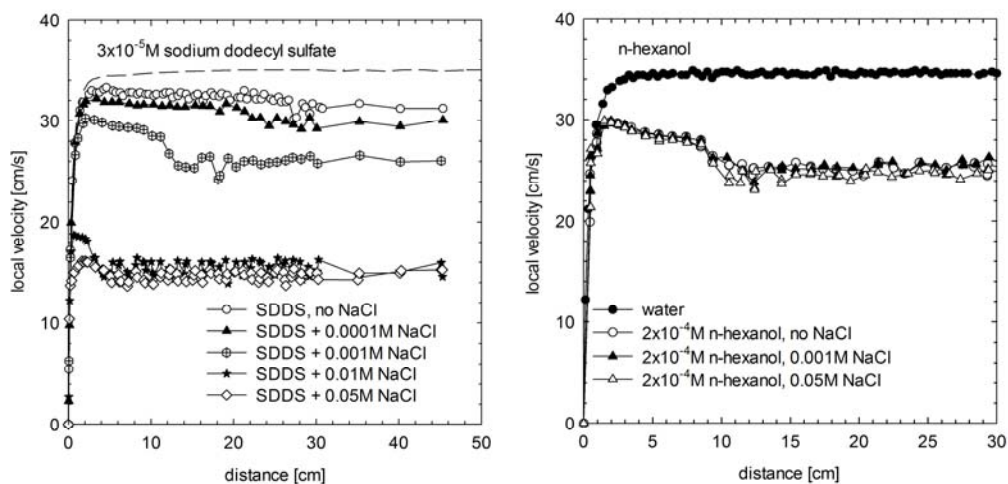


Fig. 5. Influence of electrolyte on the bubble local velocity profiles in $3 \cdot 10^{-5}$ M SDDS and $2 \cdot 10^{-4}$ M n-hexanol solutions

Figure 5 shows influence of NaCl concentration on profiles of the bubble local velocity in $3 \cdot 10^{-5}$ M sodium dodecyl sulfate SDDS (left) and $2 \cdot 10^{-4}$ M n-hexanol (right) solutions. It can be seen that the bubble local velocity profile in n-hexanol solution does not depend on concentration of the electrolyte added. The picture is completely different in the case of the $3 \cdot 10^{-5}$ M SDDS solution. Addition of 0.05 M NaCl resulted in lowering of the bubble terminal velocity by ca. 50%, from 31.4 ± 0.6 (no electrolyte) to 14.6 ± 0.5 cm/s (0.05 M NaCl). The bubble velocity profiles in $3 \cdot 10^{-5}$ M SDDS solution were significantly affected even in the presence of much smaller (0.01 and 0.001M) NaCl concentrations (Fig. 5 left). Influence of inert electrolyte and pH on parameters of the rising bubble motion in solutions of sodium n-alkylsulfates of different hydrocarbon chain length was studied earlier by Krzan and Malysa (2009, 2012) and it was concluded that electrolyte affected the bubble motion through its influence on state of the dynamic adsorption layer formed over surface of the rising bubbles. It is rather well known and documented in the literature (Kalinin and Radke, 1996; Warszynski et al., 1998, 2002; Adamczyk et al., 1999ab; Para et al., 2005; Jarek et al., 2010) that addition of electrolyte can increase adsorption of ionic surfactant. For example in the case of the SDDS solutions, the surface tension isotherm can be shifted towards lower concentrations by more than order of magnitude (Warszynski et al., 1998). This effect is related to neutralization of the surface charge of adsorbed ionic surfactant molecules by counter ions adsorbed in the stern layer. In other words, the electrolyte presence caused that the SDDS adsorption coverage at the bubble surface was increased, and therefore fluidity of the bubble surface was retarded in a higher degree. It should be added here, that at more concentrated SDDS solutions the influence of electrolyte presence is much smaller and disappears, when the SDDS adsorption coverage is high enough for a complete retardation of the bubble surface mobility (Krzan and Malysa, 2009, 2012). We would like to underline here that data presented in Fig. 5 clearly show a possibility of checking and distinguishing if samples of the contaminated waters contained ionic, nonionic and/or mixtures of ionic and nonionic surfactants and/or formulations. For this purpose the appropriate experiments and analysis of influence of the electrolyte and/or pH on the bubble velocity would have to be carried out.

Figure 6 presents the bubble velocities in samples of waters from rivers in Jaslo region and the Jaslo Refinery Channel (JRC). The bubble velocity in the Wisloka river, upstream of the Jaslo Refinery Channel (JRC) inlet was 32.5 ± 0.5 cm/s, that is practically identical as in Krakow tap water. Waters in the Jaslo Refinery channel contained a lot surface active substances (organic contaminants) since the bubble average velocity was only 15.4 ± 0.2 cm/s in these waters. Therefore, in the Wisloka waters sample collected below the JRC inlet, the bubble velocity decreased to 31.3 ± 0.5 cm/s. As the waters of the Ropa river were of similar quality so the bubble velocity in water samples from Wisloka below the Ropa inlet did not change.

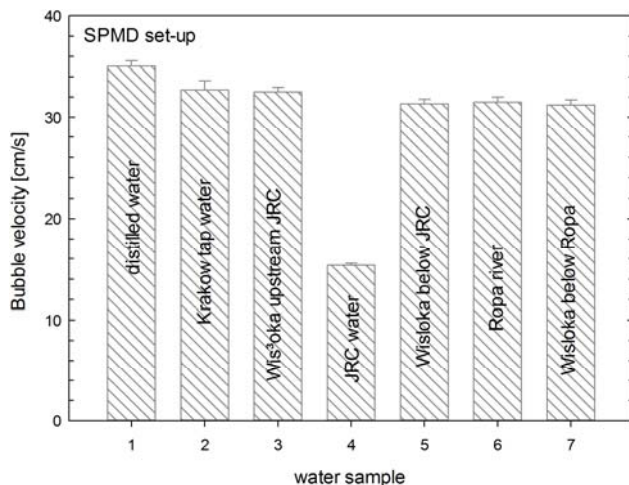


Fig. 6. Bubble velocity in samples of waters from Jaslo region – Wisloka and Ropa rivers, Jaslo Refinery Channel

Figure 7 presents the bubble velocities in samples collected at different points of the water circulation systems in Knurów and Jankowice Coal Processing Plants (Malysa et al., 2009). The bubble terminal velocity in Krakow tap water as comparison is also given. The bubble velocities in all samples from Knurów and Jankowice Coal Processing Plants were significantly lower than in tap water. The bubble velocities in samples from the Jankowice Plant were systematically much

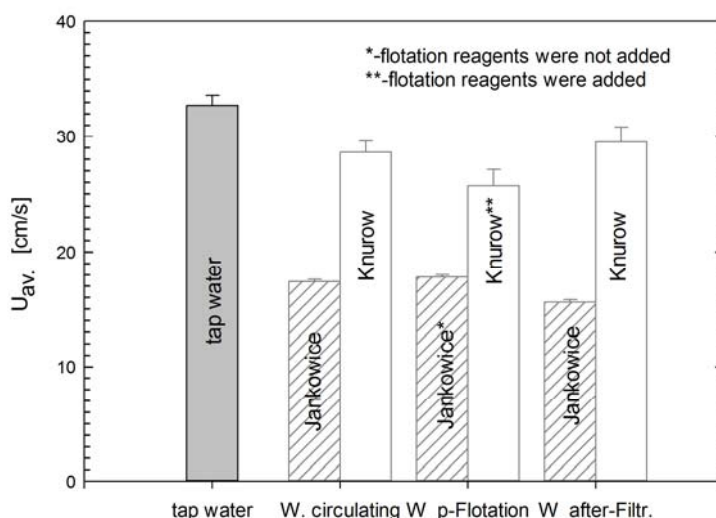


Fig. 7. Bubble velocity in various points of water circuits of the Jankowice and Knurów Processing Plant

lower than in the Knurow samples. It shows that waters of the Jankowice water circulating system contained more surface active substances (flotation reagents used in the plant). The water prior flotation sample (Fig. 7, W_p-flotation) was collected in the Jankowice Plant before the flotation reagents were added to the flotation feed, while in the case of the Knurow Plant after the reagents addition. This is immediately reflected in the bubble velocities measured. In the case of the Knurow samples the bubble velocity was the lowest in water prior flotation because of addition of the flotation reagents. These data clearly show that the bubble velocity measurements can be used as a simple method for monitoring presence and variations of the flotation reagents concentration in industrial water circulating systems.

The bubble velocity is highly dependent on concentration of surface active substances, especially at their lowest concentrations. It is very advantageous since it makes possible detection of even traces of surface active substances in environmental and industrial waters. On the other side, however, there is no a unique dependence and for different the SAS the bubble velocity variations with solution concentration can be quite different (Malysa et al., 2005, 2011) and this is the main difficulty in converting the bubble velocity variations into contaminants concentration. Therefore, a reagent "X" or commercial products "Y", "Z", etc. needs to be chosen as a "model pollutant" and used for calibration. Then, the concentration of waters contaminants can be expressed as the "equivalent concentration of "X", "Y" or "Z". Zawala et al. (2007) proposed to use the commercial detergents "Ludwik" (washing liquid) and "Vizir" (washing powder), widely used in Polish household, as the "reference detergents" for environmental waters. Montanol and Flotanol, which are mixtures of higher alcohols and esters (Malysa et al., 2009) are the flotation reagents used in Polish coal processing plants therefore, they were chosen as the "reference reagents" for the Knurow and Jankowice water circulation systems.

Figure 8 shows dependences of the bubble velocity on concentration of Ludwik, Vizir, Montanol and Flotanol solutions. From Fig. 8 it can be seen that the dependences of the bubble velocity on Montanol and Flotanol solution concentration are almost identical and quite different from that ones for Ludwik and Vizir. The highest surface activities were observed for Flotanol and Montanol, while the lowest for the Vizir washing powder. The relation between the average bubble velocity U_{av} , concentration of surface active reagent c was used to fit experimental data obtained for Ludwik, Vizir, Flotanol and Montanol solutions:

$$U_{av} = P \exp\left(\frac{Q}{c + R}\right), \quad (3)$$

where P , Q and R are fitting parameters (Fig. 8). The values of fitting parameters obtained for these "reference reagents" are collected in Table 1. The values of these parameters are very similar for Montanol and Flotanol since these reagents lower the bubble velocity in a similar way and at similar concentrations.

Rearrangement of Eq. 3 gives relation:

$$c = \frac{Q - R(\ln U_{av} - \ln P)}{\ln U_{av} - \ln P}, \quad (4)$$

which can be used to express the degree of environmental and industrial waters contaminations in a concentration scale (as equivalent concentration of either Ludwik, or Vizir, or Montanol, or Flotanol). When the bubble velocity measured in industrial and/or environmental waters is 15–16 cm/s, the samples should be diluted in the controlled manner, because such low velocity value means that the bubble surface was completely immobilized, and therefore the bubble velocity stopped to be dependent on SAS (contaminants) concentration (Malysa et al., 2011). Thus, to determine real concentration of contaminants in such samples, the bubble velocity measurements should be carried out as a function of the sample dilution.

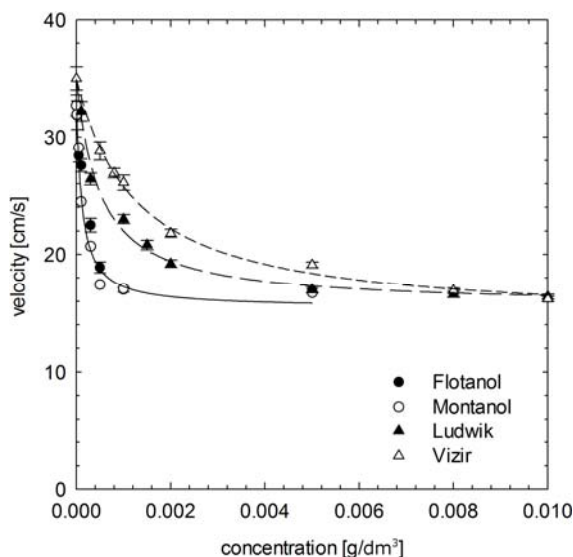


Fig. 8. The bubble velocity as a function of Ludwik (▲), Vizir (Δ), Montanol (◊) and Flotanol (◆) concentration. Lines are the exponential function (Eq. 3) fitted to Ludwik, Vizir and Montanol experimental data

Table 1. Values of the parameters P , Q , R obtained from fitting Eq. 3 to experimental data

Surfactant	P [cm/s]	Q [g/dm³]	R [g/dm³]
Montanol	15.4	$1.97 \cdot 10^{-4}$	$2.6 \cdot 10^{-4}$
Flotanol	15.4	$1.3 \cdot 10^{-4}$	$1.7 \cdot 10^{-4}$
Ludwik	15.6	$6 \cdot 10^{-4}$	$7.4 \cdot 10^{-4}$
Vizir	14.2	$1.8 \cdot 10^{-3}$	$2 \cdot 10^{-3}$

Figure 9 shows dependences of the bubble velocity on dilution of the Jaslo Refinery Channel (JRC) and Jankowice waters after filtration. Table 2 presents contaminations degree of the environmental and industrial waters calculated using the fitting parameters collected in Table 1. The results clearly illustrate possibilities and some limitations of application of the bubble velocity for monitoring presence and concentration of surface active contaminants in environmental waters. The proposed method is very sensitive and enables detection even traces of organic contaminants in environmental and industrial waters.

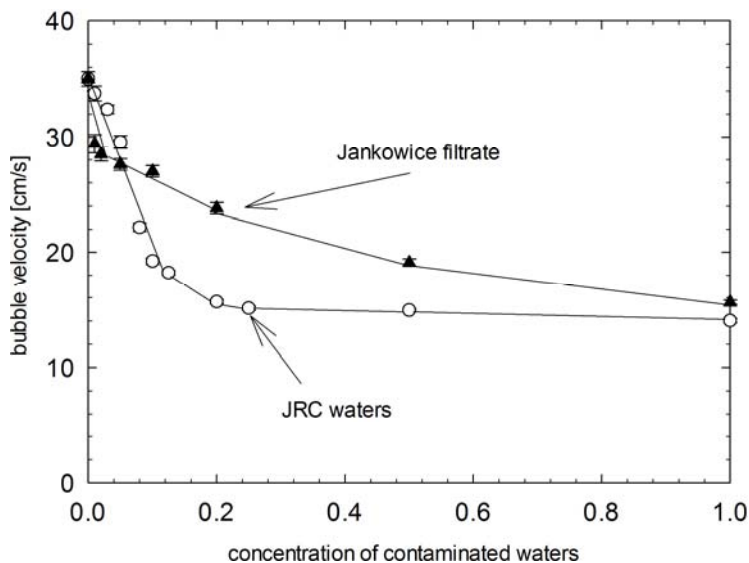


Fig. 9. The bubble velocity in diluted samples of JRC waters and Jankowice waters after filtration (lines added to guide the eye)

Table 2. Concentration of contaminants in environmental and industrial waters expressed in units of equivalent concentrations of Ludwik, Vizir and, Flotanol and Montanol

Sample	Ludwik mg/dm ³	Vizir mg/dm ³	Flotanol mg/dm ³	Montanol mg/dm ³
Distilled water	0,00	0,00	0,00	0,00
Tap water	0,07	0,16	0,00	0,00
Wisloka r. before oil renifery	0,08	0,17	0,00	0,00
Wisloka r. after oil renifery	0,12	0,28	0,01	0,02
Ropa	0,11	0,26	0,01	0,02
Knurów coal mine – water circulating	0,25	0,57	0,04	0,06
Knurów coal mine – water prior flotation	0,46	1,03	0,08	0,12
Knurów coal mine – water after filtration	0,20	0,46	0,03	0,04
Jankowice coal mine – water circulating	4,75	6,86	0,89	1,35
Jankowice coal mine – water prior flotation	3,81	5,97	0,73	1,10

In the case of nonionic surface active substances the detection limit can be even below 0.1 ppm (Table 2 for Flotanol and Montanol equivalent concentrations). When waters are contaminated by unknown mixtures of the ionic and non-ionic surface active substances, then the detection limit is shifted to higher concentrations, but this is still within the concentration range below 1 ppm, as can be observed in Table 2 (equivalent concentrations of Ludwik and Vizir). Moreover, the method is reliable, quite simple and non-expensive. In the measurements there is no need to add or use any additional reagents, and this is a big advantage of the simple physicochemical method SPMD. The SPMD can be especially useful for quick and direct controlling of variations of reagents concentration in different points of the industrial water circulating systems. On the other side, one should remember that the method can express a contamination degree only by means of the units of equivalent concentrations of some reference detergent after careful calibration.

Conclusions

The measurements of velocity variations of the rising bubbles was successfully applied for detection of organic (surface active) contaminants presence in environmental and industrial waters. The simple physicochemical method (SPMD) elaborated is based on measurements of variations of rising bubble average velocity. It was shown how highly dependent is the bubble velocity on presence of surface active substances (SAS), especially at their lowest concentrations. The bubble velocity is a very sensitive tool for detection of even traces of organic contaminant, because its detection limit of the SAS presence is lower by over order of magnitude than in the case of the surface tension measurements. The SPMD set-up is simple and non-expensive and easy to operate even under field conditions. It was shown that the SPMD method enables, when applied properly, to detect the SAS presence in concentrations, even below 1 ppm. The method can be especially useful for quick and direct controlling of variations of reagents concentration in different points of the industrial water circulating systems. Additionally, it was shown that by addition of inner electrolyte, the type of the surface active contaminant (ionic, non-ionic) can be distinguished.

The bubble velocity is highly sensitive to presence of any surface active substance and this is simultaneously a big advantage of the SPMD and difficulty in converting the bubble velocity variations into a contaminant concentration. The method of converting the bubble velocity variations into contaminants concentration expressed in terms of “equivalent concentrations of a “model contaminant” is described and its advantages and limitations are evaluated.

Acknowledgements

The study is related to the activity of the European network action COST MP1106 “Smart and green interfaces – from single bubbles and drops to industrial, environmental and biomedical applications”.

Skillful assistance of P. Zychowska in some of the experiments and financial support from AGH (grant No. 11.11.100.276) and Polish National Science Center (grant No. 2011/01/B/ST8/03717) are acknowledged with gratitude.

References

- ADAMCZYK Z., PARA G., WARSZYNSKI P., 1999, *Influence of ionic strength on surface tension of cetyltrimethylammonium bromid*, Langmuir 15, 8383–8387.
- ADAMCZYK Z., PARA G., WARSZYNSKI P., 1999, *Surface tension of sodium dodecyl sulphate in the presence of a simple electrolyte*, Bull. Pol. Ac. Sci. 47, 175–186.
- BEL FDHILA R., DUINVELD P.C., 1996, *The effect of surfactant on the rise of spherical bubble at high Reynolds and Peclet numbers*, Phys. Fluids A 8, 310–321.
- CLIFT R., GRACE J.R. and WEBER M.E., 1978, *Bubbles, drops and particles*, Academic Press, New York, San Francisco, London.
- DUKHIN S.S., KRETZSCHMAR G., MILLER R., 1995, *Dynamics of adsorption at liquid interfaces. Theory, Experiments, Application*, Elsevier, Amsterdam-Laussane-New York- Oxford-Shannon
- DUKHIN S.S., MILLER R., LOGLIO G., 1998, *Physicochemical hydrodynamics of rising bubble*, in: Studies in Interface Science, Elsevier, 367–432.
- JAREK E., JASINSKI T., BARZYK W., WARSZYNSKI P., 2010, *The pH regulated surface activity of alkanolic acids*, Colloids Surf. A. 354, 188–196.
- LEVICH V.G., 1962, *Physicochemical hydrodynamics*, Prentice-Hall, Inc., Engelwood Clift, N.J.
- LIAO Y., MCLAUGHIN J.B., 2000, *Bubble motion in aqueous surfactant solutions*, J. Colloid Interf. Sci. 224, 297–310.
- KALININ V.V., RADKE C.J., 1996, *A ion-binding model for ionic surfactant adsorption at aqueous-fluid interfaces*, Coll. Surf. A. 114, 337–350.
- KRZAN M., MALYSY K., 2002, *Profiles of local velocities of bubbles in n-butanol, n-hexanol and nonanol solutions*, Colloids and Surfaces A: 207, 279–291.
- KRZAN M., MALYSY K., 2002, *Influence of frother concentration on bubble dimension and rising velocities*, Physicochemical Problem of Mineral Processing 36, 65–76.
- KRZAN M., MALYSY K., 2009, *Influence of solution pH and electrolyte presence on bubble velocity in anionic surfactant solutions*, Physicochemical Problems of Mineral Processing 43, 43–58.
- KRZAN M., MALYSY K., 2012, *Influence of electrolyte presence on bubble velocity in solutions of sodium n-alkylsulfates (C₈, C₁₀ and C₁₂)*, Physicochemical Problems of Mineral Processing, 48, 49–62.
- KRZAN M., LUNKENHEIMER K., MALYSY K., 2004, *On the influence of the surfactant's polar group on the local and terminal velocities of bubbles*, Colloids and Surfaces A: 250, 431–441.
- KRZAN M., ZAWALA J., MALYSY K., 2007, *Development of steady state adsorption distribution over interface of a bubble rising in solutions of n-alkanols (C₅, C₈) and n-alcyltrimethylammonium bromides (C₈, C₁₂, C₁₆)*, Colloid & Surfaces A: 298, 42–51.
- LOGLIO G., DEGLI INNOCENTI N., TESEI U., CINI R., WAND Q.-S., 1989, *Il Nuovo Cimento Della Socieriae Italiana di Fisica C. 12*, 289.
- MALYSY E., IWANSKA A., HANC A., MALYSY K., 2009, *Metoda monitorowania stężenia odczynników flotacyjnych w wodach obiegowych zakładów przerobczych węgla przez pomiar prędkości pęcherzyków powietrza*, Gospod. Surowcami Mineralnymi, 25 (3) 109–120.
- MALYSY K., KRASOWSKA M., KRZAN M., 2005, *Influence of surface active substances on bubble motion and collision with various interfaces*, Adv. Colloid Interface Sci. 114–115C: 205–225.

- MALYSA K., ZAWALA J., KRZAN M., KRASOWSKA M., 2011, *Bubbles Rising in Solutions; Local and Terminal Velocities, Shape Variations and Collisions with Free Surface*, in: R. Miller, L. Liggieri (Eds.) *Bubble and Drops Interfaces*, 243–292.
- PARA, G., JAREK, E., WARSZYNSKI, P., 2005, *The surface tension of aqueous solution of cetyltrimethylammonium cationic surfactants in presence of bromide and chloride counterions*, *Colloids Surf. A* 261, 65–73.
- SAM A., GOMEZ C.O., FINCH J.A., 1996, *Axial velocity profiles of single bubbles in water/frother solutions*, *Int. J. Miner. Process.* 47, 177–196.
- WARSZYNSKI, P., BARZYK, W., LUNKENHEIMER, K., FRUHNER, H., 1998a, *Surface tension and surface potential of Na n-dodecylsulfate at the air solution interface: Model and experiment*, *J. Phys. Chem. B* 102, 10948–10957.
- WARSZYNSKI, P., LUNKENHEIMER, K., CICHOCKI, G., 2002, *Effect of counterions on the adsorption of ionic surfactants at fluid–fluid interfaces*, *Langmuir* 18, 2506–2514.
- YBERT C. and DI MEGLIO J.-M., 1998, *Ascending air bubbles in protein solutions*, *Eur. Phys. J. B* 4, 313–319.
- YBERT C. and DI MEGLIO J.-M., 2000, *Ascending air bubbles in solutions of surface active molecules: influence of desorption kinetics*, *Eur. Phys. J. E* 3, 143–148.
- ZAWALA J., SWIECH K., MALYSA K., 2007, *A simple physicochemical method for detection of organic contaminations in water*, *Colloids & Surfaces A*, 302, 293.
- ZHANG Y., FINCH J.A., 1996, *Terminal velocity of bubbles: approach and preliminary investigation*, *Column* 96, 63–69.
- ZHANG Y., FINCH J.A., 2001, *A note on single bubble motion in surfactant solution*, *J. Fluid Mech.* 429, 63–66.
- ZHANG Y., MCLAUGHIN J.B., FINCH J.A., 2001, *Bubble velocity profile and model of surfactant mass transfer to bubble surface*, *Chem. Eng. Sci.* 56, 6605–6616.
- ZHOLKOVSKIY E.K., KOVALCHUK V.I., DUKHIN S.S., MILLER R., *Dynamics of Rear Stagnant Cap Formation at Low Reynolds Numbers: 1. Slow Sorption Kinetics*, *J. Coll. Interf. Sci.*, 226 (2000), 51–59
- ZYCHOWSKA P., *Monitorowanie stanu czystości wód poprzez pomiary prędkości pęcherzyków gazowych*, M.Sc. Thesis (in Polish), Jagiellonian University, Krakow, 2012.

Received May 11, 2013; reviewed; accepted July 16, 2013

ASSESSMENT OF COAL SLURRY DEPOSITS ENERGETIC POTENTIAL AND POSSIBLE UTILIZATION PATHS

Aleksander LUTYNSKI, Marcin LUTYNSKI

Silesian University of Technology, Faculty of Mining and Geology, Gliwice, Poland,
aleksander.lutynski@polsl.pl

Abstract: Coal-slurries and post-flotation mud have the highest carbon content among other mine waste produced during coal mining and preparation. Therefore, coal slurries deposited in impoundments can be regarded as potential fuel. In the article methods of energetic potential assessments of raw and beneficiated coal slurry deposits were discussed. Results of such assessment for 21 impoundments were presented and the loss of energetic potential due to the imperfection of beneficiation method was discussed. The lowest losses were observed for beneficiation by froth flotation where the loss of energetic potential was on average 15%. The highest loss was observed for beneficiation in centrifugal separators where on average it was 68%. Possible paths of utilization of such slurries in Polish national fuel balance were studied using the SWOT analysis. The results of the SWOT analysis indicate that the internal factors, i.e. the ones related to the coal slurry processing technology have much lower impact on the possibility of using coal slurry deposits in the national fuel balance. Instead, according to the experts, external factors have much greater impact.

Keywords: coal slurry, tailings, beneficiation, SWOT analysis, fuel

Introduction

Fine grained tailings such as coal-slurries and post-flotation mud have the highest carbon content among other mine wastes produced during coal mining and preparation (Niedoba 2013, Lutynski and Szpyrka 2011, Blaschke 2005). Therefore, it is crucial to find an effective method to utilize their energetic potential, which is contained in the coal slurry deposits. Usually, coal-slurry beneficiation or direct utilization by combustion in fluidized-bed boilers is considered.

Current beneficiation methods allow obtaining fine-grained high quality coal products (Lutynski and Blaschke 2009, Lutynski 2009, Taea 2002). Nevertheless, tailing still contains some carbonaceous matter, which is inevitable despite the application of modern beneficiation methods. We performed investigations focused on

the possibility of coal slurry beneficiation by several methods. The results were described elsewhere (Szpyrka and Lutynski 2012). The applied methods included:

- centrifugal separation with the use of hydrocyclone classifier-separator and centrifugal separator,
- wet gravity separation with the use of Reichert spiral separator LD4,
- physicochemical method – flotation.

Application of each method resulted in the increase of calorific value of the concentrate in comparison to the raw coal-slurry deposited in impoundment where it was sampled. However, every single method resulted in the loss of energetic potential due to the fact that the coal matter was not completely separated from the tailing.

Determination of coal slurry deposits energetic potential

The basic quality (Lutynski et al. 2013) and quantity (Witkowska-Kita et al. 2012) analysis of coal slurries were performed allowing initial assessment of energetic potential of these deposits. In order to determine the energetic potential of the coal slurries an assessment algorithm was developed. Two options of energetic potential assessment were proposed. The first one gives a rough estimate of energetic potential of coal slurry deposit (impoundment) and is calculated taking into account the following factors:

- estimated mass of coal slurry in the impoundment,
- average calorific value determined, based on the qualitative investigation of samples collected from the impoundment.

These data serve as the approximate estimation of energetic potential which is commonly reported in qualitative studies. It is important information but for a more detailed knowledge regarding the coal slurry deposit it is necessary to give a range of energetic potential uncertainty. Therefore, in addition to the mean energetic potential, the upper and lower limits are given based on the standard deviations of calorific values in each test. It is known from the probability theory that 68% of the values (for normal distribution) are within the standard deviation from the mean, i.e. values of individual samples. The normal distribution pattern was observed for calorific values at individual impoundment. Therefore such an assumption was made (Grudzinski 2005). Thus, average energetic potential of individual coal slurry deposit (impoundment) for as received or in analytical state can be calculated using the following formula:

$$E_{avg} = M Q_{avg}^a \cdot 10^{-3} \quad (1)$$

where E_{avg} denotes mean energetic potential of the coal slurry deposit (impoundment) in GJ, M estimated mass of coal slurry in the deposit in Mg, Q_{avg}^a mean calorific value in the analytical state in kJ/kg determined by qualitative tests of individual samples collected from the impoundment. The Q_{avg}^a value can be estimated using the formula:

$$Q_{avg}^a = \frac{1}{n} \sum_{i=1}^n Q_i^a \quad (2)$$

Formulas for calculation of the maximum (E_{max}) and minimum (E_{min}) coal slurry deposit energetic potential, in GJ, are:

$$E_{max} = M (Q_{avg}^a + S_Q) \cdot 10^{-3} \quad (3)$$

and

$$E_{min} = M (Q_{avg}^a - S_Q) \cdot 10^{-3} \quad (4)$$

where S_Q is a standard deviation of calorific value calculated using the following formula:

$$S_Q = \sqrt{\frac{1}{n-1} \sum_{i=1}^n (Q_i^a - Q_{avg}^a)^2} \quad (5)$$

Results of calculations for the 21 impoundments are presented in Table 1.

Table 1. Energetic potential of coal slurry deposits at analytical state

Impoundment	Estimated mass	Average calorific value	Calorific value standard deviation	Energetic potential at analytical state		
				Average	Maximum	Minimum
	Mg	kJ/kg	kJ/kg	GJ	GJ	GJ
K13	1 000 000	15 096	1509	15095667	16604265	13587068
K14	300 000	15 646	830	4693800	4942657	4444943
K12	1 000 000	14 813	581	14812667	15393327	14232006
K18/1	100 000	9 325	2052	932547	1137768	727326
K18/2	100 000	10 073	2747	1007325	1281976	732674
K11/1	640 000	13297	2413	8509964	10054237	6965690
K3/1	1 521 000	9265	3498	14092825	19413371	8772280
K3/2	176 000	14877	5976	2618308	3670019	1566597
K2	1 117 000	12304	2803	13743987	16874910	10613064
K17	155 000	22807	1538	3535074	3773403	3296745
K1	153 000	23293	1444	3563810	3784749	3342871
K4/1	345 600	22941	590	7928525	8132297	7224753
K4/2	163 000	15813	937	2577600	2730378	2424822
K4/3	460 000	20829	2065	9581173	10530941	8631404
K5/1	130 000	12051	1504	1566590	1762060	1371119
K5/2	228 000	17802	5351	4058928	5279050	2838807
K5/3	106 000	19402	646	2056612	2125131	1988132
K5/4	102 000	20351	844	2075761	2161898	1989625
K11/2	176 000	19672	767	3462345	3597362	3327329
K6	236 000	18887	1834	4457435	4890353	4024518

The other option of coal slurry deposit energetic potential assessment is more detailed and requires data such as the type of coal slurry and method of its beneficiation. The energetic potential is calculated taking into account the following:

- mass of coal slurry in the impoundment,
- concentrate yield of beneficiation method,
- average calorific value of concentrate from technological tests.

In order to compare different beneficiation methods it was decided to estimate the energetic potential at analytical state. The average energetic potential of impoundment is calculated with the following formula:

$$E_{avg} = MU \frac{Q_{avg}^a}{10^3} \quad (6)$$

where E_{avg} is the mean energetic potential of the coal slurry deposit (impoundment) in GJ, M estimated mass of coal slurry in the impoundment in Mg, Q_{avg}^a denotes average calorific value of concentrate at analytical state determined in qualitative tests for individual beneficiation method in kJ/kg, U concentrate yield at technological test of beneficiation.

The energetic potential of coal slurries in deposits (impoundments) beneficiated with the use of four methods in comparison with the raw coal slurries energetic potential is presented in Table 2. Due to the fact that methods are not ideal, the loss of energetic potential (S) due to the beneficiation was calculated.

Coal slurry utilization analysis

Analysis of possible utilization paths of coal slurry deposits was performed with the use of the SWOT analysis. The SWOT analysis is a tool to evaluate planned process in order to optimize the strategy of reaching the objective. The main objective of analysis is to identify the current status of the process and its perspective which leads to the best possible strategy. The SWOT analysis takes its name from the abbreviations of the following:

- strengths – characteristics of the project that give it an advantage over others,
- weaknesses – are characteristics that place the project at a disadvantage relative to others,
- opportunities – elements that the project could exploit to its advantage,
- threats – elements that could cause trouble for the project.

The analysis is based on the identification of four group of factors, description if their impact on the further development and management of operations in order to improve the strategy or introduce often radical changes. In the SWOT analysis it is not required to describe and distinguish the factors but to point out key elements on which the analysis is performed. In further stages, a fixed-point scale is established where

Table 2. Energetic potential of raw coal slurry at each deposit (impoundments) and after beneficiation using four methods. The loss of potential is denoted as S

Impoundment	Hydrocyclone				Centrifugal separator, 150 g/l				Reichert spiral separator, 400g/l				Flotation, flotation agent # 2				
	E_{avg}	U	Q_r^{avg}	E_{avg}	S	U	Q_{avg}^a	E_{avg}	S	U	Q_{avg}^a	E_{avg}	S	U	Q_{avg}^a	E_{avg}	S
	GJ	–	kJ/kg	GJ	%	–	kJ/kg	GJ	%	–	kJ/kg	GJ	%	–	kJ/kg	GJ	%
K13	15095667	0,47	18121	8516870	44	0.23	18916	4350680	71	–	–	–	%	–	–	–	–
K14	4693800	0,56	20362	3420816	27	0.36	20654	2230632	52	0.29	18825	5459250	64	–	–	–	–
K12	14812667	0,50	17281	8640500	42	0.10	22042	2204200	85	0.41	20271	2493333	47	–	–	–	–
K18/1	932547	0,50	9295	464750	50	–	–	–	–	0.18	21523	3874140	74	–	–	–	–
K18/2	1007325	0,60	8576	514560	49	–	–	–	–	0.04	21042	92585	90	–	–	–	–
K11/1	8509964	0,51	15990	5219136	39	0.04	21043	538700	94	–	–	–	–	–	–	–	–
K3/1	14092825	0,57	16277	12377730	12	0.14	25840	5502369	61	0.15	20760	1992960	77	–	–	–	–
K3/2	2618308	0,63	12027	1333553	49	–	–	–	–	0.23	25843	9040657	36	0.45	24 687	1955210	25
K2	13743987	0,58	14234	9221639	33	0.48	24104	11923600	13	0.06	24258	150564	94	0.41	20 670	9466240	31
K17	3535074	0,44	13444	916880	74	0.03	18965	88187	97	0.50	24335	12602267	9	0.74	27 620	3168014	10
K1	3563810	0,52	17972	1429852	60	0.08	25046	306000	91	0.09	19136	266947	92	0.80	27 120	3319488	7
K4/1	7928525	0,51	24363	4294124	49	0.28	24095	2331625	71	0.14	24241	519000	85	0.81	26 880	7524680	5
K4/2	2577600	0,59	24557	2073136	20	0.47	24164	1851204	28	0.30	24459	2535909	68	0.65	21 525	2280574	11
K4/3	9581173	0,57	25501	6686362	30	0.52	24315	5816148	39	0.50	23763	1936684	25	0.41	24 520	4624472	51
K5/1	1566590	0,46	21415	1180617	25	0.25	24430	793975	49	0.52	24333	5820454	39	–	–	–	–
K5/2	4058928	0,48	21085	2307542	43	0.22	24043	1205997	70	0.30	23352	910728	42	0.58	24 670	3262361	20
K5/3	20566631	0,50	21161	1121533	45	0.26	23802	655983	68	0.27	23666	1456879	64	0.72	25 875	1974780	4
K5/4	2075761	0,51	21844	1136324	45	0.22	24281	544865	74	0.30	24035	764313	63	0.71	25 810	1869160	10
K11/2	3462345	0,44	12008	92999	97	0.02	18519	65187	98	0.27	24195	666330	68	0.70	25 845	3184104	8
K6	4457435	0,47	18022	1999000	55	0.08	24124	455461	90	0.07	18756	231074	93	0.72	25 465	4327013	3
average	–	0,53	16950	–	44	0.22	22846	–	68	0.14	24256	801000	82	0.64	25057	–	15

each element has an attributed value. This method of impact assessment facilitates determination of priority elements in each group. The greatest difficulties are encountered in the assessment of intangible factors where classification is not straightforward. Obviously, the analysis is not free from the subjective assessment of areas which are difficult to group but this can be minimized by public group assessment i.e. external experts or consultants not connected to the project. Commonly, the SWOT analysis is presented in a graphic form (matrix) and as a table. The internal awareness of external strengths and weaknesses of the project is essential for the marketing strategy of the company or a product.

The SWOT analysis regarding the use of coal slurry deposits in the Polish national fuel balance was conducted among ten experts i.e. employees of the Faculty of Mining and Geology of Silesian University of Technology from the Department of Mineral Processing and Waste Utilization and the Institute of Mining Engineering. The group of experts consisted of research assistants, PhD's and professor whose research field and experience was related to waste management, mining engineering and mineral processing. Information and assumptions for the analysis were the same as formulated in the scenarios of innovative hard coal mining waste management technology development (Goralczyk and Lutynski 2012). Assumptions for the SWOT analysis were as follows:

- strengths and weaknesses of coal slurry deposits use in the Polish national fuel balance were characterized by factors related to beneficiation technologies which convert them to a full value fuel,
- opportunities of using these deposits in the Polish national fuel balance are characterized by the factors associated to external conditions,
- threats related to the use of these deposits in the Polish national fuel balance are characterized by the factors associated to the external conditions being an obstacle.

Brainstorming with the expert group allowed identification of factors considered to be important in each of the four groups. These factors are presented below.

STRENGTH

- good identification of coal slurry deposits properties, amount and location
- relatively high calorific value of deposits
- waste (coal slurry) management know-how
- ease of coal slurry processing technology deployment
- low cost of fuel processing
- accessibility to coal slurry deposits
- lack of interest from the coal mines regarding the possibility of coal slurry deposit utilization in the past
- land can be used for other purposes when the processing of deposits (impoundments) is terminated.

WEAKNESS

- considerable variations of coal slurry properties between impoundments
- some variations of coal slurry properties in one deposit

- significant cost of beneficiation plant construction
- low beneficiation efficiency
- high water consumption for the purpose of coal slurry beneficiation,
- limited demand for the obtained fuel
- requirement of land reclamation after depletion of impoundments

OPPORTUNITY

- creation of new work places
- demand for conventional fuels
- depletion of conventional fossil fuels
- location of impoundments on the area where mining technologies are well known
- trend related to waste recycling
- stimulation of activities related to waste management
- actions of local authorities focused on reclamation of post-mining areas
- support by local authorities of actions focused on reclamation of post-mining areas by fiscal and legal policies.

THREAT

- insufficient funding for pro-ecological actions
- limited interest in a beneficiated product
- complex financial procedures of projects related to the use of coal slurry deposits
- appearance of a lobby acting against actions related to the use of coal slurry deposits
- legal restrictions regarding coal slurry deposits management and use of obtained fuel
- strict CO₂ emissions limits
- reluctance of land owners where deposits are located in obtaining permissions for re-use of coal slurries.

The next task was to prioritize identified factors in each group. The experts identified the impact of each factor on the possibility of using coal slurry deposits in the Polish national fuel balance. Three levels of assessment were assumed:

- very high impact – 3 points
- high impact – 2 points
- low impact – 1 point.

The above mentioned prioritization resulted in the weighted average of factor impact on the use of identified coal slurry deposits in the Polish national fuel balance.

Results of SWOT analysis

The results of the SWOT analysis are presented in Table 3. Columns labeled 3,2,1 correspond to the impact rating and indicate the number of experts who chosen particular impact factor on the possibility of using identified coal slurry deposits in Polish national fuel balance.

Table 3. Results of factor prioritization analysis – possibility of using identified coal slurry deposits in Polish national fuel balance

No	STRENGTHS	3	2	1	Average
1	good identification of coal slurry deposits properties, amount and location	4	4	2	2.2
2	relatively high calorific value of deposits	5	4	1	2.4
3	waste (coal slurry) management know-how	3	3	4	1.9
4	ease of coal slurry processing technology deployment	3	4	3	2.0
5	low cost of fuel processing	5	4	1	2.4
6	accessibility to coal slurry deposits	4	4	2	2.2
7	lack of interest from the coal mines regarding the possibility of coal slurry deposit utilization in the past	2	3	5	1.9
8	land can be used for other purposes when the processing of deposits (impoundments) is terminated	4	2	4	2.0
No	WEAKNESSES	3	2	1	Average
1	considerable variations of coal slurry properties between impoundments	1	4	5	1.9
2	some variations of coal slurry properties in one deposit	3	4	3	1.7
3	significant cost of beneficiation plant construction	6	4	0	2.6
4	low beneficiation efficiency	5	3	2	2.5
5	high water consumption for the purpose of coal slurry beneficiation	7	3	0	2.7
6	limited demand for the obtained fuel	4	5	1	2.3
7	requirement of land reclamation after depletion of impoundments	4	4	2	2.1
No	OPPORTUNITIES	3	2	1	Average
1	creation of new work places	4	4	2	2.1
2	demand for conventional fuels	6	3	1	2.7
3	depletion of conventional fossil fuels	6	3	1	2.7
4	location of impoundments on the area where mining technologies are well known,	3	4	3	2.0
5	trend related to waste recycling	4	3	3	2.1
6	stimulation of activities related to waste management	5	5	0	2.5
7	Actions of local authorities focused on reclamation of post-mining areas	3	6	1	2.2
8	support by local authorities of actions focused on reclamation of post-mining areas by fiscal and legal policies	6	4	0	2.6
No	THREATS	3	2	1	Average
1	insufficient funding for pro-ecological actions	7	3	0	2.7
2	limited interest in beneficiated product	2	5	3	1.9
3	complex financial procedures of projects related to the use of coal slurry deposits	4	4	2	2.2
4	appearance of a lobby acting against actions related to the use of coal slurry deposits	5	4	1	2.4
5	legal restrictions regarding coal slurry deposits management and use of obtained fuel	7	3	0	2.7
6	strict CO ₂ emissions limits	4	5	1	2.3
7	reluctance of land owners where deposits are located in obtaining permissions for re-use of coal slurries	6	3	1	2.5

Conclusions

Presented beneficiation tests and study of energetic potential show that during the process of coal slurry beneficiation due to the passing of fine coal into the tailing a big share of energetic potential is lost. The most promising results of beneficiation of such coal slurries were obtained for flotation which seems to be evident due to the nature of this process. An average loss of energetic potential was 15% and varied between the impoundments from 3 to 31%. The calorific value on average was 25 057 kJ/kg and was the highest among all tested methods. Unfortunately, this method was ineffective for some of the coal slurries with flotation agents used. The highest loss of energetic potential was observed for beneficiation with centrifugal separator where on average it was 68% and depending on the impoundment varied between 13 to 98%. As it is seen, these are considerable variations which indicate imperfection of the method. The calorific value of the product was on average 22864 kJ/kg which is a good result. These results are similar to the ones obtained with Reichert spiral where the loss of energetic potential was 64% and the average calorific value was 22678 kJ/kg. The lowest calorific value was obtained in case of beneficiation with hydrocyclone classifier-separator. Despite large losses of energetic potential which accounted for 53% the calorific value was on average 16950 kJ/kg and was not considerably larger than that of raw coal slurry i.e. 16427 kJ/kg.

These tests showed that it is possible to beneficiate coal slurry deposits. However, large losses of energetic potential are observed. Moreover, each method requires large quantities of water which increases the cost of operation.

The performed SWOT analysis on the use of identified coal slurry deposits in the national fuel balance revealed factors that may have the highest impact on the utilization of these coal slurries. Taking into account the average priority of the factor impact on the possible use of the identified coal slurries in the national fuel balance which was determined by experts it was assumed that the priority (i.e. above 2.0 points in a three-point scale) have the following.

STRENGTHS: relatively high calorific value of deposits (2.4) and low cost of fuel processing (2.4)

WEAKNESSES: high water consumption for the purpose of coal slurry beneficiation (2.7), significant cost of beneficiation plant construction (2.6), low beneficiation efficiency (2.5), limited demand for the obtained fuel (2.3), requirement of land reclamation after depletion of impoundments (2.1).

OPPORTUNITIES: demand for conventional fuels (2.7), depletion of conventional fossil fuels (2.7), support by local authorities of actions focused on reclamation of post-mining areas by fiscal and legal policies (2.6), stimulation of activities related to waste management (2.5), actions of local authorities focused on reclamation of post-mining areas (2.2), creation of new work places (2.1), trend related to waste recycling (2.1),

THREATS: Insufficient funding for pro-ecological actions (2.7), legal restrictions regarding coal slurry deposits management and use of obtained fuel (2.7), reluctance of land owners where deposits are located in obtaining permissions for re-use of coal slurries (2.5), appearance of a lobby acting against actions related to the use of coal slurry deposits (2.4), strict CO₂ emissions limits (2.3), complex financial procedures of projects related to the use of coal slurry deposits (2.2)

The obtained results indicate that the internal factors i.e. the ones related to the coal slurry processing technology have much lower impact on the possibility of using coal slurry deposits in national fuel balance. Instead, according to the experts, external factors have much bigger impact and at the same time the number of these factors is larger.

References

- BLASCHKE W., 2005, *Określenie wartości mulów węglowych zdeponowanych w osadnikach ziemnych*. Rocznik Ochrony Środowiska, T. III. S. 23/1–13.
- GORALCZYK S., LUTYNSKI A., 2012, *Scenariusze rozwoju innowacyjnych technologii zagospodarowania odpadów pochodzących z górnictwa węgla kamiennego w scenariuszach foresightu OGWK*. Kruszywa 3/2012, 42–48.
- GRUDZINSKI Z., 2005, *Analiza porównawcza jakości mulów węgla kamiennego pochodzących z bieżącej produkcji i zdeponowanych w osadnikach ziemnych*. Rocznik Ochrony Środowiska, T. III. P. 49/1–9.
- LUTYNSKI A., SUPONIK T., LUTYNSKI M., 2013, *Investigation of coal slurry properties deposited at impoundments*, Physicochemical Problems of Mineral Processing. Volume 49(1). 2013, 25–36.
- LUTYNSKI A., 2009, *Zagospodarowanie drobnodziarnistych odpadów węglowych*. Chapter in monograph *Innowacyjne i przyjazne dla środowiska systemy przerobcze surowców mineralnych w aspekcie zrównoważonego rozwoju*, Instytut Techniki Górniczej, Gliwice.
- LUTYNSKI A., BLASCHKE W., 2009, *Aktualne kierunki zagospodarowania odpadów przerobczych węgla kamiennego*. Przegląd Górniczy Nr. 10/2009
- LUTYNSKI A., SZPYRKA J., 2011, *Analiza jakości mulów węgla kamiennego zdeponowanych w osadnikach ziemnych*. Kwartalnik Górnictwo i Geologia. Tom 6. Zeszyt 2. Gliwice
- NIEDOBA T., 2013, *Statistical analysis of the relationship between particle size and particle density of raw coal*. Physicochemical Problems of Mineral Processing 49(1), 2013, 175–188.
- SZPYRKA J., LUTYNSKI M., 2012, *Analysis of selected methods of beneficiating coal slurries deposited in impoundments*, Physicochemical Problems of Mineral Processing Volume 48(2), 579–591.
- TAOA D., LIA B., JOHNSON B. S., PAREKHC B. K., 2002, *A flotation study of refuse pond coal slurry*. Fuel Processing Technology. Volume 76, Issue 3, 1 June 2002, 201–210.
- WITKOWSKA-KITA B., BAIC I., LUTYNSKI A., SUPONIK T., 2012, *Identyfikacja depozytów mulów węglowych – właściwości chemiczne, Baza Danych (DMW)*. Rozdział Monografii: *Innowacyjne i przyjazne dla środowiska techniki i technologie przeróbki surowców mineralnych. Bezpieczeństwo – jakość – efektywność*. Instytut Techniki Górniczej KOMAG. Gliwice, 231–244.

Received April 23, 2013; reviewed; accepted July 23, 2013

DETERMINATION OF FLOCCULATION CHARACTERISTICS OF NATURAL STONE POWDER SUSPENSIONS IN THE PRESENCE OF DIFFERENT POLYMERS

Hande K. BASARAN, Tuba TASDEMIR

Mining Engineering Department, Eskisehir Osmangazi University, 26480, Eskisehir, Turkey,
tubat@ogu.edu.tr

Abstract: In this study, flocculation behaviors of natural stone powder suspensions were determined by applying classical jar tests. The flocculation tests were performed in the presence of different types of polymers at different polymer dosages and pHs. Then, the settling rates and residual turbidity values of suspensions were recorded. The flocculation performance of flocculants possessing unique molecular architecture (UMA) and conventional polyacrylamide based flocculants was investigated for the solid-liquid separation of natural stone processing wastewater. The effects of flocculant type, dosage and pH were examined. The results obtained from this study indicated that in terms of the settling rate and turbidity, the medium anionic SPP 508 flocculant of 28% charge density showed a better flocculation performance compared to other conventional and UMA flocculants at natural pH. The SPP 508 flocculant gave the lowest turbidity value of 3 NTU (Nephelometric turbidity Unit) at dosage of 0.3 mg/dm³, while the highest settling rate (870 mm/min) for the suspensions tested was achieved at 1 mg/dm³ dosage for the same flocculant. However, the lowest settling rate was obtained by high cationic flocculant (Enflo 440 C). All flocculants showed a good flocculation performance for the settling rate and turbidity at pH 8 and 10.

Keywords: wastewater, flocculation, settling rate, turbidity

Introduction

Natural stones (marble, travertine, granite, basalt etc.) are widely used for different purposes in construction industry. Turkey has 3.8 billion m³ of exploitable marble, 2.7 billion m³ of travertine and 995 million m³ of granite reserves. According to this data, approximately 40% of world's natural stone reserves are in Turkey. The annual natural stone production capacity of Turkey is about 4 million m³ and the total slab production capacity of natural stone processing plants in Turkey is around 6.5 million m²

(www.enerji.gov.tr). Recently, there is a significant increase in production level for both domestic consumption and export markets in Turkey. However, marble factories use large amounts of water during the cutting, washing and polishing processes. Water is used as a cooler during cutting of marble blocks. The cutting of a block, for instance, produces approximately 25–40% of the weight of the block as fine particles (Onenc,2001). The particles in the wastewater are generally treated by simple solid–liquid separation. The inefficiency of the employed techniques results in the presence of fine particles in recycled water, which cause polishing problems during processing. In addition, the suspended particles in recycled water may also result in pipe clogging(Acar, 2001; Celik and Sabah, 2008).

The purpose of the flocculation process is to form aggregates or flocs from finely dispersed particles in the presence of natural or synthetic polymeric substances (flocculants). There are many types of polymeric flocculants used in various solid-liquid separation processes. The polymers are characterized by their ionic nature: cationic, anionic and non-ionic. The ionic polymers usually can be called polyelectrolytes. The most important properties of polymeric flocculants are the molecular weight and charge density. The molecular weight values range from a few thousand up to tens of millions. The charge density can be expressed in terms of mole percent of charged groups. The polyelectrolyte charge density values are regarded as low, medium or high if the mol% of ionic groups are approximately:10%, 25-40%, and 50–100%, respectively (Gregory, 2005; Gregory and Barany, 2011). The cationic flocculants are usually of lower molecular weight and are only used in the solid-liquid separation, where the fast sedimentation rates associated with the use of high molecular weight products ensured their dominance. The anionic and nonionic flocculants are currently used in mineral and natural stone tailing systems (Ipekoglu, 1997; Hendersan and Wheatley, 2007).

The flocculants bring together coagulated particles into larger aggregates and settle them. The polymer bridging and charge neutralization are the commonly encountered mechanisms in flocculation. Bridging flocculation occurs as a result of adsorption of individual polymer chains onto several particles simultaneously, forming molecular bridges between the adjoining particles in a floc. The charge neutralization becomes a major mechanism for polyelectrolytes, where significant particle surface sites with charge opposite to that of the ionic polymer functional groups are present. The flocculants are known to adsorb on particle surface through hydrogen bonding, ion binding, electrostatic interactions, chemical bonding, hydrophobic interactions and van der Waals forces (Somasundaran and Das, 1998; Hogg, 2000; Mpofu et al., 2003; Bratby, 2006; Gregory and Barany, 2011).

Flocculation of fine particle suspensions depends on a number of factors, which include type, molecular weight and charge density (ionization degree) of the flocculant, mineralogical composition and particle size of solid particles, pH and chemical composition of solutions (Ipekoglu, 1997; Somasundaran and Das, 1998; Hocking et al., 1999; Besra et al., 2000; Sworska, et al., 2000 a; Yazar, 2001; Sabah

and Cengiz, 2004; Ersoy, 2005; Gregory, 2005; Tripathy and Ranjan, 2006; Sabah and Erkan, 2006; Hendersan and Wheatley, 2007; Cengiz et al., 2009; Gregory and Barany, 2011; Tasdemir et al., 2011; Tasdemir and Kurama, 2012; Sabah and Aciksoz, 2012). The process also depends strongly on hydrodynamic conditions. The properties of floc aggregates are largely determined by mixing conditions (Gregory and Guibai, 1991; Rossini et al., 1999; Sworska, et al., 2000b; Tasdemir and Tasdemir, 2012). To achieve efficient a solid-liquid separation, different types of flocculants are used according to waste material type, since the flocculation processes are very sensitive to properties such as the surface charge of particles, solid-liquid or solid-polymer interaction, presence of different ion types in solution, structure of polymer and amount of adsorption of polymer on the particle surface. Each of them determines the flocculation rate and efficiency. Therefore, determination of the flocculation behavior of the suspensions is very important.

The standard polymer molecules of high molecular weight are considered as linear structures with two dimensions. Present day developments for polyacrylamide-based flocculants are likely to be based on the “molecular architecture” concept. This will enable a flocculant technology to produce the performance required to meet increasing and changing demands for solid-liquid separation. In recent years, a new generation of flocculants namely the unique molecular architecture (UMA) was introduced in addition to conventional flocculants to enhance the flocculation process (Pearse et al., 2001). It is claimed, that this technology covers highly branched and interactive polymer chains. They produce flocs of different characteristics than those formed by conventional flocculants. Denser and stronger flocs containing less water (Pearse, 2003) are produced with the UMA flocculants.

In the literature, many studies were conducted to determine the flocculation behavior of natural stone suspensions (Bayraktar et al. 1996; Seyrankaya et al., 2000; Nishkov and Marinov, 2003; Arslan et al., 2005; Ersoy, 2005; Tasdemir and Kurama, 2012; Sabah and Aciksoz, 2012). However, from most of them only the marble effluents were used. These studies reported that high molecular weight of anionic polymers (e.g. polyacrylamides) were commonly used in dewatering of negatively charged natural stone effluent and gave the best results on the settling rate and water clarity.

A number of studies with new unique molecular architecture type flocculants were reported in mineral processing for dewatering. These studies are related to comparison of the flocculation performances of the new generation UMA and conventional flocculants investigated in dewatering of tailings containing clay minerals (Pearse et al., 2001; Weir and Moody, 2003), coal preparation (Cengiz et al., 2004) and ceramic plant tailings (Cengiz et al., 2009). The UMA flocculants showed higher flocculation performance than the conventional flocculants in those studies. On the other hand, a limited number of researches were carried out for the flocculation performance of waste water containing natural stone fine powders by using the UMA types. Only Sabah and Aciksoz (2012) investigated the flocculation performance of a new

generation of flocculants (Magnafloc 5250 and 6260) and compared them with results with conventional (acrylamide SB 1836) for the solid-liquid separation of travertine processing wastewater. They reported that the anionic UMA flocculants showed better performance than conventional anionic flocculant (SB 1836) which is used in the travertine processing plant.

In recent years, the export potential of the natural stone industry in Turkey developed rapidly in parallel with new investments. Increased water pollution during cutting and polishing of the stones forced material suppliers to invest in new modifications on existing techniques to improve the treatment process and high performance flocculants. For this reason in this study, the sedimentation behavior of natural stone powder suspensions containing a mixture of fines such as marble, granite and travertine was investigated by using a new UMA Magnafloc polymers and conventional flocculants based on polyacrylamide. The effects of the key parameters, involving suspension pH, flocculant type and dosage, and charge density were studied on residual turbidity and settling rate for suspensions.

Materials and Method

The natural stone powder used for the flocculation tests was obtained from a local natural stone processing plant in Eskisehir region (Turkey). The plant processes different types of marbles, granite and travertine etc. blocks, therefore, the cutting fines contain mixed powders with different minerals. The sample was taken in its original waste mud state from the plant waste area and then dried. Thus mud contained coarse and fine cutting waste powders. According to the initial sieve analysis of sample, the particles are almost below 300 micrometers and 74.2% was below 20 micrometers. Since the settling rate of $-20\ \mu\text{m}$ powder is the most problematic and this size is considered as slime size, the dried particles were sieved by $20\ \mu\text{m}$ sieve. Therefore, sieved $-20\ \mu\text{m}$ powders were used in the experiments to select the most suitable flocculant type for this mixed material. The flocculation tests were conducted with suspensions of natural stone powders. The natural stone powder suspensions used in the experiments were artificially prepared as 1% (wt./vol.) in $500\ \text{cm}^3$ tap water.

The chemical composition of the natural stone powder was analyzed by a X-ray fluorescence (XRF) using a Rigaku ZSX Primus device. A mineralogical analysis of particles was characterized by X-ray diffraction (XRD) using a Rigaku Rint-2000 model diffractometer. The XRD and XRF results are given in Fig.1 and Table 1, respectively. According to the XRD data, the sample is predominately composed of calcite and quartz and also peaks of albite, muscovite and microcline occur. The XRF results showed that CaO and SiO_2 contents of the sample were 42.32% and 16.81%, respectively.

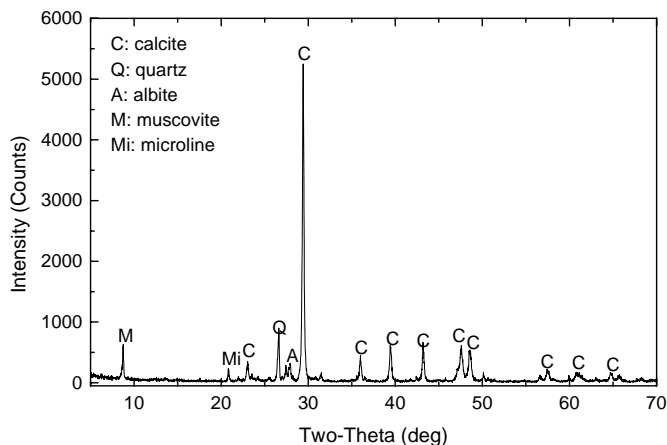


Fig. 1. X-ray diffraction pattern of natural stone powders

Table 1 Chemical analysis of the natural stone powders by XRF

CaO%	SiO ₂ %	Al ₂ O ₃ %	K ₂ O%	Na ₂ O%	MgO%	Fe ₂ O ₃ %	TiO ₂ %	LOI%
42.32	16.81	3.5	1.14	1.06	0.87	0.73	0.09	33.48

The size distribution of the sample was determined using a Malvern Mastersizer Hydro 2000G Particle Size Analyzer and result is given in Fig. 2. It was measured that d_{90} , d_{50} and d_{10} of the solid particles in the suspension by volume were 27.71, 6.84 and 1.29 μm , respectively.

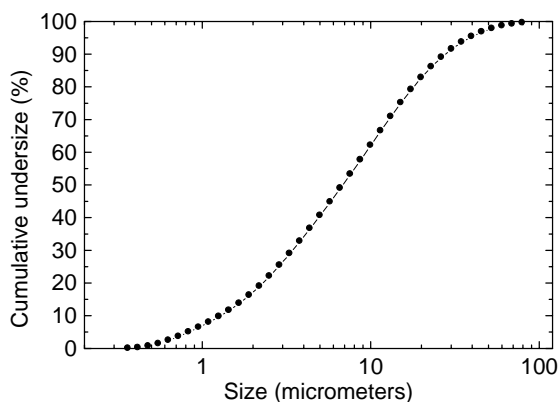


Fig. 2. Particle size distribution of sample used by laser diffraction

The zeta potential measurements for the fine particles were made by a Malvern Nano-Z model zetameter device using laser Doppler velocimeter principle. The using double distilled water was used for preparation of solid suspension in 0.1 % solid

ratio. The zeta potential of natural stone powder versus pH of suspension is presented in Fig. 3. Figure 3 shows that there is no zero zeta potential value (zpc) indicating the isoelectric point (iep) at different pH values adjusted. The highest zeta potential (-36.6 mV) was measured at pH 11. It indicates that the suspension was stable, whereas at natural pH of 8 the zeta potential of suspension was about -13.3 mV.

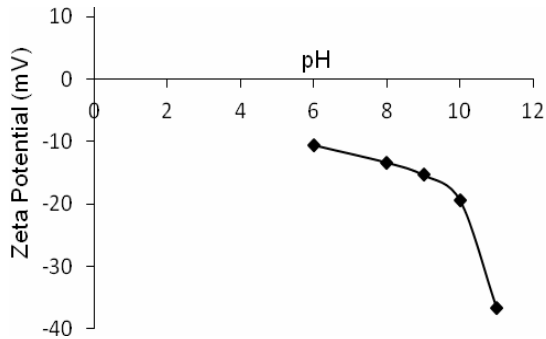


Fig. 3. Variation of zeta potential of natural stone powders

The pH, conductivity, temperature measurements of natural stone powder suspension were measured with Orion 5 star multimeter device. After settling time of 15 minutes the turbidity of suspensions was measured using a HF Scientific Turbidimeter, which gives the turbidity result as nephelometric turbidity unit (NTU). The hardness of water was determined by a volumetric method. Properties of tap and distilled waters and natural stone powder suspension used in experiments are given in Table 2. The pH and specific conductivity of the distilled water used for the preparation of stock solutions of the flocculant were 6.1 and $34 \mu\text{S}/\text{cm}$, respectively. The properties of the tap water used in the sedimentation tests were pH 7.8, specific conductivity $709 \mu\text{S}/\text{cm}$, turbidity 0.38 NTU. The natural pH value and conductivity of suspension were about 8 and $580 \mu\text{S}/\text{cm}$ respectively. The initial turbidity of natural stone powder suspension was measured as 12000 NTU and residual turbidity as 295 NTU after sedimentation time 15 min. The solutions of polymer (0.01%) were prepared using distilled water. A 1 M HCl and NaOH (analytical grade) solutions were used to adjust the suspension pH.

Table 2. Properties of tap and distilled waters and natural stone powder suspension used in experiments

	Distilled water	Tap water	Natural stone powder suspension
pH	6.1	7.8	7.96
Turbidity (NTU)	0.14	0.38	12000
Conductivity ($\mu\text{S}/\text{cm}$)	34	709	580
Temperature ($^{\circ}\text{C}$)	18.4	17.9	17.9
French hardness of water ($^{\circ}\text{F}$)	–	30	35.6

The flocculation experiments of the natural stone suspensions were carried out with a new UMA Magnafloc type flocculants and some conventional flocculants, which consist of different types of high molecular weight polyacrylamide based polymers. The polymers used for the tests are collected in Table 3. The magnafloc flocculants were provided by BASF Specialty Chemical., SPP by the Superkim and Enfloc by ECS Chemistry.

Table 3. Polymers with high molecular weight used in the experiments

Commercial name	Type	Charge Density (%)	Supplier
SPP 508	anionic	28 (medium)	Superkim
Enfloc 320A	anionic	20 (low)	ECS Chem.
Magnofloc 5250 (UMA)	anionic	30 (medium)	Basf
Magnofloc 4240 (UMA)	anionic	40 (medium)	Basf
Enfloc 440C	cationic	55 (high)	ECS Chem.
Enfloc 420C	cationic	15 (low)	ECS Chem.
SPP N 134	nonionic	–	Superkim

The flocculation experiments were carried out using a conventional jar test apparatus (Velp Scientifica FC6S) with a speed control. The desired amount of flocculant was added to the suspension and the beakers were agitated at fixed mixing time (2 min) at 200 rpm of speed. After agitation, the flocculated suspension was poured into 500 cm³ graduated cylinder and was allowed to settle. The height of the slurry and water interface was measured as a function of time and then the settling rates were calculated from the slope of the straight line portion of the plot of pulp level versus settling time. After 15 minutes of settling time, the residual turbidity values of the supernatant solutions were measured by using a Turbidimeter apparatus. The principal purpose of the flocculation experiments was to establish the optimal conditions for floc formation.

Results and discussion

Effect of flocculant type and dosage

The flocculation tests were performed in the presence of different types of polymers using the new UMA Magnafloc polymers and conventional flocculants based on polyacrylamide at different polymer dosages, which varied from 0.1 to 5mg/dm³ at natural pH of 8. Figure 4 shows the residual turbidity values as a function of polymer dosage for each type of polymer with different charge densities. The residual turbidity of the suspension decreases with an increase of polymer dosage to a certain dosage, and further increases with increasing dosages for all flocculants. It was suggested that optimum flocculation occurs, when half surface of particle is covered with

polyelectrolytes as described in many studies (Pefferkorn, 1999; Sworska et al., 2000 a; Hogg, 2000; Besra et al., 2004; Ersoy, 2005; Tripaty and Ranjan de, 2006; Boltoa and Gregory, 2007). It can be explained by the excess adsorption of polymer molecules with each other or a complete coverage of the particle surface by polymer molecules at higher dosages and steric repulsion of the adsorbed layers. Hence, the polymer to particle surface bridging mechanism is prevented (Gregory, 2005; Bratby, 2006; Gregory and Barany, 2011).

According to Fig. 4, in the flocculation process performed at natural pH, the medium anionic flocculant SPP 508 among polymers showed the lowest turbidity value of 3 NTU at the lowest dosage of 0.3 mg/dm^3 , whereas other flocculants showed the lowest turbidity values at higher dosage (1 mg/dm^3) (Kilic, 2012).

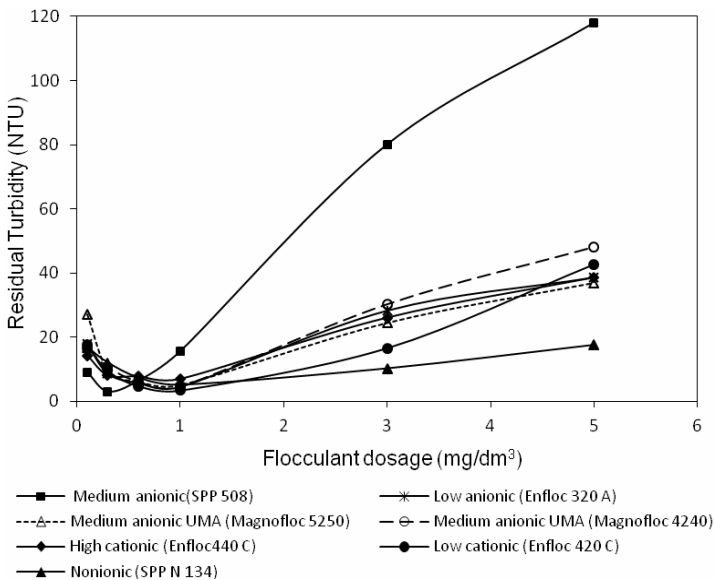


Fig. 4. Effect of flocculant type and dosage on residual turbidity (pH 8)

The settling rate curves for natural stone suspension as a function of flocculant dosage at natural pH of 8 for each flocculant type are given in Figure 5. The results of settling tests indicate that type of flocculant, charge density and dosage of the flocculant has an important effect on settling rates. From Fig. 5, it can be seen that the settling rate of particles increases rapidly with an increase in flocculant dosage for all flocculants up to a 1 mg/dm^3 dosage. After this dosage, the increase in the settling rate decreases. The settling rate increased with increasing flocculant dosage for all flocculants except the anionic SPP 508 and cationic Enfloc440 C. The settling rate for SPP 508 and 440 C reached the maximum at 1 and 3 mg/dm^3 flocculant dosage, respectively, and then further increase in the dosage leads to decrease in the settling rate. The best settling performance (870 mm/min) for the suspensions tested was

achieved at 1 mg/dm^3 dosage by the medium anionic SPP 508 flocculant. However, the lowest settling rates were obtained by the high cationic flocculant (Enfloc 440 C). Since the flocs formed by Enfloc 440 C polymer were fairly small, they had a slow-settling rate. At low polymer dosages, the settling rates were low due to insufficient polymer available for bridging particles together and the flocs were not large enough to provide adequate settling rates. As the polymer concentration increased, more particles were bridged and bigger flocs were obtained, hence a significant increase in the settling rates resulted. It was found that settling rates or hence floc sizes obtained at the same polymer dosage for each flocculant type were importantly different. It is supposed that these differences result from different mechanisms of polymer adsorption on particle surface and conformation of polymer chain in suspension (Yu and Somasundaran, 1996; Somasundaran and Krishnakumar, 1997; Hogg, 1999; Rattanakawin and Hogg, 2001; Taylor et al., 2002; Mpofu et al., 2003; Besra et al., 2004).

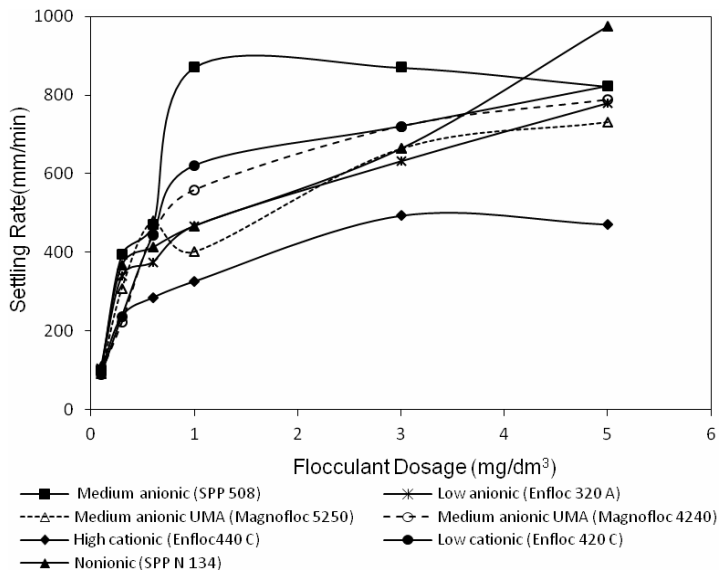


Fig.5. Effects of flocculant type and dosage on settling rate (pH 8)

The polymer bridging and charge neutralization are the commonly encountered mechanisms in flocculation (Gregory, 2005; Gregory and Barany, 2011). Bridging flocculation occurs as a result of adsorption of individual anionic polymer chains onto several particles. The most important property of the polymer bridging mechanism is to produce large sized flocs and high settling rates (Hogg, 1999; Biggs et al., 2000; Rattanakawin and Hogg, 2001). There are many possible mechanisms (hydrogen bonding, cation bridging, van der Waals forces etc.) for anionic polymers adsorption on the particle surface. Flocculation by the anionic flocculants occurs even though the

flocculant and natural stone particles have the same charge. In the flocculation tests carried out by using the anionic flocculants, it is assumed that adsorption of anionic polymers on particles is the most often attributed to cation bridging. This phenomenon was stated by several authors (Sworska, et al., 2000a; Yazar, 2001; Bentli, 2010; Sabah and Aciksoz, 2012). The divalent cations act as bridges between the anionic carboxyl groups ($-\text{COO}^-$) of polymer and the negative particlesurfaces. Sabah and Aciksoz (2012) reported that when French hardness of water is less than 9 °F, interaction between polymer molecules and particles weakens. The hardness of the natural stone suspensions tested was measured as 35.6 °F due to its high ion (Ca^{+2} and Mg^{+2}) concentrations (Table 2). This value is above the proposed limit value of 9 oF (Sabah and Erkan, 2006; Sabah and Aciksoz, 2012). Therefore, the present of divalent cations in the suspension contributes to better flocculation performance obtained with the medium anionic flocculant. The cationic flocculants adsorb on the surfaces of negatively charged particles through the charge neutralization mechanism because of electrostatic attraction between oppositely charged ionic groups. In many studies, the charge neutralization mechanism is reported to produce relatively small flocs and slow settling rates (Gregory, 2005; Tripaty and Ranjan DE, 2006; Sabah and Erkan, 2006; Bolto and Gregory, 2007; Gregory and Barany, 2011). In the case of nonionic polymers, the most likely mechanism of adsorption is through hydrogen bonding between the oxygen atoms associated with hydrated metal ions at the particle surface and amide groups ($-\text{CONH}_2$) on the polymer (Sabah and Cengiz, 2004; Bolto and Gregory, 2007).

The effectiveness of polymers as the bridging flocculants depends greatly on their properties. The most important characteristics of polymeric flocculants are molecular weight and charge density (ionization degree). The molecular weight directly influences the effective size of molecules in solution and in the adsorbed state. Polymers with higher molecular weight are found to be more effective flocculants. For a similar reason, it is generally found that linear polymers are more effective than branched or cross-linked structures for a given molecular weight (Gregory, 2005; Gregory and Barany, 2011). Therefore, it can explain that high molecular weight and linear anionic flocculants(SPP 508) are more effective than highly branched anionic UMA flocculants consisting of the same charge density. Sabah and Acksoz (2012) tried to flocculate travertine fines by using three types of anionic flocculants. They concluded that high charge density of the UMA type flocculant (Magnafloc 6260) gave the best results in terms of turbidity and settling rate while medium anionic UMA (Magnofloc 5250), which is the same flocculant used in this study and conventional medium anionic flocculants (SB 1836) showed poor performance. Many studies reported that high molecular weight polymers form large size but less compact flocs, whereas low molecular weight polymers form small and more compact flocs (Rattanakawin and Hogg, 2001; Taylor et al., 2002; Sabah and Erkan, 2006; Gregory and Barany, 2011).

The charge density can also have a large influence on the bridging effectiveness. If the charge density is high, there would be difficulty in adsorbing onto particles of the same sign of charge (as in the case of anionic polymer and negative particles). Also, the adsorbed polymer configuration may not favour bridging, when the charge density is high. However, some degree of charge is beneficial since the repulsion between charged segments gives expansion of the chain, as explained earlier, and this should enhance the bridging effect. For these reasons, there is often an optimum charge density for bridging flocculation (Ersoy, 2005; Sabah and Erkan, 2006; Bolto and Gregory, 2007; Gregory and Barany, 2011). In this study, the best flocculation performance is obtained with polymer of 28% charge density (medium anionic SPP 508) for flocculation of natural stone suspension. Similar result was found by Ersoy (2005) where 28% and 34% anionic polymers were found suitable in terms of the settling rate and turbidity for travertine and marble suspension, respectively.

Effect of pH

pH of suspension will not only affect the surface charge and stabilization of particles, but also affect the conformation of flocculants and adsorption of them onto particles in the suspension. Thus pH may directly affect the flocculating power of polymer. Figure 6 indicates the influence of suspension pH on the residual turbidity of natural stone suspension at constant flocculant dosage of 0.3 mg/dm³ for all flocculants. It is clearly seen that natural pH 8 and 10 give good flocculation performance for all flocculants, whereas at both low (6) and high (12) pH values higher supernatant turbidity values are obtained (Kılıç, 2012).

It was found that the residual turbidity of the supernatant solution decreased to the target level 20 NTU's (generally accepted turbidity level for recycled water in natural stone processing) at all pH values except 12. In the flocculation process, the potential of particle surface profoundly affects the stabilization or destabilization of the suspended particles, and therefore the efficiency of the flocculation process. In general, the stability of the particles is determined by analyzing the typical zeta potential versus pH plot. When the magnitude of zeta potential is high, the electrostatic repulsion between particles causes the particles to disperse readily and form stable suspensions. For lower magnitude of zeta potential, the repulsive force between the particles is reduced so that the particles come closer and form agglomerates resulting in faster settling characteristics. If zeta potential values of the particles are higher than the range of ± 30 mV, they are assumed to fall in a stable region (Yarar, 2001). The plot of zeta potential versus pH given in Fig. 3 shows that the zeta potential values of the natural stone particles varied between -10.5 mV and -9.36 mV at pH between 6 and 10. The particles in the suspension are assumed to fall in the unstable region due to insufficient negative surface potentials and adsorption of H⁺ ions onto negative charge centers of particles lead to the enhances flocculation of particles. It explains a good response of natural stone particles to the flocculation process given in Fig. 6.

For pH above 10, the zeta potential of particles increases to -36.6 mV. It indicates that the suspension is stable (Fig. 3). It is known that high molecular weight polymers are not effective in destabilizing such dispersed particles (Hogg, 1999). According to Hogg (1999), the addition of high molecular weight polymers to stable dispersions leads to the development of bimodal floc size distributions consisting of dispersed particles.

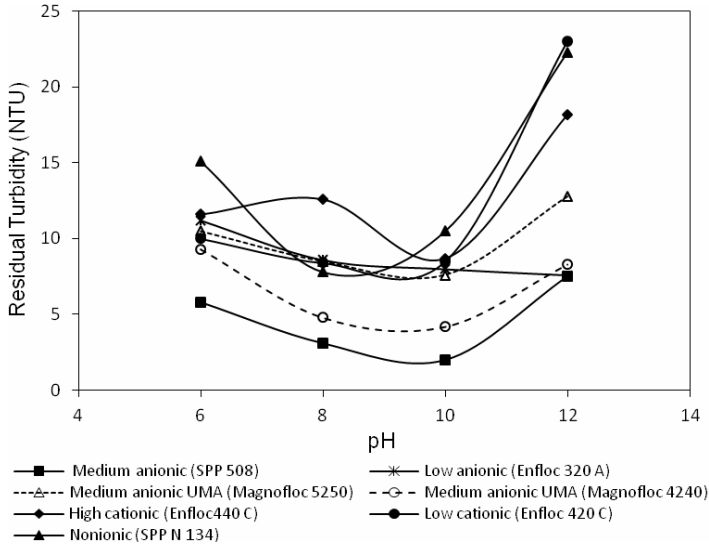


Fig. 6. Effects of polymer type and suspension pH on residual turbidity (polymer dosage 0.3 mg/dm³)

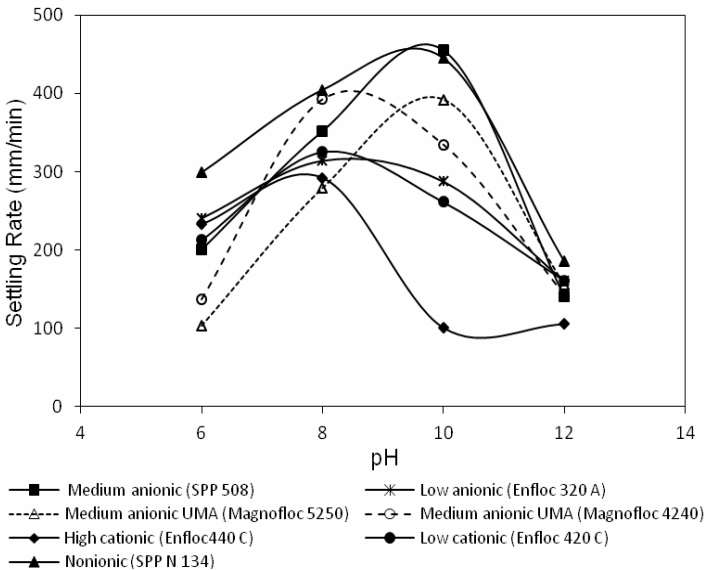


Fig. 7. Effects of polymer type and suspension pH on the settling rate (polymer dosage 0.3 mg/dm³)

Figure 7 depicts the effect of pH on settling rates of natural stone suspensions at a constant flocculant dosage of 0.3 mg/dm^3 . It can be seen that the settling rate of natural stone fine particles decreased at high and low pH values, while the settling rate significantly increased at pH 8 and 10 for all flocculants. The highest settling rates of 455, 392 and 445 mm/min were obtained with anionic SPP 508, Magnafloc 5250 and nonionic SPP N 134 flocculants respectively at pH 10 compared to other flocculants. The settling rates for other flocculants reached maximum at natural pH 8 of suspension.

Figures 6 and 7 demonstrate that both settling rate and residual turbidity of suspension are strongly dependent upon pH. This dependence arises from several factors. First, the high suspension pH increases the electrical double layer (EDL) repulsive forces between natural stone particles and anionic or nonionic polymers due to increase in the zeta potential of particles. Therefore, an attachment of polymer chain to surface can become difficult and this may adversely affect flocculation. Secondly, the conformation of the adsorbed polymer on natural stone particle surfaces, whether stretched or coiled, has a marked influence on flocculation and the polymer conformations can be changed by adjusting pH. Many studies reported that the activity of polymers is related to uncoiling or extension of the polymers (Yu and Somasundaran, 1996; Somasundaran and Krishnakumar, 1997; Sworska et al., 2000a; Taylor et al., 2002; Besra et al., 2004; Sabah and Erkan, 2006; Boltoang Gregory, 2007). At low pH values, the anionic polymers coil up and they do not adsorb on the particles or cause high polymer consumption. Increasing pH causes elongation of macromolecules through solution due to the electrostatic repulsion among negatively charged carboxyl groups and they have stretch conformation at high pH (Besra et al., 2004). That stretched conformation is very important since bridging mechanism is fully activated and flocculation performance increases due to available active polymer segments. This in turn will contribute to the enlargement and strength of the flocs.

Conclusion

Flocculation tests were carried out in the presence of different types of polymers at different polymer dosages and pHs. Flocculation and clarification behavior of natural stone suspensions were studied by determining the residual turbidity values and the settling rates of suspensions. The condition for the maximum settling rate and the minimum turbidity after settling was observed at optimum flocculant dosage for each flocculant. The critical amount of flocculant under these conditions was dependent on the type, molecular weight and charge density of flocculant and the solution pH. It was found that type and dosage of the flocculant has an important effect on the settling rate and turbidity. All flocculants used in the flocculation tests, substantially reduced the turbidity of natural stone suspensions and the settling rate of the particles increased with an increase in flocculant dosage. However, it was determined that in terms of the settling rate and turbidity, the medium anionic SPP 508 flocculant of 28% charge

density showed a better flocculation performance compared to the other conventional and UMA flocculants at natural pH of natural stone suspension SPP 508 showed the lowest turbidity value of 3 NTU at the lowest dosage of 0.3 mg/dm³. Considering only the settling rate, the large size flocs and the maximum settling rate of 870 mm/min for the suspensions tested was achieved at 1 mg/dm³ dosage by medium anionic SPP 508 flocculant. However, relatively small flocs and the lowest settling rate was obtained by the high cationic flocculant Enfloc 440 C.

The flocculation test results showed that the conformation and the charge density of polymer at high and low pH regimes played a crucial role in flocculation of the natural stone particles. All flocculants showed the good flocculation performance for the settling rate and turbidity at pH 8 and 10.

References

- ACAR H., 2001, *Attention must be paid to matters during the establishment and the running of a wastewater clarity unit for a marble processing plant*, The Third Marble Symposium, 289–296, Ankara.
- ARSLAN E.I., ASLAN S., IPEK U., ALTUN S., YAZIOGLU S. 2005, *Physico-chemical treatment of marble processing wastewater and recycling of its sludge*. Waste Management Research, 23, 550–559.
- BAYRAKTAR I., ONER M., KARAPINAR N., SAKLAR S. 1996, *Wastewater treatment in the marble industry*. In M. Kemal, V. Arslan, A. Akar, & M. Canbazoglu (Eds.), *Changing scopes in mineral processing*, 673–677, Rotterdam, NL: Balkema.
- BENTLI I., 2010, *The effect of electrolytes in flocculation of coal washing plant talings*, Ekoloji, 71–77.
- BESRA L., SENGUPTA D.K., ROY S.K., 2000, *Particle characteristics and their influence on dewatering of kaolin, calcite and quartz suspensions*, Int. J. Miner. Process. 59, 89–112.
- BESRA L., SENGUPTA D.K., ROY S.K., AY P., 2004, *Influence of polymer adsorption and conformation on flocculation and dewatering of kaolin suspension*, Separation and Purification technology, 37, 231–246.
- BIGGS S., HABGOOD M., JAMESON G.J., YAN Y., 2000, *Aggregate structures formed via a bridging flocculation mechanism*, Chemical Engineering Journal., 80, 13–22.
- BOLTOA.B., GREGORY J., 2007, *Organic Polyelectrolytes in Water Treatment*, Water Research, 41, 2301–2324.
- BRATBY J., 2006, *Coagulation and Flocculation in Water and Wastewater Treatment*, Published by IWA Publishing, London.
- CENGIZ I., SABAH E., ERKAN Z.E., 2004, *A study on the flocculation performances of traditional and UMA technology polymers*, Madencilik, 43, 15–23.
- CENGIZ I., SABAH E., OZGEN S., AKYILDIZ H., 2009, *Flocculation of Fine Particles in Ceramic Wastewater Using New Types of Polymeric Flocculants*, Journal of Applied Polymer Science, 112, 1258–1264.
- CELIK, M.Y., SABAH E., 2008, *Geological and technical characterization of Iscehisar (Afyon-Turkey) marble deposits and the impact of marble waste on environmental pollution*. Journal of Environmental Management, 87, 106–116.
- ERSOY, B., 2005, *Effect of pH and Polymer Charge Density on Settling Rate and Turbidity of Natural Stone Suspensions*, International Journal of Mineral Processing, 75, 207–216.
- GREGORY, J., 2005, *Particles in water: Properties and Process*, University College London, UK.
- GREGORY J., GUIBAI L., 1991, *Effects of dosing and mixing conditions on polymer flocculation of concentrated suspensions*, Chemical Engineering Communications, V: 108, 3–21.

- GREGORY J., BARANY S., 2011, *Adsorption and flocculation by polymers and polymer mixtures*, Advances in Colloid and Interface Science, 169, 1–12.
- HENDERSON J.M., WHEATLEY A.D. 2007, *Factors Affecting the efficient flocculation of tailings by polyacrylamides*, Coal Preparation, 1987, V 4, 1-49.
- HOCKING M.B., KLIMCHUK K.A., LOWEN S., 1999, *Polymeric flocculants and flocculation*, Polymer Reviews, 39:2, 177-203.
- HOGG R., 2000, *Flocculation and dewatering*. International Journal of Mineral Processing, V:58, pp223-236.
- HOGG R., 1999, *The role of polymer adsorption kinetics in flocculation*, Colloids and Surfaces A: Physicochemical and Engineering Aspects, 146, 253–263.
- IPEKOGLU U., 1997, *Dewatering and Methods*. Dokuz Eylül University, Mining Faculty Impress, No: 179, İzmir.
- KILIC H., 2012, *Treatment of Natural Stone Wastewaters by Flocculation and Floc-Flotation Methods*, MSc Thesis, Eskişehir Osmangazi University, Turkey.
- MPOFU P., ADDAI-MENSAH J., RALSTON J., 2003, *Investigation of the effect of polymer structure type on flocculation, rheology and dewatering behavior of kaolinite dispersions*, Int. J. Miner. Process. 71, 247–268.
- NISHKOV, I., MARINOV, M. 2003, *Calcium carbonate microproducts from marble treatment waste*. In L.Kuzey, I.Niskov, A. Boteva, D. Mochev (Eds.), Mineral processing in the 21st century (pp. 700–705), Djev Trade, Sofia.
- ONENC, D.I., 2001, *The block becoming powder and hopes*. Marble, 30, 66–68.
- PEARSE, M.J., WEIR S., ADKINS S.J AND MOODY G.M., 2001, *Advances in mineral flocculation*, Mineral Engineering, 14, 1505-1511.
- PEARSE, M.J., 2003, *Historical use and future development of chemicals for solid–liquid separation in the mineral processing industry*, Minerals Engineering, V: 16, 103–108.
- PEFFERKORN, E., 1999, *Polyacrylamide at solid/liquid interfaces*, Journal of Colloid and Interface Science, 216, 197-220.
- RATTANAKAWIN, C., HOGG R., 2001, *Aggregate size distributions in flocculation*, Colloids and Surfaces A: Physicochemical and Engineering Aspects, 177, 87–98.
- ROSSINI, M., GARRIDO J., GARCIA, GALLUZZO, M., 1999, *Optimization of the coagulation-flocculation treatment influence of rapid mix parameters*, Wat. Res., 33,8: 1817–1826.
- SABAH, E., ACIKSOZ, C., 2012, *Flocculation Performance of Fine Particles in Travertine Slime Suspension*, Physicochemical Problems of Mineral Processing 48(2), 555–566.
- SABAH, E. and ERKAN Z.E., 2006, *Interaction mechanism of flocculants with coal waste slurry*, Fuel, 85, 350–359.
- SABAH E., CENGİZ I., 2004, *An evaluation procedure for flocculation of coal preparation plant tailings*, Water Research, 38, 1542–1549.
- SEYRANKAYA A., MALAYOĞLU U., AKAR A. 2000, *Flocculation conditions of marble from industrial wastewater and environmental consideration*, In G. Ozbayoglu (Ed.), Mineral processing in the verge of the 12st century, 645–652, Rotterdam, NL: Balkema.
- SOMASUNDARAN P., DAS K.K., 1998. *Flocculation and selective flocculation - An overview*. In: Atak, S., Onal, G., Celik, M.S., (Editors), Proceedings of 7th International Mineral Processing Symposium (Innovation in mineral and coal processing), Istanbul, Turkey, Balkema, 81–91.
- SOMASUNDARAN P., KRISHNAKUMAR S., 1997, *Adsorption of surfactants and polymers at the solid-liquid interface*, Colloids Surfaces A: Physicochemical and Engineering Aspects, 491–513.
- SWORSKA A., LASKOWSKI J.S., CYMERMAN G., 2000 a, *Flocculation of the Syncrude fine tailings Part I. Effect of pH, polymer dosage and Mg²⁺ and Ca²⁺ cations*, International Journal of Mineral Processing, 60 143–152.
- SWORSKA A., LASKOWSKI J.S., CYMERMAN G., 2000 b, *Flocculation of the Syncrude fine tailings Part II. Effect of hydrodynamic conditions*, International Journal of Mineral Processing, 60, 153–161.

- TASDEMİR T., TASDEMİR A., KAKABAYEV H., 2011, *Evaluation of Flocculation Process in Natural Stone Processing Plant Wastewaters by Box-Behnken Experimental Design*, 22. International Mining Congress, 309-315, Ankara.
- TASDEMİR T., KURAMA H., 2012, *Fine Particle Removal from Natural Stone Processing Effluent by Flocculation*, Environmental Progress & Sustainable Energy, Vol. 32, No. 2, 317–324.
- TASDEMİR, T., TASDEMİR A., 2012, *Effect of Mixing Conditions on Flocculation*, Proceedings of XIIIth International Mineral Processing Symposium, 831–837, Turkey.
- TAYLOR M.L., MORRIS G.E., SELF P.G., SMART R.St.C., 2002, *Kinetics of Adsorption of High Molecular Weight Anionic Polyacrylamide onto Kaolinite: The Flocculation Process*, Journal of Colloid and Interface Science, 250, 28–36.
- TRIPATHY T., RANJAN DE B., 2006, *Flocculation : A New Way to Treat the Waste Water*, Journal of Physical Sciences, 10, 93–127.
- WEIR S., MOODY G.M., 2003, *The importance of flocculant choice with consideration to mixing energy to achieve efficient solid/liquid separation*, Minerals Engineering, V: 16, 109–113.
- YARAR B., 2001, *Evaluation of Flocculation and Filtration Procedures Applied to WSRC Sludge*, Report no: DE-AC09-96SR18500, Colarado School of Mines, 34.
- YU X., SOMASUNDARAN P., 1996, *Role of Polymer Conformation in Interparticle-Bridging Dominated Flocculation*, Journal of Colloid and Interface Science, 177, 283–287.
- <http://www.enerji.gov.tr>. Accessed on January 15, 2012.

Received May 28, 2013; reviewed, accepted July 13, 2013

APPLICATION OF THE OBSERVATIONAL TUNNELS METHOD TO SELECT A SET OF FEATURES SUFFICIENT TO IDENTIFY A TYPE OF COAL

Dariusz JAMROZ*, **Tomasz NIEDOBA****

* AGH University of Science and Technology, Faculty of Electrical Engineering, Automatics, Computer Science and Biomedical Engineering, Department of Computer Science, al. Mickiewicza 30, 30-059 Krakow, Poland, e-mail: jamroz@agh.edu.pl

** AGH University of Science and Technology, Faculty of Mining and Geoengineering, Department of Environmental Engineering and Mineral Processing, al. Mickiewicza 30, 30-059 Krakow, e-mail: tniedoba@agh.edu.pl

Abstract: Coal is a material which has many features deciding about its quality. Among them, the decisive ones are mainly ash contents, sulfur contents and combustion heat. The paper presents the investigation of coal characteristics of three selected coal types in the context of their energetic value. For this purpose samples were collected from three different Polish mines: coal types 31, 34.2 and 35 (Polish classification of coals). Each of these materials was separated into particle size fractions (9 fractions) and then into 8 density fractions by separation in heavy liquids. For each size-density fractions obtained in this way, chemical analyses were performed which allowed for determination of such features as combustion heat, sulfur contents, ash contents, volatile parts contents and analytical moisture. Altogether, seven dimensions of grained material characteristics were obtained. The data prepared in this way was subsequently analyzed for correlation with the purpose of determining significant relations between investigated features. It was stated that the most correlated coal features are density, combustion heat, ash contents and volatile parts contents.

For multidimensional analysis and identification of coal type, the modern image visualization technique, the Observational Tunnels Method, was applied. After performing seven-dimensional analysis aimed at the proper recognition of coal type, it was decided to determine the minimum amount of random variables, which describe a particular material in order to identify its type. It was stated that the crucial coal identification parameter is “analytical moisture”. Due to existing correlation between individual features, three of them were selected for testing: analytical moisture, sulfur contents and volatile parts contents. On the basis of the obtained images, it was stated that it was possible to obtain a view with the data concerning each type of coal being located in other part of the space. Subsequently, it was checked if a similar result is possible when the parameter “volatile parts contents” is replaced with highly correlated parameters “combustion heat” and “ash contents”. In both cases the exchange of these variables did not produce good enough results. This can be explained by a different scale of empirical data making it impossible to obtain a clear multidimensional image for which all three types of coal would be located in

other parts of space. However, it was proved that the modern graphical and computer methods can be successfully applied to identify the types of particulate materials.

Keywords: *multidimensional statistical analysis, observational tunnels method, coal, image visualization, energetic materials*

Introduction

Coal as energetic material is characterized by multiple parameters determining its quality. Depending on the studied type of coal (energetic, coking or semi-coking), these parameters differ significantly and allow for identifying the type of coal on the basis of its characteristics. In the paper a wide analysis of coals from three selected mines located in the Upper Silesia is carried out. They included coals types 31, 34.2 and 35 (according to Polish classification of coals). To evaluate their quality correctly, it is necessary to conduct the multidimensional statistical analysis. There are many techniques of such analysis, including:

- multidimensional distribution functions of random vector X (Lyman, 1993; Niedoba, 2009; 2011; Olejnik et al., 2010; Niedoba and Surowiak, 2012), where X is the vector describing coal properties,
- multidimensional regressive equations with the analysis of matrix coefficients of linear correlation and partial correlation between individual coal features (Niedoba, 2013; Tumidajski and Saramak, 2009),
- factor analysis (Stanisz, 2007; Tumidajski and Saramak, 2009),
- other methods including visualization by observational tunnels method (Jamroz, 2001), parallel coordinates and visualization of relations between multidimensional blocks (Jamroz, 2009).

The multidimensional distributions of vector X treated as random vector and their practical applications are widely described in the literature and will not be the subject of this paper. The other methods listed above are connected to some extent with the contents of this paper.

To carry out analyses for more than 3 dimensions, it is suitable to apply modern visualization methods which allow simultaneous analysis of many features of grained materials. One of such methods is observational tunnels method which was applied in the paper. These methods are becoming more and more useful in modern applications, which is reflected in many papers (Aldrich, 1998; Assa et al., 1997; 1999; Chatterjee et al., 1993; Chou et al., 1999; Cook et al., 1995; Heike, 2000; Hurley and Buja, 1990; Kim et al., 2000; Kraaijveld et al., 1995; Li et al., 2000). The observational tunnels method is connected with existing relations between individual coordinates of vector X (where X represents individual coal features). However, while the classical analysis of correlation is based on calculating the individual partial correlation coefficients without considering other features, the observational tunnels method considers projections of all coordinates taken together, giving a graphical image as a result. The competent change of the viewpoint gives the possibility of obtaining a view based on

which it is possible to identify the type of coal and information concerning differences between investigated materials. It also allows to select features which decide about the type of coal the investigated material is to be qualified for.

The matrices of linear coefficients and partial correlations are usually connected with existing linear models of relations between researched random variables of vector X . The coefficients of linear correlation are determined for pairs of random variables totally irrespective of other variables. The partial correlation coefficients are determined on the basis of the matrix of coefficients of linear correlation taking the role of other variables in certain equation of linear regression into consideration. In the case of analysis of three random variables from which one is treated as a dependent variable and two others as independent ones, it leads to determination of correlation coefficients for projections of points parallel to regressive plane. It allows to determine the hierarchy (power of influence) of relations between variables in researched system. On the basis of matrix of linear coefficients of correlation the factor analysis can be performed which allows for grouping the existing variables into the so-called factors representing joint influences of variables according to the results of investigated processes. Consequently, some sort of classification must be provided.

This paper also presents the methods of visualization of multidimensional data which make it possible to draw comparisons between the investigated data sets and suggest possibilities of their classification. They are a sort of continuation and development of the methods discussed above.

Observational tunnels method

The theoretical underpinnings of the Observational Tunnels Method were described in a paper by Jamroz (2001). Intuitively, it may be said that the method of observational tunnels makes use of a parallel projection with a local orthogonal projection of an extent limited by the maximal radius of the tunnel. This solution makes it possible to observe selected parts of space containing important information, which is not possible in the case of orthogonal projection. The method of projection used in this paper is roughly presented in Fig. 1. The observational plane P will be used as a screen through which any object placed in space X will be viewed. This observational plane $P \subset X$ is defined as: $P = \delta(w, \{p_1, p_2\})$, where:

$$\delta(w, \{p_1, p_2\}) \stackrel{def}{=} \{x \in X : \exists \beta_1, \beta_2 \in F, \text{ such that } x = w + \beta_1 p_1 + \beta_2 p_2\}, \quad (1)$$

X is any n -dimensional ($n \geq 3$) vector space, over an F field of real numbers, with a scalar product.

Vector w will indicate the position of the screen midpoint, whereas p_1, p_2 will indicate its coordinates. Let us assume for the moment that the space X is 3-dimensional (an example assuming a space with more dimensions would be more difficult to conceive) and that observational plane P is 1-dimensional (i.e. it is possible

to observe the pertinent reality not through a segment of 2-dimensional plane but through a segment of a line). Additionally, let us take vector r , being the proper direction of projection onto the observational plane P (The proper direction of projection r onto the observational plane $P = \mathcal{A}(w, \{p_1, p_2\})$ is defined as any vector $r \in X$ if vectors $\{p_1, p_2, r\}$ are an orthogonal system). Let's determine $k_{a,r}$ (i.e. a line parallel to r and passing through a) for observed point a . As shown in Fig. 1, the line $k_{a,r}$ need not have common points with P . However, $k_{a,r}$ always has one common point with hypersurface S containing P and being orthogonal to r . (the hypersurface $S_{(s,d)}$, anchored in $s \in X$ and directed towards $d \in X$ is defined as:

$$S_{(s,d)} \stackrel{def}{=} \{x \in X : (x - s, d) = 0\}. \tag{2}$$

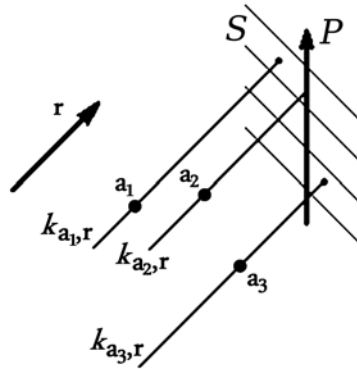


Fig. 1. Presentation of the rules of projection on plane P in the observational tunnels method

A line parallel to r and passing through a does not have to have common points with P . However, it always has exactly one common point with hypersurface S containing P and being orthogonal to r . In the above mentioned case only point a_2 will be visible using observational plane P .

In practice, some points could be viewed only at some orientations of observational plane P . This implies that in the majority of cases, when viewing a set of points using observational plane P , nothing will be seen. In order to avoid such situation, let us assume that the points visible on observational plane P do not only include points situated on lines parallel to r and passing through P , but also the points which are situated on lines parallel to r and passing through S (i.e. the hypersurface containing P and orthogonal to r) within a smaller distance from observational plane P than a certain fixed value. This distance for observed point a will be represented by vector b_a called the tunnel radius:

$$b_a = \psi r + a - w - \beta_1 p_1 - \beta_2 p_2, \tag{3}$$

where:

$$\psi = \frac{(w - a, r)}{(r, r)}, \beta_1 = \frac{(\psi r + a - w, p_1)}{(p_1, p_1)}, \beta_2 = \frac{(\psi r + a - w, p_2)}{(p_2, p_2)}. \quad (4)$$

In Eq. 4 $r \in X$ denotes a proper direction of projection onto observational plane P .

In the case presented in Fig. 2, at the point e of observational plane P , all points situated in the tunnel whose intersection is a segment of and which is spreading along r will be visible. However, generally, at the point e on the observational plane P , all points situated in the tunnel whose intersection is $n-3$ dimensional sphere and spreading along the direction of projection r will be visible.

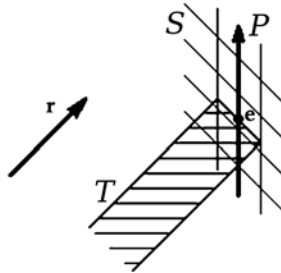


Fig. 2. Way of choosing observational tunnel T Tunnel T for point e is shown. (The area hatched with horizontal lines). All points that belong to tunnel T will be visible at point e of observational plane P

The algorithm below should be followed in order to draw the projection of observed point a consistently with the direction of projection r onto observational plane $P = \mathcal{X}(w, \{p_1, p_2\})$:

1. the distance of projection of observed point a is to be calculated using the formula:

$$\psi = (w - a, r) / (r, r) \quad (5)$$

2. the position of the projection (i.e. the pair $\beta_1, \beta_2 \in F$) of observed point a is to be calculated using the formula:

$$\beta_1 = (\psi r + a - w, p_1) / (p_1, p_1), \beta_2 = (\psi r + a - w, p_2) / (p_2, p_2) \quad (6)$$

3. the tunnel radius b_a of point a is to be calculated using the definition (3)
4. at this point it should be verified whether the scalar product (b_a, b_a) is lower than the maximum tunnel radius determined at a given time and whether the distance of the projection of observed point a is shorter than the maximum range of view

determined at a given time. If this is the case, then one should draw a point on observational plane $P=\mathcal{X}(w, \{p_1, p_2\})$ in the position of coordinates (β_1, β_2) , otherwise the point should not be drawn.

The scalar product is to be calculated using the formula:

$$(x, y) = \sum_{i=1}^n x_i y_i, \quad (7)$$

where: $x = (x_1, x_2, \dots, x_n)$, $y = (y_1, y_2, \dots, y_n)$, n - number of dimensions, $n \geq 3$.

Experimental

Three types of coal, types 31 (energetic coal), 34.2 (semi-coking coal) and 35 (coking coal) in the Polish classification were used in the investigation. They originated from three various Polish coal mines and all of them were initially screened on a set of sieves of the following sizes: -1.00, -3.15, -6.30, -8.00, -10.00, -12.50, -14.00, -16.00 and -20.00 mm. Then, the size fractions were additionally separated into density fractions by separation in dense media using zinc chloride aqueous solution of various densities (1.3, 1.4, 1.5, 1.6, 1.7, 1.8 and 1.9 g/cm³). The fractions were used as a basis for further consideration and additional coal features were determined by means of chemical analysis. For each density-size fraction such parameters as combustion heat, ash contents, sulfur contents, volatile parts contents and analytical moisture were determined, making up, together with mass of these fractions, seven various features for each coal. The examples of such data were presented in tables 1–3 showing the data for size fractions 1.00–3.15 mm for each type of coal.

Table 1. Data for size fraction 1.00–3.15 mm – coal, type 31

Density [Mg/m ³]	Mass [g]	Combustion heat [cal]	Ash contents [%]	Sulfur contents [%]	Volatile parts contents V^a	Analytical moisture W_a
<1.3	4187.8	7367	1.25	0.63	36.02	4.15
1.3–1.4	2864.0	7021	3.35	0.66	32.14	4.33
1.4–1.5	310.0	5939	18.78	1.33	27.54	2.55
1.5–1.6	102.3	5547	23.83	1.66	26.87	2.80
1.6–1.7	111.9	4911	30.54	1.91	25.98	2.65
1.7–1.8	91.3	4177	39.94	1.93	25.17	2.35
1.8–1.9	80.9	3462	47.43	1.74	24.00	2.29
>1.9	1051.8	762	82.20	1.72	13.05	1.14

Table 2. Data for size fraction 1.00–3.15 mm – coal, type 34.2

Density [Mg/m ³]	Mass [g]	Combustion heat [cal]	Ash contents [%]	Sulfur contents [%]	Volatile parts contents V^a	Analytical moisture W_a
<1.3	1803.0	8345	1.10	0.31	31.87	0.85
1.3–1.4	794.0	8032	3.70	0.38	26.52	0.88
1.4–1.5	83.3	6972	14.70	0.60	25.66	0.64
1.5–1.6	40.6	5971	24.20	0.84	24.30	0.80
1.6–1.7	25.0	5093	31.60	0.42	25.48	0.42
1.7–1.8	20.8	4571	37.00	0.86	22.08	0.56
1.8–1.9	6.7	4228	40.20	0.96	24.77	0.63
>1.9	213.7	887	79.30	0.89	13.75	0.55

Table 3. Data for size fraction 1.00–3.15 mm – coal, type 35

Density [Mg/m ³]	Mass [g]	Combustion heat [cal]	Ash contents [%]	Sulfur contents [%]	Volatile parts contents V^a	Analytical moisture W_a
<1.3	3476.2	8297	2.22	0.38	21.94	1.07
1.3–1.4	791.1	7781	7.84	0.46	19.56	0.85
1.4–1.5	264.7	6836	17.61	0.51	18.65	0.97
1.5–1.6	119.2	5830	27.70	0.62	18.22	0.93
1.6–1.7	117.0	5029	35.57	0.66	17.40	1.05
1.7–1.8	92.1	4222	43.45	0.76	16.99	1.08
1.8–1.9	72.9	3516	50.64	0.74	16.12	1.16
>1.9	1422.2	630	81.31	0.35	11.53	1.05

Searching for significant coal features

With a view to checking the relations between individual coal features, the partial correlation matrix was calculated for each type of coal. For each matrix the data concerning each particle density-size fraction (9 size fractions \times 8 density fractions = 72 data), for coal type 34.2 several measurements were performed, which resulted in the number of the data = 61 in this case) for each type of investigated coals. The correlation matrices were presented in Tables 4–6.

Table 4. Correlation matrix for coal type 31

	Density [Mg/m ³]	Mass [g]	Combustion heat [cal]	Ash contents [%]	Sulfur contents [%]	Volatile parts contents V^a	Analytical moisture W_a	Particle size d
Density [Mg/m ³]	1.00	-0.22	-0.92	0.92	0.53	-0.81	-0.86	-0.08
Mass [g]	-0.22	1.00	0.21	-0.19	-0.29	0.21	0.21	-0.29
Combustion heat [cal]	-0.92	0.21	1.00	-0.97	-0.36	0.89	0.89	-0.08
Ash contents [%]	0.92	-0.19	-0.97	1.00	0.36	-0.93	-0.92	0.06
Sulfur contents [%]	0.53	-0.29	-0.36	0.36	1.00	-0.24	-0.37	-0.31
Volatile parts contents V^a	-0.81	0.21	0.89	-0.93	-0.24	1.00	0.86	-0.03
Analytical moisture W_a	-0.86	0.21	0.89	-0.92	-0.37	0.86	1.00	-0.10
Particle size d	-0.08	-0.29	-0.08	0.06	-0.31	-0.03	-0.10	1.00

Table 5. Correlation matrix for coal type 34.2

	Density [Mg/m ³]	Mass [g]	Combustion heat [cal]	Ash contents [%]	Sulfur contents [%]	Volatile parts contents V^a	Analytical moisture W_a	Particle size d
Density [Mg/m ³]	1.00	-0.47	-0.96	0.93	0.20	-0.70	-0.44	-0.08
Mass [g]	-0.47	1.00	0.37	-0.35	-0.30	0.29	0.06	-0.18
Combustion heat [cal]	-0.96	0.37	1.00	-0.99	-0.12	0.82	0.42	0.01
Ash contents [%]	0.93	-0.35	-0.99	1.00	0.12	-0.85	-0.41	-0.02
Sulfur contents [%]	0.20	-0.30	-0.12	0.12	1.00	-0.05	-0.12	-0.29
Volatile parts contents V^a	-0.70	0.29	0.82	-0.85	-0.05	1.00	0.29	-0.07
Analytical moisture W_a	-0.44	0.06	0.42	-0.41	-0.12	0.29	1.00	0.44
Particle size d	-0.08	-0.18	0.01	-0.02	-0.29	-0.07	0.44	1.00

Table 6. Correlation matrix for coal type 35

	Density [Mg/m ³]	Mass [g]	Combustion heat [cal]	Ash contents [%]	Sulfur contents [%]	Volatile parts contents V^a	Analytical moisture W_a	Particle size d
Density [Mg/m ³]	1.00	-0.14	-0.98	0.97	0.30	-0.88	0.32	-0.08
Mass [g]	-0.14	1.00	0.05	-0.04	-0.40	0.02	-0.18	-0.28
Combustion heat [cal]	-0.98	0.05	1.00	-1.00	-0.15	0.93	-0.29	0.04
Ash contents [%]	0.97	-0.04	-1.00	1.00	0.13	-0.94	0.28	-0.04
Sulfur contents [%]	0.30	-0.40	-0.15	0.13	1.00	0.01	0.18	-0.10
Volatile parts contents V^a	-0.88	0.02	0.93	-0.94	0.01	1.00	-0.21	0.05
Analytical moisture W_a	0.32	-0.18	-0.29	0.28	0.18	-0.21	1.00	0.55
Particle size d	-0.08	-0.28	0.04	-0.04	-0.10	0.05	0.55	1.00

It is worth looking at statistical description of the considered random variables. Their characteristics were presented in Tables 7–9.

Table 7. Statistical description for coal 31

Parameter	Mass [g]	Combustion heat [cal]	Ash contents [%]	Sulfur contents [%]	Volatile parts contents V^a	Analytical moisture W_a
mean value	502.84	4827.68	30.59	1.14	26.13	2.88
standard deviation	859.77	1928.20	22.80	0.49	6.58	0.94
skewness	2.71	-0.71	0.97	0.54	-1.03	-0.21
curtosis	7.47	-0.14	0.48	-0.77	0.72	0.02
max	4187.80	7518.00	86.59	2.28	37.04	5.41
min	7.10	433.00	1.25	0.39	9.30	0.91
interval	4180.70	7085.00	85.34	1.89	27.74	4.50

Table 8. Statistical description for coal 34.2

Parameter	Mass [g]	Combustion heat [cal]	Ash contents [%]	Sulfur contents [%]	Volatile parts contents V^a	Analytical moisture W_a
mean value	170.46	5515.98	27.86	0.57	24.66	0.94
standard deviation	345.01	2390.50	23.89	0.35	5.66	0.28
skewness	3.60	-0.75	1.03	1.29	-1.48	0.35
curtosis	14.49	-0.22	0.35	2.27	1.58	0.75
max	1817.90	8367.00	81.97	1.81	31.87	1.87
min	2.20	591.00	0.79	0.05	9.77	0.37
interval	1815.70	7776.00	81.18	1.76	22.10	1.5

Table 9. Statistical description for coal 35

Parameter	Mass [g]	Combustion heat [cal]	Ash contents [%]	Sulfur contents [%]	Volatile parts contents V^a	Analytical moisture W_a
mean value	367.64	5418.26	31.60	0.56	17.65	1.27
standard deviation	631.53	2286.93	23.40	0.247	2.82	0.18
skewness	3.14	-0.67	0.73	1.09	-1.19	-0.005
curtosis	10.91	-0.27	-0.19	1.06	1.004	-0.58
max	3476.20	8383.00	82.02	1.26	22.18	1.65
min	21.00	600.00	1.84	0.18	10.60	0.85
interval	3455.20	7783.00	80.18	1.08	11.58	0.80

From the correlation analysis results it is clearly visible that the most correlated coal features are density, combustion heat, ash contents and volatile parts contents. It is presumed then that for coal type identification it is not necessary to choose all of these features, but only one of them. To perform the multidimensional analysis of the data presented above, which describes coal parameters, the observational tunnels method was applied. Each of seven dimensions was treated as one. At the beginning, it was examined whether the information contained in all parameters is sufficient to the correct identification of coal type (Niedoba and Jamroz, 2013). As a result, the 7-dimensional space was created. It turned out that the accepted parameters were sufficient for proper identification if a given sample originated from coal type 31, 34.2 or 35. Figure 3 shows an example of experiment result considering data from all types of coal: 34.2 (61 samples), 35 (72 samples) and 31 (72 samples). From this it occurs that the data representing coal of type 35 is located in other part of the space than data representing coal of type 34.2. However, it is impossible to conclude about possibility of separation of coal of type 31. Furthermore, it was impossible to achieve one view from which the conclusion about proper identification of each of three analyzed types of coal was possible. Only joined conclusions occurring from several views allowed to

state this (Niedoba and Jamroz, 2013). It proves that the nature of analyzed data is complicated.

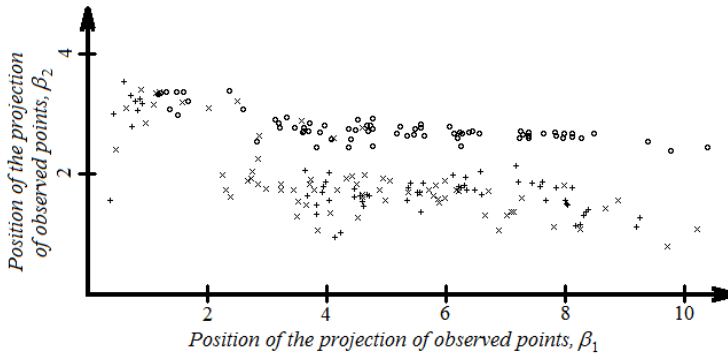


Fig. 3. Obtained view which shows that 7-dimensional data for coal 35 (“circles”) gather in other part of the space than coal 34.2 (“pluses”). From this view it is not possible to conclude about possible separation of coal of type 31 (×)

Next, the last parameter, “analytical moisture”, was deleted from the set of data. Consequently, the six-dimensional space was created. The Figs 4–5 show the experimental results for 6-dimensional data created in this way. From the view obtained in Fig. 4 it can be seen that the data concerning coal type 31 is located in other part of the space than coal type 35. On this basis it can be stated that the accepted parameters are sufficient to identify properly if certain sample origins from coal type 31 or 35. On the basis of this figure it is impossible to conclude about possible separation of the coal of type 34.2. In Fig. 5 the obtained view made it possible to state that the data concerning coal type 35 is located in other part of the space than coal type 34.2. It is possible then to state that the accepted parameters are sufficient for the proper identification whether certain sample origins from coal type 35 or 34.2. However, it was impossible to get the view from which the conclusion could be made that data concerning coal type 31 is located in other part of the space than coal of type 34.2. So, it is impossible to accept that these parameters are sufficient to the proper identification of coal type.

As it was noticed before, the seven-dimensional data created from the seven coal features described above is sufficient to the proper identification of coal type, but the same data is not sufficient for this purpose after removal of the parameter “analytical moisture”. The conclusion is that the parameter “analytical moisture” is essential to the proper identification of coal type. It was the reason for constructing the next set of data on the basis of this parameter.

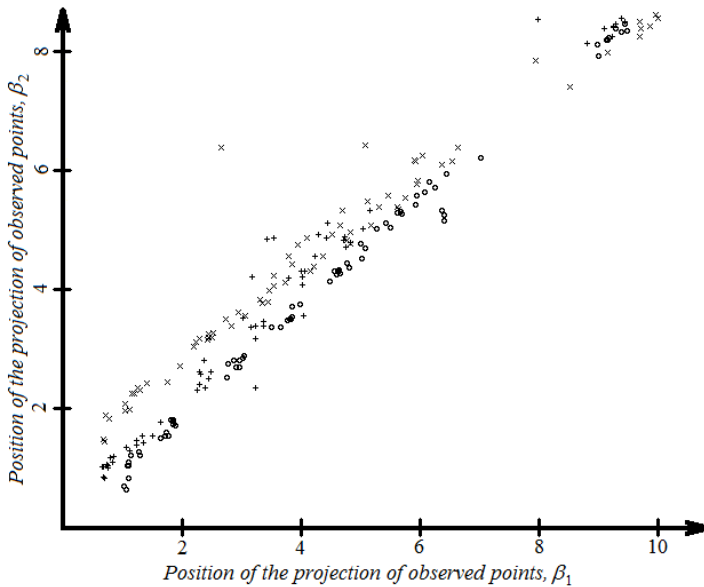


Fig. 4. View of 6-dimensional set of data created after removal of parameter „analytical moisture”. It is visible that the data representing coal of type 35 (“circles”) is located in other part of the space than data representing coal type 31 (“crosses”). From this view it is not possible to conclude about possible separation of coal of type 34.2 (“+”)

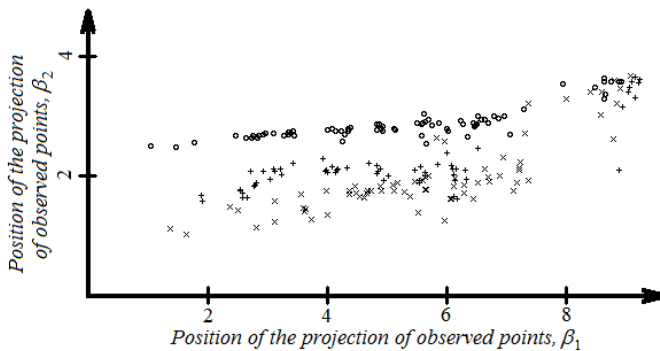


Fig. 5. View of 6-dimensional data created after the removal of parameter „analytical moisture”. It is visible that the data representing coal type 35 (“circles”) is located in other part of the space than data representing coal type 34.2 (“pluses”). From this view it is not possible to conclude about possible separation of coal of type 31 (“x”)

Based on correlation matrix results, 4 coal features were removed from the seven-dimensional set of data presented above and only 3 parameters left: analytical moisture, sulfur contents and volatile parts contents. Each of these parameters was treated as one dimension. Therefore, the three-dimensional space was created. Figures

6–7 present the results of these experiments. From the view obtained in Fig. 6 it can be seen that data concerning coal type 31 is located in other part of the space than coal type 35. On this basis it can be stated that the accepted parameters are sufficient for the proper identification if certain sample origins from coal type 31 or 35. On the basis of this figure it is impossible to conclude about possible separation of coal of type 34.2. Based on the view obtained in Fig. 7 it can be stated that data concerning coal type 34.2 is located in other part of the space than coal type 35 and simultaneously in other part of the space than coal type 31. From these two views, it can be concluded that the accepted parameters are sufficient to identify properly if certain sample origins from coal type 31, 34.2 or 35. At the same time it was impossible to get one view from which such conclusion could be made. It can be the proof that the structure of analyzed data is complicated.

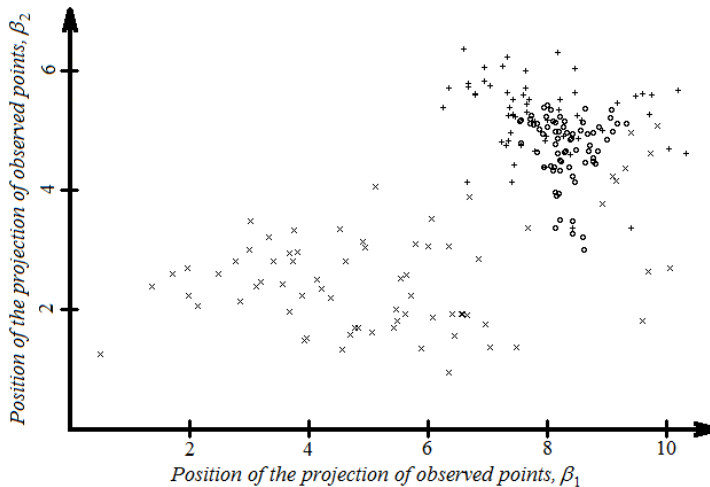


Fig. 6. View of 3-dimensional data: analytical moisture, sulfur contents and volatile parts contents. It is visible that the data representing coal type 35 (“circles”) is located in other part of the space than data representing coal type 31 (“crosses”). From this view it is not possible to conclude about possible separation of coal of type 34.2 (+)

Next, it was decided to examine the influence of potential replacement of one of the coal features with another one highly correlated with it. The correlation index of “volatile parts contents” parameter was equal to 0.93 with parameter “combustion heat” for coal type 31, 0.82 for coal type 34.2 and 0.89 for coal type 35 (see: Tables 4–6). They are parameters highly related to each other. That is why in a set of three coal features (analytical moisture, sulfur contents and volatile parts contents), which are sufficient for the correct identification of coal type as shown above, the parameter

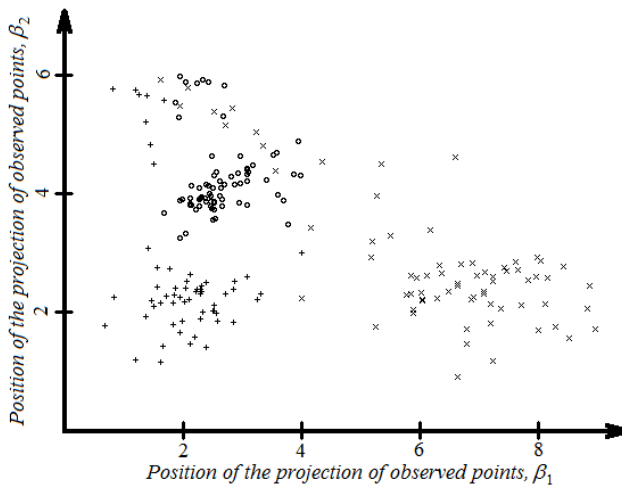


Fig. 7. View of 3-dimensional data created from features: analytical moisture, sulfur contents and volatile parts contents. It is visible that the data representing coal type 34.2 (“pluses”) is located in other part of the space than data representing coal type 31 (“crosses”) as well data representing coal type 34.2 (“pluses”) is located in other part of the space than data representing coal type 35 (“circles”)

“volatile parts contents” was replaced with parameter “combustion heat”. Figures 8-9 present the obtained results. The view obtained in Figure 8 allows to state that data concerning coal type 31 is located in other part of the space than coal type 34.2, and at the same time it is located in other part of the space than coal type 35. On this basis it can be said that the accepted parameters are sufficient to the proper identification if a particular sample originates from coal type 31 or not. All the same, it was impossible to find a view stating that the data concerning coal type 34.2 is located in other part of the space than coal type 35. The best obtained view concerning the possibility of separating the data into coals types 34.2 and 35 was shown in Figure 9. It occurs from it that the accepted parameters are sufficient to proper identification if the sample origins from coal of type 31 or 34.2. It cannot be said then that these three accepted parameters are sufficient to the proper identification of the type of coal. It proved that as a result of replacement of parameter “volatile parts contents” with “combustion heat”, the information allowing for the proper identification of coal type was lost. It occurred despite the high value of correlation index between these two coal features. Similarly, the parameter „volatile parts contents” was replaced with parameter “ash contents”. The correlation index between these two features was high and was equal to -0.94 for coal type 31, -0.85 for coal type 34.2 and -0.93 for coal type 35 (see: Tables 4–6). Consequently, the set of three parameters was created: analytical moisture, sulfur contents and ash contents. The view presented in Figure 10 allows to state that data concerning the coal type 31 is located in other part of the space than data concerning coal type 34.2 and at the same is located in other part of the space than

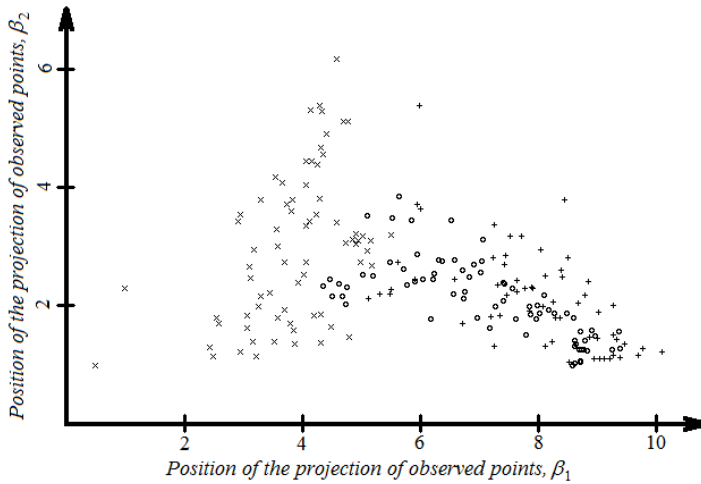


Fig. 8. View of 3-dimensional data created from features: analytical moisture, sulfur contents and combustion heat. It is visible that data representing type coal 31 (“crosses”) is located in other part of the space than data representing coal type 34.2 (“pluses”) and other part of the space than data representing coal type 35 (“circles”)

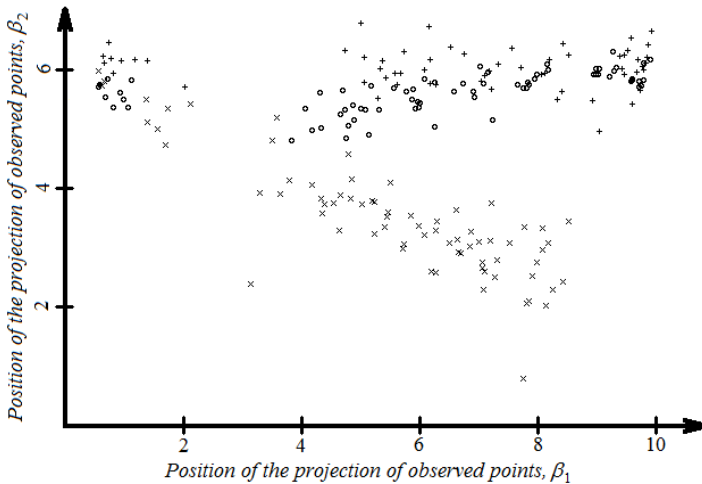


Fig. 9. View of 3-dimensional data created from features: analytical moisture, sulfur contents and combustion heat. The best view does not allow to state if the data representing type coal 34.2 (“pluses”) can be separated from the data representing type coal 35 (“circles”) – sets of points representing these two types overlap. It can be stated that the accepted parameters are sufficient to proper identification if certain sample origins from coal of type 31 (“crosses”) or 34.2 (“pluses”)

data concerning coal type 35. On this basis, similarly to the previous case, it can be stated that the accepted set of parameters is sufficient for the correct identification if certain sample originates from coal type 31 or not. All the same, it was impossible to

find a view allowing to state that the data concerning coal type 34.2 is located in other part of space than the data concerning coal type 35. The accepted parameters are then not sufficient for the proper identification of the type of coal. This proved that the replacement of the parameter “volatile parts contents” with parameter “ash contents” also resulted in a loss of information allowing for the proper identification of all three coal types despite the high value of correlation index between replaced coal features.

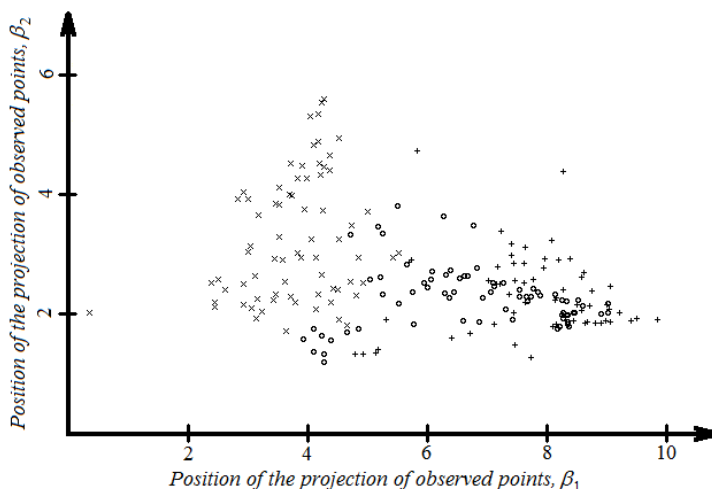


Fig. 10. View of 3-dimensional data created from features: analytical moisture, sulfur contents and ash contents. It is visible that data representing coal type 31 (“crosses”) is located in other part of the space than data concerning coal type 34.2 (“pluses”) and other part of the space than data representing coal type 35 (“circles”)

Conclusions

The visualizations of multidimensional data made it possible to arrive at the following conclusions:

- 6-dimensional data created as a result of removal of the parameter “analytical moisture” is not sufficient for the proper identification of coal type. They only allow to recognize coal types 35 and 31 as well 35 and 34.2 in pairs
- the parameter “analytical moisture” is crucial to the proper identification of coal type. Without this parameter, it would have been impossible to recognize the type of coal successfully
- three-dimensional data created from parameters: analytical moisture, sulfur contents and volatile parts contents are sufficient for the proper identification of coal type
- replacement of one of the parameters in coal features set with other highly correlated parameter does not guarantee to save the information necessary for the identification of coal type

- the system features, including analytical moisture, sulfur contents and combustion heat as well analytical moisture, sulfur contents and ash contents are not sufficient for the proper identification of coal type.

Acknowledgement

The paper is the result of scientific project No. *N N524 339040*, agreement No. *3390/B/T02/2011/40*.

References

- ALDRICH C., 1998, *Visualization of transformed multivariate data sets with autoassociative neural networks*, Pattern Recognition Letters, vol. 19, issue: 8, 749–764.
- ASSA J., COHEN-OR D., MILO T., 1997, *Displaying data in multidimensional relevance space with 2D visualization maps*, Proceedings. Visualization '97, 127–134. New York, NY, IEEE.
- ASSA J., COHEN-OR D., MILO T., 1999, *RMAP: a system for visualizing data in multidimensional relevance space*, Visual Computer, vol. 15, no. 5, 217–234.
- CHATTERJEE A., DAS P.P., BHATTACHARYA S., 1993, *Visualization in linear programming using parallel coordinates*, Pattern Recognition 26(11), 1725–1736.
- CHOU S.Y., LIN S.W., YEH C.S., 1999, *Cluster identification with parallel coordinates*, Pattern Recognition Letters 20, 565–572.
- COOK D., BUJA A., CABRERA J., HURLEY C., 1995, *Grand Tour and Projection Pursuit*, Journal of Computational and Graphical Statistics, vol. 4, no. 3, 155–172.
- HEIKE H., 2000, *Exploring categorical data: interactive mosaic plots*, Metrika 51, 11–26.
- HURLEY C., BUJA A., 1990, *Analyzing high-dimensional data with motion graphics*, SIAM Journal on Scientific & Statistical Computing, vol. 11, no. 6, 1193–1211.
- JAMROZ D., 2009, *Multidimensional labyrinth – multidimensional virtual reality*. In: Cyran K., Kozielski S., Peters J., Stanczyk U., Wakulicz-Deja A. (eds.), *Man-Machine, Interactions*, AISC, vol. 59, 445–450. Springer-Verlag, Berlin Heidelberg, Germany.
- JAMROZ D., 2001, *Visualization of objects in multidimensional spaces*. Ph.D. Thesis, AGH, University of Science and Technology, Cracow, Poland.
- KIM S., KWON S., COOK D., 2000, *Interactive visualization of hierarchical clusters using MDS and MST*, Metrika 51, 39–51, Springer-Verlag.
- KRAAIJVELD M., MAO J., JAIN A.K., 1995, *A nonlinear projection method based on Kohonen's topology preserving maps*, IEEE Trans. Neural Networks 6(3), 548–559.
- LI W., YUE H.H., VALLE-CERVANTES S., QIN S.J., 2000, *Recursive PCA for adaptive process monitoring*, Journal of Process Control, vol. 10, issue: 5, 471–486.
- Lyman G. J., 1993, *Application of Line-Length Related Interpolation Methods to Problems in Coal Preparation – III: Two dimensional Washability Data Interpolation*, Coal Preparation, vol. 13, 179–195.
- NIEDOBA T., 2013, *Statistical analysis of the relationship between particle size and particle density of raw coal*, Physicochemical Problems of Mineral Processing, vol. 49, iss. 1, 175–188.
- NIEDOBA T., SUROWIAK A., 2012, *Type of coal and multidimensional description of its composition with density and ash contents taken into consideration*, in Proceedings of the XXVI International Mineral Processing Congress, vol. 1, New Delhi, 3844–3854.
- NIEDOBA T., 2011, *Three-dimensional distribution of grained materials characteristics*, in Proceedings of the XIV Balkan Mineral Processing Congress, Tuzla, Bosnia and Herzegovina, vol. 1, 57–59.

- NIEDOBA T., 2009, *Wielowymiarowe rozkłady charakterystyk materiałów uziarnionych przy zastosowaniu nieparametrycznych aproksymacji funkcji gęstości rozkładów brzegowych*, *Górnictwo i Geoinżynieria*, iss. 4, 235–244.
- NIEDOBA T., JAMROZ D., 2013, *Visualization of multidimensional data in purpose of qualitative classification of various types of coal*, *Archives of Mining Sciences* (paper in printing).
- OLEJNIK T., SUROWIAK A., GAWENDA T., NIEDOBA T., TUMIDAJSKI T., 2010, *Wielowymiarowe charakterystyki węgla jako podstawa do oceny i korekty technologii ich wzbogacania*, *Górnictwo i Geoinżynieria*, vol. 34, iss. 4/1, 207–216.
- STANISZ A., 2007, *Przystępny kurs statystyki w oparciu o program Statistica PL na przykładach z medycyny, tom III: Analizy wielowymiarowe*, Wyd. Statsoft, Kraków.
- TUMIDAJSKI T., SARAMAK D., 2009, *Metody i modele statystyki matematycznej w przeróbce surowców mineralnych*, Wydawnictwo AGH, Kraków.

Received June 10, 2013; reviewed; accepted July 17, 2013

UPGRADING VALUABLE MINERALIZATION AND REJECTING MAGNESIUM SILICATES BY PRE-CONCENTRATION OF MAFIC ORES

N. Emre ALTUN^{*}, Trent WEATHERWAX^{**}, Bern KLEIN^{**}

^{*} Mugla University, Mining Engineering Department, 48000, Mugla, Turkey

^{**} Norman. B. Keevil Institute of Mining Engineering, University of British Columbia, Vancouver, BC, Canada

Abstract: Amenability of mafic ores to pre-concentration was investigated with respect to ore mineralization characteristics. For the pre-concentration tests seven ores from various nickel-copper operations at Sudbury, Ontario were subjected to dense medium separation. Size assays of metal values, i.e. distribution of nickel and copper with respect to size fractions, were also determined. The ores were assessed in three categories of valuable mineralization as massive pure sulphides, coarse massive sulphide grains and disseminated sulphides. For ores with massive pure sulphides and coarse massive sulphide grains even a size classification based pre-concentration route could be sought since a clear trend of metal enrichment was identified towards finer fractions. Orebodies of similar mineralogy had similar responses to pre-concentration tests. The best results were for those ore bodies with a distinct differentiation between mineralization and gangue, i.e. the ores with massive pure sulphides, where nickel recoveries of 97% and mass rejections of 38-53% were achieved. Similar results were obtained for ores with coarse massive sulphides. For disseminated sulphide mineralogy relatively lower mass rejection was attained with acceptable recoveries of metals. Rejection of magnesium bearing gangue, such as talc, was identified as another benefit of pre-concentration. The extent of magnesium rejection occurred as a function of ore mineralogy. Clear distinction between valuable mineralization and gangue provided preferential magnesium rejection at high levels with no or minor metal losses.

Keywords: mafic ores, pre-concentration, dense media separation, metallic sulphides, ore mineralogy

Introduction

Pre-concentration is a beneficiation concept with the primary goal of early waste rejection, i.e. discarding barren rock from run-off-mine ore at coarse sizes prior to downstream processes. It is not a new concept and has been in practice since early 1900's. Depending on the characteristics of the ore and scale of the process, pre-concentration can be accomplished using several methodologies ranging from simple techniques such as hand sorting and screening to conventional mineral separation

techniques such as dense medium separation (DMS) or highly advanced sorting technologies. As mentioned, it is a proven concept with practices for a wide range of ores and several large scale applications. Some of the successful applications include, pre-concentration of a Zn-sulphide ore at American Zinc Company (TN, USA), a native-Cu ore (Houghton, MI, USA), Pb-Zn sulphide ore at Mt. Isa (Australia), a Cu-sulphide ore at Copper Creek (AZ, USA), a Pb-Zn sulphide ore at Sullivan Mine (BC, Canada), a Ni-sulphide ore at Whistle Mine (Sudbury, ON, Canada). The South African Chamber of Mines also conducted an extensive research programme for more than a decade (1978-1989) to identify the potential of underground pre-concentration for several deep gold mines (Miller, 1978; Lloyd, 1979; Munro, 1982; Fiedler et al., 1984; Lloyd et al., 1986; Vatcha et al., 2000). All these applications and previous research showed that application of pre-concentration, either at the surface or underground, would potentially lead to numerous benefits by realizing early waste rejection in the mining sequence. The most significant outcomes include (Schena et al, 1990; Salter and Wyatt, 1991; Feasby and Tremblay, 1995; Peters et al., 1999; Scoble et al., 2000; Klein et al., 2002; Klein et al., 2003; Bamber et al., 2006):

- savings in material handling and transportation costs by early rejection of waste
- savings in grinding and processing costs by removing siliceous and/or Mg bearing gangue.
- increased efficiency in downstream processes due to improved feed metallurgy
- extended mine-life due to lowered cut-off grade
- possibility to use bulk-mining methods due to higher toleration of dilution in the ROM ore
- higher mining rate without installing higher capacity processing facilities
- decrease in the amount of fine wastes and slime production after concentration processes
- possibility to use rejected waste as backfill material in U/G operations.

Effective pre-concentration therefore would improve the economics, efficiency and contribute to the environmental viability of the operation. In addition, pre-concentration has been reported to be particularly in favour of operations at extreme depths and/or on low grade ores (Hinde et al., 1986). In this respect it is envisioned to contribute to the sustainability of a vast number of metal mines in the globe constrained by increasing ore depth, decreasing ore grade, and environmental measures. This paper presents results from an extensive test programme aimed at identifying the amenability of ores from some of the major nickel-copper operations at Sudbury, Ontario, Canada. These operations commonly suffer from technical restrictions such as increasing ore depth, decreasing ore grade and increasing mining costs as well as environmental pressures. The impact of ore mineralogy on the liability of the ores to pre-concentration was assessed by interpreting the results in relation to the occurrence modes of nickel and copper bearing portions, using dense medium separation.

Materials and Methods

Seven different ores from the Craig, Fraser and Thayer Lindsley mines were grouped with respect to the distinctive mineralogical characteristics of metallic sulphides in the ores. The specific names and characteristics of these ores are presented in Table 1. In all the ores, the nickel and copper values exist in the form of metallic sulphides. It is also possible to classify the ores as contact and footwall with sub-groups based on their specific mineralogical characteristics (Bamber et al., 2006):

- Contact ores with coarse grained metallic sulphides; Craig LGBX, TL Zone 2,
- Contact ores with disseminated sulphides within the host rock; Craig 8112, Fraser Ni, TL Zone 1,
- Footwall ores of narrow-vein high grade stringers containing high copper grades mostly in the form of massive pure sulphides: Fraser Cu, TL Footwall.

Table 1. Summary of the ore characteristics

Ore	Head Grades		Grain Size (mm)	Description
	Ni (%)	Cu (%)		
Fraser Copper	0.61	10.94	No discrete grains	<i>Mineralization:</i> Massive pure sulphides <i>Gangue:</i> Very minimal visual fine grained sulphides
Thayer Lindsley Footwall	1.24	8.14	No discrete grains	<i>Mineralization:</i> Massive pure sulphides <i>Gangue:</i> No visible sulphides
Craig LGBX	2.28	0.33	> 1	<i>Mineralization:</i> Coarse grained massive sulphides <i>Gangue:</i> No visible sulphide
Thayer Lindsley Zone 2	1.35	0.75	< 1	<i>Mineralization:</i> Coarse grained massive sulphides <i>Gangue:</i> No visible sulphide
Craig 8112	1.11	0.48	< 0.5	<i>Mineralization:</i> Coarse disseminated sulphides <i>Gangue:</i> No visible sulphide
Fraser Nickel	0.74	0.38	<0.1	<i>Mineralization:</i> Coarse disseminated sulphides <i>Gangue:</i> Minimal visual fine grained sulphides
Thayer Lindsley Zone 1	0.69	0.41	< 1	<i>Mineralization:</i> Coarse disseminated sulphides <i>Gangue:</i> Minimal visual fine grained sulphides

Each sample was screened into size fractions based on a $\sqrt{2}$ series. The size fractions started from a top size of 254 mm. Dense medium separation tests were conducted using a laboratory type closed-circuit vessel setup. Due to the limitations of the laboratory type DMS vessel, each ore was crushed so as to have a top particle size of 75 mm. DMS tests were conducted using a laboratory type dense media vessel. Ferro-silicon was used to adjust the separation density and was circulated through the vessel in closed circuit. The separation density in the vessel was controlled using a Marcy scale. The concentrate and waste products were weighed and assayed for nickel, copper and magnesium.

Results and discussion

Size assays

The size-assay of the crushed ore allows to identify the metal distribution and liberation data with respect to particle size fractions. This also reveals the size classes potentially available for direct rejection and the optimum cut-size for discrimination between waste material and metal enriched fractions. The observation of specific size fractions with apparently high metal grades would even allow implementation of simple screening as a possible pre-concentration tool.

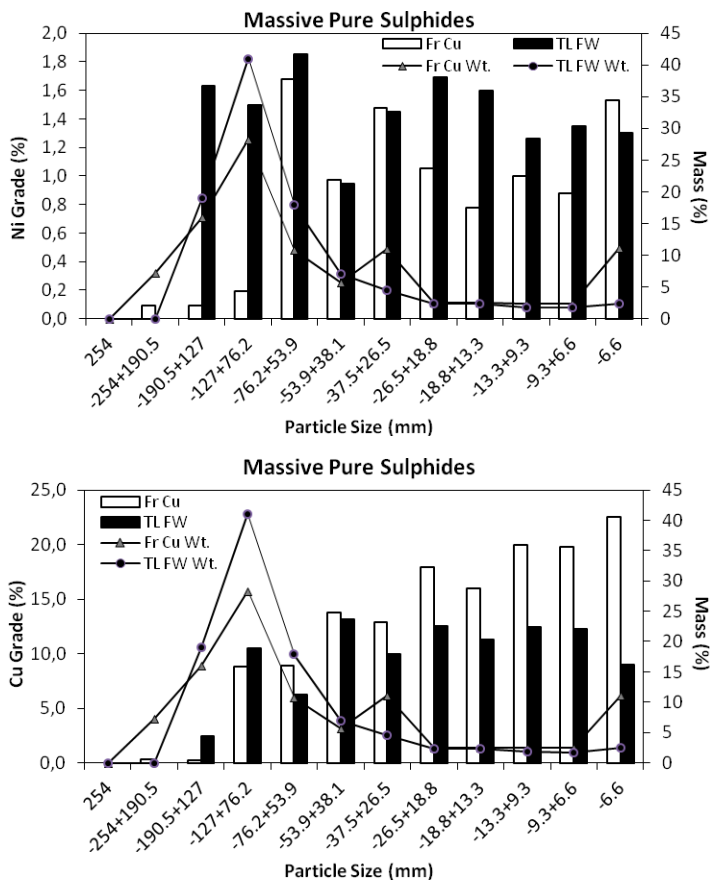


Fig. 1. Ni and Cu grade and size distribution for ores with massive pure sulphides

For the Fraser Copper and Thayer Lindsley Footwall ores, constituted of massive pure sulphide grains, nickel and copper enrichment towards finer fractions were seen. Higher grades at finer fractions were particularly clear for Fraser Cu (Fig. 1). The Ni grade in -53.9 mm fractions were higher than coarser sizes in Fraser Cu. Also for cop-

per, significant enrichment was identified for -76.2 mm fractions and Cu grades exceeding 20% were recorded. For TL Footwall, +127 mm fraction had a low Cu grade. In view of the size-assay values for both metals and considering the mass distributions, fractions coarser than 76.2 mm could be directly discarded for Fraser Cu ore. This corresponds to a mass rejection of more than 50% prior to the downstream processes. Also, +127 mm fraction is practically barren rock for TL Footwall ore and could be scalped of as waste. With a Cu grade of higher than 30%, direct addition of -26.5 mm fractions of Fraser Cu to the final flotation concentrate could be suggested.

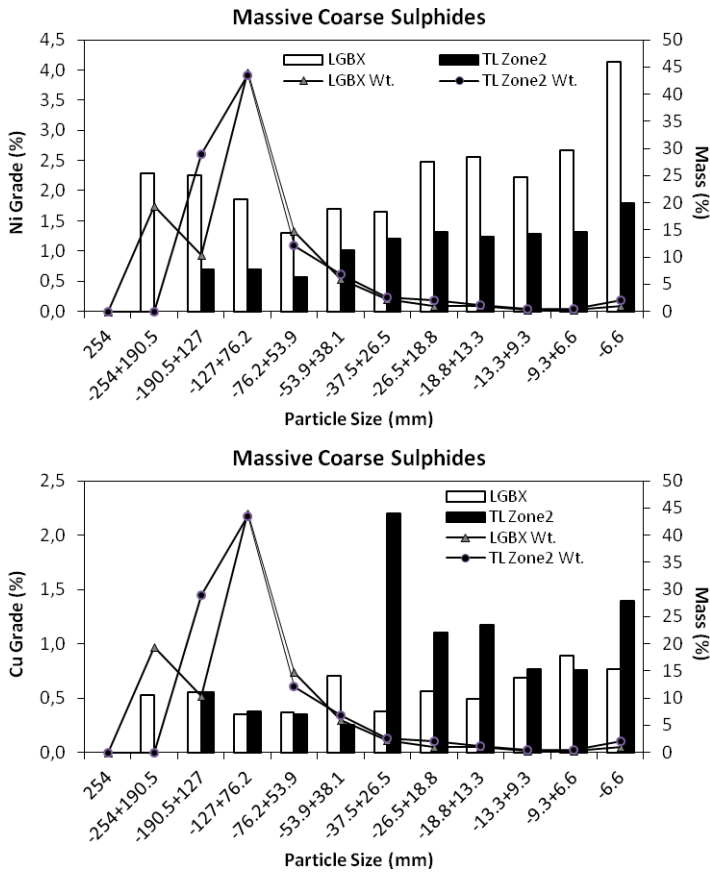


Fig. 2. Ni and Cu grade and size distribution for ores with massive coarse sulphides

For the LGBX and TL Zone 2 ores, characterized with massive coarse sulphide grains, Cu enrichment was seen for fractions finer than 37.5 mm. The Cu grades of the -37.5 mm fractions were particularly higher for TL Zone 2 ore (Fig. 2). For the same ore, there is a distinct increase in Ni grade in -53.9 mm fractions. Nickel assay in LGBX ore was more equally distributed across all size ranges except -6.6 mm fraction

(Fig. 2). Therefore a potential exists for rejection of coarser fractions of TL Zone 2 ore as waste, considering the delicate balance to recover both Ni and Cu values. Possible screening off +53.9 mm fractions corresponds to a huge mass rejection of around 85% where significant benefits would be expected.

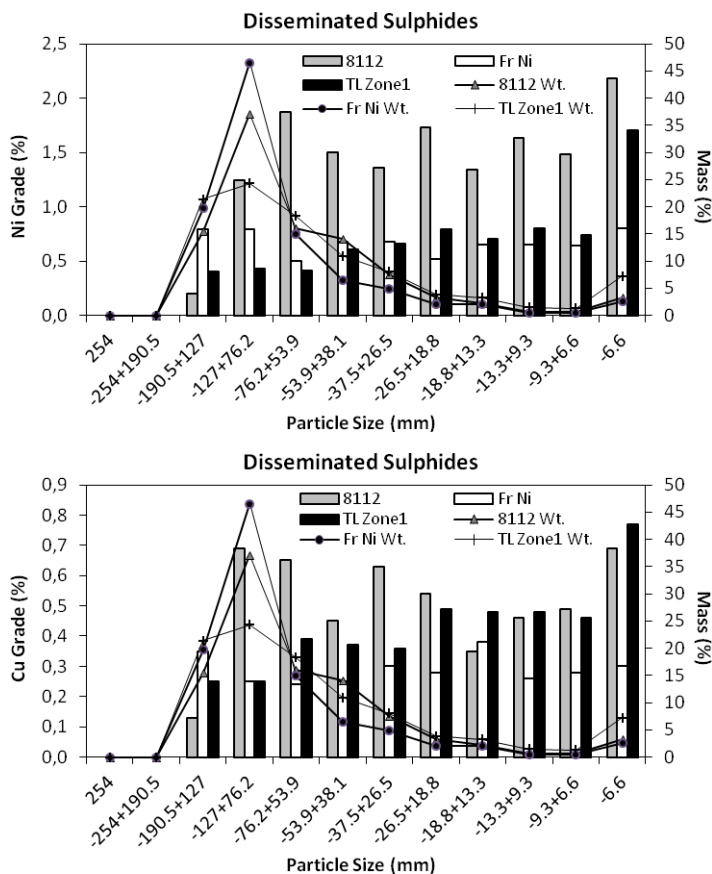


Fig. 3. Ni and Cu grade and size distribution for ores with disseminated sulphides

The ores with disseminated sulphides show relatively slight trend towards enriched fines (Fig. 3). Except -6.6 mm fraction, setting a distinct cut size is not likely particularly for Craig 8112 and Fraser Nickel ores. Only for TL Zone 1 ore, separation of +76.2 mm fractions would be sought, corresponding around 45% mass rejection with tolerable loss of metal values (Fig. 3).

The results illustrated that the ores with distinct metal sulphide mineralization provide a relatively higher trend towards enriched fines. Fraser Copper, a footwall ore with massive pure sulphides and TL Zone 2, a contact ore with massive coarse sulphide grains yielded the most promising results for size-based pre-concentration. With

these ores great extent of mass rejection was revealed with minor metal losses. All other ores with massive pure or coarse massive sulphides also showed significant potential for size-based early waste rejection. The results for ores with dissemination of metal sulphides showed relatively limited possibility for a size-based pre-concentration.

It should also be noted that regardless of ore type and mineralogy, metal enrichment in the finest fractions (-9.3+6.6 mm and -6.6 mm) were common almost for all ores. This is normally associated with the liberation of softer sulphides being readily susceptible to breakage and attrition from the host rock. Therefore, for all ores, screening of these finest fractions for by-passing into the flotation concentrates would be suggested.

DMS tests

Tables 2-4 present the results of the DMS tests with respect to ore mineralization classes. For each ore the change in the separation performances as a function of specific gravity of separation are also shown. Considering the primary objectives of pre-concentration as maximum rejection of gangue mineralization with minimum loss of metal values, i.e. with the highest possible metal recoveries, the importance of comparing different levels of separation specific gravities could be clearly understood. The results of DMS study were apparently favorable for Fraser Cu and TL Footwall ores (Table 2). For Fraser Cu, separation at both 2.9 and 3.1 yielded significant rejection of barren rock with Ni and Cu recoveries over 95 % in the concentrate.

Table 2. DMS results for ores with massive pure sulphides

Ore	Feed Grade (%)		Sep. SG	Conc. Mass (%)	Mass Rejection (%)	Concentrate Grade (%)		Recovery (%)	
	Ni	Cu				Ni	Cu	Ni	Cu
Fraser Cu	0.41	10.48	2.7	91	9	0.48	11.47	99.67	99.47
			2.9	47	53	0.84	22.01	96.01	97.95
			3.1	44	56	0.95	23.39	95.14	97.61
TL Footwall	1.19	6.99	2.7	88	12	1.35	7.92	99.93	99.85
			2.9	63	37	1.83	10.79	97.67	97.89
			3.1	59	41	1.98	11.68	96.76	96.90
			3.35	45	55	2.10	11.92	80.01	77.15

Waste rejection was slightly higher at 3.1 with similar metal recoveries in the concentrate. For TL Footwall ore, starting from 2.9 acceptable results were achieved with improved separation and waste rejection towards higher separation densities. Separation at 3.1 provided the most effective pre-concentration with 41% waste rejection and Ni and Cu recoveries around 97%. Further increase of the separation density to 3.35 caused reductions in nickel and copper recoveries (Table 2).

For ores with coarse massive sulphide grains, DMS results were also promising. At 2.95, more than 30% of the feed could be discarded as waste with a concentrate of more than 97% Ni and 81% Cu recoveries. Mass rejection was further increased to around 50% by shifting the separation density to 3.1. At this level Ni recovery remained almost similar, but Cu recovery decreased by around 10%. For TL Zone 2, Ni and Cu recoveries exceeding 95% were achieved at 2.9, but only one quarter of the feed could be discarded. Increasing the separation density to 3.1 significantly enhanced waste rejection up to 43% with a high Ni ($\approx 93\%$) and an acceptable Cu ($\approx 88\%$) recovery in concentrate (Table 3).

Table 3. DMS results for coarse massive sulphides

Ore	Feed Grade (%)		Sep. SG	Conc. Mass (%)	Mass Rejection (%)	Concentrate Grade (%)		Recovery (%)	
	Ni	Cu				Ni	Cu	Ni	Cu
LGBX			2.8	84	16	2.90	0.34	98.84	92.55
	2.46	0.31	2.95	68	32	3.52	0.38	97.18	81.55
			3.1	51	49	4.65	0.44	95.65	71.14
TL Zone 2			2.7	97	3	1.33	0.88	99.90	99.75
	1.29	0.86	2.9	74	26	1.70	1.11	97.73	95.65
			3.1	57	43	2.11	1.33	92.78	87.78

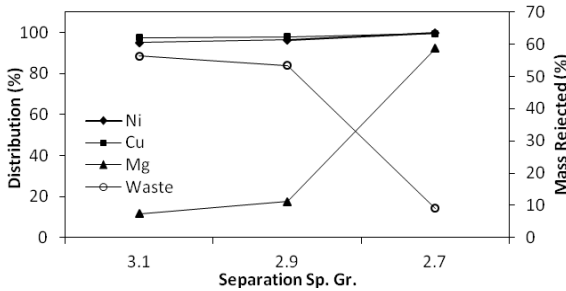
Table 4. DMS results for disseminated sulphides

Ore	Feed Grade (%)		Sep. SG	Conc. Mass (%)	Mass Rejection (%)	Concentrate Grade (%)		Recovery (%)	
	Ni	Cu				Ni	Cu	Ni	Cu
8112			2.8	94	6	1.17	0.54	98.88	98.79
	1.12	0.51	2.95	86	14	1.27	0.57	97.63	96.68
			3.1	47	53	2.12	0.93	89.39	85.41
Fraser Ni			2.7	99	1	0.68	0.40	99.87	99.87
	0.68	0.41	2.9	52	48	1.08	0.64	82.80	83.24
			3.1	21	79	1.49	0.87	45.43	45.62
TL Zone 1			2.7	99	1	0.69	0.39	99.98	99.90
	0.69	0.39	2.9	80	20	0.82	0.45	95.40	92.67
			3.1	46	54	1.23	0.63	81.21	73.77

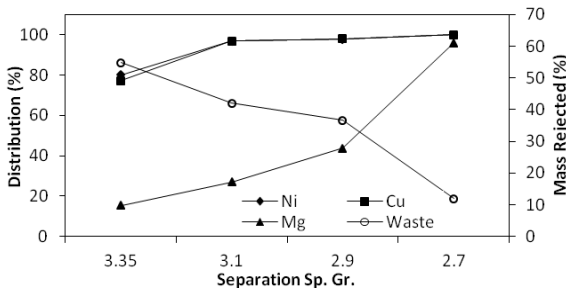
Although the separation results for the ores with disseminated sulphides can not be noted as unsatisfactory, the success of the process was relatively limited for these ores from the pre-concentration perspective. For 8112 and TL Zone 1, the nickel and copper recoveries exceeded 90% in the concentrate product when the separation was conducted at 2.95 and 2.9, respectively. However, at these separation densities mass rejection remained fairly low for both ores (Table 4). For 8112, pre-concentration could be justified at 3.1 with more than 50% mass rejection and Ni recovery close to 90% and

Cu recovery more than 85% in the concentrate. For TL Zone 1, separation at 3.1 could also yield significant mass rejection at 54%, but with lower Ni and Cu recoveries as 81.21 % and 73.77 %, respectively. At a separation density of 2.9, Fraser Ni provided similar results to TL Zone 1 in terms of mass rejection and metal recoveries. Further increase of separation density to 3.1 dramatically decreased Ni and Cu recoveries to 45% for Fraser Ni (Table 4).

Another benefit of DMS was recognized as reduced Mg in the concentrate products. The adverse effect of Mg bearing minerals and particularly talc is obvious in the flotation based beneficiation of metallic sulphides. Potential rejection of these minerals, therefore, corresponds to increased metallurgical performance in the downstream processes. The change of Mg and metal recoveries as a function of separation density was assessed and the results are presented in Figs 4–6.



Fraser Cu				
Sep SG	Mass Reject (%)	Mg Grade (%)		Mg Rec. (%)
		Feed	Conc.	
2.7	9	1.85	1.85	92.15
2.9	53	1.83	0.69	17.49
3.1	56	0.48	0.48	11.54



TL Footwall				
Sep SG	Mass Reject (%)	Mg Grade (%)		Mg Rec. (%)
		Feed	Conc.	
2.7	12	1.62	1.62	95.94
2.9	37	1.49	1.03	43.68
3.1	41	0.69	0.69	26.87
3.35	55	0.51	0.51	15.42

Fig. 4. Mg and metal recoveries for massive pure sulphide mineralogy

For the ores characterized with a massive pure sulphide mineralogy, a significant fraction of Mg was rejected at the optimum densities of separation, i.e. a concentrate product with high metal recoveries and low Mg content could be achieved at acceptable levels of waste rejection. For Fraser Cu, the concentrate product of 2.9 included only 17.49% of Mg from the feed while the Ni and Cu recoveries were over 96 %. Mg in the concentrate of 3.1 was as low as 11.54% and the metal recoveries were still high (Fig. 4). For Thayer Lindsley Footwall ore separation at 2.9 provided rejection of

more than half of the Mg with the waste. The shift of separation density to 3.1 yielded even better results. The Mg recovery in the concentrate decreased to around 27% with almost no metal loss and increased extent of waste rejection (Fig. 4). Separation at 3.35 provided further reduction of Mg in the concentrate, but at the expense of decreases in Ni and Cu recoveries.

DMS also favored Mg rejection for Craig LGBX and Thayer Lindsley Zone 2 ores which were specified by coarse grained massive sulphides. With a separation at 2.95, around 68% of Mg could be discarded with the waste (Fig. 6). Mg rejection at 3.1 was twice as high (% 34.19) at an improved mass rejection of 49%. At both separation densities, nickel recoveries remained quite significant. For TL Zone 2, Mg rejection at 2.9 and 3.1 were relatively lower than LGBX (Fig. 5). However, separation at 3.1 provided optimum results in terms of all criterions considered for possible implementation of pre-concentration. At this separation density, the concentrate included 48% Mg with significant Ni and Cu recoveries and 43% of feed could be discarded (Fig. 5).

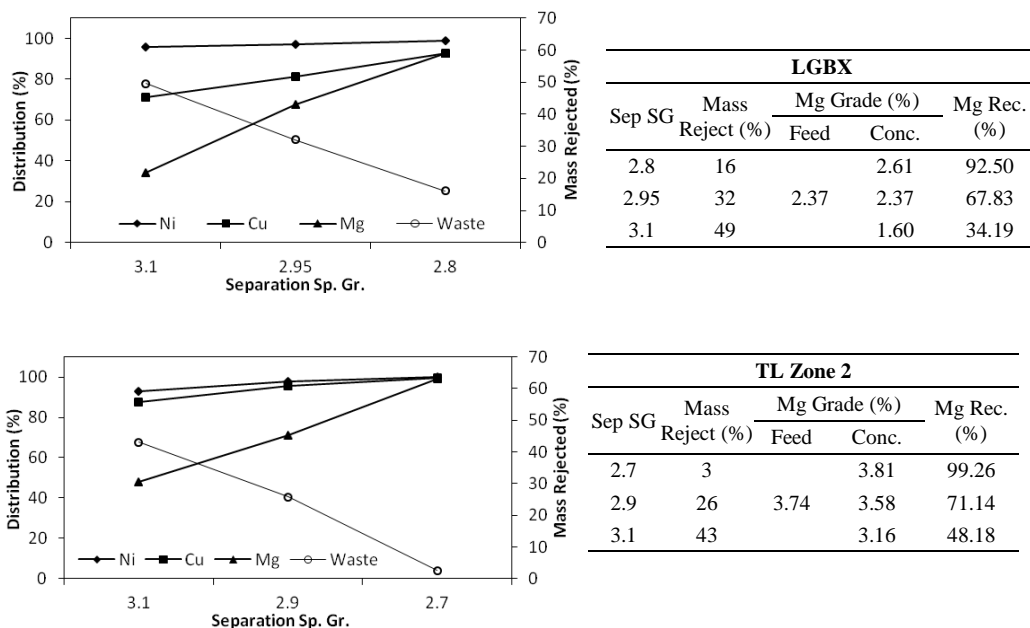


Fig. 5. Mg and metal recoveries for ores with coarse sulphide grains

For the ores categorized with disseminated sulphide inclusions, the results were rather fluctuating. Overall, separation at the highest specific gravity (3.1) provided the highest Mg rejection for all three ores. It should also be noted that a shift of separation density from the mid-level to 3.1 dramatically increased the amount of waste discarded (Fig. 6). However, it is not likely that separation at 3.1 would be justified with respect to only Mg rejection as the metal recoveries remained fairly low at this specific gravity particularly for Fraser Nickel ore. With respect to all parameters considered for

pre-concentration, Craig 8112 provided the most promising results with significant rejection of Mg and waste associated with acceptable levels of metal distributions in the concentrate at a separation specific gravity of 3.1 (Fig. 6).

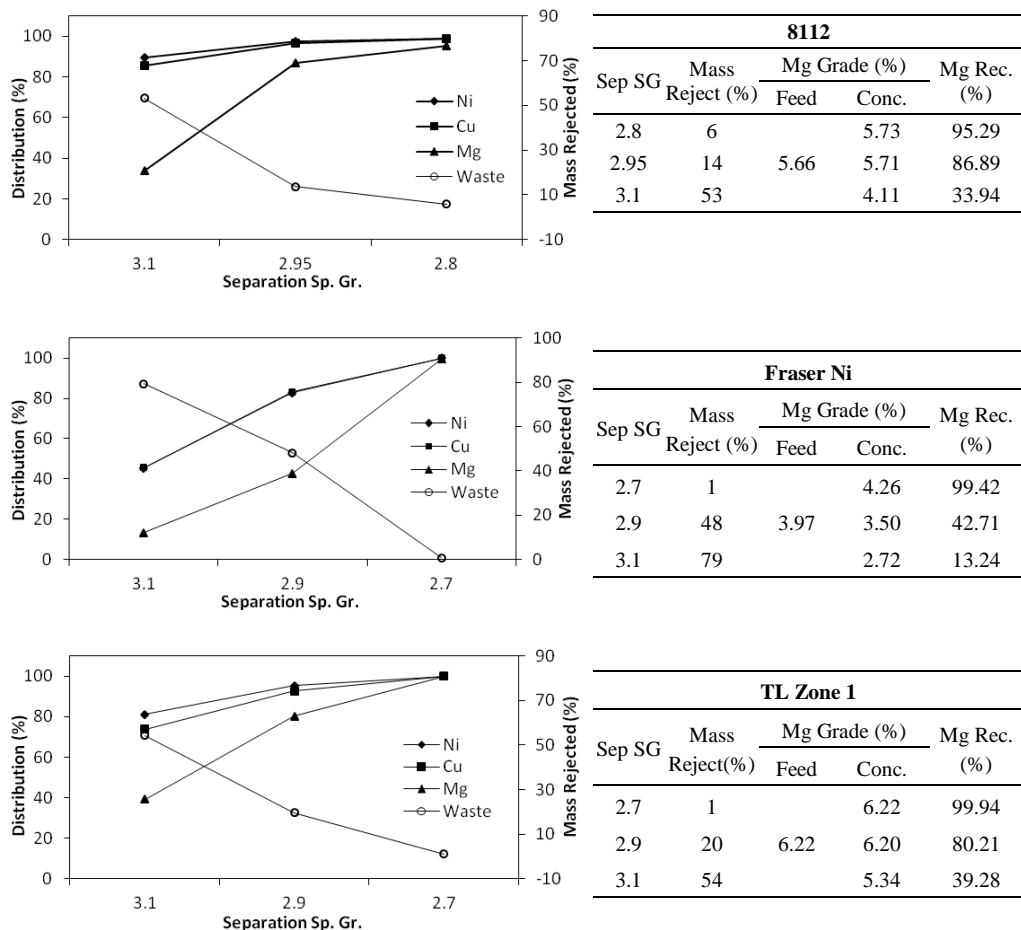


Fig. 6. Mg and metal recoveries for ores with disseminated sulphides

An overall evaluation yielded that rejection of Mg bearing entities with the waste product was closely related with the mineralogy of the ores tested. In the ores with massive pure metallic sulphides, pre-concentration by DMS resulted in a distinct separation between high-density metal-rich entities and lower density Mg-including barren part. Enhanced Mg rejection, with a higher mass rejection as the specific gravity of separation was increased, confirms this observation. Further, slight changes in the metal distributions in the concentrates as a function of the specific gravity of separation reveals that a favorable liberation could be achieved in this type of mineralogy,

i.e. metallic sulphides occurring as free entities with no or little association of Mg bearing minerals and gangue. This is an important indication directly pointing to the amenability of the ore to pre-concentration and potential for waste rejection prior to downstream processes. The same conclusions could be derived for the ores characterized with coarse massive sulphide grains, despite lower extent of Mg rejection with the waste. Significant liberation between the nickel and copper bearing sulphide grains and gangue would be possible. This provides a concentrate with favorable metal recovery, reduced Mg content at a justifiable level of mass rejection from the pre-concentration perspective. For the ores with the disseminated sulphides, a potential for early rejection of waste and specifically Mg bearing entities could still be sought, as revealed for the Craig 8112 ore. However, the amenability for pre-concentration for disseminated metallic sulphides mineralogy is relatively lower as the separation was not as distinct. An attempt to enhance mass rejection by increasing the specific gravity of separation could further increase rejection of gangue and Mg bearing entities, but resulted in subsequent loss of nickel and copper in the concentrate. This observation and lower effectiveness of pre-concentration was attributed to the disseminated form of metallic sulphides, obstructing a favorable liberation between the mineralized portions and gangue. Disseminated form of metallic sulphides would be anticipated to correspond to a higher degree of gangue associations with nickel and copper bearing sulphides.

Conclusions

All the ores tested in this study showed amenability to pre-concentration at varying levels. The effectiveness of pre-concentration, either size-based or by DMS, was linked to the occurrence modes of metallic and gangue portions. It was seen that ore mineralogy should be in favour of pre-concentration. Ores with massive pure sulphides and coarse sulphide grains, i.e. with clear differentiation between valuable mineralization and gangue, yielded an effective liberation of nickel and copper bearing entities and successful separation through DMS subsequently. Ores with disseminated form of metallic values provided relatively lower mass rejection and metal recoveries and being more sensitive to the specific gravity of separation. A potential for discarding Mg bearing minerals with early waste rejection was also identified. The significance of Mg-rejection was also related with ore mineralogy. Almost for all ores, Mg showed an apparently different separation curve from nickel and copper. Ores with distinctive metallic sulphides provided high levels of separation and a clear differentiation between valuable mineralization and gangue with Ni and/or Cu rich concentrates and Mg rich waste products. Overall, despite the variation of the performance of the ores tested, high metal recoveries with significant mass rejection could be realized through further refinement of the process.

References

- BAMBER A.S., KLEIN B., SCOBLE M.J., 2006, *Integrated Mining and Processing of Massive Sulphide Ores*, Proceedings, 39th Annual General Meeting of the Canadian Mineral Proc., Ottawa, 01/2006.
- FEASBY D.G., TREMBLAY G.A., 1995, *Role of Mineral Processing in Reducing Environmental Liability of Mine Wastes*, Proceedings, 27th Annual CMP Meeting, Ottawa, 218–231.
- FIEDLER K.J., MUNRO P.D., PEASE J.D., 1984. *Commissioning and operation of the 800 t/h heavy medium cyclone plant at Mount Isa Mines Limited*. Pro. Australasian Institute of Mining and Metallurgy, Darwin, Australia 1984. C41–C49.
- HINDE A.L., FRANKENHAUSER R.M., KRAMERS C.P., 1986, *The Benefits of Reducing the Transport, Hoisting and Processing of Barren Rock in Witwatersrand Gold Mines*, Proceedings of the SAIMM International Conference on Gold, 333–343.
- LLOYD P.J.D., *An Integrated Mining and Extraction System for Use on Witwatersrand Gold Mines*, Journal of the SAIMM, Vol. 79, January 1979.
- KLEIN B., DUNBAR W.S., SCOBLE M., 2002, *Integrating Mining and Mineral Processing for Advanced Mining Systems*, CIM Bulletin, Vol. 95, No. 1057, 63–68.
- KLEIN B., HALL R., SCOBLE M., MORIN M., 2003, *Total Systems Approach to Design for Underground Mine-Mill Integration*, CIM Bulletin, Vol. 97, No. 1067, 65–71.
- LLOYD P.J.D., VAN DER WALT J., *Critical Issues in Gold Mining: An Independent View*, Proceedings of the International Conference on Gold, SAIMM, Johannesburg 1986.
- MILLER V.R., NASH R.W., SCHWANEKE A.E., 1978. *Pre-concentration of Native Copper and Porphyry Copper Ores by Electronic Sorting*. Mining Engineering 1978:1194-1201.
- MUNRO P.D., SCHACHE I.S., PARK W.G., WATSFORD R.M.S., 1982. *The Design, Construction, and Commissioning of a Heavy Medium Plant for Silver-Lead-Zinc Ore Treatment – Mount Isa Mines Limited*. XIV International Mineral Processing Congress. Toronto, 1982: 2–21.
- PETERS O., SCOBLE M., SCHUMACHER T., 1999, *The technical and economic potential of mineral processing underground*. Annual General Meeting, Can. Inst. Min. Metall., Calgary, CD ROM.
- SALTER J.D., WYATT N.P.G., 1991, *Sorting in the Minerals Industry: Past, Present and Future*, Minerals Engineering, Vol 4, No 7–11, 779–796, 1991.
- SCHENA G.D., GOCHIN R. J., FERRARA G., 1990, *Pre-concentration by dense-medium separation – an economic evaluation*, Trans. Instn. Min. Metall. (Sect. C: Mineral Process. Extr. Metall.), 99, January-April 1990, C21–C31.
- SCOBLE M., KLEIN B., DUNBAR W.S., 2000, *Mining waste: Transforming mining systems for waste management*, 6th Int Conf on Environmental Issues and Mining Production, Calgary, 333–340.
- VATCHA M.T., COCHRANE L.B., ROUSELL D.H., 2000, *Pre-concentration by magnetic sorting of Ni–Cu ore at Whistle mine, Sudbury, Canada*, Mineral Processing and Extractive Metallurgy, Volume 109, Number 3, 156–160 (5).

Received May 30, 2013; reviewed, accepted July 23, 2013

APPLICATION OF MODIFIED CALCIUM SORBENTS IN CARBONATE LOOPING

Michalina KOTYCZKA-MORANSKA, Grzegorz TOMASZEWICZ

Institute for Chemical Processing of Coal, Zamkowa 1, 41-801 Zabrze, Poland, mmoranska@ichpw.zabrze.pl

Abstract: Reduction of CO₂ emission is essential. In this paper, a study of the behaviour of modified Polish CaO-based sorbents during calcium looping cycles has been discussed. All the related tests were conducted using the Netzsch STA 409PG Luxx thermogravimetric analyser. Samples with a weight of $m_s=10.0\pm 0.1$ mg were placed in an Al₂O₃ crucible. The calcium looping processes were performed at the carbonation temperature of 650°C and the calcination temperature of 900°C. Additionally, calcination-carbonation cycles with different gas flows were examined. The authors investigated the influence of CO₂ concentration and total gas flow on the carbonation conversion. Sorbents were studied by TG and porosimetry analysis.

Keywords: *calcium looping, CO₂ capture, CaO-based sorbents*

Introduction

It is commonly known that the rising emission of greenhouse gases causes deterioration of the global environment. In order to maintain a balanced living surrounding, mankind must control the emission of CO₂, being the main component of greenhouse gases, into the atmosphere (Wang and Lee, 2009). Using chemically and physically modified CaO samples in the Calcium Looping Process can be a good opportunity to enhance the CO₂ capture. Intensive research has been carried out to improve the performance of CaO-based sorbents by enhancing the CaO conversion and reducing the performance decay. It is expected that the use of modified sorbents will facilitate increasing the effectiveness of the CO₂ capture and improve sorbents parameters. Application of different methods aimed at increasing porosity and surface area of sorbents to enhance the conversion is a very interesting option. A carbonation process takes place in micropores, on mesopores and on grain boundaries (Bouquet et al., 2009; Manovic and Anthony, 2008). Carbonation in micropores proceeds up to pore filling. The CO₂ capture efficiency depends on many parameters, e.g. diffusion resistance, which depends on the size of the sorbent particles, volume and the pore

structure as well as the surface size and reaction kinetics (Hughes et al., 2004). Under numerous studies, the CaCO_3 layer diffusion rates as a function of CO_2 pressure, temperature and CaCO_3 porosity were examined (Mess et al., 1999). Also Oakeson and Culter (1979) studied nonporous sorbents, and their results confirmed a parabolic particle size. They formulated a law independent of the reaction rate. The particle size of pore and surface area changed in every run of the process. They also found that the CO_2 pressure has a major effect on the process rate (Oakeson et al., 1979). Bhatia and Perlmutter (1983) modelled limestone using a random pore model and found that the diffusion controlled stage was independent of the CO_2 pressure. They assumed that the carbonate product layer formed concentric shells parallel to the initial gas.

Sun et al. (2007) describe a mechanism of the limestone reactivity loss during consecutive cycles related to the changes in its porosity. They distinguish between two types of pores: the smaller ones (<200 nm) as type 1 and the larger ones (> 200 nm) as type 2. The authors claim that some of pores of the second type have also contributed to the formation of pores of the second one by sintering together. This way, the volume of pores associated with the surface of the type 1 pore is decreasing and the surface associated with the second type of pores is increasing. Having seen that the reactivity of the sample carbonation shows good correlation with the porosity of the first type, a model has been developed to predict the sorbent reactivity after a few cycles. This model, however, does not include the sample's residual activity, and in a later publication (Sun et al., 2008), the authors claim that some of the pores of the second type have also contributed to the reactivity of the sorbent. Unfortunately, this mechanism is difficult to apply in sintering of sorbents, characterised by monomodal pore distribution at the boundary between pores of the first and the second type, while during subsequent cycles, a bimodal pore size distribution is observed with the first type of pores, approaching the size of 85 nm, whereas the type 2 pore diameter is slowly increasing.

One of the solutions applied to modify sorbents is thermal pre-treatment. In their paper, Kotyczka-Moranska et al. (2011) provided a review of the known studies on the sorbent sintering. Another method of the Ca-based sorbent modification was presented in a paper by Yin et al. (2012). The authors examined reactivation of calcium based sorbents by means of ultrasounds. Application of ultrasounds during chemical reactions is referred to as sonochemistry. During the propagation of ultrasounds in a solution, microscopic bubbles filled with water vapour or gas are forming. In the next phase of the process, the bubbles implode, and this process is known as cavitation. During cavitation, "hot-spot" microareas, as they are referred to, may be formed, and the pressure inside them rises up to 500 bar and the temperature is up to 5,200 K. Ultrasounds within the frequency range of 100 kHz–1 MHz cause that average cavitation bubbles take part in sonochemical reactions. The greatest advantage of the ultrasound application is that the process can be conducted at room temperature in the presence of ultrasounds, even though the reaction normally takes place at high temperatures. Another method used in the aforementioned study for the sake of the

sorbent modification involved application of hydrochloric acid whose function was to increase the sorption capacity (expressed by an increase in the degree of carbonation). By binding calcium and magnesium in salts, the hydrochloric acid catalysed the cyclic reactions of carbonation and calcination.

The aim of this research was to modify natural calcium sorbents by different methods known from the literature, to determine their sorption parameters during the CO₂ capture process and to compare the methods analysed.

Preparation of samples and experimental systems

The authors of this paper investigated natural Polish mineral sorbents and modified mineral sorbents: raw limestone from Czatkowice, heat-treated limestone from Czatkowice, chlorine-modified limestone from Czatkowice, limestone modified with ultrasounds and HCl from Czatkowice and dolomites from Siewierz.

Application of ultrasounds in a commercial technology generally requires that an additional ultrasonic reactor should be used and the reactivated sorbent should be cooled. The Siewierz dolomites studied were modified in two ways: by rinsing in hydrochloric acid and by using both rinsing and ultrasounds in order to increase the reaction velocity and efficiency. Two hydrochloric acid concentrations were applied: 0.1 and 0.2 mol/dm³. The sorbents were immersed in hydrochloric acid and a half of them was modified with ultrasounds for 1 minute. The Czatkowice limestone was modified with ultrasounds in a water bath for 1 minute. After the modification, sorbents were dried for 48 hours at the temperature of 40° C. All tests were conducted using the STA 409PG Luxx thermogravimetric analyser (by Netzsch). Samples with a mass of $m_s = 10.0 \pm 0.1$ mg were placed in an Al₂O₃ crucible. The measurements were conducted at 650° C (carbonation temperature) and 900° C (calcination temperature), with gas flow rates of 50 cm³/min and at the CO₂ concentration of 50%. SEM figures were obtained using the Nova NANOSEM 200 scanning electron microscope (by FEJ EUROPE). The mercury porosimetry was investigated by means of Autopore IV 9500. The sample was degassed in a vacuum bellows of 100 μm for 5 minutes.

Results and discussion

Physicochemical modification of sorbents

Results of our experiments have been presented in Fig. 1 and 2. Figure 1 shows a comparison of results of consecutive carbonation and calcination cycles for raw limestone from Czatkowice, modified by means of ultrasounds and chlorine. As shown, the sorbent modified with chlorine significantly contributes to the deterioration of its performance in successive cycles, and the sorbent reactivation with ultrasounds enhances its activity, but the ratio between the amount of CO₂ absorbed in the dynamic and the static part of the carbonation process is inferior compared to the raw material.

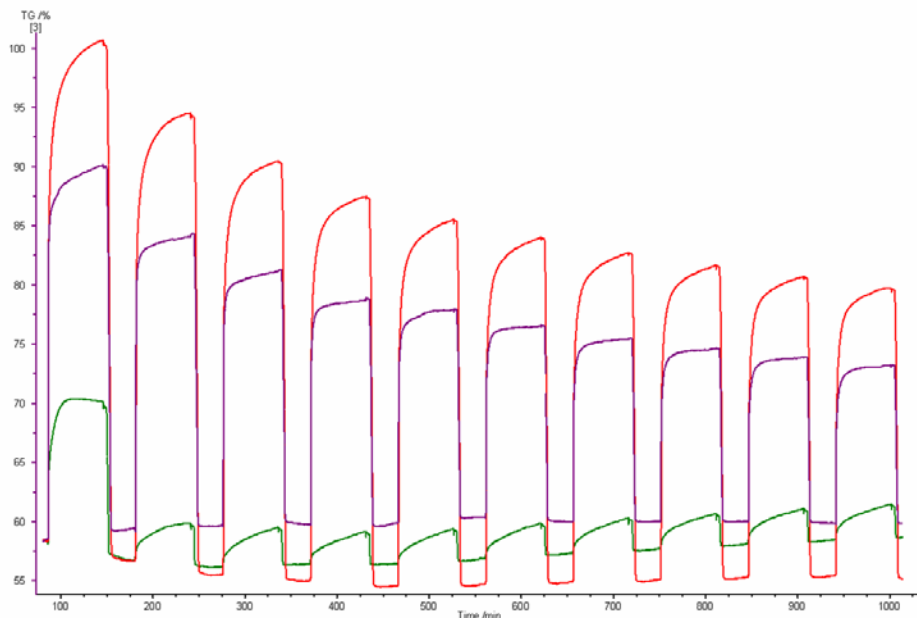


Fig. 1. Comparison of mass changes following the carbonation and calcination cycles for raw limestone from Czatkowice (red), ultrasound-modified limestone from Czatkowice (purple) and chlorine-modified limestone from Czatkowice (green)

Figure 2 illustrates a comparison of results of the consecutive carbonation and calcination cycles for the Siewierz dolomite modified with HCl in the presence of ultrasounds and that treated with HCl only. Both experiment configurations were conducted for two hydrochloric acid concentrations of 0.1 and 0.2 mol/dm³.

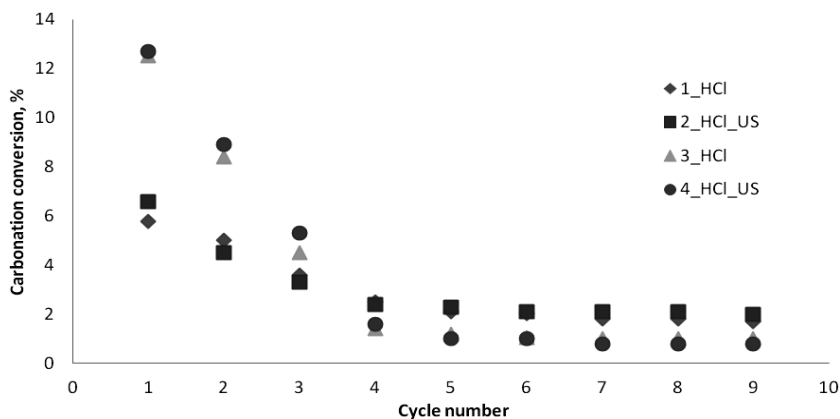


Fig. 2. Comparison of carbonation conversion degrees in consecutive carbonation and calcination cycles for dolomite from Siewierz modified with HCl and with HCl in the presence of ultrasounds (HCl_US).

Series 1 and 2 were obtained for the hydrochloric acid concentration of 0.2 mol/dm³ and series 3 and 4 for the concentration of 0.1 mol/dm³

The only result of applying the concentration of 0.2 mol/dm^3 is a lower degree of carbonation in the first cycles. The approximate degree of carbonation of modified sorbents in three cycles is comparable. The application of ultrasounds did not significantly impact the ability to bind CO_2 in the dolomite. No significant effect of the ultrasound application is probably due to the fact that the reaction between HCl and the sorbent is characterised by a very high velocity, thus the application of ultrasounds could not affect the increase in the acid penetration of the pores. However, the experimental results show no increase in the sorption capacity of the dolomite in subsequent cycles of the study.

Thermal modification of sorbents

According to the recent knowledge, thermal heating of sorbents is yet another method of their modification. In our previous experiments, pre-sintering of natural sorbents at 1000°C resulted in a significant conversion drop in the first CO_2 -capture reaction followed by enhancement throughout ~ 10 cycles. As already discussed in the authors' previously published paper (Kotyczka-Moranska et al., 2011), the decrease in the carbonation conversion is probably associated with sintering of the sorbent's active surface. In this paper, the authors have presented results of the structure examinations for thermally pre-treated sorbents. Figs 4 and 5 illustrate the morphology of raw (A) and thermally modified sorbents (B).

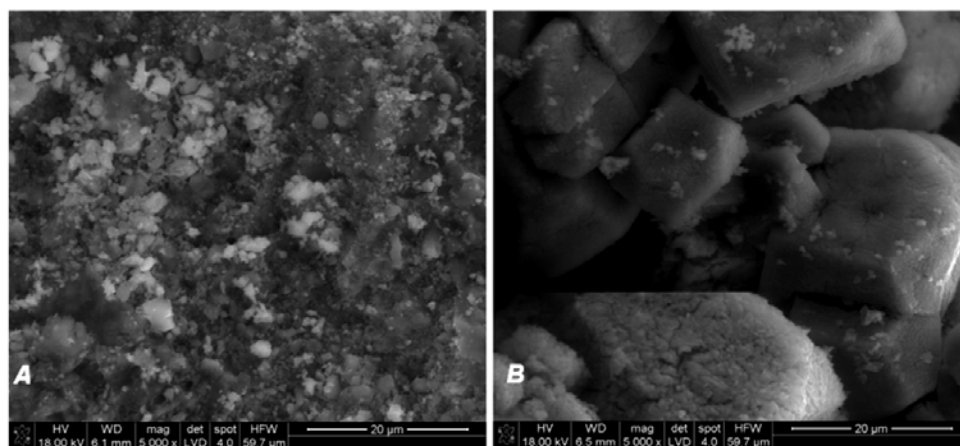


Fig. 3. SEM photo of raw (a) and thermally pre-treated (b) limestone

Manovic and Anthony (2008) have claimed that, after heating the sorbent, the surface is composed of large grains and pores of the order of $1 \mu\text{m}$. They have similar dimensions and smooth surfaces which mean that small pores have been eliminated by heating and consequently the number of large pores has increased. It is consistent with the SEM photos provided in Figs 3 and 4 as well as results of the mercury porosimetry (Fig. 5).

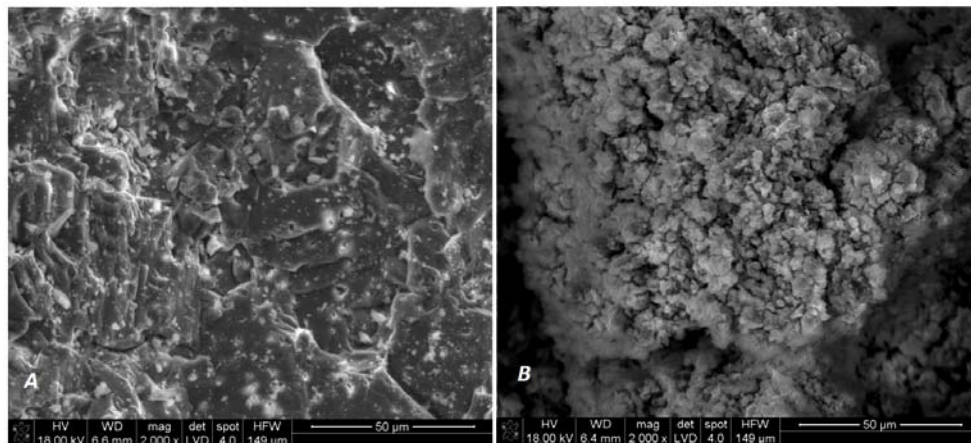


Fig. 4. SEM photos of raw (a) and thermally pre-treated (b) dolomite

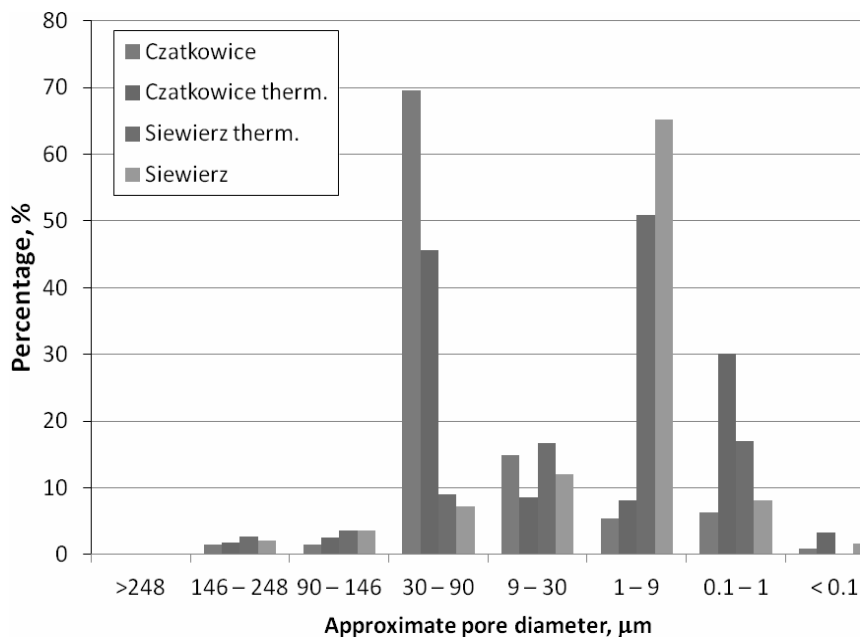


Fig. 5. Approximate pore diameter of the sorbents examined

Table 1 contains results of the mercury porosimetry testing of raw and sintered sorbents. One may clearly notice that, in both cases, the total pore area increases and the bulk density is reduced after the thermal pre-treatment for the Czatkowice limestone and the Siewierz dolomite examined. The median pore diameter clearly increases slightly for the Czatkowice limestone and the Siewierz dolomite as well.

Table 1. Results of porosimetry testing of raw and sintered sorbents

Parameter	Unit	Sorbent tested			
		Czatkowice	Czatkowice therm.	Siewierz	Siewierz therm.
Total Intrusion Volume	cm ³ /g	0.2889	0.9239	0.3173	0.6376
Total Pore Area	m ² /g	0.476	7.917	1.042	1.724
Median Pore Diameter (Volume)	μm	24.73	30.13	4.15	5.86
Bulk Density at 0.43 psia	g/cm ³	1.50	0.73	1.41	1.01
Apparent (skeletal) Density	g/cm ³	2.66	2.24	2.57	2.83
Porosity	%	43.48	67.47	44.93	64.36

Unfortunately, based on results provided, it is difficult to state what the exact amount of type 1 pores is. Because of that, one can only infer conclusions about the changes to the pore structure of the sorbents tested from the fluctuations in the number of pores of the second type. As for the raw limestone sorbent from Czatkowice, the number of pores of less than 1 μm in size was smaller than in preheated sorbent. In the case of preheated limestone, there was a significant increase in the number of pores in the category of less than 1 μm, which may suggest an inclination towards monomodal distribution of pores at the boundary between pores of the first and the second type. This conclusion is supported by a drastic decrease in the activeness of the preheated sorbent (Kotyczka-Moranska et al., 2011).

Conclusions

The purpose of the authors' study was to determine the best way to modify mineral CO₂ sorbents for calcium looping processes. Taking the results presented into consideration, one may claim that the most interesting modification method is the application of ultrasounds. All attempts to modify the sorption parameter of sorbents by applying chlorine have failed. A thorough analysis has led the authors to a conclusion that chlorine salts do not perform the function of a framework in modified sorbents. This phenomenon occurred in both the sorbents studied, i.e. limestone and dolomite. The next step in the research will be testing of the influence ultrasounds exert on parameters of sorbents. This paper also provides a discussion on the effects of preheating on the morphology of sorbents. One may notice that the results provided reflect the phenomenon known from the literature, i.e. sintering of pores on the surface of sorbents.

Acknowledgements

The research presented herein was conducted in the course of the project entitled "Development of coal gasification technology for high-efficiency production of fuels and energy", Task No. 3 of the Strategic

Programme for Research and Development: “Advanced energy generation technologies” funded by the National Centre for Research and Development, Poland.

References

- BHATIA S., PERLMUTTER D., 1983, *Effect of the product layer on the kinetics on the CO₂-lime reaction*, *AICHe J.*, 29, 79–86.
- BOUQUET E., LEYSSENS G., SCHONNENBECK C., GILOT P., 2009, *The decrease of carbonation efficiency of CaO along calcination–carbonation cycles: Experiments and modeling*, *Chem. Eng. Sci.*, 64, 2136–2146.
- HUGHES R., LU D., ANTHONY E., WU Y., 2004, *Improved long-term conversion of limestone-derived sorbents for in situ capture of CO₂ in a fluidized bed combustor*, *Ind. Eng. Chem. Res.*, 43, 5529–5539.
- KOTYCZKA-MORANSKA M., TOMASZEWICZ G., LABOJKO G., 2011, *Comparison of different methods for enhancing CO₂ capture by CaO-based sorbents – review*, *Physicochem. Probl. Miner. Process.* 48(1), 77–90.
- MANOVIC V., ANTHONY E., GRASA G., ABANADES J., 2008, *CO₂ Looping Cycle Performance of a High-Purity Limestone after Thermal Activation/Doping*, *Fuel*, 87, 3344–3352.
- MESS D., SAROFIM A., LONGWELL J., 1999, *Product layer Diffusion during the Reaction of Calcium Oxide with Carbon Dioxide*, *Energy & Fuels*, 13, 999-1005.
- OAKESON W., CULTER I., 1979, *Effect of CO₂ pressure on the reaction with CaO*, *J. Am. Ceram. Soc.* 62, 556-558.
- SUN P., GRACE J., LIM C., ANTHONY, E., 2007, *The effect of CaO sintering on cyclic CO₂ capture in energy systems*. *AICHe Journal*, 53 (9), 2432–2442.
- SUN P., LIM C., GRACE J., 2008, *Cyclic CO₂ capture by limestone-derived sorbent during prolonged calcination/carbonation cycling*. *AICHe Journal*, 54(6), 1668–1677.
- WANG M., LEE C., 2009, *Absorption of CO₂ on CaSiO₃ at high temperatures*, *Energy Conv. Mgmt* 50, 636–638.
- YIN J., ZHANG C., QIN C., LIU W., AN H., CHEN G., FENG B., 2012, *Reactivation of calcium –based sorbent by water hydration for CO₂ capture*, *Chem. Eng. J.* 108–199, 38-44.

Received May 31, 2013; reviewed; accepted July 23, 2013

SYNTHESIS OF HYDROXYAPATITE IN THE PRESENCE OF ANIONIC SURFACTANT

**Agnieszka KOŁODZIEJCZAK-RADZIMSKA^{*}, Marlena SAMUEL^{*},
Dominik PAUKSZTA^{*}, Adam PIASECKI^{**}, Teofil JESIONOWSKI^{*}**

^{*} Poznan University of Technology, Institute of Chemical Technology and Engineering, Faculty of Chemical Technology, M. Skłodowskiej-Curie 2, PL-60-965, Poznan, Poland; e-mail: Agnieszka.Kolodziejczak-Radzimska@put.poznan.pl

^{**} Poznan University of Technology, Faculty of Mechanical Engineering and Management, Institute of materials Science and Engineering, Jana Pawła II 24, PL-60-965, Poznan, Poland

Abstract: Hydroxyapatite was synthesized by precipitation method using an anionic surfactant (SDS) template, at ambient temperature and normal pressure. Phosphoric acid and disodium phosphate were used as a precursor of phosphorous, whereas calcium hydroxide and chloride were used as a precursor of calcium. The obtained hydroxyapatite was subjected to a wide range of physicochemical analysis using various measurement techniques. In order to get information about the properties of the obtained products, the following analysis of characteristics was performed: dispersion (NIBS), morphological (SEM), adsorptive (BET) and structural (XRD). Energy-dispersive X-ray spectroscopy and elemental analysis were also applied.

Keywords: *hydroxyapatite, precipitation, anionic surfactant*

Introduction

Biomaterials belong to a unique materials group. They are distinguishable by their specific composition, structure, and properties. The feature determining their specific character is that they are accepted by the human organism (Cheng, 2010).

Hydroxyapatite (HA) is an interesting example of biomaterials that belong to the apatite group. HA occurs in mineralogical, biological, and synthetic forms (Joschek, 2000; Ferraz, 2004; LeGeros, 2008). Hydroxyapatite is biocompatible, osteoconductive and can easily be processed to matrices with interconnecting pores to allow for no ingrowths (Nunes, 1997). Although it has been reported that HA is almost water insoluble, it is nevertheless biodegradable, though at a very slow rate (Joschek, 2000). In nature, it can be found mainly as a component of metamorphic and

sedimentary rocks, especially in rocks of volcanic origin. Biological hydroxyapatite contains a small amount of fluorine, magnesium and sodium, as well as carbonate and citrate ions (Shi, 2010). Synthetic HA, with the chemical formula of $\text{Ca}_{10}(\text{PO}_4)_6(\text{OH})_2$, includes hydroxyl groups. The Ca/P ratio in the feed decides whether pure hydroxyapatite and CaO, biphasic calcium phosphate (BCP, HA + β -TCP) or β -tricalcium phosphate ($\text{Ca}_3(\text{PO}_4)_2$, β -TCP) is formed. The critical Ca/P ratio for which pure hydroxyapatite is obtained is 1.67 (Afshar, 2003; Salma, 2010; Cho, 2011).

The presence of surfactants in a precipitation process influences the dispersion and morphology of obtained products. Numerous reports in the literature have shown that the most widely used surfactants are cationic surfactants (CTAB) (Wang, 2006; Salarian, 2009; Shanti, 2009; Coelho, 2010) or a mixture of cationic/anionic surfactants (CTAB/SDS) (Yan, 2001; Ma, 2011). Therefore, in this study an anionic surfactant (SDS) was used. Sodium dodecyl sulfate (SDS), as one of the macromolecules, is used to control the morphology of HA in aqueous synthetic methods (Tari, 2011). Sodium dodecyl sulfate is an organic compound with the formula $\text{CH}_3(\text{CH}_2)_{11}\text{OSO}_3\text{Na}$. It is an anionic surfactant used in many cleaning and hygiene products. The salt is an organosulfate consisting of a 12-carbon tail attached to a sulfate group, giving the material the amphiphilic properties required of a detergent.

The main aim of this work was the synthesis of hydroxyapatite by precipitation method using sodium dodecyl sulfate, SDS. The obtained hydroxyapatite was characterized by dispersive and morphological analysis, BET surface area analysis, and structural, elemental and energy dispersive analysis.

Experimental

Synthesis of hydroxyapatite (HA)

The hydroxyapatite (HA) was obtained in a precipitation process. The process was performed in a reactor of 0.5 dm^3 capacity, equipped with a fast-rotating stirrer (Eurostar digital IKA–Werke GmbH, 1200 obr/min). In the first stage, a reactor was charged with a solution containing PO_4^{3-} ions (H_3PO_4 or Na_2HPO_4 from Sigma-Aldrich) and anionic surfactant (SDS from Sigma-Aldrich). The mixture was intensively stirred for about 15 min. The pH was adjusted to 12 with 1N NaOH. In the second stage, the solution containing Ca^{2+} ions ($\text{Ca}(\text{OH})_2$ or CaCl_2 from Sigma-Aldrich) was dosed using an Ismatec ISM833A type peristaltic pump at the rate of $2 \text{ cm}^3/\text{min}$, into a reactor. A white milky solution was obtained. After 24 h of aging, the solution was filtered along with repeated washing to remove residues of the surfactant. Then the filtrate cake was dried out.

Table 1. Experimental conditions of the precipitation process

Sample symbols	Source of Ca ²⁺ ions	Concentration of Ca ²⁺ ions [M]	Source of PO ₄ ³⁻ ions	Concentration of PO ₄ ³⁻ ions [M]	Concentration of SDS [g]
HA0	CaCl ₂	1	H ₃ PO ₄	0.6	-
HA0'			Na ₂ HPO ₄		
HA1	Ca(OH) ₂	1	H ₃ PO ₄	0.6	0.8
HA2	CaCl ₂				
HA3	Ca(OH) ₂	1	Na ₂ HPO ₄	0.6	0.8
HA4	CaCl ₂				

Four samples, labelled as HA1, HA2, HA3 and HA4 were obtained. Table 1 presents the conditions of precipitation and main data of the samples, while Figure 1 shows the schema for obtaining hydroxyapatite from the precipitation method.

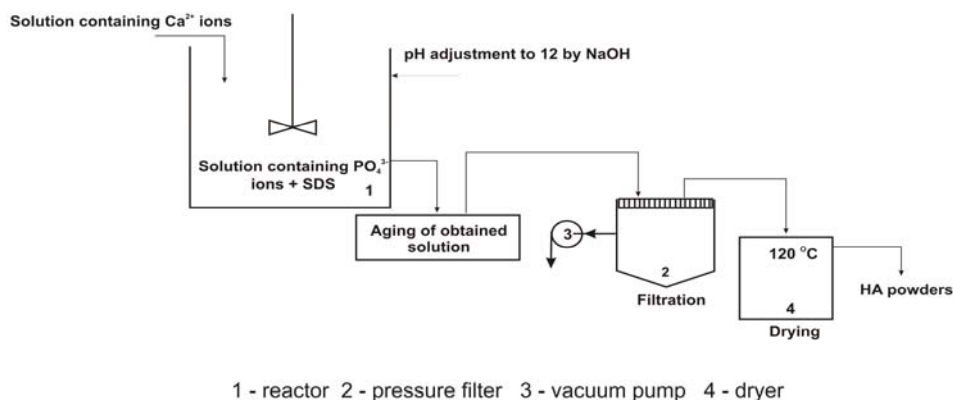


Fig. 1. Preparation of hydroxyapatite – a schematic presentation

Physicochemical evaluation

The dispersive characteristics of obtained hydroxyapatite samples were determined by using an a Zetasizer Nano ZS and Mastersizer 2000, both made by Malvern Instruments Ltd., operating on the non-invasive back-scattering method and laser diffraction method measuring particles of sizes ranging from 0.6 to 6000 nm and from 0.2 to 2000 μm , respectively. Measurements of particle size were repeated at least ten times for each sample. At the next stage, the morphology and microstructure of hydroxyapatite were investigated using a Zeiss EVO40 Scanning Electron Microscope. In order to characterise the adsorption properties, nitrogen adsorption/desorption isotherms at 77 K and parameters such as surface area (A_{BET}), total volume (V_p) and mean size (S_p) of pores were determined using an ASAP 2020 instrument (Micromeritics Instrument Co.). All samples were degassed at 120 °C for

4 h prior to measurement. The surface area was determined by the multipoint BET (Brunauer-Emmett-Teller) method using the adsorption data as a function of relative pressure (p/p_0). The BJH (Barrett-Joyner-Halenda) algorithm was applied to determine the total pore volume and the average pore size. The crystalline structure of individual samples was resolved using the X-ray diffraction method. The diffractograms were recorded using a TUR-M-62 horizontal diffractometer, equipped with HZG-3 type goniometer. To obtain the radiation intensity distribution curve $I = f(\theta)$, a counting rate gauge interoperated with the counter and electronically coupled to a graphic recorder was used. Moreover, the surface composition of hydroxyapatite (contents of Ca and P) was analyzed by energy dispersive X-ray spectroscopy (EDS) using a Princeton Gamma-Tech unit equipped with a prism digital spectrometer. EDS technique is based on an analysis of X-ray energy values using a semiconductor. Before the analysis, the sample was placed on the ground with a carbon paste or tape. The presence of carbon materials is needed to create a conductive layer, which ensures the delivery of electric charge from the sample. Representative parts ($500 \mu\text{m}^2$) were analyzed for proper surface composition evaluation.

Results and discussion

Dispersive and morphological characteristic

Figure 2 presents particle size distributions of obtained hydroxyapatite without and in the presence of SDS, using different initial substrates. Analyzing the presented distribution curves, it was found that hydroxyapatite precipitated without SDS characterized by higher particles in relation to the HA samples precipitated in presence of SDS. In this case, the obtained samples were characterized by particles above 1000 nm. The maximum diameter (close to 20% for sample HA0 and 10% for HA0') came from particles of 4600 nm (HA0) and 2300 nm (HA0'). Hydroxyapatite samples precipitated from calcium hydroxide characterized by significantly smaller particles in relation to the HA samples precipitated from calcium chloride. The smallest particles were obtained for HA3 samples (hydroxyapatite precipitated from $\text{Ca}(\text{OH})_2$ and Na_2HPO_4). In this case, the obtained particles have a diameter in the range of 78–164 nm, where the maximum diameter (close to 34%) came from particles of 106 nm diameter. Results of the analysis, obtained from Mastersizer 2000, revealed that in sample HA3 10% of particles [d(0.1)] have diameter not greater than $3.29 \mu\text{m}$, 50% of particles [d(0.5)] have diameter not greater than $18.53 \mu\text{m}$, and 90% [d(0.9)] have diameters not greater than $52.69 \mu\text{m}$. The mean diameter of particles in this sample [D[4.3]] equals to $23.90 \mu\text{m}$. The hydroxyapatite precipitated as the HA1 sample (obtained from $\text{Ca}(\text{OH})_2$ and H_3PO_4) contains minimal greater size of particles (106–220 nm). In this sample, the maximum volume contribution of about 36.6% came from particles of 142 nm diameter. According to the micrometric particles size (Table 2), the sample contains 90% of particles of diameters smaller than $46.49 \mu\text{m}$, 50% of particles have diameter of $22.23 \mu\text{m}$, and 10% of particles of diameters not greater

than 6.88 μm . The mean diameter of particles in this sample [D[4.3]] equals to 24.85 μm . However when CaCl_2 (Figs 2b, d, Table 2) is used as a source of calcium ionic, we obtain particles in the significantly larger size, and an agglomerate occurs above 1000 nm. The hydroxyapatite precipitated as a HA2 had diameters in the range 1280–2300 nm, and the maximum volume contribution of about 34% came from particles of 1720 nm diameter. In addition, the micromeritic particles (for HA2 and HA4 samples) have the higher sizes. The SEM images of the particles morphology of HA1 (obtained from CaCl_2 and H_3PO_4) and HA3 (obtained from CaCl_3 and Na_2HPO_4) samples show that they are characterized by a greater homogeneity, compared to the samples precipitated as a HA2 and HA4 (Fig. 2). In interpreting the SEM images of HA1 and HA3 samples, we can also see that this hydroxyapatite sample demonstrates (displays) a tendency to create agglomerates.

Comparing our results with the literature data, we can say that using a different surfactant, particles of HA of various structure and size can be obtained. Liu et al. (2004) synthesized HA nanorods of 50–80 nm in diameter and 0.5–1.2 μm in length using surfactants of CTAB and PEG 400. Shanti et al. (2009) obtained hydroxyapatite rods with diameter 20 nm and length in the range of 100–120 μm using only cationic surfactant (CTAB). Yan et al. (2001) used an anionic surfactant (SDS) as regulator of the nucleation and crystal growth in the synthetic method of preparing HA. The obtained hydroxyapatite had particles of nanorods structure (150 nm/10 nm).

Table 2. Dispersive characteristics of obtained hydroxapatite

Sample number	Zetasizer Nano ZS		Mastersizer 2000			
	Particle diameter (nm)	Polidispersity index (Pdl)	Particle diameter (μm)			
			d(0.1)	d(0.5)	d(0.9)	D[4.3]
HA0	68–122 3090–6440	0.734	5.88	37.44	80.91	41.12
HA0'	1110–3580	0.395	5.02	40.75	92.38	45.40
HA1	106–220	0.393	6.88	22.23	46.49	24.85
HA2	1280–2300	0.491	4.41	38.92	89.88	33.37
HA3	98–164	0.436	3.29	18.53	52.69	23.90
HA4	396–1110	0.232	3.94	33.18	85.06	39.36

X-Ray diffraction

The XRD pattern of the synthesized sample in the presence of SDS is shown in Fig. 3. From the XRD pattern, we can say that in all cases there is only HA. Four intensive peaks are located in $2\theta = 25.9^\circ$ (002), $2\theta = 31.5$ (211), $2\theta = 32.2$ (112) and $2\theta = 32.7$ (300), which indicate the high crystallinity of HA particles. Phase identification of the synthesized powders was accomplished by comparing the experimental XRD patterns with the database compiled by the Joint Committee on Powder Diffraction Standards (JCPDS), namely the following card number: 9-432 for $\text{Ca}_{10}(\text{PO}_4)_6(\text{OH})_2$ (Salarian, 2009). Our observations are in agreement with previous research (Tari, 2011; Yan, 2001; Yu, 2011).

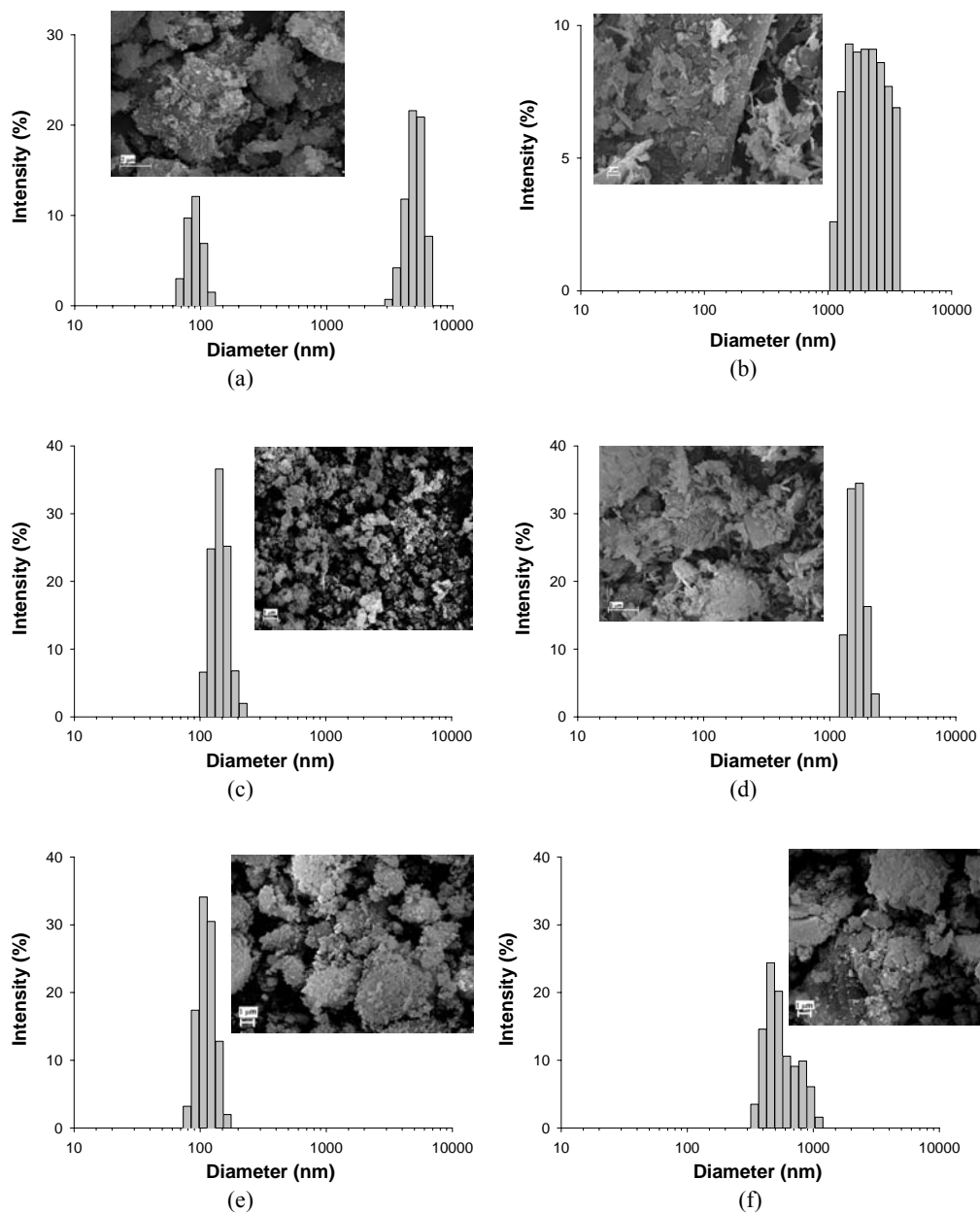


Fig. 2. Particle size distribution (Zetasizer Nano ZS) and SEM microphotographs of hydroxyapatite obtained from different compounds: (a) HA0 – CaCl_2 , H_3PO_4 without SDS; (b) HA0' – CaCl_2 , Na_2HPO_4 without SDS; (c) HA1 – $\text{Ca}(\text{OH})_2$, H_3PO_4 ; (d) HA2 – CaCl_2 , H_3PO_4 ; (e) HA3 – $\text{Ca}(\text{OH})_2$, Na_2HPO_4 ; (f) HA4 – CaCl_2 , Na_2HPO_4

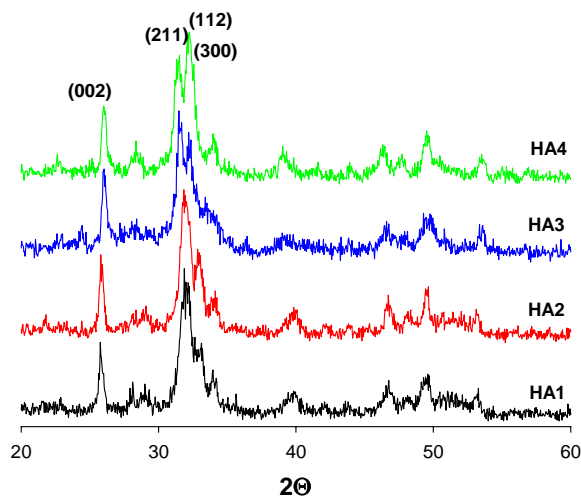


Fig. 3. XRD diffraction patterns of hydroxyapatite structures

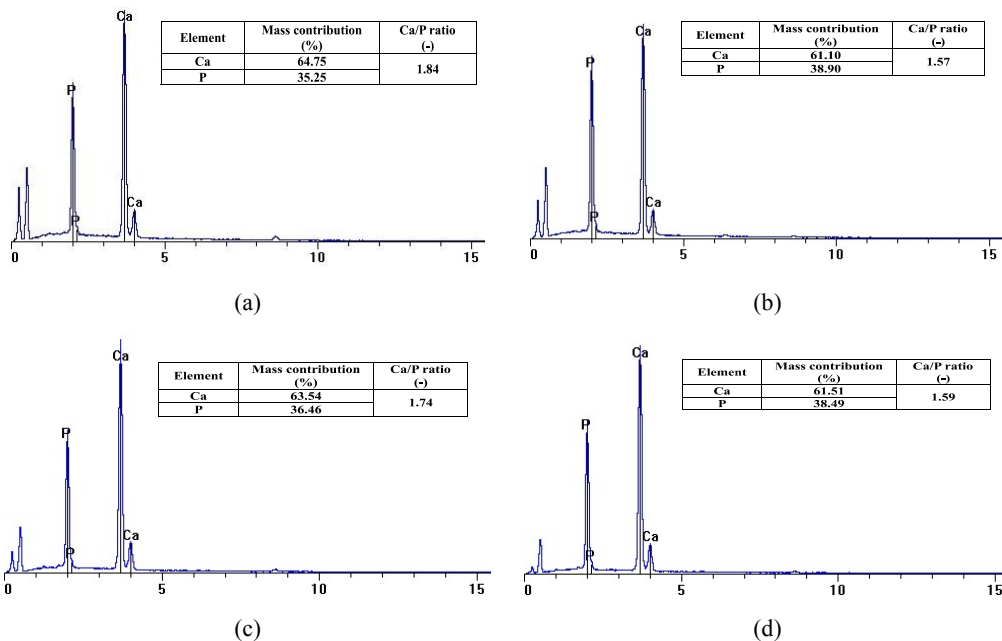


Fig. 4. Energy dispersive spectroscopy (EDS) analysis of hydroxyapatite samples: (a) HA1, (b) HA2, (c) HA3 and d) HA4

Energy dispersive characterization

The Ca/P ratio in the obtained HA was calculated based on the content of Ca and P. Energy dispersive spectroscopy (EDS) analysis of the products (Fig. 4) shows that the

Ca/P ratio is 1.59–1.84:1. The Ca/P ratio in the HA2 and HA4 samples is in the range 1.5–1.67 and is most similar to the stoichiometric hydroxyapatite (1.67). Whereas, the HA1 and HA3 samples are characterized by the Ca/P ratio 1.74–1.84, which indicates the presence of hydroxyapatite with an excess of calcium. Josheck et al. (2000) and Ooi et al (2007) observed analogous results.

Elemental analysis

In order to determine the degree elute of the surfactant from the obtained hydroxyapatite samples, an elemental analysis was performed. This analysis enables one to determine the carbon, hydrogen and sulfur amount. Analyzing the data presented in Table 3, a small amount of sulfur (< 0.05%) was determined, which may indicate a sufficient washing of the samples.

Table 3. Elemental content of the hydroxyapatite samples obtained in presence of SDS

Sample number	C	H	S
	(%)		
HA1	0.64	0.69	0.04
HA2	0.26	0.82	0.05
HA3	1.23	0.57	0.04
HA4	0.27	0.54	0.04

Characteristics of porous structure of obtained hydroxyapatite

Nitrogen adsorption/desorption isotherms and pore size distributions of the obtained hydroxyapatite samples (HA1 and HA3) are shown in Figure 5. The isotherms were classified as type IV and the hysteresis loops as type H3, which points to the mesoporous structure of the HA samples. A type IV isotherm is related to capillary condensation taking place in mesopores. As can be seen in Table 4, the HA samples obtained in the presence of SDS has the largest specific surface areas in comparison with samples obtained without SDS, the largest (115.1 m²/g) being recorded for sample HA3. The pore volume and mean pore diameter in this sample were 0.502 cm³/g and 17.4 nm respectively. The smallest specific surface area (30.9 m²/g) was determined for sample HA2 (Table 4), and the pore volume and mean pore diameter in this sample were 0.021 cm³/g and 2.8 nm. The specific surface areas of sample HA1 and sample HA4 (Table 2) were 84.0 and 83.5 m²/g, while their pore volumes were 0.270 and 0.057 cm³/g and the mean pore diameters 12.9 and 2.7 nm, respectively. From analysis of the parameters of the HA precipitation process, it can be concluded that with an increase in the size of particles diameter there is a decrease in the specific surface area of the resulting samples.

Table 4. Characteristics of porous structure of obtained hydroxyapatite

Sample number	Specific surface area (m ² /g)	Pore volume (cm ³ /g)	Pore diameter (nm)
HA0	20.4	0,015	2.8
HA0'	17.7	0.012	2.8
HA1	84.0	0.270	12.9
HA2	30.9	0.021	2.8
HA3	115.1	0.502	17.4
HA4	83.5	0.057	2.7

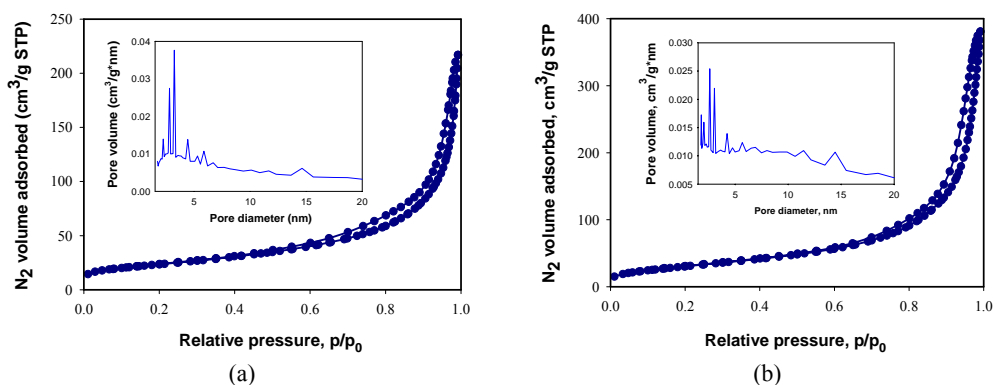


Fig. 5. Nitrogen adsorption/desorption isotherms and pore size distributions of hydroxyapatite samples a) HA1 and b) HA3

Figure 6 presents a probable mechanism for the formation of hydroxyapatite particles in the compositions containing the anionic surfactant. Earlier studies show that the sulfate groups are able to interact with calcium ions present in an aqueous solution. Surfactant molecules in micelles or as emulsion droplets interact with Ca²⁺ ions to form zwitterions (Zhao, 2009). These numerous calcium-rich domains lead to the rapid formation of HA particles on contact with phosphate in the aqueous phase. In addition, the positional stabilization of Ca²⁺ ions within each zwitterions structure as a result of the electrostatic interaction effect by SDS molecules favours the formation of ordered HA crystals (Tari, 2011).

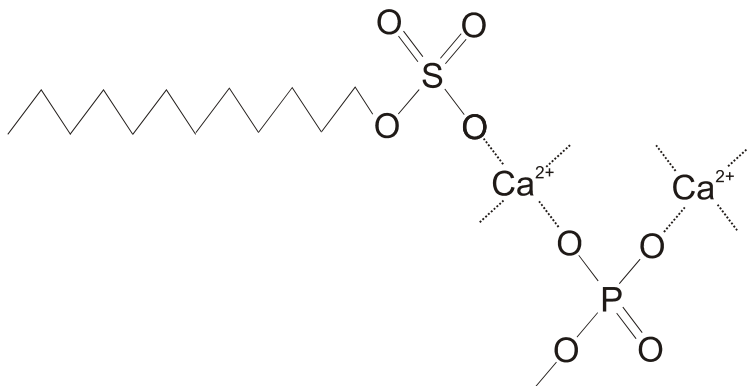


Fig. 6. A schematic drawing showing the interaction between the surfactant anion and calcium cation (Tari, 2011)

Conclusions

Crystalline hydroxyapatite was successfully prepared by adding anionic surfactant at ambient temperature and normal pressure. The XRD studies confirm the pure crystalline structure of HA. The investigated dispersive-morphological research shows that hydroxyapatite obtained from hydroxide calcium and disodium phosphate (sample HA3) is characterized by the smallest particles. Their diameters varied in the range from 78-164 nm and have regular structure. Additionally, the largest specific surface area was observed (115.1 m²/g) for this sample. The greatest size particles were obtained in sample HA2; their diameters varied in a range from 1280-2300 nm. This sample is also characterized by the smallest specific surface area (30.9 m²/g). The maximum volume contribution (close to 34%) came from particles of 1720 nm diameter. Energy dispersive analysis showed that the obtained hydroxyapatite samples are characterized by Ca/P ratio in the range of 1.59-1.84. This range indicates that some of the HA samples contain excess calcium. The small amount of the sulfur (□0.05%) in the obtained HA samples points to sufficient washing of the surfactants residue.

Acknowledgements

This work was supported by Poznan University of Technology Research Grant no. 32-396-2013 DS MK.

References

- AFSHAR A., GHORBANI M., EHSANI N., SAERI M.R., SORRELL C.C., 2003, *Some important factors in the wet precipitation process of hydroxyapatite*, Materials and Design, 24, 197–202.
- CHENG, H.N., GROSS R.A., 2010, *Green polymer chemistry: biocatalysis and biomaterials*, ACS Symposium Series, American Chemical Society, Washington, DC, Chapter 1, 1–14.

- CHO J.S., RHEE S.H., 2011, *The densification mechanism of hydroxyapatite particles during spray pyrolysis with variable carrier gas rates of flow*, Journal of Biomedical Materials Research B: Applied Biomaterials, 2, 493–500.
- COELHO J.M., MOREIRA J.A., ALMEIDA A., MONTEIRO F.J., 2010, *Synthesis and characterization of HAp nanorods from a cationic surfactant template method*, Journal of Materials Science: Materials in Medicine, 21, 2543–2549.
- FERRAZ M.P., MONTEIRO F.J., MANUEL C.M., 2004, *Hydroxyapatite nanoparticles: a review of preparation methodologies*, Journal of Applied Biomaterials & Biomechanics, 2, 74–80.
- JOSCHEK S., NIES B., KROTZ R., GOPFERICH A., 2000, *Chemical and physicochemical characterization of porous hydroxyapatite ceramics made of natural bone*, Biomaterials, 21, 1645–1658.
- LIU Y., HOU D., WANG G., 2004, *A simple wet chemical synthesis and characterization of hydroxyapatite nanorods*, Material Chemistry and Physics, 86, 69–73.
- MA T., XIA Z., LIAO L., 2011, *Effect of reaction system and surfactant additives on the morphology evolution of hydroxyapatite nanorods obtained via a hydrothermal route*, Applied Surface Science, 257, 4384–4388.
- NUNES C.R., SIMSKE S.J., SACHADEVA R., WOLDORD L.M., 1997, *Long-term ingrowth and apposition of porous hydroxyapatite implants*, Journal of Biomedical Material Research, 36, 560–563.
- LEGEROS R.Z., 2008, *Calcium phosphate-based osteoinductive materials*, Chemical Reviews, 108, 4742–4753.
- OOI C.Y., Hamdi M., RAMESH S., 2007, *Properties of hydroxyapatite produced by annealing of bovine bone*, Ceramics International, 33, 1171–1177.
- SADAT-SHOJAI M., KHORASANI M.-T., DINPANAH-KHOSHDARGI E., JAMSHIDI A., 2013, *Synthesis methods for nanosized hydroxyapatite with diverse structures*, Acta Biomaterialia, 9, 7591–7621.
- SALARIAN M., SOLATI-HASHJIN, SHAFIEI S.S., GOUDARZI A., SALARIAN R., NEMATI A., 2009, *Surfactant-assisted synthesis and characterization of hydroxyapatite nanorods under hydrothermal conditions*, Materials Science-Poland, 27, 961–972.
- SALMA K., BERZINA-CIMDINA L., BORODAJENKO N., 2010, *Calcium phosphate bioceramics prepared from wet chemically precipitated powders*, Processing and Application of Ceramics, 4, 45–51.
- SHANTI P.M.S.L., ASHOK M., BALASUBRAMANIAN T., RIYASDEEN A., AKBARSHA M.A., 2009, *Synthesis and characterization of nan-hydroxyapatite at ambient temperature using cationic surfactant*, Materials Letters, 63, 2123–2125.
- SHI D., 2004, *Biomaterials and tissue engineering*, Springer Berlin Heidelberg, Germany
- TARI N.E., MOTLAGH M.M.K., SOHRABI B., 2011, *Synthesis of hydroxyapatite particles in cationic mixed surfactants template*, Materials Chemistry and Physics, 131, 132–135.
- WANG Y.J., CHEN J.D., WEI K., ZHANG S.H., WANG X.D., 2006, *Surfactant-assisted synthesis of hydroxyapatite particles*, Materials Letters, 60, 3227–3231.
- WANG Y., ZHANG S., WEI K., ZHAO N., CHEN J., WANG X., 2006, *Hydrothermal synthesis of hydroxyapatite nanopowders using cationic surfactant as a template*, Materials Letters, 60, 1484–1487.
- YAN L., LI Y., DENG Z.X., ZHUANG J., SUN X., 2001, *Surfactant-assisted hydrothermal synthesis of hydroxyapatite nanorods*, International Journal of Inorganic Materials, 3, 633–637.
- YU G., SHAO W., 2011, *Synthesis of hydroxyapatite assisted by surfactants*, 4th International Conference on Biomedical Engineering and Informatics (BMEI), 1260–1263.

ZHAO J., LIU J., JIANG J., 2009, *Interaction between anionic and cationic gemni surfactants at air/water interface and in aqueous bulk solution*, *Colloids and Surfaces A: Physicochemical and Engineering Aspects*, 350, 141–146.

Received June 9, 2013; reviewed, accepted July 23, 2013

SELECTIVE REMOVAL OF Ag(I) AND Cu(II) BY PLASTICIZER MEMBRANES WITH *N*-(DIETHYLTHIOPHOSPHORYL)- AZA[18]CROWN-6 AS A CARRIER

Marta KOŁODZIEJSKA*, Cezary KOZŁOWSKI**, Jolanta KOZŁOWSKA**,
Malgorzata ULEWICZ***

* Department of Metal Extraction and Recirculation, Czestochowa University of Technology, 42-200 Czestochowa, Armii Krajowej 19, Poland

** Institute of Chemistry and Environment Protection, Jan Dlugosz University of Czestochowa, 42-201 Czestochowa, Armii Krajowej 13/15, Poland, e-mail: c.kozlowski@ajd.czyst.pl

*** Department General Building Engineering and Building Physics, Faculty of Civil Engineering, Czestochowa University of Technology, Akademicka 3, 42-200, Czestochowa, Poland

Abstract: The competitive transport of equimolar mixtures of Ag(I) and Cu(II) ions from aqueous source phase ($c_{Me} = 0.001 \text{ mol/dm}^3$) across polymer inclusion membranes PIMs with *N*-(diethylthiophosphoryl)-aza[18]crown-6 as ion carriers, was studied. The influence of pH of source phase and metal concentration on an efficiency of silver(I) transport through polymer inclusion membranes containing cellulose triacetate as the support and *o*-nitrophenyl pentyl ether as the plasticizer was studied. The transport selectivity order for the PIM with *N*-(diethylthiophosphoryl)-aza[18]crown-6 was: Ag(I) \gg Cu(II). The metal cations transport rate can be explained by size and nature of substituent in lariat ether molecule, which prefer formation of Ag(I) complex in the membrane phase.

Keywords: plasticizer membranes, lariat ether, separation, silver(I), copper(II)

Introduction

Transport of metal ions across liquid membranes (LMs) is a powerful tool, which combines extraction and stripping into one step process. LMs play important role in science and technology, and many efforts were made for development of these kind of membranes (Kislik, 2010). Liquid membrane systems include bulk liquid (BLMs), emulsion liquid (ELMs) and supported liquid membranes (SLMs) (de Gyves and de Miguel, 1999). Polymer inclusion membranes (PIMs) were developed as an alternative of SLMs. This kind of liquid membranes was reviewed recently by Nghiem et al.

(2006). PIMs are formed by casting cellulose triacetate (CTA) or polyvinyl chloride (PCV) from an organic solvent solution to form a thin stable film. The organic solution also contains an ion carrier and a plasticizer (usually *o*-nitrophenyl alkyl ethers). The prepared membrane is used to separate source and receiving aqueous phases, but it does not contain an organic solvent to allow the transport of ions or molecules through PIMs.

The most common group of macrocyclic compounds constitute crown ethers, which contain oxygen, sulfur and nitrogen atoms as donor sites. The first crown ether was synthesized by Pedersen (1967). He obtained dibenzo-18-crown-6, which gained attention for its ability to form stable complexes with metal ions within its central cavity. The stability of the crown ether-metal ion complex is dependent on the number of ethers donor atoms. Of particular importance is the size and shape of the cavity relative to the cation size. Due to differences in polarizability, the nitrogen-containing crown ethers (azacrowns) and sulfur-containing crown ethers (thiacrowns) display different ionic selectivities than oxygen-containing crown ethers.

The introduction of one or more side arms into monocyclic crown ethers gives the lariat ethers and may enhance the metal ion binding strength and selectivity over monocyclic crown ethers by providing donor sites in addition to those found in the macro ring. The modified crown ethers, i.e. lariat ethers, have acceptable complexation-decomplexation dynamics connected with the possibility of three-dimensional cation encapsulation by the crown ether unit and the side arm. In order to achieve effective transfer of the metal ion in a separation process, the system must have a counter anion that is soluble in both aqueous and organic phases. However, the distribution coefficients of complexes formed with common anions, such as chlorides, sulfates or nitrates, between an aqueous phase and an organic phase are too low to be useful. The attachment of a proton-ionizable sidearm to the crown ether ring can eliminate the need to transfer aqueous phase anions into the organic phase. Another advantage of proton-ionizable lariat ethers as ion carriers in the liquid membranes transport processes is coupling of metal ions transport from the aqueous source phase into the aqueous receiving phase with back-transport of a proton. Thus, pH gradient provides the potential for metal ions transport. A variety of proton ionizable lariat ethers were synthesized and investigated by Bartsch and his coworkers (1992).

The transport of Pb(II) was studied by Aguilar et al. (2001). They synthesized a series of diazadibenzocrown ethers and found that two of them possessed a high selectivity for lead(II) over cadmium(II) and zinc(II), when using the polymer inclusion membrane (PIM). Hydrophilic diazadibenzocrown ethers were reported to have higher selectivity for Pb(II) over Zn(II) and Cd(II) than the more hydrophobic derivatives. Moreover, the high selectivity transport of silver ions over other metals was maintained when the above tribenzylated ligand (O_2N_3 -ring) was incorporated as the ionophore in the polymer inclusion membrane system (Kim et al., 2001).

Cho et al. (1996) proved that transport of Cu^{2+} from 0.4 mol/dm^3 SCN^- aqueous solution across the emulsion liquid membranes doped with tetrathia-18-crown-6

reaches 73.0%; increase to 89.1% was found by applying analogous hexathia-18-crown-6 (HT18C6). They also noticed that dithia-18-crown-6 much more effectively transported Cu(II) ions (68.2%) compared to Pb(II) (57.7%), Cd(II) (15.2%), and Zn(II) (13.3%). Shamsipur et al. (2002) showed that transport of mercury(II) ions into 0.05 M ethylenediaminetetraacetic acid (EDTA) receiving phase at pH 6.0 through a chloroform-tetrathia-12-crown-4 bulk liquid membrane runs with efficiency equal to 98%. They also revealed that among a wide variety of tested cations, only Ag(I) ions affect a little the transport of Hg(II) ions from mixture of Hg(II), Cd(II), and Ag(I) ions. In recent years, the transport across plasticized cellulose triacetate membranes doped with dibenzo-18-crown-6, hexathia-18-crown-6, diaza-18-crown-6 and hexaaza-18-crown-6 were investigated by Gherrou et al. (2002). They showed that dibenzo-18-crown-6 carrier was the most selective for silver(I), copper(II) and gold(III).

The competitive transport of zinc(II), cadmium(II), and lead(II) ions from dilute aqueous solutions across PIMs containing imidazole azacrown ether derivative and ionizable crown ether was studied by Ulewicz et al. (2007a, b). The kind of carriers had an influence on the rate of constant transport of Pb(II), as well as Zn(II) and Cd(II). The selectivity order of metal ion fluxes for azacrown ether and ionizable lariat ether was: Pb(II) > Cd(II) > Zn(II). Also, using azacrown ethers in the presence of other metal ions. The highest initial fluxes were obtained for Pb(II) ions. Moreover, the acidity and HCl concentration in the source phase had the influence on the selectivity coefficient value. A relationship was found to exist also between the initial fluxes of transported ions and the hydrophile-lipophile balance of crown ethers used. The initial fluxes of Zn(II), Cd(II), and Pb(II) ions decrease with the increase in azacrown ethers hydrophile-lipophile balance. Pyrrole azacrown ethers in ordinary bulk membrane system were also found to preferentially transport lead(II) from equimolar mixture of Co^{2+} , Ni^{2+} , Cu^{2+} , Zn^{2+} , Cd^{2+} , Ag^+ and Pb^{2+} ions (Luboch et al., 2006).

A considerable number of studies on PIMs to date used polyethers. The sizes of the polyether cavities and of the inserted ions are fundamental parameters that make polyethers effective in the selective transport of metal ions across the liquid membrane. A series of polyesters were examined for the transport abilities toward the mixture of Pb(II), Cu(II), Cd(II), Zn(II), and Ni(II) ions by Hayashi et al. (2003). They used ionizable polyethers with different alkyl chain lengths (from $-\text{C}_7\text{H}_{15}$ to $-\text{C}_{16}\text{H}_{33}$) and found that one of them had a high selectivity for Pb(II). The metal ions were transported across PIMs in the following sequence: $\text{Pb}^{2+} > \text{Cu}^{2+} > \text{Cd}^{2+} > \text{Zn}^{2+} > \text{Ni}^{2+}$. On the other hand, Lee et al. (2000), using lipophilic acyclic polyether dicarboxylic acid, studied the transport of Pb(II), Cu(II), Co(II), Zn(II), and Ni(II) ions across PIMs. This PIM system exhibited a selective transport of Pb^{2+} over other transition metal ions. Kim et al. (2001) also found a highly selective transport of Ag(I) in the presence of Cd(II), Pb(II), Zn(II), Co(II), and Ni(II).

In this work, the competitive transport of equimolar mixtures of Ag(I) and Cu(II) ions from aqueous source phase across PIM containing aza[18]crown-6 or *N*-(diethylthiophosphoryl)-aza[18]crown-6 as an ion carrier was studied. The influence of carrier concentration on the selectivity and efficiency was investigated.

Experimental part

Reagents

The inorganic chemicals, i.e. silver(II) and copper(II) nitrates were of analytical grade and were purchased from POCh (Gliwice, Poland). The organic reagents, i.e. cellulose triacetate (CTA, $M_n = 72,000\text{--}74,000$), *o*-nitrophenyloctyl ether (*o*-NPOE) and dichloromethane were also of analytical grade and were purchased from Fluka and used without further purification.

The general procedure to phosphorylation of the aza[18]crown-6 according to (Maeda et al., 1983) leading to *N*-(diethylthiophosphoryl)-aza[18]crown-6 is as follows: the starting aza[18]crown-6 1 (0.01 mol/dm^3) was dissolved in absolute chloroform (25 dm^3), and dry triethylamine (0.05 mol/dm^3) was added (Fig 1). This mixture was cooled in the ice bath and the solution of the appropriate diethyl chlorothiophosphate (0.01 mol/dm^3) in the dry chloroform (10 dm^3) was added dropwise in 30 minutes. The reaction mixture was stirred for 1 hour in the ice bath for overnight at room temperature. The precipitate was filtered off and washed with dry chloroform. Then, the filtrate was evaporated and dried in high vacuum for 8 h at $40\text{ }^\circ\text{C}$. The obtained *N*-(diethylthiophosphoryl)-aza[18]crown-6 was a colorless viscous liquid.

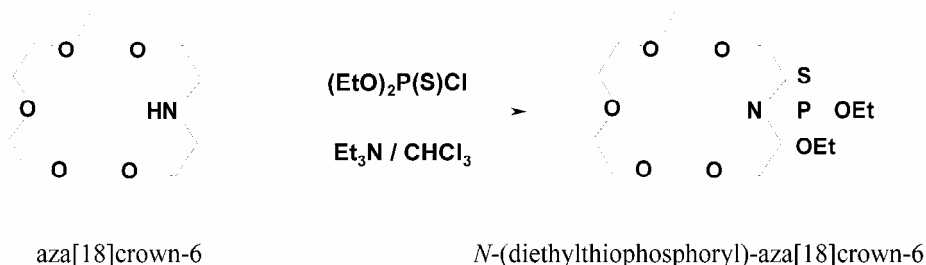


Fig. 1. The diagram of phosphorylation of the aza[18]crown-6. ^1H NMR of *N*-(diethylthiophosphoryl)-aza[18]crown-6: (ppm; CDCl_3): 1.32 (t, 6 H, CH_3), 3.4 (m, 4 H, NCH_2), 3.65 (m, 20 H, $\text{CH}_2\text{CH}_2\text{O}$), 3.96 (m, 4 H, CH_3CH_2). ^{31}P (ppm; CDCl_3): 10.49. Yield 82 %.

Polymer membrane preparation and characterization

The polymer membranes were prepared according to the procedure reported in the previous paper (Kozłowski, 2007). The organic solutions of support (CTA), the ion carrier (lariat ether), and the plasticizer (*o*-nitrophenyl octyl ether) in dichloromethane

were prepared. A portion of this solution was poured into a membrane mold comprised of a 6.0 cm glass ring attached to a glass plate with CTA - dichloromethane glue. The organic solvent was allowed to evaporate overnight and the resulting membrane was separated from the glass plate by immersion in cold water.

The thickness of the PIM samples was measured using a digital micrometer (Mitutoyo) with an accuracy of 0.0001 mm. The thickness of membrane was measured 10 times for each case and shown as average value of these measurements with the standard deviation below 1%. The thickness of membrane before and after the transport was the same. The prepared membranes had thickness equal to 27 μm .

The each experiential point was repeated 4 times, *i.e.* formed membrane by immobilization, thickness measured and transport parameters calculated. Experimental reproducibility was high with standard deviation below 1% measured values.

Transport studies

Transport experiments were carried out in a permeation module cell described in our previous paper (Ulewicz et al., 2007b). The membrane film (at surface area of 4.9 cm^2) was tightly clamped between two cell compartments. Both, *i.e.* the source and receiving aqueous phases (45 cm^3 each) were mechanically stirred at 600 rpm. As the receiving phase the deionized water was used. The transport experiments were carried out at temperature of 20 ± 0.2 $^\circ\text{C}$. Metal concentration was determined by withdrawing small samples (0.1 cm^3 each) of the aqueous receiving phase at different time intervals and analyzing by an atomic absorption spectroscopy method (AAS Spectrometer, Solaar 939, Unicam). The source phase pH was kept constant (pH = 5.0) and controlled by a pH meter (pH meter, CX-731 Elmetron, with combine pH electrode, ERH-126, Hydromet, Poland). The permeability coefficient (P , m/s) of metal ions across membranes was described by the following equation (Danesi, 1984):

$$\ln\left(\frac{c}{c_i}\right) = -\frac{A}{V}Pt \quad (1)$$

where c is the metal ions concentration (mol/dm^3) in the source aqueous phase at some given time, c_i initial metal ions concentration in the source phase, t time of transport (s), V volume of the aqueous source phase (m^3), and A is an effective area of membrane (m^2).

A linear dependence of $\ln(c/c_i)$ in the source phase versus time was obtained and the permeability coefficient was calculated from the slope of the straight line that fits the experimental data. The initial flux (J_i) was determined as equal to:

$$J_i = P \cdot c_i \quad (2)$$

The selectivity coefficient (S) was defined as the ratio of initial fluxes for M1 and M2 metal ions, respectively:

$$S = \frac{J_{i,M1}}{J_{i,m2}} \quad (3)$$

The reported values correspond to the average values of three replicates, with the standard deviation within 5%.

Results and discussion

Permeation of Ag(I) influenced by *N*-(diethylthiophosphoryl)-aza[18]crown-6 in the CTA-based polymer inclusion membrane system

The flux (J) of ions transported in the liquid membrane systems is defined as follows

$$J_M = \frac{c_{(receiving)} \cdot V}{(A \cdot t)} \quad (5)$$

where A and V stand for the effective surface area of the membrane and volume of the source phase, respectively. dc/dt denotes a derivative of the concentration (c) of ions in the source phase versus time (t). The derivatives of the concentration (c) of ions in the source phase versus time (t) $d(\ln c)/dt$ for Ag(I) transported in the considered membrane system depended upon the initial total concentration of silver(I) in the source phase ranging from 0.0002 to 0.010 mol/dm³, but in every case constant values were found irrespective of the elapsed time. The results of Ag(I) transport experiments were interpreted in terms of changes of the initial flux. According to (Danesi, 1984) the permeation coefficient (P) was computed from the changes of the total silver concentration in the source phase at time 0 and elapsed time t , respectively. The effect of pH values in the source phase, ranging from 1 to 7, was studied for 0.25 mol/dm³ *N*-(diethylthiophosphoryl)-aza[18]crown-6 in the membrane phase based on the plasticizer. The initial concentration of Ag(I) in the source phase was 0.001 mol/dm³. The initial flux reaches maximum at pH 2.8 and then decreases with further increase of nitric acid concentration in the source phase (Fig. 2). It is obvious that this effect is parallel to that observed for metal ion extraction with lariat ethers and can be discussed from a similar point of view, namely, taking into account the effective concentration of protonated ion carrier in the membrane phase, and the influence of strong hydrolysis form of metal species.

At constant pH 3.0 in the source phase, the linear dependence $\log J_i$ versus \log of the initial concentration of Ag(I) was found (Fig. 3). The initial Ag(I) concentrations (0.002–0.01 mol/dm³) in the source phase were small in comparison to the concentration (0.25 mol/dm³) of *N*-(diethylthiophosphoryl)-aza[18]crown-6 in the membrane phase. Therefore, the linear dependence of slope 1 indicates that metal-extracted complexes in the membrane phase at stoichiometry 1:1 was formation

resulting from the better fitting of silver(I) diameter (0.22 nm) to the diameter of the crown cavity (0.24 nm).

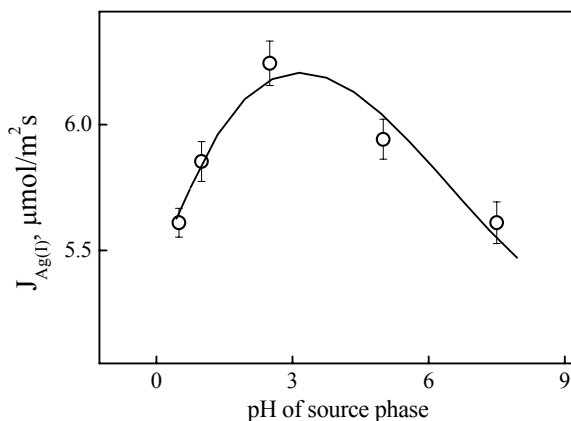


Fig. 2. Dependence of initial flux on pH values in source phase at constant concentration ($2.0 \text{ mmol}/\text{dm}^3$) of Ag(I). Concentration of *N*-(diethylthiophosphoryl)-aza[18]crown-6 in the CTA-membrane phase, $0.25 \text{ mol}/\text{dm}^3$ (based on the plasticiser); the receiving phase: $0.10 \text{ mol}/\text{dm}^3 \text{ Na}_2\text{S}_2\text{O}_3$

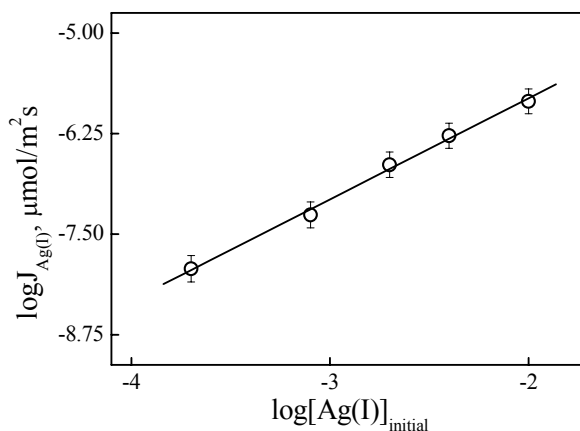


Fig. 3. The log–log plot of initial flux vs. the initial concentration of Ag(I) at 3.0 pH value in source phase; $0.25 \text{ mol}/\text{dm}^3$ (based on plasticizer) and $0.10 \text{ mol}/\text{dm}^3 \text{ Na}_2\text{S}_2\text{O}_3$ in the receiving phase

Competitive separation of Ag(I) and Cu(II) using lariat ether

In the study of Ag(I), and Cu(II) ions transport across PIMs containing *N*-(diethylthiophosphoryl)-aza[18]crown-6 lariat ether as the ion carrier were conducted. The kinetic parameters of this process were determined in the aspect of its effectiveness and selectivity. The extraction ability of ion carrier is not reflected as

expected by the pKa values. Phosphate lariat ethers have two different donor sites, which provide weak complementarily and a rugged coordination site. Furthermore, since the P=S group in *N*-(diethylthiophosphoryl)-aza[18]crown-6 is located at the side arm, if a metal ion complex is formed with the phosphorylated aza[18]crown-6, its complexation is apparently preferred due to the presence of the oxygen atoms.

The membranes containing 0.25 mol/dm³ solution of *N*-(diethylthiophosphoryl)-aza[18]crown-6 lariat ether in the plasticizer, *i.e.* in ONPPE were used for investigations. The aqueous solutions containing equimolar mixture of metal ions of 1.0·10⁻⁴ mol/dm³ concentration served as a source aqueous phases and 0.10 mol/dm³ Na₂S₂O₃ were received as the aqueous phase. Table 1 shows the selectivity order and selectivity coefficients of the above metal ions removed by the transport across PIMs. The transport of Ag(I) is faster due to its larger ionic radius. In the case of Cu(II) much lower transport rate is probably determined by the formation of “sandwich” complexes for lariat ethers (Shampsipur et al., 2003). The selectivity of the metal ion transport for *N*-(diethylthiophosphoryl)-aza[18]crown-6 lariat decreases in the order: Ag(I) >> Cu(II), with the Ag(I)/Cu(II) selectivity coefficient equal to 180 for membrane containing 0.3 mol/dm³ of ion carrier. The large separation factors among divalent heavy metal cations rival those reported by Hayashi et al. (2003) for separation of lead from copper in a PIM transport system with proton-ionizable polyether as a carrier, as well as those reported by Sgarlata et al. (2008). Although these papers deal with the separation of some transition metal ions, only Ulewicz et al. (Ulewicz et al., 2007a, b) report on the selective separation of Zn(II), Cd(II) and Pb(II) from mixtures using macrocyclic carriers. However these results show lower selectivity and efficiency. To our knowledge, this is the first report of successful separation with a PIM system of Ag(I) from the source phase solutions containing Cu(II) ions.

Table 1. Results of measurements of Ag(I), and Cu(II) transport across PIMs containing 0.30 mol/dm³ of *N*-(diethylthiophosphoryl)-aza[18]crown-6 lariat ether. Source phase: 1.0·10⁻³ mol/dm³ metal ions (pH=3.0). Receiving phase: 0.10 mol/dm³ Na₂S₂O₃. PIM: 0.30 mol/dm³ lariat ether and *o*-NPPE (4.0 cm³ *o*-NPOE per 1.0 g CTA)

Concentration of lariat ether, mol/dm ³	Metal ion	Flux, μmole/m ² ·s	Selectivity order and coefficient
0.2	Ag(I)	4.0	Ag(I) >> Cu(II) 60
	Cu(II)	0.07	
0.1	Ag(I)	2.4	Ag(I) >> Cu(II) 40
	Cu(II)	0.06	
0.3	Ag(I)	6.8	Ag(I) >> Cu(II) 180
	Cu(II)	0.04	
0.5	Ag(I)	5.0	Ag(I) >> Cu(II) 70
	Cu(II)	0.07	

Conclusions

In this paper it was demonstrated that *N*-(diethylthiophosphoryl)-aza[18]crown-6 could be regarded as an effective agent used for separation of Ag(I) from aqueous solutions of nitric acid. The crown ether, *i.e.* *N*-(diethylthiophosphoryl)-aza[18]crown-6 used as an ion carrier for competitive transport of Ag(I), and Cu(II) give preferential selectivity order: Ag(II) >> Cu(II). The *N*-(diethylthiophosphoryl)-aza[18]crown-6 applied as ionic extractant gives very high removal for silver cations with good selectivity and the entire amount of Ag(I) can be removed from source aqueous phase under pH 3.0.

Acknowledgments

This work is part of the project no. 2011/01/D/ST5/05781. The authors acknowledge Polish National Science Centre for financial support of this project.

References

- AGUILAR J. C., MIGUEL E.R.D.S., GYVES J. D., BARTSCH R. A., KIM M., 2001, *Design, synthesis and evaluation of diazadibenzocrown ethers as Pb²⁺ extractants and carriers in plasticized cellulose triacetate membranes* Talanta, 54, 1195–1209.
- BARTSCH R. A., YANG I. W. JEON E-G, WALKOWIAK W., CHAREWICZ W. A., 1992, *Selective transport of alkali metal cations in solvent extraction by proton-ionizable dibenzo-crown ethers*, J. Coord. Chem., 27 75–85.
- CHO M. H., CHUN H. S., KIM J. H., RHEE C. H., KIM S. J., 1991, *Study on separation of heavy metal ions in a natural macrocycle-mediated emulsion liquid membrane system*, Bull. Korean Chem. Soc., 12, 474–477.
- CHO M. H., LEE S. Ch., YANG S. Ch, SHIN S. S., KIM K., 1996, *Podand-mediated transport of Ag⁺ in a bulk liquid membrane System*, Bull. Korean Chem. Soc., 17, 1109–1111.
- CHO M. H., SEON-WOO K. H., HEO M. Y., LEE I.C., YOON C.J., KIM S. J., 1988, *Studies on the macrocycles mediated transport in bulk liquid membrane system of transport metal ions*, Bull. Korean Chem. Soc., 9, 292–295.
- DANESI P.R., 1984, *Separation of metal species by supported liquid membranes*, Sep. Sci. Technol., 19, 857-894.
- de GYVES J., de S. MIGUEL E. R., 1999, *Metal ion separations by supported liquid membranes*, Ind. Eng. Chem. Res., 38 (6), 2182-2202.
- GHERROU A., KERDJOUJ H., 2002, *Specific membrane transport of silver and copper as Ag(CN)₃²⁻ and Cu(CN)₄³⁻ ions through a supported liquid membrane using K⁺-crown ether as a carrier*, Desalination, 151, 87–94.
- GHERROU A., KERDJOUJ H., MOLINARI R., SETA P., DRIOLI E., 2004, *Fixed sites plasticized cellulose triacetate membranes containing crown ethers for silver(I), copper(II) and gold(III) ions transport*, J. Membr. Sci., 228, 149–157.
- HAYASHI R., HAYASHITA T., YOSHIKAWA T., HIRATANI K., BARTSCH R. A., 2003, *Design of a polymer inclusion membrane having proton-ionizable carriers and their separation function for lead ion*, Bunseki Kagaku, 52, 755–762.
- KIM J., AHN T. H., LEE M., LEONG A. J., LINDOY L. F., RUMBEL B. W., SKELTON B. W., STRIXNER T., WEI G., WHITE A. H., 2002, *Metal ion recognition. The interaction of cobalt(II)*,

- nickel(II), copper(II), zinc(II), cadmium(II), silver(I) and lead(II) with N-benzylated macrocycles incorporating O₂N₂⁻, O₃N₂⁻ and O₂N₃⁻ donor sets*, J. Chem. Soc. Dalton Trans., 21, 3993–3998.
- KIM J. S., KIM S. K., CHO M. H., LEE S. H., KIM J. Y., KWON S.-G., LEE E.-H., 2001, *Permeation of silver ion through polymeric CTA membrane containing acyclic polyether bearing amide and amine end-group*, Bull. Korean Chem. Soc., 22, 1076–1080.
- KISLIK V.S., 2010, *Liquid membranes. Principles and application in chemical separation and wastewater treatment*, Elsevier, UK.
- KOZŁOWSKI C.A., 2007, *Kinetics of chromium(VI) transport from mineral acids across cellulose triacetate (CTA) plasticized membranes immobilized by tri-n-octylamine*, Ind. Eng. Chem. Res., 46, 5420–5428.
- KUBOTA F., GOTO M., 2005, *Recent advances in liquid membrane technology*, Solv. Extr. Res. and Developm., 12, 11–26.
- LAMB J. D., CHRISTENSON M. D., 1998, *Macrocyclic ligands in separations*, J. Inclusion Phenom. Mol. Recognit. Chem., 32, 107–111.
- LAMB J. D., NAZARENKO A. Y., 1997, *Lead(II) ion sorption and transport using polymer inclusion membranes containing tri-octylphosphine oxide*, J. Membr. Sci., 134, 255–259.
- LEE S.C., LAMB J.D., CHO M.H., RHEE C.H. KIM J.S., 2000, *A lipophilic acyclic polyether dicarboxylic acid as Pb²⁺ carrier in polymer inclusion and bulk liquid membranes*, Sep. Sci. Technol., 35, 5, 767–778.
- LUBOCH E., WAGNER-WYSIECKA E., FAINERMAN-MELNIKOVA M., LINDOY L. F., BIERNAT J. F., 2006, *Pyrrole Azacrown Ethers. Synthesis, Complexation, Selective Lead transport and ion-selective membrane electrode studies*, Supramol. Chem., 18, 593–601.
- MAEDA H., FURUYOSHI S., NAKATSUJI Y., OKAHARA M., 1983, *Synthesis of Monoaza Crown Ethers from N,N-Di[oligo(oxyalkylene)]amines and Oligoethylene Glycol Di(p-toluenesulfonates) or Corresponding Dichlorides*, Bull. Chem. Soc. Jpn., 56, 212.
- NABESHIMA T., TSUKADA N., NISHIJIMA K., OHSHIRO H., YANO Y., 1996, *Remarkably selective Ag(+) extraction and transport by thiolariet ethers*, J. Org. Chem., 61, 4342–4350.
- NAZARENKO A. Y., LAMB J. D., 1997, *Selective transport of lead(II) and strontium(II) through a crown ether-based polymer inclusion membrane containing dialkyl naphthalenesulfonic acid*, J. Inclusion Phenom. Mol. Recognit. Chem., 29, 247–258.
- NGHIEM L. D., MORNANE P., POTTER J. D., PERERA J. M., CATTRALL R. W., KOLEV S. D., 2006, *Extraction and transport of metal ions and small organic compounds using polymer inclusion membranes (PIMs)*, J. Membr. Sci., 281, 7–41.
- PEDERSEN C. J., 1967, *Cyclic Polyethers and Their Complexes with Metal Salts* J. Am. Chem. Soc., 20, 7017–7022.
- SASTRE A. M., KUMAR A., SHUKLA J. P., and SINGH R. K., 1998, *Improved techniques in liquid membrane separations: an overview*, Sep. and Purif. Methods, 27, 213–298.
- SGARLATA C., ARENA G., LONGO E., ZHANG D., YANG Y., BARTSCH R. A., 2008, *Heavy metal separation with polymer inclusion membranes*, J. Membr. Sci., 323, 444–451.
- SHAMSIPUR M., AZIMI G., MASHHADIZADEH M. H., MADAENI S. S., 2001, *Selective transport of silver ion through a supported liquid membrane using hexathia-18-crown-6 as carrier*, Anal. Sci., 17, 491–499.
- SHAMSIPUR M. S., KAZEMI Y., AZIMI G., MADAENI S.S., LIPPOLIS V., GARAU A., ISAIA F., 2003, *Selective Transport of Silver Ion through a Supported Liquid Membrane Using Some Mixed Aza-Thioether Crowns Containing a 1,10-Phenanthroline Sub-Unit as Specific Ion Carriers*, J. Membr. Sci., 215, 87–93.

- SHAMPSIPUR M., MASHHADIZADEH M. H., 2000, *Highly efficient and selective membrane transport of silver(I) using hexathia-18-crown-6 as a specific ion carrier*, Sep. Purif. Technol., 20, 147–153.
- SHAMSIPUR M., MASHHADIZADEH M. H., AZIMI A., 2002, *Highly selective and efficient transport of mercury(II) ions across a bulk liquid membrane containing tetrathia-12-crown-4 as a specific ion carrier*, Sep. Purif. Technol., 27, 155–161.
- ULEWICZ M., 2007a, *Transport jonów Zn(II) i Pb(II) przez polimerowe membrany inkluzyjne przy użyciu D2EHPA*, Przemysł Chemiczny, 86/9, 861-865.
- ULEWICZ M., KOZŁOWSKI C., WALKOWIAK W., 2004, *Removal of Zn(II), Cd(II) and Cu(II) ions by polymer inclusion membrane with side-armed diphosphaza-16-crown-6 ethers*, Physicochem. Probl. Miner. Process., 38, 131–138.
- ULEWICZ M., LESINSKA U., BOCHENSKA M., WALKOWIAK W., 2007b, *Facilitated transport of Zn(II), Cd(II) and Pb(II) ions through polymer inclusion membranes with calix[4]-crown-6 derivatives*, Sep. Purif. Technol., 54, 299-305.
- ULEWICZ M., SADOWSKA K., BIERNAT J. F., 2007, *Facilitated transport of Zn(II), Cd(II) and Pb(II) across polymer inclusion membranes doped with imidazole azacrown ethers*, Desalination, 214, 352-364.
- ULEWICZ M., SADOWSKA K., BIERNAT J. F., 2007, *Selective transport of Pb(II) across polymer inclusion membrane using imidazole azacrown ethers as carriers*, Probl. Miner. Process., 41, 133–143.
- ULEWICZ M., SADOWSKA K., BIERNAT J.F., SZCZYGELSKA-TAO J., 2009, *Selectivity of Pb(II) transport across polymer inclusion membranes doped with imidazole azathiacrown ethers*, J. Membr. Sci., 344, 32–38.
- ULEWICZ M., WALKOWIAK W., 2006, *Removal of Zn(II), Cd(II) and Pb(II) using polymer inclusion membrane transport with proton ionizable DB-16-C-5 crownethers*, Physicochem. Probl. Miner. Process., 40, 185-194.
- YANG X. J., FANE A. G., SOLDENHOFF K., 2003, *Comparison of liquid membrane processes for metal separations: permeability, stability, and selectivity*, Ind. Eng. Chem. Res., 42, 392–403.

Received August 16, 2013; reviewed, accepted September 3, 2013

APPLICATION OF STATISTICAL PROCESS CONTROL FOR PROPER PROCESSING OF THE FORE-SUDETIC MONOCLINE COPPER ORE

Adem TASDEMIR*, Przemyslaw B. KOWALCZUK**

* Department of Mining Engineering, Division of Mineral Processing, Eskisehir Osmangazi University, 26480, Eskisehir, Turkey, atasdem@ogu.edu.tr, Tel: +90 222 239 37 50

** Wrocław University of Technology, Wybrzeże Wyspińskiego 27, 30-370 Wrocław, Poland, przemyslaw.kowalczuk@pwr.wroc.pl

Abstract: The paper deals with Statistical Process Control (SPC) applied to three original and three generated variables of copper ore upgrading by flotation. The six variables were evaluated by the SPC charts based on industrial upgrading of copper ore data gathered during one month of operation in the form of copper content in feed, concentrate and tailing. The remaining three upgrading variables were concentrate yield, copper recovery in concentrate and non-copper components recovery in tailing. Although, all variables obeyed normal distribution, considerable autocorrelation was detected between observations for all variables. For this reason, the traditional Shewhart control charts, that assume the process data generated are normally and independently distributed, resulted in many of out-of-control points which may lead to wrong decisions regarding the control of process variables. The most suitable ARIMA time series models were determined for all variables to remove autocorrelations. The ARIMA(0,1,1) model was found the best for copper content in feed, copper content in concentrate, concentrate yield and non-copper components recovery in tailing, while the AR(1) model was suitable for copper content in tailing and copper recovery in concentrate.

keywords: *copper, upgrading, statistical process control, ARIMA model, Shewhart's chart, autocorrelation*

Introduction

Each separation process provides a set of results, which can be used for evaluation, analysis and optimization of the process. The obtained data from industrial processing of raw materials are always scattered. It is due to fluctuation of operational variables and variation of feed composition (Mukherjee and Chandra, 2002; Drzymala et al., 2010). Moreover, most separation processes are specific and typical statistical methods applied for analysis and evaluation of separation results are very often not

applicable (Drzymala and Kowalczyk, 2010). It causes a need for appropriate processing of separation results data.

The processing of an ore in beneficiation plants is mainly controlled by the grade of feed, concentrate and tailing. These data, and some new parameters of the ore upgrading such as recovery and yield can be calculated and used for evaluation of the overall plant performance (Wills and Napier-Munn, 2006; Drzymala, 2007). Therefore, the process data must be gathered and analysed to determine control limits of variables and to monitor them. During industrial processing two types of variability occur. The first one is the common cause variability that occurs with the nature of any process and cannot be avoided. The second one is a special cause variability, which is not a part of process characteristics and exists almost in all processes. The special cause variability can be identified and eliminated by the Statistical Process Control (SPC) charts. The SPC chart is a guide during decision making on the process and taking the corrective actions. If there is no special cause in the process, the SPC methods are also used to check its working conditions at a predetermined level (Smeti et al., 2006; Psarakis and Papaleonida, 2007).

The control charts represent a very important tool in statistical quality control used to monitor a process and detect shifts in values of its variables. Traditional control charts are based on the assumption that process outputs obtained at each time period are normally distributed and independent (Alwan and Roberts, 1988; Zhang, 1997; Castagliola and Tsung, 2005). Many research studies showed that violation of these assumptions resulted in many false alarms which caused wrong decisions about the process (Alwan and Roberts, 1988; Stoumbos and Reynolds, 2000; Bisgard and Kulahci, 2005). Therefore, both normality and independence assumptions should be satisfied since most industrial data are usually non-normal and auto-correlated.

The dynamics of any process induces correlated variables, which are closely spaced in time. Therefore, in the process outputs some correlations, called autocorrelation, can occur. The autocorrelation may have serious effects on the properties of standard control charts developed under independence assumption (Singh and Prajapati, 2011). Hence, the process mean is not constant if there is autocorrelation between variables (Thaga, 2008).

It is well known that the autocorrelation may significantly degrade the in-control performance of the control charts due to frequent false alarms (Testik, 2005). The effect of autocorrelation on the performance of the Statistical Process Control (SPC) charts were reported by many authors (Alwan and Roberts, 1988; Montgomery and Mastrangelo, 1991; Reynolds and Lu, 1997; Zhang, 1997; Lu and Reynolds, 1999; 2001; Bisgaard and Kulahci, 2005; Testik, 2005; Singh and Prajapati, 2011). However, the data generated are assumed independent (not autocorrelated), and normally distributed in many SPC applications of mineral and/or mining industry and assumptions for the monitoring and process control aims. On the other hand, satisfaction of normality and dependence assumptions of the SPC is necessary to avoid wrong decisions due to false alarms on the charts (Bhattacharjee and Samanta, 2002).

A significant effect of autocorrelation on the SPC charts was considered in mineral and mining applications by a limited number of studies (Samanta and Bhattacharjee, 2001; Bhattacharjee and Samanta, 2002; Samanta, 2002; Elevation et al., 2009; Tasdemir, 2012a; 2013).

In the case of autocorrelation, it is necessary to make some modifications for traditional control charts. Fitting a time series model to the traditional control charts, which display the original observations was suggested by Alwan and Roberts (1988), Reynolds and Lu (1997), Lu and Reynolds (1999, 2001). A suitable time series model for the investigated quality parameter of the process is required to apply this method (Apley and Lee, 2003). The individual control chart applied to the residuals is called the Special Control Chart (SCC), which is also known as the X residual or the Shewhart chart. The first residual control chart was developed by Alwan and Roberts (1988). In residual charts, an appropriate time series model is fitted to autocorrelated observations and residuals are plotted on the SCC (Demirkol, 2008). More detailed information can be found in Psarakis and Papaleonida (2007) and the references therein.

As in the many industrial plants, large amounts of data are obtained over time at mineral processing plants. The analyses of these resulting data by a suitable method are very important steps to understand the plant performance (Ketata and Rockwell, 2008). Application of times series to many data sets from mineral processing plants was shown to be a suitable method (Napier-Munn and Meyer, 1999; Meyer and Napier-Munn, 1999; Ganguli and Tingling, 2001) since the data structure is identical to the time series form. Many ore quality characteristic values in mineral processing are good examples of the time series that is correlated in time domain (Ganguli and Tingling, 2001; Elevation et al., 2009; Tasdemir, 2012a, b, 2013). Therefore, usage of the ARIMA time series for removing the autocorrelation to detect correct ore quality limits by the SPC is advantageous, since we can also use this time series model for near future estimation of ore quality characteristics. Two examples were reported for the short-term prediction of recovery and ore quality variables at a chromite preparation plant by using the AR(1) time series model (Tasdemir, 2012b, 2013).

In this work we investigate the individual control charts based on the original observations of residuals obtained by the time series of ARIMA models to monitor three original and three generated upgrading variables of the Fore-Sudetic Monocline copper ores by a flotation process, that are copper content in the feed, concentrate and tailing, and three generated upgrading parameters, that are concentrate yield, Cu recovery in concentrate and non-Cu components recovery in tailing. The ARIMA models were developed for the copper ore parameters to characterize the autocorrelation between observations. Finally, we compare the performance of the standard Shewhart chart, which ignores subgroup correlations with the X- individual control charts of ARIMA residuals.

Methods

The data sets were obtained from the Fore-Sudetic Monocline copper ore flotation process gathered during one-month production (Drzymala and Kowalczuk, 2010) in the form of copper content in feed α , concentrate β and tailing \mathcal{G} , and three generated upgrading parameters, namely concentrate yield $\gamma = \left(\frac{\alpha - \mathcal{G}}{\beta - \mathcal{G}} \right) \cdot 100\%$, copper recovery

in the concentrate $\varepsilon = \frac{\beta(\alpha - \mathcal{G})}{\alpha(\beta - \mathcal{G})} \cdot 100\%$, and non-copper components recovery in

tailing $\varepsilon_o = \frac{(\beta - \alpha)(100 - \mathcal{G})}{(\beta - \mathcal{G})(100 - \alpha)} \cdot 100\%$ (Drzymala, 2007), to monitor the changes in the

industrial processing plant. The plant works three shifts in a day, therefore 93 records were used to investigate the effect of autocorrelation on the performance of the Shewhart individual control charts based on the original observations or the residual charts from the ARIMA models.

The SPC chart is used to present sample quality for one parameter measured in control samples. If the data occur outside the limits, the process is out-of-control and has to be stopped and inspected of causes, when the out-of-control points are detected. More detailed information on this topic can be found in Montgomery and Runger (2011) and Tasdemir (2012a,b).

The parameters of time series models were estimated from the ARIMA models using Minitab 16 and Statgraphics Centrion XVI softwares. The softwares were also used for constructing and evaluation the SPC charts and for statistical analysis of residuals from the ARIMA models. More details on the ARIMA estimation methodology and model selection can be found in the work of Montgomery et al. (2008) and two examples for coal washing data were applied by Tasdemir (2012a). In this study, the Akaike Information Criterion (AIC) was considered during the selection of a suitable ARIMA model for the Cu upgrading variables. Finally, the Shewhart charts of individual observations were compared with the Shewhart charts of residuals to investigate the autocorrelation effect on the performance of the SPC charts.

Results and discussion

Normality and autocorrelation of upgrading parameters

The process control charts can be applied, when the normality assumption is satisfied. Without a normal distribution, correct limits of control charts may fail. Montgomery and Runger (2011) studied behaviour of the Shewhart control chart for non-normal process data. According to Montgomery and Runger (2011), even if the process shows evidence of moderate departure from normality, the given control limits may be entirely inappropriate. In situations involving a large number of measurements, it may

be possible to subgroup the data and construct the mean chart (\bar{X}) instead of the X individual chart. However, the measurements should not be subgrouped arbitrarily for this purpose (Srinivasan, 2011). If subgrouping is not possible, two alternatives of the normality of data occur. One approach attempts to transform data. A number of mathematical transformations were developed over the years. The data transformation means performing the same mathematical operation on each piece of original data, preferably with a transformation method like the Box-Cox or the Johnson (Chou et al., 1998). Another approach is to modify the usual limits based on a suitable model for the data distribution (Castagliola and Tsung, 2005). Identifying a mathematical distribution can help to develop alternate control limits. Thus, it can be identified if the data belong to a particular class of distribution.

The normal probability graphs of six copper upgrading variables are plotted with 95% confidence interval (Fig. 1). The p values, which test normal distribution, for all variables were higher than 0.05. It means that all the considered process data have normal distribution. It indicates that normality, the first assumption needed for applying the traditional Shewhart control charts, was satisfied.

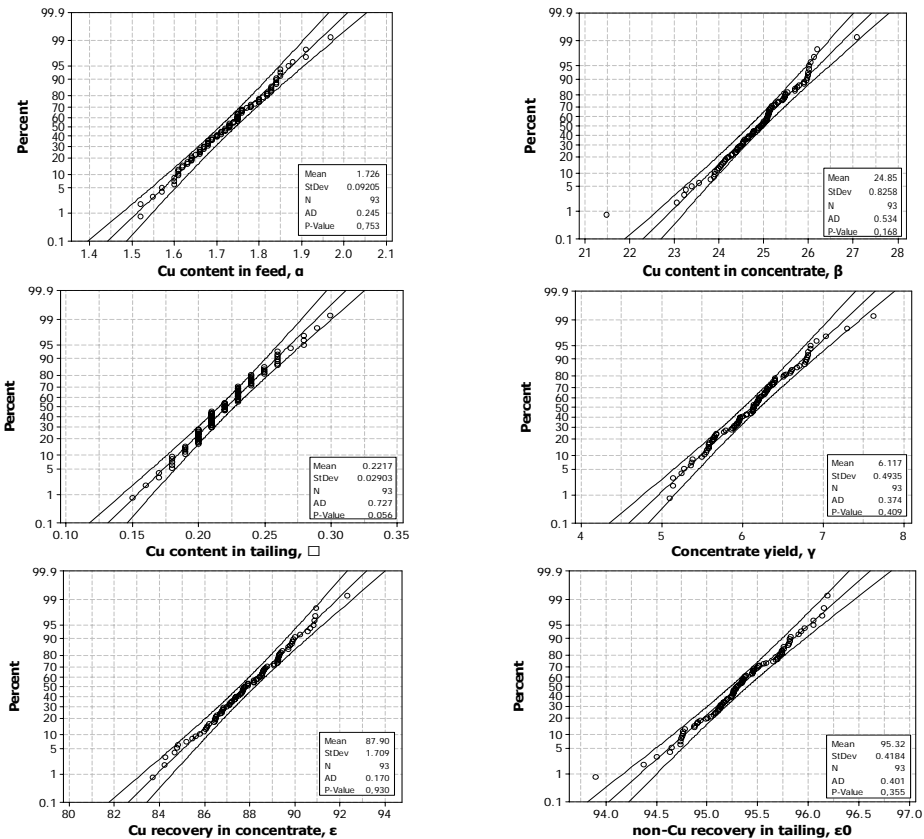


Fig. 1. Normal probability plots of considered copper upgrading variables

The statistical process control (SPC) can only be applied for a process, when the independence of data is also satisfied. If any correlation of data is detected, it has to be eliminated before use for the standard control charts. Data are autocorrelated when each value is correlated to the previous one. The autocorrelation (or time dependency) builds up automatically and occurs between observed data. It can be checked by scatter diagrams of each value (lag plot) against the previous one (Stapenhurst, 2005; Drzymala and Kowalczuk, 2010; NIST/SEMATECH, 2010). Figure 2 shows the scatter diagrams of six copper upgrading variables, where considerable positive correlations between two consecutive data values of all variables are observed. It means that there is no non-random pattern in the data. Since each individual observation is dependent upon the previous one, the degree of autocorrelation should be determined and removed before constructing the SPC charts. It can be done by using the ARIMA time series models.

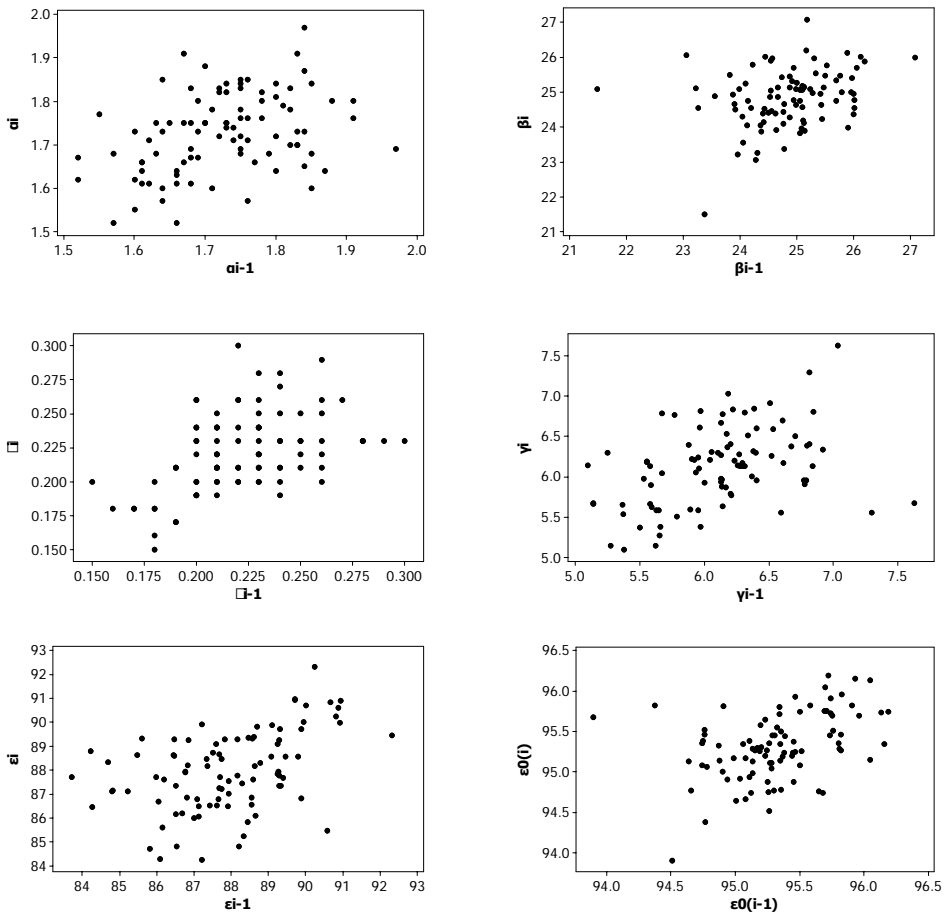


Fig. 2. The lag plots of copper upgrading variables

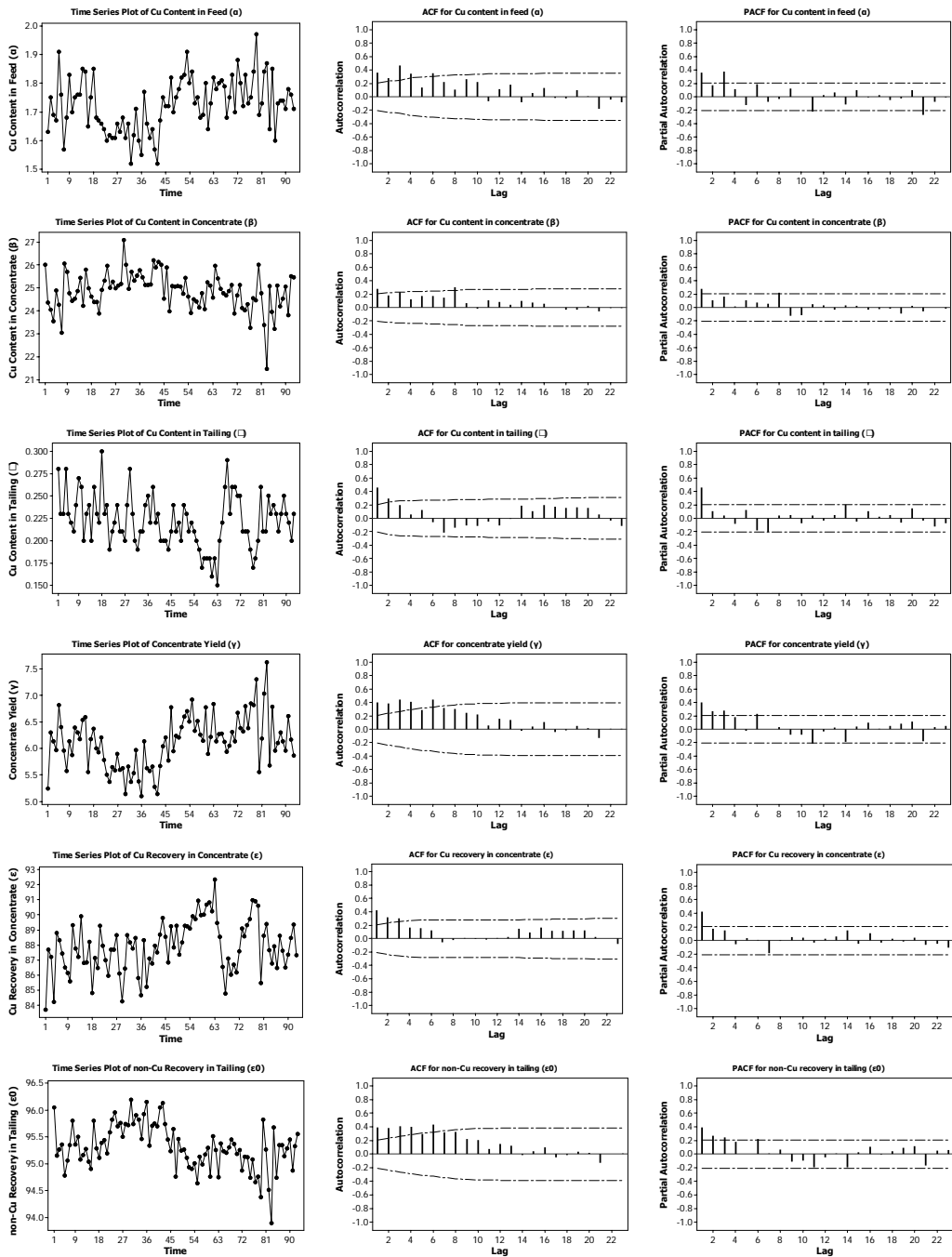


Fig. 3. Time series, ACF and PACF plots of copper upgrading variables

The assumptions of independence and stationary were also checked for six upgrading variables using the autocorrelation (ACF) and partial autocorrelation (PACF) functions. Figure 3 shows the time series plots of six data sets together with their ACF and PACF plots. The ACF plots show the correlation between X_t and X_{t-k} , where X_t is the response variable at time t , and k lag between two measurements. The PACF plots show the partial autocorrelation function for a given lag k , where the partial autocorrelation at lag k is the autocorrelation between X_t and X_{t-k} , that is not accounted for lags 1 through $k-1$ (NIST/SEMATECH, 2010). These plots are generated for 25 lags. The ACF and PACF plots (Fig. 3) clearly confirm the existence of autocorrelation between values of all upgrading variables. It can be seen that the data are highly autocorrelated with the lag one autocorrelation of 0.472 for Cu content in tailing (ϑ) and 0.462 for Cu recovery in concentrate (ε). According to the autocorrelation plots of these variables, the ACF of the time series values cuts off quickly after few lags, then they can be considered stationary. The autoregressive models are indicated by exponential decay to zero of the ACF plot and order of the autoregressive model is determined by the initial peaks in the PACF plots. The ACF and PACF plots for ϑ and ε indicate the autoregressive model with lag 1, since they have one important spike at first lag in their PACF plots. For these reasons, the AR(1) model was suitable for fitting the data of copper content in tailing ϑ and copper recovery in concentrate ε .

The autocorrelation of copper content in feed α and concentrate β , concentrate yield γ and non-copper components recovery in tailing ε_o can be also described by the ARIMA time series model. The autocorrelation values at first lag were determined as 0.361, 0.279, 0.402 and 0.399 for the copper content in feed (α), concentrate grade (β), yield of product (γ) and non-copper components content in tailing (ε_o), respectively (Fig. 3). The slow decay of autocorrelation coefficients for these variables in the ACF plots implies that they are not stationary. The stationary characters were achieved by applying first order differencing. After that, all upgrading variables showed one significant spike at the first lag of the ACF plots suggesting the first order of the moving average model MA(1). Finally, the ARIMA (0,1,1) model was found to be the most suitable for these variables. In the ARIMA (0,1,1) model the autoregressive parameter is zero, number of differencing passes is one and moving average parameter is one.

ARIMA models and residual analysis

The ARIMA time series models were used to remove autocorrelations. The models were fitted by using the Statgraphics software, which optimizes the model parameters according to the selection criteria of the model. The models with the lowest values of the Akaike Information Criterion (AIC) were selected as the best describing model of the variables. More detailed information about the AIC can be found in Tasdemir (2012a).

It was mentioned before that among different ARIMA models, the ARIMA(0,1,1) was found the best one for α , β , γ and ε_o , while the first order autoregressive time series model AR(1) was the most suitable for \mathcal{G} and ε . The AR(1) model was used by many authors for daily metal recovery or concentrate grade at a zinc flotation plant, daily gold feed grade and gold recovery data (Napier-Munn and Meyer, 1999; Meyer and Napier-Munn, 1999), B₂O₃% contents in two colemanite concentrator plants (Elevli et al., 2009), Al₂O₃% and SiO₂% constituents of a bauxite ore (Bhattacharjee and Samanta, 2002), forecasting chromite feed grade and product quality parameters (Tasdemir, 2013), and prediction of Cr₂O₃ recovery in a chromite preparation plant (Tasdemir, 2012b). Except the AR(1), other time series models were reported for mineral processing data such as the ARMA models for flotation (Trybalski and Cieply, 2000), SO₂ emissions (Gleit, 1985) and coal preparation (Tasdemir, 2012a).

Validation of the models obtained for the Cu upgrading variables was checked for the adequacy. The model is adequate if residuals are uncorrelated and normally distributed. The evaluation results of the ARIMA models as the so-called 4-plot of data and residual ACF plots for β as an example are presented in Fig. 4. It clearly indicates that the residuals are uncorrelated within (or very close to) 95% confidence limits and distributed randomly. The residuals of other parameters are also found uncorrelated and normally distributed. Therefore, they can be considered as a white noise allowing to work on the traditional SPC charts.

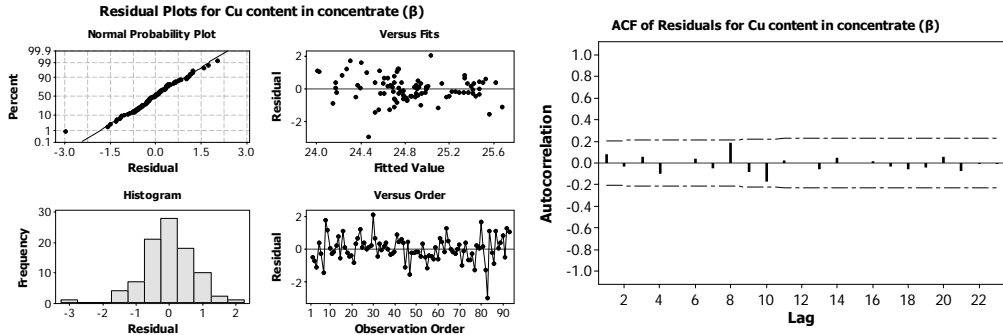


Fig. 4. Residual plots from ARIMA model and ACF chart for Cu content in concentrate β

The calculated parameters of the AR(1) and ARIMA(0,1,1) models for Cu upgrading variables are given in Tables 1 and 2, respectively. It can be seen that the p -values of all model parameters are less than 0.05, so they are significantly different from zero at the 95.0% confidence level. We obtained the following AR(1) models for copper content in tailing \mathcal{G} and copper recovery in concentrate ε :

$$X_t = 0.472 X_{t-1} + 0.117 \quad \text{with the AIC of } -7.278 \text{ (for } \mathcal{G}\text{),}$$

$$X_t = 0.462 X_{t-1} + 47.308 \quad \text{with the AIC of } 0.894 \text{ (for } \varepsilon\text{).}$$

and ARIMA(0,1,1) models (Eq. 8) for copper content in feed α and concentrate β , concentrate yield γ and non-copper compounds recovery in tailing ε_o :

$$X_t = X_{t-1} + 0.759 a_{t-1} \quad \text{with the AIC of } -4.977 \text{ (for } \alpha),$$

$$X_t = X_{t-1} + 0.846 a_{t-1} \quad \text{with the AIC of } -0.4804 \text{ (for } \beta),$$

$$X_t = X_{t-1} + 0.751 a_{t-1} \quad \text{with the AIC of } -1.7362 \text{ (for } \gamma),$$

$$X_t = X_{t-1} + 0.754 a_{t-1} \quad \text{with the AIC of } -2.0624 \text{ (for } \varepsilon_o),$$

where a_t is the independent error term (random shock term) at time t , which reflects the amount of variation in data.

Table 1. Summary of AR(1) model parameters for copper content in tailing ϑ and Cu recovery in concentrate ε . WNV means white noise variance of random shock term (a_t) in the model

Upgrading variable	Model descriptors and statistics				
	Parameter	Estimate	Standard error	<i>t</i> -value	<i>p</i> -value
Cu content in tailing, ϑ , %	AR(1)	0.471505	0.0908267	5.19126	0.000001
	Mean	0.222053	0.0048676	45.6189	0.000000
	WNV	0.000666			
Cu recovery in concentrate, ε , %	AR(1)	0.461607	0.0911491	5.0643	0.000002
	Mean	87.8695	0.287521	305.611	0.000000
	WNV	2.36768			

Table 2. Summary of ARIMA(0,1,1) model parameters for Cu content in feed α and concentrate β , concentrate yield γ , and non-copper components recovery in tailing ε_o . WNV means white noise variance of random shock term (a_t) in the model

Upgrading variable	Model descriptors and statistics				
	Parameter	Estimate	Standard error	<i>t</i> -value	<i>p</i> -value
Cu content in feed, α , %	MA(1)	0.75944	0.068817	11.0356	0.00000
	WNV	0.00682			
Cu content in concentrate, β , %	MA(1)	0.84585	0.061638	13.7229	0.00000
	WNV	0.62394			
Concentrate yield, γ , %	MA(1)	0.75112	0.067773	11.0828	0.00000
	WNV	0.17818			
Non-Cu recovery in tailing, ε_o , %	MA(1)	0.75425	0.067943	11.1013	0.00000
	WNV	0.12881			

Individual control charts and ARIMA residuals

The original and ARIMA residual values of the control chart parameters used for constructing the statistical process control chart (SPC) are given in Tables 3 and 4,

respectively. In Tables 3 and 4, \bar{X} is the mean of individual values and σ is standard deviation which is calculated from $\overline{MR}/1.128$ formula, where \overline{MR} is the average moving range value of individual observations. The SPC charts are designed to allow determining whether the data come from a process which is in a state of statistical control. The individual Shewhart charts of six upgrading copper variables based on the original data and residuals obtained from the ARIMA models are presented in Fig. 5. Figure 5 compares the individual charts of the Shewhart (left hand side plots), and ARIMA residuals (special cause charts, right hand side plots) with additional Western Electric rules, which are applied to improve the efficiency of control charts for small shifts. The number of the Western Electric rules applied was four. The same run rules were used in our previous study (Tasdemir, 2012a). More details regarding the method can be found in Montgomery and Runger (2011). A common calculation is to plot the SPC with z-score when comparing multiple control charts. Therefore, the numerical values of the original and ARIMA residual data set in Fig. 5 were presented as z-score values. The z-scores standardize $\pm 3\sigma$ values. The calibrated z-values of control charts presented in Fig. 5 were calculated from formula $\frac{UCL_X - \bar{X}}{\sigma}$ for the upper control limit and $\frac{LCL_X - \bar{X}}{\sigma}$ for the lower control limit.

Table 3. Individual Shewhart's chart parameters of Cu upgrading variables

Chart parameters	α	β	ϱ	γ	ε	ε_o
Upper control limit, $UCL_X (\bar{X} + 3\sigma)$	1.942	26.81	0.284	7.199	91.676	96.219
Mean of individual values (\bar{X})	1.726	24.85	0.222	6.117	87.903	95.319
Lower control limit, $LCL_X (\bar{X} - 3\sigma)$	1.508	22.89	0.159	5.035	84.129	94.419
Average of moving average (\overline{MR})	0.082	0.736	0.024	0.407	1.419	0.338
$\sigma(\overline{MR}/1.128)$	0.072	0.652	0.021	0.361	1.258	0.300
2σ	0.144	1.305	0.042	0.722	2.516	0.600
3σ	0.216	1.956	0.063	1.083	3.774	0.900

Table 4. ARIMA residual chart parameters of Cu upgrading variables

Chart parameters	α	β	ϱ	γ	ε	ε_o
Upper control limit, $UCL_X (\bar{X} + 3\sigma)$	0.244	2.063	0.077	1.205	4.694	0.975
Mean of individual values (\bar{X})	0.002	-0.019	-0.0003	0.016	0.025	-0.013
Lower control limit, $LCL_X (\bar{X} - 3\sigma)$	-0.239	-2.1	-0.077	-1.173	-4.644	-1.001
Average of moving average (\overline{MR})	0.091	0.783	0.029	0.447	1.755	0.371
$\sigma(\overline{MR}/1.128)$	0.081	0.694	0.026	0.396	1.556	0.329
2σ	0.161	1.388	0.052	0.793	3.112	0.659
3σ	0.242	2.081	0.077	1.189	4.669	0.988

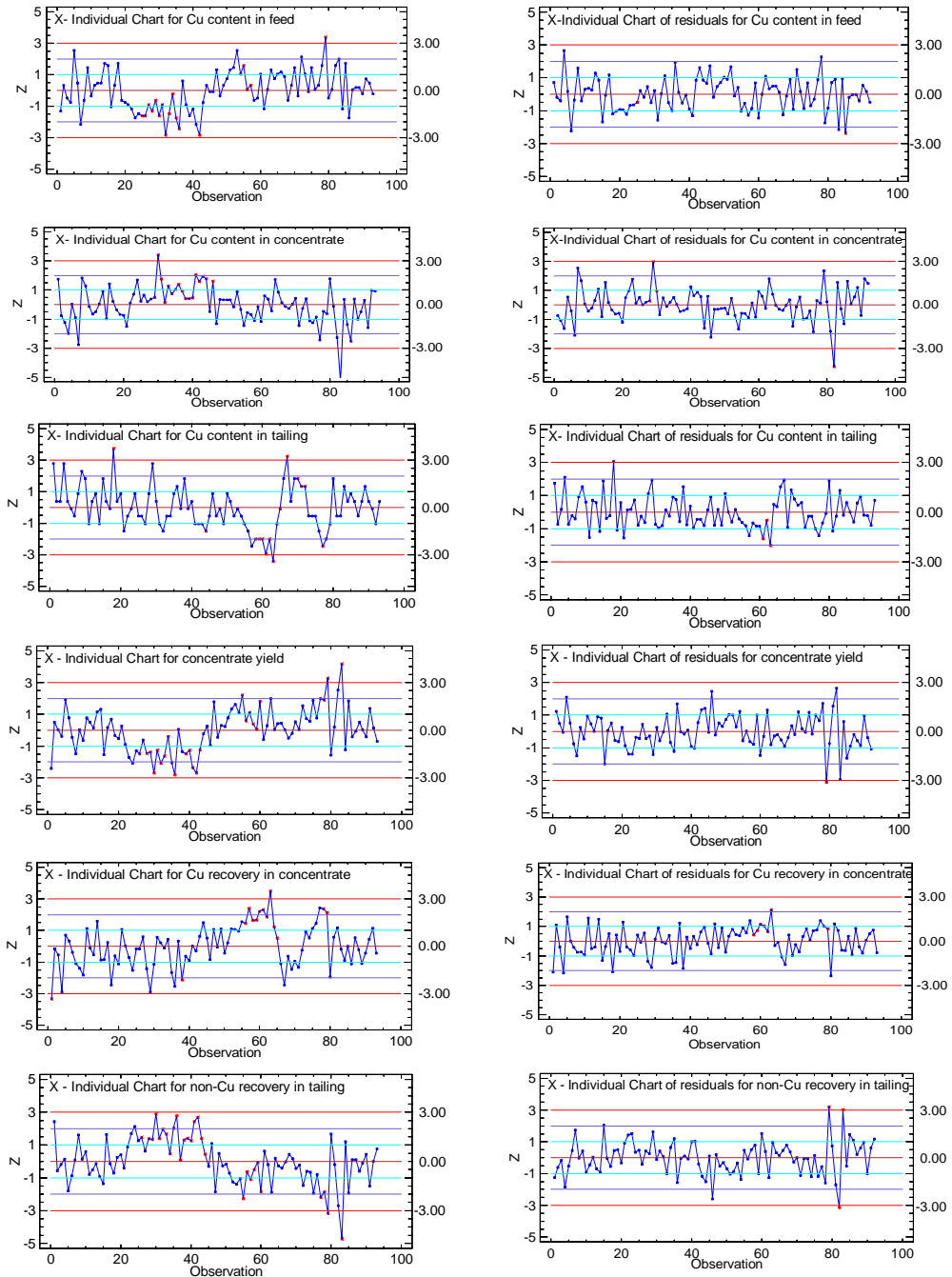


Fig. 5. Comparison of Shewhart's chart of original data (left) and ARIMA residuals (right) with unusual points determined by run rules

From Fig. 5, it can be seen that the number of out-of-control points on the original and residual SPC charts are different. Higher number of out-of-control points are given on the SPC charts (Fig. 5, left), which only assume the independence of data and use original data values. From 93 individual observations unusual points were determined as 18 for α , 19 for β , 16 for ϑ , 25 for γ , 14 for ε and 28 for ε_o by applying the run rules. On the other hand, the residual charts (Fig. 5, right), which consider the autocorrelation give less uncontrolled data points: 2 for α , 4 for β , 4 for ϑ , 1 for γ , 7 for ε and 3 for ε_o . This clearly indicates that wrong decisions can be made about uncontrolled number of process variables, when the data used are autocorrelated. Therefore, if there is any autocorrelation between the consecutive observations it should be taken into account during the process control of the Cu beneficiation variables. The autocorrelation effect on the SPC charts was already shown as the important factor in some mineral processing and mining applications (Samanta and Bhattacharjee, 2001; Bhattacharjee and Samanta, 2002; Samanta, 2002; Eleveli et al., 2009; Tasdemir, 2012a; 2013). Also, the performance of the Shewhart individual chart was shown to be better for weak positive and negative autocorrelation, and it is advisable only for small values of autocorrelation (Karaoglan and Bayhan, 2011; Tasdemir, 2013).

Conclusions

The methodology for monitoring a plant scale copper flotation process was proposed. The technique was based on the statistical quality control charts used to monitor the process and detect shifts in values of its variables. As in the many modern applications of statistical process control charts, the autocorrelation has an important effect on mining and mineral industry data and it should be considered. When the data are autocorrelated the wrong decisions can be made about uncontrolled number of process variables. If there is any autocorrelation between the consecutive observations, it should be taken into account during the process control of the Cu beneficiation parameters.

The data showed that copper upgrading variables obtained during the beneficiation of the copper ore from the Fore-Sudetic Monocline (SW Poland) were autocorrelated over time. It was shown that the typical Shewhart charts are inappropriate for controlling the upgrading variables of the copper ore due to the existence of autocorrelation. The autocorrelation can be described by the suitable ARIMA time series models. It was found that the upgrading variables of copper content in feed, concentrate, product yield and non-copper components recovery in concentrate can be modelled by the ARIMA(0,1,1), while copper content in tailing and copper recovery in concentrate were described by the AR(1).

It was determined that the standard control charts are not capable of detecting right unusual points of the copper ore upgrading variables, when the data are autocorrelated from one time period to the next one. Usage of the residual charts is more suitable to

monitor or control the Cu ore upgrading variables, since the residuals resulted from the ARIMA models consider the dynamics of the process. Since the time series are often used for near future estimation aims, the ARIMA models developed in this research to remove autocorrelation of the Cu upgrading variables can be considered as a useful tool for the short-term process control functions.

Acknowledgements

The authors thank Prof. Jan Drzymala (Wroclaw University of Technology) for his help in many aspects of this work. Financial support by the Polish Statutory Research Grants (S20119 and B20073), the Foundation for Polish Science (FNP), and a Fellowship co-financed by the European Union within the European Social Fund are also greatly acknowledged.

References

- ALWAN L.C., ROBERTS H.V., 1988, *Time Series Modelling for Statistical Process Control*, Journal of Business and Economic Statistics, 6: 86–95.
- APLEY D.W., LEE H.C., 2003, *Design of Exponentially Weighted Moving Average Control Charts for Autocorrelated Processes With Model Uncertainty*, Technometrics, 45(3): 187–198.
- BHATTACHERJEE A., SAMANTA B., 2002, *Practical Issues in the Construction of Control Charts in Mining Applications*, The Journal of The South African Institute of Mining and Metallurgy, 173–180.
- BISGAARD S., KULAHCI M., 2005, *Quality Quandaries: The Effect of Autocorrelation on Statistical Process Control Procedures*, Quality Engineering, 17: 481–489.
- CASTAGLIOLA P., TSUNG F., 2005, *Autocorrelated SPC for non-normal situations*, Qual. Reliab. Engng. Int., 21, 131–161.
- CHOU Y.M., POLANNSKY A.M., MASON R.L., 1998, *Transforming non-normal data to normality in statistical process control*, Journal of Quality Technology, 30(2), pp. 133–141.
- DEMIRKOL Ş., 2008, *Comparison of Control Charts for Autocorrelated Data*, Master Thesis, Graduate School of Natural and Applied Sciences of Dokuz Eylül University.
- DRZYMALA J., 2007, *Mineral processing. Foundation of Theory and Practice of Metallurgy*. Oficyna Wydawnicza PWr, Wrocław.
- DRZYMALA J., LUSZCZKIEWICZ A., FOSZCZ D., 2010, *Application of Upgrading Curves for Evaluation of Past, Present and Future Performance of a Separation Plant*, Mineral Processing and Extractive Metallurgy Review, 31(3), 165–175.
- DRZYMALA J., KOWALCZUK P.B., 2010, *Problems with Statistical Evaluation of Separation Results*, Proceedings of The XIIIth International Mineral Processing Symposium, Cappadocia, Turkey, 1191–1202.
- ELEVLİ S., UZGÖREN N., SAVAS M., 2009, *Control Charts for Autocorrelated Colemanite Data*, Journal of Scientific & Industrial Research, 68: 11–17.
- GANGULI R., TINGLING J.C., 2001, *Algorithms to Control Coal Segregation Under Non-Stationary Conditions Part II: Time Series Based Methods*, International Journal of Mineral Processing, 61, 261–271.
- GLEIT A., 1985, *SO₂ Emissions and Time Series Models*, Journal of Air Pollution Control Association, 35(2), 115–120.
- KETATA C., ROCKWELL M.C., 2008, *Stream Material Variables and Sampling Errors*, Mineral Processing & Extractive Metall. Rev., 29, 104–117.

- KARAOGLAN A.D., BAYHAN G.M., 2011, *Performance Comparison of Residual Control Charts for Trend Stationary First Order Autoregressive Processes*, Gazi University Journal of Science, 24(2):329–33.
- LU C.W., REYNOLDS Jr. M.R., 1999, *Control Charts for Monitoring the Mean and Variance of Autocorrelated Processes*, Journal of Quality Technology, 31: 259–274.
- LU C.W., REYNOLDS, Jr. M.R., 2001, *CUSUM Charts for Monitoring an Autocorrelated Process*, Journal of Quality Technology 33: 316–334.
- MEYER D., NAPIER-MUNN T., 1999, *Optimal Experiments for Time-Dependent Mineral Processes*, Austral. & New Zealand J. Statist., 41(1), 3–17.
- MUKHERJEE A.M., CHANDRA S., 2002, *A Robust Statistical Method to Evaluate Unit Operation in Coal Washery*, International Journal of Mineral Processing, 66, 145–162.
- MONTGOMERY D.C., MASTRANGELO C.M., 1991, *Some Statistical Process Control Methods for Autocorrelated Data*, Journal of Quality Technology, 23: 179–293.
- MONTGOMERY D.C., JENNINGS C.L., KULAHÇI M., 2008, *Introduction to Time Series Analysis and Forecasting*, Wiley Series in Probability and Statistics.
- MONTGOMERY D.C., RUNGER G.C., 2011, *Applied Statistics and Probability for Engineers*, Fifth Edition, John Wiley&Sons, Inc.
- NAPIER-MUNN T.J., MEYER D.H., 1999, *A Modified Paired t-Test for the Analysis of Plant Trials with Data Autocorrelated in Time*, Minerals Engineering, 12(9), 1093–1100.
- NIST/SEMATECH *e-Handbook of Statistical Methods*, 2010, free access at <http://www.itl.nist.gov/div898/handbook/>, 2/16/2010 and 4/15/2013.
- PSARAKIS S., PAPALEONIDA G.E.A., 2007, *SPC Procedures for Monitoring Autocorrelated Processes*, Quality Technology & Quantitative Management, 4(4), 501–540.
- REYNOLDS JR. M.R., LU C.W., 1997, *Control Charts for Monitoring Processes with Autocorrelated Data*, Nonlinear Analysis, Theory, Methods & Applications, 30(7): 4059–4067.
- SAMANTA B., BHATTACHERJEE A., 2001, *An Investigation of Quality Control Charts for Autocorrelated Data*, Mineral Resources Engineering, 10: 53–69.
- SAMANTA B., 2002, *Multivariate Control Charts for Grade Control Using Principal-Component Analysis and Time Series Modelling*, Trans. Inst. Min. Metall. (Sect A: Min Technol), 307: 149–157.
- SINGH S., PRAJAPATI D.R., 2011, *Behavior of CUSUM Chart for Autocorrelated Data*, International Journal of Engineering Sciences Research, Vol. 02, Issue 04, 1–8.
- SMETI E.M., KOUSOURIS L.P., TZOUMERKAS P.C., GOLFINOPOULOS S.K., 2006, *Statistical Process Control Techniques on Autocorrelated Turbidity Data from Finished Water Tank*, Proceedings of An International Conference on Water Science and Technology Integrated Management on Water Resources, AQUA 2006, Athens, Greece.
- SRINIVASAN A., 2001, *Application of information technology and statistical process control in pharmaceutical quality assurance & compliance*, MSc Thesis in Electrical Engineering & Computer Science, Massachusetts Institute of Technology.
- STOUMBOS Z.G.B., REYNOLDS Jr. M.R., 2000, *Robustness to non-normality and auto-correlation of individuals control charts*, Journal of Statistical Computation and Simulation, 66(2), pp. 145–187.
- STAPENHURST T., 2005, *Mastering Statistical Process Control*, A Handbook for Performance Improvement Using Cases, Elsevier.
- TASDEMIR A., 2012a, *Effect of Autocorrelation on the Process Control Charts in Monitoring of a Coal Washing Plant*, Physicochemical Problems of Mineral Processing, 48(2), 495–512.

- TASDEMIR A., 2012b, *Prediction of Chromite Concentrate Recovery in A Chromite Processing Plant by ARIMA Model of Time Series*, Proceedings of XIIIth International Mineral Processing Symposium, Bodrum, Turkey, 911–918.
- TASDEMIR A., 2013, *Analysis of Chromite Processing Plant Data by First Order Autoregressive Model*, Physicochemical Problems of Mineral Processing, 49(1), 157–174.
- TESTIK M.C., 2005, *Model Inadequacy and Residuals Control Charts for Autocorrelated Processes*, Quality and Reliability Engineering International, 21, 115–130.
- THAGA K., 2008, *Control Chart for Autocorrelated Process with Heavy Tailed Distributions*, Economic Quality Control, 23(2): 197–206.
- TRYBALSKI K., CIEPLY J., 2000, *ARMA Type Model for Copper Ore Flotation*, Proceedings of the XXI International Mineral Processing Congress, Developments in Mineral Processing C3(72–78).
- WILLS B.A., NAPIER-MUNN T., 2006, *Mineral Processing Technology, An Introduction to the Practical Aspects of Ore Treatment and Mineral Recovery*, Elsevier Science & Technology Books.
- ZHANG N.F., 1997, *Detection Capability of Residual Control Chart for Stationary Process Data*, Journal of Applied Statistics, 24(4): 475–492.

Received May 30, 2013; reviewed; accepted, July 23, 2013

SYNTHESIS AND PHYSICOCHEMICAL CHARACTERISTICS OF TITANIUM DIOXIDE DOPED WITH SELECTED METALS

**Katarzyna SIWINSKA-STEFANSKA^{*}, Dominik PAUKSZTA^{*},
Adam PIASECKI^{**}, Teofil JESIONOWSKI^{*}**

^{*} Poznan University of Technology, Faculty of Chemical Technology, Institute of Chemical Technology and Engineering, Marii Skłodowskiej-Curie 2, PL-60-965, Poznan, Poland; e-mail: Katarzyna.Siwinska-Stefanska@put.poznan.pl, phone: +48 616653626, fax: +48 616653649

^{**} Poznan University of Technology, Faculty of Mechanical Engineering and Management, Institute of Materials Science and Engineering, Jana Pawla II 24, PL-60-965, Poznan, Poland

Abstract: The paper details with of the preparation and physicochemical characterisation of nano- and microstructured TiO₂ doped with Fe and Co produced by the sol-gel method using titanium alkoxide as the precursor of titania as well as iron or cobalt nitrates as dopant sources. Fe and Co doped TiO₂ materials were successfully prepared with two different methods. The effect of the dopant type on the synthesis of TiO₂ powders was investigated. The physicochemical properties of the studied samples were determined. The characterisation included determination of the dispersion and morphology of the systems (particle size distribution, SEM images), characteristics of porous structure (BET isotherms), crystalline structure (XRD), surface composition (EDS), as well as thermal stability (TG/DTA).

Keywords: titanium dioxide, sol-gel method, doping, TiO₂ surface modification, Fe and Co dopant

Introduction

Titanium dioxide (TiO₂) has emerged as one of the most fascinating materials in the modern era. It has captured the attention of physical chemists, physicists, material scientists, and engineers exploring distinctive semiconducting and photocatalytic properties (Wu, 2007; Huang, 2009; Wang, 2009; Xu, 2011; He, 2012). Inertness to the chemical environment and long-term photostability has made TiO₂ an important component in many practical applications and in commercial products. From drugs to doughnuts, cosmetics to catalysts, pigments to pharmaceuticals, and sunscreens to solar cells, TiO₂ is used as a desiccant, brightener, or reactive mediator.

Titanium dioxide represents an effective photocatalyst for water and air purification and for self-cleaning surfaces. Additionally, it can be used as an antibacterial agent because of strong oxidation activity and superhydrophilicity (Fujishima, 2006). TiO_2 shows relatively high reactivity and chemical stability under ultraviolet light ($\lambda < 387 \text{ nm}$), whose energy exceeds the band gap of 3.3 eV in the anatase crystalline phase. The development of photocatalysts exhibiting high reactivity under visible light ($\lambda > 400 \text{ nm}$) should allow the main part of the solar spectrum to be used, even under poor illumination of interior lighting. Several approaches to modifying TiO_2 have been proposed: metal-ion implanted TiO_2 (using transition metals: Cu, Co, Ni, Cr, Mn, Mo, Nb, V, Fe, Ru, Au, Ag, Pt) (Anpo, 2000; Fuente, 2001; Yamashita, 2001), reduced TiO_x photocatalysts (Takeuchi, 2000; Ihara, 2001), non-metal doped- TiO_2 (N, S, C, B, P, I, F) (Ohno, 2003; Yu, 2003; Liu, 2005), composites of TiO_2 with semiconductor having lower band gap energy (e.g., Cd-S particles (Hirai, 2001), sensitizing of TiO_2 with dyes (e.g., thionine) (Chatterjee, 2001) and TiO_2 doped with upconversion luminescence agent (Zhou, 2006; Wang, 2007).

The aim of the study was verification of preparation methods of TiO_2 doped with metallic species, including two types of dopants and doping methods. The effect of the doping process on the fundamental physicochemical properties for all obtained samples was evaluated.

Experimental

Materials

The pure and doped TiO_2 powders were synthesized employing the sol-gel method, in which titanium tetraisopropoxide ($\text{Ti}(\text{OC}_3\text{H}_7)_4$, 97%) was used as the precursor of titania, ammonia (NH_4OH , 25%) as catalyst, 2-propanol ($\text{C}_3\text{H}_7\text{OH}$, 99.5%) as solvent, iron(III) nitrate ($\text{Fe}(\text{NO}_3)_3 \cdot 9\text{H}_2\text{O}$, 98%) and cobalt(II) nitrate ($\text{Co}(\text{NO}_3)_2 \cdot 6\text{H}_2\text{O}$, 98%) as dopant sources.

Synthesis of TiO_2 via sol-gel method

TiO_2 powder was prepared by a sol-gel process, in which sol was prepared by mixing titanium tetraisopropoxide (TTIP), 2-propanol, and ammonia at room temperature. 15 cm^3 (0.049 mole) of TTIP as the starting material was dissolved in 100 cm^3 (1.304 mole) of 2-propanol. Upon stirring the catalyst, ammonia was introduced at a constant rate of 1 cm^3/min . The titanium alkoxide solution was hydrolysed by adding 15 cm^3 (0.033 mole) of ammonia. The initially clear solution turned into a white emulsion. This solution was vigorously stirred for 1 h. The entire system was transferred to a round-bottomed flask and placed in a vacuum rotary evaporator, in order to remove the solvent (water bath temperature 60 °C, pressure 136 mbar). The subsequent stage involved filtration of the mixture under reduced pressure. The sample obtained in this way was washed with distilled water. At the terminal stage, the sample was dried by

convection at 105 °C for 18 h. The sample was then calcined at 600 °C for 2 h. The proposed method for preparing TiO₂ is presented schematically in Fig. 1a.

Synthesis of doped-TiO₂

The doped-TiO₂ materials were prepared following two different methods. The first method: solution A was prepared by adding 15 cm³ (0.049 mole) of titanium tetraisopropoxide to 100 cm³ (1.304 mole) of 2-propanol. A certain amount of Fe(NO₃)₃ or Co(NO₃)₂ was dissolved in 100 cm³ (0.782 mole) of 2-propanol (solution B). Subsequently, solution B and ammonia (catalyst – solution C) were introduced to solution A, at a constant rate of 5 and 1 cm³/min, respectively. The resulting solution was vigorously stirred. When dosing of solutions B and C was terminated, the emulsion obtained was mixed for 30 min. The second method: solution A was prepared by adding 15 cm³ (0.049 mole) of titanium tetraisopropoxide to 50 cm³ (0.670 mole) of 2-propanol. At first, a certain amount of Fe(NO₃)₃ or Co(NO₃)₂ was dissolved in 100 cm³ (0.782 mole) of 2-propanol and then the solution obtained (solution B) was dosed to solution A at a constant rate of 5 cm³/min. The obtained solution was vigorously stirred. Next, 15 cm³ (0.033 mole) of ammonia was dissolved in 50 cm³ (0.670 mole) of 2-propanol (solution C) and then the resulting mixture was introduced to a mixture of solution A and B, at a constant rate of 1 cm³/min. When dosing of solution C was terminated, the obtained emulsion was mixed for 30 min. The concentrations of Fe and Co calculated for mass of the dry sample of titania were 0.10; 0.25; 0.57; 0.75; 1.00; 1.70 and 2.80% mass, respectively. Classification of the obtained products was realised in analogous way as in the case of preparation titanium dioxide. The final products of Fe- and Co-doped titania have a yellow/orange and green colour, respectively. Fig. 1 b and c presents two doping methods of titania.

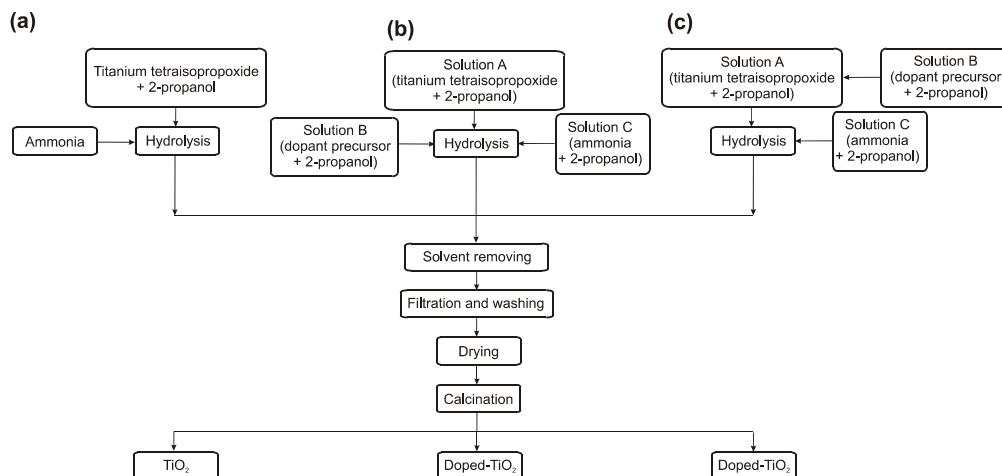


Fig. 1. Preparation of (a) TiO₂ and doped-TiO₂ by (b) first method, (c) second method via sol-gel method

Determination of physicochemical properties

The doped-TiO₂ samples were subjected to comprehensive characterisation using the most advanced analytical methods and techniques. The dispersive properties of TiO₂/Fe and TiO₂/Co samples were evaluated based on the particle size distributions and polydispersity index (PDI) determined using a Zetasizer Nano ZS made by Malvern Instruments Ltd. operating based on non-invasive back scatter technique. The samples of doped-TiO₂ were also subjected to morphological and microstructural analysis using a scanning electron microscope – Zeiss EVO40. In order to characterise their porous structure, nitrogen adsorption/desorption isotherms at 77 K and parameters such as surface area (A_{BET}), pore volume (V_p) and average pore size (S_p) were determined using an ASAP 2020 instrument (Micromeritics Instrument Co.). All samples were degassed at 120 °C for 4 h prior to measurement. The surface area was determined by the multipoint BET (Brunauer–Emmett–Teller) method using the adsorption data in the relative pressure (p/p_0). The BJH (Barrett–Joyner–Halenda) method was applied to determine the pore volume and the average pore size. The doped-TiO₂ samples were also subjected to crystalline structure determination using the WAXS method (wide-angle X-ray scattering). X-ray diffraction measurements were performed using Cu K α ($\lambda=1.54056$ Å) radiation. The accelerating voltage and the applied current were 30 kV and 15 mA respectively. The samples were scanned at a rate of 0.04° over an angular range of 5–60°. Moreover, the surface composition of the obtained materials was analysed using an EDS technique (energy dispersive X-ray spectroscopy) using a Princeton Gamma-Tech unit equipped with a prism digital spectrometer. Thermogravimetric analysis was performed using a Jupiter STA 449 F3 (Netzsch GmbH). Samples weighing approximately 10.0 mg were placed in an Al₂O₃ crucible, and heated at a rate of 10 °C/min from 30 to 1000 °C in a nitrogen atmosphere.

Results and discussion

The aim of the first stage of the study was to characterise the dispersive properties and morphology of the pure TiO₂ obtained via the sol-gel method. The titanium dioxide is characterised by a monomodal particle size distribution with a relatively wide band covering the diameter range of 955–2670 nm. The maximum volume contribution of 28.4% corresponds to agglomerates of 1720 nm in diameter (Fig. 2a). The polydispersity index of TiO₂ is 0.153, which means that this sample is rather homogeneous. The SEM microphotograph of the titanium dioxide studied presented in Fig. 2b confirms the presence of particles of micro-sized diameter (corresponding to those indicated in the particle size distribution), their almost spherical shape and high homogeneity.

The structure of obtained sample was studied using the WAXS method. The crystalline structure of sample determines their suitability for particular applications (catalysis, paints, lacquers, and polymer fillers). Titania of well-defined crystalline

structure shows diffraction maxima at certain specific 2-theta values. Figure 2c shows the WAXS pattern of prepared TiO₂ sample of the anatase structure, characterised by the presence of maxima at 2 Θ values of 25, 38, 48, 54 and 55, which is a confirmation of the effective preparation process (JCPDS, Card 21-1272.).

Characterisation of the porous structure of pure TiO₂ included determination of the nitrogen adsorption/desorption isotherms and calculation of the surface area, size and volume of pores. Synthetic TiO₂, obtained via the sol-gel method, has defined surface activity, which is indicated by its specific surface area of 17.4 m²/g. It can be classified as mesoporous adsorbent as its pore volume is $V_p = 0.013$ cm³/g and pore diameter is $S_p = 2.9$ nm.

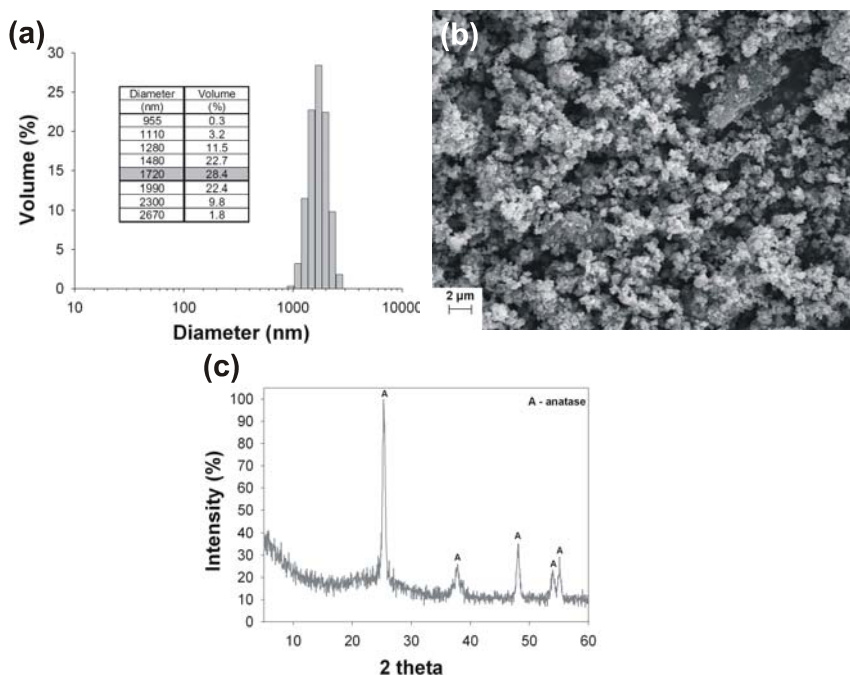


Fig. 2. Particle size distribution (a), SEM microphotograph (b) and WAXS pattern (c) of TiO₂ obtained via sol-gel method

At the next stage, the titanium dioxide preparation process was supplemented with doping using selected metals (Fe and Co). The main aim of the study was to evaluate the efficiency of the doping process of synthetic titanium dioxide and to determine its influence on the fundamental physicochemical properties of the obtained systems. Samples of TiO₂ doped with Fe and Co were subjected to dispersive and morphological characterisation. Table 1 presents the dispersive characteristics of doped-TiO₂ samples. The results prove that the doping process caused significant changes in the dispersive character of the obtained systems.

Table 1. Dispersive properties of doped-TiO₂ obtained via sol-gel method

Amount of metal dopant (% mass)	Particle size distributions by volume (nm) and maximum volume contribution (%)	Polydispersity index
TiO ₂ /Fe (first method)		
0.10	295–1110 (531 nm – 24.9)	0.329
0.57	255–825 (459 nm – 25.5)	0.191
1.00	220–615 (396 nm – 27.3)	0.298
2.80	190–825 (396 nm – 8.7) 3090–6440 (5560 nm – 25.7)	0.424
TiO ₂ /Fe (second method)		
0.10	342–955 (615 nm – 29.2)	0.079
0.57	342–1280 (712 nm – 23.4)	0.342
1.00	531–1990 (1280 nm – 20.2)	0.099
2.80	396–1480 (712 nm – 23.7)	0.264
TiO ₂ /Co (first method)		
0.10	531–1480 (955 nm – 26.3)	0.098
0.57	615–1720 (1110 nm – 25.3)	0.247
1.00	255–615 (459 nm – 28.6)	0.417
2.80	295–825 (531 nm – 27.7)	0.205
TiO ₂ /Co (second method)		
0.10	531–2300 (1280 nm – 19.7)	0.267
0.57	459–1720 (955 nm – 23.4)	0.305
1.00	531–1990 (1110 nm – 22.4)	0.195
2.80	342–1280 (615 nm – 22.8)	0.260

The substantial differences in the mean diameters of TiO₂ particles doped with two different metals in different amounts, imply that the dopant type have a great effect on the dispersive parameters of the final products. The dispersive characteristics show that noticeable changes in the particle size of all doped TiO₂ appear independently of the type and quantity of the dopant as well as the doping method. According to the results, by far the best dispersive properties are shown by materials doped with iron. All samples of the doped materials have particles of smaller diameter than those determined in the sample of pure titanium dioxide. In most samples, the doping of pure TiO₂ with selected dopant (in relation to the amount of dopant used) contributed to a decrease in the sample's homogeneity (higher polydispersity index) – see Table 1 – compared to that of pure titania.

The SEM microphotographs of the samples studied presented in Fig. 3 confirm the presence of particles of micro-sized diameter (corresponding to those indicated in particle size distributions), high homogeneity, almost spherical shape and showing a small tendency to form agglomerate structures.

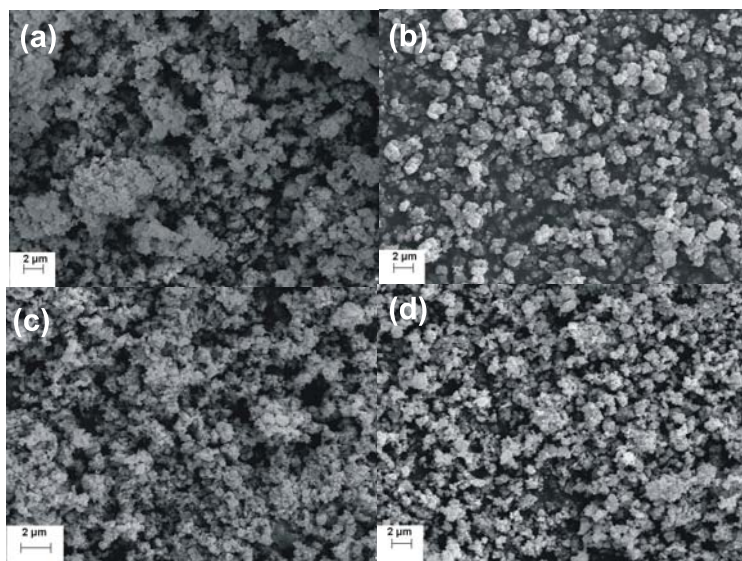


Fig. 3. SEM microphotographs of TiO₂ doped with 1.0% mass of Fe (first method – a), 1.0% mass of Fe (second method – b), 1.0% mass of Co (first method – c) and 1.0% mass of Co (second method – d)

The XRD patterns of different TiO₂ samples (pure, Fe and Co doped) are shown in Fig. 4. The XRD pattern of pure TiO₂ shows five primary peaks at 25, 38, 48, 54 and 55, which can be attributed to different diffraction planes of anatase. The XRD patterns of doped samples show different peaks at 28, 36, 39, 41, 44, 54 and 57, which resulted from different diffraction planes of the rutile form of TiO₂. Results show that the addition of iron or cobalt to the titania preparation process has a significant effect on crystalline structure formation. The XRD patterns of Fe and Co doped TiO₂ samples almost coincide with that of pure TiO₂, showing no diffraction peaks related

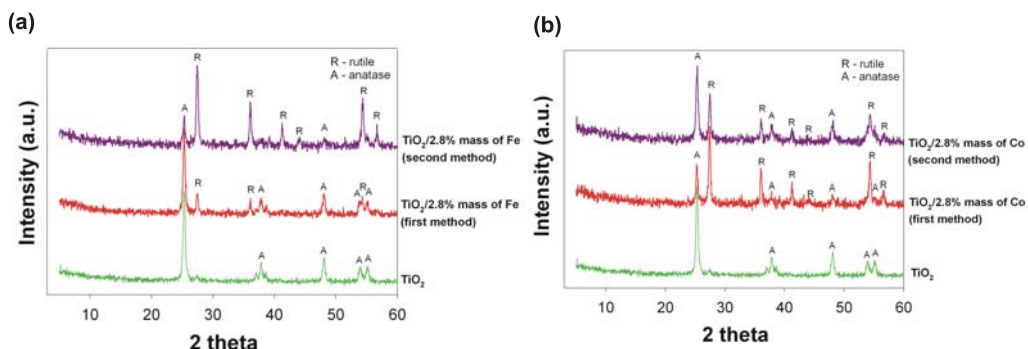


Fig. 4. WAXS patterns of TiO₂ doped with Fe (a) and Co (b)

with iron and cobalt. Our observations are in agreement with previous research (Amadelli, 2008; Ambrus, 2008; Hamadani, 2010). It can be concluded that selected dopants are not incorporated directly onto titania structure, but are placed onto the TiO_2 surface. Fe^{3+} and Co^{2+} ions influence the crystalline structure formation of TiO_2 and cause the transformation of the anatase phase to rutile.

At the next stage of the study, the adsorption abilities of the doped titanium dioxide samples were characterised. The fundamental parameters determining the surface activity of the doped samples, the surface area (BET) and pore size distribution, are given in Table 2.

Table 2. Porous structure parameters of native and doped- TiO_2

Amount of metal dopant (% mass)	A_{BET} (m^2/g)	V_p (cm^3/g)	S_p (nm)	A_{BET} (m^2/g)	V_p (cm^3/g)	S_p (nm)
	TiO_2/Fe (first method)			TiO_2/Co (first method)		
0.10	10.2	0.009	3.1	9.9	0.008	3.0
0.57	8.7	0.006	2.9	8.4	0.006	2.6
1.00	6.7	0.005	2.8	6.9	0.004	2.5
2.80	4.5	0.003	2.8	4.3	0.004	2.5
	TiO_2/Fe (second method)			TiO_2/Co (second method)		
0.10	12.8	0.012	3.2	14.5	0.013	3.3
0.57	6.2	0.004	2.8	13.6	0.009	2.7
1.00	5.8	0.004	2.8	9.8	0.008	2.6
2.80	4.7	0.003	2.8	7.3	0.007	2.6

A considerable decrease in the surface area relative to that of the pure sample was observed for all doped samples. Addition of any of dopants also resulted in a decrease in the pore diameters relative to those of native TiO_2 , irrespective of the quantity of dopant. The BET surface areas decrease was observed together with increasing Fe and Co amount in the sample structure. The TiO_2 doped with Co obtained via first method has the lowest BET surface area as compared to Co doped TiO_2 obtained according to second method.

The surface composition of the obtained samples was studied by the EDS technique. EDS results are given in Table 3. From the elemental mapping mode, highly and uniformly dispersed Fe and Co on the TiO_2 support were observed. This implies good interaction between dopant and support in the preparation process using the sol-gel method. The EDS technique was used to detect the amount of Fe and Co in the titania structure. Doped titania samples contain ca. 0.12 and ca. 0.56% mass of Fe were produced via first method using 0.10 and 0.57% mass of Fe as a dopant. It can be seen that Fe amount is very close to the initial values. Wen et al. (2012) have observed

the analogous results. The EDS analysis of Fe and Co doped TiO₂ confirmed the presence of Fe and Co ions in the powder structure, as the opposite of XRD patterns. The XRD patterns do not show any peaks related to Fe and Co, presence in TiO₂ structure.

Table 3. Surface composition of doped-TiO₂

Amount of metal dopant (% mass)	Compound content (%)					
	Ti	O	Fe	Ti	O	Co
	TiO ₂ /Fe (first method)			TiO ₂ /Co (first method)		
0.10	54.92	44.95	0.12	52.10	47.85	0.05
0.57	51.08	48.36	0.56	55.44	44.13	0.43
1.00	50.06	49.12	0.82	51.63	47.74	0.63
2.80	54.13	43.82	2.05	55.86	42.18	1.96
	TiO ₂ /Fe (second method)			TiO ₂ /Co (second method)		
	Ti	O	Fe	Ti	O	Co
0.10	50.61	49.19	0.20	50.11	49.83	0.06
0.57	48.77	50.62	0.61	50.80	48.78	0.42
1.00	52.32	46.79	0.89	52.01	47.41	0.58
2.80	51.07	46.83	2.10	51.13	47.08	1.79

Investigation of the effectiveness of the doped process has been broadened by thermal analysis TG/DTA (Fig. 5) of the pure TiO₂, and selected doped materials. The results of TG/DTA analysis allowed for an estimate of the temperature range that corresponds to important chemical and structural transitions of the obtained systems.

Figure 5a shows TGA thermograms of pure titanium dioxide and systems obtained by doping titania with 2.8% mass of Fe. Analysis of the obtained systems was performed in order to determine thermal stability. In case of pure titania, first mass loss is observable in a temperature range of 30 to 300 °C, and most likely corresponds to loss of physically and chemically bound water. At this point mass loss is slightly above 0.4%. Total mass loss of pure TiO₂ is equal to ~0.9%. The TGA thermograms of doped-TiO₂ with iron show similar changes in thermal stability in comparison to pure titania. Total mass loss of doped samples via first and second method is equal to ~0.7 and ~1.2%, respectively. A similar change of thermal stability was observed of Co-doped TiO₂ (Fig. 5b). Total mass loss of Co-doped samples via the first and second method is equal to ~0.75 and ~0.8%, respectively.

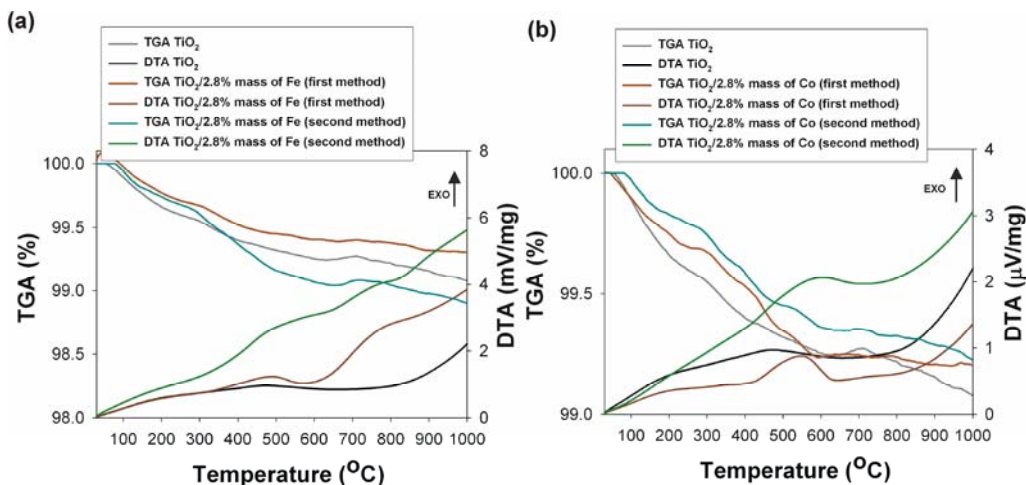


Fig. 5. Thermograms of doped TiO₂ with Fe (a) and Co (b) obtained by sol-gel method

Conclusions

According to the results presented above, the systems obtained after doping of selected dopants (Fe and Co) on titania were characterised by particles of smaller diameter and lower homogeneity compare to pure TiO₂.

The XRD patterns show that the addition of iron or cobalt to the titania preparation process has a significant effect on crystalline structure formation. The XRD patterns of Fe and Co doped TiO₂ samples almost coincide with that of pure TiO₂, showing no diffraction peaks related with iron and cobalt.

The type of dopant and doping method has a significant influence on the surface activity of the systems obtained by sol-gel method. The porous structure of the doped titania decreased proportionally with increasing concentration of the dopant. Surface area measurements were carried out on TiO₂ samples doped with Fe and Co, indicating that the adopted doping procedure brought some surface area change with respect to the pristine oxide.

Iron and cobalt were found to be effectively doped on the surface of synthetic the TiO₂ sample. EDS analysis of Fe and Co doped TiO₂ confirmed the presence of Fe and Co ions in the powder structure,

The Fe and Co doped titania acquired via doping of selected dopants are characterised by a small shift in thermal stability. However, a small change in the mass loss of doped samples, in comparison to pure titania, was observed.

Acknowledgements

This work was supported by Polish National Centre of Science research grant no. 2011/01/B/ST8/03961.

References

- AMADELLI R., SAMIOLO L., MALDOTTI A., MOLINARI A., VALIGI M., GAZZOLI D., 2008, *Preparation, characterisation, and photocatalytic behaviour of Co-TiO₂ with visible light response*, International Journal of Photoenergy, Article ID 853753, 9 pages, doi: 10.1155/2008/853753.
- AMBRUS Z., BALÁZS N., ALAPI T., WITTMANN G., SIPOS P., DOMBI A., MOGYORÓSI K., 2008, *Synthesis, structure and photocatalytic properties of Fe(III)-doped TiO₂ prepared from TiCl₃*, Applied Catalysis B: Environmental 81, 27–37.
- ANPO M., 2000, *Use of visible light. Second-generation titanium dioxide photocatalysts prepared by the application of an advanced metal ion-implantation method*, Pure and Applied Chemistry 72, 1787–1792.
- CHATTERJEE D., MAHATA A., 2001, *Demineralization of organic pollutants on the dye modified TiO₂ semiconductor particulate system using visible light*, Applied Catalysis B: Environmental 33, 119–125.
- FUERTE M.D.H.A., MAIRA A.J., MARTINEZ-ARIAS A., FERNADEZ-GARCIA M., CONESA J.C., SORIA J., 2001, *Visible light-activated nanosized doped-TiO₂ photocatalysts*, Chemical Communications 24, 2718–2719.
- FUJISHIMA X., ZHANG C.R., 2006, *Titanium dioxide photocatalysis: Present situation and future approaches*, Chimie 9, 750–760.
- HAMADANIAN M., REISI-VANANI A., MAJEDI A., 2010, *Sol-gel preparation and characterization of Co/TiO₂ nanoparticles: application to degradation of Methyl Orange*, Journal of the Iranian Chemical Society 7, S52–S58.
- HE Z.L., QUE W.X., XIE H.X., CHEN J., YUAN, P. SUN., 2012, *Facile synthesis of self-sensitized TiO₂ photocatalysts and their higher photocatalytic activity*, Journal of the American Ceramic Society 95, 3941–3946.
- HIRAI T., SUZUKI K., KOMASAWA I., 2001, *Preparation and photocatalytic properties of composite CdS nanoparticles-titanium dioxide particles*, Journal of Colloid and Interface Science 244, 262–265.
- HUANG D.G., LIAO S.J., ZHOU W.B., QUAN S.Q., LIU L., HE Z.J., WAN J.B., 2009, *Synthesis of samarium- and nitrogen-co-doped TiO₂ by modified hydrothermal method and its photocatalytic performance for the degradation of 4-chlorophenol*, Journal of Physics and Chemistry of Solids 70, 853–859.
- IHARA T., MIYOSHI M., ANDO M., SUGIHARA S., IRIYAMA Y., 2001, *Preparation of a visible-light-active TiO₂ photocatalyst by RF plasma treatment*, Journal of Materials Science 36, 4201–4207.
- JCPDS International Center of Diffraction Data (1980), JCPDS Powder Diffraction File, Card 21-1272.
- LIU Y., CHEN X., LI J., BURDA C., 2005, *Photocatalytic degradation of azo dyes by nitrogen-doped TiO₂ nanocatalysts*, Chemosphere 61, 11–18.
- OHNO T., MITSUI T., MATSUMURA M., 2003, *Photocatalytic activity of S-doped TiO₂ photocatalyst under visible light*, Chemistry Letters 32, 364–365.
- TAKEUCHI K., NAKAMURA I., MATSUMOTO O., SUGIHARA S., ANDO M., IHARA T., 2000, *Preparation of visible-light-responsive titanium oxide photocatalysts by plasma treatment*, Chemistry Letters 29, 1354–1355.
- WANG J., MA T., ZHANG G., ZHANG Z., ZHANG X., JIANG Y., ZHAO G., ZHANG P., 2007, *Preparation of nanometer TiO₂ catalyst doped with upconversion luminescence agent and investigation on degradation of acid red B dye using visible light*, Catalysis Communications 8, 607–611.

- WANG J., TAFEN D.N., LEWIS J.P., HONG Z.L., MANIVANNAN A., ZHI M.J., LI M., WU N.Q., 2009, *Origin of photocatalytic activity of nitrogen-doped TiO₂ nanobelts*, Journal of the American Ceramic Society 131, 12290–12297.
- WEN L., LIU B., ZHAO X., NAKATA K., MURAKAMI T., FUJISHIMA A., 2012, *Synthesis, characterization, and photocatalysis of Fe-doped TiO₂: a combined experimental and theoretical study*, International Journal of Photoenergy, Article ID 368750, 10 pages, doi: 10.1155/2012/368750.
- WU X.H., QIN W., DING X.B., WEN Y., LIU H.L., JIANG Z.H., 2007, *Photocatalytic activity of Eu-doped TiO₂ ceramic films prepared by microplasma oxidation method*, Journal of Physics and Chemistry of Solids 68, 2387–2393.
- XU X.J., FANG X.S., ZHAI T.Y., ZENG H.B., LIU B.D., HU X.Y., BANDO Y., GOLBERG D., 2011, *Tube-in-tube TiO₂ nanotubes with porous walls: Fabrication, formation mechanism, and photocatalytic properties*, Small 7, 445–449.
- YAMASHITA H., HARADA M., MISAKA J., 2001, *Application of ion beam techniques for preparation of metal ion-implanted TiO₂ thin film photocatalyst available under visible light irradiation: Metal ion implantation and ionized cluster beam method*, Journal of Synchrotron Radiation 8, 569–571.
- YU J.C., ZHANG L., ZHENG Z., ZHAO J., 2003, *Synthesis and characterization of phosphated mesoporous titanium dioxide with high photocatalytic activity*, Chemistry of Materials 15, 2280–2286.
- ZHOU W., ZHENG Y., WU G., 2006, *Novel luminescent RE/TiO₂ (RE=Eu, Gd) catalysts prepared by in-situ sol-gel approach construction of multi-functional precursors and their photo or photocatalytic oxidation properties*, Applied Surface Science 252, 1387–1392.

Received May 17, 2013; reviewed; accepted July 17, 2013

EFFECT OF SILVER, NICKEL AND COPPER CYANIDES ON GOLD ADSORPTION ON ACTIVATED CARBON IN CYANIDE LEACH SOLUTIONS

Baris SAYINER*, Neset ACARKAN**

* Kozagold Corp. Kaymaz Gold Mine, P.O. Box 26640, Eskisehir, Turkey, baris.sayiner@gmail.com

** Istanbul Technical University, Mineral Processing Eng. Faculty, P.O. Box 34469, Istanbul, Turkey, acarkan@itu.edu.tr

Abstract: The effect of Ag, Ni and Cu cyanides on gold adsorption on activated coconut carbon in cyanide leach solutions was investigated by synthetic cyanide leach solutions containing gold and other metal cyanides. According to the adsorption tests Ag remarkably reduces the gold adsorption on activated carbon by competing with gold to adsorption sites. When the Ag concentration in solution increases up to 200 ppm the carbon adsorption method for gold recovery becomes inapplicable. Ni has an effect on gold adsorption on activated carbon, however even at as high concentrations of Ni as 250 ppm residual Au in solution is still below 1 ppm. Cu addition up to 300 ppm does not affect the gold loading significantly. According to the adsorption test studies, it is concluded that the metal-cyanides diminish the gold adsorption on activated carbon by adsorbing themselves and competing with gold. When the metals are present in the leach solution all together with gold, they also prevent adsorption of themselves as well as gold. Thus, when Au, Ag, Ni and Cu are present in solution simultaneously, the adsorption of all these metals decreases. The adsorption results were modeled by Fleming k_n adsorption kinetic model.

Keywords: gold, silver, nickel, copper, cyanide leaching, activated carbon adsorption

Introduction

Gold is recovered from its ores hydrometallurgically by the cyanide leach process. The gold reacts with cyanide according to reaction (Davidson and Sole, 2007):



The gold ore after grinding to 80% –5 micrometers, is fed to leaching tanks in the form of slurry including 45% solid. Gold is dissolved from its ore by cyanide, according to reaction 1 in leaching tanks and then the slurry passes through adsorption tanks containing activated granular coconut carbon dispersed in the slurry. The system

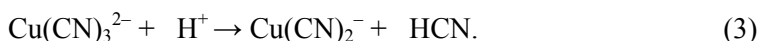
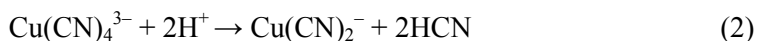
where gold is recovered from the leach solution by activated carbon is named the CIP (carbon in pulp) process. In the adsorption unit cyanide leach slurry first goes through the last adsorption tank and the carbon from the last tank through the first adsorption tank due to counter current flow. The dissolved gold-cyanide complex ($\text{Au}(\text{CN})_2^-$) is adsorbed on the activated carbon (Ibrado and Fuerstenau, 1995; Rees and Van Deventer, 2001). The barren slurry leaves the process from the last tank and gold loaded carbon is driven from the first adsorption tank. Gold loaded carbon is taken to the elution column in which gold is stripped from carbon and directed to the electrolysis process.

Many other metals, such as Ag, Ni, Cu, Fe, Zn etc., are dissolved with gold from ores as cyanide species. Thus, after cyanide leaching of ores, there are many other metal impurities in the leach solution, competing with gold to be adsorb on activated carbon.

According to the previous studies present in the literature, in cyanide leaching Ag dissolves as $\text{Ag}(\text{CN})_2^-$ complex and adsorbs on carbon better than the cyanides of Ni and Cu. When the concentration ratio of $[\text{Ag}]/[\text{Au}]$ reaches 2:1, Ag starts to inhibit the Au adsorption on activated carbon (Vegter and Sandebergh, 1997; Adams, 1992).

Ni dissolves as a $\text{Ni}(\text{CN})_4^{2-}$ complex, adsorbs on activated carbon and at high concentrations decreases the Au adsorption (Xie, 2010). Besides, if the gold ore has significant content of Ni that dissolves and adsorbs on activated carbon, Ni comes with gold up to smelting stage and increases the smelting temperature of the metal mixture, because of the high melting point of Ni at 1455 °C comparing with Au melting point of 1063 °C.

Among these metals, Cu has a special place. Cu forms complexes with cyanide as $\text{Cu}(\text{CN})_2^-$, $\text{Cu}(\text{CN})_3^{2-}$ and $\text{Cu}(\text{CN})_4^{3-}$. The $\text{Cu}(\text{CN})_2^-$ complex adsorbs on carbon much stronger than the gold complex, that it stripes the previously adsorbed gold from activated carbon placing on carbon itself. However, adsorption of $\text{Cu}(\text{CN})_3^{2-}$ and $\text{Cu}(\text{CN})_4^{3-}$ complexes is so much lower that these species exert approximately no effect on gold adsorption (Dai and Breuer, 2009). The Cu-cyanide complexes change accordingly to the free cyanide concentration and the pH of the solution. When pH decreases the formation of $\text{Cu}(\text{CN})_2^-$ complex occurs according to reactions:



Thus, because pH of the cyanide leach solutions is as high as 10.5 and the leach solution contains as much free cyanide as 200 ppm NaCN, it might be expected that $\text{Cu}(\text{CN})_3^{2-}$ and $\text{Cu}(\text{CN})_4^{3-}$ forms are obtained and they have no significant effect on the gold adsorption (Xie, 2010). This phenomenon is confirmed by adsorption tests with synthetic Cu-cyanide presented in this paper.

Iron dissolves from its sulfide minerals as a $\text{Fe}(\text{CN})_6^{4-}$ strong complex. However this complex does not either adsorb on the carbon or prevent the adsorption of gold

even at as high concentrations as 1000 ppm (Romero and Sampaio, 1993; Sheya and Palmer, 1989).

Besides, Zn-cyanide has no significant effect on adsorption of gold between pH of 6 and 12 according to the previous studies (Romero and Sampaio, 1993; Sheya and Palmer, 1989).

Also, the SCN^- complex formed by dissolution of sulfide minerals by cyanide at as high concentrations of cyanide as 1000-2000 ppm decreases gold adsorption to some degree but not as much as Ag (Romero and Sampaio, 1993).

Thus, many metal-cyanide species occur in cyanide leaching process, but many of them adsorb weakly on carbon without affecting the gold adsorption. Among these metals, Ag and Ni exert negative effect on gold adsorption and in the case of Cu this effect depends on pH and free cyanide concentrations (Poinern et al., 2011; Fleming et al., 2011; Yin et al., 2011; Petersen et al., 1993). Therefore, in this paper, the effect of Ag, Ni and Cu on the Au adsorption on activated carbon was investigated with synthetic cyanide solutions one by one and all together.

The adsorption of metal-cyanides on activated carbon is selective and the strongest adsorbed complex is $\text{Au}(\text{CN})_2^-$. The $\text{Ag}(\text{CN})_2^-$ complex adsorbs strongly but not as strong as $\text{Au}(\text{CN})_2^-$. The $\text{Cu}(\text{CN})_2^-$ and $\text{Cu}(\text{CN})_3^{2-}$ complexes shows different adsorption features; $\text{Cu}(\text{CN})_2^-$ complex adsorbed strongly while the adsorption of $\text{Cu}(\text{CN})_3^{2-}$ complex is insignificant. The $\text{Ni}(\text{CN})_4^{2-}$ complex adsorbs weaker than $\text{Au}(\text{CN})_2^-$, $\text{Ag}(\text{CN})_2^-$, $\text{Cu}(\text{CN})_2^-$ complexes but stronger than $\text{Cu}(\text{CN})_3^{2-}$, and $\text{Ni}(\text{CN})_4^{2-}$ can reduce $\text{Au}(\text{CN})_2^-$ adsorption significantly when there is as much as 250 ppm in leach solution. $\text{Fe}(\text{CN})_6^{4-}$ and $\text{Zn}(\text{CN})_4^{2-}$ adsorption and effects on gold adsorption are insignificant.

The adsorption of metal-cyanide species on activated carbon occurs selectively. First, it was thought that it is because of the difference between ionic diameters of the metal-cyanide complexes. However, although strongest adsorption on activated carbon occurs for the $\text{Au}(\text{CN})_2^-$ complex, the ionic diameter is higher than many other cyanide species. Thus, according to the recent studies, the reason for the selective adsorption of metal-cyanide species would be the differences in the levels of hydration of the metal-cyanide molecule. Due to the hydration of the metal-cyanide complex in solution, a water shell occurs around the molecule increasing their diameter at different degrees. The hydration of the molecule relates to the cyanide molecules binding to the metal ion. Thus, increased quantity of CN^- of a metal-cyanide complex will lead to increased hydration level and thus, increased diameter of metal-cyanide molecule. So metal-cyanide could not enter through the micropores of the activated carbon and adsorption of the metal cyanide species will decrease.

On the other hand hydrophobicity increases by decreasing hydration level. Hydrophobic metal-cyanide species tends to form clusters by binding together. Forming clusters is another mechanism of adsorption of the metal-cyanides that they settle down to the activated carbon to increase the adsorption of these metal-cyanide species. Confirming these results of the studies, for example $\text{Fe}(\text{CN})_6^{4-}$ and $\text{Zn}(\text{CN})_4^{2-}$

complexes are found to adsorb more weakly on activated carbon than these species contain 6 and 4 CN^- molecules, and thus, have increased hydration level and decreased hydrophobicity. As a result they are well dispersed in the solution without forming clusters. The $\text{Ni}(\text{CN})_4^{2-}$ complex can serve as a similar example but it has not been studied in the literature as to the hydration levels. Also, $\text{Cu}(\text{CN})_3^{2-}$ complex is well dispersed in water and its hydration level is relatively high. Three cyanide bearing complexes, $\text{Au}(\text{CN})_2$, $\text{Ag}(\text{CN})_2^-$ and $\text{Cu}(\text{CN})_2^-$, have the lowest hydration state and form clusters adsorbed on activated carbon. They can be classified from the strongest adsorbed to the least strong: $\text{Au} > \text{Ag} > \text{Cu}$ (Yin et al., 2011).

In this paper, the effect of Ag, Ni and Cu on Au adsorption on activated carbon was investigated, one by one at 10 ppm Au and all together at 10 ppm Au. Because the effect of Ni-cyanide on Au adsorption was less investigated in the literature, detailed investigation of Ni effect would be a beneficial study in concept of this paper.

Materials and methods

Adsorption kinetic tests were performed by bottle rolling using 0.5 dm^3 synthetic solution and 0.6 g/dm^3 granulated activated coconut carbon of 2.36-1.7 mm size range. The bottles were rolled at 30 rpm at 20 °C for 48 hours. 15 cm^3 solution samples were taken after 1, 3, 5, 7, 22 and 30 hours. The sample solutions were analyzed for Au, Ag, Ni and Cu.

The synthetic solutions were prepared according to the AARL (Anglo American Research Laboratories) procedure. That solution contained: 3.1 g/dm^3 H_3BO_3 , 3.2 g/dm^3 $\text{CaCl}_2 \cdot 2\text{H}_2\text{O}$ and 200 ppm NaCN in pure water. pH was maintained at 10.7–11 by NaOH. It is shown that high ionic strength of the solution increases the gold adsorption on activated carbon. As the ionic strength of the process waters of cyanide leaching plants is rather high, the AARL procedure applies a high ionic strength of the test solutions simulating plant process solutions. $\text{Au}(\text{CN})_2^-$ in solution was supplied by a 1000 ppm standard AuCl_3 solution. NaCN was used as analytical quality reagent. For $\text{Ag}(\text{CN})_2^-$, analytical grade AgNO_3 , for $\text{Cu}(\text{CN})_3^{2-}$ analytical grade $\text{CuCl}_2 \cdot 2\text{H}_2\text{O}$, for $\text{Ni}(\text{CN})_4^{2-}$ analytical grade $\text{NiCl}_2 \cdot 6\text{H}_2\text{O}$ reagents were used. The adsorption test conditions are shown in Table 1.

Table 1. Composition of experimental adsorption solutions

	Metal content of adsorption solutions, ppm													
Au ppm	5	15	10	10	10	10	10	10	10	10	10	10	10	10
Ag ppm	0	0	0	20	50	100	200	0	0	0	0	0	0	200
Ni ppm	0	0	0	0	0	0	0	40	80	160	250	0	0	200
Cu ppm	0	0	0	0	0	0	0	0	0	0	0	90	180	300

To model the adsorption results the Fleming k,n method was used. The k,n model is defined as

$$\Delta Auc = k \cdot Aus \cdot t^n \tag{4}$$

In this equation *k* and *n* are model parameters: *k* is a kinetic constant (1/hours), and *n* is a model parameter, *t* is adsorption time (hours), *Aus* is gold in solution at time *t*, ppm, and ΔAuc is defined as the gold adsorbed on carbon from *t*=0 up to a certain time *t* (ppm). The equation can be linearized:

$$\ln\left(\frac{\Delta Auc}{Aus}\right) = \ln k + n \ln t \tag{5}$$

Results and discussion

Gold adsorption

Adsorption tests for aqueous solutions containing Au at the concentrations of 5, 10 and 15 ppm and 200 ppm NaCN at pH 10.7–11.0 were performed at 20 °C during 48 hours. Granulated activated carbon (0.6 g/dm³) was used. The adsorption recovery of Au is presented in Fig. 1.

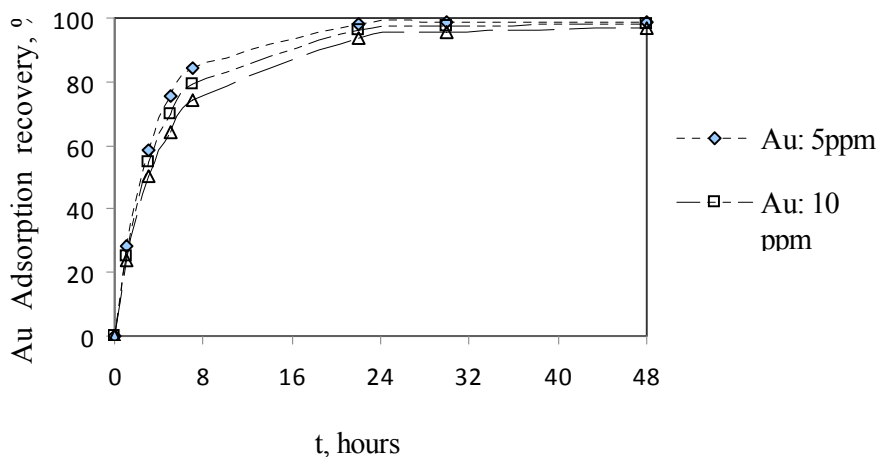


Fig. 1. Adsorption recoveries vs. time at 5, 10 and 15 ppm Au solution concentrations

According to Fig. 1 the adsorption of gold from solution on activated carbon is very fast up to 7 hours and slows down after 7 to 22 hours finally reaching equilibrium between 30 and 48 hours.

Silver effect on gold adsorption

Au adsorption tests at 10 ppm of Au and Ag concentrations of 20, 50, 100 and 200 ppm were performed. The results are presented in Fig.2.

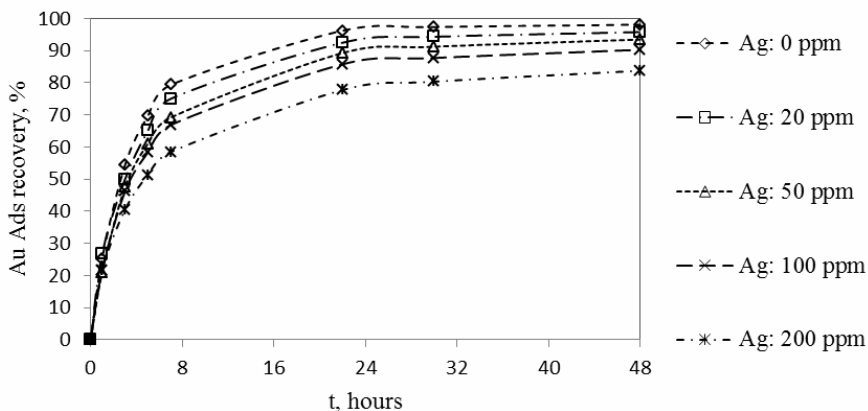


Fig. 2. Gold adsorption recovery at different Ag concentrations

As presented in Fig. 2, the Au adsorption recoveries decrease according to increasing silver concentration starting with as low as 20 ppm Ag up to 200 ppm. At 200 ppm Ag concentration gold adsorption efficiency decreased by as much as 20% (Fleming and Nicol, 1984; Romero and Sampaio, 1993; Vegter and Sanderbergh, 1997; Yin et al., 2011). Also silver loading to carbon is shown in Table 2.

Table 2. Adsorption of Ag with Au on activated carbon

	Ag: 20 ppm	Ag: 50 ppm	Ag: 100ppm	Ag: 200ppm
Ag on carbon after 48 h.	5915 ppm	10261 ppm	11216 ppm	24986 ppm
Ag adsorption rec. after 48 h.	46.90%	31.69%	17.33%	18.83%

Nickel effect on gold adsorption

Au adsorption tests at the Ni concentrations of 40, 80, 160 and 250 ppm and 10 ppm Au were performed. The results are presented in Table 3 and Fig. 3. As represented in Fig. 3 the inhibition of the Au adsorption is lower than in the case of Ag. $\text{Ni}(\text{CN})_4^{2-}$ complex has 4 CN^- ions compared to 2 CN^- in $\text{Ag}(\text{CN})_2^-$ which results in higher hydration. Thus, it is better dispersed in the solution without forming clusters which enables the adsorption on activated carbon (Yin et al., 2011).

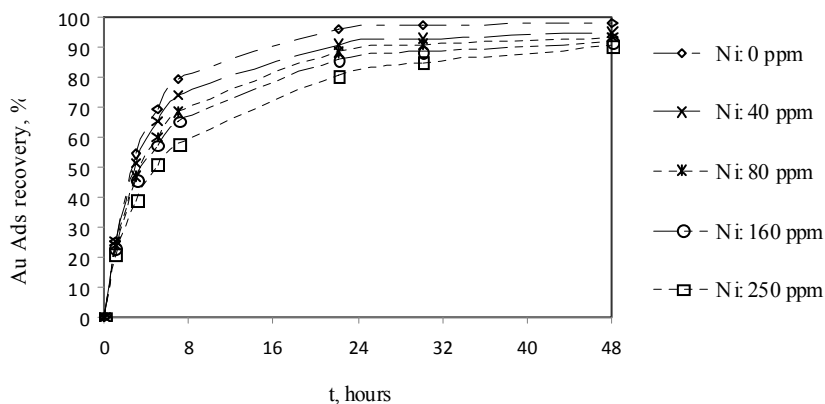


Fig. 3. Gold adsorption recovery at different Ni concentrations

Table 3. Adsorption of Au with Ni on activated carbon

	Ni: 40 ppm	Ni: 80 ppm	Ni: 160 ppm	Ni: 250 ppm
Ni on carbon in 48 h	2034 ppm	2356 ppm	5561 ppm	4706 ppm
Ni adsorption rec. in 48 h	8.38%	4.77%	5.46%	3.08%

Table 3 confirms that the Ni adsorption is lower than that of Ag and this phenomenon indicates higher hydration of $\text{Ni}(\text{CN})_4^{2-}$.

Copper effect on gold adsorption

Cu concentrations of 90, 180 and 300 ppm with 10 ppm Au were used for adsorption tests. The results are presented in Table 5 and Fig. 4.

According to Fig. 4 and Table 4, copper concentration at 90 ppm has no effect on Au adsorption and with 180 ppm Cu the Au adsorption starts decreasing slightly up to 300 ppm Cu. However, Cu effect on Au adsorption is very limited. With 300 ppm Cu in solution the decrease of gold adsorption recovery was as low as 3%. This phenomenon indicates that the Cu-cyanide species are in the forms of $\text{Cu}(\text{CN})_3^{2-}$ and $\text{Cu}(\text{CN})_4^{3-}$ of which hydration levels are higher than $\text{Cu}(\text{CN})_2^-$ which adsorbs strongly on activated carbon preventing Au adsorption. Besides, the conditions of solution of adsorption tests (pH 10,7–11 with 200 ppm NaCN) represent a typical process solution of Au cyanide leaching at plants where $\text{Cu}(\text{CN})_3^{2-}$ and $\text{Cu}(\text{CN})_4^{3-}$ species are formed rather than $\text{Cu}(\text{CN})_2^-$.

As presented on Table 4, Cu adsorptions on activated carbon are lower than that of Ag and Ni indicating that Cu shows lower effect on gold adsorption on activated carbon.

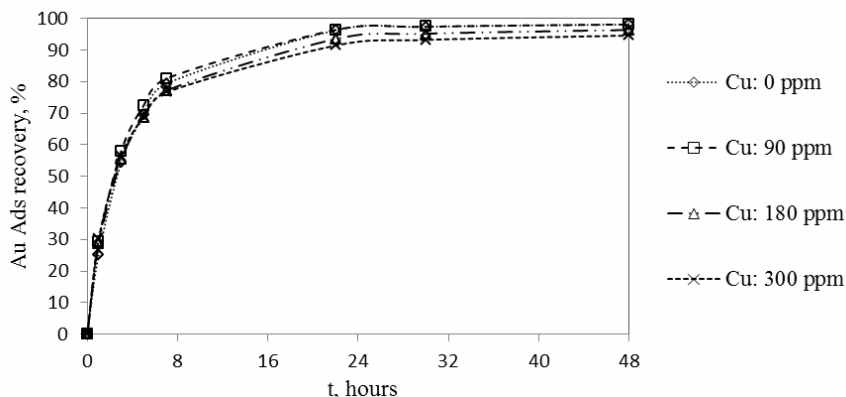


Fig. 4. Gold adsorption recovery at different Cu concentrations

Table 4. Adsorbed Cu with Au on activated carbon

	Cu: 90 ppm	Cu: 180 ppm	Cu: 300 ppm
Cu on carbon in 48 h	3038 ppm	2889 ppm	4135 ppm
Cu adsorption rec. in 48 h	5.40 %	2.59 %	2.26 %

Simultaneous effect of Ag, Ni and Cu on gold adsorption

Ag, Ni and Cu cyanide complexes were added together to the adsorption solution to have 200 ppm of Ag and Ni, and 300 ppm Cu at 10 ppm of Au. The test parameters were: solution temperature, 20 °C, 200 ppm NaCN, pH 10.7–11. Results are shown in Fig. 5.

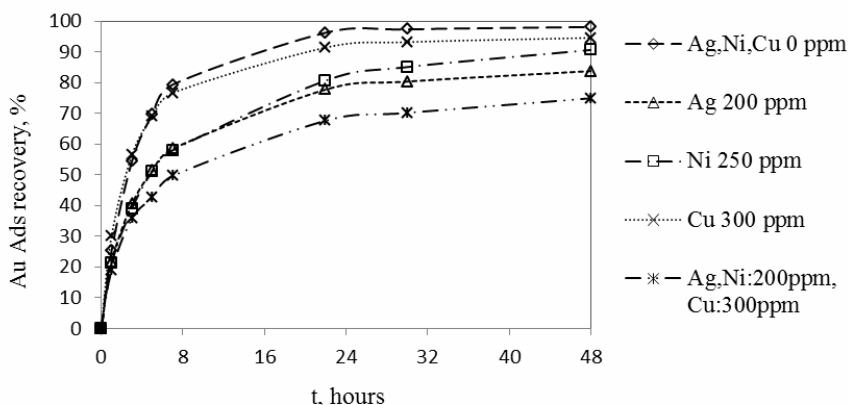


Fig. 5. Comparative results of Ag, Ni: 200 ppm and Cu:300 ppm with metals one by one

As shown in Fig. 5, 200 ppm Ag has more decreasing effect than 250 ppm Ni on Au adsorption while Ag, Ni 200 ppm and Cu:300 ppm has the most significant effect. Besides, when Ag, Ni and Cu placed all together in the same solution with 10 ppm Au, they prevent adsorption of each other. The comparative results are presented in Table 5.

Table 5. Comparative results of adsorption of metals together and separately

Solution metal contents	Adsorption of Ag, Ni and Cu		
	Ag	Ni	Cu
Ag,Ni: 200 ppm; Cu:300 ppm together	11.69%	4.43%	0.66%
Ag:200 ppm separately	18.83%		
Ni: 160 ppm separately		5.46%	
Cu:300 ppm separately			2.26%

As shown in Table 5 the test: Ag, Ni: 200 ppm and Cu, 300 ppm together with 10 ppm Au, presents the results that Ag, Ni and Cu adsorption on activated carbon decreased to a lower level than that of the separate tests with Ag 200 ppm; Ni 160 ppm and Cu 300 ppm. Ni at 160 ppm test shows more Ni adsorption recovery than that of the test with Ni at 200 ppm with Ag and Cu together. These results indicate the metals prevent adsorption of each other when present in the solution together.

Modeling of the Au adsorption data adsorption by the Fleming k,n model

The Fleming k,n modeling is applied to 48 hour adsorption data as shown in Fig. 6 (Fleming and Nicol, 1984).

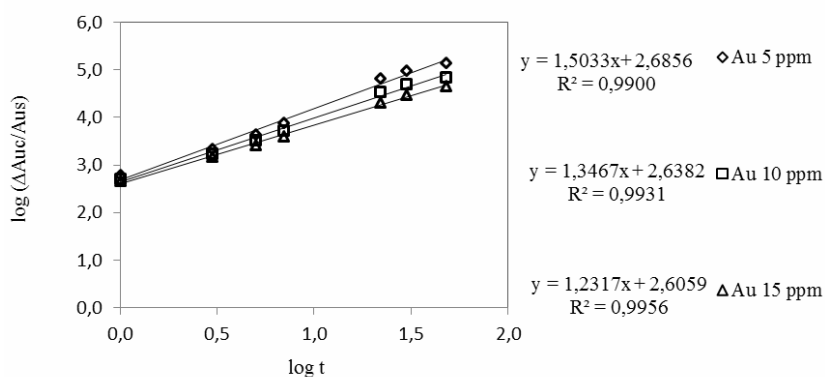


Fig. 6. The Fleming k,n model application graphs for 48 hours gold adsorption data.

As shown in Fig. 6, the Fleming k,n model fits well to the adsorption data giving R² values that are very close to 1. Model parameters *k* and *n* were found by an non-

linear regression analysis. According to Fig. 6, increased n values indicate rapid adsorption of Au on activated carbon. Thus, with decreasing concentration of the Au solution the slope of the model graphs increases indicating increased n values. Parameter n is presented as adsorption strength and k is a parameter representing Au adsorption capacity of carbon.

Conclusions

Adsorption tests regarding Au concentrations of 5, 10 and 15 ppm were performed. For 48 hours adsorption tests the Au adsorption recoveries were 99.04%, 98.13% and 97.16% for 5, 10 and 15 ppm Au in solution, respectively.

The test with 200 ppm Ag showed the strongest decreasing effect on Au adsorption recovery decreasing it from 98.13% to 83.77%. 250 ppm Ni decreased the Au adsorption recovery to 90.65% and 300 ppm Cu decreased it to 94.59%.

When metals are added together to the same solution (Ag, Ni 200 ppm and Cu 300 ppm) Au adsorption recovery decreased to 74.92%. When the metals are added together, the adsorption recovery of Au decreased more than that of the metals used separately. Also metals prevent adsorption of themselves as well as that of gold, when they are present in the solution together.

The data of Au adsorption recoveries for 48 hours adsorption time modelled by the Fleming k, n adsorption kinetic, where k and n are the model parameters which could be used to design and optimize an adsorption unit of a gold cyanide leach plant. Knowing k and n values such variables as adsorption tank quantities and volumes, carbon concentrations (g carbon/dm³ slurry) for each tank and weekly carbon stripping quantities can be determined.

References

- ADAMS M.D., 1992, *The mechanisms of adsorption of $Ag(CN)_2^-$ and Ag^+ on to activated carbon* Hydrometallurgy, Vol. 31, Iss. 1–2, September 1992, 121–138.
- DAI X., BREUER P.L., 2009, *Cyanide and copper cyanide recovery by activated carbon* Minerals Engineering, Vol. 22, Iss. 5, 469–476.
- DAVIDSON R.J., SOLE M.J., 2007, *the major role played by calcium in gold plant circuits*. The Journal of The Southern African Institute of Mining and Metallurgy, Vol. 107 refereed paper July, 463–468.
- FLEMING C.A., MEZEI A., BOURRICAUDY E., CANIZARES M., ASHBURY, M., 2011, *Factors influencing the rate of gold cyanide leaching and adsorption on activated carbon, and their impact on the design of CIL and CIP circuits* Minerals Engineering, Vol. 24, Iss. 6, 484–494.
- FLEMING C.A., NICOL M.J., 1984, *The adsorption of gold cyanide onto activated carbon. III. Factors Influencing the Rate of Loading and the Equilibrium Capacity*. J. S. Afr. Inst.Min. Metall., Vol. 84, No. 4, 85–93.
- IBRADO A.S., FUERSTENAU D.W., 1995, *Infrared and X-ray photoelectron spectroscopy studies on the adsorption of gold cyanide on activated carbon*. Minerals Engineering, Vol. 8, Iss. 4–5, April–May 1995, 441–458.

- PETERSEN F.W., VAN DEVENTER J.S.J., LORENZEN L., 1993, *The interaction between metal cyanides, fine particles and porous adsorbents in an agitated slurry*, Chemical Engineering Science, Vol. 48, Iss. 16, 2919–2925.
- POINERN G.E.J., SENANAYAKE G., SHAH N., THI-LE X.N., PARKINSON G.M., 2011, *Adsorption of the aurocyanide $Au(CN)_2^-$ complex on granular activated carbons derived from macadamia nut shells – A preliminary study*. Minerals Engineering 24, 1695–1702.
- REES K.L., VAN DEVENTER J.S.J., 2001, *Gold process modeling. I. Batch modeling of the processes of leaching, preg-robbing and adsorption onto activated carbon* Minerals Engineering, Vol. 14, Iss. 7, 753–773.
- ROMERO A., SAMPAIO C. H., 1993, *Characterization of Activated Carbons for the Extractive Metallurgy of Gold*. Turkey XML.
- SHEYA S.A.N., PALMER G.R., 1989, *Effect of metal impurities on adsorption of gold by activated carbon in cyanide solutions*. U.S. Bureau of Mines, Technical Note, 1–13.
- VEGTER N.M., SANDERBERGH R.F., 1997, *Communications Discussion of -The Adsorption Kinetics of Dicyanoaurate and Dicyanoargentate Ions in Activated Carbon*. Metallurgical and Materials Transactions B, Vol. 28B, April, 345–347.
- XIE F., 2010, *Solvent extraction of copper and cyanide from waste cyanide solution*, Doktorate Thesis, The University of British Columbia, April 2010.
- YIN X., OPARA A., DU H., MILLER J.D., 2011, *Molecular Dynamics Simulations of metal-cyanide complexes: Fundamental considerations in gold hydrometallurgy*. Hydrometallurgy 106, 64–70.

Received May 20, 2013, reviewed, accepted July 24, 2013

HYDROCARBONS REMOVAL FROM UNDERGROUND COAL GASIFICATION WATER BY ORGANIC ADSORBENTS

Marcin LUTYNSKI, Tomasz SUPONIK

Faculty of Mining and Geology, Silesian University of Technology, Gliwice, Poland, marcin.lutynski@polsl.pl

Abstract: The main problems in the case of the underground coal gasification process is the possible pollution of surrounding aquifers. The underground gasification cavity is a source of both gaseous and liquid pollutants and these are mainly aromatic hydrocarbons, phenols, heavy metals and others. In order to prevent underground water from pollution a permeable reactive barrier was proposed. The filling was granulated activated carbon and SPILL-SORB (peat) – two commonly available sorbents adequate for hydrocarbons removal. The wastewater (synthetic solution which simulated groundwater contaminated with the UCG products) was prepared by mixing distilled water with desired amounts of substances such as phenols, benzene, toluene, xylene, naphthalene etc. Batch tests were performed in order to measure sorption of phenols and benzene from the post-UCG water on the mentioned sorbents. Experimental results were fitted with linear and non-linear Freundlich and Langmuir isotherm models. The obtained data showed that removal of phenols and benzene in case of GAC was much more efficient. However, sorption was lower than in the case of literature data and can be explained by complex composition of the solution and pre-treatment of the samples. The Langmuir model gave a better fit in the case of GAC, whereas Freundlich isotherm model was matching the data better in case of SPILL-SORB.

Keywords: *underground coal gasification, permeable reactive barrier, Langmuir adsorption isotherm*

Introduction

Underground coal gasification (UCG), the technology which dates back to the beginning of the XX century is an alternative technology of energy extraction from coal. Despite the fact that various field and laboratory tests were performed, it has never been implemented on a full technical scale. The main drawback of UCG is the environmental risk associated with water pollution in surrounding aquifers. The underground gasification cavity is a source of both gaseous and liquid pollutants which may get into contact with water and in future cause threat to water aquifers. The substances leached from the gasification zone are mainly mono- and polycyclic

aromatic hydrocarbons, phenols, heavy metals, cyanides, ammonium, chloride, sulphate (Humenick et al. 1980; Stuermer et al. 1982; Humenick 1984; Liu et al. 2006; Kapusta et al. 2010; Kapusta and Stanczyk 2011). Among many water treatment technologies the PRB (Permeable Reactive Barrier) is one of the considered method of UCG water treatment. It is a passive technology where contaminants are removed from an aquifer by flowing through a “reactive material” (Puls et al. 1998; Gavaskar et al. 2000; Gavaskar et al. 2003; ITRC 2005; Suponik 2011).

As the contaminated groundwater moves through the reactive barrier, the contaminants are removed by physicochemical, chemical and/or biological processes (Puls et al. 1998; Meggyes et al. 1998; Gavaskar et al. 2000; Meggyes et al. 2000; Suponik and Lutynski 2009, Suponik 2013). The mechanism involved in contaminant removal are listed below (Roehl et al. 2005; ITRC 2005; Suponik 2011).

- Biochemical reactions which lead to:
 - biodegradation of organic compound
 - precipitation of heavy metals by sulphate-reducing bacteria.
- Redox reactions which lead to:
 - chemical detoxification
 - precipitation of heavy metals.
- pH control (precipitation).
- Adsorption.

The type of mechanism which removes contaminants depends on the material used for filling and on the contaminant to be removed. In case of this study it was assumed that for removing aromatic hydrocarbons the filling for PRB would be granulated activated carbon or peat. These materials were selected based on literature review (U.S. DOE 1998, Gavaskar et al. 2003). In both cases the leading reaction which retains contaminants is adsorption. The uptake of adsorbate by the adsorbent can be described by various models where the most commonly applied are Freundlich and Langmuir isotherm models.

In this study results of batch tests of benzene and phenols removal from synthetic solution of post-UCG water by granulated activated carbon and peat are presented. Experimental results are fitted with linear and non-linear forms of Freundlich and Langmuir models.

Materials and methods

Two reactive materials were selected for the study, i.e. granulated activated carbon (GAC) and peat in form of the commercial adsorbent SPILL-SORB. The granular activated carbon was WACC 8X30 made from coconut shells by steam gas-method. SPILL-SORB (peat) is a fully organic industrial adsorbent of high moisture adsorbancy. Properties of GAC and peat are presented in Table 1. Methodology of the tests was typical for experiments of sorption from aqueous solution (Gulgonul 2012).

Table 1. Properties of sorbents used in the study
(SPILL-SORB MSDS 2012, ELBAR Katowice MSDS 2013)

Property, unit	GAC Value	SPILL-SORB Value
Particle size distribution, mm	0.6–2.4	–
Specific surface, m ² /g	min. 1000	200
Iodine number, mg/g	min. 1000	–
Moisture, %	max. 5	10%
Ash, %	max. 12	6
pH	ca. 8	4–6
Hardness, %	min. 98	–
Bulk density, g/dm ³	480±30	150±2

The wastewater (synthetic solution which simulated groundwater contaminated with UCG products) was prepared by mixing distilled water with desired amounts of the following pure substance: phenols, benzene, toluene, xylene, naphthalene, fluorene, phenanthrene, pyrene, anthracene, CuSO₄·5H₂O, NiSO₄·7H₂O, ZnSO₄·7H₂O, NaCl, K₂CrO₄, (NH₄)₂S₂O₈, KCN. The concentrations of contaminants in the solution were similar to the values reported in the literature (Liu et al. 2006; Kapusta and Stanczyk 2011). Chemical composition of solution is presented in Table 2. The initial conductivity and pH of the solution was 22 mS/cm and 7.9 respectively. Since pH after adding the substances was 5.5, it was adjusted to the intentional value by slow titration with ultra-pure sodium hydroxide.

Table 2. Initial chemical composition of synthetic UCG wastewater used for the test

Parameter/ chemical compound	Value	Unit
pH	7.9	–
Conductivity	22	mS/cm
TOC	4.48	mg/dm ³
Phenols	15.4	mg/dm ³
NH ₄ ⁺	3280	mg/dm ³
CN ⁻	1.84	mg/dm ³
Benzene	0.540	mg/dm ³
Toluene	0.141	mg/dm ³
Xylene (sum)	0.121	mg/dm ³
Cr ⁶⁺	0.091	mg/dm ³
Cu	0.55	mg/dm ³
Ni	1.24	mg/dm ³
Zn	0.16	mg/dm ³
SO ₄ ⁻	550	mg/dm ³
Cl	784.1	mg/dm ³

The concentration of contaminants in wastewater during the tests was measured with the use of:

1. UV-Vis Spectrophotometer DR5000 HachLange – diazotised 4-nitroaniline method, wavelength 550 nm (phenols)
2. HPLC – UVD 340u Gynkotek, column RP-18 Hypersil Gold, flow 1 cm³/min in gradient analysis Me/H₂O (benzene).

The installation in which batch tests were carried out was a programmable rotator equipped with 50 cm³ plastic tubes. In the rotator, the 2 minutes reciprocal rotation was used for every sample (with turning angle 90° and speed range 50 rpm) after which a short pause (15 second) followed. The solutions were poured into plastic tubes (50 cm³ to every sample) and then a specified mass of reactive material was added to every sample. Later, the tubes were closed with corks. After shaking the samples for 2 hours, the solutions were flowed through thick filters and the concentrations of particular chemicals were measured. The temperature in laboratory air and in tested water was about 19 °C.

The amount of solute adsorbed per unit weight of material (mg/g) was calculated with the use of the following formula:

$$q_e = \frac{V(C_0 - C_e)}{W} \quad (1)$$

where C_0 and C_e are the initial and equilibrium adsorbate concentrations (mg/dm³), respectively, V is the volume of solution (dm³) and W is the weight of the adsorbent (g).

Results and discussion

Sorption of benzene on GAC and SPILL-SORB is shown in Fig. 1, whereas sorption of phenols on GAC and SPILL-SORB is shown in Fig. 2. The mechanism of adsorbate removal in both cases is the hydrophobic adsorption to GAC and peat. Therefore, it was decided to fit Freundlich and Langmuir models in order to explain interactions between the adsorbate and adsorbent and to compare the constants with literature data.

The isotherms were fitted with linear and non-linear forms of Freundlich and Langmuir isotherm models. These two models are the most common and fairly accurate ones that describe sorption of substances from aqueous solutions (McKay et al. 1985; Kumar 2006). The intention was to assess if the non-linear forms give a better fit than commonly applied linear forms. In case of linear forms, the sum of square residuals is not minimized as it is in formulas presented below for the Freundlich and Langmuir model respectively:

$$\sum_i (q_{ei} - K_F C_e^n)^2 \quad (2)$$

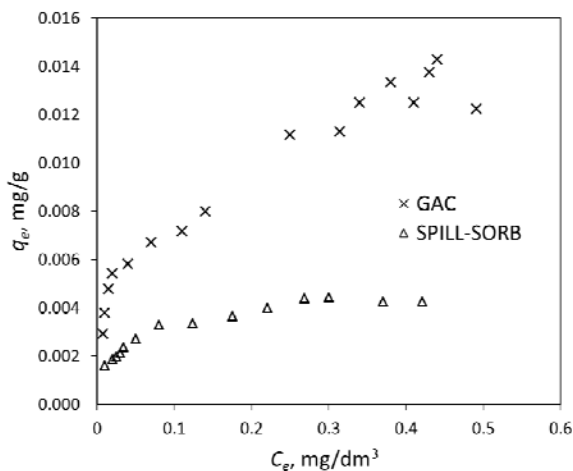


Fig. 1. Adsorption isotherms of benzene from UCG wastewater solution on GAC and SPILL-SORB at 19 °C

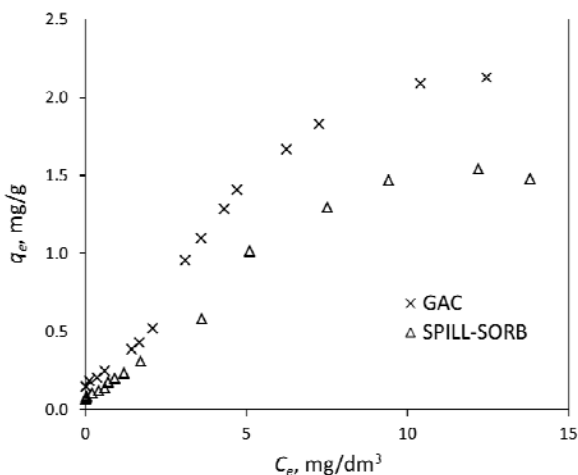


Fig. 2 Adsorption isotherm of phenols from UCG wastewater solution on GAC and SPILL-SORB at 19 °C from wastewater

$$\sum_i \left(q_{ei} - \frac{Q K_L C_e}{1 + K_L C_e} \right)^2 \tag{3}$$

Langmuir model has four linear forms and all of them were assessed in terms of best model fit to the experimental results. The linear and non-linear forms of equations assessed in the study are presented in Table 3.

Table 3. Linear and non-linear forms of Freundlich and Langmuir models

Isotherm model	General equation (non-linear form)	Linear form
Freundlich	$q_e = K_F C_e^n$	$\log q_e = \log K_F + n \log C_e$
Langmuir-1		$\frac{C_e}{q_e} = \frac{1}{Q} C_e + \frac{1}{K_L Q}$
Langmuir-2	$q_e = \frac{Q K_L C_e}{1 + K_L C_e}$	$\frac{1}{q_e} = \frac{1}{K_L Q} \frac{1}{C_e} + \frac{1}{Q}$
Langmuir-3		$q_e = Q - \left(\frac{1}{K_L} \right) \frac{q_e}{C_e}$
Langmuir-4		$\frac{C_e}{q_e} = K_L Q + K_L q_e$

Experimental data were plotted in linear forms and fitted with regression lines. Constants for each model i.e. K_F and n for Freundlich and K_L and Q for Langmuir were calculated based on the general form of the linear equation of regression line. Coefficients for the non-linear forms of the models were calculated by minimizing residual sum of squares to the experimental values. The coefficient of determination was calculated for each form of the models and summarized for GAC and SPILL-SORB in Table 4 and 5 respectively. Table 3 and 4 present Freundlich and Langmuir constants calculated by using linear and non-linear forms of the equations for benzene and phenols adsorption on GAC and SPILL-SORB at 19 °C.

Table 4. Freundlich and Langmuir constants calculated using linear and non-linear forms of the equations for benzene and phenols adsorption on GAC at 19 °C

Isotherm	Benzene			Phenols		
	K_F dm ³ /mg	n	R^2	K_F dm ³ /mg	n	R^2
Freundlich (linear)	0.0172	0.3343	0.9667	0.5668	0.4234	0.8421
Freundlich (non-linear)	0.0175	0.3443	0.9639	0.4510	0.6558	0.9604
	K_L , dm ³ /mg	Q , mg/g	R^2	K_L , dm ³ /mg	Q , mg/g	R^2
Langmuir-1	17.7436	0.0144	0.9667	0.1765	3.3333	0.6422
Langmuir-2	75.5384	0.0102	0.8647	31.6666	5.2632	0.5327
Langmuir-3	56.4972	0.0116	0.6476	12.3609	1.0619	0.1851
Langmuir-4	36.6690	0.0129	0.6476	2.2869	1.6796	0.1851
Langmuir (non-linear)	17.7260	0.0142	0.9810	0.1005	4.07291	0.9753

Table 5. Freundlich and Langmuir constants calculated using linear and non-linear forms of the equations for benzene and phenols adsorption on SPILL-SORB at 19 °C

Isotherm	Benzene			Phenols		
	K_F dm ³ /mg	n	R^2	K_F dm ³ /mg	n	R^2
Freundlich (linear)	0.00604	0.2865	0.9717	0.3462	0.3843	0.7792
Freundlich (non-linear)	0.00585	0.2702	0.9604	0.2836	0.6806	0.9650
	K_L dm ³ /mg	Q mg/g	R^2	K_L dm ³ /mg	Q mg/g	R^2
Langmuir-1	33.8750	0.0046	0.9914	0.0967	3.3333	0.6728
Langmuir-2	56.3111	0.0039	0.8671	4700	0.2128	0.3306
Langmuir-3	46.7289	0.0042	0.8054	113.6363	0.6009	0.0643
Langmuir-4	37.664	0.0044	0.8054	7.2998	1.2313	0.0643
Langmuir (non-linear)	31.8979	0.0046	0.9547	0.0945	2.8633	0.9895

Comparison of correlation coefficients for both linear and non-linear models shows that GAC adsorption equilibrium data follow predominantly the Langmuir non-linear model for benzene and phenols. In the case of SPILL-SORB the sorption data for benzene are described more accurately by Langmuir-1, whereas phenols follow the Langmuir non-linear model. In both materials the Freundlich model gives a slightly less accurate fit. In case of GAC some of the Langmuir non-linear models have unacceptable fitting and therefore should be rejected for further assessment. Experimental data with best-fit models are presented in Figs 3 and 4.

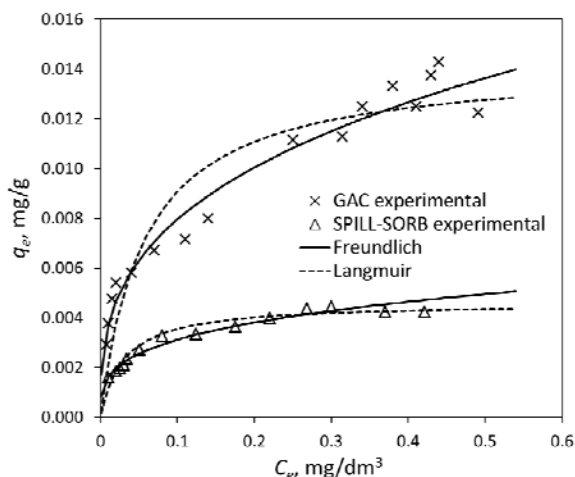


Fig. 3. Freundlich and Langmuir best model fitting for sorption of benzene on GAC and SPILL-SORB at 19 °C from wastewater

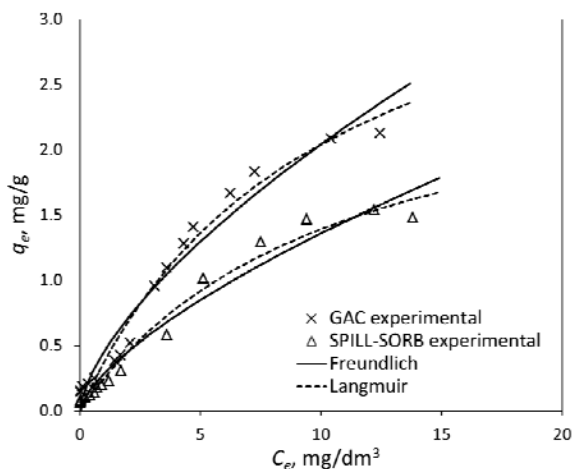


Fig. 4. Freundlich and Langmuir best model fitting for sorption of phenols on GAC and SPILL-SORB at 19 °C from wastewater

The isotherm data clearly show that removal of phenols and benzene in case of GAC is much more efficient. It can be explained by much larger specific surface of GAC and its pH which is more favorable for organic compounds sorption (Villacanas et al. 2006). Nevertheless, the Langmuir and Freundlich constants are significantly lower than those reported in literature (Maarof et al. 2004; Villacanas et al. 2006; Vijana and Neagu 2012). There might be several reasons of this phenomenon. The first one is the method of sample preparation. In our study the GAC and SPILL-SORB were not pre-treated neither by thermal nor chemical treatment (eg. with nitric acid). Those procedures could not be followed in case of PRB, therefore were rejected. Another explanation could be the fact that the experiments were not conducted under vacuum and in the access of oxygen. The tendency of carbon to chemisorb oxygen is greater than the tendency to adsorb any other species. Oxygen chemisorbs on the surface of GAC to form carbon–oxygen functional groups that may be acidic, neutral, or basic. These phenomena has been observed in other studies (Tessmer et al. 1997; Dabrowski et al. 2005). We can assume that this effect is not valid for peat. Low adsorption of these two measured compounds could be explained by the number of other chemical compounds in the solution which most probably occupy sorption sites of adsorbents. Therefore, the obtained values were lower than those reported in the literature for less complex solutions.

Conclusions

Granulated activated carbon and peat were tested as possible filling for PRB installed around UCG site. The reason for choosing these materials was their accessibility and relatively high sorption properties of organic compounds. Sorption of phenols and

benzene was much higher on GAC than on peat (SPILL-SORB). In the case of GAC the model which describes more accurately sorption equilibrium is the Langmuir non-linear model whereas in case of SPILL-SORB a slightly better fit was obtained with Langmuir-1 linear isotherm model for benzene and as Langmuir non-linear for phenols. Calculated constants for the models were lower than usually reported in the literature which can be explained by the fact that the material were not pre-treated and the experiments were conducted in the access of oxygen. Another factor could be the complex composition of the synthetic solution used for the tests where other compounds were most probably adsorbed.

Acknowledgments

The work presented in this paper has been performed in the frame of HUGE2 project (Hydrogen Oriented Underground Coal Gasification for Europe - Environmental and Safety Aspects) co-financed by the EU within the Research Fund for Coal and Steel under grant agreement no RFCR-CT-2011-00002

References

- DABROWSKI A., PODKOSCIELNY P., HUBICKI Z., BARCZAK M., 2005, *Adsorption of phenolic compounds by activated carbon—a critical review*, Chemosphere 58, 1049–1070.
- ELBAR Katowice MSDS (Material Safety Data Sheet), 2013, *WACC 8X30*, www.wegiel-aktywny.pl, accessed June 2013.
- GAVASKAR A., GUPTA N., SASS B., JANOSY R., HICKS J., 2000, *Design guidance for application of permeable reactive barriers for groundwater remediation*. Florida, Battelle Columbus Operations, Ohio 2000.
- GAVASKAR A., SASS B., GUPTA N., DRESCHER E., YOON W.S., SMINCHAK J., HICKS J., CONDIT W., 2003, *Evaluating the longevity and hydraulic performance of Permeable Reactive Barriers at Department of Defence Sites*. Battelle Columbus Operations Ohio; 2003.
- GULGONUL I., 2012. *Evaluation of Turkish bentonite for removal of deys from textile wastewaters*, Physicocheical Problems of Mineral Processing, 48(2), 2012, 369–380.
- HUMENICK M. J., 1984, *Water pollution control for underground coal gasification*. Journal of Energy Engineering, 110(2), 100–112.
- HUMENICK M.J., MATTOX C.F., 1980, *Organic groundwater contaminants from underground coal gasification*. In Situ, 4(2), 78–85.
- ITRC (Interstate Technology & Regulatory Council), 2011, *Permeable Reactive Barrier: Technology Update, PRB-5*. Washington, D.C.: Interstate Technology & Regulatory Council, PRB: Technology Update Team. Washington: <http://www.itreweb.org>.
- KAPUSTA K., STAŃCZYK K., 2011, *Pollution of water during underground coal gasification of hard coal and lignite*. Fuel, 90(2011), 1927–1934
- KAPUSTA K., STAŃCZYK K., KORCZAK K., PANKIEWICZ M., WIATOWSKI M., 2010, *Wybrane aspekty oddziaływania procesu podziemnego zgazowania węgla na środowisko wodne*, Prace Naukowe GIG, Górnictwo i Środowisko, nr 4, Główny Instytut Górnictwa Katowice 2010.
- KUMAR V.K., 2006, *Comparative analysis of linear and non-linear method of estimating the sorption isotherm parameters for malachite green onto activated carbon*. Journal of Hazardous Materials, Vol. 136, Iss. 2, 197–202.

- LIU SHUQIN, WANG YONGTAO, YU LI, OAKLEY JOHN., 2006, *Volatilization of mercury, arsenic and selenium during underground coal gasification*, Fuel, Vol. 85, Iss. 10–11, July–August 2006, 1550–1558.
- MAAROF H.I., HAMEED B. H., LATIF A.A., 2004, *Adsorption Isotherms For Phenol Onto Activated Carbon*. ASEAN Journal of Chemical Engineering, 4 (1), 70–76.
- MCKAY G., BINO M.J., ALTAMEMI A.R., 1985, *The adsorption of various pollutants from aqueous solutions on to activated carbon*. Water Research, Vol. 19, Iss. 4, 1985, 491–495.
- MEGGYES T., HOLZLOHNER U., AUGUST H., 1998, *A multidisciplinary approach to improving the safety and durability of landfill barriers*. In *Contaminated and derelict land* (Sarsby R.W. (ed)), Kraków. Thomas Telford, London, 413–420.
- MEGGYES T., SIMON F.G., DEBRECZENI E., 2000, *New developments in reactive barrier technology, The exploitation of natural resources and the consequences*, Greek International Symposium on Geotechnics Related to the European Environment, Berlin.
- PULS R.W., POWELL M.R., BLOWES D.W., GILLHAM R. W., SCHULTZ D., SIVAVEC T., VOGAN J. L., POWELL P. D., 1998, *Permeable reactive barrier technologies for contaminant remediation*, Washington: United States Environmental Protection Agency.
- ROEHL K.E., MEGGYES T., SIMON F.G. STEWART D.I., 2005, *Long-term Performance of Permeable Reactive Barriers*, Trace metals and other contaminants in the environment, Vol. 7, Elsevier 2005.
- SPILL-SORBMSDS (Material Safety Data Sheet), 2012, www.spillsorb.com, accessed June 2013
- STUERNER D.H., DOUGLAS J.N., MORRIS C.J., 1982, *Organic contaminants in groundwater near an underground coal gasification site in northeastern Wyoming*. *Environmental Science Technology*, 16, 582–587.
- SUPONIK T., 2011, *Optimization of the PRB (Permeable Reactive Barriers) parameters for selected area of dumping site*, The Publishing House of the Silesian University of Technology (monographs no 328), Gliwice 2011.
- SUPONIK T., 2013, *Groundwater treatment with the use of zero-valent iron in the Permeable Reactive Barrier Technology*, *Physicochemical Problems of Mineral Processing*, Vol. 49, Iss. 1, 2013, 13–23.
- SUPONIK T., LUTYNSKI M., 2009, *Possibility of Using Permeable Reactive Barrier in Two Selected Dumping Sites*. *Archives Of Environmental Protection*, Vol. 35, No. 3, 109–122.
- TESSMER C.H., VIDIC R.D., URANOWSKI L.J., 1997, *Impact of Oxygen-Containing Surface Functional Groups on Activated Carbon Adsorption of Phenols*, *Environmental Science Technology*, 1997, 31 (7), 1872–1878.
- U.S. DEPARTMENT OF ENERGY, 1998, *Research and Application of Permeable Reactive Barriers*, Grand Junction Office 1998.
- VIJANA L.E., NEAGU M., 2012, *Adsorption isotherms of phenol and aniline on activated carbon*, *Revue Roumaine de Chimie*, 57(2), 85–93.
- VILLACANAS F., MANUEL FERNANDO R. PEREIRA M.F.R., ORFAO J.J.M., FIGUEIREDO J.L., 2006, *Adsorption of simple aromatic compounds on activated carbons*, *Journal of Colloid and Interface Science* 293 (2006), 128–136.

Received June 6, 2013; reviewed; accepted June 28, 2013

EFFECT OF TWO-STAGE STIRRED PULP-MIXING ON COAL FLOTATION

Xiahui GUI*, Yongtian WANG**, Haijun ZHANG**, Shulei LI*

* School of Chemical Engineering and Technology, China University of Mining & Technology, Xuzhou, Jiangsu 221116, China, Corresponding author, guixiahui1985@163.com

** Chinese National Engineering Research Center of Coal Preparation and Purification, Xuzhou 221116, Jiangsu, China

Abstract: Stirred pulp-mixing is performed before coal flotation. In this study, a two-stage stirred pulp-mixing tank was designed based on the single-stirred process to intensify the mixing effect of pulp and flotation reagents. A tank has a pitched-impeller opening-type turbine. Stirred pulp-mixing and flotation experiments were conducted on a sample of anthracite fine coal (-0.5mm) from the Xuehu Coal Preparation Plant in Henan Province, China. The results of the two-stage stirred pulp-mixing were compared with those of a single-stage stirred pulp-mixing in terms of flotation performance. Compared with the single-stage stirred pulp-mixing, two mixing areas and double-layer impeller were able to strengthen the energy input to the stirred system, thereby improving the mixing efficiency of flotation reagents and coal particles in the pulp. The two-stage stirred pulp-mixing significantly increased the flotation feed rate of the cyclone-static micro-bubble flotation column and concentrate yield, enhanced the combustible matter recovery effect of coarse particles at a suitable flotation feed rate, and ensured the recovery effect of fine particles at high flotation feed rate.

Keywords: *mixing, stirred, two stage, fine coal, flotation*

Introduction

Stirred pulp-mixing is the first process in fine particle separation. With “poor, miscellaneous, and difficult” mineral characteristics, suitable conditions for mineralization are prerequisites for efficient recovery of fine and micro-fine mineral particles (Akdemir and Sonmez, 2003; Sun et al., 2006; Negri et al., 2007). The conventional mechanical cell, flotation column and Jameson cell are the main devices used in fine particle flotation. Mechanical flotation machines typically work as a mixing device. A high stirring intensity in flotation cell may lead to a low recovery of particles because of high detachment probability of mineral particles from bubbles (Cheng et al., 1998; Rubinstein, 2004). However, a highly turbulent environment is

required for the sufficient mixing of particles and flotation reagents. These two distinct fluid environments cannot be provided simultaneously by the stirring mechanism of a flotation cell (Dobby and Finch, 1986). The flotation column has no stirring device, and thus, the mixing effect of pulp and reagents is particularly important for the subsequent separation process (Clayton et al., 1991; Harbort et al., 1994; Liu et al., 2000).

Stirred pulp-mixing is related to the dispersion of pulp and reagents, contact of mineral particles with reagents, and mineral surface modification. The adequacy of stirred pulp-mixing is directly related to the flotation effects. A lot of works were done and meaningful conclusions were obtained about mixing before mineral flotation. Strong pulp-mixing pretreatment significantly improves flotation performance, including the improvements in the selectivity and recovery of valuable metals (Engel et al., 1997). High-shearing pulp-mixing improves the flotation effect through the surface cleaning and shear flocculation of mineral particles (Chen et al., 1999). A shearing force is a key factor for separation efficiency (Valderrama and Rubio, 1998). Coal oxidation also has a significant effect on floatability. Feng et al. (2005) found that the hydrophilic oxide layer of a mineral particle surface can be removed effectively by high-shearing pulp-mixing. The oxidized coal is also difficult to float with the common collectors (Xia et al., 2012a, b, 2013). In fine coal flotation, higher combustible matter recovery can be obtained by enhancing the impeller speed of mixing operation prior to flotation. However, concentrate ash content also increases by different degrees (Li et al., 2009; Liu et al., 2009; Liang et al., 2011).

Considerable research and development were conducted on fine coal stirring equipment, particularly on pulp pre-processor (Yu, 2005), emulsifiers (Jiang et al., 2006), surface-modified separators (Wang, 2003), static mixers (Zhang et al., 2006), and a variety of stirring tanks (Wang, 2004). These studies significantly improved pulp efficiency circulation and shearing and reduced the dosage of flotation reagents. Studies on stirred pulp-mixing focused mainly on the cycle efficiency, which significantly influences the macro-mixing of mineral particles and improves homogenization in a stirring tank. With the improvement in the proportion of mechanical coal-mining and the rapid development of heavy-medium coal preparation, the fine coal of China is characterized gradually by size reduction, ash increase, and higher intergrowth content (Xu et al., 2003). The fine coal separation problem became prominent (Li et al., 2013; Ding et al., 2006). A high fine coal particle content in stirred pulp-mixing can agglomerate the mixing system, pollute the micro-fine heterogeneous mud in clean coal flocs, and significantly affect the flotation reagents and coal particle surface. A short circuit in the stirred pulp-mixing process affects the recovery of flotation devices because parts of the flotation reagents and pulp would be overflowed by the surface material flow given a horizontal circulation of single-stage mixing (Gui et al., 2013). To solve this problem, the current study proposes a two-stage stirred pulp-mixing process. The effect of two-stage stirred pulp-mixing is compared with that of single-stage stirred pulp-mixing by analyzing their

mixed characteristics. The results of this study can serve as references for new, efficient mixing mechanisms.

Experimental

Method

The experimental samples were fine anthracite coal from the Xuehu Preparation Plant in Henan Province, China. The feed slurry was a mixture of fine coal particles, water, and flotation reagents. The feed had solid concentration of 100 g/dm³ to 120 g/dm³ and pulp density of 1,035 kg/m³ to 1,050 kg/m³. The optimum flotation conditions were obtained in the experiment. Collector dosage was 320 g/Mg, frother dosage was 110 g/Mg, and feed concentration was 90 g/dm³. Figure 1 shows the equipment flowchart.

With valves 1 and 3 opened and valves 2 and 4 closed, coal slime and flotation reagents were fed into a two-stage stirring tank with diameter of 2.5 m. With valves 1 and 3 closed and valves 2 and 4 opened, coal slime and flotation reagents were fed into a single-stage tank with diameter of 2.5 m. Impeller speed was changed by adjusting drive motor speed through the inverter. The strength of the flow field in the stirring tank was adjusted by replacing the stirring impeller with one of a different diameter. The coal slurry was fed into a FCSMC 3000×6000 cyclone-static micro-bubble flotation column after stirred pulp-mixing. The cyclonic-static micro-bubble flotation column (FCSMC) was researched by the China University of Mining and Technology widely used in coal preparation, polymetal sulfide flotation and magnetite/hematite reverse flotation, where higher separation efficiency, especially of fine and micro fine particles, was demonstrated. FCSMC is composed of the separation zone, cyclonic separation zone, bubble producer and pipe flow mineralized zone. The separation zone is on the top of the column. FCSMC is a combination of column flotation and cyclonic separation and is a multi-separation structure, combining column-separation, cyclonic-separation and pipe flow mineralization. It can maintain the selective superiority of flotation column separation and at the same time further improve the recovery and separation efficiency, which can make this kind of equipment highly efficient in fine and micro-fine particle separation. In this study, FCSMC 3000×6000 was used as a flotation equipment, which width and length are 3000 and 6000 millimeters, respectively (Cao et al., 2011; Zhang et al., 2013). The effect of two-stage stirred pulp-mixing on the flotation device was compared with that of single-stirred pulp-mixing by changing feed rate.

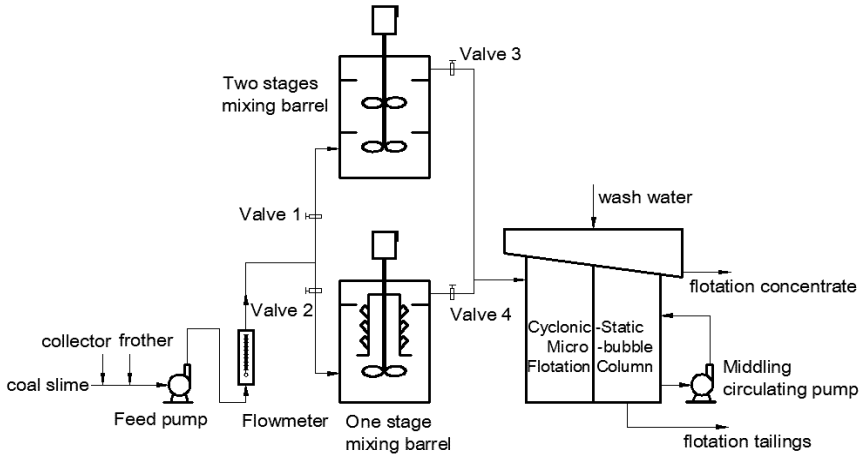


Fig.1. Equipment flow chart

Stirred mixing tank

The two-stage stirring tank consists of two mixing areas, tank, shaft, two impellers, baffles, and ring plate. Upper and lower impellers and ring plate are removable, allowing the switch from the two-stage stirring tank to the single one. In the preliminary tests, the impeller forms were fixed as pitched-impeller opening-type turbines, and the impeller number was 4 with alternating diameters (600, 650, and 700 mm). The motor and stirring shaft speeds were adjusted using the inverter. Table 1 shows the size of the stirring barrel and accessories.

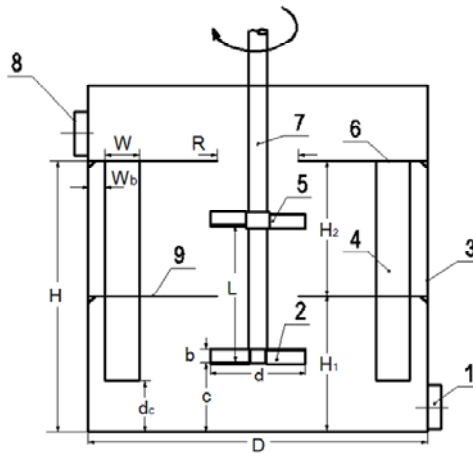


Fig. 2. Schematic diagram of two-stage compulsory-stirred tank. 1 – Feed inlet; 2 – Lower impeller; 3 – Mixing tank; 4 – Baffle; 5 – Upper impeller; 6 – Upper ring-plate; 7 – Stirring shaft; 8 – Discharge port; 9 – Low ring-plate

The coal slurry was mixed in different axial positions through stirred pulp-mixing by two impellers in two different positions in two sections of the tank area. Figure 2 shows the structure diagram of the two-stage stirring tank. The coal slurry was fed into the first stirring section through feed inlet 1. The coal slurry then entered the second stirring section after the stirring action of lower impeller 2. Then, the second mixing process was completed by the action of upper impeller 5. The material was forced-modified by the mechanical fluid force. The modified pulp was discharged from discharge port 8. When the upper impeller 5 and lower ring plate were removed and a loop sleeve was added, the two-stage stirred pulp-mixing was changed to single mixing, allowing for comparative tests on the two stirring forms. Figure 3 shows the schematic diagram of the single-stage stirring tank

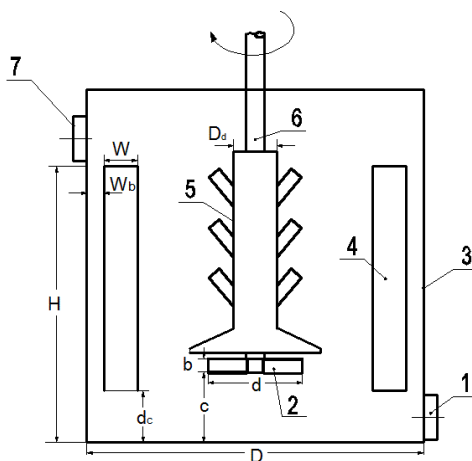


Fig. 3. Schematic of single-stage stirred tank. Feed inlet; 2 – Impeller; 3 – Mixing tank; 4 – Baffle; 5 – Circulation sleeve; 6 – Stirring shaft; 7 – Discharge port

Table 1. Structure size of two- and single-stage stirring tanks. Symbols: D – Tank diameter; H – Tank height; W_b – Distance between baffle and tank; W – Width of baffle; C – Distance between lower impeller and bottom of the tank; L, d – Impeller diameter; D_d – Cycle sleeve diameter; b – Impeller height; R – Inner circle radius of the ring plate; H_1 – Distance between lower ring plate and bottom of the tank; H_2 – Distance between the two ring plates; θ – Blade angle

Dimension (mm)	D	H	W_b	W	C	L	d	D_d	b	R	H_1	H_2	$\theta, ^\circ$
Two-stage	2500	2500	125	250	500	1000	600/650/700	/	100	600	1000	1000	45
Single-stage	2500	2500	125	250	500	/	600/650/700	324	100	/	/	/	45

Results and discussion

Effect of stage stirring on coal flotation index

Figure 4 shows a relationship between flotation index and stirring speed. Test conditions were characterized by a dry fine coal with 30 Mg/h and pulp feed rate of 380 m³/h. Concentrate yield and ash content increased with increasing shaft speed, although the increasing trend slowed down. The previous studies showed that coal floatability decreases in the flotation cell and that the flotation rate constant is reduced gradually with the flotation process (Li et al., 2013). In other words, many materials of low ash content float during early flotation, and only a few materials of high ash content and poor floatability float during late flotation. Thus, the increase in the shaft speed is equivalent to increase in energy input in the stirring system. The excess energy is reflected mainly in the recovery of coal particles that are difficult to float. Impellers with large diameters can obtain higher concentrate yield at the same coal ash content or obtain lower ash content at the same concentrate yield. The concentrate yield can be increased and high-quality clean coal can be obtained by increasing energy input in the stirred system.

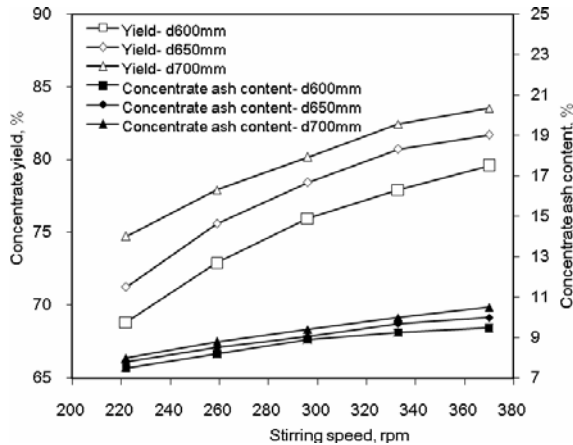


Fig. 4. Relationship between flotation index and stirring speed

Figure 5 shows the relationship between the power consumption of the unit volume and the flotation index. The power consumption of the unit volume in a stirred tank (P_V) can be expressed as:

$$P_V = \frac{P}{V} \quad (1)$$

where P_V is the input power of fluid in the tank (W) and V is the effective volume of the tank (m^3). Figure 5 shows that the power consumption of unit volume reached the maximum value of 2877, 3415, and 4140 W/m^3 with the maximum speed of 370 rpm at the corresponding impeller diameter of 600, 650, and 700 mm, respectively. The flotation concentrate yield and ash content increased with increasing power input per unit volume, but the rate of increase gradually slowed. The power input per unit volume with the same speed increased and the concentrate yield increased with larger impeller diameter. However, with the same power input per unit volume, the smaller impeller diameter generated higher concentrate yield and lower ash content. These results indicate that more energy is required in the late stage of the flotation process of hard-to-float particles. In actual production, flotation index requirements and the power consumption of unit volume are considered comprehensively to determine impeller diameter and speed in the two-stage stirring tank.

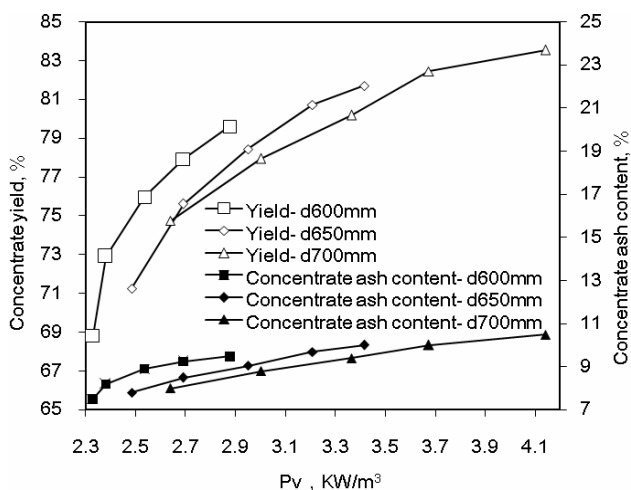


Fig. 5. Relationship between concentrate ash content, yield, and power consumption of unit volume in a stirred tank P_V

Mixing characteristics were evaluated comprehensively by investigating the flow and power dimensionless numbers, shearing and cycle characteristics, and mixing efficiency of the two-stage compulsory-stirred system. Efficient mixing means that the same mixing level was achieved at the lowest energy consumption. Thus, mixing efficiency of different stirring mechanisms is combined with the mixing time and energy consumption. The mixing time per unit of energy consumption is characterized by K (dimensionless). Smaller K indicates shorter mixing time with the same energy consumption and higher mixing efficiency. K can be expressed as follows (Wang and Yu, 2003; Zhang et al., 2003; Li, 2010):

$$N = \left(\frac{\rho N_p d^5}{P} \right)^{\frac{1}{3}} \tag{2}$$

$$\theta_m = \frac{N_\theta}{N} = N_\theta N_p^{\frac{1}{3}} d^{\frac{5}{3}} (\rho / P)^{\frac{1}{3}} = N_\theta N_p^{\frac{1}{3}} (d / D)^{\frac{5}{3}} (D)^{\frac{5}{3}} (\rho / P)^{\frac{1}{3}} \tag{3}$$

$$K = N_\theta N_p^{\frac{1}{3}} \left(\frac{d}{D} \right)^{\frac{5}{3}} \tag{4}$$

Combination of $N_\theta = \theta_m N$, $N\theta_m = 5 \left(\frac{2H_L}{d} + \frac{D}{d} \right) \frac{C}{d}$ and $N_p = \frac{P}{\rho N^3 d^5}$, then

$$K = \frac{5 \left(2 \frac{H_L}{d} + \frac{D}{d} \right) \frac{C}{d}}{N} \left(\frac{P}{\rho D^5} \right)^{\frac{1}{3}} \tag{5}$$

where N is the stirring speed (rpm), ρ pulp density (kg/m^3), d impeller diameter, N_p power dimensionless number, P input power in the tank (W), H_L liquid height in the tank, D tank diameter and C is the distance between impeller and bottom of the tank .

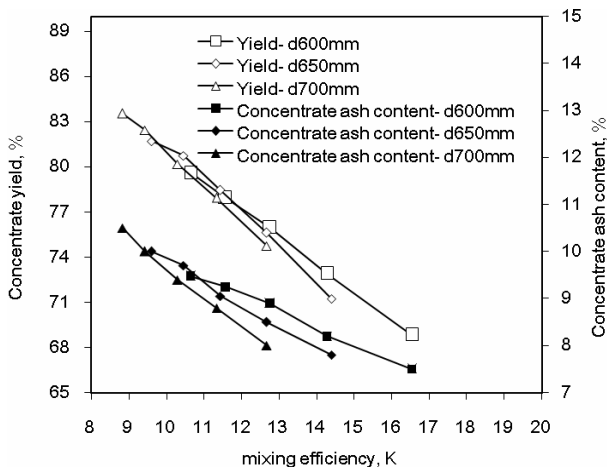


Fig. 6. Relationship between concentrate ash, yield, and mixing time per unit of energy consumption K

Figure 6 shows a relationship between the mixing efficiency and flotation index. The yield and ash content of flotation concentrate decreases with increasing mixing time per unit of energy consumption K . Higher K is detrimental to concentrate

flotation, while smaller K is more conducive to concentrate flotation. Based on the relationships between blade diameter, rotational speed, and K , the mixing time per unit of energy consumption is small when blade diameter is large. With the same K , larger blade diameter could obtain lower ash content of concentrate as well as concentrate yield.

Effect of stirred form on the feed rate of the flotation column

Stirred pulp-mixing and flotation experiments were conducted in the single- and two-stage stirring tanks at different feed rates to investigate the effect of stirred form on the feed rate of flotation column. The flotation concentrate ash content was controlled as qualified ash with intervals of 8.5% to 10% through forth overflow operation. The ash content of the flotation tailings of the two-stage stirred pulp-mixing was compared to that of the single-stage stirred pulp-mixing at different feed rates. The results of the prediction tests show that shaft speed was fixed at 333 rotation per min (rpm) (Fig. 7). The ash of the flotation tailings significantly decreased with the increasing feed rate of the cyclone-static micro-bubble flotation column. At a low feed rate, the ash content of the flotation tailings of two-stage stirred pulp-mixing did not exhibit obvious advantages over the single-stage stirred pulp-mixing.

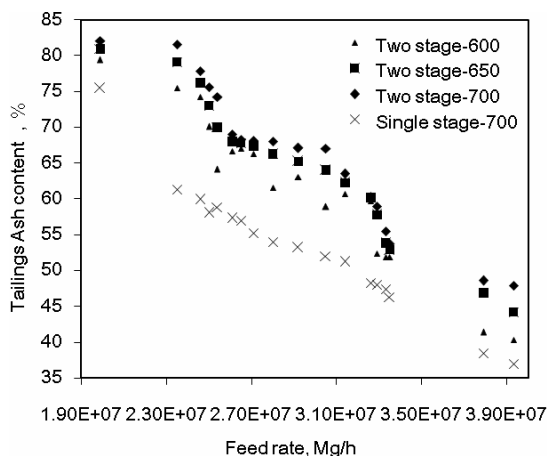


Fig. 7. Effect of different stirred mechanisms on flotation feed rate

For more in-depth analysis of superiority of the two-stage stirred mixing to the single-stage stirred mixing, the particle sizes of flotation tailings of the two stirring modes were analyzed at different flotation feed rates and at an impeller diameter of 700 mm. Figure 8 shows the ash distribution of the flotation tailings in different size fractions. In each grain size and feed rate, the ash content of tailings in the two-stage stirred pulp-mixing was higher than that of single-stage stirred pulp-mixing. In the two-stage stirred mode, fine particles (-0.074 mm) exhibited a good recovery effect

with low flotation feed rate, and tailings with higher ash content were obtained with coarse fractions (+0.125mm). The two-stage stirred pulp-mixing obtained tailings with higher ash content, when the flotation feed rate was high. Fine particle recovery was better in the two-stage stirred pulp-mixing than in the single-stage pulp-mixing. These results show that the two-stage stirred process strengthens the sufficient contact of micro-grain and flotation reagents in fine-coal flotation and intensifies flotation.

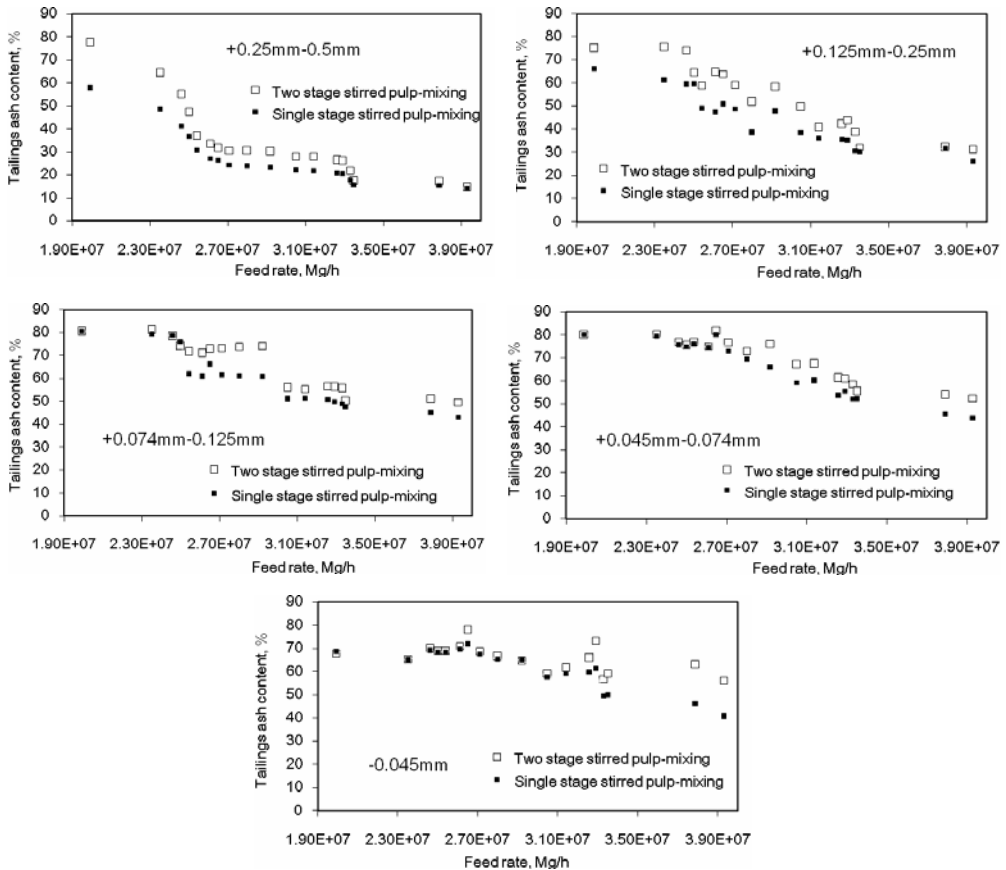


Fig. 8. Ash distribution in grain size of flotation tailings for different stirring mechanisms

Conclusions

In this study, the two-stage stirred pulp-mixing system was found to strengthen the mixing efficiency of pulp and flotation reagents and significantly increase the flotation concentrate yield and feed rate of the cyclone-static micro-bubble flotation column. Moreover, recycling of poor-floatability particles in the latter part of the flotation process in the two-stage stirring process could be strengthened with increasing

impeller diameter and shaft speed. Unlike the single-stage stirred pulp-mixing, the two-stage stirred pulp-mixing enhanced coarse particle recovery at a suitable flotation feed rate and ensured fine particle recovery at a high flotation feed rate.

Future research could focus on the relationships between the impeller diameter and stirring tank diameter, and the effect of distance of two stirring impellers. These relationships can possibly improve unsuitable mixing zones, reduce energy consumption and optimize the tank structure.

Acknowledgements

This research was supported by the National Key Basic Research Program of China (Grant no. 2012CB214905) and National Nature Science Foundation of China (Grant no. 51074157) for which the authors express their appreciation.

References

- CAO Y., GUI X., MA Z., YU X., CHEN X., ZHANG X., 2009. *Process mineralogy of copper-nickel sulphide flotation by a cyclonic-static micro-bubble flotation column*. Mining Science and Technology, 19, 784–787.
- CHENG H., CAI C., ZHANG X., ZHANG J., 1998. *Flotation microscopic kinetics and mathematical model*. Journal of China Coal Society, 23(5), 545–548 (in Chinese).
- DING K., JANUSZ S, LASKOWSKI, 2006. *Coal reverse flotation. Part I, Separation of a mixture of subbituminous coal and gangue minerals*. Minerals Engineering, 19 (1), 72–78.
- DOBBY G S, FINCH J A, 1986. *Particle size dependence in flotation derived from a fundamental model of the capture process*. International Journal of Mineral Processing, 21(3–4), 241–260.
- CHEN G., GRANO S., SOBIERAJ S., RALSTON J., 1999. *The effect of high intensity conditioning on the flotation of a nickel ore, part1, size-by-size analysis*. Minerals Engineering, 12(10), 1185–1200.
- GUI X., HUANG G., YUAN C., LIANG H., WANG Y., 2013. *Mixing characteristics of two-stage compulsory stirred pulp-mixing and its influence on fine coal flotation*. Journal of University of Science and Technology Beijing, 35(4), 423–431.
- HARBORT G. J., JACKSON B. R., MANLAPIG E. V., 1994. *Recent advances in jameson flotation cell technology*. Minerals Engineering, 7(2), 319–332.
- JIANG M., YAN R., YU Y., 2006. *The popularization and application of the flotation emulsion system in coal preparation plants*. Coal Quality Technology, 4, 7–10 (in Chinese).
- LI Y., ZHAO W., GUI X., ZHANG X., 2013. *Flotation Kinetics and Separation Selectivity of Coal Size Fractions*. Physicochemical Problems of Mineral Processing, 49(2), 387–395.
- LI Z., 2010. *Study on the stirred pulp-mixing process intensification and multi-stage compulsory mixing mechanism*. Xuzhou, China University of Mining and Technology, 49–55 (in Chinese).
- LI Z., LIU J., CAO Y., 2009. *Review of stirred pulp-mixing technology in flotation process*. Metal Mine, 10), 5– 11 (in Chinese).
- LIANG H., XU N., SHAO Y., 2011. *Flotation process optimization and mixing transformation of Xuehu coal preparation plant*. Coal Engineering, 6 , 60– 62 (in Chinese).
- LIU J., HU J., MA L., 2000. *Development and application of column flotation separation technology*. Coal Processing and Comprehensive Utilization, 1, 1–5 (in Chinese).
- LIU L., LIU J., SHANG L., XU M., 2009. *Stirring on the impact of coal flotation process*. Coal Preparation Technology, 1, 22–25 (in Chinese).

- ENGEL M.D., MIDDLEBROOK P.D., JAMESON G.J., 1997. *Advances in the study of high intensity conditioning as a means of improving mineral flotation performance*. Minerals Engineering, 10(1), 55–68
- FENG D., ALDRICH C., 2005. *Effect of Preconditioning on the Flotation of Coal*. Chem. Eng. Comm. 192, 972–983.
- CLAYTON R., JAMESON G.J., MANLAPIG E.V., *The development and application of the Jameson cell*. Minerals Engineering, 1991, 4(1), 925–933.
- RUBINSTEIN J. B. 2004. *Design, simulation, and operation of the flotation column*. Metallic Ore Dressing Abroad. 7, 16–20.
- SUN W., HU Y., DAI J., 2006. *Observation of fine particle aggregating behavior induced by high intensity conditioning using high speed CCD*. Transactions of Nonferrous Metals Society of China (English Edition), 16 (1), 198–202.
- NEGRI T, ZHANG L., LI C., 2007. *The measurement and scaling of flotation pulp mixing intensity*. Metallic Ore Dressing Abroad, 4, 22–25.
- VALDERRAMA L , RUBIO J, 1998. *High intensity conditioning and the carrier flotation of gold fine particle*. International Journal of Mineral Processing, 52(4), 273–285
- WANG F., MAO Z., SHEN X., 2004. Numerical study of solid-liquid two-phase flow in stirred tanks with Rushton impeller. (II) Prediction of critical impeller speed. Chinese Journal of Chemical Engineering, 12(5):610-614.
- WANG K., YU J., 2003. Chemical equipment design – mixing equipment. Beijing, Chemical Industry Press, 57–58 (in Chinese).
- XIA W., YANG J., ZHU B., 2012a. *Flotation of oxidized coal dry-ground with collector*. Powder Technology, 228, 324–326.
- XIA W., YANG J., ZHAO Y., ZHU B., WANG Y., 2012b. *Improving floatability of Taixi anthracite coal of mild oxidation by grinding*. Physicochemical Problems of Mineral Processing, 48 (2), 393–401.
- XIA W., YANG J., LIANG C., 2013. *A short review of improvement in flotation of low rank/oxidized coals by pretreatments*. Powder Technology, 237, 1–8.
- XU Z., LIU, J., CHOUNG J.W., ZHOU Z., 2003. *Electrokinetic study of clay interactions with coal in flotation*. International Journal of Mineral Processing, 68 (1–4), 183–196.
- YU H., 2005. XY–3.5 *The application of pulp preprocessor in coal preparation plant*. Mining and Processing Equipment, 5, 120–121. (In Chinese)
- ZHANG C., WU J., GONG B., 2006. *Flow resistance researches for SK static mixer tube of turbulent flow*. Chemical Engineering, 34(10), 27–30 (in Chinese).
- ZHANG H., LIU J., WANG Y., CAO Y., MA Z., LI X., 2013. *Cyclonic–static micro-bubble flotation column*. Minerals Engineering, 45, 1–3.
- ZHANG Q., MAO Z., YANG C., ZHAO C., 2008. *Research progress of liquid–phase mixing time in stirred tanks*. Chemical Industry and Engineering Progress, 27(10), 1544–1550.

Received: June 14, 2013; reviewed, accepted: August 6, 2013

RECOVERY OF MAJOR COMPONENTS OF SPENT ZINC ELECTROLYTE WITH DI(2-ETHYLHEXYL)PHOSPHORIC ACID (DEHPA) USED AS A ZINC(II) EXTRACTANT

Leszek GOTFRYD, Grzegorz PIETEK, Zbigniew SZOŁOMICKI,
Ksawery BECKER

Institute of Non-Ferrous Metals, Sowińskiego 5; 44-100 Gliwice, Poland, leszekg@imn.gliwice.pl

Abstract: Industrial acidic zinc electrolyte has been treated with calcium compounds and/or concentrated ammonia solution and resulting crystalline phases as well as equilibrium mother liquors were analyzed in detail for dependence on preliminary dilution of electrolyte with water. Neutralized zinc electrolyte was an object of investigation in zinc(II) extraction with di(2-ethylhexyl)phosphoric acid (DEHPA) as an extractant. Dependencies of zinc(II) and contaminants extraction on equilibrium pH, isotherms of zinc(II) extraction and stripping have been studied. During simulated laboratory counter-current trial of zinc extraction a new zinc electrolyte (stripped solution) has been produced. Raffinates left after the process were purified and qualified as mineral magnesium-ammonium fertilizer solutions.

Keywords: *zinc electrolyte, zinc solvent extraction, DEHPA, mineral fertilizer*

Introduction

Zinc electrolyte, circulating within zinc electrowinning system, contains mainly zinc sulphate, free sulphuric acid, and, in smaller amounts, magnesium and manganese sulphates. Such elements as Na, K, Cl, F are usually present within their permissible limits. The crude pregnant leach zinc-bearing solution is usually purified by chemical methods. Fe, As, Al, Si, Sb, Ge are rejected by oxyhydrolysis while Cd, Cu, Co, Ni, Pb are removed by cementation. Irremovable by these methods are Mg, Ca, Na, K, chlorides and fluorides. Generally, zinc electrolyte, used in electrolytic zinc metal production, because of necessity to maintain high parameters of current efficiency and quality of zinc cathodes, constitutes a product of very high purity (Ni, Co, Cu, Cd and others $< 0.001 \text{ g/dm}^3$). The exception is Mg, Mn or Na tolerated on higher levels. In particular zinc electrolyte contains only very limited amounts of iron as well as aluminium and silica. This favours application of the solvent extraction technique to

zinc recovery from this part of the solution, which from technological reasons has to be removed from the circuit.

Purification and concentration of metal salt from rich but contaminated solutions constitutes one of rather typical problems in industry. As for waste zinc bearing industrial solutions quite common problem pertain to hydrochloric acid spent pickling solutions, containing mainly zinc and iron. Crude zinc sulphate solutions are more often produced by leaching of industrial zinc-bearing dusts. They are also created within typical zinc hydrometallurgy process RLE (roasting – leaching – electrowinning).

Regel-Rosocka propose solvent extraction technique with use of tributyl phosphate organic solution for zinc(II), iron(II) and iron(III) extraction in form of their chloride anionic species (Regel et al., 2001; Regel-Rosocka et al., 2002). The work of other authors suggests similar approach (Rozenblat et al., 2004).

The ZINCEX™ technology developed by Technicas Reunidas, Spain, has been successfully applied in four industrial plants (Frias et al. 2009). The most important ones were domestic battery recycling plant in Spain (Frias et al. 2004) and Skorpion project in Namibia, Africa (Garcia 2005). This adaptable and flexible technology is based on natural (without external pH regulations) zinc solvent extraction technique from low and moderately concentrated zinc-bearing solutions with DEHPA organic solution as an extractant.

Gotfryd and Szymanowski published their results of zinc(II) extraction with Cyanex 272 and DEHPA organic solutions as extractants from highly contaminated zinc sulphate solutions of industrial origin (Gotfryd et al., 2004). In later works (Gotfryd et al., 2011a and 2011b) the authors have successfully treated by extraction concentrated but crude zinc solutions, obtained by sulphuric acid leaching of industrial zinc and lead bearing flue dusts. They used sodium hydroxide solution as neutralizing agent for current pH maintenance on the desired level of ≥ 2.0

Applying, in course of extraction, NaOH as well as NH₃ solutions, as current neutralizing agents, allows the effective treatment by solvent extraction technique also definitely highly concentrated zinc feed solutions.

Materials and reagents

The composition of the original (industrial) electrolyte is shown in Table 1.

Table 1. Composition of acidic zinc electrolyte used in investigations

H ₂ SO ₄	Zn	Mg	Mn	Na	K	Ca	Al	Si	Pb	Cl	F
155.3	59.3	14.3	2.84	5.23	1.43	0.55	0.011	0.058	<0.001	0.36	0.0055

For effective zinc extraction the treated solution must be nearly neutral. One of the early ideas of this work was applying ammonia solution for sulphuric acid

neutralization, both present originally in electrolyte and evolving during extraction. Using 25% ammonia for neutralization of free sulphuric acid leads to precipitation over 70% of zinc, and to a lesser extent, the other cations in the form of hydrated crystalline sulphate phases. Detailed discussion of this problem, especially regarding the influence of preliminary dilution on composition of crystalline phases and resulting mother liquors is provided in Results chapter.

The solution for zinc(II) extraction investigations has been prepared by using mineral calcium carbonate fines for acid neutralization. Crystalline gypsum ($\text{CaSO}_4 \cdot 2\text{H}_2\text{O}$) was produced as a by-product. The composition of resulting solution, further subjected to zinc extraction, is revealed in Table 2.

Table 2. Composition of zinc electrolyte after neutralization

Zn	Mg	Mn	Na	K	Ca	Cl	F	pH
51.70	12.6	2.65	4.99	1.38	0.56	0.305	0.007	g/dm^3 5.6

The solutions of ammonia (25%), NaOH (2.0 M) and sulphuric acid (2.4 M) (all POCH Gliwice) were used as reagents for neutralization and/or stripping purposes. Di(ethylhexyl)phosphoric acid (DEHPA) dissolved in hydrocarbon diluent Exxsol D80 (Exxon Mobile/Brenntag Polska) was applied as the extractant (DEHPA concentration was 18 and 36 % vol.).

Experimental

Acid neutralization and preparation of solutions for extraction

Two series of experiments leading to electrolyte neutralization with ammonia solution have been performed. During the first one the volume of electrolyte was 2.0 dm^3 (to observe the thermal effects). The second one has been performed on a smaller scale (250 cm^3). In both cases portions of electrolyte were diluted to the different extent with water and next, mixed and treated slowly with 25% ammonia solution, controlling the pH (final pH level 5.0). Next, the solution/suspension has been mixed gently during its natural cooling, to avoid excessive hardening of precipitating crystals at the bottom of vessel (in form of a coarse 1–2 cm crystalline compact crust). Mixing was continued until temperature reached a constant level and spontaneous crystallization was stopped. The obtained crystals were filtered and drained on filter paper.

To avoid contamination of the crystals with insoluble forms of Mn(IV) compounds, before experiment the zinc electrolyte was discoloured (colour was caused by MnO_4^-) using small amount of reducing agent (30% H_2O_2).

To obtain solutions for extraction investigations the method of neutralization with fine calcium carbonate particles has been used. Limestone powder was added slowly

to mixed solution to rich pH of about 5.5. Precipitated gypsum was filtered on vacuum filter.

Methods of zinc extraction and additional raffinates purification

First trials of zinc extraction were done with 36% (vol.) di(ethylhexyl)phosphoric acid (DEHPA) dissolved in hydrocarbon diluent Exxsol D80. Due to high viscosity, the concentration in further experiments has been limited to 18% (vol.) (about 0.50 M).

Elementary extractive experiment consisted of period of mixing (usually 10 minutes) of the two particular reacting phases, period of their natural gravitational separation and analysing of the samples obtained.

First experiments covered recognition and establishing zinc(II) and contaminants extraction dependences on pH. Reacting phases (e.g. 500 cm³/500 cm³) were repeatedly mixed for ten minutes, with aliquot of 50 cm³ samples taken after that for analysis. A small volume (1–2 cm³) of neutralizing agent has been gradually added each time to the remaining volume of reacting phases at the beginning of mixing period.

Afterwards, the measurements of zinc(II) extraction isotherms at two levels of temperature (20 and 40 °C) and isotherm of stripping with 2.4 M sulphuric acid (at 20 °C) were conducted. All trials of zinc(II) extraction were performed, using, as a feed solution, zinc electrolyte, neutralized with limestone powder (Table 2). However, in all cases of acid neutralization in the course of zinc(II) extraction 25% ammonia solution has been used. Additionally, for comparison purpose, the isotherm of zinc(II) extraction with 5.0 M NaOH used as neutralizing agent also has been measured. In these studies, in order to obtain individual data points which provide isotherms, specific method was applied. It consists of radical changes of organic-to-aqueous ratio within a wide range of O: W = 10:1 to 1:10. Next the isotherms were supported with the McCabe-Thiele constructions, which supply information about the parameters of the counter-current system, necessary for effective extraction/stripping of zinc(II) (number of counter-current stages, optimal phase ratios, etc.).

Basing on collected data an extraction scheme has been designed and used in the laboratory trial, imitating configuration and performance of counter-current systems. All stripped liquors, as well as raffinates, remaining after the process, were analyzed.

Cumulative post-extraction raffinates (two batches) were subjected to a further treatment for purification from the residual organic phase. Next they were purified from manganese(II) and residual amounts of zinc(II). The aim was to obtain either solutions or crystalline phases of magnesium-amonium salt, which can be used as fertilizer.

The following reagents have been tested as purifying agents (in parenthesis temperature of action is given):

- saturated solution of NH₄HCO₃ (80 °C)
- saturated solution of (NH₄)₂CO₃ (60 °C),
- 30% H₂O₂ + 25% NH₃ (80 °C),

- magnesium oxide – MgO (60 °C),
- magnesium carbonate – MgCO₃ (60 °C),
- solid ammonium persulphate NH₄)₂S₂O₈ (90 °C) + NH₄HCO₃ for neutralization

Results

Electrolyte neutralization with ammonia

In the case of 2.0-dm³ sample of undiluted electrolyte neutralized with 25 % ammonia, to obtain nearly neutral pH of about 5.0 in hot suspension, 493 g of ammonia solution was used. A temperature increase to the level of 63 °C has been observed. Products of reaction occupied 2.45 dm³ while the crystals, lying on the bottom of beaker – 0.75 dm³ (apparent bulk volume). Poured out after several hours saturated solution of pH 6.33 had volume of 1.42 dm³. Its composition was as follows; g/dm³: NH₄⁺ 23.2; Zn 11.3; Mg 6.9; Mn 2.6.

For the other trials of series 1 the procedure was similar except for the fact that the electrolyte was pre-diluted with water. Likewise, but on a smaller scale, experiments have been carried out as series 2. Selected results of the tests of series 1 are shown in Table 3 and more complete results of series 2 in graphical form in Figs 1–4.

Table 3. Changes in composition of obtained crystalline phases, depending on degree of dilution of initial electrolyte

Experiment No.		0	1	2	3	4
Water/electrolyte	dm ³ /dm ³	0.0	0.4	0.8	1.2	1.6
Concentrations in crystalline phases						
Mn		0.17	0.14	0.13	0.12	0.12
Mg		1.69	1.49	1.36	1.29	1.20
NH ₄ ⁺	%	8.94	8.44	8.40	8.52	8.47
Zn		11.46	11.85	12.18	12.32	13.64

Figure 1 shows the effect of dilution of the initial electrolyte on the composition of both crystalline phases and the mother liquors in the form of their interrelations. In addition to that, the data for each particular sample were clustered with dashed lines. Figure 2 shows the shares of the individual components of the electrolyte in the precipitated crystals depend on the degree of dilution of the initial electrolyte.

Concentrations of individual components of the zinc electrolyte neutralized with ammonia and their shares in the solutions, in the equilibrium state with the precipitated crystals (if present), versus initial dilution of the electrolyte are shown in Figs 3 and 4.

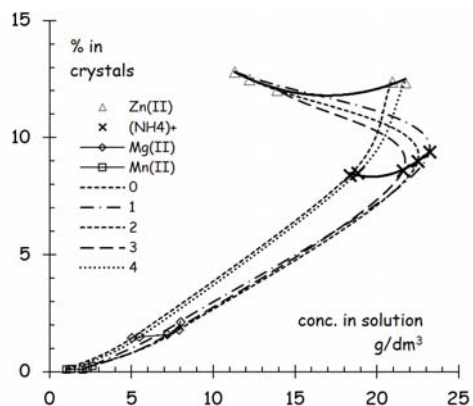


Fig. 1. Effect of the initial electrolyte dilution on the changes of phases composition of reaction mixtures, being in equilibrium state

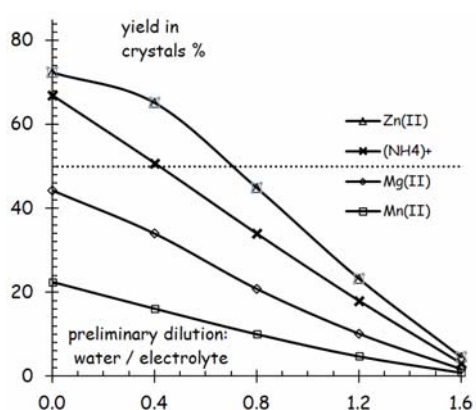


Fig. 2. The shares of the individual components in crystals in equilibrium with the saturated solutions depending on the initial dilution of the electrolyte

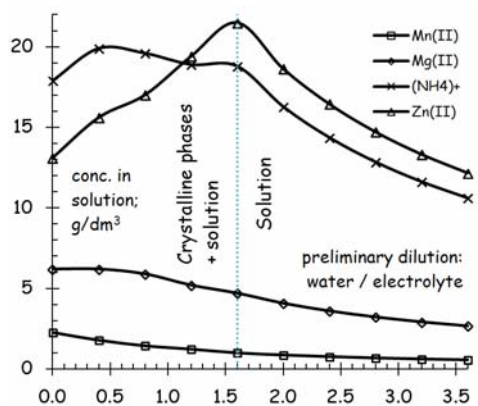


Fig. 3. Composition of solutions, resulting from zinc electrolyte neutralization with 25% ammonia, in equilibrium with crystals (if present), versus water/electrolyte initial ratio

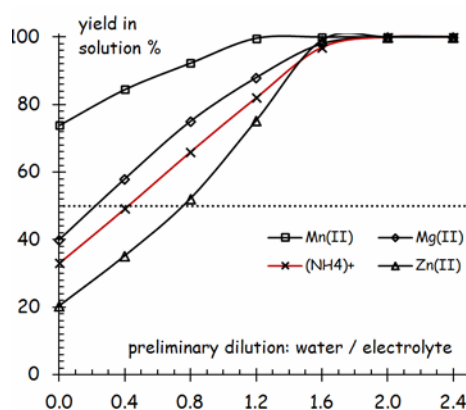


Fig. 4. Yield of particular component of neutralized with ammonia zinc electrolyte into solution versus water/electrolyte initial ratio

It can be seen that there is no possibility to separate constituents of neutralized electrolyte basing on such methods. On the other hand, to keep all the components of the electrolyte in solution, it should be pre-diluted with water used in an amount of $\geq 1.6 \text{ dm}^3$ per 1 dm^3 of electrolyte. Therefore, trials to utilize ammonia in order to prepare the solution for zinc extraction with conversion of free sulphuric acid into ingredient of ammonia-magnesium type fertilizer do not justify themselves. Thus, further zinc extraction tests were carried out with a solution neutralized with calcium carbonate.

Zinc(II) extraction

Figures 5 and 6 show concentrations of Zn and contaminants in organics versus equilibrium pH. The 36% organic phase, as more viscous, bears increased amounts of impurities. The relationships were investigated using 25% ammonia as pH neutralizing agent.

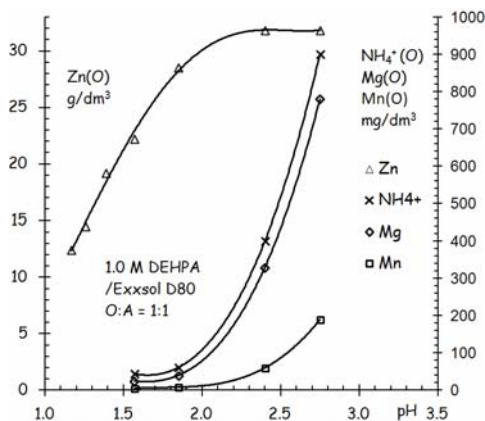


Fig. 5. Concentrations of Zn and contaminants in organics versus equilibrium pH (36% DEHPA)

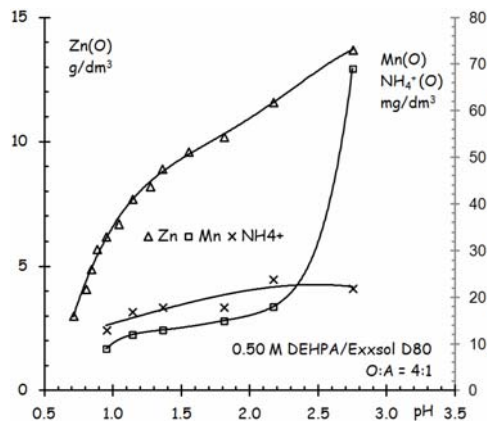


Fig. 6. Concentrations of Zn and contaminants in organics versus equilibrium pH (18% DEHPA)

The next step involved zinc extraction isotherm examination at equilibrium pH of 2.5 ± 0.1 . The isotherms have been obtained with 25% NH₃ at ambient and elevated (40 °C) temperatures and 5.0 M NaOH (at ambient temp.) used as neutralizing agents. The results are shown in Figs 7 and 8.

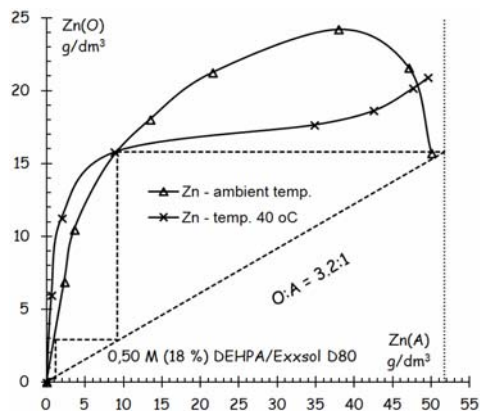


Fig. 7. Zn extraction isotherms with ammonia used as neutralizing agents

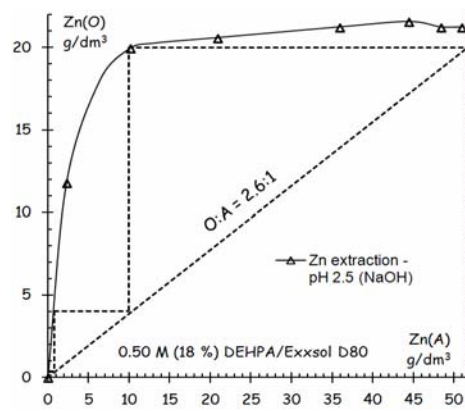


Fig. 8. Zn extraction isotherms with NaOH used as neutralizing agents

The results obtained with NaOH are superior. The extractions can be conducted at a lower phases ratio (O:A) because of practical possibility to utilize higher level of organic phase saturation with Zn(II) $\geq 20 \text{ g/dm}^3$. More on this one can find in earlier works of the authors (Gotfryd et al., 2011a and 2011b) and on the so-called pre-neutralization of the extractant with soda lye in other references, e.g. Swain et al. 2006.

Stripping isotherm (Fig. 9), prepared with organic phase saturated to the level of 13.7 g/dm^3 Zn(II) (at $\text{pH} = 2.5 \pm 0.1$, stabilized by ammonia) and 2.4 M sulphuric acid, indicate that concentrations of about 155 g/dm^3 Zn(II) can be obtained in the stripped solution applying only two steps of counter-current stripping.

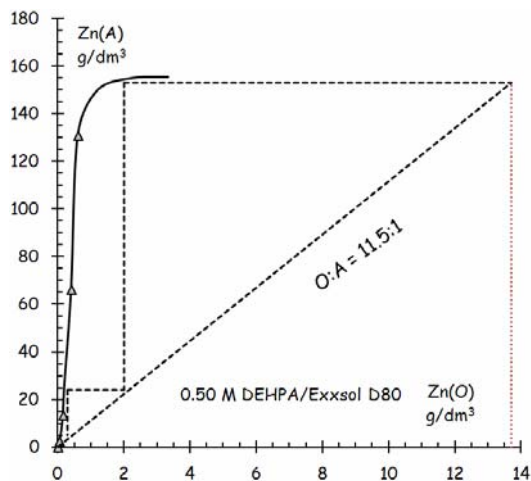


Fig. 9. Zn stripping isotherm with 2.4 M sulphuric acid

Basing on obtained isotherms and their McCabe–Thiele interpretations, a multistage laboratory trial has been carried out. The way it was done is shown as a scheme in Fig. 10.

Starting from the cycle E, amount of organic phase was increased to 1.20 dm^3 . The results obtained are presented in the Table 4. It contains ammonia consumption, obtained equilibrium pH and concentrations of components in the raffinates and stripped solutions.

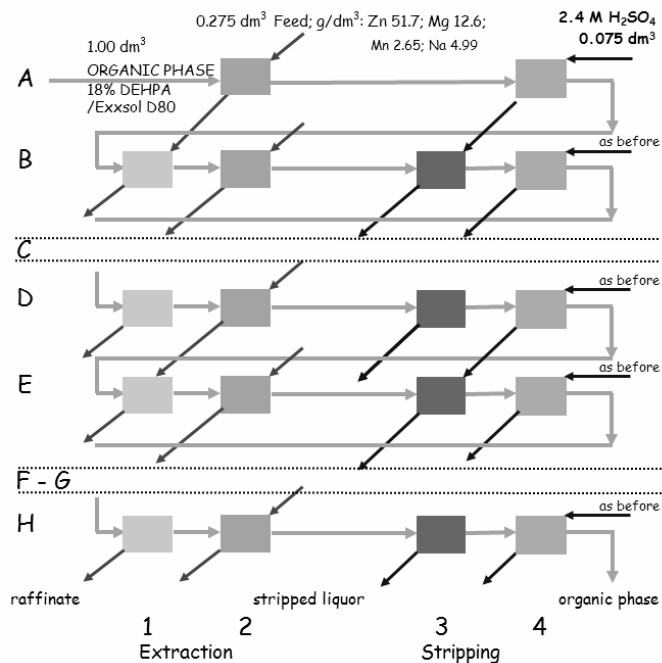


Fig. 10. Scheme of extractive system realizing course of counter-current extraction and stripping of zinc(II)

Table 4. Results of pseudo counter-current trials of zinc(II) extraction

Cycle	Raffinates					Strip liquors				
	1 (final)		2 (immediate)			3 ^{*)}		4		
	NH ₃ ml	pH –	Zn g/dm ³	Mg g/dm ³	Mn g/dm ³	NH ₃ ml	pH –	Zn g/dm ³	Zn g/dm ³	Zn g/dm ³
A	–	–	–	–	–	32.0	2.52	6.86	–	–
B	7.0	2.50	0.099	–	1.1	23.0	2.58	16.34	157.2	134.7
C	11.0	2.60	0.22	–	–	20.0	2.70	22.88	156.9	143.9
D	14.5	2.70	0.39	12.6	2.7	15.0	2.61	30.07	150.7	141.5
E	17.5	2.55	1.40	–	–	12.0	2.53	36.28	157.6	144.8
F	23.0	2.65	0.82	–	2.2	13.5	2.50	33.34	164.1	150.7
G	21.0	2.50	0.17	–	2.6	15.5	2.50	38.90	161.5	152
H	24.0	2.60	3.40	12.4	2.5	8.0	2.65	43.15	147.1	150
Cumulative stripped liquors ^{*)}										
Sample (cumulative)	Zn	Mg	Mn	NH ₄ ⁺	Cl	F				
	g/dm ³	g/dm ³	g/dm ³	g/dm ³	mg/dm ³	mg/dm ³				
B3 + C3 + D3	154.0	1.46	0.54	0.095	42	< 1.0				
E3+F3+G3+H3	157.5	1.38	0.29	0.13	52	< 1.0				

As in case of stripped liquors, two collective samples of raffinates have been prepared by mixing a few particular samples, each of 200 cm³ in volume, namely Raffinate 1 (B1+C1+D1) and Raffinate 2 (E1+F1+G1+H1).

The detailed composition of these raffinates is given in Table 5.

Table 5. Composition of raffinates obtained by counter-current zinc(II) extraction in comparison with original composition of acidic and neutralized zinc electrolyte

Solut.\ ingr.	NH ₄ ⁺	Mg	Mn	Zn	Na	K	Ca	Al	Si	Cl	F	g/dm ³
Electrolite	0.00	14.3	2.84	59.3	5.23	1.43	0.55	0.011	0.058	0.36	0.0055	
Neut. electr.	0.00	12.6	2.65	51.7	4.99	1.38	0.56	–	–	0.305	0.007	
Raffinate 1	25.0	12.4	2.43	0.24	4.8	1.3	0.5	–	–	≥0.25	0.005	
Raffinate 2	24.5	14.95	2.67	1.45	5.0	1.4	0.5	–	–	≥0.25	0.005	

Generally the composition of these two solutions (Raffinate 1 and 2) is such, that they are close to saturation. The main ingredient is ammonium sulphate and the next is magnesium sulphate. Magnesium and manganese, like sodium, potassium and chlorides are present in raffinates in amounts almost equal to their original concentrations in the zinc electrolyte.

Raffinates processing

First two rows of Table 6 repeat composition of both cumulative raffinates. First of them has been preliminary purified and neutralized by adding 30% hydrogen peroxide and 25% ammonia and then, after filtration, used for further purposes. Feed 2 row shows also composition of first crystals being in equilibrium with the solution.

Table 6 gives names of reagents used and conditions of physical/chemical treatment of raffinates and the compositions of the solutions obtained. In cases where solid sediments and/or hydrated sulphate crystals have appeared, there are given composition and further data, pertaining to these solid phases.

Discussions

Neutralization of acidic zinc electrolyte with ammonia and spontaneous crystallisation

Neutralization of acidic zinc electrolyte with 25% ammonia warms up the solutions, and after cooling, precipitation of large amount of crystals occurs. Neutralization without dilution causes binding in the structure of a mixed sulphate crystals over 70% of zinc mainly as zinc-ammonium sulphate phases but with admixture of magnesium and slight admixture of manganese.

On the other hand, to maintain all electrolyte components in solution one should dilute it with water taken in amounts of ≥ 1.6 dm³ per 1 dm³ of electrolyte. This leads to a total dilution of zinc from an initial value of about 60 g/dm³ up to about 22 g/dm³

Table 6. Conditions and results of raffinates purification and composition of precipitated solid phases in equilibrium with solutions

No.	Date 2013	Feed	Vol. dm ³	Reagent		Conditions		Sediment		Solid phases				Solutions					
				Sort	Quantity g (ml)	Temp. °C	Time h	– g	Crystals g	NH ₄ ⁺ %	Mn %	Mg %	Zn %	Vol. dm ³	pH	NH ₄ ⁺ g/dm ³	Mn g/dm ³	Mg g/dm ³	Zn g/dm ³
Feed 1	1	0.600	–	–	20	–	–	–	–	–	–	–	0.600	2.4	25.0	2.43	12.4	0.24	
Feed 2	2	0.800	merely natur. crystallization	–	20	–	–	–	(5)	9.20	0.43	6.0	1.80	0.800	2.2	24.5	2.67	14.95	1.45
1*	1402	1	0.600	25 % NH ₃ 30 % H ₂ O ₂	(14.5) (5.0)	80	3	no inf. –	– lack	– –	– –	– –	– –	0.600	8.20	>25	<2.0	12.3	0.15
2/3	1502	1*	0.050	(NH ₄) ₂ CO ₃ (solution)	(till the effect)	60	0.5	3.43 –	– traces	– –	– –	– –	– –	0.067	8.65	>25	0.014	<12	0.092
2/4	1502	1*	0.050	MgO	0.6	60	0.5	1.12 –	– lack	– –	– –	– –	– –	0.050	8.37	25	0.7	>12	0.11
5/1	2202	1*	0.400	NH ₄ HCO ₃ (solution)	10.0	80	0.25	1.38 –	– 21.5	– –	– 1.30	– –	– <0.005	0.050	8.11	30.7	0.68	<11	0.17
5/2	2202	1*	0.350	NH ₄ HCO ₃ (solution)	13.8	80	0.25	0.79**(+) –	– 29.5	– –	– 28.0	– 5.8	– 2.7	0.050	8.32	34.0	0.094	<10	0.062
5/3	2202	1*	0.300	NH ₄ HCO ₃ (solution)	21.8	80	0.25	0.00 –	– 33.1	– –	– –	– –	– <0.005	0.29	7.85	41.5	0.066	8.9	0.080
2/1	1502	2	0.050	MgCO ₃	2.5	60	0.5	1.84 /white/	– lack	– –	– –	– –	– –	0.055	8.09	>25	0.079	>12	0.41
2/2	1502	2	0.050	MgO	1.0	60	0.5	1.33 /brown/	– lack	– –	– –	– –	– –	0.047	8.28	>25	1.10	>12	1.25
3	1902	2	0.100	MgO (NH ₄) ₂ S ₂ O ₈ 30 % H ₂ O ₂	2.0 1.5 (2.0)	80	0.5	2.4 /brown/	– lack	– –	– –	– –	– –	0,080	8.54	>25	1.09	>12	1.57
4/1	2002	2	0.100	NH ₄ HCO ₃ (NH ₄) ₂ S ₂ O ₈	for neutral. 2.0	95	1.0	1.84 /white/	– 3.65	– 10.9	– 0.15	– 6.71	– 0.36	0.082	7.19	31.5	0.70	10.33	0.83
4/2	2002	2	0.100	NH ₄ HCO ₃ (NH ₄) ₂ S ₂ O ₈	for neutral. 4.0	95	1.0	0.20 /black/	– 7.86	– 9.53	– 0.54	– 6.13	– 1.43	0.079	2.96	31.3	2.37	10.21	0.71
4/3	2002	2	0.100	(NH ₄) ₂ S ₂ O ₈ NH ₄ HCO ₃	2.0 for neutral.	95	1.0	1.02 /creamy–c./	– 9.89	– 9.70	– 0.10	– 6.63	– 0.075	0.060	7.42	34.7	0.75	8.70	1.18

** – analyzed together with sample 5/1

(Fig. 3). At the same time it is the maximum value of the concentration, because under lesser dilution the crystallization of common with ammonium salts causes a decrease of the equilibrium zinc(II) concentration in the solution up to a level of about 11.5 g/dm^3 . Therefore, attempts to utilize ammonia in order to prepare the solution for zinc extraction with conversion of all free sulphuric acid into ingredient of ammonia-magnesium type fertilizer do not justify themselves.

Neutralization of zinc electrolyte with calcium compounds

Attempts to use slaked lime or quicklime for zinc electrolyte neutralization proved that they are not good reagents for this purpose. Much better results are obtained by using for this purpose fines of calcium carbonate (limestone). This leads to a good use of raw material (CaCO_3) and provides valuable product - gypsum of commercial value.

Zinc(II) extraction from zinc electrolyte neutralized with limestone

Investigations with use of about 36% (vol.) di(2-ethylhexyl)phosphoric acid (DEHPA) as an extractant proved that zinc(II) extraction takes place already at pH 2.0–2.5 and the saturated with zinc(II) organic phases are very viscous. This leads to slowing down of phases separation and tendency to emulsification. In practice it means carrying out organic phase with microdrops of raffinate transferred to stripping solution (undesirable mechanical transport of contaminants). Reducing the concentration of the extractant to the level of 18% has decreased significantly these trends. The determined on this stage capacity of 36% of extractant has reached the level of about 32 g Zn(II)/dm^3 and after dilution by half it has been a commensurately reduced.

The 18% extractant was also examined in terms of its usefulness in the extraction process of a continuous counter-current character by determining their zinc(II) extraction isotherms (iso-pH 2.5) and their McCabe-Thiele interpretation. The recognition was done at ambient ($20 \text{ }^\circ\text{C}$) and elevated ($40 \text{ }^\circ\text{C}$) temperatures. In both cases optimally designed McCabe-Thiele diagram indicates the possibility for effective extraction of zinc(II) using merely two-step counter-current system, if we assume the working zinc(II) concentration within extractant at the level of about $14 \text{ g/dm}^3 \text{ Zn(II)}$.

Studies of stripping isotherms with sulphuric acid at a concentration of about 2.4 M allow concluding, that it is possible, after applying two-stage counter-current stripping, to reach practically complete uptake of available acid and to achieve the concentration of zinc in the stripped phase of about $\geq 155 \text{ g/dm}^3$. To achieve this one should work with a high proportion of the organic phase in relation to the aqueous phase (acidic) O: A = 11.5:1.

Simulations trials of the counter-current system of SX was carried out using periodically the same portion of 1.00 (1.20) dm^3 of 18% DEHPA in turns into two-stage counter-current extraction of zinc from neutralized zinc electrolyte, and then performing a two stage of counter-current stripping. There was no washing step

between extraction and stripping inserted, in order to observe the transport of impurities.

This effect was treated as an indicator of the level of microdrops of raffinate mechanical transmission to the stripped phase.

Efficiency of the extraction system was substantial with zinc extraction of about 99.6% (raffinate 1) and zinc accumulation in the sulphate form as a highly concentrated solution.

The excessive transfer of impurities to the stripped phases has been found. Reason for this is relatively high viscosity of the organic phase saturated with zinc in the presence of ammonia. Using of washing stage of the organic phase, higher extraction temperature and lower pH of extraction (to about 2.0-2.3) should effectively prevent the presence of impurities in stripped phases.

Purification and crystallization of the raffinates

At the first stage of experiments it has been attempted to get crystalline phases or solutions of the fertilizer character during neutralization of all the acid present in the electrolyte using 25% ammonia solution. However, zinc, not other species, is the major component of the spontaneously precipitating crystals (they contained it at the level of 11.5–13.6% Zn). In the post-crystallization solution the lowest concentration of zinc was about 11.5–13 g/dm³.

Further tests were carried out with the electrolyte neutralized with calcium carbonate, although for current neutralization during extraction 25% solution of ammonia was used. In this way, raffinates obtained in the second period of tests, after thorough cleaning, potentially could also be treated as a source of chemical compounds in the type of mineral magnesium-ammonium fertilizers.

Basing on the data obtained in the trials of raffinates purification, it can be concluded, that

- before the actual precipitation of impurities, acid remnants should be neutralized (pH of 2.2–2.5 level should be increased to approximately ≥ 8.2),
- methods of disposal of manganese(II) by its oxidation using ammonium persulphate or hydrogen peroxide or even their combination, are moderately effective,
- because under these oxidative conditions pH decreases, it should be re-adjust to a level of > 8.2 to 8.5 by addition of ammonium carbonate, preferably in neutral form, as ammonium bicarbonate gives a slightly worse results,
- the presence of significant amounts of ammonium salt in the solution makes it difficult to achieve significant removal of impurities. This applies to a greater extent for zinc(II) than for the manganese(II).

Finally, it was possible to obtain the concentration of manganese(II) and zinc(II) at 0.015-0.095 and 0.06-0.09 g/dm³, respectively, levels. This allows to crystallize the solid phases containing 9.5-10.5% NH₄⁺, to 6.8% Mg, approximately 0.015% Mn and several times less Zn (<0.005 %). Ambiguity of correlations between low contents of

Mn and Zn in the crystals of ammonium-magnesium sulphates and their concentration (at low levels) in the pregnant solutions, can be explained by changes of the levels of moisture contained in the crystals separated from the solution. These, separated by filtration, crystals were not washed but merely dried on the filter paper. The effectiveness of this procedure was better in the case of coarser crystals.

Summary

Generally it can be stated, that

1. there is no possibility for separation of components of ammonia neutralized zinc electrolyte by simple crystalline and mother liquor phases separation
2. zinc recovery from preneutralized acidic zinc electrolyte, using solvent extraction technique with 18% vol. DEHPA as extractant and 25% ammonia as neutralizing agent, with the aim of parallel utilization of raffinate as a mineral fertilizer solution, can be realized in two ways:
 - after electrolyte substantial dilution with water to the level of some 3.0 dm³ from one dm³ of electrolyte, neutralization with ammonia and zinc(II) extraction at O:A ratio of about 1.5–2:1; or
 - after acid removal by crystalline gypsum precipitation and zinc(II) extraction at O:A ratio of some 3.6–4:1
3. to stop an excessive transport of contaminants by organic phase to strip solution it is recommended:
 - performing the extraction at the temperature of about 40–45 °C,
 - maintain comparatively low pH of extraction of about 2.0–2.5,
 - utilize extractive washing system of loaded organic phase
4. such method of treatment (with ammonia used) slightly spoils conditions of zinc(II) extraction (higher viscosity of loaded organic) in comparison with extraction with the use of soda lye, but it is compensated by obtaining potentially useful solutions of ammonia-magnesium sulphates suitable for fertilising purposes
5. it is possible to purify the post-extractive raffinates to obtain solutions or even crystalline phases. It can be used as an ammonia-magnesium fertilizer.

References

- FRIAS C., DIAZ G., MARTIN D., SANCHEZ F., 2009, *Implementation of first ZINCEX commercial plant treating zinc secondaries*; Proc. Europ. Met. Conf., June 28–July 1, Innsbruck, Austria.
- FRIAS C., MARTIN D., DIAZ G., FALGUERAS J., BAYLINA V., 2004, *Highlights of domestic battery recycling plant based on Modified ZINCEX process after five years successful operation*. In: Global Symposium on Recycling, Waste Treatment and Clean Technology; REWAS'04 Conference, Madrid, Spain.
- GARCIA M. A., SANCHEZ F., MEJIAS A., FRADES M., 2005, *The Skorpion zinc plant, ZINCEX solvent extraction. The best expectations confirmed after commissioning*. In: International Symposium Lead/Zinc 2005, Kyoto, Japan.

- GOTFRYD L., CHMIELARZ A., SZOŁOMICKI Z., 2011, *Recovery of zinc from arduous waste using solvent extraction technique. Part I. Preliminary laboratory studies*. Phys. Probl. Min. Proc. 47, 149–158
- GOTFRYD L., CHMIELARZ A., SZOŁOMICKI Z., 2011, *Recovery of zinc from arduous waste using solvent extraction technique. Part II. Pilot plant tests*. Phys. Probl. Min. Proc. 47, 183–192.
- GOTFRYD L., SZYMANOWSKI J., 2004, *Recovery of zinc(II) from acidic sulfate solutions. Simulations of counter-current extraction-stripping process*. Phys. Probl. Min. Proc. 38, 113–120.
- REGEL M., SASTRE A. M., SZYMANOWSKI J., 2001, *Recovery of zinc(II) from HCl spent pickling solutions by solvent extraction*, *Envir. Sci. Technol.*, Vol. 35, 630–635.
- REGEL-ROSOCKA M., MIESIĄC I., SASTRE A.M., SZYMANOWSKI J., 2002, *Screening of reagents for recovery of zinc(II) from hydrochloric acid spent pickling solutions*. Proc. ISEC'2002. Chris van Rensburg Publ. Ltd. Cape Town, South Africa, Vol. 2, 768–773.
- ROZENBLAT M., REGEL-ROSOCKA M., SZYMANOWSKI J., 2004, *Metal removal from spent pickling solution of high zinc(II) concentration*, Phys. Probl. Min. Proc. 38, 121–129.
- SWAIN B., JEONG J., LEE J., LEE G.-H., 2006, *Separation of cobalt and lithium from mixed sulphate solution using Na-Cyanex 272*. Hydrometallurgy 84, 130–138.

Received July 3, 2013; reviewed, accepted July 26, 2013

COPPER(II) EXTRACTION FROM AMMONIA LEACH SOLUTION

Katarzyna OCHROMOWICZ, Magdalena JEZIOREK, Katarzyna WEJMAN

Wrocław University of Technology, Faculty of Chemistry, Division of Chemical Metallurgy, Wybrzeże Wyspiańskiego 23, 50-370 Wrocław, Poland, k.ochromowicz@gmail.com

Abstract: Hydrometallurgical processing of copper-bearing materials (ores, concentrates, by-products) is usually done with the use of acidic or ammonia leaching. In the case where a leaching feed material contains significant amounts of carbonate rocks and iron minerals the second method is preferential due to a higher process selectivity. However, it can also be problematic considering possible ammonia transfer during the subsequent extraction process. The paper presents results of extraction of copper(II) from ammonia leach solutions. The effect of a type of extractant, its concentration and type of diluent in organic phase on extraction efficiency and ammonia transfer was studied. A few commercial extractants were examined, namely LIX 84-I, LIX 984N, LIX 54-100. The results clearly indicate that in the case of extraction systems using hydroxyoximes the extraction efficiency is remarkably higher than for β -diketone reagent. Presented studies proved that extraction efficiency of Cu(II) is also dependent on the type of diluent and is less favourable for systems with non-aliphatic diluents. It was observed that ammonia co-extraction occurs and depends on examined parameters. Scrubbing of loaded organic phase showed that ammonia can be removed almost completely using double wash with sulfuric acid solution.

Keywords: *hydrometallurgy, hydroxyoximes, LIX, copper ore, copper concentrate*

Introduction

Ammonia leaching is frequently used in hydrometallurgy for processing of oxide and sulfide ores, concentrates or by-products, particularly those containing significant amounts of carbonate rocks, which during the acidic leaching contribute to increased acid consumption. Ammonia and its salts (carbonate or sulfate) are very effective and selective leaching agents. They can be a good alternative to acidic oxidative solutions, considering high stability constants of formed ammonia complexes of Ag, Au, Co, Cu, Ni and Zn. In the case of materials containing copper-iron and iron minerals (chalcopyrite, bornite, pyrite, pyrrhotite) ammonia leaching can be beneficial because of its selectivity. The selectivity means solubilization of desired metals and

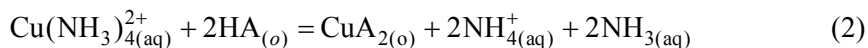
precipitation of undesirable iron in one unit operation (Chmielewski et al., 2009). Iron can pose a real problem in further stages of hydrometallurgical processing, in operations such as solvent extraction.

Ammonia leaching of sulfide copper concentrates generate buffer type liquors (pH ranges from 9 to 10), because of the excess of ammonia and significant amount of ammonia sulfate as a leaching agent. Metals such as Cu, Ni, Co and Zn occur in ammonia systems as a cationic amminacomplexes. Alkalinity of the solution and free ammonia concentration affect route of extraction (Miller et al., 1981).

Solvent extraction (SX) of copper(II) from ammonia solutions proceeds similarly to that from acidic solutions, but complexation of metal (M) by ammonia ligands must be considered:



During extraction ammonia ligands are pushed out and a new chelate complex with hydroxyoxime is formed in organic phase. Copper(II) extraction from ammonia solution with acidic extractant HA is described as:



where aq and o subscripts denote the aqueous and organic phases, respectively.

Extraction of metals from ammonia solutions seems to be more complicated comparing to acidic environment. Initially, considering that extraction reaction is reversible it should be expected that the increase of ammonia or ammonium ion concentration in the aqueous phase will deteriorate extraction. Moreover, according to Jergensen (1999) the increase of pH of the aqueous phase or extractant concentration in the organic phase is not necessarily beneficial for extraction. The reason for this is that both parameters favour ammonia transfer to the organic phase. The type of hydroxyoxime extractant and diluent and content of metal in the organic phase also significantly contribute to ammonia extraction. The observed phenomenon is dangerous and should be avoided. The contact of loaded organic phase containing ammonia with a spent electrolyte can lead to formation of ammonium sulfate (carbonate or chloride) in liquors directed to electrowinning section. Crystallization of ammonium salts can be observed in tanks after few recycles of spent electrolyte to the stripping section. It is the main disadvantage of metals extraction from ammonia solutions. It complicates a technological process and negatively affects its economy. Scrubbing of the loaded organic phase before stripping with spent electrolyte significantly reduce ammonia concentration in strip liquors (Flett and Melling, 1979; Ritcey, 2006).

In the case of multicomponent solutions, extraction of metals can be held in two ways. The first one is selective sequential extraction – stripping, while the second one is co-extraction – selective stripping. Very often it appears that the second method is

more cost-effective, because it requires less stages comparing to the first way of separation. The concept of co-extraction (selective stripping) was used for many metal couples. It was also adopted in ammonia systems for Cu-Ni separation.

The paper presents the results of extraction of copper(II) from ammonia pregnant leach solutions (PLS), coming from leaching of copper sulfide concentrates. Some commercial extractants were examined, namely LIX 84-I, LIX 984N, LIX 54-100. The extractive properties of selected reagents prepared as the organic solutions in hydrocarbon diluents were examined and compared. Moreover, the effect of extractant concentration in the organic phase on the extraction efficiency and ammonia transfer were studied.

Experimental

Reagents and solutions

Aqueous feed solutions used in solvent extraction (SX) studies were pregnant leach solutions (PLS) generated in pressure ammonia leaching of commercial flotation concentrate. Leaching with ammonia/ammonium sulfate solution resulted in leach liquors (PLS) containing 8 g/dm^3 Cu(II), 0.58 g/dm^3 Zn(II), 15 mg/dm^3 Ni(II) and 45 mg/dm^3 Co(II). The solution pH was 9.7 ± 0.15 .

The commercial extractants LIX84-I, LIX®984N and LIX 54-100, applied in SX laboratory tests, were manufactured by Cognis and supplied by Cognis Ireland Ltd. The active substance of LIX84-I is oxime of 2-hydroxy-5-nonylacetophenone. LIX®984N is a mixture of oximes: 5-nonylsalicylaldoxime and 2-hydroxy-5-nonylacetophenone oxime. The active substance of diketone type extractant LIX 54-100 is 1-phenyldecane-1,3-dion. Escaid®100 (Exxon Mobil Chemical), Exxsol D80 (Exxon Mobil Chemical) and toluene (POCh Gliwice) were used as diluents. The chosen diluents differ in aromatic compounds content, which is equal to 19, 0.5 and 100%, respectively. No extraction modifiers were used.

Analytical methods

The aqueous solutions were analyzed for metals concentration by atomic absorption spectrometry (AAS) using a Varian SpectrAA 20Plus. The concentration of copper in the organic phase was calculated from a difference between its initial metal concentration in PLS and its concentration in raffinate at fixed organic to the aqueous (O/A) phase ratios. The measurements of pH were carried out with Elmetron CX-731 pH-meter using a Hydromet glass electrode. Ammonia concentration was determined spectrophotometrically with the Nessler reagent.

Results and discussion

The effect of type of extractant

Extraction of copper(II) was performed with the use of chosen extractants diluted in aliphatic diluent Exxsol D80. The concentration of extractants in the organic phase was equal to 10% (v/v). The pregnant leach solution from ammonia leaching was used as an aqueous phase. Extraction was performed at ambient temperature. Aqueous (A) and organic (O) phases were mixed for 5 min at different A/O ratio from 10/1 to 1/10. The McCabe-Thiele diagrams were constructed on extraction equilibrium isotherms for each system (Figs. 1-3).

The efficiency of examined systems was estimated considering few parameters, namely organic phase loading, concentration of copper(II) in the raffinates and number of theoretical stages required to reach target extraction. The McCabe-Thiele diagrams (Figs. 1-3) show that in all investigated systems it is possible to reduce copper(II) concentration to the level below 0.5 g/dm^3 . It was also observed that full loading of the organic phase is possible only, when diketone reagent is used as Cu(II) extractant. However, it is quite easy to see that in the case of diketone extractant LIX 54-100 the number of extraction stages is much greater than for remaining systems. Therefore, the comparison of test data shows that extraction systems using the hydroxyoxime reagents are preferred over the one with β -diketone reagent. Therefore, LIX 54-100 was phased out from further experiments. Similar conclusions can be found in Pietek et al. (2011). The authors investigated the behavior of the same extractants during extraction of copper(II) from ammoniacal leach solutions containing around 45 g Cu/dm^3 . They also chose LIX 84-I as the best extractant based on a few criteria: good stability of reagent, no propensity towards emulsion formation, low number of extraction stages and low amount of acid needed in stripping stage.

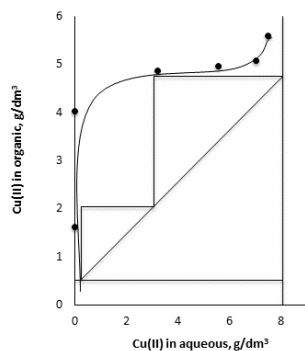


Fig. 1. Copper(II) extraction isotherm for 10% LIX 84-I in Exxsol D 80, A/O = 0.55

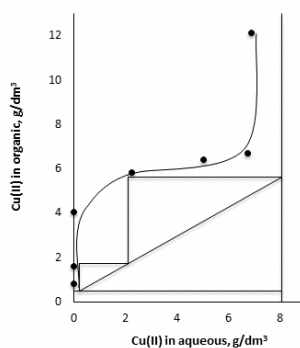


Fig. 2. Copper(II) extraction isotherm for 10% LIX 984N in Exxsol D 80, A/O = 0.65

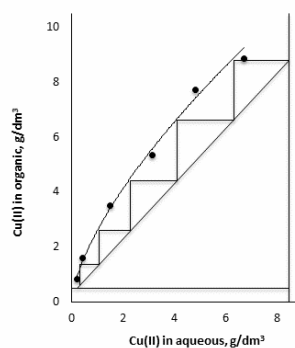


Fig. 3. Copper(II) extraction isotherm for 10% LIX 54-100 in Exxsol D 80, A/O = 1

The effect of type of diluent

Next experiments were performed in order to study the effect of type of a diluent in organic phase. LIX 84-I and LIX 984N were diluted in Escaid 100 and toluene. The concentration of extractants was equal to 10% (v/v). The obtained isotherms were compared with results from previous section for aliphatic diluent Exxsol D80 (Fig. 4). The direct evaluation of extraction curves shows that in the case of both extractants the use of aliphatic diluent (Exxsol D80) results in better extraction efficiency. The slope of isotherms indicates that extraction conditions (the number of extraction stages, organic phase loading or advance phase ratio A/O) will be less favourable for systems with non-aliphatic diluents. Moreover, the shape of generated isotherms can suggest that co-extraction of the contamination compounds (probably ammonia) takes place. It is particularly apparent in the following systems LIX 84 + Escaid 100, LIX 984 + Escaid 100 and toluene, where copper(II) loading is initially delayed and decreased at the end. Flett and Melling (1979) showed that the increase of aromatic compounds content in the hydrocarbon diluent causes greater ammonia transfer to the organic phase.

To verify this assumption the series of single extraction experiments were performed and ammonia concentration in the aqueous phase was determined. The ammonia concentration in the organic phase was calculated from a difference between its initial PLS and raffinate concentration. The obtained results are presented in Table 1. The comparison shows that the NH_3 transfer is dependent on the type of diluent and increases with the increase of aromatic compounds content. The lowest concentration of ammonia in organic phase was noted in the case of LIX 84-I diluted in Exxsol D80. Therefore, this system was chosen to further investigation.

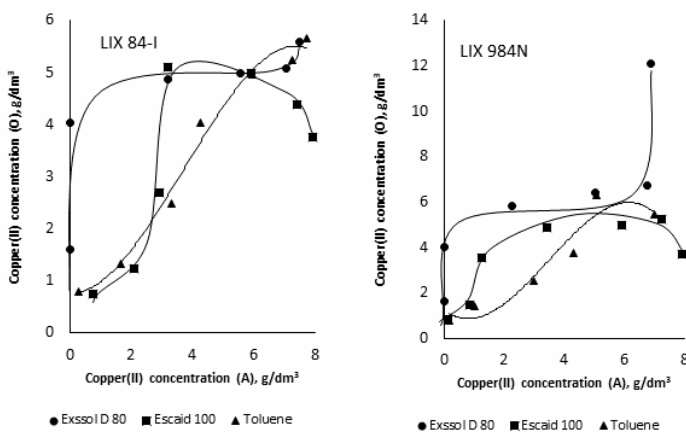


Fig. 4. The effect of diluent on extraction isotherms for Cu(II) extraction from ammonia solutions

Table 1. Concentration of ammonia in organic phase after extraction with hydroxyoxime extractants in different diluents

Diluent	LIX 84-I	LIX 984 N
	NH ₃ , mg/dm ³	
Exxsol D 80	126	258
Escaid 100	1183	921
Toluene	2237	1579

The effect of extractant concentration

To study the effect of extractant concentration the content of LIX 84-I in the organic phase was varied in the range of 5-30% (v/v). As before, extraction was performed using different A/O ratios to generate extraction isotherms. The obtained results are presented in Fig. 5. Figure 5 shows that the positive effect of LIX 84-I concentration increase in the organic phase. As expected, the copper(II) extraction efficiency was improved with increasing concentration of extractant. However, according to Fu et al. (2011) the hydroxyoxime extractants are not the most suitable reagents in the ammonia solution in spite of their high affinity towards copper(II). It is due to their high tendency to co-extract ammonia to organic phase. Considering that fact, additional tests were conducted to measure ammonia loading during copper(II) extraction. For this purpose freshly prepared organic solutions of LIX 84-I in Exxsol D80 were contacted with PLS solution at the phase ratio A/O equal to 1. After given contact time the phases were separated and filtrated. The concentration of ammonia in the organic phase was calculated as before.

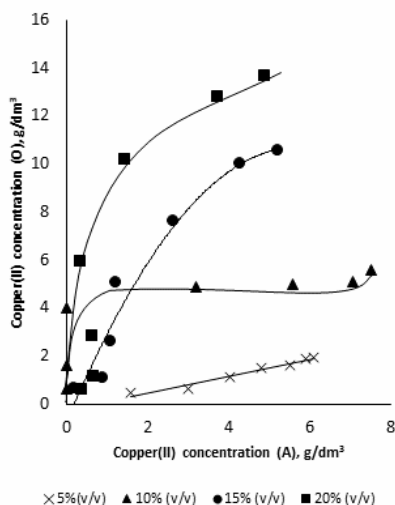


Fig. 5. The effect of LIX 84-I concentration on Cu(II) extraction from ammonia solutions

The obtained results indicate that the amount of co-extracted ammonia decreases with the increase of extractant concentration (Table 2). However, it should be noticed that at the same time loading of the organic phase with copper(II) also increases. It means that extracted metal ions replace ammonia from the organic phase

Table 2. The effect of extractant concentration in organic phase on ammonia transfer

LIX 84 % (v/v)	Cu(II) (O) mg/dm ³	NH ₃ , mg/dm ³
5	2172	3947
10	5221	1316
15	5655	1184
30	6494	658

Washing of NH₃ from loaded organic phase

The problems described previously indicate that it is necessary to remove ammonia from the loaded organic phase before stripping of copper(II). For this purpose controlled washing with sulfuric acid solutions of different pH was used. First organic phase was contacted with PLS at phase ratio A/O equal to 1, to obtain the organic phase loaded with Cu(II) and NH₃. Then, the organic solutions were contacted with H₂SO₄ solutions at the same phase ratio. The aqueous solutions obtained after washing of the organic phase were analyzed for the concentration of copper(II) and ammonia.

The obtained results (Table 3) indicate that the increase of scrubbing solution acidity results in a greater efficiency of ammonia washing from the organic phase, although it is not complete. Only 80% of ammonia was removed in a single test after contact with pH 2 solution, with negligible losses of copper(II). Further testing was necessary to check possibilities of total washing of ammonia. The loaded organic solutions were doubly-contacted with sulfuric acid solutions of pH 2 and 3. The analysis showed that it is possible to increase the effectiveness of washing to 66 and 96%, respectively for pH 3 and pH 2 solutions. In the latter case copper losses were noticed to be at the same level as in the first scrub stage.

Removal of ammonia from loaded organic phase was also studied by Parija et al. (2000), as the scrub stage was necessary before nickel(II) stripping. They described selective stripping of Cu(II) and Ni(II) after co-extraction from PLS containing above 10 kg/m³ of both metals. The loaded organic phase obtained in a two stage counter-current study contained Cu(II) 6.91 kg/m³, Ni(II) 5.35 kg/m³ and NH₃ 1.92 kg/m³. The obtained in this work results showed that almost complete (99.5%) ammonia removal with irrelevant nickel(II) losses (36 g/m³) is possible with the use of 6.75 kg/m³ sulfuric acid.

It is known that in the case of copper(II) extraction by LIX 84 from typical ammoniacal solutions, co-extraction of Cu(II) and Ni(II) takes place. Therefore, a further step in the treatment of loaded organic solutions is selective reextraction of

nickel(II) before stripping of copper(II). Usually sulfuric acid solutions of different concentrations are used as a stripping agent.

Table 3. The effect of acidity of a scrubbing solution on ammonia washing

Initial pH	Equilibrium pH	Washing efficiency %	Cu(II) conc. mg/dm ³
6	10.66	35.4	89
4	10.65	40.4	80
3	10.49	50.4	111
2.5	10.25	55.4	321
2	9.60	80.4	54
1.5	9.01	80.4	64

Conclusions

This paper refers to copper(II) extraction from ammonia leach liquors. Special attention was paid to the problem of ammonia transfer to the organic phase. Significant differences in extraction performance were observed for examined extractants. This applies particularly to the organic phase loading, concentration of copper(II) in raffinate and number of theoretical stages required to reach target extraction. The results clearly indicate that in the case of systems using hydroxyoximes extraction efficiency is much better than for β -diketone reagent.

The results proved that extraction efficiency of Cu(II) is also dependent on the type of diluent and is less favorable for the systems with non-aliphatic diluents. Additionally it was observed that transfer of ammonia increases with the increase of aromatic compounds content in the diluent. Moreover, ammonia extraction to the organic phase was shown to be inversely proportional to extractant concentration in organic phase. This is probably related to the replacement of ammonia by copper(II) during its extraction.

The presence of ammonia in the organic phase forces the need to its elimination before stripping. The results showed that the effectiveness of washing depends on acidity of scrubbing solution. The best results were obtained when loaded organic was doubly-washed with pH 2 sulfuric acid solution.

Acknowledgments

The work was supported by Wrocław Research Centre EIT+ within project "The Application of Nanotechnology in Advanced Materials" – NanoMat (POIG.01.01.02-02-002/08) co-financed by the European Regional Development Fund (Operational Programme Innovative Economy, 1.1.2).

References

CHMIELEWSKI T., WÓDKA J., IWACHÓW Ł., 2009, *Ammonia pressure leaching for Lubin shale middlings*, *Physicochemical Problems of Mineral Processing*, 43, 5–20.

- FLETT D.S., MELLING J., 1979, *Extraction of ammonia by commercial copper chelating extractants*, Hydrometallurgy, 4, 135–146.
- FU W., CHEN Q., HU H., NIU CH., ZHU Q., 2011, *Solvent extraction of copper from ammoniacal chloride solutions by sterically hindered b-diketone extractants*, Separation and Purification Technology 80, 52–58.
- JERGENSEN G.V., 1999, *Copper Leaching, Solvent Extraction, and Electrowinning Technology*, SME Inc., Littleton, USA, 267–268.
- MILLER J.D., HAUNG H.H., PEREIRA E.F., 1981, *Equilibrium and kinetics of copper extraction from ammonia solutions by hydroxyoximes with particular emphasis on transport phenomena, Process and fundamental considerations of selected hydrometallurgical systems*, Society of Mining Engineers of American Institute of Mining, Metallurgical, and Petroleum Engineers, 221–241.
- PARIJA CH., BHASKARA SARMA P.V.R., 2000, *Separation of nickel and copper from ammoniacal solutions through co-extraction and selective stripping using LIX84 as the extractant*, Hydrometallurgy, 54, 195–204.
- PIETEK G., GOTFRYD L., SZOŁOMICKI Z., BECKER K., PIWOWOŃSKA J., KWARCIŃSKI M., 2011, *Ekstrakcja miedzi(II) z roztworów amoniakalnych*, Rudy i Metale Nieżelazne 56 (10), 511–516.
- RITCEY G.M. 2006, in *Solvent Extraction. Principles and Applications to Process Metallurgy*, Rev. 2nd ed. Ottawa.

Received May 20, 2013; reviewed, accepted September 1, 2013

INFLUENCE OF SELECTED WORK PARAMETERS OF THE ROLLING SCREEN OPERATION ON SCREENING EFFECTS

Tomasz GAWENDA, Daniel SARMAK

AGH University of Science and Technology, Faculty of Mining and Geoengineering, al. Mickiewicza 30, Krakow, Poland, gawenda@agh.edu.pl, dsaramak@agh.edu.pl

Abstract: The paper deals with effectiveness of particle size separation. The investigations of limestone screening were run on a laboratory scale using a rolling screen. Batch tests were run for various batch outputs as well as different angles of deviation of motovibrators. Quantitative and qualitative effectiveness indices were calculated as well as the imperfection and probable error, which depend on the sieve mesh. A model of determining the screening effectiveness as a function of four independent variables: the amplitude of vertical vibrations of sieve decks (described by means of the angle of deviation of motovibrators), screening time, batch output and the mesh sizes of respective sieves was proposed. The results presented in the paper and the applied approach to stochastic modeling can be used under industrial conditions for rolling screens with variable dynamic parameters at different screening parameters.

Keywords: *screen, screening, effectiveness, separation sharpness*

Introduction

The size separation of particles below 3 mm in size and size separation of fine particles of about 0.1 mm in size creates numerous problems in industrial comminution circuits. It is especially connected with technological crushing and screening circuits either preparing the material for downstream beneficiation processes or producing the final fine-particle products for building industry (Gawenda 2013a, Saramak 2012, Saramak et al., 2010). The key works on mineral processing (Banaszewski 1990, Battaglia and Banaszewski 1972, Dietrych 1962, Sztaba 1993, Wodzinski 1988, Modrzewski and Wodzinski 2013, Lawinska and Wodzinski 2012, Gawenda 2013b) show many aspects of problems of screening fine particles.

Technological screening processes depend on three basic characteristic factors: technical parameters of the screen, physico-mechanical properties of screened materials and the method of conducting the screening. These factors interact, determining the

quality and efficiency of screening. Therefore, designing and modernizing screening is important to recognize and consider all the factors of screening.

Investigations of the screening process on the rolling screen

The investigations of screening of fine 0–2 mm particles of limestone were performed with a rolling screen located in the Department of Technology and Apparatuses of Chemical and Food Industry of University of Technology and Life Sciences in Bydgoszcz (Pocwiardowski et al., 2012, Pocwiardowski and Wodzinski 2011, Pocwiardowski 2011). They aimed at analyzing a hypothesis stating that the application of vertical vibrations (vertical amplitude) at an optimum selection of remaining parameters of screening would increase significantly the effectiveness of the screening process. The investigations were carried out with a rotational screen, designed for sieving of fine particles. This machine performs a complex spatial rotational motion and the main resistance of the screening is caused by the layer of particles, not by the sieve. As known, the problem of such machines is blocking of the sieve meshes, resulting from the movement of the material on the sieve surface and adhesive susceptibility of fine particles which results in lower effectiveness of screening and separation sharpness. Therefore, to increase screening effectiveness, additional vertical vibrations (vertical amplitude) were introduced by means of the drive of two rotating motovibrators operating with mutual self-synchronization. In this way the screen obtained torsional vibrations and additional vertical ones. It was possible to install five screen decks with different sieve meshes in the screen and to change the angle of motovibrators i.e. the alternation of amplitude values of vertical vibrations, as presented in in Table 1. In this way the screen has become an important experimental base, enabling to evaluate both the effects and dynamic parameters of the screening process and the parameters of declassified fractions of fine-particle material.

Table 1 lists the selected (optimum) parameters of screen operation used during laboratory tests (Pocwiardowski et al., 2012, Pocwiardowski and Wodzinski 2011, Pocwiardowski 2011). The frequency of vibrations was constant an equal to 1500 s^{-1} . For registration the amplitude volume a PULSE system of Bruel and Kjaer was

Table 1. Values of amplitudes for respective angles of deviation of motovibrators and for the data of screen decks in mm. Data were taken from Pocwiardowski et al., 2012, Pocwiardowski and Wodzinski 2011, Pocwiardowski 2011

Sieve mesh [mm]	Angle of motovibrators [°]			
	20	30	45	50
0.1	0.22	0.34	0.49	0.54
0.2	0.31	0.41	0.53	0.59
0.4	0.29	0.40	0.54	0.60
0.8	0.31	0.46	0.58	0.62
1.6	0.30	0.43	0.58	0.62

applied. The sensor in this set measures the amplitude of vibration in three dimensions of XYZ axes. The sieve meshes were 0.1, 0.2, 0.4, 0.8 and 1.6 mm. Material moisture was 0.14%. In order to investigate the accurate screen work and its efficiency the authors provided analyses according to the sampling of the performed screening process of different screen capacities, i.e. 12, 19 and 26 kg/h.

The results obtained in the screening experiments were used to evaluate indices of the screening process such as screening effectiveness, imperfection and probable dissipation. Applying these indices the authors analyzed the correlations of screen work and screening effects as well as determined the model of screen work.

Analysis of effects of rolling screen performance

Evaluation of screening effectiveness

Qualitative and quantitative effectiveness values were taken into account to estimate technological criteria of effectiveness of the screening process. When evaluating effectiveness, as a rule the recovery of the finest size fraction, denoted either as S_i or ε_d in the undersize product is taken into consideration, determining quantitative effectiveness (Sztaba 1993):

$$S_i = \gamma_d \frac{a_{dd}}{a_{nd}} = \varepsilon_d \quad [\%] \quad (1)$$

where: γ_d –yield of the lower (undersize) product [%], a_{nd} –content of fine particles in the feed [%], a_{dd} –content of fine particles in the lower product [%], which should be equal to 100%.

Table 2. Average quantitative effectiveness S_i for different angles of deviation of motovibrators and average batch screening outputs $Q_1=12$, $Q_2=19$ and $Q_3=26$ [kg/h]

Capacity	Q_1				Q_2				Q_3			
Sieving time [h]	0.5	1.0	1.5	2	0.5	1.0	1.5	2	0.5	1.0	1.5	2
motovibrators angle, [°]												
20°	99.0	90.8	85.8	81.7	99.4	87.3	81.1	77.1	89.0	77.4	71.4	65.5
30°	99.2	96.6	92.4	91.0	98.9	93.8	88.8	84.6	97.4	93.6	89.9	87.0
45°	99.0	98.9	98.1	97.7	98.8	98.5	98.5	98.2	98.5	98.2	97.3	95.1
50°	98.4	98.3	98.2	97.9	97.6	97.6	97.4	94.0	99.0	98.7	96.1	91.3

The effectiveness values were calculated for each sieve in the set, for each angle of deviation of motovibrators and for every output Q , according to the assumptions of experiments (Table 1). Table 2 presents average effectiveness for the whole set of the sieves.

While analyzing the data it can be observed that the most favourable screening results, regardless of the time of execution of the experiment, were obtained for the 45° angle of deviation of motovibrators (amplitude of vertical vibrations equal to 0.49-0.58 mm) at average output of $Q_1 = 12$ and $Q_2 = 19$ kg/h. The obtained effectiveness was over 98%. For the output of $Q_3 = 26$ kg/h the most favourable results were also obtained in relation to the remaining values of angles of deviation of motovibrators but slightly worse than those at the output of Q_1 and Q_2 . It proves that Q_3 value was too high for the machine due to which a part of the material could not be sieved properly because of the too thick layer of material on the sieves, i.e. too high screen overload.

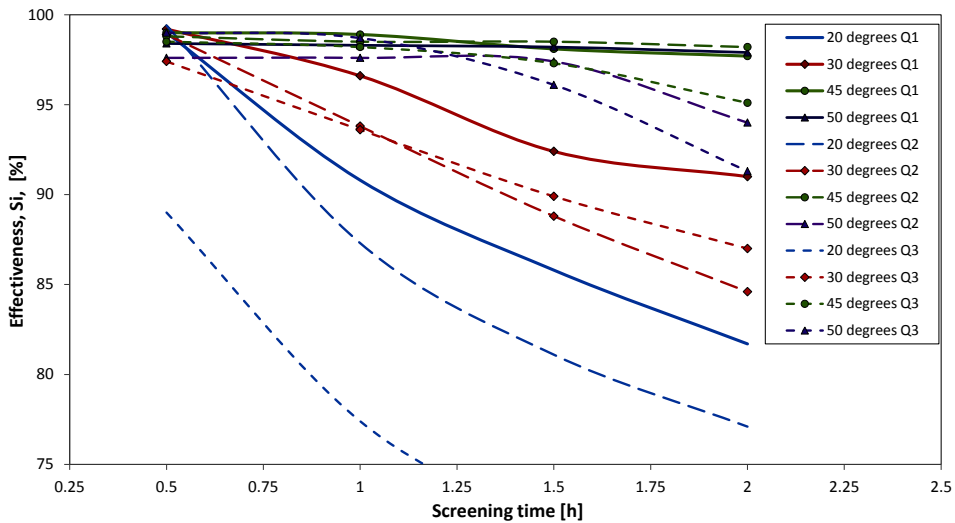


Fig. 1. Relationship between screening time and the results of quantitative effectiveness

The decrease of sieving effectiveness with time of the experiment was also observed, especially for angles equal to 20° and 30° . It was caused by blocking of sieves, especially those of finer meshes, and the fine particles, instead of passing through the sieves, were transported together with the upper product, forming the so-called subparticle. It is confirmed by the results of analysis of dependence between the time of screening and quantitative effectiveness, presented in Fig. 1. It can be easily observed that for the angles of 45° and 50° the best average effectiveness values were obtained, regardless of experiment duration, because the increase of the amplitude of vertical vibrations prevented the sieves from blocking by the so-called difficult and fine particles as well as from gluing by means of adhesive forces.

Screening effectiveness is significantly connected and directly proportionally with the dimension of sieves in the screen which was shown more precisely when analyzing correlative relations further on. Qualitative effectiveness was calculated according to formula:

$$Sj_2 = 100 - a_{gd} \text{ [%]} \tag{2}$$

where: a_{gd} – content of fine particles in the oversize product [%]. Sj_2 was calculated for each angle of deviation of motovibrators and for each sieving output Q .

Table 3 presents the results in the form of average effectiveness values for the whole range of sieves for different angles of deviation of motovibrators and average batching efficiencies.

Table 3. List of values of average qualitative effectiveness for different angles of deviation of motovibrators and average batch screening outputs $Q_1 = 2$, $Q_2 = 19$ and $Q_3 = 26$ kg/h

Capacity	Q_1				Q_2				Q_3			
Sieving time [h]	0.5	1.0	1.5	2	0.5	1.0	1.5	2	0.5	1.0	1.5	2
motovibrators												
angle, [°]												
20°	99.0	97.2	95.6	93.3	99.4	92.9	88.9	85.3	94.1	88.5	82.9	76.9
30°	99.0	98.5	97.3	97.0	99.0	97.7	95.7	93.8	98.1	97.1	95.9	94.7
45°	96.8	97.3	97.3	96.9	97.6	98.3	98.6	98.5	97.3	97.9	97.8	95.7
50°	95.0	96.1	96.9	96.9	96.0	97.2	97.2	94.0	98.3	98.1	95.8	93.3

According to the collected results it can be easily observed that, similarly as in the case of quantitative effectiveness, regardless of the duration of the experiment, the most favourable screening results were obtained for 45° angle of deviation of motovibrators (amplitude of vertical vibrations 0.49-0.58 mm). The results for the remaining angles are characterized by much larger scatter, which indicates an inappropriate selection of process dynamic parameters, which affects sieve blocking, improper distribution of material on the sieve, lack of mixing of the material layer and prevention of contact of fine particles with the sieve surface.

Evaluation of imperfection and separation sharpness

The work of a screen can be characterized by such indices as productivity and efficiency, connected with effectiveness and separation sharpness. The authors applied the method of determining the cut size d_{50} , imperfection index I and separation sharpness in the form of probable error E_p for analytical investigations of the screening results according to the performed sampling and analyses. Separation sharpness, i.e. probable error E_p , was calculated from the formula (Kelly and Spottiswood 1989, Drzymala 2007):

$$E_p = \frac{d_{75} - d_{25}}{2} \text{ [mm]} \tag{3}$$

where: d_{75} – 75 percentage particle size, d_{25} – 25 percentage particle size.

Imperfection index I was calculated from the formula (3):

$$I = \frac{E_p}{d_{50}} \quad (4)$$

Table 4. The values of imperfection and probable error for 45° angles of deviation of motovibrators and average batch screening outputs $Q_1 = 12$, $Q_2 = 19$ and $Q_3 = 26$ kg/h

Sieving time [h]		0.5	1.0	1.5	2
Q_1					
Sieve mesh [mm]					
0.4	I	0.1681	0.1682	0.1685	0.1685
	E_p [mm]	0.1518	0.1519	0.1521	0.1519
0.8	I	0.1700	0.1703	0.1698	0.1691
	E_p [mm]	0.0767	0.0768	0.0766	0.0763
1.6	I	0.0264	0.0222	0.0219	0.0217
	E_p [mm]	0.0329	0.0278	0.0274	0.0272
Q_2					
0.4	I	0.1692	0.1691	0.1689	0.1688
	E_p [mm]	0.1527	0.1526	0.1524	0.1523
0.8	I	0.1714	0.1732	0.1729	0.1716
	E_p [mm]	0.0772	0.0780	0.0779	0.0773
1.6	I	0.0214	0.0206	0.0203	0.0202
	E_p [mm]	0.0268	0.0257	0.0254	0.0253
Q_3					
0.4	I	0.1690	0.1689	0.1688	0.1686
	E_p [mm]	0.1525	0.1525	0.1523	0.1521
0.8	I	0.1718	0.1718	0.1705	0.1699
	E_p [mm]	0.0771	0.0772	0.0766	0.0763
1.6	I	0.0217	0.0206	0.0204	0.0203
	E_p [mm]	0.0272	0.0258	0.0255	0.0253

The smaller values for these indices (close to 0) are obtained, the more accurate is the process. In this way the values of imperfection and probable errors were determined for different angles of deviation of motovibrators. The values of indices I and E_p , calculated for sieves of 0.4, 0.8 and 1.6 mm for 45° angles of deviation of motovibrators are shown in Table 4.

Analyzing the results it can be observed that both the screening time and process productivity do not influence significantly the values of imperfection and probable error whereas both indices decrease with the increase of sieve dimensions.

For the sake of comparison, Fig. 2 presents the values of indices of imperfection and probable error for the angles of 20, 40 and 50° of deviation of motovibrators. It can be observed, for the angle of 20° the values of I and E_p are higher than for 45 or

50°. This confirms that less accurate separation of material occurs at lower amplitudes. For 45 and 50° the values I and E_p are close to each other. It means that both amplitudes have been chosen properly for the process.

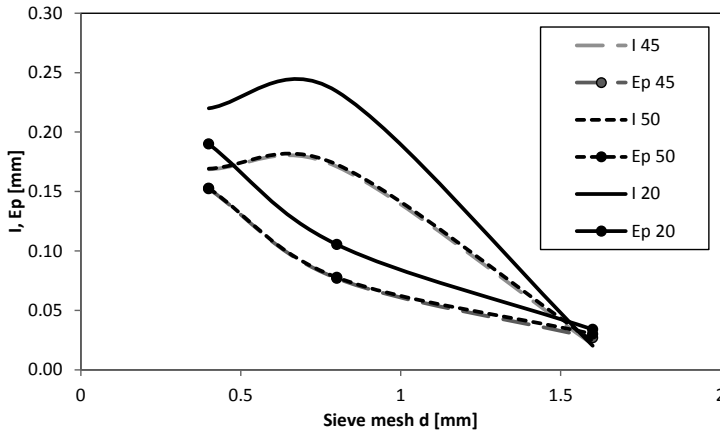


Fig. 2. Dependences of imperfection (I) and probable error (E_p) for the angles of 20, 45 and 50° for the sieves of 0.4, 0.8 and 1.6 mm (curves I_{50} and I_{45} , similarly as E_{p50} and E_{p45} , overlap)

To make the screening process run optimally in industrial conditions, the set of dynamic parameters of the rolling screen should be selected properly. Here the most important role is played by the amplitude since with its increase the screening accuracy is greater.

Analysis of correlations of parameters of the screen work and screening effects

Table 5 presents correlations between the effectiveness (S_i) and analyzed independent variables, like the amplitude of vertical vibrations of sieve decks (described by means of the angle of deviation of motovibrators), screening time, efficiency/productivity understood as a batch screening output and the mesh sizes of respective sieves. The frequency of rotations was constant and was 1500 rotations/minute.

Table 5. Correlation coefficient values between screening effectiveness (S_i) and selected process parameters

Independent variable	Correlation coefficient, R
Screening output	-0.148
Amplitude	0.484
Screening time	-0.260
Sieve mesh	0.410

All the correlation coefficients are significant at the 95% confidence level. Screening effectiveness S_i , according to Table 5, is the most strongly connected with the value of amplitude of vertical vibrations (which increases with the growth of the angle of deviation of motovibrators). The size of the sieve mesh reveals a slightly lower correlation with S_i value. Both variables are positively correlated with screening effectiveness S_i which means that it grows with the increase of amplitude of vertical vibrations and mesh size.

The screening time and output are negatively correlated with the S_i which means that quantitative effectiveness decreases with the growth of screening time or the output. Screening efficiency is the lowest variable correlated with the effectiveness. The negative correlation between quantitative effectiveness and screening time can be explained by the fact that sieves were blocked, especially for low values of amplitudes of vertical vibrations. This is important because when the working parameters of the screen are properly selected, the sieve should not be blocked and it is logical that the longer is the process of screening, the more accurately the material is sieved. That means that effectiveness S_i should grow but, on the other hand, the longer the process, the more material passes on the sieve deck and more probably the sieves could be blocked. Disregarding the type of materials used for the production of sieves, they should clean easily as a result of vertical vibrations whereas at too high amplitudes the sieves (wire bridges) can throw fine particles, preventing them from passing the meshes.

Model of work of the rolling screen

The determination of the model of work of the screen was carried out with the application of multiple regression. The general functional model of screen work effectiveness, i.e. screening effectiveness, can be represented by means of the following equation:

$$\text{Quantitative effectiveness } S_i = f(\text{amplitude, time, output, sieve mesh}) \quad (5a)$$

According to the performed calculations the following model of screening effectiveness was obtained for the analyzed screen:

$$\text{Quantitative effectiveness } S_i = 76.56 + 56.12A - 0.44B - 7.88C + 19.86D \quad (5b)$$

where: A – amplitude of vertical vibrations (angle of deviation of motovibrators, B – the output, C – screening time, D – sieve mesh.

All model indices are significant, therefore all independent variables affect significantly the change of screening effectiveness S_i . The amplitude of vertical vibrations reveals the highest influence upon effectiveness of screening, i.e. effectiveness increases by 5.6% on the average with the growth of amplitude by 0.1 mm. The mesh size is another variable; effectiveness increases by 1.9 % with the

growth of mesh size by 0.1 mm. The process efficiency, in turn, has reasonably low influence upon effectiveness. The model accuracy reaches an average level and is equal to $R^2 = 0.418$ which means that about 42% of effectiveness is explained by this model. The remaining 58% of the unexplained effectiveness is caused by other factors, not included in the discussed considerations, which may have some influence (e.g. frequency of vibrations and moisture, already accepted as constants and errors connected with averaging of samples).

When the work effectiveness of the screen is evaluated, attention should be drawn to the problem of decrease of screening effectiveness with increasing duration of screening. When the time of screening is prolonged, its efficiency is limited and it should increase its effectiveness. The decrease of screening effectiveness with the growth of its duration, as observed during the tests, cannot be accepted. This phenomenon can be explained by filling the sieve meshes with the passage of time. This problem is strictly connected with the value of toss index. The index affects not only the conditions of segregation of the material layer but also promotes the sieve opening to be free of particles (Banaszewski 1990, Battaglia and Banaszewski 1972, Dietrych 1962, Sztaba 1993).

The toss index can be calculated from the formula:

$$u = \frac{A\omega^2 \sin \gamma}{g \cos \beta} \quad (6)$$

where: A – amplitude of vibrations in mm, ω – frequency of vibrations in rad./s, β – angle of deviation of sieve deck, γ – angle of deviation of forced force, g – acceleration of gravity m/s^2 .

The condition of motion of the screen with the particle toss is: $u > 1,2$. It can be observed in Table 6 that this condition is fulfilled at the rotations $n = 1500 \text{ s}^{-1}$ only for the amplitude of about 0.5–0.6 mm. The above calculation is in agreement with the experimental results for which at the amplitude < 0.5 mm the decrease of screening effectiveness occurred with lengthening of time. The condition of proper work of the tested screen consists in, apart from obtaining a spatial motion of the screen, maintaining the toss index at $1.2 < u < 1.5$. This condition is especially significant for the sieves with the smallest meshes.

Table 6. The calculated toss indices for different values of vibration amplitudes

$n \text{ [s}^{-1}\text{]}$	u		
	$A = 0.4 \text{ mm}$	$A = 0.5 \text{ mm}$	$A = 0.6 \text{ mm}$
1500	1.00	1.26	1.51

Summary

According to the analyses of quantitative and qualitative effectiveness the most favourable screening results, regardless the time of the experiment execution, were obtained for torsional and vertical vibrations for the angles of 45° of motovibrators (the amplitude of vertical vibrations was 0.49-0.58 mm). A too low amplitude will cause blocking of sieve openings, lack of mixing of the material layer and preventing the fine particles from contacting the sieve surface and thus the decrease of effectiveness of the screening process.

The best indices of the particle size classification by screening (high effectiveness of about 98% and good separation sharpness in the form of probable error under 0.17 mm) were achieved in the laboratory conditions in the rolling screen at vibration frequency 1500 s^{-1} , amplitude 0.49-0.58 mm and toss index 1.2-1.5 of value g , at the screen load from $8\text{ kg/m}^2\text{h}$ for the 0.1 mm sieve up to $16\text{ kg/m}^2\text{h}$ for the 0.8 mm sieve.

The obtained results involving a laboratory screen and the applied approach to stochastic modeling can be used in industrial screening using rolling screens with variable dynamic parameters for different screening conditions.

Acknowledgement

The article was prepared as part of the research project no NN524 466139 of Ministry of Science and Higher Education.

References

- BANASZEWSKI T., *Przesiewacze*. Wyd. Śląsk, 1990.
- BATTAGLIA A., BANASZEWSKI T., *Maszyny do przeróbki węgla, rud i surowców mineralnych. Część I. Maszyny do przesiewania i rozdrabniania*. PWN. Warszawa – Kraków 1972.
- DIETRICH J., *Teoria i budowa przesiewaczy*. WGH Katowice 1962.
- DRZYMAŁA J., *Mineral Processing. Foundations of theory and practice of minerallurgy*. Oficyna Wydawnicza PWR, Wrocław 2007,
- GAWENDA T., *Analiza porównawcza mobilnych i stacjonarnych układów technologicznych przesiewania i kruszenia*. Annual Set of Environment Protection, Vol. 15, 2013b.
- GAWENDA T., *Wpływ rozdrabniania surowców skalnych w różnych kruszarkach i stadiach kruszenia na jakość kruszyw mineralnych*. Gospodarka Surowcami Mineralnymi, Vol. 29 (1), 2013a.
- KELLY E., SPOTTISWOOD D., *Introduction To Mineral Processing*. John Wiley and Sons Ltd, New York, 1989.
- LAWIŃSKA K., WODZIŃSKI P., *Determination of the effective sieve blocking coefficient*. Physicochemical Problems of Mineral Processing, Vol. 48 (1), 2012.
- MODRZEWSKI R., WODZIŃSKI P., *Analysis of screening proces of crushed basalt performer by a double-frequency screen*. Physicochemical Problems of Mineral Processing, vol. 49 (1), 2013.
- POĆWIARDOWSKI W., WODZIŃSKI P., KANIEWSKA J., *Investigation of the Rolling Screen*. AGH Journal of Mining and Geoinengineering, Vol. 36 (4), 2012.
- POĆWIARDOWSKI W., WODZIŃSKI P., *Przesiewanie surowców mineralnych na przesiewaczu zataczającym*. Prace Naukowe Instytutu Górnictwa Politechniki Wrocławskiej, 2011, nr 132.

- POĆWIARDOWSKI W., *Sprawozdanie z badań przesiewania na przesiewaczu zataczającym*. Uniwersytet Technologiczno-Przyrodniczy w Bydgoszczy, Katedra Technologii i Aparatury Przemysłu Chemicznego i Spożywczego. Bydgoszcz 2011, materiały niepublikowane.
- SARAMAK D., TUMIDAJSKI T., GAWENDA T., NAZIEMIEC Z., BROŻEK M., *Aspect of comminution flowsheet design in processing of mineral raw materials*. *Gospodarka Surowcami Mineralnymi*, Vol. 26 (4), 2010.
- SARAMAK D., *De-agglomeration in high pressure grinding roll based crushing circuits*. *Physicochemical Problems of Mineral Processing*, vol. 48 (1), 2012.
- SZTABA K., *Przesiewanie*. Śląskie Wyd. Techniczne, Katowice 1993.
- WODZIŃSKI P., *Potrzeby, możliwości i perspektywy przesiewania bardzo drobno ziarnowego*. III Seminarium Materiały Bardzo Drobno Uziarnione. Zeszyty naukowe AGH. Górnictwo, Zeszyt 140. Kraków 1988.
- WODZIŃSKI P., *Przesiewanie i przesiewacze*. Monografie, Wyd. Pol. Łódzkiej. Łódź 1997.

Received July 11, 2012; reviewed; accepted July 22, 2013

ASSESSING INFLUENCE OF HYDROCHLORIC ACID LEACHING ON STRUCTURAL CHANGES AND BLEACHING PERFORMANCE OF NIGERIAN CLAY FROM UDI

Regina O. AJEMBA, Okechukwu D. ONUKWULI

Department of Chemical Engineering, Nnamdi Azikiwe University, P. M. B. 5025, Awka, Anambra State, Nigeria, ginaajemba@rocketmail.com

Abstract: Clay from Udi in Nigeria was mined, ground, and acid-leached at different concentrations of hydrochloric acid to produce adsorbents of varying properties. The raw and acid-leached samples were characterized using x-ray fluorescence (XRF) and Fourier transforms infra-red spectroscopy (FTIR) to examine the structural modifications in the clay as a result of acid-leaching. The analysis showed that the acid-leaching process caused several modifications of the clay samples. The surface area, Si/[Al + Fe + Mg] ratio, adsorption capacity were found to have increased in the acid-leached samples. The acid-leached samples were tested in order to ascertain their performance in bleaching palm oil and it was observed that the bleaching efficiency increased from 29.8% to 66.7%. The acid-leached sample prepared with 7M hydrochloric acid yielded an adsorbent that was efficient in bleaching palm oil under the experimental conditions. The isotherm analysis showed that the bleaching process followed the Freundlich equation.

Keywords: acid-leaching, adsorption, bleaching, hydrochloric acid, isotherm

Introduction

Impurities present in palm oil can be reduced appreciably by adsorption process or bleaching by using clay mineral adsorbents. Clay minerals may be used both naturally and after some chemical or physical treatments such as acid activation, calcination, and ion exchange according to their area of application (Ayari et al., 2005, 2007). Clay minerals generally show limited adsorption capacity in their natural state, but their adsorption capacity is greatly enhanced by being treated with strong acids at slightly elevated temperature (Foletto et al., 2003; Nguetnkam et al., 2008). When clay minerals are acid activated, initially interlayer cations are replaced with hydrogen ions of the acid with subsequent dissolution of structural cations. The desired changes in

the adsorptive properties of clay minerals occurring as a result of acid activation depend considerably on the acid leaching conditions (Motlagh, et al., 2011). Several acid activation experiments under different operating conditions have been reported in the literature, in particular the choice of acid concentration, activation time and temperature, and clay-to-acid ratio (Al-Zahrani et al., 2000; Bakhtyar et al., 2011; Motlagh et al., 2008; Diaz and Santos, 2001; Makhoukhi et al., 2009; Salawudeen et al., 2007; Zhansheng et al., 2006; Foletto et al., 2011; Motlagh et al., 2011; Temuujin et al., 2006; Woumfo et al., 2007; Onal et al., 2002; Temuujin et al., 2004). Activation is the chemical or physical treatment applied to certain types of clays to develop a capacity to adsorb coloring matter and other impurities in oils (vegetable, animal, and petroleum). Acid activated clay materials are widely used in various fields, for example, catalysts, catalyst beds, adsorbents, and bleaching earth. The most important applications of the bleaching earth are purification, decolorization, and stabilization of vegetable oils, otherwise, bleaching. They are able to remove undesirable colors by decreasing the levels of chlorophyll, carotene, and other color species, to reduce traces of Cu^{2+} , Fe^{3+} , phospholipids, and soaps. Christidis et al. (1997) examined the bleaching capacity and acid activation of bentonite from Aegean, Greece, observing a five-fold increase of the specific surface area of the raw materials. The activated samples were rendered suitable for bleaching of rapeseed oil. It was determined that the optimum bleaching capacity is not associated with maximum surface area and the optimum conditions for activation are obtained by using a variety of combinations of acid strength and residence time. The preparation of acid-activated clay materials must be controlled in order to obtain maximum bleaching capacity (Kirali and Lacin, 2006; Rozic et al., 2010). Usman et al. (2012) investigated the applicability of clay from Ibeshe in bleaching palm oil. They observed that the clay after acid activation only increased the color reduction from 9.1 % to 27.3%, a poor performance as an adsorbent. Motlagh et al. (2011) reported that acid activation of clay from Khorasan, Iran, increased its adsorbing ability from 6.35% to 96.4% efficiency using 5N sulfuric acid.

This work was carried out in order to investigate the structural effects on Udi natural clay after acid-leaching with hydrochloric acid and also verify the performance of the said acid-leached clay in bleaching palm oil.

Materials and Methods

Materials

Brown-colored clay material from Udi (N: 6° 31' 00"; E: 7° 43' 00"; A: 327 m) was used as the primary raw material. Refined palm oil was obtained at oil mill located at Isuofia (N: 6° 1' 60"; E: 7° 2' 60"; A: 361 m). All chemicals used were analytical grade, bought from Conraws Company Ltd, Enugu.

Experimental Methods

Acid activation of the clay sample

The clay material was prepared for activation by air-drying and grinding to a particle size of 0.212 mm. 10 g of the prepared sample was weighed into flask (250 ml capacity) and 100 ml of hydrochloric acid solution was added. The resulting suspension was heated on a magnetically stirred hot plate at the temperature of 90 °C for 2 hours 30 minutes. At the end of the experiment duration the resulting slurry was poured into a Buchner funnel to separate the acid and the clay. The residual clay was washed severally with distilled water until neutral point was obtained with pH indicator. The clay residue was dried in an oven at 80 °C for 4 hours. The dried samples were crushed and sieved again to 0.212 mm particle size. The activation process was repeated with varying acid concentrations of 2–7M of HCl, varying time of 30–150 minutes, and varying temperatures of 70–120 °C. The clay samples thus prepared were labeled UD0, UD2, UD4, UD5, UD6, and UD7, where the numbers indicate the acid concentrations used in the activation step.

Characterization

The chemical and mineralogical compositions of the natural and activated clay samples were determined. The chemical composition was determined using X-ray fluorescence (XRF), Philips PW 2400 XRF spectrometer; while the mineralogical composition was determined using Fourier transform infrared (FTIR), Shimadzu S8400 spectrophotometer, with samples prepared by the conventional KBr disc method. The specific surface area was measured at 77 K by BET method with a Micromeritics Gemini 2360 instrument using N₂ gas.

Adsorption experiment

The adsorption/bleaching experiments were carried out in a batch process. 50 g of the refined palm oil were charged into a 250 ml beaker and 2 g of the activated clay samples were also added. The mixture of clay and oil were placed in a water bath and heated to a temperature of 80 °C for 30 minutes under continuous stirring. At the end of the reaction the slurry formed was filtered through a dry filter paper. The bleaching capacity of the acid activated clays was then determined by measuring the color of the bleached oils using a UV-Vis spectrophotometer (Shimadzu UV mini 1240) at wavelength of 450 nm. The bleaching efficiency of the acid activated clay was calculated in this study using the following equation:

$$\% \text{ bleaching efficiency} = [A_{\text{unbleached}} - A_{\text{bleached}} / A_{\text{unbleached}}] \times 100 \quad (1)$$

where $A_{\text{unbleached}}$ and A_{bleached} are the absorbencies of the unbleached and bleached oils, respectively.

Results and Discussions

Characterization

The modifications observed in the chemical composition, surface area, bleaching efficiency, Si/[Al + Fe + Mg] ratio, and cation exchange capacity (CEC) of the natural and acid-leached clay samples are shown in Table 1. The table shows that the acid leaching process modified the chemical composition of the samples. As can be seen in the table, the Si^{4+} cations are not removed, but increased with increase in acid treatment, this could be as a result of depletion of the cations from the interlayer and octahedral sheets of the clay (Motlagh et al., 2011). More of the exchangeable cations were easily removed under mild treatment with the acid; such cations include Ca^{2+} and K^+ . Their dissolution remained almost constant after treating with 4M acid concentration. The dissolution of the octahedral cations (Al^{3+} , Fe^{3+} , and Mg^{2+}) was continuous as the acid concentration increased.

As the acid activation is increased, the surface area increased rapidly and reached a maximum and dropped. The rise in specific surface area is as a result of the unoccupied octahedron spaces remaining from Al^{3+} , Fe^{3+} , and Mg^{2+} ions that have left the layer. Then as the activation progresses, the empty spaces grow larger and the micro pores are transformed into mesopores and finally, because of the decomposition of the crystal structure at some locations, some of the mesopores disappear, leading to a drop in specific surface area (Onal et al., 2002; Motlagh et al., 2011). The maximum bleaching efficiency does not correspond to the maximum surface area value. As can

Table 1. Chemical analysis, specific surface area, maximum bleaching efficiency and cation exchange capacity (CEC) of the natural and acid activated Udi clay samples

Chemical composition (%)	Clay sample					
	UD0	UD2	UD4	UD5	UD6	UD7
Al_2O_3	24.42	19.75	17.42	15.06	14.27	13.04
SiO_2	42.28	52.69	59.76	64.48	67.33	70.47
Fe_2O_3	17.25	13.61	11.12	9.53	8.06	7.12
CaO	0.14	0.06	0.05	0.03	0.03	0.03
MgO	3.60	1.74	1.23	1.02	0.89	0.75
K_2O	2.33	1.03	0.87	0.72	0.71	0.71
TiO	4.35	2.31	1.95	1.47	1.25	1.07
LOI	5.73	3.28	2.65	2.33	2.06	1.92
S_{BET} (m^2/g)	70.2	187	207	232	245	237
Max. Bleaching efficiency (%)	29.8	37.5	46.4	51.8	58.9	66.7
Si/(Al + Fe + Mg)	0.93	1.50	2.01	2.52	2.90	3.37
Cation exchange capacity (CEC), meq/100g	78	67	60	51	45	38

be observed from Table 1, UD6 has a surface area of 245 m²/g and a maximum bleaching efficiency of 78.9%, while UD7 has a surface area of 237 m²/g with a maximum bleaching efficiency of 82.7%. Naturally, UD6 should be expected to have higher bleaching efficiency as a result of higher surface area value. It has been reported by researchers (Inglethorpe et al., 1993; Diaz et al., 2001; Engelhard, 1996) that the optimum decolorization ability of activated clay (for a given set of activating conditions) may or may not coincide with its maximum value of the surface area attained under those conditions.

FTIR analysis

The FTIR spectra of the untreated and treated clay samples are shown in Figs 1 and 2, respectively. Comparing Figs 1 and 2, it is clear that there were some structural modifications on the clay sample as a result of acid activation. The untreated clay sample shows absorption bands at 473, 559, 685, 793, 920, 1038, 1104, 1640, 3450, 3525, 3626 and 3692 cm⁻¹. After acid treatment, the bands at 3692.04 and 3626.29 cm⁻¹ attributed to the O–H stretching of kaolinite were modified to 3694 and 3623 cm⁻¹, respectively. The vibrational bands at 3525 and 1104 cm⁻¹ associated with Al–O–Al were completely absent after acid activation, while bands at 1037, 920, 792, 685, and 559 cm⁻¹ related to the Si–O–Si and O–Si–O stretching remained after acid leaching. This verifies the x-ray fluorescence analysis report that the Si⁺⁴ ion increases with acid treatment while the octahedral cations Al³⁺, Fe³⁺, and Mg²⁺ decreases with acid activation. This indicates that there is a minimal damage to the crystal structure of the clay material. This result is in agreement with the findings of other researchers (Mohamedbakr and Burkitbaev, 2009; Temunjin et al., 2004; Low et al., 1998; Chaisena and Rangswatananon, 2004; Hula et al., 2007; Taha et al., 2011).

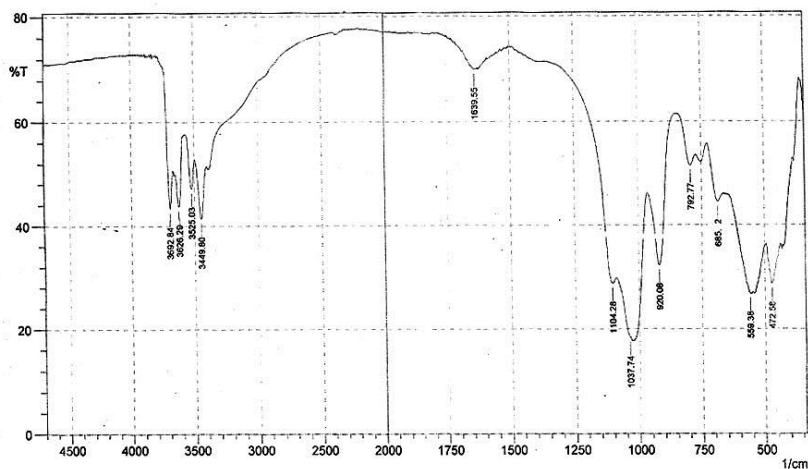


Fig. 1. FT-IR spectra of natural Udi clay

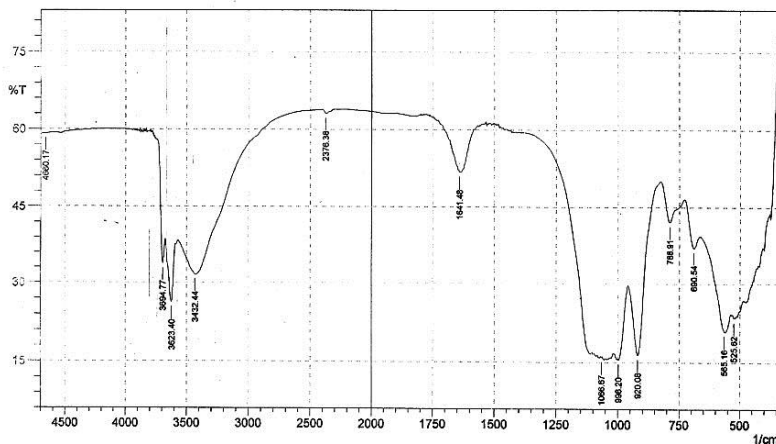


Fig. 2. FT-IR spectra of acid-activated Udi clay

Bleaching efficiency

The results of the bleaching studies performed using the natural and acid-leached samples are shown in Figure 3. The figure shows that the bleaching efficiency increases with an increase in the acid concentration used in the activation step. It is to be seen from the figure that the sample activated with 7M hydrochloric acid shows the highest bleaching efficiency. The figure also shows that time is an important factor, as can be seen, the bleaching efficiency increases with increase in time.

Figure 4 indicates that the bleaching efficiency of the clay samples increases with loss of octahedral cations of Al^{3+} , Fe^{3+} , and Mg^{2+} during the activation process.

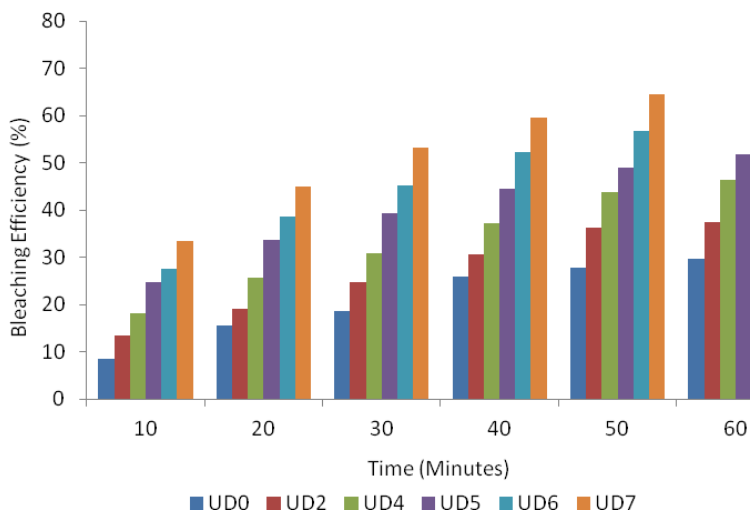


Fig. 3. Bleaching efficiency of the natural and acid-activated clay samples

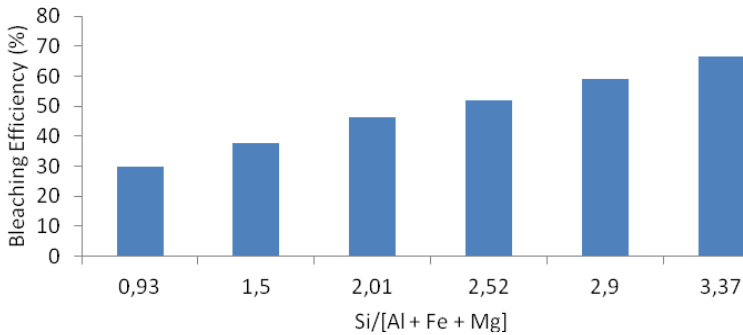


Fig. 4. Variation of bleaching efficiency with Si/[Al + Fe + Mg]

Adsorption isotherms

Langmuir considered adsorption to distribute molecules over the surface of the adsorbent in the form of a monomolecular layer and for the dynamic equilibrium between adsorbed and free molecules. He proposed the following relation:

$$\frac{P}{X/m} = \frac{1}{a} + \frac{a}{b}P \quad (2)$$

where P is equilibrium pressure for a given amount of substance adsorbed, X is the amount of substance adsorbed, m is the amount of adsorbent, a and b are constants.

The mathematical expression relating adsorption to residual solute concentration was developed by Freundlich:

$$\frac{X}{m} = K C^n \quad (3)$$

where C is the amount of residual substance, and K and n are constants.

Since the absorbance measurements are taken in all experiments for the bleaching process, the relative amount of pigment adsorbed (X) and the residual relative amount at equilibrium (X_e) are obtained from Eqs 2 and 3:

$$X = \frac{A_0 - A_t}{A_0} \quad (4a)$$

$$X_e = \frac{A_t}{A_0} = 1 - X \quad (4b)$$

where A_0 is the absorbance of unbleached (crude) palm oil and A_t is the absorbance of bleached oil at time t . Thus, by means of Eqs 4a and 4b, by writing X_e instead of

equilibrium pressure P and the residual substance C , Equations 2 and 3 are rearranged as follows (Topallar, 1998):

$$\frac{X_e}{X/m} = \frac{1}{a} + \frac{a}{b} X_e \tag{5}$$

$X/m = K X_e^n$ or the linear form

$$\log \frac{X}{m} = \log K + n \log X_e \tag{6}$$

A plot of $X_e/(X/m)$ versus X_e and $\log X/m$ versus $\log X_e$ should give straight lines and the least squares analysis can be used to calculate the parameters (a, b) and (K, n) from intercept and slope of straight lines of the isotherms.

Plots of the Freundlich isotherm for the differently prepared adsorbents are depicted in Fig. 5. As can be seen in the figure, straight lines were obtained in the plots with high regression coefficient.

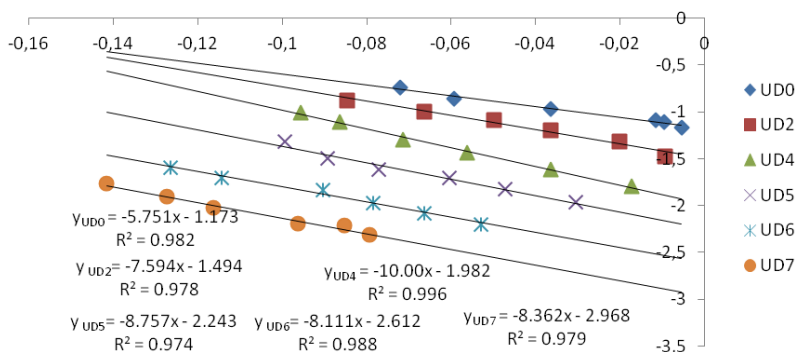


Fig. 5. Freundlich isotherm plot for color pigment removal from palm oil using Udi clay activated with different concentrations of hydrochloric acid

Table 2. Isotherm constants for the un-activated and HCl activated samples

Isotherm	Constants	Clay type					
		UD0	UD2	UD4	UD5	UD6	UD7
Langmuir	a	-0.028	-0.041	-0.065	-0.076	-0.084	-0.089
	b	-2.57	-2.15	-2.08	-1.97	-1.82	-1.70
	R^2	0.876	0.869	0.890	0.881	0.889	0.888
Freundlich	N	-5.751	-7.794	-10.00	-8.757	-8.111	-8.362
	K	0.067	0.032	0.010	0.006	0.002	0.001
	R^2	0.982	0.978	0.996	0.974	0.988	0.979

Since the fit of the plots of Freundlich isotherm is more linear, it can be concluded that the Freundlich isotherm is more applicable to the bleaching performance of acid activated clay from Udi. The values of the constants calculated from the slopes and intercepts of the plots are presented in Table 2.

Conclusion

The effect of hydrochloric acid activation on the structural and bleaching performance of Udi clay has been successfully investigated. The structure of the clay was modified by the acid activation process and the bleaching efficiency was increased from 29.8 to 66.7%. Based on the results activated clay from Udi performs better than the un-activated one and the acid concentration play an important role in the activation step.

References

- AJEMBA R.O., 2012, *Characterization, dissolution, and adsorptive applications of Ukpor, Udi, and Nteje clays*, PhD. Thesis, Nnamdi Azikiwe University, Awka, Anambra, Nigeria.
- AL-ZAHRANI A.A., AL-SHAHRANI S.S., AL-TAWIL Y.A., 2000, *Study on the activation of Saudi natural bentonite, part II: characterization of the produced active clay and its test as an adsorbing agent*, J. King Saud Univ., 13, Eng. Sci. (2), 193 – 203.
- AYARI, F., SRASRA, E., TRABELSI-AYADI, M., 2005, *Characterization of bentonitic clays and their use as adsorbent*, Desalination, 185, 391 – 397.
- AYARI F., SRASRA E., TRABELSI-AYADI M., 2007, *Retention of organic molecule by bentonitic clay saturated with different cations*, Desalination, 206, 499–506.
- BAKHTYAR K.A., MUHAMMAD A.A., KARIM J.J., 2011, *Acid activation and bleaching capacity of some local clays for decolourizing used oils*, Asian J. Chem., 23 (6), 113–122.
- CHRISTIDIS G.E., SCOTT P.W., DUNHAM A.C., 1997, *Acid activation and bleaching capacity of bentonite from the Islands of Milos and Chios, Aegean, Greece*, Appl. Clay Sci., 12, 329–347.
- DIAZ F.R.C., SANCTOS P.S., 2001, *Studies on the acid activation of Brazilian smectitic clays*, Quim. Nova, 24 (3), 345–353.
- ENGELHARD, 1996, *Raising performance standards in catalysts and sorbents for fats and oils*; Engelhard; Houston.
- EZE K.A., NWADIOGBU J.O., NWAMKWERE E.T., 2012, *Effect of acid treatment on the physicochemical properties of kaolin clay*, Archives Appl. Sci. Res., 4 (2), 792–794.
- FOLETTTO E.L., VOLZONE C., PORTO L.M., 2003, *Performance of an Argentinian acid-activated bentonite in the bleaching of soybean oil*, Brazilian J. Chem. Eng., 20, 139–145.
- FOLETTTO E.L., COLAZZO G.C., VOLZONE C., PORTO L.M., 2011, *Sunflower oil bleaching by adsorption onto acid-activated bentonite*, Brazilian J. Chem. Eng., 28 (1), 169–174.
- HULA N., MUSERRET O., YUKSEL S., 2007, *The effect of sulphuric acid activation on crystallinity, surface area, porosity, surface acidity, and bleaching power of bentonite*, Food Chem., 105, 156–163.
- TOPALLAR H., 1998, *Bleaching kinetics of sunflower seed oil*, JAOCS, 75 (4), 531–533.
- INGLETHORPE S.D.J., MORGAN D.J., HIGHLEY D.E., BLOODWORTH A. J., 1993, *Industrial mineral laboratory manual- bentonite*, British Geological Survey Technical Report. WG/93/20.
- KIRALI E.G., LACIN O., 2006, *Statistical modeling of acid activation on cotton oil bleaching by Turkish bentonite*, J. Food Eng., 75, 137–141.

- LOW S.K., LEE C.K., KONG L.Y., 1998, *Decolourization of crude palm oil by activated spent bleaching earth*, J. of Chem. Tech. Biotechnol., 72, 67–73.
- MAKHOUKHI B., DIDI M.A., VILLEMIN D., AZZOUZ A., 2009, *Acid activation of bentonite for use as a vegetable oil bleaching agent*, Grasas Y. Aceites, 60 (4), 343–349.
- MOHAMEDBAKR M., BURKITBAEV M., 2009, *Elaboration and characterization of natural diatomite in Aktyubinsk/Kazakhstan*, The Open Mineral Journal, 3, 12–16.
- MOTLAGH M.M.K., YOUZBASHI A.A., RIGI Z.A., 2011, *Effect of acid activation on structural and bleaching properties of a bentonite*, Iranian J. Mat. Sci. Eng., 8 (4), 50–56.
- MOTLAGH M.M.K., Z. RIGI Z.A., YUZBASHI A.A., 2008, *To evaluate an acid activated bentonite from Khorasan (Iran) for use as bleaching clay*, Int. J. Eng. Sci., 19 (5-2), 83–87.
- NGUETNKAM J.P., KAMGA R., VILLIERAS F., EKODECK G.E., YVON J., 2008, *Assessing the bleaching capacity of some Cameroonian clays on vegetable oils*, Appl. Clay Sci., 39, 113–121.
- ONAL M., SARIKAYA Y., ALEMDAROGLU T., 2002, *The effect of acid activation on some physicochemical properties of a bentonite*, Turk. J. Chem., 26, 409–416.
- ROZIC L., NOVKOVIC T., PETROVIC S., 2010, *Modeling and optimization process parameters of acid activation of bentonite by response surface methodology*, Appl. Clay Sci., 48, 154–158.
- SALAWUDEEN T.O., DADA E.O., ALAGBE S.O., 2007, *Performance evaluation of acid treated clays for palm oil bleaching*, J. Eng. Appl. Sci., 2 (11), 1677–1680.
- TAHA K.K., TAGELSIR M.S., MUSA A.M., 2011, *Performance of Sudanese activated bentonite in bleaching cotton seed oil*, J. Bangladesh Chem. Soc., 24 (2), 191–201.
- TEMUUJIN J., JADAMBAA T., AMARSANAA J., MACKENZIE K.J.D., 2004, *Characterization of acid activated montmorillonite clay from Tuulant (Mongolia)*, Ceramics Int., 30, 251–255.
- TEMUUJIN J., SENNA M., JADAMBAA T., BURMAA D., ERDENECHIMEG S., MACKENZIE K.J.D., 2006, *Characterization and bleaching properties of acid-leached montmorillonite*, J. Chem. Technol. Biotechnol., 81, 688–693.
- TOMIC Z.P., MLADENOVI S.B., BABIE B.M., LOGAR V.A., DORDEVIC A.R., CUPAC S.B., 2011, *Modification of smectite structure by sulphuric acid and characteristics of the modified smectite*, J. Agric. Sci., 56 (1), 25–35.
- USMAN M.A., EKWUEME V.I., ALAJE T.O., MOHAMMED A.O., 2012, *Characterization, acid activation, and bleaching performance of Ibeshe clay, Lagos, Nigeria*, ISRN Ceramics, doi:10.5402/2012/658508.
- WOUMFO D., KAMGA R., FIGUERAS F., NJOPWOUO D., 2007, *Acid activation and bleaching capacity of some Cameroonian smectite soil clays*, Appl. Clay Sci., 37, 149–156.
- ZHANSHENG W., LI C., XIFANG S., XIAOLIN X., DAI B., JIN'E L., HONGSHENG Z., 2006, *Characterization, acid activation, and bleaching performance of bentonite from Xinjiang*, Chinese J. Chem. Eng., 14 (2), 253–258.

Received May 13, 2013; reviewed; accepted August 11, 2013

REMOVAL OF HEAVY METALS FROM GROUNDWATER AFFECTED BY ACID MINE DRAINAGE

Tomasz SUPONIK*, **Miguel BLANCO****

* Politechnika Śląska, Wydział Górnictwa i Geologii, ul. Akademicka 2; 44-100 Gliwice, Poland,
Tomasz.Suponik@polsl.pl

** University of Vigo, Spain

Abstract: Batch tests have been used to assess the level of the removal of metals (copper, nickel, cobalt, zinc, and chromium, in cationic and in anionic forms) from water at low pH values affected by acid mine drainage. The predominant processes which result in the removal with the use of zero-valent iron (Fe⁰) in Permeable Reactive Barrier Technology were evaluated. The most probable processes for each metal have been presented in drawings. There are: reductive precipitation leading to the metallic form, co-precipitation mainly with iron in the form of oxides and/or hydroxides and adsorption on the surface of iron corrosion products or on the surface of zero-valent iron.

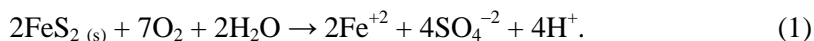
Keywords: coal mine waste dumps, acid mine drainage, groundwater, PRB Technology, metals, zero-valent iron

Introduction

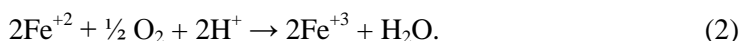
A large number of coal mines are located in the southern Poland and in the North-East and West of Spain. The dumping sites established there have a significant impact on the quality of ground and surface water. The leachates from these waste dumps may contain barium, boron, copper, cadmium, chromium, cobalt, lead, lithium, arsenic, zinc, nickel, molybdenum, manganese, selenium, and thallium. To protect ground and surface water from these contaminants the permeable reactive barrier (PRB) technology may be applied.

The coal mine waste material contains large amount of sulphide minerals. The predominant sulphides in coal mines are pyrite and marcasite (FeS₂), but other minerals may also be found, e.g. covellite (CuS), chalcopyrite (CuFeS₂), sphalerite ((Zn,Fe)S) and galena (PbS). When sulphide minerals are exposed to water and air, minerals are oxidized and create acidic, sulphate-rich drainage which is called the acid

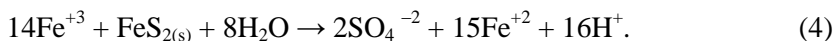
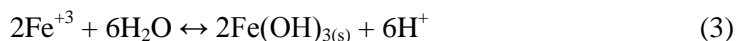
mine drainage (AMD) (Groudev et al., 2007). The reaction of pyrite with water and oxygen produces a solution of sulphuric acid and ferrous sulphate:



In non-altered natural systems, this reaction proceeds slowly in geologic time periods. When environment of this new solution is rich in O_2 , Fe^{2+} is oxidized to Fe^{3+} :



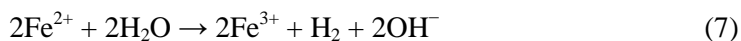
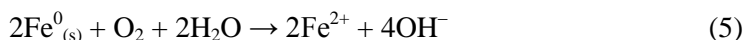
Fe^{3+} can react either with water (reaction 3) creating $\text{Fe}(\text{OH})_3$ or with water and pyrite (reaction 4), thereby decreasing the pH in both equations and increasing ferrous iron in Eq. 4 (Jennings et al., 2008). These processes cause water to gain characteristic orange colour.



Mobility of metals is increased at acidic pH created this way.

The paper aims to evaluate the level of copper, nickel, cobalt, zinc and chromium removal from solution (simulated groundwater affected by coal mine dumping sites) at neutral and low pH values. In order to achieve this objective zero-valent iron ($\text{Fe}(0)$) (ZVI) was employed as a reactive material in the PRB technology (Suponik, 2012). In this technology, the contaminants dissolved in groundwater are removed directly from aquifer by flowing through a permeable barrier filled with a reactive material. The application of zero-valent Iron to remove metals in cationic and anionic forms has been investigated (Wilkin and McNeil, 2003; Rangsvik and Jekel, 2005; Li and Zhang, 2007; Fiore and Zanetti, 2009; Puls et al., 1998; Groudev et al., 2007, Klimkova et al., 2011). In the paper by Suponik (2013), it was concluded that rapid removal of metals in the ZVI occurs likely due to the reductive precipitation/coprecipitation and/or due to the adsorption onto the iron metal surface or/and onto the iron corrosion products. The type of mechanism depends on the type of metal removed, the other accompanying substances and physicochemical conditions in the ZVI bed.

The oxidation of zero valent iron to ferrous and ferric iron causes the increase in pH, the decrease in ORP, the consumption of dissolved oxygen and the generation of hydrogen (Puls et al., 1999). The chemical reactions proceeding in this material are the reactions of iron corrosion:



(see also: reaction 2 and 3).

The paper shows a decrease in the concentration of metals in the aqueous solution for pH 3, 5 and 7. The matter in question is the type of predominant processes which cause the removal of these metals. The answer can be obtained by using advanced techniques such as X-Ray Photoelectron Spectroscopy, Energy-dispersive X-ray spectroscopy and X-ray diffraction. The authors of the paper, however, attempted to answer this question by analyzing the changes of physicochemical parameters and some chemicals in low and neutral pH.

Materials and method

The evaluation of the possibility of the removal of heavy metals from solution was performed in the form of batch tests in a MULTI BIO RS-24 BIOSAN programmable rotator equipped with 50 ml plastic tubes. For these tests the synthetic solutions with the initial pHs of ca. 3.0, 5.0, 7.0 were prepared – pHs of the solutions were adjusted by slow titration with ultra-pure sulphuric acid or with ultra-pure sodium hydroxide. The batch tests were carried out in five separate solutions: chromium, zinc, copper, nickel and cobalt. The synthetic solutions have simulated groundwater contaminated by coal mine waste dumps located in the Upper Silesia, Poland and in the North-East and West of Spain. Solutions containing metal (copper, chromium, zinc, nickel and cobalt) ions were prepared by adding the desired amounts of metal salts ($\text{CuSO}_4 \cdot 5\text{H}_2\text{O}$, $\text{K}_2\text{Cr}_2\text{O}_7$, $\text{ZnSO}_4 \cdot 7\text{H}_2\text{O}$, CoCl_2 , $\text{NiSO}_4 \cdot 7\text{H}_2\text{O}$) into bottles and pouring distilled water; only one metal was dissolved in each sample.

In the batch tests, the solutions (copper, chromium, zinc, nickel and cobalt solution for every value of pH) were poured into five plastic tubes (50ml per each sample) and then 20, 30, 50, 75, 100 mg of ZVI was added to each sample. The tubes were then closed with corks. Each sample had to undergo two minutes of orbital rotation in a programmable rotator (with a speed range = 40 rpm) after which a 6 second reciprocal motion (with turning angle = 90°) with vibration motion followed. This sequence of shaking was repeatedly reiterated. The sequence continued for 1 hour (after this time constant value was achieved). After shaking the samples the solutions were passed through thick filters and assessed. The quantitative analysis of heavy metals (Cr^{6+} , Cu_{total} , Co_{total} , Ni_{total} , Zn_{total}) in solutions was carried out in the UV-Vis Spectrophotometer DR5000 HachLange. The concentrations of Ni, Co, Cu or Zn in the solutions were measured in a Spectrophotometer as a total value. Since there were no metals speciation (at the beginning) other than Ni^{2+} , Co^{2+} , Cu^{2+} or Zn^{2+} cations in the solutions the removal of the metals in the second oxidation state has been assessed in the paper.

Scrap iron (in the form of chips and swarfs (Fig. 1)) used in the batch tests was obtained from a machining plant. Table 1 presents grain-size distribution of scrap iron (Suponik, 2013). The material used in the batch tests has been cleaned before using – first with a thinner (painter's naphtha), dried in the moisture teller, and then, just

before the application, cleaned with distilled water. The density of this material amounted to 7.85 g/cm^3 (Suponik, 2013).

Table 1. Particle size distribution of zero-valent iron used in batch test (Suponik, 2013)

Particle size, mm	4.0–2.0	2.0–1.6	1.6–1.0	1.0–0.71	0.71–0.5	<0.5
Mass fraction, %	1.77	1.28	7.26	38.79	36.57	14.33

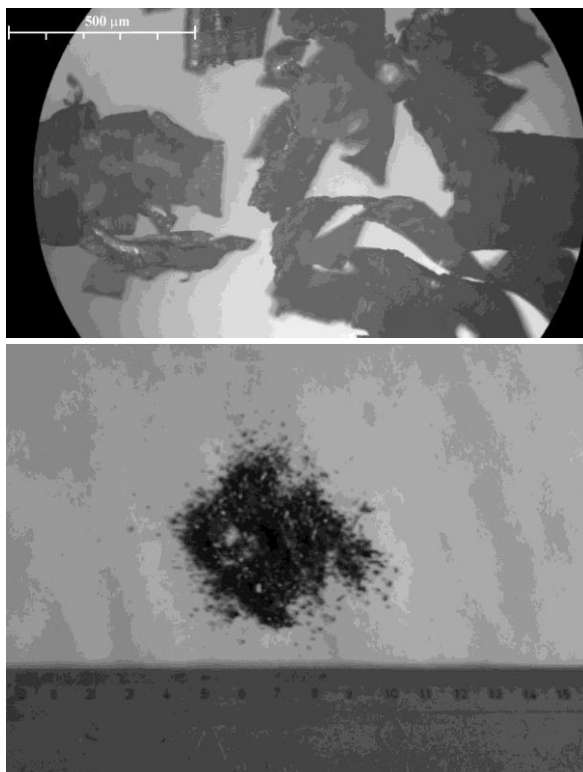


Fig.1. Zero-valent iron (Fe(0)) used in batch test

Results and discussion

The concentration of metals measured in the tests decreased with the increase of the mass of ZVI applied in the tubes (Fig. 2). This phenomenon was observed for all assessed values of pH, however the lower was the value of pH in the metal ion solution the slower was the observed decrease of Ni(II), Co(II), Zn(II), Cr(VI) or Cu(II) concentration. In the case of Chromium and Copper that partially occurred due to the easy precipitation of copper and chromium(III) hydroxides at higher values of pH (i.e. for pH = 7). Moreover, in every test, at higher value of pH (i.e. for pH amounting to 5 and 7) the ferric hydroxides (e.g. FeOOH , $\text{Fe}(\text{OH})_3$) may be created on

the surface of zero-valent iron, on which metals in cationic forms may be sorbed. These compounds (iron corrosion products) appear as a result of Fe^0 oxidation to Fe^{2+} and then to Fe^{3+} , mainly in the presence of dissolved oxygen in aqueous solutions.

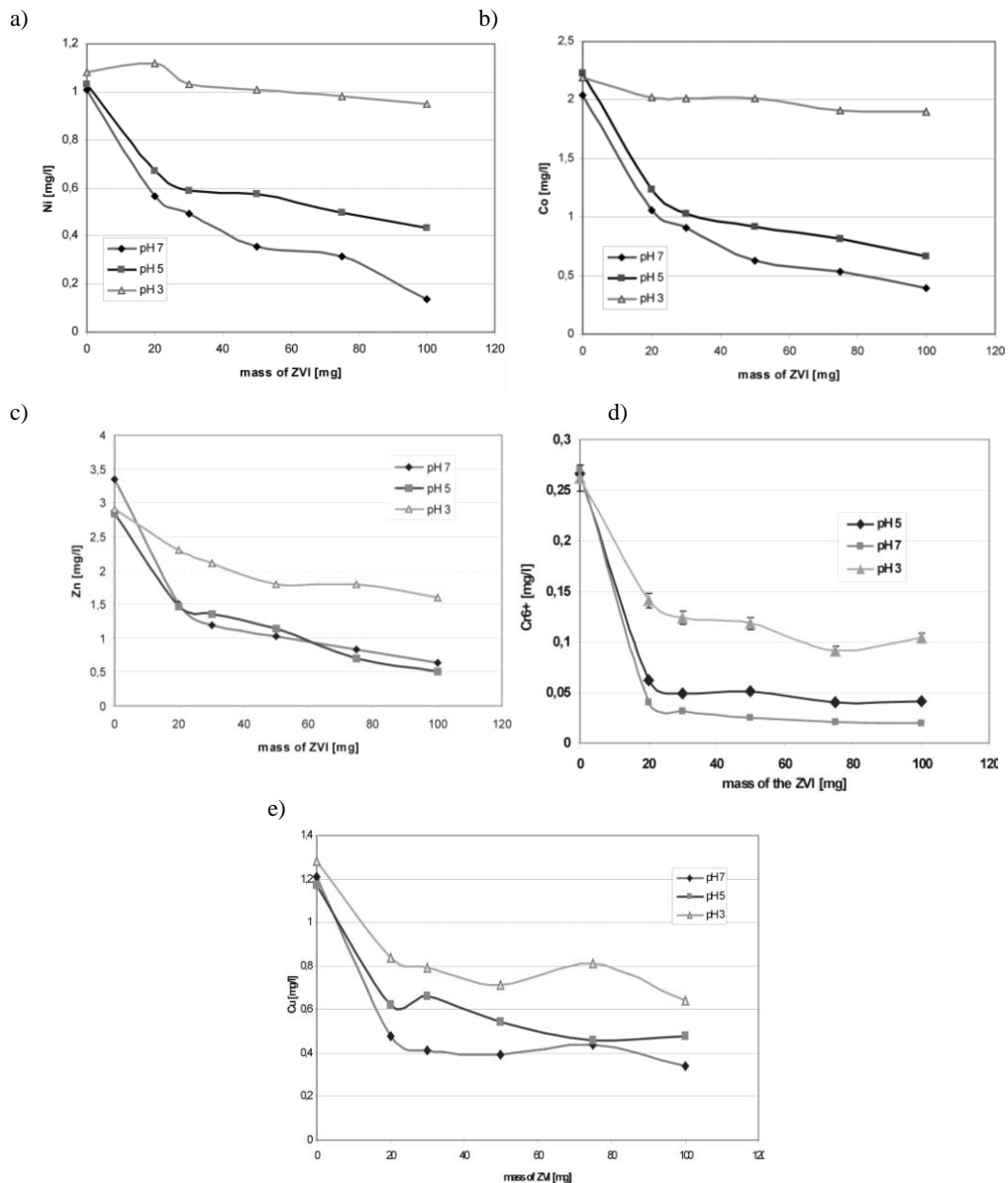


Fig 2. The concentration of: a) Ni(II); b) Co(II); c) Zn(II); d) Cr(VI); e) Cu(II); in three solutions (the initial pH = 3; 5; 7) for various masses of ZVI

In accordance with one of the author's previous work (Suponik, in press) the oxidation of Fe^0 to Fe^{2+} was evidenced by creation of reduction conditions in the water which was in contact with the reactive material as well as by the formation of ferrous iron in it. In this work, it has been presented that more ions of divalent iron appeared in water with lower initial pH value than in water which was characterized by higher value of pH. Thus, it was concluded that the oxidation of ZVI proceeds faster in low pH, which has also been found by other researchers, e.g. Kowal and Swiderska-Broz (1996). This occurs mostly due to the processes described by reactions 5 and 6. With high probability, as a result of reactions 2, 7 and others Fe(II) may be oxidized to Fe(III), which is then (under suitable conditions) precipitated in various forms. These precipitates cover ZVI with thin shell. In the said article (Suponik, in press) it has also been confirmed that more ferric iron is formed in solution with high pH values than in solutions with lower values of pH.

Iron oxides and oxyhydroxides are widespread in the nature and play an important role in many geological and biological processes. All together, there are many iron oxides and oxyhydroxides. They may be divided into (Cornell and Schwertmann, 2003):

- oxides: iron(II) oxide – FeO ; iron(II,III) oxide – Fe_3O_4 ; iron(III) oxide – Fe_2O_3 among which are alpha phase ($\alpha\text{-Fe}_2\text{O}_3$), beta phase ($\beta\text{-Fe}_2\text{O}_3$), gamma phase ($\gamma\text{-Fe}_2\text{O}_3$), epsilon phase ($\epsilon\text{-Fe}_2\text{O}_3$),
- hydroxides: iron(II) hydroxide ($\text{Fe}(\text{OH})_2$) and iron(III) hydroxide ($\text{Fe}(\text{OH})_3$),
- oxide/hydroxides: goethite ($\alpha\text{-FeOOH}$), akaganeite ($\beta\text{-FeOOH}$), lepidocrocite ($\gamma\text{-FeOOH}$), feroxyhyte ($\delta\text{-FeOOH}$), ferrihydrite ($\text{Fe}_5\text{HO}_8 \cdot 4\text{H}_2\text{O}$ approx.), high-pressure FeOOH and green rust ($\text{Fe}^{\text{III}}_x\text{Fe}^{\text{II}}_y(\text{OH})_{3x+2y-z}(\text{A}^-)_z$; where A^- is Cl^- or 0.5SO_4^{2-}).

In accordance with James Newton Butler (1998) the form of the precipitated phase for ferric oxyhydroxides depends strongly on the composition of the precipitating solution and the age of the precipitate. It also depends on the redox potential and the value of pH. Thus, it is difficult to foresee the type of iron compound formed on the surface of scrap iron used in the tests.

In the research presented in paper by Suponik (in press) it has also been shown that during the metals removal pH increased. Higher increases of pH were observed for its low initial value (i.e. $\text{pH} = 3$), as the oxidation of $\text{Fe}(0)$ proceeded more rapidly in low pH. Similar results were obtained in the experiments presented in this paper. Figure 3 shows changes of pH (mean values of all tests) during application of different ZVI masses used in plastic tubes.

Most of heavy metals precipitated at basic conditions, but the optimum pH for precipitation of various heavy metals varies significantly. Table 2 presents the theoretical equilibrium concentrations of different metals hydroxides at pH 4.11, 5.81, 7.21 (the pH values correspond to 100 mg of ZVI used in the tests). They were calculated according to solubility product (K_{sp}) of metals hydroxides.

Although the redox potential is a very important parameter in regard to precipitation of metals hydroxides (that can not be neglected), the values presented in Table 2 show the compounds which are readily precipitated. $\text{Fe}(\text{OH})_3$ and especially FeOOH and Fe_3O_4 (not included in the Table 2) are sparingly soluble compounds, so in the presence of Fe^{3+} in water (under appropriate conditions) these compounds are easily precipitated.

Xu et al. (2010), Huang et al. (2005), Music and Ristic (1988), Lagashetty et al. (2010) and Djafer et al. (1989) studied the adsorption of heavy metals (Cr(VI), Cu(II), Zn(II), Pb(II) and others) on iron oxides and hydroxides (e.g. FeOOH , $\text{Fe}(\text{OH})_3$, Fe_2O_3). They have shown that these metals are easily removed from water, hence it can be claimed that these compounds are a good medium for the removal of metal ions from groundwater. Djafer et al. (1989) also claimed that the adsorption of metallic cations increased with the increase in pH of water.

It can be hypothetically said that the co-precipitation of metals analyzed in this work with ferric ions (crating metal-iron hydroxides or oxides, e.g. $\text{Fe}_2\text{Me}_1\text{O}_4$ – where Me means metal ions) may also be one of the processes of metal removal from water in reactive barrier. The same applies to the adsorption of heavy metals directly on the surface of zero-valent iron (although this is less likely).

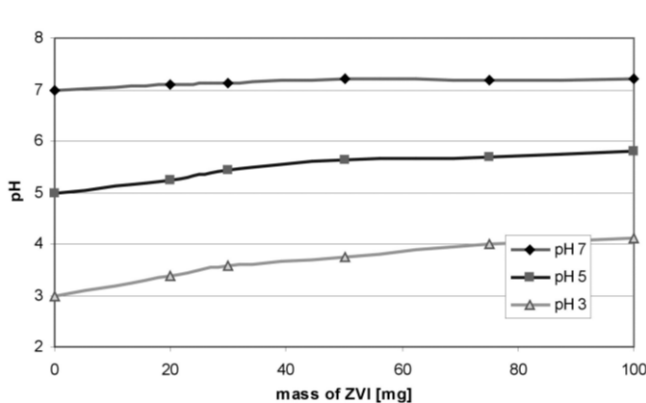


Fig. 3. The mean value of pH for solutions (copper, chromium, zinc, nickel and cobalt) tested for various masses of ZVI and for various initial values of pH (pH = 3; 5; 7)

As the pH of the water passing through zero-valent iron substantially increases, the precipitation of metal hydroxides may play an important role in the immobilization of metals. This fact has also been noticed by Li and Zhang (2007). In accordance with Table 2 the following hydroxides are characterized by a low solubility at pH >7.21: $\text{Cu}(\text{OH})_2$, $\text{Cr}(\text{OH})_3$ – while in lower pH values, copper hydroxide readily dissolves in water.

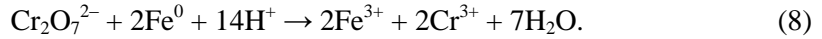
Table 2. Theoretical equilibrium concentrations of different metals hydroxides and oxides at 4.11, 5.81, 7.21 pH (these values correspond to 100 mg of ZVI used in the tests) which were calculated based on the solubility product constant K_{sp}

Metal hydroxide	K_{sp}	pH	$[Me^{n+}]$, mol/dm ³	$C[Me^{n+}]$, mg/dm ³
Fe(OH) ₂	$4.8 \cdot 10^{-16}$	pH = 4.11	28922.86	$2.60 \cdot 10^9$
		pH = 5.81	11.5144	1034798.949
		pH = 7.21	0.0182	1640.05
Fe(OH) ₃	$3.8 \cdot 10^{-38}$	pH = 4.11	$1.78 \cdot 10^{-08}$	$1.90 \cdot 10^{-03}$
		pH = 5.81	$1.41 \cdot 10^{-13}$	$1.51 \cdot 10^{-08}$
		pH = 7.21	$8.90 \cdot 10^{-18}$	$9.51 \cdot 10^{-13}$
Cu(OH) ₂	$5.6 \cdot 10^{-20}$	pH = 4.11	3.373	329151.8072
		pH = 5.81	0.00134	130.7438
		pH = 7.21	$2.13 \cdot 10^{-6}$	0.2078241
Ni(OH) ₂	$1.6 \cdot 10^{-14}$	pH = 4.11	963855.422	$8.94 \cdot 10^{10}$
		pH = 5.81	383.69	35572182.25
		pH = 7.21	0.6084	56401.52091
Co(OH) ₃	$2.5 \cdot 10^{-43}$	pH = 4.11	$1.17 \cdot 10^{-13}$	$1.72 \cdot 10^{-08}$
		pH = 5.81	$9.29 \cdot 10^{-19}$	$1.37 \cdot 10^{-13}$
		pH = 7.21	$5.84 \cdot 10^{-23}$	$8.60 \cdot 10^{-18}$
Co(OH) ₂	$1.6 \cdot 10^{-18}$	pH = 4.11	96.3855	8959036.145
		pH = 5.81	0.0383693	3566.427
		pH = 7.21	$6.08 \cdot 10^{-5}$	5.65136
Zn(OH) ₂	$1.3 \cdot 10^{-17}$	pH = 4.11	783.133	77851204.82
		pH = 5.81	0.31175	30991.1271
		pH = 7.21	$4.90 \cdot 10^{-4}$	49.138
Cr(OH) ₃	$5.4 \cdot 10^{-31}$	pH = 4.11	0.253	26022.54
		pH = 5.81	$2.01 \cdot 10^{-06}$	$206.83 \cdot 10^{-3}$
		pH = 7.21	$1.27 \cdot 10^{-10}$	$1.30 \cdot 10^{-05}$

In accordance with standard electrode potential, the metals in cationic and anionic forms, such as Ni^{2+} , Cu^{2+} , Co^{2+} and $Cr_2O_7^{2-}$, $HCrO_4^-$, CrO_4^{2-} , may also be removed from groundwater as a result of reductive precipitation/coprecipitation, as all these ions are characterized by a higher standard electrode potential than iron (Fe^0). Finally, these metals may be precipitated out in a reactive material as Ni^0 , Cu^0 , Co^0 and $Cr_xFe_{(1-x)}OOH$ (see reaction 11) (Puls et al., 1998), $Cr(OH)_3$ and Cr_2O_3 (ITRC, 2011).

Figures 4–8 show the conceptual models for Ni^{2+} , Co^{2+} , Cu^{2+} , Zn^{2+} and Cr^{6+} removal from water with the use of ZVI.

The overall reaction for the hexavalent chromium, which occurs in water as an oxyanion in the form of CrO_4^{2-} or as $Cr_2O_7^{2-}$ can be presented as (Suponik, in press, Suponik, 2013):

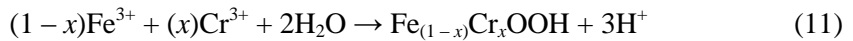


In further steps, chromium Cr(III) may be removed from solution by (Fig. 4):

- precipitation as chromium hydroxides and oxides, such as $\text{Cr}(\text{OH})_3$ (reaction 9) and Cr_2O_3 (reaction 10),



- co-precipitation with iron as mixed chromium-iron oxyhydroxide (Puls et al., 1998),



- adsorption on the surface of iron corrosion products e.g. FeOOH ,



- adsorption on the surface of zero-valent iron.

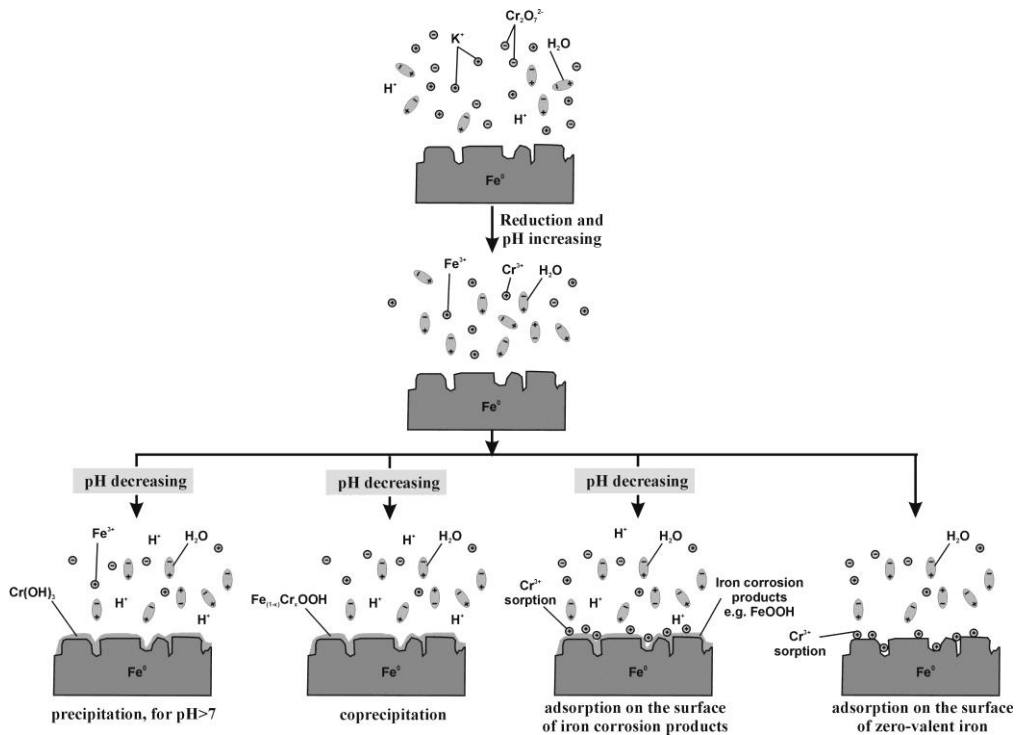


Fig. 4. Conceptual model for chromium(VI) removal from water with the use of ZVI

Cu(II), Ni(II), Co(II) also have a higher standard electrode potential than Fe(0), thus, iron may displace these hazardous cations from groundwater. Although the reduction and precipitation of Cu (to metallic form) is more probable, some Cu(II) may be adsorbed on the surface of iron corrosion products (see reaction 12) or on the surface of zero-valent iron (less likely). Moreover, low solubility of copper hydroxide at $\text{pH} > 7$ indicates that this compound may also precipitate in this condition. In the case of metals analyzed, it should be also noted that co-precipitation in the form of metal-iron hydroxides or oxides (e.g. Fe_2CuO_4) may result in the removal of metal ions:

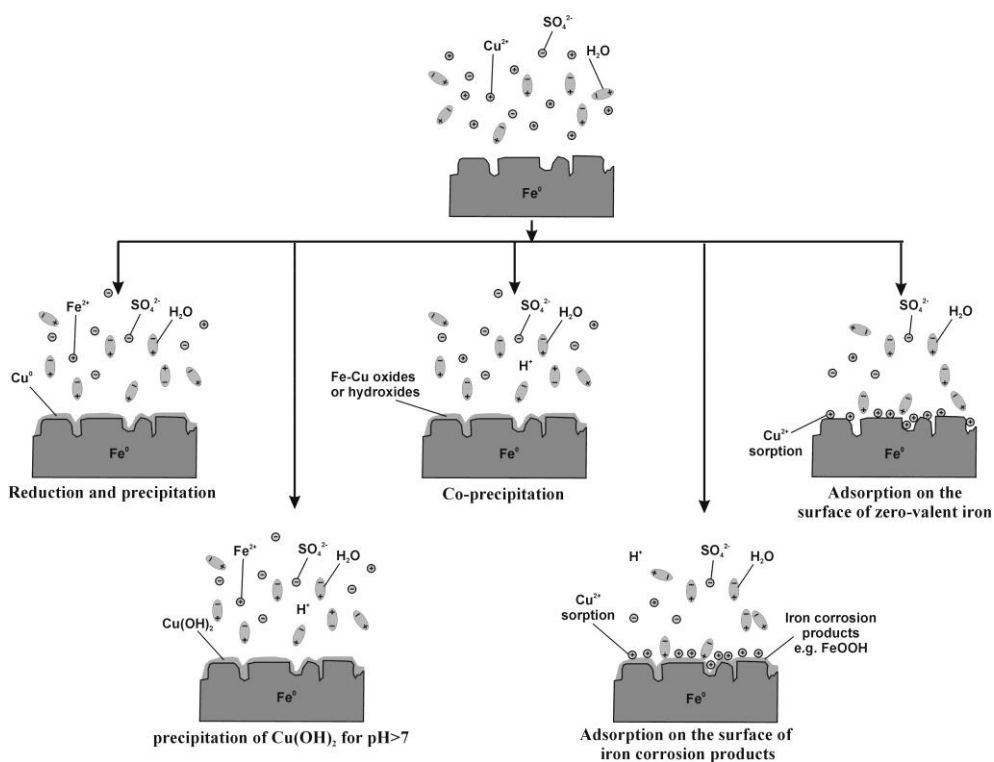


Fig. 5. Conceptual model for copper(II) removal from water with the use of ZVI

According to the study by Li and Zhang (2007), the sorption/surface complex formation is the removal mechanism for metal ions with a standard potential very close to or more negative than that of iron. The predominant removal mechanism, for metals with a considerably more positive and slightly more positive standard electrode potential than that of iron is respectively the reductive precipitation and the sorption and/or reductive precipitation. Thus it can be said with a high probability that the main processes for nickel(II), cobalt(II) and zinc(II) removal are the adsorption on the

surface of iron corrosion products and the adsorption directly on the surface of zero-valent iron (less likely). It should not be forgotten in this place about the possibility of co-precipitation with iron, forming oxides and/or hydroxides (e.g. $Fe_{(1-x)}Ni_x(OH)_2$, $Fe_{(1-x)}Co_x(OH)_2$, $Fe_{2.5}Zn_{0.5}O_4$). In the case of cobalt and zinc, the process of reductive precipitation into metallic form is also possible, but a small difference between the standard electrode potential of Fe^0 and Co^0 and Ni^0 reduces this probability (Figs 6, 7).

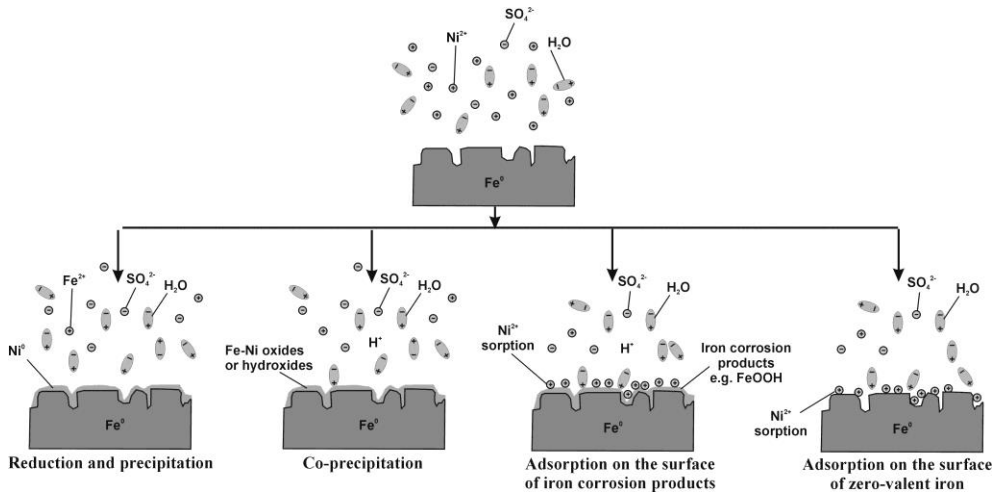


Fig. 6. Conceptual model for nickel (II) removal from water with the use of ZVI

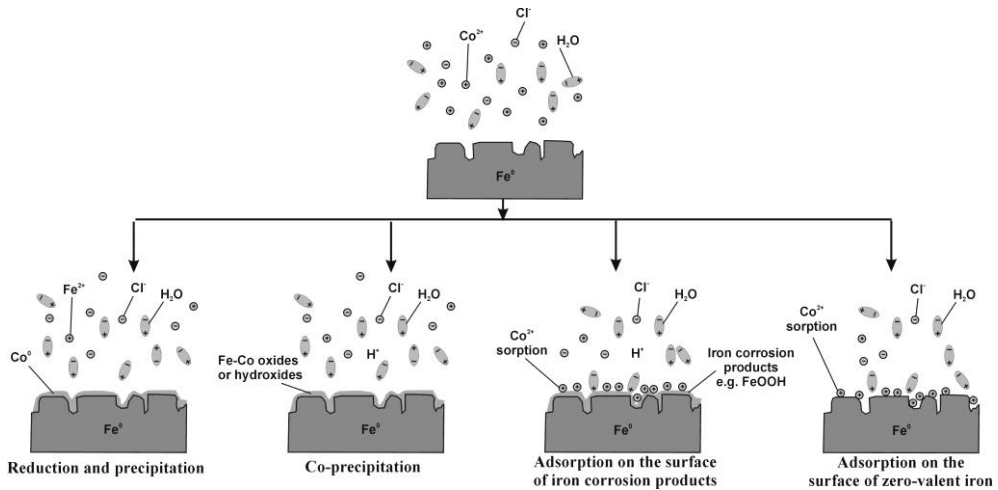


Fig. 7. Conceptual model for cobalt(II) removal from water with the use of ZVI

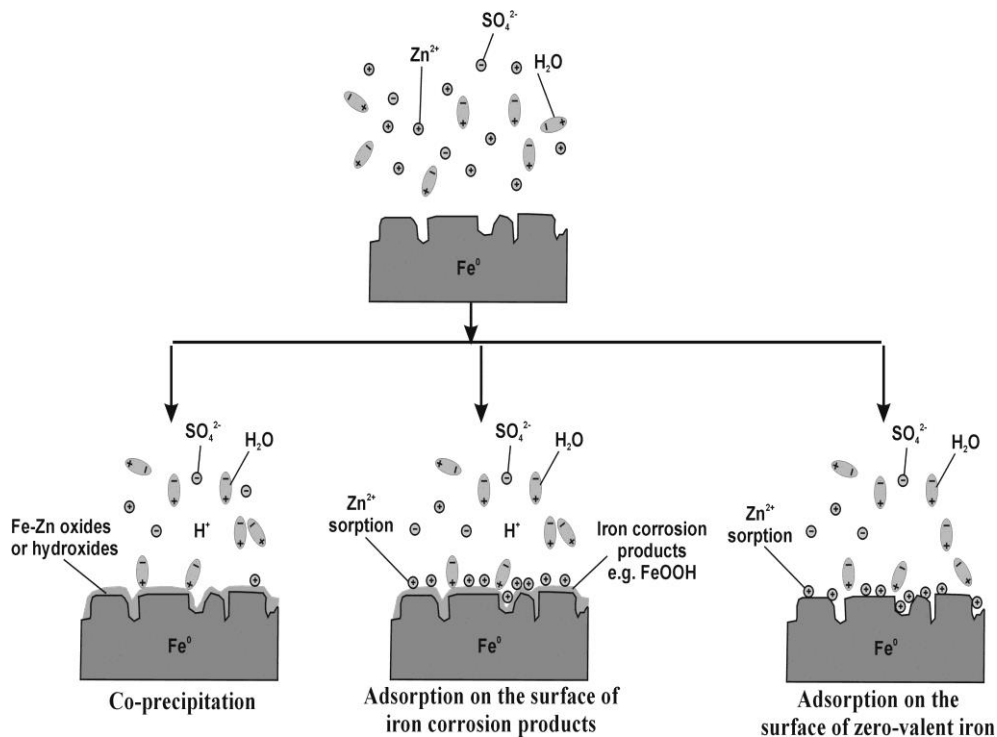


Fig. 8. Conceptual model for zinc(II) removal from water with the use of ZVI

Conclusions

All metals analyzed in the article have been removed from water when ZVI was used as a reactive material of PRB. pH had a large impact on the degree of removal, and on the processes which influence the removal of the individual metals. In general, the lower the pH, the slower is the removal of metals.

The processes that can result in the removal of copper, nickel, cobalt, zinc and chromium from water with the use of zero-valent iron are:

- reductive precipitation leading to the metallic form – relates mainly to copper, but also to a lesser extent nickel and cobalt;
- co-precipitation with iron in the form of oxides and/or hydroxides, e.g. for successive metal: $\text{Fe}_{(1-x)}\text{Cr}_x\text{OOH}$, $\text{Fe}_2\text{Cu}_1\text{O}_4$, $\text{Fe}_{(1-x)}\text{Ni}_x(\text{OH})_2$, $\text{Fe}_{(1-x)}\text{Co}_x(\text{OH})_2$, $\text{Fe}_{2.5}\text{Zn}_{0.5}\text{O}_4$;
- precipitation as a result of increase in pH – relates mainly to copper $\text{Cu}(\text{OH})_2$ and chromium $\text{Cr}(\text{OH})_3$, only for pH higher than 7;
- adsorption on the surface of iron corrosion products or on the surface of zero-valent iron – for all of the analyzed metals, although sorption directly on the surface of zero-valent iron is highly unlikely.

References

- BUTLER J.N. WITH A CHAPTER BY COGLEY D. R., 1998, *Ionic equilibrium, solubility and pH calculations*, John Wiley and Sons, Inc.
- CORNELL R.M., SCHWERTMANN U., 2003, *The iron oxides: structure, properties, reactions, occurrences and uses*, Wiley VCH.
- DJAFER M., LAMY I., TERCE M., 1989, *Interaction of metallic cations with the hydrous goethite (α -FeOOH) surface*, Progress in Colloid and Polymer Science, vol. 79, 150–154.
- FIORE, S., ZANETTI M. C., 2009, *Preliminary Tests Concerning Zero-Valent Iron Efficiency in Inorganic Pollutants Remediation*, American Journal of Environmental Sciences, 5(4), 556–561.
- GROUDEV S., SPASOVA I., NICOLOVA M., GEORGIEV P., 2007, *Acid Mine drainage cleanup in a uranium deposit by means of a passive treatment system*, Physicochemical Problems of Mineral Processing, vol. 41, 265–274.
- HUANG H.H., TWIDWELL L.G., YOUNG C.A., 2005, *Point of Zero Charge (PZC) and Double Layer Adsorption – An Equilibrium Calculation Approach*, Computational Analysis in Hydrometallurgy, COM 2005 Calgary Canada August.
- ITRC (Interstate Technology & Regulatory Council), 2011, *Permeable Reactive Barrier: Technology Update*, PRB-5. Washington, D.C.: Interstate Technology & Regulatory Council, PRB: Technology Update Team. Washington: <http://www.itrcweb.org>.
- JENNINGS S.R., NEUMAN D.R., BLICKER P.S., 2008, *Acid mine drainage and effects on fish health and ecology: a review*, Reclamation Research Group Publication, Bozeman, MT.
- KLIMKOVA S., CERNIK M., LACINOVA L., FILIP J., JANCIK D., ZBORIL R., 2011, *Zero-valent iron nanoparticles in treatment of acid mine water from in situ uranium leaching*, Chemosphere, Vol. 82, Iss. 8, 1178–1184.
- KOWAL L. A., ŚWIDERSKA-BRÓŹ M. 1996, *Oczyszczanie wody*, PWN, Warszawa–Wrocław.
- LI, X.-Q., ZHANG W. X., 2007, *Sequestration of Metal Cations with Zerovalent Iron Nanoparticles: A Study with High Resolution X-Ray Photoelectron Spectroscopy (HRXPS)*, Journal of Physical Chemistry, 111(19), 6939–6946.
- LAGASHETTY A., VIJAYANAND H., BASAVARAJA S., MALLIKARJUNA N.N., VENKATARAMAN A., 2010, *Lead adsorption study on combustion derived γ -Fe₂O₃ surface*, Bulletin of Materials Science, Vol. 33, Iss. 1, 1–6.
- MUSIC S., RISTIC M., 1988, *Adsorption of trace elements or radionuclides on hydrous iron oxides*, Journal of Radioanalytical and Nuclear Chemistry, Vol. 120, No. 2, 289–304.
- PULS R. W., POWELL M. R., BLOWES D. W., GILLHAM R. W., SCHULTZ D., SIVAVEC T., VOGAN J. L., POWELL P. D., 1998, *Permeable reactive barrier technologies for contaminant remediation*, Washington: United States Environmental Protection Agency.
- PULS R.W., PAUL C.J., POWELL R.M., 1999, *The application of in situ permeable reactive (zero-valent iron) barrier technology for the remediation of chromate-contaminated groundwater: a field test*, Applied Geochemistry, 14, 989–1000.
- RANGSIVIEK, R., JEKEL M. R., 2005, *Removal of Dissolved Metals by Zero-Valent Iron (ZVI): Kinetics, Equilibria, Processes and Implications for Stormwater Runoff Treatment*, Water Research 39, 4153–4163.
- SUPONIK T., 2012, *Removing contaminants from groundwater polluted by the Trzebieńka Mine Settling Pond located in Upper Silesia (Poland)*, Physicochemical Problems of Mineral Processing, Vol. 48, issue 1, pp. 169–180.
- SUPONIK T., 2013, *Groundwater treatment with the use of zero-valent iron in the Permeable Reactive Barrier Technology*, Physicochemical Problems of Mineral Processing, Vol. 49, Iss. 1, 13–23.

- SUPONIK T., in press, *Zero-valent iron for inorganic contaminants removal from low pH water*, accepted for publication in *Environment Protection Engineering*.
- WILKIN R. T., MCNEIL M. S., 2003, *Laboratory evaluation of zero-valent iron to treat water impacted by acid mine drainage*, *Chemosphere*, 53, 715–725.
- XU CHUNHUA, CHENG DANDAN, YUE QINYAN, YIN ZHILEI, GAO BAOYU, ZHAO XIAN, 2010, *Adsorption of Cr (VI) from Aqueous Solution with nano β -FeOOH*, International Conference on Bioinformatics and Biomedical Engineering – ICBBE, 1–4.

Received July 5, 2013; reviewed; accepted August 13, 2013

WETTING PROCESSES IN SUPPORTED IONIC LIQUID MEMBRANES TECHNOLOGY

**Iwona CICHOWSKA-KOPCZYNSKA,
Monika JOSKOWSKA, Robert ARANOWSKI**

Department of Chemical Technology, Gdansk University of Technology, ul. Narutowicza 11/12, Gdansk, Poland, kopczynska.i@gmail.com

Abstract: Ionic liquids are widely used in supported ionic liquid membranes technology, especially in gas separation and purification processes. This work characterizes the ability of ionic liquids to wet commercially available porous supports used for such purposes. Characterization of supports and membrane phases was carried out in order to determine factors influencing wetting process. Experimental method based on capillary rise is widely used for porous media characterization (i.e. pore radius, contact angle). Measurements of penetration distance or liquid mass are two main experimental methods, in which the Washburn equation is a basic instrument to analyze the obtained results. However, polymeric porous supports do not meet Washburn assumptions and the method is loaded with human errors, so the sessile drop method was used. The rate of wetting influences swelling effects and therefore changes in permeation path during gas separation processes are observed. Influence of ionic liquids structure on wetting and swelling of porous supports was investigated. The families of 1-alkyl-3-methylimidazolium ($C_n\text{mim}$), ammonium (N_{nmn}), 1-alkyl-1-methylpyrrolidinium ($C_n\text{Pyr}$) and 1-alkylpyridinium ($C_n\text{Py}$) compounds with variable alkyl chain lengths in cation structures and changeable anions were taken into account in wetting and swelling experiments.

Keywords: ionic liquid, supported ionic liquid membrane, contact angle, wettability, swelling

Introduction

Supported liquid membrane (SLM) is a two phase system of porous support and liquid phase held in the membrane pores by capillary forces (Walczyk, 2006). Industrial application of liquid membrane systems usually covers usage of ethanolamine (MEA), diethanolamine (DEA), chloroform, dichloromethane, tetrachloromethane, chlorobenzene and toluene. These traditional solvents present high absorption capacity of CO_2 at low temperature and under pressure (Schaffer et al., 2011). However, they also present high heat absorption, corrosiveness (Kittel et al., 2009), high vapor pressure, lack of possibility of recovery and high toxicity. Pure MEA vapor pressure is

about 64 Pa. However, while using water solutions, vapor pressure is much higher. DEA acute toxicity in the form of LD_{50} is from 1.41 g/kg to 2.83 g/kg (Expert Panel of the Cosmetic Ingredient, 1983), DEA is irritant to skin, eyes and cause systemic toxicity mainly in liver, kidney, red blood cells and the nervous system following oral and/or dermal exposure of laboratory animals (Gamer et al., 2008). Therefore, while using these traditional organic solvents several disadvantages can be observed such as secondary stream pollution or loss of membrane phase caused by vaporization or displacement of liquid from the pores under transmembrane pressure (Teramoto, 2000). Many efforts have been made to improve the lifetime of SLMs. Gelation, applying top layers or replacing traditional solvent to ionic liquid (IL) were employed to prevent instability mechanisms (Danesi et al., 1987; Naplenbroek et al., 1992). Great issue is noticed in using ionic liquids as a replacement for toxic, flammable and volatile organic solvents. Calculated vapor pressure for 1-ethyl-3-methylimidazolium bis(trifluoromethylsulfonyl)imide in 298K is $12 \cdot 10^{-6}$ Pa (Berthod et al., 2008). Ionic liquids are class of solvents that are composed of large asymmetric organic cation and smaller organic or inorganic anion. Ionic liquids present many unique properties, they have negligible vapor pressure, they are non-flammable and stay liquid in a wide range of temperatures, moreover ILs solvate many of organic and inorganic species (Cadena et al., 2004). These properties make them very attractive in many industrial applications. However, complete design of industrial processes using ILs can be performed only having knowledge on their physicochemical properties such as viscosity, density or surface tension.

Ionic liquids present surface tensions lower than those observed for traditional solvents as water, however these values are still much higher than observed for organic solvents (Sohn et al., 2000). Freie et al. (2007) presented the dependence of surface tension on the strength of interactions between cation, anion and hydrogen bonds.

Ionic liquids also have higher viscosity than other typical solvents used in separation processes. Dynamic viscosity of ILs in room temperature is situated in a range from about 10 mPa·s to 500 mPa·s. In comparison, viscosity of chloroform, tetrachlorocarbon and ethanolamine in 293K is 0.89; 16.1; and 20 mPa·s respectively (Wasserscheid and Keim, 2000; Chiappe and Pieraccin, 2005).

Properties of ionic liquids mentioned above give supported ionic liquid membranes (SILMs) predominance over traditional SLMs (Gamer et al., 2008; Letcher, 2007; Hernandez-Fernandez et al., 2009). SILMs present several advantages, such as requirement of very small quantities of solvent and high selectivity. Key aspect in obtaining satisfying effectiveness and long membrane lifetime is the proper choice of ionic liquid and polymeric or ceramic support. Properties of both affect the processes of obtaining useful supported ionic liquid membrane. Perfect wetting of supports with ionic liquids is required for complete pores saturation and applying high operating pressures without pushing the liquid out of the pores. Contact angles of some ionic

liquids are described in the literature, for example on Si wafers (Tadkaew et al., 2011), PTFE and glass (Nguyen et al., 2012; Cichowska-Kopczynska et al., 2013).

This work characterizes the ability of ionic liquids to wet polymeric porous supports and the rate of swelling of these supports that are used in SILMs technology. Wetting of supports affects membrane stability, whereas swelling effect causes fluctuations in gas diffusion path. Experimental method based on capillary rise is widely used for porous media characterization (i.e. pore radius, contact angle). Measurements of penetration distance and liquid mass are two main experimental methods, in which Washburn equation is a basic instrument to analyze the obtained results (Dang-Vu and Hupka, 2005; Ferraris et al., 2001). However, this method is loaded with human errors, so the sessile drop method was used for measurements. The families of 1-alkyl-3-methylimidazolium ($C_n\text{mim}$), ammonium ($N\text{nnnn}$), 1-alkyl-1-methylpyrrolidinium ($C_n\text{Pyr}$) and 1-alkylpyridinium ($C_n\text{Py}$) compounds with variable alkyl chain lengths in cation structures and changeable anions were taken into account in order to discuss the influence of ionic liquids structure on wetting and swelling of porous supports.

Materials

Several imidazolium, ammonium, pyridinium and pyrrolidinium ionic liquids were used in this study:

- 1-ethyl-3-methylimidazolium bis(trifluoromethylsulfonyl)imide [Emim][Tf₂N],
- 1-ethyl-3-methylimidazolium trifluoromethanesulfonate [Emim][TfO],
- 1-butyl-3-methylimidazolium bis(trifluoromethylsulfonyl)imide [Bmim][Tf₂N],
- 1-butyl-3-methylimidazolium trifluoromethanesulfonate [Bmim][TfO],
- 1-hexyl-3-methylimidazolium bis(trifluoromethylsulfonyl)imide [Hmim][Tf₂N],
- trimethylbutylammonium bis(trifluoromethylsulfonyl)imide [N1114][Tf₂N],
- triethylbutylammonium bis(trifluoromethylsulfonyl)imide [N2224][Tf₂N],
- triethylhexylammonium bis(trifluoromethylsulfonyl)imide [N2226][Tf₂N],
- triethyloktylammonium bis(trifluoromethylsulfonyl)imide [N2228][Tf₂N],
- 1-butyl-1-methylpyrrolidinium bis(trifluoromethylsulfonyl)imide [BPyr][Tf₂N],
- 1-hexyl-1-methylpyrrolidinium bis(trifluoromethylsulfonyl)imide [HPyr][Tf₂N],
- 1-butyl-1-methylpyrrolidinium trifluoromethanesulfonate [BPyr][TfO]
- 1-butylpyridinium bis(trifluoromethylsulfonyl)imide [BPy][Tf₂N],
- 1-hexylpyridinium bis(trifluoromethylsulfonyl)imide [HPy][Tf₂N].

All chemicals were supplied by IOLITEC, Heilbronn, Germany with purity about 99%. The molecular structures of ILs cations and anions used in this study are shown in Figs. 1–2.

In order to determine the effect of chemical structure of the ionic liquids on wetting, different alkyl chain lengths of the cations and different anions were selected.

The four hydrophilic membranes were applied: GH Polypro (polypropylene) – PP, FP VericeITM (polyvinylidene fluoride) – PVDF, NylafloTM (polyamide) – PA, Supor® (polyethersulfone) - PES, (Pall, Gelman Laboratory, USA). The surface of PP membrane occurred modified with compounds containing C-O-C bonds, so the surface of PP membrane is also hydrophilic. This was evidenced by IR spectra previously (Joskowska et al., 2012).

Table 1 presents the physicochemical properties of polymeric supports declared by Pall, Gelman Laboratory.

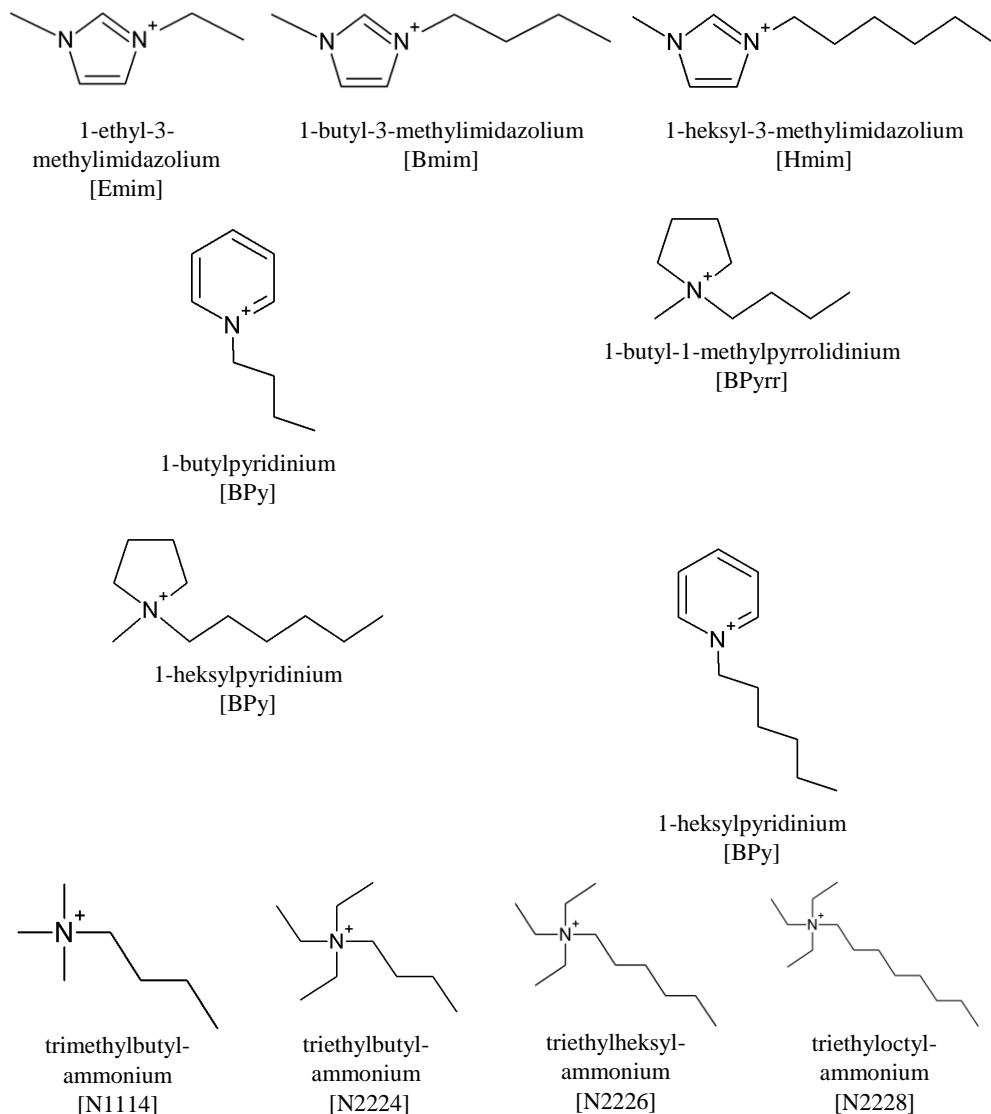


Fig. 1. The structure of ionic liquids cations used in the experiments

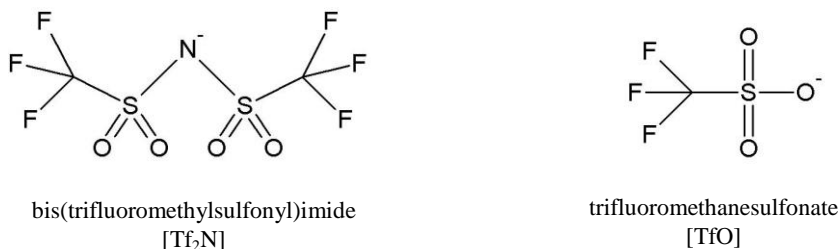


Fig. 2. The structure of ionic liquids anions used in the experiments

Table 1. Physicochemical parameters of polymeric supports*

Membrane	Density [kg/m ³]	Pore size [μm]	Porosity [%]	Thickness [μm]
PP	900	0.2	80	92
PVDF	1790	0.2	80	123
PA	1130	0.2	80	110
PES	1370–1510	0.2	80	148

* data provided by producer

Experimental

Wetting experiments

Contact angles of porous and powdered materials are usually measured using capillary rise method. However, as we have indicated in the previous paper, examined support do not meet assumptions of Washburn equation (Joskowska et al., 2012). In this paper contact angle determination was carried out using the dynamic sessile drop method. The size of membranes pores is much smaller than the drop size, therefore the method could be applied. Dynamic sessile drop study determines the largest contact angle possible without increasing solid/liquid interfacial area by dynamically adding volume of liquid. This maximum angle is the advancing angle θ_a , whereas the smallest possible angle, the receding angle θ_r . The difference between the advancing and receding angle $\theta_a - \theta_r$ is the contact angle hysteresis. The shape of air/liquid interface of a drop is detected using digital system and matched to a numeric model (Sohn et al., 2000). The results are shown in Fig. 9.

The surface tensions of the ionic liquids were determined by the pendant drop method using Tensiometer Krüss DSA 10. The uncertainty of the surface tension measurements was ± 0.2 mN/m.

Traces of water and volatile contaminants were removed from ionic liquids in a vacuum dryer in 353 K for 24 h. The measurements were carried out in 298 K and the relative humidity of the air was 60-70%. The humidity of the air can affect the values of measured surface tension due to hygroscopicity of ILs, therefore the time of

stabilization was not longer than 5 min to minimize the effect. Still, measured values can be loaded with error following the water content fluctuations. The changes in water content after the experiment were not recorded.

Swelling rate experiments

Swelling rate of polymeric supports was determined on the basis of thickness of supports saturated with ionic liquids. Polymer supports and ionic liquids were kept in vacuum dryer VacuCell 55, according to procedure described in literature (Hernandez-Fernandez et al., 2009; Fortunato et al., 2004; 2005). Degassed polymeric supports were saturated with 0.1 cm^3 of ionic liquids per 1.0 cm^2 of support surface. The excess of ionic liquid was removed from membrane surface using blotting paper until the mass of immobilized membrane was stable. Thickness was determined by optical method. The accuracy of this method is better than gravimetric due to difficulties in removing excess ionic liquid from the surface. Measurements were conducted using epi-fluorescent microscope L3001 equipped with digital camera with high resolution. Membrane was placed in glass holder in Z direction according to the procedure described in literature (Izak et al., 2007). Swelling rate was determined using optical method by measuring thickness of the membrane after 2, 24, 72 and 120 hours from the immobilization procedure. In the time intervals between each measurement membranes were kept in a dessicator containing self-indicating silica gel. The humidity of air in the dessicator was 19%.

Results

Wetting experiments

Values of ionic liquids surface tension are located between values for alkanes and for water. There is a large number of publications dealing with surface tension of ionic liquids. Vakili-Nezhaad et al. performed experiments of effect of temperature on the surface tension, density and viscosity of 1-butyl-3-methylimidazolium combined with thiocyanate and tetrafluoroborate anions and 1-hexyl-3-methylimidazolium with tetrafluoroborate and hexafluorophosphate anions and they reported a decrease of physicochemical parameters as the temperature increased (Lee and Prausnitz, 2010). Sanchez et al. provided data on the temperature effect on physicochemical properties of imidazolium, pyridinium and pyrrolidinium ionic liquids, and observed the same trends (Khupse and Kumar, 2010). Similar conclusions were published by Klomfar et al. on the behavior of 1-alkylimidazolium based ionic liquids with hexafluorophosphate anion (Klomfar et al., 2009). The values reported in the literature for the same ionic liquids can differ significantly. The reason is water content in the ionic liquid. Moreover no direct relation between surface tension and alkyl chain length is observed. Sedev performed the attempt to provide an empirical description of the dependence of surface tension and molecular volume. The data set was approximated

with the equation $\gamma = a + bV_M^{-4}$ (Sedev, 2011), where γ is the surface tension and V_M is the molecular volume that was derived from molecular weight (M) and density (ρ) on the basis of the following equation: $V_M = M/(\rho \cdot N_A)$. This approximation is only a guide for the eye. Though, molecular volume is affected by the length of the alkyl chain, other factors should be taken into account when describing the correlation of surface tension and IL structure, like the distribution of intermolecular attractive forces. Moreover, it was reported that ammonium and phosphonium ionic liquids present no correlation between surface tension and molecular volume. It is confirmed by this research (Fig. 3).

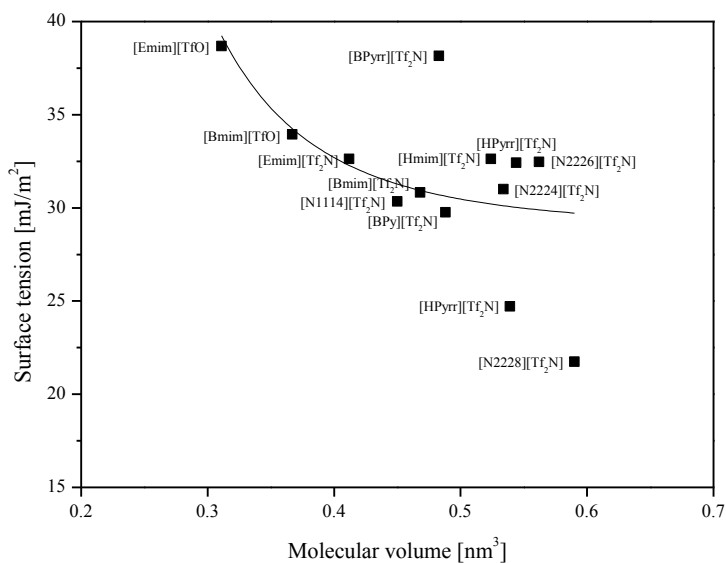


Fig. 3. Surface tension of selected ionic liquids at 298 K

The sessile drop method showed that advancing contact angles of all examined membranes in most cases are below 20 deg. These values demonstrate very good wettability of supports with ionic liquids used in the experiments. Contact angles for imidazolium and pyrrolidinium increase with the alkyl chain length in the ionic liquid cation structure (Figs 4–5). The opposite situation was recorded for ammonium and pyridinium ionic liquids (Figs 6–7).

The parameter deciding on this behaviour is ionic liquid polarity. The polarity of ILs is very sensitive to temperature changes (Lee and Prausnitz, 2010). It has been noticed that the polarity of pyridinium and pyrrolidinium ionic liquid decreases with temperature and this situation is in contrast to that observed for phosphonium ILs (Khupse and Kumar, 2010).

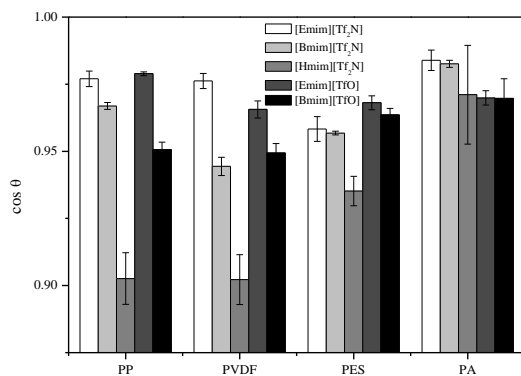


Fig. 4. The relation of carbon atoms number of [C_nmim][Tf₂N] based ionic liquids and cos θ

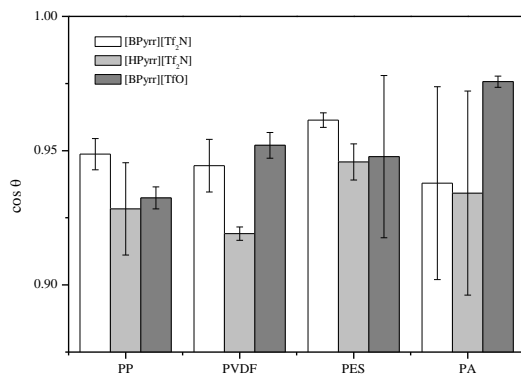


Fig. 5. The relation of carbon atoms number of [C_nPyr][Tf₂N] ionic liquids and cos θ

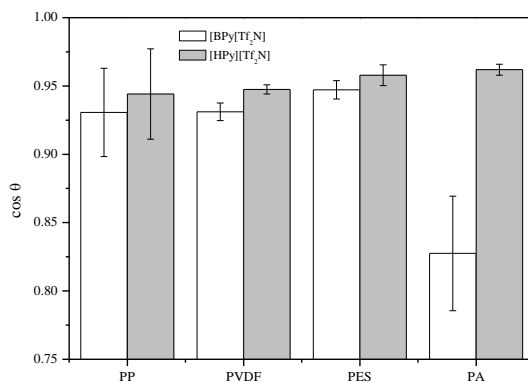


Fig. 6. The relation of carbon atoms number of [C_nPy][Tf₂N] ionic liquids and cos θ

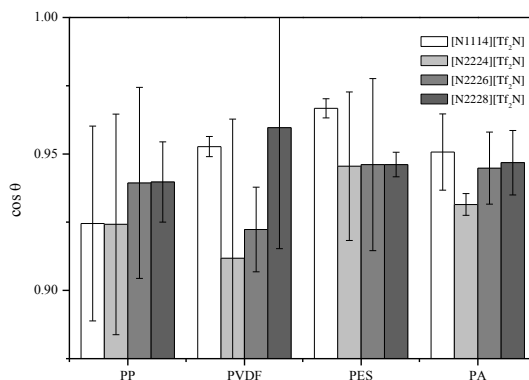


Fig. 7. The relation between carbon atoms number of [Nnnnn][Tf₂N] ionic liquids and $\cos \theta$

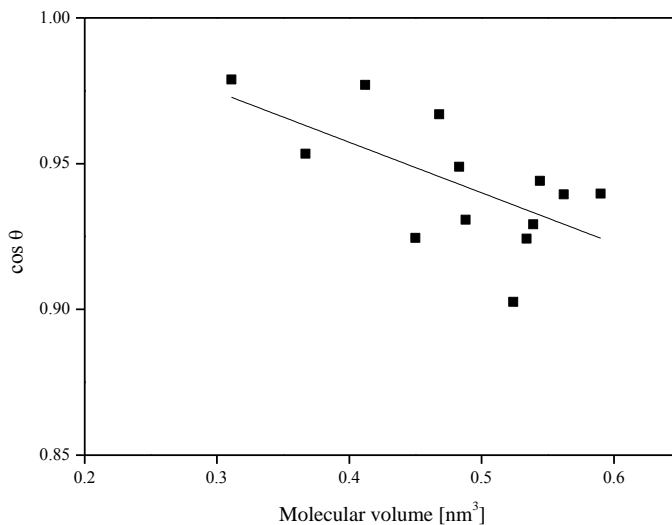


Fig. 8. The dependence of advancing contact angle on polypropylene support on molecular volume of the liquid

Figure 8 presents the overall trend of increasing contact angle value with the increase of molecular volume of ionic liquid and this behavior is preserved for all of examined supports. In most cases the best wettability was obtained for PA support and successively for PP, PES and PVDF.

Supports examined in this study do not meet Young equation foundations, the drop remains in the metastable state and therefore the hysteresis is observed. The hysteresis value is a result of the thermodynamic hysteresis that is dependent on the surface roughness and heterogeneity, and the second one that is the dynamic hysteresis connected to chemical interactions of liquid and solid, penetration of liquid into

polymer pores and the ability of atoms or functional groups to change its positions. The first component is not affected by the time of liquid drop – solid contact, whereas dynamic hysteresis is, and moreover is dependent on the properties of polymer and ionic liquid. The hysteresis of contact angle measured on the PA support was the lowest (Fig. 9), therefore it can be concluded that the heterogeneity and porosity of the PA support surface is the lowest of all examined supports, whereas the highest is observed for PVDF.

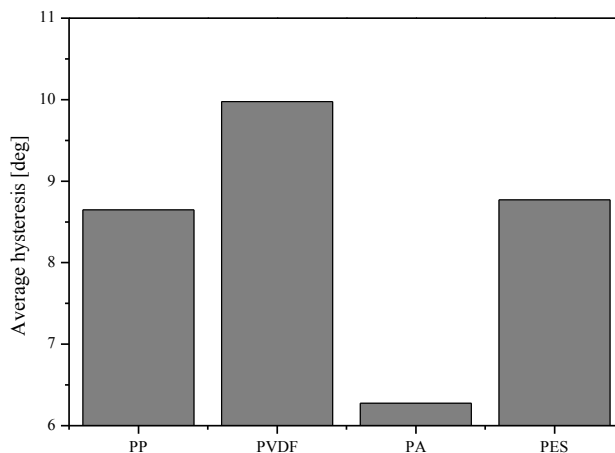


Fig. 9. The average hysteresis of contact angles for examined supports

Swelling rate experiments

Izak et al. (2007) stated, that rate of support swelling depends on the water content in ionic liquid. Therefore, before each experiment, ionic liquids were remained in the vacuum dryer in 343 K for 12 hours. However, swelling effect was observed even if extremely dried ionic liquids were used. Still, the water content could change during the experiments due to water vapor absorption from the atmosphere (Poleski et al., 2013). All the investigated supports showed higher thickness after saturation with ionic liquid. Swelling behavior of polymeric membranes can affect mechanical stability of the membranes and affects value of maximum possible gas pressure without support breakage (Cichowska-Kopczynska et al., 2013).

The obtained results suggest that the longer hydrocarbon chain in the cation structure is, the higher swelling effect is observed. Ionic liquid penetrates into the support pores between polymer particles and fibers and reorientates functional groups, so the particles in the ionic liquid-polymer interface reach the minimum of free interface energy. The longer alkyl chain length the greater space is occupied with the ionic liquid and the greater polymer expansion is observed. Taking into account swelling of the supports, it is observed that the polypropylene support gains similar

thickness immediately after impregnation for all ionic liquids used in the study and it can be assumed that the hysteresis is dependent only on the roughness and heterogeneity of support surface. Further changes in thickness of the supports are

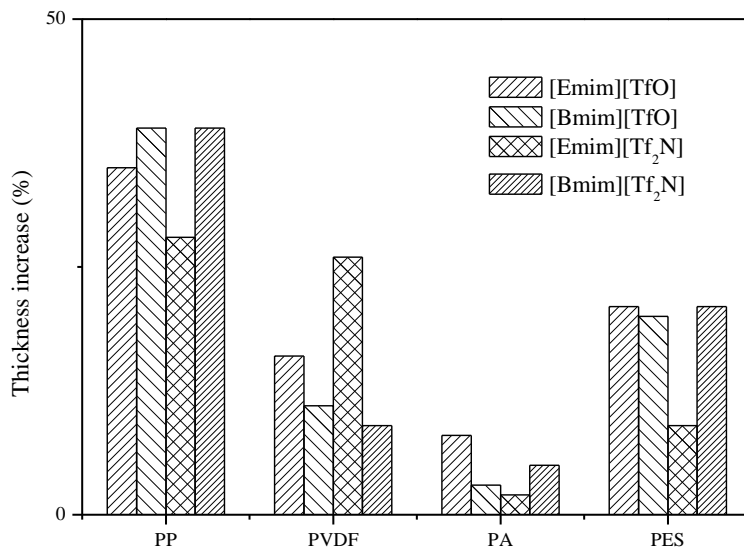


Fig. 10. Thickness increase of supports saturated with imidazolium ionic liquids

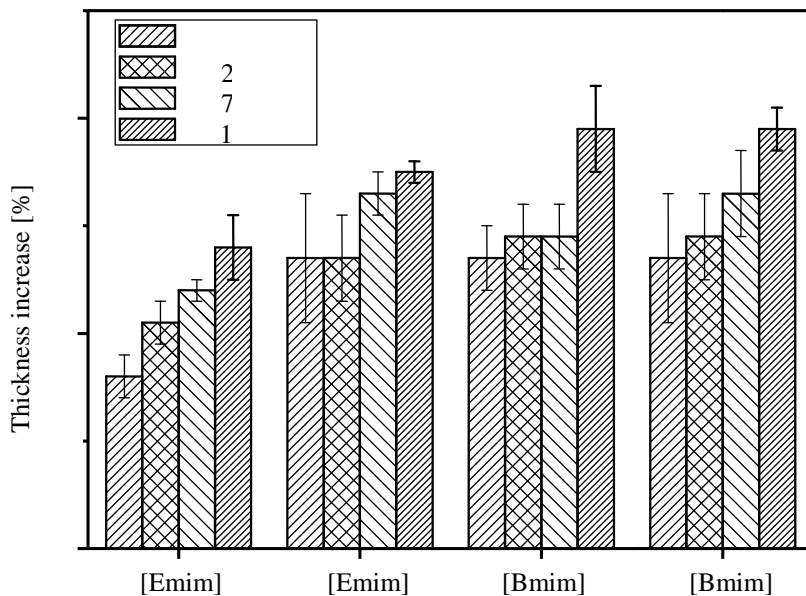


Fig. 11. Thickness increase of polypropylene support saturated with imidazolium ionic liquids

connected to the liquid penetration into the free space between polymer molecules and reorientation ionic liquid structure to the position that is energetically favorable. Polypropylene supports gain about 30–40% of thickness and yet PA ones gain only about 4%, nevertheless wetting of PA occurred to be the best.

The highest thickness increase was observed during two hours since the saturation with ionic liquid was performed. Again, the slight correlation with alkyl chain length and the type of anion is visible for imidazolium ionic liquids in contrast to ammonium, pyridinium and pyrrolidinium. Presumably, this is the consequence of heterogeneity of supports, differences in the structure of each support used in the experiments and possible water gaining from air in the dessicator between measurements. After 120 h since the saturation of supports with ionic liquids, supports gain their terminal thickness. There is no further thickness increase observed.

Conclusions

As indicated by this research, obtaining good effectiveness of the separation process requires proper support and membrane phase, forming stable supported ionic liquid membrane. One of the issues that have to be taken into consideration when choosing proper system should be wettability of the polymeric or ceramic supports in order to ensure that the liquid is not pushed out of the support pores in high pressures. It has been revealed that porous polymer supports are perfectly wetted with ionic liquids, however degradation of polymers is observed in a form of swelling. The surface tension, viscosity, density and contact angles can be tuned by selection of proper combination of cation and anion. Our results confirmed the results of Sedev (2011), hinting that the surface tension of ionic liquids is not directly affected by the alkyl chain length and other factors should be taken into account when describing the correlation of surface tension and IL structure, like the distribution of intermolecular attractive forces. Polymeric supports used in this study occurred to be suitable in order to low values of contact angles. However, due to the high rate of swelling that occurs, mechanical stability should be taken into account. The selection of suitable support is crucial in the development and obtaining highly stable supported ionic liquid membranes.

Acknowledgements

This research was supported by the National Science Centre, grant No. 7563/B/T02/2011/40 under the title Removal of Volatile Organic Compounds from Gas Phase using Ionic Liquids. Financial support of this work was provided also by the National Centre for Research and Development of Poland, grant 04/strategic program/2010 about Advanced Technologies of Energy Generation, Pilot Agricultural Biogas Microstation and Fermentation and Separation of Carbon Dioxide from Biogas with Ionic Liquids Application. We are very grateful for financial support provided by the Ministry of Science and Higher Education, grant no 1815/B/H03/2009/36.

References

- BERTHOD A., RUIZ-ANGEL M.J., CARDA-BROCH S., 2008, *Ionic liquids in separation techniques*, J. Chromatogr. A 1184, 6–18.
- CADENA C., ANTHONY J.L., SHAH J.K., MORROW T.I., BRENNECKE J.F., MAGINN E.J., 2004, *Why is CO₂ so soluble in imidazolium-based ionic liquids?*, J. Am. Chem. Soc. 126, 5300–5308.
- CHIAPPE C., PIERACCIN D., 2005, *Ionic liquids: solvent properties and organic reactivity*, J. Phys. Org. Chem. 18, 275–297.
- CICHOWSKA-KOPCZYNSKA I., JOSKOWSKA M., DĘBSKI B., ŁUCZAK J., ARANOWSKI R., 2013, *Influence of Ionic Liquid Structure on Supported Ionic Liquid Membranes Effectiveness in Carbon Dioxide/Methane Separation*, J. Chem. 2013, 1–10.
- CICHOWSKA-KOPCZYNSKA I., JOSKOWSKA M., WOJCIECHOWSKA A., ARANOWSKI R., 2013, *Preparation and physicochemical characterisation of ceramic supports for supported liquid membranes*, Physicochem. Probl. Miner. Process. 49, 287–300.
- DANESI P.R., REICHLEY-YINGER L., RICKERT P.G., 1987, *Lifetime of supported liquid membranes: the influence of interfacial properties, chemical composition and water transport on the long-term stability of the membranes*, J. Membr. Sci. 31, 117–145.
- DANG-VU T., HUPKA J., 2005, *Characterization of porous materials by capillary method*, Physicochem. Probl. Miner. Process. 39, 47–65.
- EXPERT PANEL OF THE COSMETIC INGREDIENT, 1983, *Final report on the safety assessment of triethanolamine, diethanolamine, and monoethanolamine*, Int. J. Toxicol., 183–235.
- FERRARIS M., SALVO M., SMEACETTO F., AUGIER L., BARBIERI L., CORRADI A., LANCELLOTTI I., 2001, *Glass matrix composites from solid waste materials*, J. Eur. Ceram. Soc. 21, 453–460.
- FORTUNATO R., AFONSO C.A.M., BENAVENTE J., RODRIGUEZ-CASTELLÓN E., CRESPO J.G., 2005, *Stability of supported ionic liquid membranes as studied by X-ray photoelectron spectroscopy*, J. Membr. Sci. 256, 216–233.
- FORTUNATO R., AFONSO C.A.M., REIS A.M., CRESPO J.G., 2004, *Supported liquid membranes using ionic liquids: study of stability and transport mechanisms*, J. Membr. Sci. 242, 197–209.
- FREIE M.G., CARVALHO P.J., FERNANDEZ A.M., MARRUCHO I.M., QUEIMADA A.J., COUTINHO J.A.P., 2007, *Surface tensions of imidazolium based ionic liquids: Anion, cation, temperature and water effect*, J. Colloid Interface Sci. 314, 621–630.
- GAMER A.O., ROSSBACHER R., KAUFMANN W., VAN RAVENZWAAY B., 2008, *The inhalation toxicity of di- and triethanolamine upon repeated exposure*, Food Chem. Toxicol. 46, 2173–2183.
- HERNANDEZ-FERNANDEZ F.J., DE LOS RIOS A.P., ALONSO F.T., PALACIOS J.M., WILLORA G., 2009, *Preparation of supported ionic liquid membranes: Influence of the ionic liquid immobilization method on their operational stability*, J. Membr. Sci. 341, 172–177.
- IZAK P., HOVORKA S., BARTOVSKY T., BARTOVSKA L., CRESPO J.G., 2007, *Swelling of polymeric membranes in room temperature ionic liquids*, J. Membr. Sci. 296, 131–138.
- JOSKOWSKA M., KOPCZYNSKA I., DEBSKI B., HOLOWNIA-KEDZIA D., ARANOWSKI R., HUPKA J., 2012, *Wetting of supports by ionic liquids used in gas separation processes*, Physicochem. Probl. Miner. Process. 48, 129–140.
- KHUPSE N.D., KUMAR A., 2010, *Contrasting Thermosolvatochromic Trends In Pyridinium-, Pyrrolidinium-, and Phosphonium-Based Ionic Liquids*, J. Phys. Chem. B 114, 367–381.
- KITTEL J., IDEM R., GELOWITZ D., TONTIWACHWUTHIKUL P., PARRAIN G., BONNEAU A., 2009, *Corrosion in MEA units for CO₂ capture: pilot plant studies*, Energy Procedia 1, 791–797.

- KLOMFAR J., SOUCKOVA M., PATEK J., 2009, *Surface Tension Measurements for Four 1-Alkyl-3-methylimidazolium-Based Ionic Liquids with Hexafluorophosphate Anion*, J. Chem. Eng. Data 54, 1389–1394.
- LEE J.M., PRAUSNITZ J.M., 2010, *Polarity and hydrogen-bond-donor-strength for some ionic liquids: Effect of alkyl chain length on the pyrrolidinium cation*, Chem. Phys. Lett. 492, 55–59.
- LETCHER T.M., 2007, *Thermodynamics, solubility and environmental issues*, Elsevier, Amsterdam.
- NAPLENBROEK A.M., BARGEMAN D., SMOLDERS C.A., 1992, *Supported liquid membranes: instability effects*, J. Membr. Sci. 67, 121–132.
- NGUYEN L.N., HAI F.I., PRICE W.E., NGHIEM L.D., 2012, *Removal of trace organic contaminants by a membrane bioreactor–granular activated carbon (MBR–GAC) system*, Bioresour. Technol. 113, 169–173.
- POLESKI M., ŁUCZAK J., ARANOWSKI R., JUNGNIKKEL C., 2013, *Wetting of surfaces with ionic liquids*, Physicochem. Probl. Miner. Process. 49, 277–286.
- SCHAFFER A., BRECHTEL K., SCHEFFKNECHT G., 2011, *Comparative study on differently concentrated aqueous solutions of MEA and TETA for CO₂ capture from flue gas*, Fuel 101, 148–153.
- SEDEV R., 2011, *Surface tension, interfacial tension and contact angles of ionic liquids*, Curr. Opin. Colloid Interface Sci. 16, 310–316.
- SOHN W.I., RYU D.H., OH S.J., KOO J.K., 2000, *A study on the development of composite membranes for the separation of organic vapors*, J. Membr. Sci. 175, 163–170.
- TADKAEW N., HAI F.I., MCDONALD J.A., KHAN S.J., NGHIEM L.D., 2011, *Removal of trace organics by MBR treatment: the role of molecular properties*, Water Res. 45, 2439–2451.
- TERAMOTO M., SAKAIDA Y., FU S., OHNISHI N., MATSUYAMA H., MAKI M., FUKUI T., ARAI K., 2000, *An attempt for the stabilization of supported liquid membrane*, Sep. Purif. Technol. 21, 137–144.
- TRONG D., HUPKA J., DRZYMAŁA J., 2006, *Impact of roughness on hydrophobicity of particles measured by the Washburn method*, Physicochem. Probl. Miner. Process. 40, 45–52.
- TRONG D., HUPKA J., 2005, *Characterization of porous materials by capillary rise method*, Physicochem. Probl. Miner. Process. 39, 47–65.
- WALCZYK H., 2006, *Niskotemperaturowa kondensacja lotnych związków organicznych w obecności gazu inertnego w spiralnym wymienniku ciepła*, Prace Naukowe ICh PAN 6, 7–127.
- WASSERSCHIED P., KEIM W., 2000, *Ionic Liquids – New „Solutions“ for Transition Metal Catalysis*, Angew. Chem. Int. Ed. 39, 3772–3789.

Received May 29, 2013; reviewed; accepted August 11, 2013

A STUDY OF SELECTED PROPERTIES OF RHENIUM SULPHIDE DISPERSION

Dariusz W. PAWLAK*, **Jozef L. PARUS***, **Ewa SKWAREK***,
Wladyslaw JANUSZ**

* Radioisotope Centre POLATOM, National Centre for Nuclear Research, Otwock, Poland

** Maria Curie Skłodowska University, Pl. M. Curie Skłodowskiej 3, 20-031 Lublin, Poland
wladyslaw.janusz@umcs.lublin.pl

Abstract: Due to potential application of rhenium sulphide in medicine and industry, this study is focused on the properties of synthetic and commercial rhenium sulphide. The main reaction of rhenium sulphide preparation involves potassium perrhenate and sodium thiosulphate in the acidic environment giving a mixture of rhenium sulphide and sulphur. The next step is removing sulphur by its dissolution in ether. Stabilization by Povidone K-25 is needed to obtain rhenium sulphide dispersed with the grain size of 0.5–4 μm . The extrapolated value of pH_{iep} for synthesised rhenium sulphide is 2.3 whereas for commercial samples this value is lower than 2. For synthetic sample a dependence of zeta potential on the carrier electrolyte concentration is found. It is larger than that for the commercial sample, probably due to surface oxidation during synthesis or purification.

Keywords: *rhenium sulphide, particle size distribution, zeta potential*

Introduction

The method of rhenium sulphide preparation and its properties are studied in relation to its potential application in nuclear medicine as a catalysts in hydrogenation, hydrodesulphurization, hydronitriding (Klett et al., 2007, De Los Reyes, 2007) as well as in the form of nanoparticles in electronics (Coleman et al., 2002). Rhenium sulphide is the most common carrier of radioactive rhenium in nuclear medicine (Junfeng et al., 2007). Though there have been developed a number of procedures for sulphide preparation, they produce rhenium sulphides of different structures which is still the subject of studies.

Traore described preparation of Re_2S_7 using the acidified solution of potassium perrhenate and thiosulphate or hydrogen sulphide (Escalona et al., 2007). After annealing at 110 °C for a few days, the obtained black precipitate was identified as

Re_2S_7 of the tetragonal structure. According to the authors, this sulphide can be readily decomposed in hydrogen atmosphere to give amorphous rhenium trisulphide, ReS_3 , which is a precursor of rhenium disulphide, ReS_2 . It can be obtained in vacuum at high temperature as the reaction product of metallic rhenium and elementary sulphur. It is regarded as the most stable rhenium sulphide. It has a hexagonal structure ($a = 3.14$ and $c = 12.2$ Å), but its parameters can differ insignificantly depending on the excess of sulphur.

Amorphous Re_2S_7 was also obtained in the reaction of potassium perrhenate and sodium thiosulphate in the acidic medium and studied by means of X-ray adsorption XAS method. The results showed that it has the rhombic cluster with metal-metal combination as a basic unit of the structure (Hibble et al., 1996).

The studies carried out by Schwarz et al. (2004) on the ReS_4 , Re_2S_7 , ReS_2 characteristics indicate the presence of sulphur in the forms S^{2-} and S_2^{2-} in the compounds ReS_4 and Re_2S_7 whereby the content of S_2^{2-} in both ReS_4 and Re_2S_7 is larger than that in S^{2-} . The authors also suggest that the phases ReS_4 and Re_2S_7 are closely structurally connected. Given the fact that both sulphides transform into ReS_2 during heating, they proposed to treat them as components of the continuous structure $\text{ReS}_{1.5-1}(\text{S}_2)_{1-1.5}$ which differs in the $\text{S}_2^{2-}/\text{S}^{2-}$ ratio.

Startsev et al. (1996) described the preparation of ReS_2 by means of the reaction of HReO_4 with H_2S at 450°C . The TEM studies revealed the presence of spheres of a diameter ~ 6 Å which is consistent with the inner distance $d_{002} = 6.1$ Å in the ReS_2 structure. However, the studies using the X-ray diffraction method showed that the structure is strongly disordered. Similarly, spherical ReS_2 particles of the size 0.1 to 1 µm were obtained as a result of the reaction of ReCl_4 with Li_2S in ethyl acetate. The XRD studies confirmed partially crystalline structure of the obtained substance.

For the purpose of the use in radiosynovectomy some attempts were made to synthesize colloidal rhenium sulphide based on the reaction of potassium perrhenate solution with thiosulphate solution in the acid medium (Junfeng et al., 1999) or using the method described by Tui and Denizot (Tu et al., 2007) in which the reagents (sodium thiosulphate and potassium perrhenate) were added in the solid state to the ethyl glycol/ethanol/distilled water mixture.

Though ReS_2 was investigated by many scientists, its structure is still studied. Murray et al. (1994) claim that ReS_2 has a triclinic crystalline structure and the elementary cell is characterized by the parameters: $a = 6.417$ Å, $b = 6.510$ Å, $c = 6.461$ Å, $\alpha = 121.10^\circ$, $\beta = 88.38^\circ$, $\gamma = 106.47^\circ$. The structure described by the authors is composed of asymmetric elementary cells with almost hexagonal, closed and packed layers.

In this paper the electrokinetic properties, particle size distribution and FTIR study of rhenium sulphide dispersions are presented. The electrokinetic properties as a function of pH reflect acid base properties of surface groups that may be interesting for catalytic behaviour of this compound (Stelzer et al., 2005). Moreover, the study of the particle size distribution of the rhenium sulphide suspension in the presence of

gelatin and Povidon K-25 can be interesting for pharmaceutical applications in the radiosynovectomy.

Experimental

Materials and methods

The studies were carried out using a commercial Re_2S_7 sample purchased from Alfa Aesar and the rhenium sulphide sample prepared according to the Jungfeng et al. procedure. The XRD analysis of the commercial Re_2S_7 showed its amorphous structure. The synthesis performed according to the Jungfeng et al. (1999) procedure confirmed that the concentration ratio of the solutions, $\text{Na}_2\text{S}_2\text{O}_3:\text{KReO}_4 = 70:1$ at the concentrations of $C_{\text{Na}_2\text{S}_2\text{O}_3}$ equal to 0.0394 M and C_{KReO_4} to 0.000563 M, and the heating time 30 min is optimal. Using this procedure the synthesis was repeated many times to determine the sulphur content in the samples and to remove elementary sulphur.

Methods of measurements

Measurement of particle size distribution was made using the Mastersizer 2000 apparatus (Malvern) with the hydro 2000 μP (A) unit. The suspension containing 0.05 g sample in 50 ml of water was transferred to the measuring cell. The rate of suspension flow through the measuring cell was chosen adjusting the rotation speed of the pump and ultrasound intensity.

Distribution of sulphide particle sizes after washing the sample in the aqueous medium and dispersion subjected to stabilization using gelatin and Povidone K-25 were measured.

Zeta potential measurements of NaCl solution of the concentrations of 1, 10^{-1} , 10^{-2} , 10^{-3} M NaCl were made using the Zetasizer 3000 apparatus (Malvern). 0.02 g of commercial rhenium sulphide was added to the solution of a given concentration and subjected to dispersion using the ultrasound probe Sonicator XL 2020 (Misonix). Then, the suspension was transferred into 125 ml flasks, and pH was adjusted in the range from 3 to 9 in the presence of nitrogen using 0.1 M HCl and NaOH solutions. Four measurements of zeta potential were made for each solution. Infrared spectra were registered by means of the FTIR spectrometer Nicolet 8700A with the smart Orbit TR diamond ATR module.

Results and discussion

Specific surface area of Re_2S_7

As follows from the characteristics of the surface area of rhenium sulphide samples in Table 1, the studied samples have a similar specific surface area determined by the

BET method, whereas the synthetic samples are characterized by a slightly larger pore volume and larger average pore radius.

Table 1. Characteristics of the specific surface area and porosity of the commercial and synthetic rhenium sulphides

Rhenium sulphide	Commercial.	Synthetic
Surface area from the BET isotherm [m^2/g]	5.18	6.26
Surface area from the Langmuir isotherm [m^2/g]	7.45	9.11
Total pore volume from adsorption $1.7 \text{ nm} < d <$ and 300 nm diameter calculated by means of the BJH method [cm^3/g]	0.025	0.018
Total pore volume from desorption $1.7 \text{ nm} < d <$ and 300 nm diameter calculated by means of the BJH method [cm^3/g]	0.025	0.0185
Average pore radius from adsorption – BJH method [nm]	17.86	12.9
Average pore radius from desorption – BJH method [nm]	16.1	10.5

Measurement of particle sizes

As follows from the comparison of Re_2S_7 particle size distribution before and after the ultrasound treatment, the commercial sample contains a large number of aggregates of different particle sizes from 1 to 1000 μm whereby the fraction $>30\mu\text{m}$ in the sample not subjected to the ultrasound treatment is predominant. Treating the sample with ultrasounds for 6 min causes its unification and the particle size is from 0.2 to 2 μm (Fig. 1). Both numerical and volumetric distributions indicate monomodal particle distribution. The numerical distribution is characterized by: $d(0.1) = 0.27 \mu\text{m}$, $d(0.5) = 0.40 \mu\text{m}$ and $d(0.9) = 0.73 \mu\text{m}$.

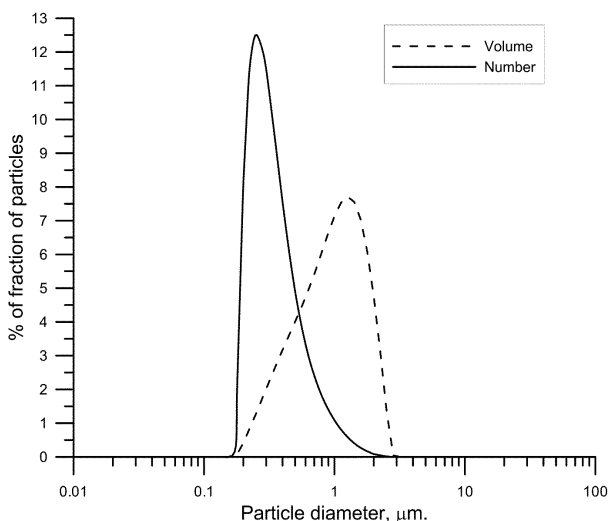


Fig. 1. Volumetric and numerical particle size distribution of the commercial sample Re_2S_7 after the six-minute ultrasound action

Figure 2 presents the volumetric particle size distribution of rhenium sulphide synthesized according to the Junfeng et al. procedure. As can be seen the radius of particles is from 3 to 50 μm . Because during the Junfeng et al. (1999) synthesis of rhenium sulphide the precipitation of elementary sulphur takes place and kinetics of precipitation of rhenium sulphide and sulphur is fast, so it is difficult to control the precipitation process. In the following experiments sulphur was removed by dissolution in ether. In several runs 1.16 g of precipitate was produced and it was washed with 400ml of ether. From the mass loss (0.5731 g) it was calculated that the content of elementary sulphur in the sample was 49%. After sulphur removal the rhenium sulphide sample was subjected to the particle size analysis (Fig. 2).

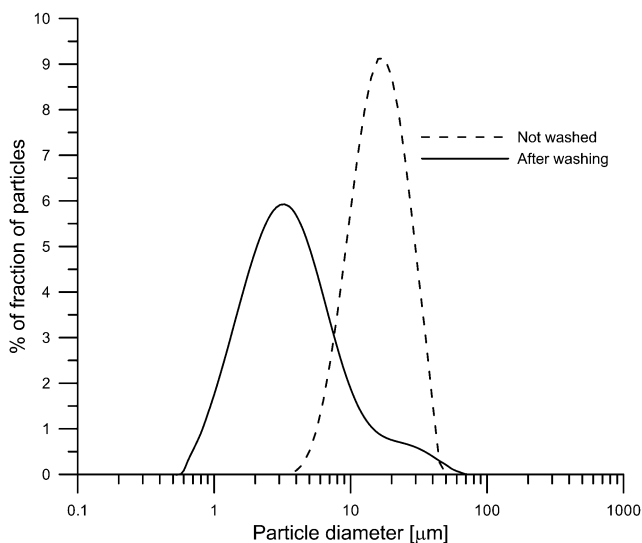


Fig. 2. Particle size distribution of the rhenium sulphide sample after sulphur washing

Table 2. Quantities characterizing the particle size distribution of the rhenium sulphide sample after washing with ether and stabilized with the pharmaceutical gelatine solution (2.3 mg/ml)

V ml	Dose mg/g	$d(0.1)$ μm	$d(0.5)$ μm	$d(0.9)$ μm
0	0	1.27	3.24	10.62
3	138	1.09	2.43	6.62
6	276	0.84	1.76	3.74
10	460	2.62	91.66	162.5
20	920	0.86	2.02	18.08

Washing the obtained precipitate with ether changed the grain size distribution increasing the contribution of smaller agglomerates. Repetition of syntheses and washings with ether resulted in similar distribution of grain size as shown in Fig. 2.

Analyzing the particle size distribution in Fig. 3 and the quantities characterizing the particle size distribution in Table 2 one can see that the optimal dose for suspension stabilization is 276 mg/g. When this dose is larger the steric aggregation process is observed. When it is lower the gelatine stabilization process is not sufficiently efficient.

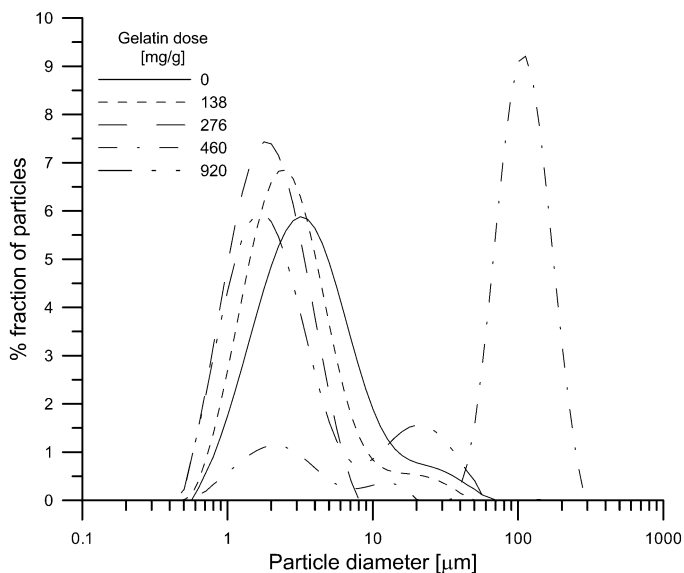


Fig. 3. Particle size distribution of the rhenium sulphide sample stabilized with gelatine

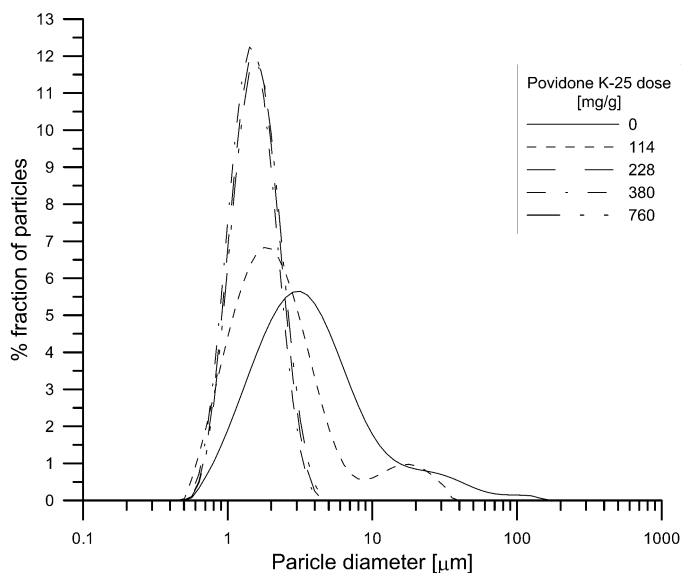


Fig. 4. Particle size distribution of the rhenium sulphide sample stabilized with Povidone K-25

Table 3. Quantities characterizing particle size distribution of rhenium sulphide sample after washing with ether and stabilizing with Povidone K-25 (1.9 mg/ml)

V [ml]	Dose mg/g	d (0.1) μm	d (0.5) μm	d (0.9) μm
0	0	1.27	3.24	10.62
3	114	0.89	1.92	6.62
6	228	0.90	1.44	2.31
10	380	0.87	1.39	2.21
20	760	0.92	1.48	2.39

Application of 228 mg/g dose of the Povidone K-25 resulted in the shift of suspension particle size distribution towards smaller particle size, $d(0.5) = 1.4 \mu\text{m}$. Like for gelatine, this dose was sufficient for dispersion of rhenium sulphide aggregates due to steric stabilization. However, compared to other stabilizers the essential difference was that successive increase in the Povidone K-25 dose did not cause suspension destabilization and the obtained particle size distribution of the sample remained unchanged.

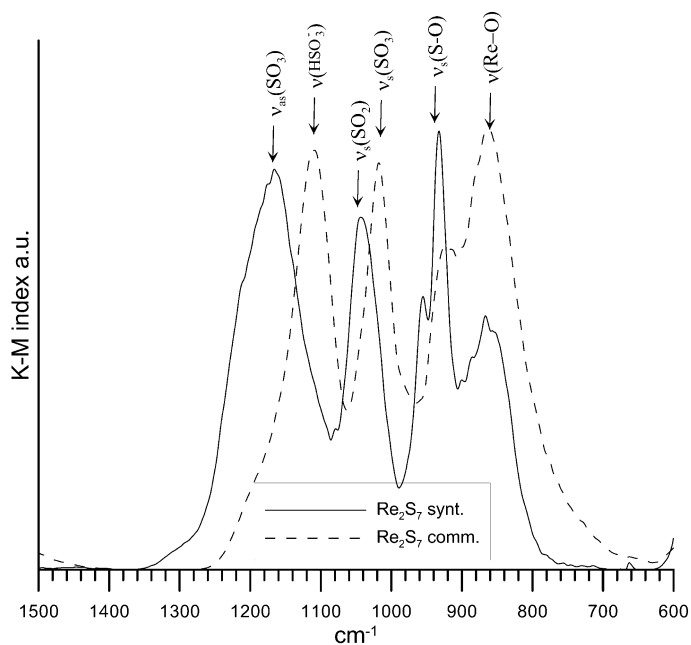


Fig 5. FTIR spectra of rhenium sulphide samples

Figure 5 presents the FTIR ATR spectra of the commercial rhenium sulphide sample and the sample prepared by synthesis. The commercial sample is characterized

by vibration bands at the wave numbers 1109.1, 1018.05, 922.5 and 863.25 cm^{-1} . The stretching vibrations (the bond Re-O) are responsible for the band at 863.25 cm^{-1} (Luo et al., 2004), whereas stretching (ν) vibrations of hydrosulphite ions are responsible for the band at 1109.1 cm^{-1} (Herlinger and Long, 1969). The bands at 1018.05 and 922.5 cm^{-1} result from the stretching vibrations of S-O groups in $\text{S}_2\text{O}_5^{2-}$ (Townsend et al., 2012). In the case of the sample prepared by the synthesis, the bands at 1166.1 and 1042.05 cm^{-1} formed due to stretching bonds in the sulphate group are visible (Peak et al., 1999).

Zeta potential

Figure 6 presents the change of the zeta potential of the commercial rhenium sulphide as a function of pH and electrolyte concentrations. As can be seen the potential decreases with the increasing pH and the background electrolyte concentration. However, within the given background electrolyte concentration the difference in the zeta potential is only about 15 mV. It should be mentioned that for all concentrations the zeta potential is negative which is characteristic of most metal sulphides because sulphide surface is rather easily oxidized which results in the presence of acidic groups and low pH_{iep} . The point pH_{iep} determined by extrapolation from the dependence of zeta potential on pH has the value of about 2. A similar shape of zeta potential as a function of pH and electrolyte concentration was observed for the zinc sulphide/NaCl solution system (Zhang et al., 1995). The charge formation at the sulphide/solution interface comes from the acid-base reactions of the =SH and =ZnOH groups as well as desorption/adsorption of Zn^{2+} ions (Rönngren et al., 1991).

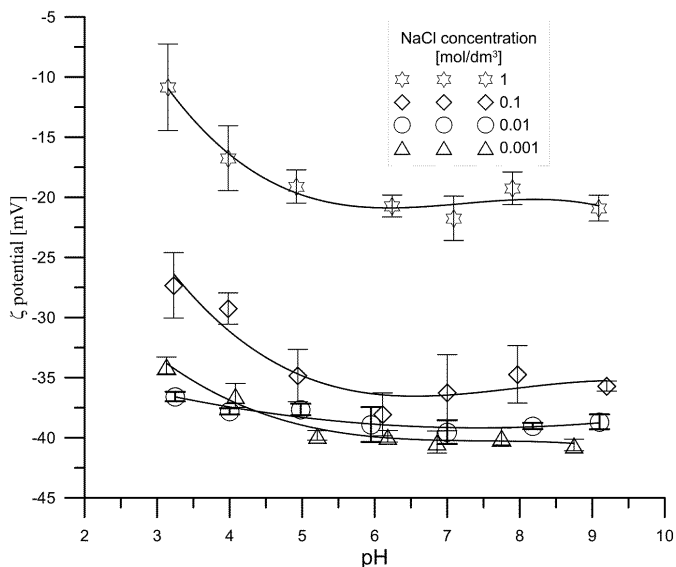


Fig. 6. Dependence of ζ potential of commercial rhenium sulphide in NaCl solutions as a function of pH

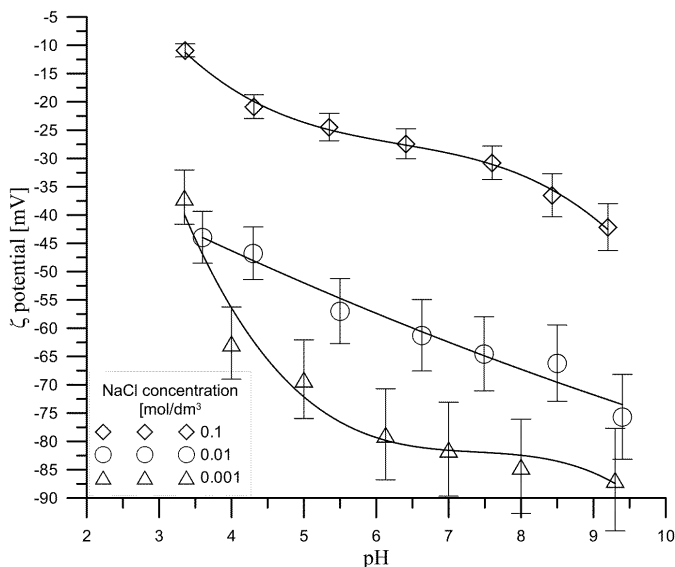


Fig. 7. Dependence of ζ potential of synthetic rhenium sulphide in NaCl solutions as a function of pH

Figure 7 presents the dependence of zeta potential of synthetic rhenium sulphide on pH in NaCl solutions of different background electrolyte concentrations. Like in the case of commercial rhenium sulphide the decrease in the zeta potential value with the increasing pH is observed. However, contrary to the commercial rhenium sulphide, the background electrolyte concentration in the case of the synthetic one has a stronger effect on the zeta potential value. In the case of the synthetic rhenium sulphide sample there were found surface sulphate groups (Fig. 5), formed due to oxidation of the sulphide surface, but sulphate ions can readily pass into the solution (Gård et al., 1995). However, these ions can take part in the surface group complexation reaction and compete with the adsorption of background electrolyte ions. It was shown that copper sulphide oxidation results in the increasing zeta potential value as the hydrogen sulphate groups are replaced on the sulphide surface with the hydroxyl groups (Fullston et al., 1999). In the case of rhenium sulphide, rhenium oxide formed due to oxidation is characterized by acidic properties $\text{pH}_{\text{iep}} = 4.22$ (Luxton et al., 2011). Thus stronger dependence of zeta potential on the electrolyte concentration, as in the case of many oxides, was observed for synthetic rhenium sulphide. As in the case of synthetic sulphide, sulphate groups were found which can form surface complexes with rhenium hydroxyl groups and in which sulphate ion can be exchanged into chloride ion of the background electrolyte. Thus, synthetic rhenium sulphide can exhibit dependence on pH and electrolyte concentration.

Conclusions

Synthesis of rhenium sulphide through the reaction of potassium perrhenate with sodium thiosulphate in the acidic medium leads to the preparation of the rhenium sulphide and sulphur mixture. In order to obtain pure sulphide it is necessary to remove sulphur by its dissolution in ether. To obtain rhenium sulphide in the form of dispersion of the grain sizes 0.5–4 μm it requires dispersion stabilization using Povidone K-25. The extrapolated pH_{Hiep} value of synthetic rhenium sulphide is 2.3 for 0.001 mol/dm³ NaCl. As for the commercial sample the extrapolated value pH_{Hiep} is lower than 2. The synthetic sample exhibits stronger dependence of the zeta potential on the background electrolyte concentration than the commercial one due to surface oxidation during synthesis and/or purification.

References

- COLEMAN K.S., SLOAN J., HANSON N.A., BROWN G., CLANCY G.P., TERRONES M., TERRONES H., GREEN M.L.H., 2002, *The Formation of ReS₂ Inorganic Fullerene-like Structures Containing Re₄ Parallelogram Units and Metal-Metal Bonds*, J. Am. Chem. Soc., 124, 11580–11581.
- DE LOS REYES J. A., 2007, *Ruthenium sulphide supported on alumina as hydrotreating catalyst*, Appl. Catal. A. 322, 106–112.
- ESCALONA N., VRINAT M., LAURENTI D., GIL F.J., 2007 *Llambí'as, Rhenium sulphide in hydrotreating*, Appl. Catal. A. 322, 113–120.
- FULLSTON D., FORNASIERO D., RALSTON J., 1999, *Zeta potential study of the oxidation of copper sulphide minerals*: Colloids and Surfaces A: Physicochem. Eng. Aspects 146, 113–121.
- GÄRD R., SUN Z., FORSLING W., 1995, *FT-IR and FT-Raman Studies of Colloidal ZnS: 1. Acidic and Alkaline Sites at the ZnS/Water Interface*, J. Colloid Interface Sci., 169, 393–399.
- HERLINGER' A.W., LONG T.V., 1969, *An Investigation of the Structure of the Disulfite Ion in Aqueous Solution Using Raman and Infrared Spectroscopies*, Inorg. Chem., 8, 2661–2665.
- HIBBLE S. J., WALTON R.I., 1996, *X-Ray absorption studies of amorphous Re₂S₇*. Chem. Commun., 169, 393–399.
- JUNFENG, Y. DUANZHI, M. XIAOFENG, G. ZILI, Z. JIONG, W. YONGXIAN, F.F. KNAPP JR., 1999, *[¹⁸⁸Re] Rhenium Sulphide Suspension: A Potential Radiopharmaceutical for Tumor Treatment Following Intra-Tumor Injection*, Nucl. Med. Biol., 26, 573–579.
- KLETT R., LANGE U., HAAS H., VOTH M., PINKERT J., 2007, *Radiosynoviorthesis of medium-sized joints with rhenium-186-sulphide colloid: a review of the literature*, Rheumatology; 46(10), 1531–1537.
- LUO J., ALEXANDER B., WAGNER T.R., MAGGARD P.A., 2004, *Synthesis and Characterization of ReO₄-Containing Microporous and Open Framework Structures*, Inorg. Chem., 43, 5537–5542.
- LUXTON T.P., EICK M.J., SCHECKEL K.G., 2011, *Characterization and dissolution properties of ruthenium oxides*, J. Colloid Interface Sci., 359, 30–39.
- MURRAY H.H., KELTY S.P., CHIANELLI R.R., 1994, *Structure of Rhenium Disulphide*, Inorg. Chem., 33, 4418–4420.
- PEAK D., FORD R.G., SPARKS D.L., 1999, *An in Situ ATR-FTIR Investigation of Sulfate Bonding Mechanisms on Goethite*, J. Colloid Interface Sci. 218, 289–299.

- RÖNNGREN L., SJÖBERG S., SUN Z., FORSLING W., SCHINDLER P.W., 1991, *Surface reactions in aqueous metal sulphide systems: 2. Ion exchange and acid/base reactions at the ZnS single bond H₂O interface*. J. Colloid Interface Sci., 145, 396–404.
- SCHWARZ D.E., FRENKEL A.I., NUZZO R.G., RAUCHFUSS T.B., VAIRAVAMURTHY A., 2004, *Electrosynthesis of ReS₄. XAS Analysis of ReS₂, Re₂S₇, and ReS₄*. Chem. Mater., 16, 151–158.
- STARTSEV A.N., RODIN V.N., ZAIKOVSKII V.I., KALINKIN A.V., KRIVENTSOV V.V., KOCHUBEI D.I., 1996, *Silica-supported Sulphide Catalysts: IX. Synthesis and Properties of Structural Analogs of the Active Component of Hydrodesulphurization Catalysts*. Kinet. Catal., 38 (4) 548–555.
- STELZER J.B., NITZSCHE R., CARO J., 2005, *Zeta Potential Measurement in Catalyst Preparations*. Chem. Eng. Technol., 28, 182–186.
- TOWNSEND T.M., ALLANIC A., NOONAN C., SODEAU J.R., 2012, *Characterization of Sulphurous Acid, Sulfite, and Bisulfite Aerosol Systems*, J. Phys. Chem. A., 116, 4035–4046.
- TU W., DENIZOT B., 2007, *Synthesis of small-sized rhenium sulphide colloidal nanoparticles*, J. Colloid Interface Sci., 310, 167–170.
- ZHANG Q., XU Z., FINCH J.A., 1995, *Surface Ionization and Complexation at the Sphalerite/Water Interface: I. Computation of Electrical Double-Layer Properties of Sphalerite in a Simple Electrolyte*, J. Colloid Interface Sci., 169, 468–475.

Received August 1, 2013; reviewed; accepted August 29, 2013

LEACHING KINETICS OF COPPER FROM CHALCOPYRITE CONCENTRATE IN NITROUS-SULFURIC ACID

Ozge GOK*, **Corby G. ANDERSON****, **Gorkem CICEKLI***, **E. Ilknur COCEN***

* Mining Engineering Dept., Faculty of Engineering, Dokuz Eylul University, Izmir, 35160, Turkey;
e-mail: ozge.solak@deu.edu.tr

** Department of Metallurgical and Materials Engineering, Colorado School of Mines, CO, 80401, USA

Abstract: Treating chalcopyrite flotation concentrates by hydrometallurgical techniques seems to be the most convenient method for leaching copper due to concerns over air pollution and regulations regarding the emission of sulfur dioxide that result from smelting. In this study, the leaching recovery-time trajectories of bulk chalcopyrite concentrate obtained from a flotation plant in the Kastamonu region of Turkey are presented. The effects of various parameters were elucidated in the nitrous-sulfuric acid electrolyte (C_{NaNO_2} :0.05 M–0.15 M, $C_{\text{H}_2\text{SO}_4}$:1 M) at a moderate temperature (80–120 °C). A high level of copper recovery (98%) from bulk chalcopyrite concentrate was obtained under a total pressure of 6 atm at 120°C within 2 h when using small amounts of nitrite species due to their autocatalytic behavior in acidic solutions. The kinetics were well correlated with the shrinking core model for the diffusion controlled mechanism with an apparent activation energy of 34.06 kJ·mol⁻¹. Elemental sulfur was the primary leaching product on the mineral surface, as confirmed using XRD and SEM/EDX. The semi-empirical equation explaining the reaction rate under the present conditions was expressed as follows:

$$1 - \frac{2}{3}X - (1 - X)^{\frac{2}{3}} = 56.53 \cdot 10^{-4} C_{\text{NaNO}_2}^{0.96} \gamma_0^{-0.83} e^{-\frac{4096.7}{T}t}$$

Keywords: *chalcopyrite, pressure leaching, nitrogen species, kinetics*

Introduction

Concerns over air pollution and strict environmental regulations regarding the emission of sulfur dioxide, combined with the increased demand of treating complex chalcopyrite ores and concentrates with high recoveries, have led to the development of hydrometallurgical processes as alternatives to smelting. Advances in construction materials, successful implementation of autoclave technology and development of

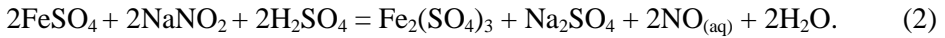
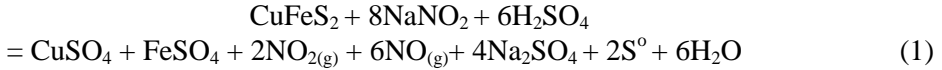
more efficient mills for the fine or ultrafine grinding of sulfides have made chalcopyrite concentrate leaching more reliable and cost-competitive (Wang, 2005).

In the last two decades, although some hydrometallurgical processes have been conducted at the lab/pilot scale, only a few have been built at the plant scale (Corrans and Angove, 1993; Dreisinger et al., 2003; Jones, 1996; Kofluk and Collins, 1998; Dreisinger et al., 2002; Stanley and Submanian, 1977; Ferron et al., 2001; Marsden et al., 2003). Typically, most of these methods promote the oxidation of copper from chalcopyrite concentrate in the presence of several species such as ferric ions, ferrous ions, cupric ions, silver ions, bacteria, pyrite and oxygen (Dixon et al., 2008; Dreisinger and Abed, 2002; Dutrizac et al., 1969; Hackl et al., 1995; Hirato et al., 1987; Hiroyoshi et al., 2000; Linge, 1976; Miller and Portillo, 1979; Munoz et al., 1979).

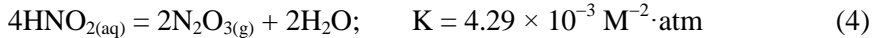
Sulfuric acid processing with the addition of a small amount of nitrogen species has been employed for a long time in some industrial applications. The first patented commercial process by Sunshine Precious Metals (Idaho, USA) used a sulfuric and dilute nitric acid mixture to leach silver- and copper-bearing ores (Caldon, 1978). Subsequently, "nitric acid" leaching was practiced under various process acronyms such as NSL (Brennecke et al., 1981), NITROX (Van Weert et al., 1986), ARSENO, and REDOX (Beattie et al., 1989). More recently, a novel process involving nitrogen species-catalyzed pressure leaching (NSC) was commissioned and performed successfully on an industrial scale at Sunshine Precious Metals (Anderson et al., 1992; Anderson et al., 1993). It was reported that silver and copper were successfully recovered from a complex sulfide concentrate at temperatures between 145°C and 155°C and at a total pressure of 7 atm (Ackerman et al., 1993). The NSC pretreatment process was proposed as a potential alternative process capable of being performed at "modest" process temperatures and pressures (125-170°C and 6-10 atm) and with a lower oxygen demand (associated with the partial oxidation of sulfide to zero-valence sulfur). The process employs sulfuric acid to achieve high proton activity, oxygen/air as the primary oxidant, and a low concentration of nitrite, which, in a broad sense, acts in a "catalytic" role (Baldwin and Van Weert, 1996; Anderson, 2003). The reasons for favoring nitrogen species are (i) they are powerful oxidizing agents, (ii) the NO_x gases produced (NO, NO₂, etc.) remove other reaction products from the mineral surfaces, (iii) high temperatures increase the reaction rates, and (iv) the oxidant can be regenerated autocatalytically.

Reaction Sequence of Chalcopyrite Dissolution

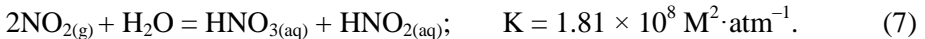
The complex chemistry of chalcopyrite leaching in acidic nitrite electrolyte can be explained based on data (Gok and Anderson, 2013) for the CuFeS₂-H₂SO₄-NaNO₂-H₂O system as follows:



In that study, it was found that both nitric oxide ($\text{NO}_{(\text{g})}$) and nitrogen dioxide ($\text{NO}_{2(\text{g})}$) were most likely to be generated as products of chalcopyrite leaching with nitrite. During the oxidation, in addition to $\text{NO}_{(\text{g})}$ and $\text{NO}_{2(\text{g})}$, the system may contain a number of other nitrogen compounds (HNO_2 , N_2O_4 , NO_2^- , N_2O_3 , HNO_3 and NO_3^-) that have various catalytic activities. Nitrous acid (HNO_2) has been predicted to be the most kinetically reactive form when nitrite salt is introduced into the acidic solution. The two-step disproportionation reaction mechanism of HNO_2 to $\text{NO}_{(\text{g})}$ and $\text{NO}_{2(\text{g})}$ has been described by Eqs. 3-5 (Park and Lee, 1988).



The convincing work by Markovitz et al. (1981) showed that the rate of homolysis of $\text{N}_2\text{O}_{3(\text{g})}$ to $\text{NO}_{(\text{g})}$ and $\text{NO}_{2(\text{g})}$ was much greater than hydrolysis to HNO_2 . Nitric oxide is more likely to be in the gas phase due to its lower solubility and is re-oxidized to HNO_2 in the oxidizing environment (Awad and Stanbury, 1993), as indicated in Eq. 6. Nitrogen dioxide immediately reacts with water to form two oxyacids, nitric acid and nitrous acid (Kameoka and Pigford, 1977), according to Eq. 7. The cyclic NO_x redistribution mechanism is completed by this equilibrium, and only one fourth of the initial amount of nitrous acid is lost. Finally, all of the nitrogen species that evolve in the electrolyte from the nitrite salt, except $\text{NO}_{(\text{g})}$, are oxidized to nitrate (NO_3^-) (Gok, 2009).



The reaction scheme explained above takes into account both the steady-state absorption of NO_x gases into the electrolyte and the disproportionation reactions. These non-elementary reaction steps also give a more complete understanding of the regeneration process.

The present study provides an extensive investigation into the leaching kinetics of copper from bulk chalcopyrite concentrate in nitrous-sulfuric acid with an emphasis on the roles of temperature, initial nitrite concentration, and particle size, which have not been sufficiently studied from a theoretical or practical point of view.

Material and Methods

Materials

Experiments were implemented with bulk concentrate obtained from the Küre Copper Concentrator Plant, Eti Bakır A.Ş., Kastamonu-Turkey, where $\text{CuFeS}_2\text{-ZnS-FeS}_2$ complex ore is treated. The chemical and mineralogical compositions of the “as-received” bulk concentrate are presented in Table 1.

Mineralogical analyses performed by scanning electron microscopy (SEM) coupled with energy dispersive spectroscopy (EDS) and X-ray diffraction of the bulk concentrate revealed that the sample contained mainly chalcopyrite with sphalerite, pyrite and small amounts of bornite. The primary gangue mineral was quartz. Chemical analyses by atomic absorption spectrometry (AAS) in conjunction with the mineralogical findings were used to determine mineralogical composition.

Table 1. Results of the chalcopyrite concentrate head sample assay

Chemical Analysis		Mineralogical Analysis	
Element	%	Mineral	%
Cu	11.21	CuFeS_2	28
Fe	32.36	Cu_3FeS_4	3
Zn	5.10	ZnS	8
S	36.8	FeS_2	51
Co	0.06	SiO_2	4
Pb	0.02	CaO	0.35
Ag (g/t)	27		

Experimental Procedure

Experiments were conducted using a Parr 1 L 4520 M model vertical reactor constructed from titanium and controlled to within ± 2 °C using a Parr 4843 model temperature controller. Typically, the vessel was charged with electrolyte containing NaNO_2 , H_2SO_4 and 5% w/v pulp density bulk chalcopyrite concentrate. Sodium nitrite immediately dissociated to produce nitrous acid in acid solution as described in Eq. 3. The experiments were initiated by introducing nitrite salt into the electrolyte at a concentration of 0.05–0.15 M. The system was then pressurized with oxygen on a continuous basis to maintain a total pressure of 6 atm. The temperature of the solution was varied over the range of 80–120 °C and the reaction sustained for 2 h. The initial sulfuric acid concentration was 1.0 M and the reaction was mixed well by stirring at 400 rpm by a magnetically driven twin impeller. Samples from each experiment were taken at the selected time intervals and analyzed using an atomic absorption spectrophotometer (Analytik Jena NovaA 300). XRD and SEM analyses were performed using a Rigaku Miniflex II diffractometer with Cu K α radiation and a JEOL JXA-733 Superprobe, respectively. The particle size (d_{80}) of the received

samples, determined from measurements on an HORIBA/Partica LA-950V2 Particle Size Analyzer, was 35 μm . Ultrafine milling of the as-received material to 15 μm was performed using a ball mill. The size of the product was confirmed by particle size analysis.

Results and Discussion

Effects of parameters

The influence of the concentration of nitrite on copper recovery was investigated using an electrolyte containing various initial sodium nitrite concentrations in the range of 0.05 M–0.15 M at 120 °C. The results are plotted in Fig. 1. Although the recovery-time curves overlapped during the first 15 min, the reaction rates were enhanced after the dissociation of nitrite into $\text{NO}_{2(\text{g})}$ and $\text{NO}_{(\text{g})}$ in acidic electrolyte. Additionally, the *in situ* regeneration of NO_x during the dissolution process minimized the need to add additional exogenous nitrite over the course of the reaction.

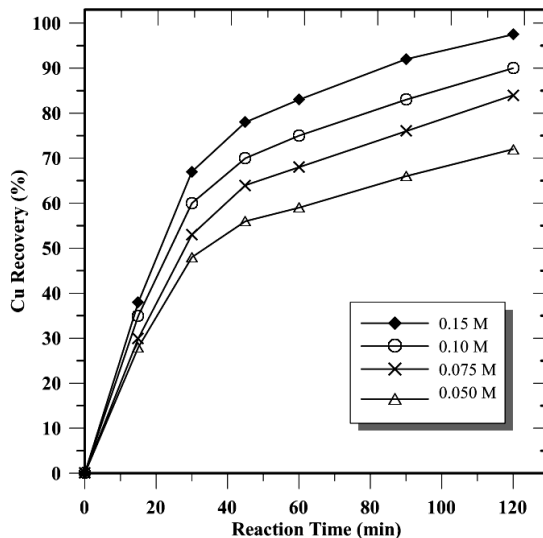


Fig. 1. Effect of the nitrite concentration on copper recovery. Initial electrolyte conditions: $\text{C}_{\text{H}_2\text{SO}_4} = 1 \text{ M}$, $d_{\text{mean}} = 15 \mu\text{m}$, $T = 120^\circ\text{C}$, $P_{\text{tot}} = 6 \text{ atm}$

The extraction of copper at various temperatures (80–120 °C) was implemented in the electrolyte containing 0.10 M NaNO_2 and 1 M H_2SO_4 as depicted in Fig. 2. Copper recovery was enhanced by increasing temperature; 90% extraction was obtained at 120 °C, whereas only 60% copper extraction was obtained at 80 °C within 2 h. This is likely due to slower dissolution kinetics as temperature decreases due to the increasing viscosity of molten sulfur (Papangelakis, 2005).

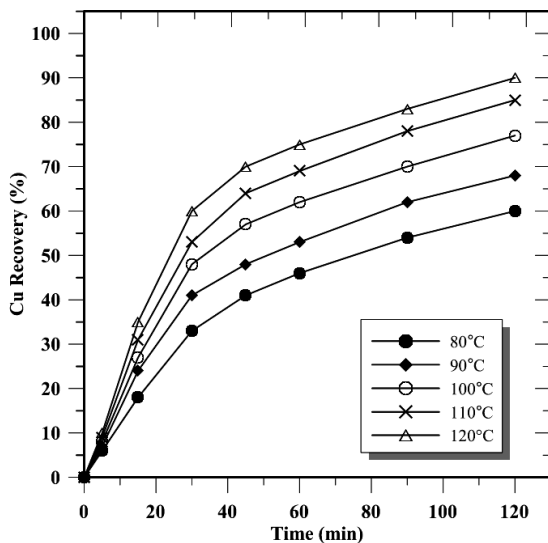


Fig. 2. Effect of the temperature on copper recovery. Initial electrolyte conditions:
 $C_{\text{NaNO}_2} = 0.10 \text{ M}$, $C_{\text{H}_2\text{SO}_4} = 1 \text{ M}$, $d_{\text{mean}} = 15 \mu\text{m}$, $P_{\text{tot}} = 6 \text{ atm}$

In this study, a set of grinding tests were performed to determine the effect of particle size on copper recovery. Tests were performed for three different particle sizes (35 μm , 25 μm , and 15 μm) at 120 °C under a total pressure of 6 atm. The results are illustrated in Fig. 3. Reducing the material size significantly increased copper recovery

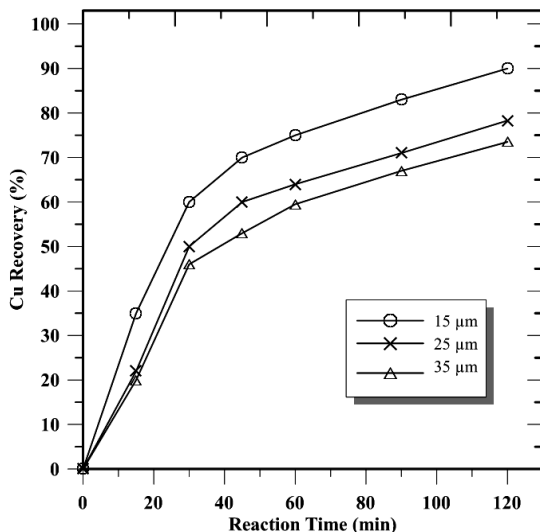


Fig. 3. Effect of the particle size of concentrate on copper recovery. Initial electrolyte conditions:
 $C_{\text{NaNO}_2} = 0.10 \text{ M}$, $C_{\text{H}_2\text{SO}_4} = 1 \text{ M}$, $T = 120^\circ\text{C}$, $P_{\text{tot}} = 6 \text{ atm}$

(from 70% to 90%). These findings revealed that this is a classic heterogeneous reaction system in which the larger surface area due to the smaller particle size has a beneficial effect. Similar behavior has been reported for the nitric-sulfuric acid system (Anderson et al., 1991). Researchers have explained that this type of dramatic improvement in conversion is usually indicative of a reaction controlled by diffusional effects. Less encapsulation of the particle in molten sulfur could be observed by grinding the material to increase its total surface area. Size reduction also enables more copper to be solubilized by generating more NO and NO₂ gas according to the reaction shown in Eq. 1.

Kinetic Analysis

A non-catalytic heterogeneous reaction model was conducted to evaluate the kinetic parameters and the rate-controlling step of the chalcopyrite dissolution in acidic nitrite solutions. The rate controlling step of the reaction between solid particles and electrolyte can be due to one of the following: external diffusion of the reactant through the boundary layer of the fluid surrounding the particle, reaction on the surface between the fluid reactant and the solid, or internal diffusion of the reactant through the reaction products on the particle (Levenspiel, 1972; Mazet, 1992). Three shrinking core models were tested to better understand the leaching mechanism of chalcopyrite in acidic nitrite solutions (Aydogan et al., 2005; Levenspiel, 1972):

$$X = \frac{3b'k_g C_A}{\rho_B r_o} t \quad (\text{film diffusion control}) \quad (8)$$

$$1 - (1 - X)^{\frac{1}{3}} = \frac{b'k_r C_A}{\rho_B r_o} t \quad (\text{surface chemical reaction control}) \quad (9)$$

$$1 - \frac{2}{3}X - (1 - X)^{\frac{2}{3}} = \frac{2b'k_d D_e C_A}{\rho_B r_o^2} t \quad (\text{ash diffusion control}). \quad (10)$$

Rate constant values and their correlation coefficients in these models are presented in Table 2. Detailed analysis of the data revealed that diffusion through the product layer is the limiting step in the dissolution reaction. Therefore, subsequent linearization of the values obtained from temperature-, particle size- and nitrite concentration-related experiments was performed by the model equation $1 - 2/3X - (1 - X)^{2/3} = k_d t$. The model plots for nitrous acid concentration and temperature are given in Fig. 4 and Fig. 5. Apparent rate constants k_1 and k_2 were found from the slopes of the straight lines.

Table 2. Apparent rate constants and correlation coefficients for shrinking core model

	Surface chemical reaction $1 - (1 - X)^{1/3}$		Diffusion through product layer $1 - 2/3X - (1 - X)^{2/3}$	
	k_r (min ⁻¹)	R ²	k_d (min ⁻¹)	R ²
Concentration (M)				
0.05	0.0035	0.7019	0.008	0.9768
0.075	0.0044	0.8199	0.012	0.9840
0.10	0.0052	0.8238	0.016	0.9830
0.15	0.0066	0.9008	0.023	0.9902
Particle Size (mm)				
0.035	0.0035	0.8203	0.0008	0.9812
0.025	0.0039	0.8014	0.0010	0.9798
0.015	0.0052	0.8238	0.0016	0.9830
Temperature (K)				
353	0.0026	0.8411	0.0005	0.9939
363	0.0031	0.8031	0.0007	0.9928
373	0.0038	0.8032	0.0010	0.9860
383	0.0045	0.8377	0.0013	0.9890
393	0.0052	0.8238	0.0016	0.9830

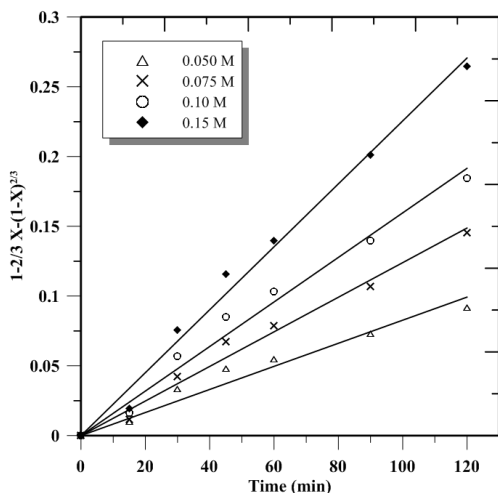


Fig. 4. Plot of the shrinking core model for the effect of nitrite concentration on the reaction rate

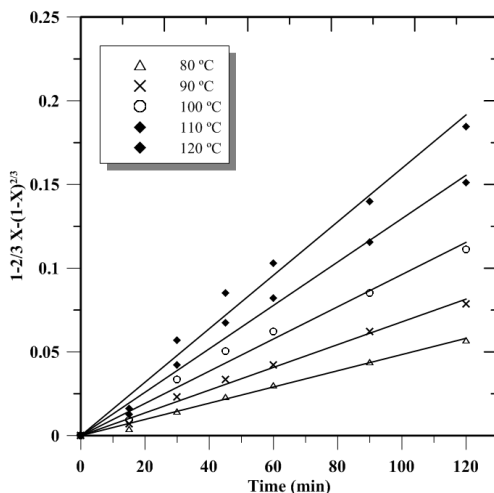


Fig. 5. Plot of the shrinking core model for the the effect of temperature on the reaction rate

When temperature is selected as a variable factor, activation energy of the leaching reaction can be calculated by the expression below. The value of activation energy, E_a , and the pre-exponential factor, A , are estimated to be $34.06 \text{ kJ} \cdot \text{mol}^{-1}$ and 56.26 min^{-1} , respectively, from Fig. 6.

$$k_d = Ae^{\frac{-E_a}{RT}} \quad (11)$$

Typically, low activation energy ($<20 \text{ kJ}\cdot\text{mol}^{-1}$) confirms the presence of a diffusion-controlled system (Jackson, 1982). However, Baba et al. (2009) and Olanipekun (1999) have claimed that some diffusion-controlled reactions have unexpectedly high activation energies (Tsuchida et al., 1982; Baba and Adekola, 2010).

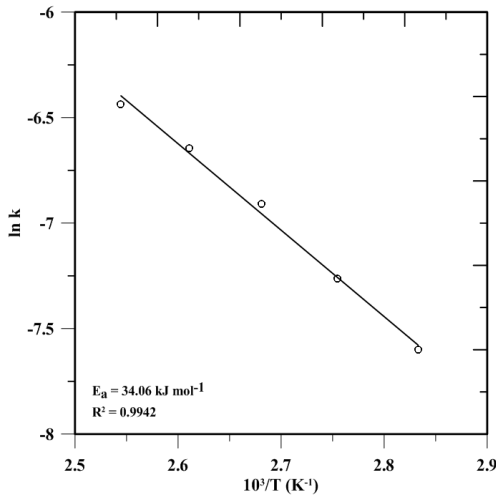


Fig. 6. Plot of parabolic leaching rate constants vs. inverse of temperature (Arrhenius plot)

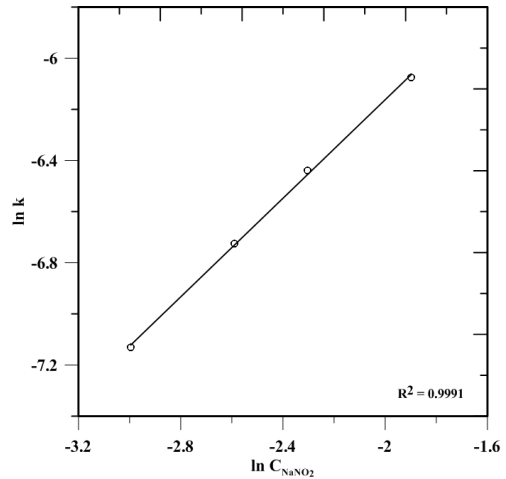


Fig. 7. Determination of reaction order for chalcopyrite dissolution in acidic nitrite electrolyte

It should be noted that in some instances the rate controlling mechanism of the heterogeneous dissolution process can be predicted better from the kinetic equations rather than the activation energy. Aydogan et al. (2007) demonstrated that a diffusion-controlled process is slightly dependent on temperature, while the chemically controlled process is strongly dependent on temperature. Researchers found the activation energy to be $42.26 \text{ kJ}\cdot\text{mol}^{-1}$ in the range of $27\text{--}60 \text{ }^\circ\text{C}$ for the Turkish galena concentrate in 0.5 M HNO_3 and $1.0 \text{ M H}_2\text{O}_2$ electrolyte. Based on discussions in literature and the correlation coefficients given in Table 2, it was concluded that the dissolution mechanism is controlled by diffusion through the product layer.

The effect of nitrite concentration on the reaction rate was investigated from a plot of $\ln k_1$ vs. $\ln C_{\text{HNO}_2}$. The slope of the plot (Fig. 7) reveals that the reaction order is 0.96 with respect to nitrous acid. Aydogan et al. (2007) obtained a similar reaction order for leaching in nitric acid and hydrogen peroxide.

To elucidate the rate-determining step for this study, kinetic curves (presented in Fig. 3) were linearized by means of Eq. 10. Generally, if diffusion controls the reaction rate, there is a linear relation between the apparent rate constant, k_3 , and the

reciprocal of the square of particle radius, $1/r_0^2$. A linear dependence between k and $1/r_0^2$ values is observed in Fig. 8 which confirms that diffusion through the product layer is the rate-limiting step for this process.

A semi-empirical model describing the effects of the reaction parameters on the rate constant of the reaction can be written as follows:

$$k_d = k_o C^a \gamma_o^b e^{\frac{-E_a}{RT}} \quad (12)$$

Combining Eqs. (11) and (12), the following equation is obtained:

$$1 - \frac{2}{3} X - (1 - X)^{\frac{2}{3}} = k_o C^a \gamma_o^b e^{\frac{-E_a}{RT}} t \quad (13)$$

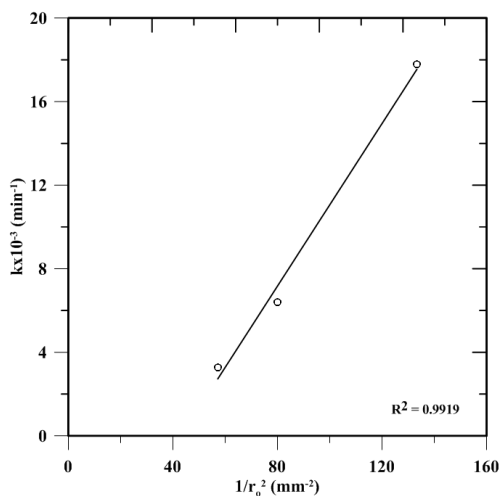


Fig. 8. Dependence of rate constant on particle size radius

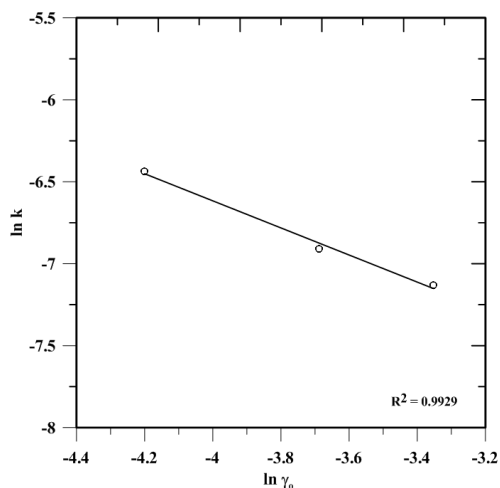


Fig. 9. Determination of constant b in semi-empirical model equation

The constant a was estimated to be 0.96 from the slope of the line in Fig. 7. The order of the initial particle radius, b , was found to be -0.83 from the $\ln k$ vs. $\ln \gamma_o$ plot in Fig. 9. Substituting the values of a , b , and E_a into Eq. 13, the value of k_o is calculated to be $56.53 \cdot 10^{-4}$. Hence, the proposed model equation to describe chalcopyrite leaching in acidic nitrite electrolyte is described as follows:

$$1 - \frac{2}{3} X - (1 - X)^{\frac{2}{3}} = 56.53 \cdot 10^{-4} C_{\text{NaNO}_2}^{0.96} \gamma_o^{-0.83} e^{\frac{-4096.7}{T}} t \quad (14)$$

The agreement between experimental results and theoretical calculations (Eq. 13) was tested (Fig. 10). The correlation is reasonably satisfactory and suggests that Eq. 14 can be used to predict the leaching rate for the ranges of particle size, acid concentrations and temperatures used in this study.

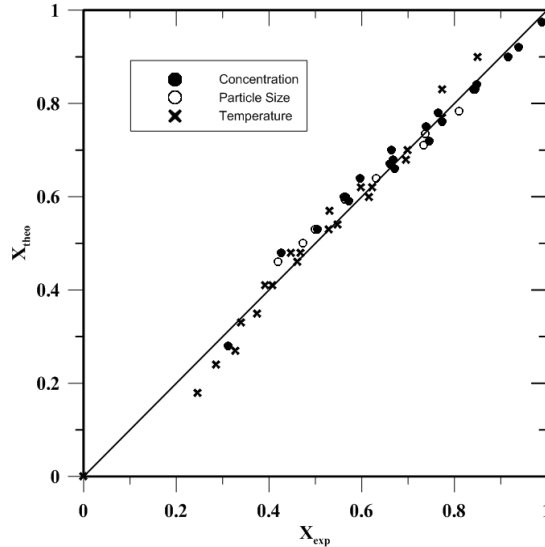


Fig. 10. Correlation of the observed and estimated values of reaction rate constants

Characterization of Solid Residue

Chemical (AAS) and physical analyses (SEM and XRD) were performed to explain the behavior of the sulfide concentrate during the leaching of chalcopyrite with nitrite. Chemical analyses of the solid residue indicated that during the first hour most of the pyrite and sphalerite were leached. The dissolution of chalcopyrite, pyrite and sphalerite over time can also be observed from the XRD analyses of the head sample (Fig. 11a) and residues obtained after 2 h (Fig. 11b). SEM micrographs and X-ray diffraction spectra revealed non-conductive sulfur layers and quartz to be the major components. The micrographs and spectra of product layers formed on the particle surface are presented in Fig. 11 and Fig. 12 for the optimum chalcopyrite dissolution conditions: 0.10 M NaNO_2 , 1 M H_2SO_4 at 393 K. As the sulfur layer builds, it impedes the reaction so that diffusion through the product layer is a major reaction barrier. However, it is clear that the formation of elemental sulfur does not hinder the reaction within two hours at higher temperatures.

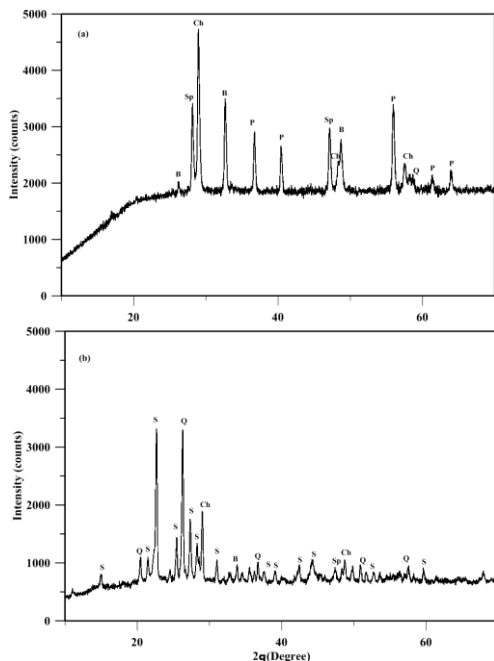


Fig. 11. XRD patterns of (a) bulk concentrate, (b) solid residue at 120 °C after 2 h. In the figure: Ch = chalcopyrite, P = pyrite, Sp = sphalerite, B = Bornite, S = Sulfur, Q = Quartz

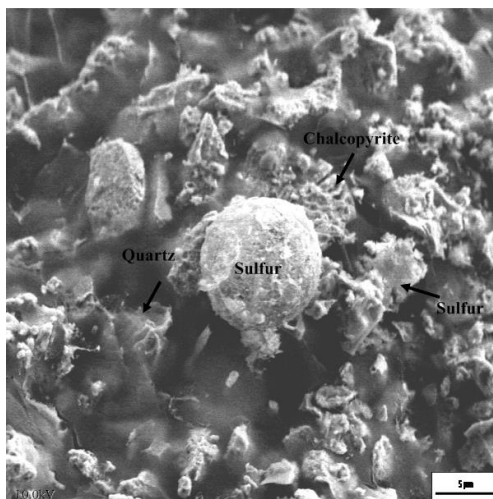


Fig. 12. SEM micrographs of solid residue at 120 °C after 2 h at magnification 1500×

Conclusions

The kinetics of dissolution of bulk chalcopyrite concentrate in acidic nitrite electrolyte have been investigated in the temperature range of 80–120 °C. On the basis of the results provided by the experiments, the following can be concluded.

- An increase in nitrite concentration from 0.05 M to 0.15 M caused a significant increase in leaching from 72% to 98% over the course of 120 min.
- The dissociation products of nitrous acid, NO and NO₂, were realized during the withdrawn of the liquid samples. The rapid extraction of copper from the complex mineral matrix with such small amounts of nitrite revealed that NO reacted with oxygen to regenerate HNO₂. Accordingly, nitrous acid could follow a second reaction path by reacting with a nitrate ion, reducing the nitrate to form NO₂ and water. The key intermediate product of the reaction, nitrous acid, serves both to reduce nitrate and to oxidize NO. Overall, more nitrous acid is produced than consumed.

- The leaching of chalcopyrite concentrate with a particle size of 15 μm in nitrite-containing solutions had a high reaction rate. Over 98% of the copper was dissolved in 120 min at 120 $^{\circ}\text{C}$. Pyrite and sphalerite were completely dissolved within 120 min, as confirmed with X-ray diffraction measurements.
- The extraction of copper obeyed a shrinking core model with a diffusion-controlled mechanism in which the diffusion through the product layer was the rate-limiting step. The value of activation energy was calculated to be 34.06 $\text{kJ}\cdot\text{mol}^{-1}$ and the reaction order with respect to nitrite concentration was 0.96. This is consistent with the following semi-empirical relation:

$$1 - \frac{2}{3}X - (1 - X)^{\frac{2}{3}} = 56.53 \times 10^{-4} C_{\text{NaNO}_2}^{0.96} \gamma_o^{-0.83} e^{\frac{-4096.7}{T} t}.$$

- The results of the post-leaching process indicated the presence of a residue containing elemental sulfur and quartz as its major constituents. This was confirmed by both X-ray diffraction spectra and SEM micrographs.

Acknowledgement

The author wish to express appreciation to Eti Bakir A.S. for supplying the Küre chalcopyrite concentrate. Dr. Hatice Yilmaz is also acknowledged for the acquisition of XRD and SEM data. Appreciation is extended to Dr. Erkan Güler for his invaluable comments.

References

- ACKERMAN J.B., ANDERSON C.G., NORDWICK S.M., KRYS L.E., 1993. *Hydrometallurgy at the Sunshine Mine metallurgical complex*. In: Hiskey B., Wadsworth M. (Eds.), *Proceedings of AIME Meeting, Hydrometallurgy-Fundamentals, Technology and Innovations*, Littleton, Colorado, 477–498.
- ANDERSON C.G., KRYS, L.E., HARRISON, K.D., 1992. *Treatment of metal bearing mineral material*. Chemical Abstract, US Patent No. 5096486.
- ANDERSON C.G., HARRISON K.D., KRYS L.E., 1993. *Process Integration of sodium nitrite oxidation and fine grinding in refractory precious metal concentrate pressure leaching*. In: Mishra R.K. (Ed.), *Precious Metals*, Allentown, Pennsylvania, 19–45.
- ANDERSON C.G., HARRISON K.D., KRYS L.E., 1996. *Theoretical considerations of sodium nitrite oxidation and fine grinding in refractory precious metals concentrate pressure leaching*. *Minerals and Metallurgical Processing*, AIME-SME, 4.
- ANDERSON C.G., 2003, *Treatment of copper ores and concentrates with industrial nitrogen species catalyzed pressure leaching and non-cyanide precious metals recovery*. *J. Metals*, 55, 32–36.
- AYDOGAN S., ARAS A., CAMBAZOGLU M., 2005, *Dissolution kinetics of sphalerite in acidic ferric chloride leaching*. *Chem. Eng. J.*, 114, 67–72.
- AYDOGAN S., ARAS A., UCAR G., ERDEMOGLU M., 2007, *Dissolution kinetics of galena in acetic acid solutions with hydrogen peroxide*. *Hydrometallurgy*, 89, 189–195.
- AWAD H.H., STANBURY D.M., 1993, *Autooxidation of NO in aqueous solution*, *Int. J. Chem. Kin.*, 25, 375–381.
- BABA A.A., ADEKOLA F.A., BALE, R.B., 2009, *Study of dissolution kinetics of a Nigerian cassiterite ore by hydrochloric acid*. *Sci. Focus*, 14 (2), 198–207.

- BABA A.A., ADEKOLA F.A., 2010, *Hydrometallurgical processing of a Nigerian sphalerite in hydrochloric acid: characterization and dissolution kinetics*. Hydrometallurgy, 101 (1–2), 69–75.
- BALDWIN S.A., VAN WEERT G.V., 1996, *On the catalysis of ferrous sulphate oxidation in autoclaves by nitrates and nitrites*. Hydrometallurgy, 42, 209–219.
- BEATTIE M.J.V., RANDSEPP R., ISMAY A., 1989. *Arseno/Redox Process for Refractory Gold Ores*. in: Dobby, G.S., Rao, S.R. (Eds.), Intern. Symp. Processing Complex Ores, Pergamon, Oxford, 431–439.
- BRENNECKE H.M., BERGMANN O., ELLEFSON R.R., DAVIES D.S., LEUDERS R.E., SPITZ R.A., 1981, *Nitric-sulfuric leach process for recovery of copper from concentrate*. J. Min. Eng., 12, 20–24.
- CALDON F., 1978. *Treatment of metal bearing mineral material*. Chemical Abstract, US Patent No. 4084961.
- CORRANS I.J., ANGOVE J.E., 1993. *Activation of a Mineral Species*, Chemical Abstract, US Patent No 232491.
- DIXON D.G., MAYNE D.D., BAXTER K.G., 2008, *GalvanoxTM – a novel galvanically assisted atmospheric leaching technology for copper concentrate*. Canadian Metallurgical Quarterly, 47, 327–336.
- DREISINGER D., ABED N.A., 2002, *Fundamental study of the reductive leaching of chalcopryrite using metallic iron part I: Kinetic analysis*. Hydrometallurgy, 66, 37.
- DREISINGER D., RICHMOND G., HESS F., LANCASTER T., 2002. *The competitive position of the Mt. Gordon copper process in the copper industry*. ALTA 2002 Copper 7 Forum. ALTA Metallurgical Services, Melbourne, 14.
- DREISINGER D.B., STEYL J.D.T., SOLE K.C., GNOINSKI J., DEMPSEY P., 2003. *The Anglo American Corporation/University of British Columbia (AAC/UBC) chalcopryrite process: An integrated pilot–plant evaluation*. in: Rivieros, A., Dixon, D.G., Dreisinger, D.B., Menacho, J. (Eds.), Copper 2003-Cobre 2003, Vol VI, Hydrometallurgy of copper, Montreal, 223–237.
- DUTRIZAC J.E., MACDONALD R.J.C., INGRAHAM T.R., 1969, *The kinetics of dissolution of synthetic chalcopryrite in aqueous acidic ferric sulphate solutions*. AIME, 245, 955–959.
- FERRON C.J., FLEMING C.A., O’KAN P.T., DREISINGER D.B., 2001, *Application of the PLATSOL process for simultaneous dissolution of copper, nickel, gold, and PGMs from sulfide concentrates and autocatalysts*. Precious Metals, 129–157.
- GOK O.S., 2009. *On the role of low-concentration nitrite in oxidative-leaching with oxygen*, PhD Thesis, Colorado School of Mines, CO, USA.
- GOK O., ANDERSON C.G., 2013, *Dissolution of Low-Grade Chalcopryrite Concentrate in Acidified Nitrite Electrolyte*, Hydrometallurgy, DOI No: 10.1016/j.hydromet.2013.01.021.
- HACKL R.P., DREISIGER D.B., PETERS E., KING J.A., 1995, *Passivation of chalcopryrite during oxidative leaching in sulfate media*. Hydrometallurgy, 39, 25–48.
- HIRATO T., KINOSHITA M., AWAKURA Y., MAJIMA H., 1986, *The leaching of chalcopryrite with ferric chloride*. Metallurgical Transactions B, Process Metallurgy, 17, 19–28.
- HIROYOSHI N., MIKI H., HIRAJIMA T., TSUNEKAWA M.A., 2000, *Model for ferrous promoted chalcopryrite leaching*. Hydrometallurgy, 57, 31–38.
- JACKSON E., 1982, *Hydrometallurgical extraction and reclamation*. Chichester: Ellis Horwood Ltd., 46–47.
- JONES D.L., 1996. *CESL Copper Process*. Alta Copper Hydrometallurgy Forum, Brisbane, Australia, 24.
- KAMEOKA Y., PIGFORD R.L., 1977, *Adsorption of nitrogen dioxide into water, sulfuric acid, sodium hydroxide, and alkaline sodium sulfite aqueous solutions*. Ind. Eng. Chem. Fundam., 16, 163–169.

- KOFLUK D.K., COLLINS M.J., 1998. *Hydrometallurgical process for the extraction of copper from sulphidic concentrates*. Chemical Abstract, US Patent No. 5730776.
- LEVENSPIEL O., 1972. *Chemical Reaction Engineering*, 2nd ed., John Wiley & Sons, New York, 361–371.
- LINGE H.G., 1976. *A study of chalcopyrite dissolution in acidic ferric nitrate by potentiometric titration*. Hydrometallurgy, 2, 51–64.
- MARKOVITZ G.Y., SCHWARTZ S.E., NEWMAN L., 1981. *Hydrolysis equilibrium of dinitrogen trioxide in dilute acid solution*. Inorg. Chem., 20, 445–450.
- MARSDEN J.O., BREWER R.E., HAZEN N., 2003. *Copper concentrate leaching developments by Phelps Dodge corporation*, Young, C.A. (Ed.), Electrometallurgy and Environmental Hydrometallurgy, TMS, PA, 1429–1446.
- MAZET N., 1992. *Modeling of gas–solid reactions. 1. Nonporous solids*, Int Chem Eng, 32, 271–284.
- MILLER J.D., PORTILLO H.Q., 1979. *Silver catalysis in ferric sulfate leaching of chalcopyrite*. In: Laskowski, J. (Ed.), XIII International Min. Proc. Conf., Elsevier, Amsterdam, 851–901.
- MUNOZ P.B., MILLER J.D., WADSWORTH M.E., 1979. *Reaction mechanism for the acid ferric sulfate leaching of chalcopyrite*. Metallurgical Transactions B: Process Metallurgy, 10B, 149–158.
- OLANIPEKUN E.O., 1999. *A kinetics study of the leaching of a Nigerian ilmenite ore by hydrochloric acid*. Hydrometallurgy, 53, 1–10.
- PAPANGELAKIS V., 2005. *Surface chemistry of molten sulfur on nickel sulfides. Pressure Oxidation-Modelling, Reactor Design, and Processes*. Presentation to CSIRO Minerals Symposium, Perth, Australia, 14th April,
- PARK J.Y., LEE Y.N., 1988. *Solubility and decomposition kinetics of nitrous acid in aqueous solution*, J. Phys. Chem., 92, 6294–6302.
- STANLEY R.W., SUBRAMANIAN K.N., 1977. *Recovering copper from concentrates with insoluble sulfate forming leach*. Chemical Abstract, US Patent No. 4039406.
- TSUCHIDA T., NARRITA E., TAKUECHI H., ADACHI M., OKABE T., 1982. *Manufacture of high pure titanium (IV) oxide by the chloride process. I: Kinetic study on leaching of ilmenite ore in concentrated hydrochloric acid solution*. Bull. Chem. Soc. Jpn., 55 (6), 1934–1938 (In: Olanipekun, E.O., 1999. Hydrometallurgy 53, 1–10).
- VAN WEERT G., FAIR K.J., SCHNEIDER J.C., 1986. *The NITROX process for treating gold bearing arsenopyrite*. In: 116th Annual TMS/AIME Meeting, CO.
- WANG S., 2005. *Copper leaching from chalcopyrite concentrates*. J. of Metals, 57, 48–51.

Nomenclature

a	order of sodium nitrite concentration	k_0	constant of semi-empirical equation
A	pre-exponential factor (min^{-1})	k_r	rate constant of surface reaction
b	order of particle diameter	K	equilibrium constant
b^1	stoichiometric coefficient	r_0	radius of unreacted core (mm)
C_A	bulk concentration of the fluid ($\text{mol}\cdot\text{m}^{-3}$)	R	universal gas constant ($\text{J}\cdot\text{mol}^{-1}\cdot\text{K}^{-1}$)
C_{NaNO_2}	initial concentration of sodium nitrite (M)	t	reaction time (min)
D_B	effective diffusion coefficient ($\text{m}^2\cdot\text{s}^{-1}$)	T	temperature (K)
E_A	activation energy ($\text{kJ}\cdot\text{mol}^{-1}$)	X	fractional conversion
k_d	apparent reaction rate constant (min^{-1})	ρ_B	molar density of B in the solid ($\text{mol}\cdot\text{m}^{-3}$)
k_g	rate constant of film diffusion	γ_0	initial size of solid particle (mm)

ISSN 1643-1049

Physicochemical Problems of Mineral Processing, 50(1), January 1, 2014